Janice Aldrich-Wright

Editor

Metallo-
intercalators

Synthesis and Techniques to Probe their Interactions with Biomolecules

SpringerWienNewYork

Janice Aldrich-Wright

Editor

Metallointercalators

Synthesis and Techniques
to Probe Their Interactions
with Biomolecules

SpringerWienNewYork

Editor
Janice Aldrich-Wright
University of Western Sydney
School of Biomedical & Health Sciences
Penrith South DC New South Wales
Sydney
Australia
J.Aldrich-Wright@uws.edu.au

To my husband James and my children Elisé and Nathan

Preface

This book provides an introduction for students and interested researchers who wish to explore the biological interactions of metallointercalators. The emphasis is on what techniques can be used to synthesise, characterise and assess the biological interactions of these metal complexes. There are many research articles in the literature but what was lacking was a book that brought all of this basic information together. I hope that this book provides a good starting point for your research journey with metallointercalators.

The book is composed of four parts where we introduce some of the biomacromolecules that metallointercalators have been reported to target; explore the synthesis and characterisation of some examples; use several biophysical techniques to probe the interactions with biomacromolecules and lastly use *in vitro* and *in vivo* assays to assess the biological activity of metallointercalators.

Sydney, Australia   J. Aldrich-Wright

Acknowledgements

Contents

Contributors

Janice Aldrich-Wright University of Western Sydney, School of Biomedical & Health Sciences, Penrith South DC New South Wales, Sydney, Australia, J.Aldrich-Wright@uws.edu.au

Jennifer L. Beck School of Chemistry, University of Wollongong, Wollongong, NSW, Australia

Patrick J. Bednarski Department of Pharmaceutical and Medicinal Chemistry, Institute of Pharmacy, University of Greifswald, Greifswald, Germany, bednarsk@pharmazie.uni-greifswald.de

Albert Bolhuis Department of Pharmacy and Pharmacology, University of Bath, Bath, UK, a.bolhuis@bath.ac.uk

Florence Bouyer Equipe Avenir, INSERM, UMR 866, University of Burgundy, Dijon, France, florence.bouyer@u-bourgogne.fr

Damian P. Buck School of Physical, Environmental and Mathematical Sciences, University College, University of New South Wales, Australian Defence Force Academy, Canberra, ACT 2600, Australia

Magdalena Buczkowska Department of Pharmaceutical and Medicinal Chemistry, Institute of Pharmacy, University of Greifswald, Greifswald, Germany

Bruno Chauffert Equipe Avenir, INSERM, UMR 866, University of Burgundy, Dijon, France; GF Leclerc Regional Anticancer Centre, Dijon, France

J. Grant Collins School of Physical, Environmental and Mathematical Sciences, University College, University of New South Wales, Australian Defence Force Academy, Canberra, ACT 2600, Australia, g.collins@adfa.edu.au

Carolyn T. Dillon School of Chemistry, University of Wollongong, Wollongong, NSW, Australia, carolynd@uow.edu.au

Dianne M. Fisher Centre for Heavy Metals Research, School of Chemistry, The University of Sydney, Sydney, NSW, Australia

Nichola C. Garbett Biophysical Core Facility, James Graham Brown Cancer Center, University of Louisville, Louisville, KY, USA, nichola.garbett@louisville.edu

K. Benjamin Garbutcheon-Singh Nanoscale Organisation and Dynamics Group, School of Biomedical and Health Sciences, College of Health and Science, University of Western Sydney, Sydney, NSW, Australia

David Geny School of Natural Sciences, College of Health and Science, University of Western Sydney, Penrith South, NSW, Australia

Maxine P. Grant Nanoscale Organisation and Dynamics Group, School of Biomedical and Health Sciences, College of Health and Science, University of Western Sydney, Sydney, NSW, Australia

Renate Grünert Department of Pharmaceutical and Medicinal Chemistry, Institute of Pharmacy, University of Greifswald, Greifswald, Germany

Christopher Hammang School of Natural Sciences, College of Health and Science, University of Western Sydney, Penrith South, NSW, Australia

Mareike Hänsch Department of Pharmaceutical and Medicinal Chemistry, Institute of Pharmacy, University of Greifswald, Greifswald, Germany

Benjamin W. J. Harper Nanoscale Organisation and Dynamics Group, School of Biomedical and Health Sciences, College of Health and Science, University of Western Sydney, Sydney, NSW, Australia

Vincent J. Higgins School of Biomedical and Health Sciences, College of Health and Science, University of Western Sydney, Penrith South, NSW, Australia

Sybil Grünert Department of Pharmaceutical and Medicinal Chemistry, Institute of Pharmacy, University of Greifswald, Greifswald, Germany

Anwen M. Krause-Heuer Nanoscale Organisation and Dynamics Group, School of Biomedical and Health Sciences, College of Health and Science, University of Western Sydney, Sydney, NSW, Australia

Per Lincoln Department of Chemistry and Bioscience Chalmers, University of Technology, Gothenburg, Sweden

Victoria Lyons School of Biomedical and Health Sciences, College of Health and Science, University of Western Sydney, Penrith South, NSW, Australia

Madhura Manohar Nanoscale Organisation and Dynamics Group, School of Biomedical and Health Sciences, College of Health and Science, University of Western Sydney, Sydney, NSW, Australia

Johnny Moretto Equipe Avenir, INSERM, UMR 866, University of Burgundy, Dijon, France; Department of Hematology, Dijon University Hospital, Dijon, France

Simon Myers Nanoscale Organisation and Dynamics Group, School of Biomedical and Health Sciences, College of Health and Science, University of Western Sydney, Sydney, NSW, Australia

Nikita Orkey School of Biomedical and Health Sciences, College of Health and Science, University of Western Sydney, Penrith South, NSW, Australia

William S. Price Nanoscale Organisation and Dynamics Group, College of Health and Science, University of Western Sydney, Sydney, NSW 1797, Australia, w.price@uws.edu.au

Stephen F. Ralph School of Chemistry, University of Wollongong, Wollongong, NSW, Australia, sralph@uow.edu.au

Adair D. Richards Molecular Organisation and Assembly in Cells DTC, University of Warwick, Coventry, UK

Alison Rodger MOAC Doctoral Training Centre, University of Warwick, Coventry, UK, a.rodger@warwick.ac.uk

Anya Salih School of Natural Sciences, College of Health and Science, University of Western Sydney, Penrith South, NSW, Australia, a.salih@uws.edu.au

Jihan Talib School of Chemistry, University of Wollongong, Wollongong, NSW, Australia

Allan M. Torres Nanoscale Organisation and Dynamics Group, School of Biomedical and Health Sciences, College of Health and Science, University of Western Sydney, Sydney, NSW, Australia, A.Torres@uws.edu.au

Thitima Urathamakul School of Chemistry, University of Wollongong, Wollongong, NSW, Australia

Marcelis van Holst Nanoscale Organisation and Dynamics Group, School of Biomedical and Health Sciences, College of Health and Science, University of Western Sydney, Sydney, NSW, Australia

Shaoyu Wang School of Biomedical and Health Sciences, College of Health and Science, University of Western Sydney, Penrith South, NSW, Australia

Aron Westendorf Department of Pharmaceutical and Medicinal Chemistry, Institute of Pharmacy, University of Greifswald, Greifswald, Germany

Paul Wormell School of Natural Sciences, College of Health and Science, University of Western Sydney, Penrith South, NSW, Australia

Elise P. Wright School of Medicine, College of Health and Science, University of Western Sydney, Penrith South, NSW, Australia, E.Wright@uws.edu.au

Gang Zheng Nanoscale Organisation and Dynamics Group, College of Health and Science, University of Western Sydney, Sydney, NSW 1797, Australia

Abbreviations and Acronyms

Hoechst 33258	(2′-[4-Hydroxyphenyl]-5-[4-methyl-1-piperazinyl]-2,5′-bi-1H-benzimidazole trihydrochloride pentahydrate
BPG	(Bis(2-pyridylmethyl)amino)acetate
BENA435	(N-(2,8-Dimethoxy-12-methyl-dibenzo[c,h][1,5]naphthyridin-6-yl)-N,N-dimethyl-propane-1,3 diamine)
RR4M	[(4-Methyl-1,10-phenanthroline)(1R,2R-diaminocyclohex-ane)platinum(II)]$^{2+}$
56MERR	[(5,6-Dimethyl-1,10-phenanthroline)(1R,2R-diaminocyclo-hexane)platinum(II)]$^{2+}$
56MESS	[(5,6-Dimethyl-1,10-phenanthroline)(1S,2S-diaminocyclohex-ane)platinum(II)]$^{2+}$
56MEEN	[(5,6-Dimethyl-1,10-phenanthroline)(ethylenediamine)plati-num(II)]$^{2+}$
hpip	1,4-Diazacycloheptane
hnpip	1-(1H-Imidazo[4,5-f]-1,10-phenanthrolin-2-yl)naphthalen-2-ol
phen	1,10-Phenanthroline
phendo	1,10-Phenanthroline-5,6-dione
phehat	1,10-Phenanthrolino[5,6-b]1,4,5,8,9,12-hexaazatriphenylene
bfed	1,2-Bis(4-fluorophenyl)-1,2-ethylenediamine
dach	1,2-Diaminocyclohexane
en	1,2-Diaminoethane
DMH	1,2-Dimethyl-hydrazine
dpen	1,2-Diphenylethanediamine
PTA	1,3,5-Triaza-7-phosphatricyclo[3.3.1.1]decane
RAPTA	1,3,5-Triaza-7-phosphatricyclo[3.3.1.1]-decane
tmcp	1,3-Diamino-1,2,2-trimethylcyclopentane
1,3-pn	1,3-Diaminopropane
HAT	1,4,5,8,9,12-Hexaazatriphenylene
12S4	1,4,7,10-Tetrathiatetradecane
1,4-bn	1,4-Diaminobutane
COD	1,5-Cyclooctadiene

(AO(CH$_2$)$_6$en)	10-(6-(2-Aminoethylamino)hexyl)-3,6-bis(dimethylamino) acridinium
11,11′-didppz	11,11′-Bis(dipyrido[3,2-a:2′3′-c]phenazinyl
appo	11-Aminopteridino[6,7-f][1,10]phenanthrolin-13(12h)-one
IP	1H-Imidazo[4,5-f]-1,10-phenanthroline
MeIm	1-Methylimidazole
R,R-dach	1R,2R-Diaminocyclohexane
oxaliplatin	1*R*,2*R*-Diaminocyclohexane oxalatoplatinum(II)
POC-Nmet	2-(2-((6-Chloronaphthalen-1-yl)(methyl)amino)ethylthio)-N-(1,10-phenanthrolin-5-yl)acetamide
mopip	2-(2-Methoxyphenyl)imidazo[4,5-f][1,10]-phenanthroline
dptap	2-(2-Pyridylimino)-2h-1,2,4-thia-diazolo [2,3-a] pyridine
mhpip	2-(3-Methoxy-4-hydroxyphenyl)imidazo[4,5-f]1,10-phenanthroline
BPIP	2-(4′-Biphenyl)imidazo[4,5-f][1,10]phenanthroline
Hoechst 33342	2′-(4′-Ethoxyphenyl)-5-(4-methylpiperazin-1-yl)-2,5′-bis-1H-benzimidazole trihydrochloride trihydrate
pmip	2-(4-Methylphenyl)imidazo[4,5-f]1,10-phenanthroline
o-npip	2-(4-Nitrophenyl)imidazo[4,5-f]-1,10-phenanthroline
mcmip	2-(6-Methyl-3-chromonyl)imidazo[4,5-f][1,10]-phenanthroline
bdip	2-(Benzo[d][1,3]dioxol-4-yl)-1H-imidazo[4,5-f]-1,10-phenanthroline
tap	2-(m-Tolylazo)pyridine
azpy	2-(Phenylazo)pyridine
PYNI	2-(Pyridin-2-yl)-2,9a-dihydro-1H-naphtho[2,3-d]imidazole
pyip	2-(Pyridin-3-yl-1h-imidazo [4,5-f][1,10]phenanthroline
terpy	2,2′:6′,2″-Terpyridine
bmp	2,2′-Bipyrimidine
btb	2,2′-*Bis*(1,2,4-triazin-3-yl)-4,4′-bipyridine
bdapb	2,2′-*Bis*(1,2,4-triazino[5,6-f]acenaphthylen-3-yl)-4,4′-bipyridine
bdptb	2,2′-*Bis*(5,6-biphenyl-1,2,4-triazin-3-yl)-4,4′-bipyridine
bpy	2,2′-Bipyridine
dipy	2,2′-Dipyridylamine
XTT	2,3-*Bis*(2-methoxy-4-nitro-5-sulfophenyl)-5[(phenylamino)carbonyl]-2H-tetrazolium hydroxide
2,3-bn	2,3-Butanediamine
2,9-Me$_2$phen	2,9-Dimethyl-1,10-phenanthroline
IC$_{20}$	20% Inhibitory Concentration
HET	2-Hydroxyethane-thiolato
AET	2-Mercapoethylamine
pip	2-Phenylimidazo[4,5-f][1,10]phenanthroline
PAIDH	2-Pyridyl-1h-anthra[1,2-d]imidazole-6,11-dione
2*R*,3*R*-Bn	2*R*,3*R*-Diaminobutane

R,R-Me$_2$-trien	2R,9R-Diamino-4,7-diazadecane
2S,3S-Bn	2S,3S-Diaminobutane
MTT	3-(4,5-Dimethylthiazol-2-yl)-2,5-diphenyltetrazolium bromide
DiOC$_6$(3)	3,3′-Dihexyloxacarbocyanine iodide
TMP	3,4,7,8-Tetramethyl-1,10-phenanthroline
3,4,7,8-Me$_4$-phen	3,4,7,8-Tetramethyl-1,10-phenathroline
MPA	3-Mercaptopropionic acid
DSS	4,4-Dimethyl-4-silapentane-1-sulfonic acid
taptp	4,5,9,18-Tetraazaphenanthreno[9,10-b] triphenylene
flone	4,5-Diazafluorene-9-one
DAPI	4′,6-Diamidino-2-phenylindole
ppz	4,7-Phenanthroline[6,5-b]-pyrazine
terpyanth	4-Anthracene-2,2′:6′,2″-terpyridine-platinum(II)
4-Mephen	4-Methyl-1,10-phenanthroline
Pt-terpy	4-Picoline-2,2′:6′,2″-terpyridine-platinum(II)
aa-dUTP	5-(3-Aminoallyl)-2′-deoxyuridine-5′-triphosphate
tbz	5-(4-Methylpiperazin-1-yl)-2-[2′[2″-(4-hydroxy-3-methoxy-phenyl)-5″-benzimidazolyl]-5′-benzimidazolyl] benzimidazole
5,6-Me$_2$phen	5,6-Dimethyl-1,10-phenanthroline
GI$_{50}$	50% Growth inhibition
IC$_{50}$	50% Inhibitory concentration
5-NH$_2$-phen	5-Amino-1,10-phenanthroline
5-Cl-phen	5-Chloro-1,10-phenanthroline
mitatp	5-Methoxy-isatino[1,2-b]-1,4,8,9-tetraazatriphenylene
5-Me-phen	5-Methyl-1,10-phenanthroline
5-NO$_2$-phen	5-Nitro-1,10-phenanthroline
nitatp	5-Nitro-isatino[1,2-b]-1,4,8,9-tetraazatriphenylene
MDPZ	7,7′-Methylenedioxyphenyldipyrido[3,2-a:2′,3′-c]-phenazine
Fluorescein	9-(2-Carboxyphenyl)-6-hydroxy-3H-xanthen-3-one
phi	9,10-Phenanthrenequinone diimine
Fmoc	9-Fluorenylmethyl chloroformate
BDF1 mice	A cross between female C57BL/6 and male DBA/2
A$_{iso}$	Absorbance of an unoriented sample
AO	Acridine orange
A	Adenine
AO(CH$_2$)$_6$en	3,6-Bis(dimethylamino)-l0-[6-[(2-aminoethyl)amino]hexyl] acridinium chloride
dA	Adenine nucleotide (DNA monomer)
d(ACG)TP	Adenine, cytosine, guanidine nucleotide
APC	Adenomatous polyposis coli gene
APS	Advanced photon source
AMACR	Alpha-methylacyl CoA racemase
T$_R$	An appropriate reference temperature
ANOVA	Analysis of variance

A_L	Ancillary ligand
anthryl	Anthracene
AOI	Area of interest
Amber	Assisted model building and energy refinement
APDs	Avalanche photodiodes
B. subtilis	*Bacillus subtilis*
b	Bandwidth
BE	Binding energy
n	Binding stoichiometry
bip	Biphenyl
acphen	*Bis*(acetophenone)ethylenediamine
JM216	*Bis*-acetato-ammine-dichloro-cyclohexylamine platinum(IV) or Satraplatin
BFP	Blue fluorescent proteins
Met_b	Bound metallointercalator
BSA	Bovine serum albumin
BL	Bridging ligands
C2′-endo	C2′-endo deoxyribose ring puckering of B-DNA
C3′-endo	C3′-endo deoxyribose ring puckering of B-DNA
C. elegans	*Caenorhabditis elegans*
ct-DNA	Calf thymus DNA
CX[n]	calix[*n*]arenes
CPMG	Carr-Purcell-Meiboom-Gill
CICD	Caspases-independent cell death
δ_b	Chemical shifts of the resonances of the bound metal complex
δ_f	Chemical shifts of the resonances of the free metal complex
CD	Circular dichroism
carboplatin	*cis*-Diammine(1,1-cyclobutandicarboxylato)platinum(II)
cisplatin	*cis*-Diamminedichloroplatinum(II)
nedaplatin	*cis*-Diammineglycolatoplatinum(II)
cDNA	Complementary deoxyribonucleic acid
[*DL*]	Concentration of ligand–DNA complex
[DA]	Concentrations of the donor–acceptor
[D_{total}]	Concentrations of the total donor
CSLM	Confocal scanning laser microscopy
COSY	Correlation spectroscopy
CV	Crystal violet
CFP	Cyan fluorescent proteins
Cy3	Cyanine 3 dye
Cy5	Cyanine 5 dye
n-CD	Cyclodextrin
Cym	Cymene
C	Cytosine
°C	Degrees Celsius

Δ	Delta
DNA	Deoxyribonucleic acid
dTTP	Deoxythymidine triphosphate
S(θ)	Describes the orientational distribution of the long axis of the molecules in the film or flow
ΔH_b	Determination of the binding enthalpy
D_2O	Deuterium oxide
HDO	Deuterium protium oxide
dien	Diethylenetriamine
DTC	Diethylthiocarbocyanine iodide
W	Differential power signal
DSC	Differential scanning calorimetry
DHA	Dihydroanthracene
DMSO	Dimethyl sulfoxide
DD	Dipole–dipole
dpqC	Dipyrido[3,2-*a*:2′,3′-*c*](6,7,8,9-tetrahydro)phenazine
dppzMe$_2$	Dipyrido[3,2-*a*:2′,y-*c*]-7,8-dimethylphenazine
dppz	Dipyrido[3,2-*a*:2′3′-*c*]phenazine
dpq	Dipyrido[3,2-*d*:2′,3′-*f*]quinoxaline
DHD/K12	DMH-induced colon tumour
DQFCOSY	Double-quantum-filtered correlation spectroscopy
dsDNA	Duplex DNA
TE	Echo time
EPR	Electron paramagnetic resonance
ESI	ElectroSpray ionisation
ESI-MS	ElectroSpray ionisation mass spectrometry
ESI-QToF	Electrospray ionisation quadrupole time of flight
ER	Endoplasmic reticulum
EDXA	Energy dispersive X-ray analysis
EDXS	Energy dispersive X-ray spectroscopy
ΔH	Enthalpy
ΔH_{vH}	Enthalpy per mole of cooperative unit
ΔS	Entropy
K_a	Equilibrium binding constant
Equiv.	Equivalent
E. coli	*Escherichia coli*
E. coli K12	*Escherichia coli* K-12
EtBr	Ethidium bromide
EDTA	Ethylenediaminetetraacetic acid
EMEA	European agency for the evaluation of medicinal products
ESRF	European synchrotron radiation facility
ΔC_p^{ex}	Excess heat capacity
EXAFS	Extended X-ray absorption fine structure
ε_λ	Extinction coefficient at wavelength λ

ECM	Extracellular matrix
FDR	False discovery rate
FNR	False negative rate
FCS	Fluorescence correlation spectroscopy
FLIM	Fluorescence lifetime imaging microscopy
FRAP	Fluorescence recovery after photobleaching
FISH	Fluorescent in situ hybridization
FID	Fluorescent intercalator displacement
FPs	Fluorescent proteins
FDA	Food and drug administration
ΔG_{mol}	formation of non-covalent molecular interactions between ligand and DNA
R_o	Förster radius
FRET	Förster resonant energy transfer
ΔG_{conf}	Free energy associated with conformational changes
ΔG_{r+t}	Free energy associated with restriction of rotational and translational motions
ΔG_{hyd}	Free energy associated with the hydrophobic transfer of ligand from an aqueous environment to the DNA binding site
FID	Free induction decay
$[Met_f]$	Free metallointercalators
E	FRET efficiency
E_{max}	FRET efficiency of the interacting complex
R	Gas constant, 8.314 J/K mol
GEO	Gene expression omnibus
GO	Gene ontology
ΔG°	Gibbs free energy
ΔG	Gibbs free energy change
GFAAS	Graphite furnace atomic absorption spectroscopy
GFP	Green fluorescent protein
GuSCN	Guanidium thiocyanate
G	Guanine
ΔC_p	Heat capacity change
H_b	Hemoglobinemia
HMBC	Heteronuclear multiple bond correlated spectroscopy
HMQC	Heteronuclear Multiple-Quantum Correlated Spectroscopy
C-1311	Imidazoacridinone
Im	Imidazole
ILS	Increased life span
idpq	Indeno[1,2-b]dipyrido[3,2-f:2′,3′-h]-quinoxaline-6-one
ICD	Induced circular dichroism
IR	Infra-red
I	Intensity of the light beam
I_L	Intercalating ligand

IP	Intraperitoneal
IV	Intravenous
IMMS	Ion mobility mass spectrometry
LDH	Lactate dehydrogenase
Λ	Lambda
LC	Ligand-centred transitions
LD	Linear dichroism
LOWESS	Locally weighted scatterplot smoothing
MRI	Magnetic resonance imaging
MS	Mass spectrometry
m/z	Mass to charge ratio
MALDI	Matrix assisted laser desorption ionisation
MTD	Maximal tolerated dose
T_{max}	Maximum temperature of the excess specific heat capacity
MCHC	Mean corpuscular hemoglobin
MCV	Mean corpuscular volume
meso-2,3-Bn	*meso*-2*S*,3*R*-Diaminobutane
mRNA	Messenger ribonucleic acid
MC	Metal-centred transitions
MLCT	Metal-to-ligand charge transfer
MRSA	Methicillin-resistant *Staphylococcus Aureus*
MB	Methylene blue
MTOC	Microtubule-organising centres
MBC	Minimal bactericidal concentration
MIAME	Minimal information about a microarray experiment
MIC	Minimal inhibitory concentration
min	Minutes
ΔH_{cal}	Model-independent calorimetric enthalpy
χ_b	Mole fractions of bound metal complex or oligonucleotide
χ_f	Mole fractions of free metal complex or oligonucleotide
MD or MDS	Molecular dynamics simulations
MQ	Multi-quantum
M. tuberculosis	*Mycobacterium tuberculosis*
C_4(cpdppz)	N,N'-*Bis*(12-cyano-12,13-dihydro-11h-8-cyclopenta[b]dipyrido [3,2-h:2'3'-j]phenazine-12-carbonyl)
Tel01	*N,N'-Bis*(2-morpholinylpropyl)-3,4,9,10-perylenetetracar-boxylic acid diimide
DMF	N,N-Dimethylformamide
NNEM	Nearest neighbour exclusion model
NMR	Nuclear magnetic resonance
NOE	Nuclear overhauser effect
NOESY	Nuclear overhauser enhancement spectroscopy
n	Number of binding sites (in base pairs)

δ_{obs}	Observed chemical shift of the metal complex or oligonucleotide resonances
ΔG_{obs}	Observed free energy
1D	One-dimensional
ORF	Open reading frame
S	Orientation parameter
PIXE	Particle-induced X-ray emission
ppm	Parts per million
T/C	Percent of tumour mass in treated animal/tumour mass in control animals
% T/C	Percent test/control
phenanthryl	Phenanthrene
PBS	phosphate buffered saline
PAFPs	PhotoActivatable fluorescent proteins
PALM	PhotoActivation localization microscopy
AMD473	Picoplatin or *cis*-(amminedichloro-2-methylpyridine)platinum (II))
PAMAM	Poly(amidoamine)
ΔG_{pe}	Polyelectrolyte contribution to the free energy of binding
PE	Polyethylene
PCR	Polymerase chain reaction
PVA	Polyvinylalcohol
PCA	Principal components analysis
PI	Propidium iodide
POT1	Protection of telomere-1
s-CX[n]	p-Sulfonatocalix[*n*]arenes
PGSE	Pulsed gradient spin-echo
pyrenyl	Pyrene
qRT-PCR	Quantitative real time polymerase chain reaction
RF	Radio-frequency
DsRed	Red fluorescent proteins
LD^{r}	Reduced linear dichroism
[*D*]	Represent the concentration of DNA
[*L*]	Represent the concentration of unbound ligand
$\Delta H_{vH}/\Delta H_{cal}$	Represents the enthalpy per mole of cooperative unit and the ratio is typically used to comment on the cooperativity of the process
RNA	Ribonucleic acid
rRNA	Ribosomal RNA
RMA	Robust multi-chip average
RT	Room temperature
ROESY	Rotating-frame overhauser spectroscopy
Ru-DHA	Ru-dihydroanthracene
S. cerevisiae	*Saccharomyces cerevisiae*

SGD	Saccharomyces genome database
s	Scan speed
SCID	Severe combined immunodeficiency
ssDNA	Single-stranded DNA
SDS	Sodium dodecyl sulphate
C_p^{max}	Specific heat capacity profile
S. aureus	*Staphylococcus aureus*
STE	Stimulated echo
STORM	STochastic optical reconstruction microscopy
SAR	Structure activity relationship
SRB	Sulforhodamine B
SR	Super-resolution
SPring8	Synchrotron photon ring 8 (GeV)
SRXRF	Synchrotron radiation X-ray fluorescence
SRIXE	Synchrotron radiation-induced X-ray emission
TTAGGG	Telomere sequence
TRF1 and TRF2	Telomeric repeat-binding factor
T	Temperature at the completion of the transition
T_o	Temperature at the onset of the transition
$T_{1/2}$	Temperature at which 50% of the sample has denatured
THA	Tetrahydroanthracene
T_I	Therapeutic index
3D	Three-dimensional
T	Thymine
dT	Thymine nucleotide (DNA monomer)
ToF	Time of flight
τ	Time over which the machine averages each data point
TCSPC	Time-correlated single photon counting
TOPO I	Topoisomerase I
TOPO II	Topoisomerase II
TOCSY	Total correlation SpectroscopY
[DNA$_{tot}$]	Total DNA concentration
[Met$_{tot}$]	Total metallointercalator concentration
[M$_{tot}$]	Total molar concentration in the sample cell
tri-Pt	*trans*-[7_2{*trans*-$(NH_3)_2(dpzm)_2$}]$^{2+}$
tRNA	Transfer RNA
T_m	Transition midpoint
α	Transition polarized angle to the stretch direction
TEM	Transmission electron microscopy
ITC	Tsothermal titration calorimetry
2D	Two-dimensional
UV	Ultra violet
[DNA$_f$]	Unbound DNA or Free DNA
NCI	United state national cancer institute

U	Uracil
ΔH_{vH}	van't Hoff enthalpies
VRE	Vancomycin resistant *Enterococci*
xg	Xenograft
XANES	X-ray absorption near edge spectroscopy
XAS	X-ray absorption spectroscopy
XRF	X-ray fluorescence
YPD	Yeast proteome database
YFP	Yellow fluorescent proteins

Cell Lines

5637	Bladder carcinoma with epithelial-like characteristics
HeLa	Cervical cancer cells taken from Henrietta Lacks
V79	Chinese hamster lung cells
NCH89	Glioma
MCF-7	Hormone dependent breast cancer cell lines
MDB-MB 231	Hormone independent breast cancer cell lines
HL-60	Human acute promyelocytic leukemia
RT-4	Human bladder cancer
KB-3-1	Human carcinoma cells lines
SISO	Human cervical cancer
LCLC-103H	Human large cell lung carcinoma
Molt-4	Human leukaemia
A-427	Human lung cancer
A549	Human lung cancer
KYSE 520	Human oesophagal cancer
KYSR-70	Human oesophagal cancer
CH1	Human ovarian cancer
CH1cis^R	Human ovarian cancer with acquired resistance to cisplatin
CHIdox^R	Human ovarian cancer with acquired resistance to doxorubicin
2008	Human ovarian carcinoma
SKOV-3	Human ovarian carcinoma cell line with intrinsic resistance to cisplatin
C13*5	Human ovarian carcinoma with acquired resistance to cisplatin
HX/110	Human ovarian carcinoma with acquired resistance to cisplatin
A2780	Human ovarian carcinoma
A2780CIS^R	Human ovarian carcinoma with acquired resistance to cisplatin
PXN/65	Human ovarian carcinoma, relatively sensitive to cisplatin, formerly known as PXN/lO9T/C
HX/62	Intrinsically resistant human ovarian-carcinoma
LLC	Lewis lung cancer
colon 26	Mouse colorectal adenocarcinoma-26
colon 28	Mouse colorectal adenocarcinoma-28
colon 38	Mouse colorectal adenocarcinoma-38
L1210	Murine lymphocytic leukaemia
L1210cis^R	Murine lymphocytic leukaemia cell lines resistant to cisplatin
B16	Murine melanoma
M5076 Fibrosarcoma	Murine reticulum cell sarcoma
C22LR	Osteosarcoma solid tumour
P388	Murine lymphocytic leukaemia cell line
P388cis^R	P388 tumours resistant to cisplatin

ADJ/PC6	Plasmacytoma, L1210 leukemia
ADJ/PC6cis^R	Plasmacytoma, L1210 leukemia with acquired resistance to cisplatin
AkR leukemia	T-cell lymphoma cell line from a spontaneous thymic lymphoma/ leukemia that developed in an AKR/Cum mouse

Chapter 1
Target Biological Structures: The Cell, Organelles, DNA and RNA

Marcelis van Holst, Maxine P. Grant, and Janice Aldrich-Wright

1.1 Introduction

Living organisms are self replicating molecular factories of staggering complexity [1]. As a result, we are often overwhelmed when trying to identify potential targets for therapeutics. Water, inorganic ions and a large array of relatively small organic molecules (e.g., sugars, vitamins and fatty acids) account for approximately 80% of living matter, with water being the most abundant. Macromolecules such as proteins, polysaccharides, ribonucleic acid (RNA) and deoxyribonucleic acid (DNA) constitute the rest. The majority of potential therapeutic targets are found within the cell. Small molecules which are vital for cellular function are imported into the cell by a variety of mechanisms but unlike smaller molecules, macromolecules are assembled within the cell itself. Drugs are usually designed to target cellular macromolecules, as they perform very specific roles in the metabolic processes.

1.2 Cell Types

Whilst cells can vary greatly in shape and size depending on their function, they can be separated into two distinct types; eukaryotic and prokaryotic [1]. Eukaryotic cells are characterised by their highly organised membrane bound organelles such as the nucleus. Prokaryotic cells are considered to be simpler, more primitive and lacking most of the structures and organelles found in eukaryotic cells. As this book is mainly concerned with DNA intercalating agents, our primary focus in this chapter will be on nucleic acids and related structures contained within animal eukaryotic cells [2].

J. Aldrich-Wright (✉)
University of Western Sydney, School of Biomedical & Health Sciences, Penrith South DC New South Wales, Sydney, Australia
e-mail: J.Aldrich-Wright@uws.edu.au

1.3 Eukaryotic Cell Structure

Eukaryotic cells are enclosed by a plasma membrane that separates the cell from the outside world and defines the cell as a distinct entity. The plasma membrane helps maintain a life-supporting internal environment by regulating the passage of materials in and out of the cell [1]. The compartmentalisation of the cell, by internal membranes, allows incompatible chemical processes to occur simultaneously within the confines of the cell. In general, these membranes consist of a layer of lipids and phospholipids with proteins either imbedded in, or attached to, its surface. Additionally, each type of membrane has a unique composition of lipids and proteins to suit its function, e.g., enzymes embedded in the membrane of the mitochondria allow cellular respiration to occur there [2]. The most important compartment is the nucleus, this contains the cell's DNA.

1.3.1 The Nucleus

The nucleus controls the functions of the cell. This large structure (~5 μm) is surrounded by a double membrane (separated by 20–40 nm) containing the nucleolus and chromosomes (Fig. 1.1) [1]. Nuclear pores (~100 nm in diameter, Fig. 1.1) allow the passage of material in and out of the nucleus. The shape of the nucleus is maintained by proteins called the nuclear lamina, which line the inside of the
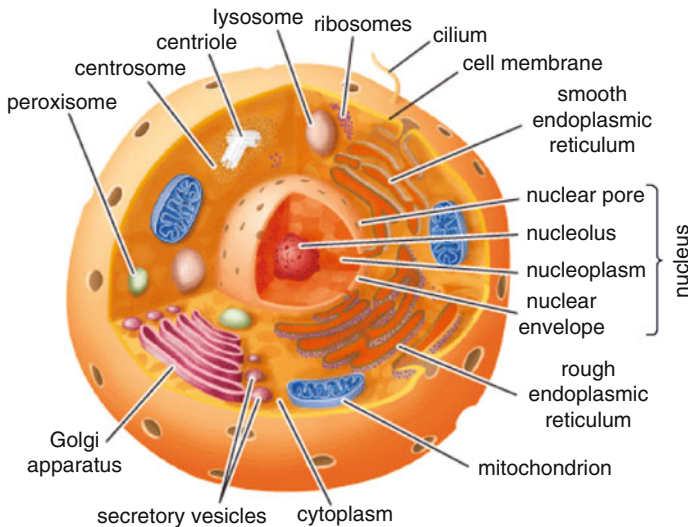

Fig. 1.1 A simple schematic of a cell. Reprinted with permission from the British Encyclopaedia Britannica

nuclear membrane with a net-like structure. The nuclear matrix consists of fibres extending throughout the nuclear interior, though their function is not completely understood. DNA and its associated proteins form thin fibres called chromatin. Chromatin condenses as it coils up before cell division and then forms chromosomes. Each eukaryotic species has a characteristic number of chromosomes (e.g., 46 in *Homosapiens*) that contain genes (units of hereditary information that govern the structures and activity of the cell). Genetic instructions from DNA are transcribed by the process of RNA synthesis, which involves the formation of messenger RNA (mRNA). Within the nucleus there is a granular body called the nucleolus, consisting of RNA and protein. Sometimes there are two or more nucleoli depending on the species and current stage of the cell's reproductive cycle [2]. The nucleolus is the site of ribosomal RNA (rRNA) synthesis and ribosome subunit assembly [3]. It adjoins part of the chromatin where the instructions for making rRNA are found. Ribosome subunits leave the nucleus through the nuclear pores and travel to the cytoplasm, where they assemble to form complete ribosomes.

1.3.2 Ribosomes

Ribosomes do not have a surrounding membrane and are composed of RNA and protein. Some are attached to inner membranes of the endoplasmic reticulum (rough endoplasmic reticulum, Fig. 1.1) or nuclear membrane, whilst others are free in the cytosol [3]. Ribosomes are responsible for the synthesis of polypeptides and proteins. Bound ribosomes make proteins mainly destined for use in membranes whereas free ribosomes make proteins that are usually dissolved in the cytosol [1].

1.3.3 Endoplasmic Reticulum

The endoplasmic reticulum (ER) is continuous with the nucleus. It is involved in constructing membranes and performs many other biosynthetic functions (Fig. 1.1). The ER consists of a network of membranous tubules and sacks called cisternae, which are kept separate from the cytosol by an encompassing membrane. The ER has two regions: the rough and smooth ER. The rough ER has ribosomes attached to the cytoplasmic surface of the membrane while the smooth ER is involved in various processes in different cell types, such as the synthesis of lipids, steroids (sex and adrenal hormones), phospholipids and oils (including the lipid components of lipoproteins), metabolism of carbohydrates and detoxification of drugs and poisons [3]. Smooth ER is found in kidney and liver cells, cardiac and skeletal muscle cells, intestinal cells and testosterone-synthesising cells, while other cells have little or no smooth ER. Many specialised cells secrete proteins synthesised by ribosomes attached to the ER. These polypeptides enter the cisternal space through

a pore formed by a protein in the ER membrane, as it enters, a polypeptide acquires its final conformation [2]. Many secretory proteins are proteins covalently bonded to a carbohydrate and are kept separate from cytosol proteins in the ER. Specialised molecules built into the ER membrane catalyse the formation of the bond between the polypeptide and carbohydrate. These proteins leave the ER wrapped by membranes that form a vesicle (small sac). The rough ER makes the integral proteins, phospholipids and cholesterol to form part of all cellular membranes and as the ER membrane expands, some of it is used to make transport vesicles [1].

1.3.4   Golgi Apparatus

The Golgi apparatus is characterised by stacks of flattened membrane sacs with internal spaces also known as cisternae (Fig. 1.1). The role of Golgi apparatus is to receive proteins transported by vesicles, which are made in the ER. After modifying these proteins the Golgi apparatus packages them into vesicles to be sent to other parts of the cell [3]. The Golgi apparatus also manufactures macromolecules. The *cis* face of the Golgi stack faces the ER and receives protein filled vesicles. The *trans* face produces transport vesicles which pinch off and transport materials to other parts of the cell. Products of the ER are modified during their transit through Golgi apparatus [2]. These modified molecules are sorted and targeted to various parts of the cell. The cisternae move forward from the *cis* to the *trans* face carrying and modifying their protein cargo as they move, this is called the cisternal maturation mode. Finished products may be excreted or incorporated into the plasma membrane or into lysosomes, etc. [1].

1.3.5   Lysosomes

Lysosomes are membranous sacs found in most eukaryotic cells that sometimes arise from the *trans* face of the Golgi apparatus as illustrated in Fig. 1.1. Digestive (hydrolytic) enzymes are stored in lysosomes and are isolated from the rest of the cell. Lysosomes fuse with food vacuoles and digest any engulfed particles in a process called phagocytosis, they are also responsible for digesting bacteria and damaged organelles. Additionally, lysosomes engulf small portions of the cytoplasm and organelles in a process called autophagy [1, 3].

1.3.6   Vacuoles

Vacuoles are water filled compartments within the cell. They may contain inorganic and organic molecules and include various soluble enzymes and solid material.

Vacuoles are formed by the fusion of multiple membrane vesicles and vary greatly in size depending on storage function and cell type. Vacuoles are responsible for the isolation of potentially harmful material including metabolic waste products, the storage of molecules and food, maintaining hydrostatic pressure and pH [3]. Vacuoles play a central role in a process known as autophagy which maintains a balance between the biogenesis and degradation of many substances and cell structures, they also aid in the elimination of bacteria and misfolded proteins. In eukaryotic cells, vacuoles assist in the processes of exocytosis and endocytosis [2].

1.3.6.1   Exocytosis

Exocytosis is a process whereby material is secreted by the cell. Proteins and lipids are firstly absorbed into secretory granules within the Golgi apparatus and are then transported via the vacuoles to the cell membrane and secreted outside the cell [1, 3].

1.3.6.2   Endocytosis

Endocytosis is the reverse process of exocytosis. Phagocytosis is an example of endocytosis, whereby bacteria and other organic material are engulfed by cells [3]. The plasma membrane makes contact with the material and then engulfs it. The membrane then is pinched off. This produces a vacuole filled with material, whilst the integrity of the cell membrane in maintained. Pinocytosis is a similar, generally smaller volume process whereby the cell engulfs water and soluble substrates (Fig. 1.2) [1, 2].
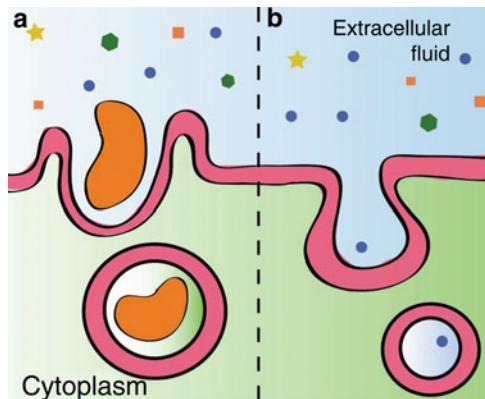

Fig. 1.2 Endocytosis is a process where cells deliver material (such as proteins) from the outside by engulfing it with their cell membrane

1.3.7   Mitochondria

Mitochondria are involved in energy transformation within the cell. Mitochondria (singular mitochondrion, Fig. 1.1) are the sites of cellular respiration and are found in almost all eukaryotic cells. Some cells have a single large mitochondrion, whilst others have hundreds or thousands of smaller mitochondria [3]. The number of mitochondria correlates to the metabolic activity level of the cell. They appear as long sacs (1–10 μm) consisting of two membranes, each a phospholipid bilayer with an inter-membrane space [2]. The inner membrane is folded to form cristae and encloses a matrix of macromolecules. The matrix contains various enzymes, RNA, DNA and ribosomes. Enzymes found in the matrix catalyse some steps of cellular respiration, for example, the enzyme involved in the synthesis of ATP is part of the inner membrane. Interestingly, mitochondria are capable of self-replication by fission and then growth [1].

1.3.8   Peroxisomes

Peroxisomes and glyoxysomes are protein based structures that are not made by the ER (Fig. 1.1). Instead, their membranes grow by incorporating proteins and lipids from the cytosol and when they reach a critical size they split. Peroxisomes are roughly spherical with a crystalline core. This single membrane sacs are involved in metabolic reactions where hydrogen is transferred to oxygen to make H_2O_2. They use molecular oxygen (O_2) to detoxify harmful substances like alcohol and formaldehyde [2], they also render free radicals harmless by converting O_2^- (superoxide ion) and hydroxyl radicals to H_2O_2 and this is then reduced to H_2O by the enzyme catalase. Additionally, they are involved in the break down of fatty acids into smaller molecules which can be transported into the mitochondria for fuel in cellular respiration. Peroxisomes and glyoxysomes are abundant in the kidneys and liver, where they detoxify alcohol by transferring hydrogen from the alcohol to oxygen. Peroxisomes in the liver are also involved in the formation of bile acids, which are hydrophilic derivatives of cholesterol. Synthesised bile acids are exported to the small intestine via the gall bladder, where they aid in lipid digestion [3].

1.3.9   Cytoskeleton

The cytoskeleton is a network of fibres extending throughout the cytoplasm. It plays a major role in organising the structures and activities of the cell. The cytoskeleton provides structural support to the cell by maintaining its shape and also assists in cell motility. It separates the chromosomes during cell division, provides anchorage and controls the movement of organelles within the cell. Cell motility involves the

displacement of cells from one location to another, movement of parts of the cell such as cilia and flagella, shape changes, muscle cell contraction, phagocytosis, vacuole formation and the movement of vesicles within the cell. The cytoskeleton is made of three types of fibres: microfilaments, intermediate filaments and microtubules [1, 3, 4].

1.3.9.1 Microfilaments and Intermediate Filaments

Microfilaments are solid helical structures, ~6–7 nm in diameter. They form when two subunits of the protein actin twist together. They are involved in the changing of cell shape and cell movement, e.g., amoeboid movement and endocytosis. They play a key role in the contraction of muscle cells, this involves interaction with filaments of myosin. Each cell appears to have its own arrangement of microfilaments forming a complex cross-linked network. They are constantly breaking down and being reassembled to meet the needs of the cell. Intermediate filaments are ~8–12 nm in diameter and constitute a diverse intermediate structure between microtubules and microfilaments. Intermediate filaments are constructed from keratin proteins and are abundant in parts of the cell that are frequently subjected to mechanical stress. They are a major constituent of the nuclear lamina inside the nuclear envelope where they are involved in disassembling and reassembling the nuclear membrane during mitosis. Intermediate filaments also fix the nucleus in a relatively permanent position [1–3].

1.3.9.2 Microtubules

Microtubules are hollow tubes (25–200 nm in diameter and up to 25 μm in length), made of subunits of the globular protein tubulin. They constantly grow, disassemble and reassemble. Microtubules provide structural support and shape to the cell, anchorage points for organelles allow them to move within the cytoplasm and act as a guide for the movement of chromosomes when the cell divides. They also play a role in the movement of cilia and flagella and are important components in centrioles and basal bodies [1–3].

1.3.9.3 Centrosomes and Centrioles

Centrosomes are clouds of cytoplasmic material that exist in animal cells and contain centrioles, which are also commonly referred to as microtubule-organising centres (MTOC) are shown in Fig. 1.1. Microtubules are produced and grow out of this region of the cytoplasm. Centrioles are found in the centrosome of animal cells and appear as nine sets of three microtubules forming a hollow tube. Centrioles are thought to organise microtubule assembly, the mitotic spindle in cell division and are the main structural components of cilia and flagella.

1.3.10   Cilia and Flagella

Cilia (singular cilium, Fig. 1.1) are short projections (2–20 μm in length and 0.25 μm in diameter) covered by plasma membrane and are usually present on the cell surfaces in almost all eukaryotic cells. They consist of two central and nine peripheral microtubules, are anchored inside the cell by a basal body similar in structure to centrioles and are responsible for the movement of some single-celled organisms whilst being used elsewhere to move materials on the surface of some tissues, e.g., mucous in the respiratory tract of mammals [3]. Cilia and flagella have the same internal structure. Flagella (singular flagellum) are long projections (10–20 μm in length) usually found singularly or in small numbers. They are also anchored inside the cell by a basal body similar in structure to centrioles, and are responsible for the movement of some single-celled organisms and gametes (such as sperm). A motor protein called dynein is involved in the movement of flagella.

1.3.11   The Plasma Membrane

Although the plasma membrane is considered to be the boundary of the cell, many cells secrete coats of different kinds beyond this membrane. The function of the plasma membrane is to protect the cell, maintain its cellular shape and prevent excessive intake of water. Cell membranes can vary in thickness from 1 μm to several micrometers and the composition of the membrane varies from species to species and from one cell type to another. However, the basic structure of the cell wall is consistent. Microfibrils of cellulose embed in the polysaccharides and proteins matrix. Most eukaryotic cells are also surrounded by a glycocalyx or cell coat which is formed by polysaccharide chains of proteins (glycoproteins) and lipids (glycolipids) that are part of the plasma membrane. These substances surround the cell and form the extracellular matrix (ECM). Different cell types have different glycocalyx, providing a highly specific biological marker by which cells recognise each other, make contact and form associations. Other molecules contribute to the mechanical strength of tissues. Animal cells have a glycocalyx gel made of carbohydrates and fibrous proteins. Collagen, a glycoprotein, is the main structural protein of the ECM.

1.3.11.1   Collagen Fibres

Collagen fibres are embedded in a network of proteoglycan fibres. Proteoglycans are rich in carbohydrates (up to 95%) and the remainder is protein. Fibronectin proteins are bound to collagen and receptor proteins called integrins which are part of the plasma membrane. Integrins cross the plasma membrane and bind to the cell cytoskeleton making integrins capable of transmitting changes in the ECM to the

cytoskeleton assisting in the regulation of cell functions [3]. Changes in the ECM may influence the activity of genes in the nucleus, by triggering a combination of mechanical and chemical pathways [2].

1.4 DNA

DNA is the template of life. Our genome encodes the structure and function of the organs that sustain us, the skeletal and muscular features that define us, and at times, the diseases that afflict us. A single unit of DNA commonly referred to as a "nucleotide", is characterised by three main structural features: (1) a five-membered carbohydrate ring, deoxyribose; (2) a heterocyclic base, either adenine (A), guanine (G), cytosine (C) or thymine (T) attached to the C1' of the carbohydrate ring in the β-conformations; (3) a 3'–5' phosphodiester linker, which spans the gap between individual DNA units. Complementary strands of DNA are stabilised by hydrogen bonding between guanine and cytosine (G-C) and adenine and thymine (A-T), and held in the anti-parallel double helix motif by stacking interactions between parallel oriented bases [2, 5, 6].

1.4.1 DNA Geometry and Dynamics

Probing the geometry and dynamics of DNA interactions by both NMR spectroscopy and X-ray diffraction has remained a field of intense interest since the double helical structure was first published in 1953 [7]. Many spatial configurations of DNA have since been proposed based on the results of such studies. Franklin played a major role in the original elucidation of the structure of DNA and was the first to discover that DNA fibres yield two distinct diffraction patterns depending on whether they are "crystalline" or "wet". These were designated as the A and B forms of DNA. The most predominant conformation of DNA under physiological conditions is referred to as the B form. The base pairs of B-DNA are stacked 0.34 nm (3.4 Å) apart with ten base pair residues per full rotation of the helix. Thus, the length of a DNA strand required for a full rotation is 34 Å with a diameter of 20 Å. This structure forms two distinct grooves, labelled minor and major. The minor groove is narrow (4.8 Å), whilst the major groove is wide (10.5 Å) though their depths are identical.

Double stranded DNA can adopt several recognised structures. A-DNA consists of 11 base residues per full turn with a closer distance of 2.25 Å between the bases. The major groove is deep, while the minor groove is wide and shallow. A-DNA is also characterised by a 20° tilting of the base pairs and their net migration away from the central axis. This produces a more compacted structure with a hollow core. Li and Na-DNA fibres adopt the C form of DNA under low hydration conditions which is when the salt content is between that which would induce the formation of

either A- or B-DNA. D-DNA has also been identified where the DNA strand consists of alternating purine and pyrimidine sequences (Table 1.1).

The Z-DNA conformation is adopted at high salt concentrations and is characterised by the adoption of left-handed geometry. The Z-DNA helix is elongated and slender (diameter 18 Å), and can be induced by the covalent binding of various metal complexes. It has 12 base pairs per turn with the sugar phosphate adopting a "zig-zag" shape. The orientation of the carbohydrate groups alternates every second unit, revealing a departure from the standard mononucleotide repeating unit of B-DNA in favour of a dinucleotide motif. The minor groove of Z-DNA is also deeper than the minor groove of B-DNA, extending all the way down to the axis of the molecule, whilst the major groove is absent [6].

1.4.2 Chromosome Structure

The double helix is condensed in a highly ordered fashion which enables the genome to physically fit within the nucleus. This is achieved by the wrapping of 146 bp DNA stretches around a specialised protein complex, histone octamers to form "bead-like" units called nucleosomes. Collections of nucleosomes are then organised into higher order structures such as chromatin fibres, the end point of which is the formation of chromosomes [4, 10, 11].
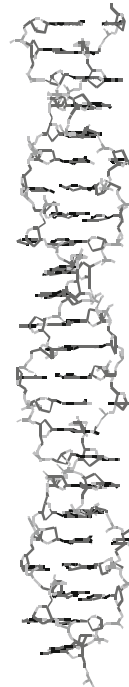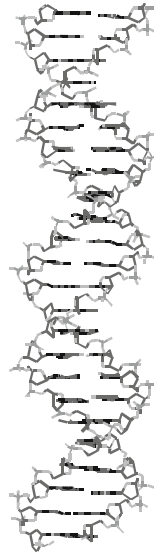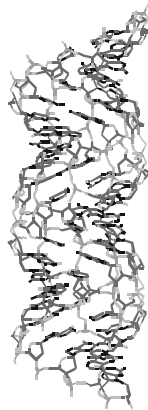
1.4.3 Telomeres and Telomerase

Chromosomes are capped with long tandem repeats of double stranded DNA, known as telomeres. these modulate chromosome replication [12, 13]. Their primary role is to protect chromosomes from degradation and loss of essential genes during replication [14]. Telomere-specific proteins, such as protection of telomere-1 (POT1) and telomeric repeat-binding factor (TRF1 and TRF2), bind directly to the single- and double-stranded telomere regions to form a complex, thus providing a protective cap over the chromosome. Telomere length is maintained by a balance between processes that lengthen telomeres, such as the enzyme telomerase, and processes that shorten telomeres, such as incomplete DNA synthesis. As DNA polymerase assembles DNA in the 5'–3' direction and requires a primer, replication cannot be completed to the 5' end, as after removal of the primer there is nothing for the DNA polymerase to extend from. After many rounds of cell division and replication, chromosomes become progressively shorter due to the gap left after primer removal. Telomeres themselves consist of a repeated DNA sequence; TTAGGG (in humans they are of 10–15 kb in length). The sequence, TTAGGG is repeatedly added to by the 3' termini of chromosomal DNA by telomerase [6].

This elongation provides space for the primer to bind and initiate lagging-strand synthesis on the complementary strand, thus maintaining the approximate length of

Table 1.1 Comparison of A-, B- and Z-DNA [8, 9]

Parameter	A-DNA	B-DNA	Z-DNA
Helical sense	Right handed	Right handed	Left handed
Diameter	~25.5 Å	~23.7 Å	~18.4 Å
Sugar conformation	$C_{3'}$-endo	$C_{2'}$-endo	$C_{3'}$-endo/$C_{2'}$-endo
Glycosidic bond	Anti	Anti	Anti (C), syn(G)
Base roll (twist)	12°	0°	1°
Base tilt	20°	5°	9°
Base pairs per helical turn	11	10	12 (6 dimers)
Helix axis location	Major groove	Through base pairs	Minor groove
Helical twist per base pair	32°	36°	60° (per dimer)
Helix pitch (rise per turn)	28 Å	34 Å	45 Å
Helix rise per base pair	2.3 Å	3.3 Å	3.8 Å
Major groove	Extremely narrow but very deep	Wide and with intermediate depth	Flattened out on helix surface
Minor groove	Wide, shallow	Narrow, deep	Narrow, deep
Overall proportions	Short and broad	Longer and thinner	Elongated and slim
The general structures of A-, B- and Z-DNA. All three structures are 24 base pair segments			
Orthogonal view of the helix			
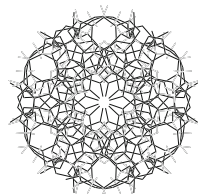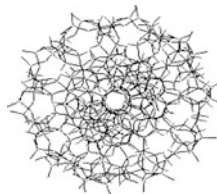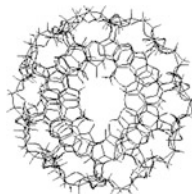
the chromosome and preventing the loss of coding sequences. Telomerase adds nucleotides without the use of a DNA primer. This is possible due to the presence of an essential RNA oligonucleotide that is complementary to the telomeric sequence being synthesised, which acts as a template. Telomerase is present in embryonic cells and in male germline cells. Telomerase is not detectable in normal somatic cells except for proliferative cells of renewal tissues. Telomeres and telomerase may perform other roles in addition to the prevention of chromosome shortening. It is possible that the G-rich stretches, typical of telomeres may aid in chromosome pairing by forming four-strand structures known as guanine quadruplexes as shown in Fig. 1.3. These structures are stabilised by the propensity of guanine bases to associate with each other in a stable hydrogen-bonded arrangement. This arrangement involves four DNA strands, resulting in a range of four-stranded quadruplex structural motifs. This is dependant on a number of factors such as: the strand orientation; and whether the quadruplex is formed from one, two or four separate strands.

1.4.3.1 Telomerase and Cancer

There is a strong correlation between aging, cell senescence (the period between maturity and death) and low levels of telomerase. The correlation between
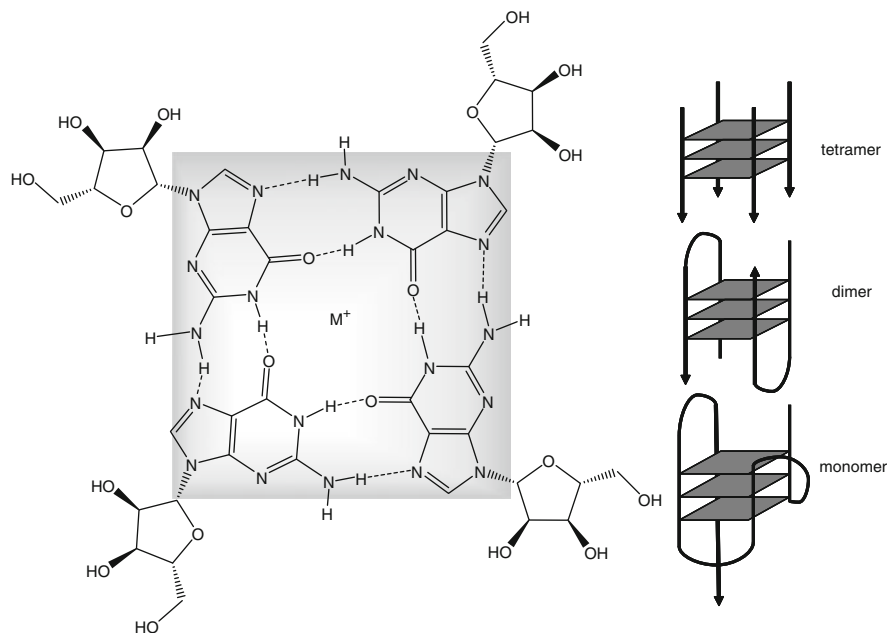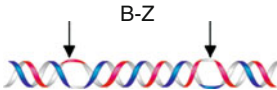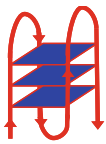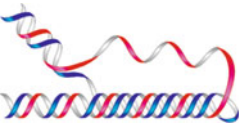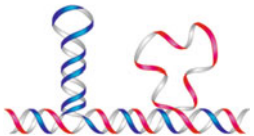

Fig. 1.3 The telomere sequence (TTAGGG in humans) can hydrogen bond with itself (*left*) and fold upon itself to form quadruplex structures each composed of three hydrogen bonded G-quartets, a tetrameric, dimeric and monomeric

telomerase activity and the growth of tumours has been demonstrated by many researchers [15, 16]. The 2009 Nobel Prize in Physiology or Medicine was awarded to Blackburn, Greider and Szostak for the discovery of how chromosomes are protected by telomeres and the enzyme telomerase. For example, in comparison to normal cells, tumour cells typically have short telomere length and do not show shortening with successive cell divisions. This suggests that telomere stability may be necessary for cells to proliferate indefinitely and by-pass cell senescence. Telomerase is present in 80–85% of proliferating tumour cells, but absent in most normal cells, it plays an important role in maintaining malignant growth by stabilising telomere length. Thus the link between telomere length, telomerase activity and malignant cells has attracted much interest. One approach to future cancer therapy is the development of small molecules that can act as telomerase inhibiters by either interacting with the telomeric G-rich DNA sequence or the enzyme itself. This enables these molecules to return control of malignant cells to the mechanisms of the natural cell cycle [6].

1.4.4 Higher Ordered DNA Structures

DNA can also adopt other, higher order, formations, which may provide alternative targets for DNA binding therapeutics. For example, self complimentary sections of single stranded DNA can form hairpin structures and cruciforms (which consist of two opposing hairpins as shown in Table 1.2) [17, 18]. Hairpin structures in particular, have been identified in genomic DNA and are considered to be potential sites for controlling gene expression. Many structures adopted by single stranded DNA are associated with regions of the DNA that are involved in the regulation of transcription, such as promoter sites [17, 18]. Drugs that can target hairpin and cruciform structures in promoter regions may be able to modify transcription and control gene expression [17, 19–23]. Higher order structures in ssDNA can be accurately predicted and synthesized. They are an important tool in unravelling the biological function of genes and proteins. Such molecules can be structured to form targeted catalytic molecules such as the class of "DNAzymes" which can specifically cleave other nucleic acid sequences. Double stranded DNA can also bind to a third strand under some conditions, to form a triple helix. The bases of the third strand bind to the existing base pairs via Höögsten base pairing, where T binds to A in a novel fashion and protonated C binds to G, forming the triplets T.AT and C.GC (Table 1.2). This permits a strand with long pyrimidine stretches to bind to its complementary sequence of duplex DNA, forming a triple helix. Triple helices are not as stable as duplexes, and are thought to relieve torsional stress caused by supercoiling. Some molecules preferentially bind to triple helices providing stability to these elusive structures. Many of these binding molecules are characterised by large planar aromatic surfaces that are capable of binding DNA by intercalation, and may have side chains which are capable of associating in the multiple grooves of the triple helix.

Table 1.2 Higher ordered DNA structures

Designation	Sequence requirements	Structure
Z-DNA	(YR YR)$_n$ such as 5′-CGCGTGCGCTG-3′	
Tetraplex/ G-Tetrad	Oligo (G)$_n$ repeats such as 5′-AG$_3$(T$_2$AG$_3$)$_3$-3′	
Cruciform	Inverted repeats such as 5′-TCGGTACCGA-3′	
Triplex	(R·Y)$_n$ mirror repeats such as 5′-AAGAGGGGAGAA-3′	
Hairpin	Direct repeats such as 5′-TCGGTTCGGT-3′	

1.4.5 DNA Specific Proteins and Enzymes

To perform its role, DNA must interact and associate with a diverse collection of proteins. These proteins vary greatly in size, regulation, sequence specificity and binding motif, whilst regulating a broad range of nuclear metabolic processes. For example, topoisomerase enzymes are involved in solving topological perturbations in DNA, such as superhelical tension which result from normal nuclear processes. To do this, Topoisomerase I (TOPO I) can induce a break in a single strand of the duplex, whilst Topoisomerase II (TOPO II) can induce a double-strand break. Several intercalating agents target the activity of TOPO II, by stabilising the break in the DNA made by the enzyme and preventing repair. Anthracycline

doxorubicin achieves this through an association with DNA, whilst epipodophyllo-toxin etoposide binds directly to the enzyme. Other molecules inhibit the catalytic activity of TOPO without stabilising the cleavage complex [6].

1.5 DNA Binding Interactions

DNA offers many potential sites for molecules to bind due to its size and complex-ity. Compounds are able to bind to DNA via two main modes of interaction: irreversible covalent/coordinate binding and reversible intermolecular associations, which can then be further divided into electrostatic binding, groove binding and intercalation. Transition metal complexes, such as *cis*-$[Pt(NH_3)_2Cl_2]$ (cisplatin) or $[Ru(bpy)_2(dppz)]^{2+}$ (where bpy is 2,2′-bipyridine and dppz is dipyrido[3,2-a:2′3′-c] phenazine) can bind DNA via coordinate bond formation or reversible intermolecular associations. Transition metal complexes may exhibit a preference for a particular binding mode or nucleotide sequence, depending on the size and shape of the molecule.

1.5.1 Irreversible Covalent/Coordinate Binding

Unsaturated metal complexes, such as $[PtCl_4]^{4+}$ and cisplatin bind coordinately to DNA (Fig. 1.4) [24]. When cisplatin is introduced into the body the chloride groups of cisplatin are replaced by water to give a reactive positively charged species. These complexes bind strongly to DNA through coordination to the guanine N7 nitrogen atom by inter- or intrastrand cross-linking thus forming Pt-DNA links. The hydrogen bonds involved in base-pairing guanine to cytosine are disrupted by these
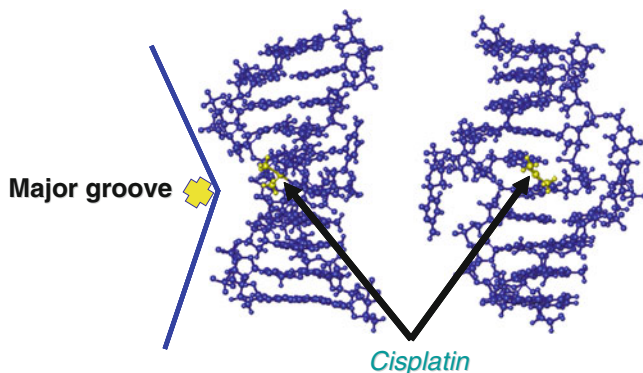

Major groove

Cisplatin

Fig. 1.4 A ball and stick model of the duplex d(CATAGCTATG)$_2$, where the helix is distorted by the covalent binding of *cis*-$[Pt(NH_3)_2]^{2+}$ in the major groove

cross-links causing unwinding of the DNA helix and inhibition of transcription. This explains the mode of action for disruption of cellular function of this well used anticancer compound. Other metal complexes including $[Co(H_2O)_6]^{2+}$ [25] and [Ru (phen)$_2$Cl$_2$] [26] also bind coordinately. For many molecules covalent binding is not the only mode of binding. Such complexes include $[Pt(AO(CH_2)_6en)Cl_2]$ [27] and $[Co(phen)_2]^+$ [28] which intercalate in the DNA strand as well as covalently binding over a period of time.

1.5.2 Reversible Intermolecular Associations

Reversible intermolecular associations such as electrostatic binding occur due to the interaction between cations, such as Na$^+$ and $[Mg(H_2O)_6]^{2+}$ with the negatively charged phosphate backbone at the exterior surface of the DNA helix [29]. Dimers, trimers and polymers of positively charged planar molecules, such as proflavine form, aggregates (stack with themselves) along the outside of the double helix [30]. The reduction in net charge of the complex produces conformational changes in the DNA.

Compounds with topologies that are flat and crescent shaped, complimentary to the particular groove of the DNA helix, preferentially participate in groove binding. The minor and major grooves differ significantly in size, shape, hydration, electrostatic potential and position of hydrogen bonding sites. Most organic groove binders, including distamycin and Hoechst 33258, show a preference for AT DNA base sequences in the minor groove where binding is stabilised by van der Waals interactions at the AT sequences [31, 32].

1.5.2.1 Intercalation

Intercalation is a mode of DNA binding that has been studied in detail via a broad spectrum of techniques. The alteration of the tertiary structure of DNA, induced by intercalation, can lead to changes in topology which can cause a blockade of functions at a biochemical level [33–37]. Thus molecules that are capable of intercalation are of great interest as potential medicinal agents. The model for intercalation was first proposed in 1961 by Lerman [38] after conducting a number of physical studies. Intercalation occurs when a chromophoric or planar part of a molecule is inserted perpendicular to the helical axis of adjacent base pairs of DNA in the minor and/or major groove of double stranded DNA (Fig. 1.5) [38, 39].

Intercalation is reversible, though it is stabilised by a combination of electrostatic, entropic, hydrogen bonding, van der Waals and hydrophobic interactions. As a consequence, DNA is lengthened, stiffened and unwound as well as losing regular helical structure in its backbone [33, 40]. This is the result of a change in the sugar-phosphate torsional angles, as the base pairs are forced apart to accommodate the insertion of an aromatic molecule. The degree to which the DNA helix can be lengthened by intercalation has been studied by electric dichroism, and suggests
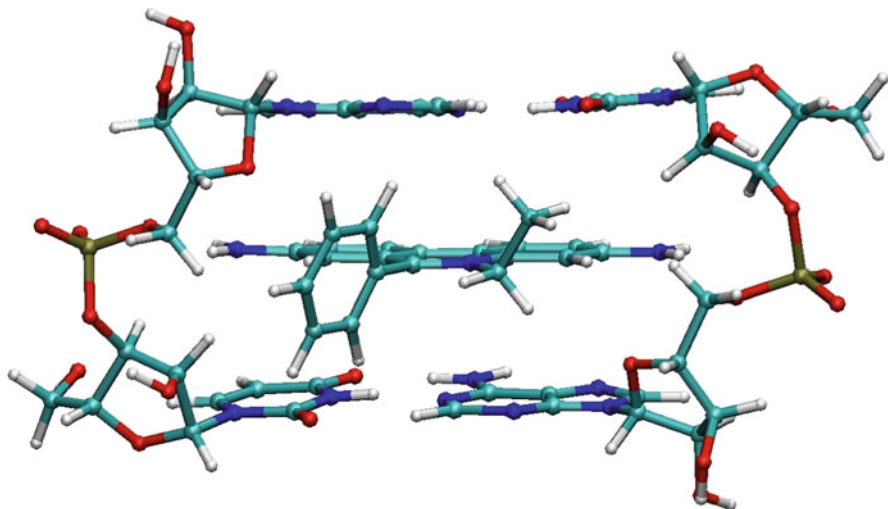
Fig. 1.5 Ethidium intercalated between two adenine–uracil base pairs

a range of extensions, from 2.0 to 3.7 Å [7, 36], depending on the intercalating moiety. In addition to this the usual offset angle of one base to the next is decreased from 36° to 26° as a result of intercalation [6, 35, 41–43].

There are a number of physical and spectroscopic techniques available to investigate the intercalative binding mechanisms with DNA. These techniques include: viscosity and sedimentation experiments [35, 44–56], UV-Vis spectroscopy [57–68], and electric dichroism [35, 43, 50, 59, 60, 64, 65, 68–76], electrophoresis [66, 77–83], NMR [40, 54, 56, 74, 84–94] and X-ray crystallography [33, 74, 78, 95–98]. Compounds that intercalate into DNA in general cause an increased relative viscosity, reduced sedimentation coefficients due to the increased length of DNA, wavelength shifts in their absorption spectrum, increased induced linear dichroism spectra, as well as changes in the extent of supercoiling in closed-circular DNA (typically plasmid DNA) [99, 100].

Some physical and spectroscopic techniques have shown that the effect on DNA is dependant upon the "depth of penetration" [34, 37, 101]. Intercalation (Fig. 1.6a) occurs when the planar portion of the intercalating molecule fully penetrates and stacks over the adjacent base pairs of the DNA helix [37, 102] and as a result the DNA is lengthened [101]. Partial intercalation (Fig. 1.6b–d) occurs when the planar portion of the intercalating molecule does not fully penetrate two adjacent base pairs or displaces a base [37, 101, 102]. Partial intercalation can be further broken down into two types: semi-intercalation and quasi-intercalation [101]. Semi-intercalation occurs when the intercalator is wedged between two stacked base pairs causing a partial opening, which may result in the DNA becoming bent (Fig. 1.6b) or kinked (Fig. 1.6c). Quasi-intercalation occurs when the base pairs at the binding site are shifted out-of-plane in order to accommodate the intercalating molecule (Fig. 1.6d) [101].
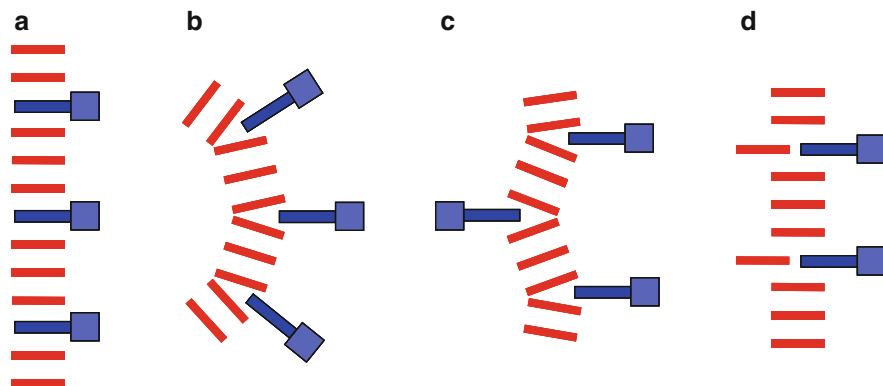
Fig. 1.6 A representation of different proposed intercalative binding modes with DNA. The base pairs are in *red*, and the intercalators are in *blue* (**a**) = intercalation, (**b**) and (**c**) = semi-intercalation, and (**d**) = quasi-intercalation
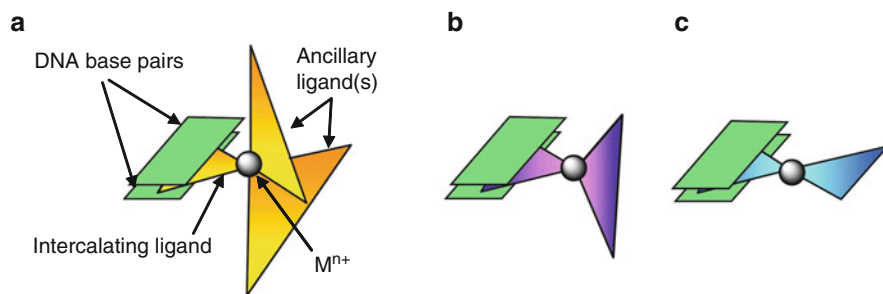

Fig. 1.7 Generic representations of metallointercalators with: (**a**) octahedral, (**b**) tetrahedral and (**c**) square-planar geometry

Once the intercalating portion of the molecule has been inserted into the DNA, regardless of the type of intercalation, it is stabilised by π–π (or π-stacking) interactions between the intercalator and the base pairs, as well as dipole–dipole interactions [103–105]. The non-intercalated portion of the molecule may also stabilise the intercalation of the drug through hydrogen bonding, electrostatic and van der Waals interactions with the sugar–phosphate backbone of the DNA [34, 39, 103, 106, 107]. X-ray structural analyses of several intercalating complexes have shown that these interactions, along with hydrophobic forces, contribute to their DNA binding affinity [98].

Intercalation anchors the metal complex with a distinct orientation within the intercalation site allowing functional groups to interact with the DNA grooves. The metal complex, 2-hydroxyethane-thiolato (2,2′:′0,2″-terpyridine) platinum(II), ([Pt (terpy)HET]$^{2+}$, where terpy is 2,2′:6′,2″-terpyridine and HET is 2-hydroxyethane-thiolato) intercalates but this is not limited to square planar complexes [108]. Tetrahedral ([Co(phen)$_2$]$^{2+}$) [109] and octahedral ([Ru(bpy)$_2$(dppz)]$^{2+}$) [110] complexes also intercalate into DNA. The coordination geometry of square planar complexes allows for deeper intercalator insertion than octahedral or tetrahedral

geometries (Fig. 1.7) [111, 112]. Platinum(II) complexes containing intercalating ligands stack between the base pairs of DNA [77, 97] and, depending on the choice of the ancillary ligands, may insert beyond the Pt(II) centre [39, 113, 114]. In the case of octahedral and tetrahedral complexes the arrangements of the ancillary ligands in relation to the intercalating ligand produces steric interactions with the DNA which can prevent full insertion [111, 112].

This model of interaction can be further complicated if the molecule has two intercalating moieties [35, 115–117]. Organic bisintercalators, such as echinomycin and triosin may intercalate into two base pairs of DNA [118]. These compounds are composed of positively charged fused rings that are attached by flexible linkers. They exhibit higher affinity for DNA and have a slower dissociation rate than mono-intercalators. Metallo-bisintercalators will be discussed in Chap. 4.

1.5.2.2 The Nearest Neighbour Exclusion Model

The presence of an intercalator inserted between two base pairs excludes the neighbouring intercalation sites from being occupied [33, 35, 40]. This phenomenon is referred to as the Nearest Neighbour Exclusion Model (NNEM) [35, 70, 119]. It results in periodic intervals of 10.2 Å between two drugs binding as it spans three individual 3.4 Å binding sites (Fig. 1.8). This principle is supported by the results of X-ray diffraction studies which have demonstrated the upper limit of binding to be one drug molecule for every four nucleotides [33, 35, 40, 97]. X-ray crystallographic studies showed conformational changes in the puckering of the sugars surrounding the intercalation site [96]. Upon intercalation, the normal C2′-*endo* deoxyribose ring puckering of B-DNA is altered to a mixture of C3′-*endo* and C2′-*endo* sugar puckering in the 3′–5′direction [33, 40, 113]. These conformational changes create sites at neighbouring base pairs to which additional intercalating ligands cannot bind [40]. The NNEM is illustrated by the X-ray fibre diffraction patterns observed on binding a metallointercalator [Pt(terpy)HET]$^{2+}$ to DNA [78, 95].
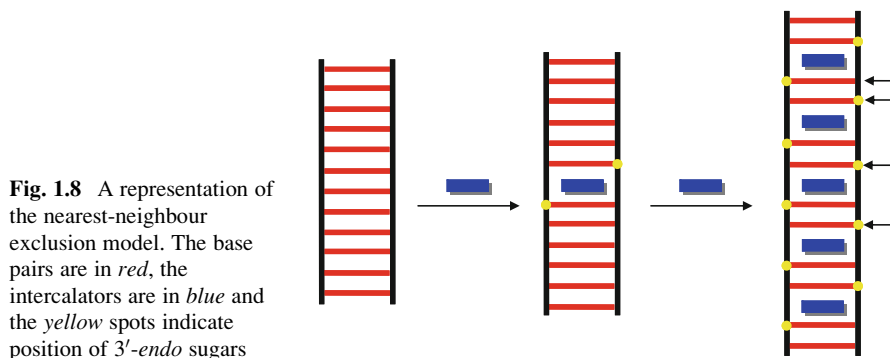

Fig. 1.8 A representation of the nearest-neighbour exclusion model. The base pairs are in *red*, the intercalators are in *blue* and the *yellow* spots indicate position of 3′-*endo* sugars

1.5.2.3 Biological Effects of Intercalators

The structural changes in the topology of DNA resulting from the intercalation of a drug are recognised as a factor contributing to their biological activity [34, 36, 37, 120–123]. Intercalation has been reported to inhibit the synthesis of DNA and RNA and ultimately diminish the capacity for cell replication [36, 120, 121]. Intercalation may also render affected or diseased cells more susceptible to normal defence mechanisms [40].

The effectiveness of intercalators is particularly evident in rapidly growing cells. This is evidenced by the reports that many of these compounds exhibit antibacterial, antiparasitic and antitumour properties [36, 120, 122, 123]. Cells exhibit good permeability to a number of intercalators [35]. Intercalative drugs typically hinder nuclear processes involving DNA-dependent enzymes such as DNA polymerases [123–125], RNA polymerases [126, 127] and nucleases [128] by disrupting their binding along the DNA. As a consequence, a number of mechanisms including replication, translation and repair are inhibited [122]. For example, 9-aminoacridine inhibits the initiation of RNA synthesis, whereas actinomycin D inhibits the elongation step [127]. Intercalators have been shown to produce single strand breaks in the DNA of mammalian cells [122, 129, 130]. Ethidium bromide (EtBr), for example, has been reported to induce DNA lesions photochemically, in the absence of enzymes; however, it has been suggested that nicks can also be created by inducing nuclease activity and inhibiting repair mechanisms subsequent to the excision of DNA [122, 131, 132]. Intercalators have also been reported to propagate cleavage breaks by TOPO II in DNA, by binding to the cleaved DNA-protein adduct and prevent the bond between the phosphates of DNA from reforming [123, 133].

Frame-shift mutagenesis is the deletion or insertion of base pairs within a DNA sequence. During the transcription and translation processes an intercalator can resemble a base pair and mistranscription through addition of an extra base causes a shift in the codon reading frame, resulting in the generation of an altered sequence [36, 120]. Alternatively, for example, 9-aminoacridine has been reported to cause deletion mutations in bacteria [134]. Some intercalators effect their therapeutic action by a combination of mechanisms, imidazoacridinone (C-1311) is an example of one of these. It has been reported to inhibit cellular nucleic acid synthesis [135, 136], trap TOPO II cleavage complexes [137] and block the G2 stage of the mitotic cell cycle leading to cell death [138, 139].

1.6 RNA

There are several different forms of RNA and each one perform very specific and vital roles in genetic processes. RNA is a pivotal component in the synthesis of proteins as it is used to transfer the genetic information stored in DNA to sites where it can be translated [4, 5]. Fundamentally, RNA is very similar to DNA although it has some key structural differences. RNA utilises the nitrogenous base

uracil (U) instead of thymine (T) which features in DNA. RNA primarily exists as single-stranded form and contains ribose which replaces the deoxyribose found in DNA. The presence of the hydroxyl group in ribose causes the helix to adopt A-form geometry in preference to the B-form conformation favoured by DNA. Like DNA, RNA is polyanionic, having multiple negative charges due to a phosphate backbone. Additionally, most forms of RNA have self-complementary sequences that allow parts of the RNA to fold and form a double helix. This small amount of tertiary structure allows some RNA to act in a catalytic capacity similar to enzymes. For example, the active site of the ribosome is composed entirely of RNA. Ribosomes are the apparatus that makes proteins from amino acids in the cells. The amino acids are attached to transfer RNA (tRNA) and the ribosome facilitates "reading" and then binding to (mRNA) to produce amino acids of a specific sequence.

1.6.1 Transcription

RNA strands are synthesised by the enzyme RNA polymerase directly from the code contained in DNA. This process is called transcription. Transcription produces messenger RNA (mRNA) which travels out of the nucleus to the ribosomes in the cytoplasm where protein synthesis occurs. Transcription begins with the binding of RNA polymerase to a DNA promoter sequence. The enzyme causes local unwinding of the double helix, then progresses along the DNA in the $3'-5'$ direction, synthesising a complementary RNA strand. Once synthesised, eukaryotic mRNA undergoes post-transcriptional modification, where a polyadenine tail and a $5'$ cap is added and non-coding introns are removed by spliceosomes (which themselves are protein-RNA complexes) [1–3].

1.6.2 Translation

Translation is a process occurring in the cytosol that is responsible for the synthesis of a protein from a mRNA During this process the ribosome continues along the mRNA and allows a triplet of ribonucleotides (codon) to specify the addition of a particular amino acid to the increasing chain. Like transcription, translation has specific start and stop signals which are also codons. The sequence of mRNA that is read and translated is the open reading frame (ORF), which specifies the order of linked amino acids. In addition to the importance of mRNA and ribosomes, tRNA also plays a significant role. There is no actual affinity between codons and the amino acids they specify. tRNA acts as an adaptor by attaching itself to the specified amino acid and carrying it to the codon during protein synthesis [1–3].

1.6.3 Ribosomal RNA

Ribosomes are composed of specific proteins and RNA molecules. The ribosome provides a scaffold for mRNA and aminoacyl-tRNA to assemble and a cavity for polypeptide synthesis. Ribosomes consist of two subunits each containing different sized RNA molecules. Eukaryotic ribosomes contain a 60S and a 40S subunit which make an 80S ribosome. Each ribosome subunit contains a set of rRNAs, those of eukaryotes contain 28S, 18S, 5.8S and 5S rRNA molecules. When these various subunits combine they undergo conformational changes forming a groove in which the mRNA molecule fits. The ribosomal subunits only assemble during protein synthesis and otherwise dissociate from one another [1–3].

References

1. Knox I, Ladiges P, Evans B, Saint R. Biology. 2nd ed. Roseville: MaGraw Hill; 2001.
2. Alberts B, Johnson A, Lewis J, Raff M, Roberts K, Walter P. Garland science. 5th ed. New York: Taylor and Francis Group; 2008. p. 1268.
3. Lodish H, Berk A, Kasier CA, Krieger M, Scott MP, Bretscher A, et al. Molecular cell biology. 6th ed. New York: W.H. Freeman and Company; 2008.
4. Bolsover SR, Hyams JS, Shephard EA, White HA, Wiedemann CG. Cell biology, a short course. 2nd ed. Hoboken: Wiley; 2004.
5. Sriram AHJW. Bioorganic chemistry: nucleic acids. Oxford: Oxford University Press; 1999.
6. Sarma RH. Nucleic Acid Geometry and Dynamics. New York: Pergamon; 1979, p. 424.
7. Watson JD, Crick FHC. Nature. 1953;171:737.
8. Rodger A, Nordén B. Circular dichroism and linear dichroism. 1st ed. Oxford: Oxford University Press; 1997.
9. Voet D, Voet JG. Biochemistry. 2nd ed. New York: Wiley; 1995.
10. Blackburn EH, Szostak JW. Annu Rev Biochem. 1984;53:163.
11. Blackburn EH. Nature. 1991;350:569.
12. Watson JD. Nat New Biol. 1972;239:197.
13. Olovnikov A. J Theor Biol. 1973;41:181.
14. McEachern M, Krauskopf A, Blackburn E. Annu Rev Genet. 2000;34:331.
15. Counter CM, Botelho FM, Wang P, Harley CB, Bacchetti S. J Virol. 1994;68:3410.
16. Greider CW, Blackburn EH. Cell. 1985;43:405.
17. Wadkins RM. Curr Med Chem. 2000;7:1.
18. Ying L, Wallace MI, Klenerman D. Chem Phys Lett. 2001;334:145.
19. Francois J-C, Thuong NT, Helene C. Nucleic Acids Res. 1994;22:3943.
20. Henderson PT, Armitage B, Schuster GB. Biochemistry. 1998;37:2991.
21. Chen F-M, Jones CM, Johnson QL. Biochemistry. 1993;32:5554.
22. Brown DR, Kurz M, Kearns DR, Hsu VL. Biochemistry. 1994;33:651.
23. Lian C, Robinson H, Wang AH. J Am Chem Soc. 1996;118:8791.
24. Huang H, Zhu L, Reid BR, Drobny GP, Hopkins PB. Science. 1995;270:1842.

25. Caradonna JP, Lippard SJ, Gait MJ, Singh M. J Am Chem Soc. 1982;104:504.
26. Barton JK, Lolis E. J Am Chem Soc. 1985;107:708.
27. Sundquiat WI, Bancroft DP, Lippard SJ. J Am Chem Soc. 1990;112:1590.
28. Grahman DR, Marshall LE, Reich KA, Sigman DS. J Am Chem Soc. 1980;102:5419.
29. Gessner RV, Quigley GJ, Wang AH-J, GAvd Marel, JHv Broom, Rich A. Biochemistry. 1985;24:237.
30. Record MT, Lohman TM, PJd Haseth. Mol Biol. 1976;107:145.
31. Robinson H, Wang AH-J. Nucleic Acids Res. 1996;24:676.
32. Kopka ML, Yoon C, Goodsell D, Pjura P, Dickerson RE. J Mol Biol. 1984;183:553.
33. Saenger W. Principles of nucleic acid structure. New York: Springer; 1984.
34. Pindur U, Haber M, Sattler K. J Chem Edu. 1993;70:263.
35. Blackburn GM, Gait MJ. Nucleic acids in chemistry and biology. 2nd ed. New York: Oxford University Press; 1996.
36. Berman HM, Young PR. Annu Rev Biophys Bioeng. 1981;10:87.
37. Werner MH, Gronenborn AM, Clore GM. Science. 1996;271:778.
38. Lerman LS. J Mol Biol. 1961;3:18.
39. Barton JK. Science. 1986;233:727.
40. Wilson WD, Jones RL. Adv Pharmacol Chemother. 1981;18:177.
41. Bauer W, Vinograd J. Basic principles in nucleic acid chemistry. New York: Academic; 1974. p. 265.
42. Jones RL, Lanier AL, Keel RA, Wilson WD. Nucleic Acids Res. 1980;8:1613.
43. Wang JC. J Mol Biol. 1974;89:783.
44. Cohen G, Eisenberg H. Biopolymers. 1969;8:45.
45. Gabbay EJ, Scofield R, Baxter CS. J Am Chem Soc. 1973;95:7850.
46. Saucier JM, Festy B, LePecq JB. Biochimie. 1971;53:973.
47. Luck G, Zimmer C, Reinert K-E, Arcamone F. Nucleic Acids Res. 1977;4:2655.
48. Balcarova Z, Kleinwachter V, Koudelka J, Lober G, Reinert K-E, Wakelin LPG, et al. Biophys Chem. 1978;8:27.
49. Dahl KS, Pardi A, Tinoco Jr I. Biochemistry. 1982;21:2730.
50. Banville DL, Wilson WD, Marzilli LG. Inorg Chem. 1985;24:2479.
51. Liu F, Meadows KA, McMilin DR. J Am Chem Soc. 1993;115:6699.
52. Cusumano M, Di Pietro ML, Giannetto A, Nicolo F, Rotondo E. Inorg Chem. 1998;37:563.
53. Zhen Q-X, Ye B-H, Zhang Q-L, Liu J-G, Li H, Ji L-N, et al. J Inorg Biochem. 1999;76:47.
54. Collins JG, Aldrich-Wright J, Greguric ID, Pellegrini P. Inorg Chem. 1999;38:5502.
55. Luedtke NW, Hwang JS, Nava E, Gut D, Kol M, Tor Y. Nucleic Acids Res. 2003;31:5732.
56. Brodie CR, Collins JG, Aldrich-Wright JR. Dalton Trans 2004; 1145.
57. Bloomfield VA, Crothers DM, Tinoco Jr I. Physical chemistry of nucleic acids. New York: Harper and Row; 1974. p. 373.
58. Chaires JB, Dattagupta N, Crothers DM. Biochemistry. 1982;21:3933.
59. Adlam G, Blagbrough IS, Taylor S, Latham HC, Haworth IS, Rodger A. Bioorg Med Chem Lett. 1994;4:2435.
60. Rodger A, Taylor S, Adlam G, Blagbrough IS, Haworth IS. Bioorg Med Chem. 1995;3:861.
61. McCoubrey A, Latham HC, Cook PR, Rodger A, Lowe G. FEBS Lett. 1996;380:73.
62. Choi S-D, Kim M-S, Kim SK, Lincoln P, Tuite E, Nordén B. Biochemistry. 1997;36:214.
63. Rodger A, Latham HC, Wormell P, Parkinson A, Ismail M, Sanders KJ. Enantiomer. 1998;3:395.
64. Ismail MA, Sanders KJ, Fennell GC, Latham HC, Wormell P, Rodger A. Biopolymers. 1998;46:127.
65. Rodger A, Sanders KJ, Hannon MJ, Meistermann I, Parkinson A, Vidler DS, et al. Chirality. 2000;12:221.
66. Parkinson A, Hawken M, Hall M, Sanders KJ, Rodger A. Phys Chem Chem Phys. 2000;2:5469.
67. Rodger A, Parkinson A, Best S. Eur J Inorg Chem. 2001;9:2311.

68. Patel KK, Plummer EA, Darwish M, Rodger A, Hannon MJ. J Inorg Biochem. 2002;91:220.
69. Lerman LS. J Cell Comp Physiol. 1964;64:1.
70. Crothers DM. Biopolymers. 1968;6:575.
71. Nordén B, Tjerneld F. Biophys Chem. 1976;4:191.
72. Nordén B, Tjerneld F. FEBS Lett. 1976;67:368.
73. Hogan M, Jardetzky O. Proc Natl Acad Sci U S A. 1979;76:6341.
74. Sarma RH. Nucleic acid geometry and dynamics. New York: Pergamon; 1980.
75. Hiort C, Nordén B, Rodger A. J Am Chem Soc. 1990;112:1971.
76. Halsall DJ, Rodger A, Dafforn TR. Chem Commun. 2001;23:2410.
77. Howe-Grant M, Wu KC, Bauer WR, Lippard SJ. Biochemistry. 1976;15:4339.
78. Lippard SJ, Bond PJ, Wu KC, Bauer WR. Science. 1976;194:726.
79. Barton JK. J Biomol Struct Dyn. 1983;1:621.
80. Barton JK, Danishefsky AT, Goldberg JM. J Am Chem Soc. 1984;106:2172.
81. Fitzsimons MP, Barton JK. J Am Chem Soc. 1997;119:3379.
82. Gisselfalt K, Lincoln P, Nordén B, Jonsson M. J Phys Chem B. 2000;104:3651.
83. Novakova O, Chen H, Vrana O, Rodger A, Sadler PJ, Brabec V. Biochemistry. 2003;42:11544.
84. Krugh TR, Nuss ME. Biological applications of magnetic resonance. Shulman RG, editor. New York: Academic press; 1979. p. 113.
85. Wilson WD, Tanious FA, Watson RA, Barton HJ, Strekowska A, Harden DB, et al. Biochemistry. 1989;28:1984.
86. Collins JG, Sheilds TP, Barton JK. J Am Chem Soc. 1994;116:9840.
87. Hudson BP, Dupureur CM, Barton JK. J Am Chem Soc. 1995;117:9379.
88. Odani A, Sekiguchi T, Okada H, S-i Ishiguro, Yamauchi O. Bull Chem Soc Jpn. 1995;68:2093.
89. Dupureur CM, Barton JK. Inorg Chem. 1997;36:33.
90. Greguric I, Aldrich-Wright JR, Collins JG. J Am Chem Soc. 1997;119:3621.
91. Franklin SJ, Treadway CR, Barton JK. Inorg Chem. 1998;37:5198.
92. Collins JG, Rixon R, Aldrich-Wright JR. Inorg Chem. 2000;39:4377.
93. Proudfoot EM, Mackay JP, Karuso P. Biochemistry. 2001;40:4867.
94. Greguric A, Greguric ID, Hambley TW, Aldrich-Wright JR, Collins JG. J Chem Soc Dalton Trans. 2002;6:849.
95. Bond PJ, Langridge R, Jennette KW, Lippard SJ. Proc Natl Acad Sci U S A. 1975;72:4825.
96. Sobell HM, Reddy BS, Bhandray KK, Jain SC, Sakore TD, Seshadri TP. Cold spring harbor symposia on quantitative biology, Cold Spring Harbor Lab, Cold Spring Harbor: New York; 1977. p. 87.
97. Lippard SJ. Acc Chem Res. 1978;11:211.
98. Kennard O, Hunter WN. Angew Chem Int Ed Engl. 1991;30:1245.
99. Bauer WR, Vinograd J. Prog Mol Subcell Biol. 1971;2:181.
100. Jennette KW, Lippard SJ, Vassiliades GA, Bauer WR. Proc Natl Acad Sci U S A. 1974;71:3839.
101. Lincoln P, Nordén B. J Phys Chem B. 1998;102:9583.
102. Sobell HM, Tsai C-C, Gilbert SG, Jain SC, Sakore TD. Proc Natl Acad Sci U S A. 1976;73:3068.
103. Pyle AM, Rehman JP, Meshoyrer R, Kumar CV, Turro NJ, Barton JK. J Am Chem Soc. 1989;111:3051.
104. Long EC, Barton JK. Acc Chem Res. 1990;23:271.
105. Mudasir N, Yoshioka H, Inoue J. Inorg Biochem. 1999;77:239.
106. Friedman AE, Kumar CV, Turro NJ, Barton JK. Nucleic Acids Res. 1991;19:2595.
107. Krotz AH, Kuo LY, Sheilds TP, Barton JK. J Am Chem Soc. 1993;115:3877.
108. Wang AH-J, Nathans J, Gvd Marel, JHv Boom, Rich A. Nature. 1978;276:471.
109. Thederahn TB, Kuwabara MD, Sigman TALDS. J Am Chem Soc. 1989;111:4941.
110. Hartshorn RM, Barton JK. J Am Chem Soc. 1992;114:5919.
111. Cusumano M, Petro MLD, Giannetto A, Nicolo F, Rotondo E. Inorg Chem. 1998;37:563.
112. Fisher DM, Honours Thesis, The University of Sydney (Sydney), 2000.
113. Wang AHJ, Nathans J, van der Marel G, van Boom JH, Rich A. Nature. 1978;276:471.

114. Barton JK. Science. 1986;15:8.
115. Capelle N, Barbet J, Dessen P, Blanquet S, Roques BP, LePecq JB. Biochemistry. 1979;18:3354.
116. Lowe G, Droz AS, Vilaivan T, Weaver GW, Park JJ, Pratt JM, et al. J Med Chem. 1999;42:3167.
117. Chan H-L, Ma D-L, Yang M, Che C-M. Chem Biol Chem. 2003;4:62.
118. Holmlin RE, Stemp EDA, Barton JK. Inorg Chem. 1998;230:412.
119. Bauer W, Vinograd J. J Mol Biol. 1970;47:419.
120. Gale EF, Cundliffe E, Reynolds PE, Richmond MH, Waring MJ. The molecular basis of antibiotic action. London: Wiley; 1972. p. 173.
121. Neidle S. Prog Med Chem. 1979;16:151.
122. Schwartz HS. Adv Cancer Chemother. 1979;1:1.
123. Denny WA. Anti-Cancer Drug Des. 1989;4:241.
124. Hurwitz J, Furth JJ, Malamy M, Alexander M. Proc Natl Acad Sci U S A. 1962;48:1222.
125. Bohner R, Hagen U. Biochim Biophys Acta. 1977;479:300.
126. Waring MJ. Mol Pharmacol. 1965;1:1.
127. Sarris AH, Niles EG, Canellakis ES. Biochim Biophys Acta. 1977;474:268.
128. Eron LJ, McAuslan BR. Biochim Biophys Acta. 1966;114:633.
129. Kanter PM, Schwartz HS. Cancer Res. 1979;39:3661.
130. Ross WE, Glaubiger DL, Kohn KH. Biochim Biophys Acta. 1979;562:41.
131. Paoletti C, Couder H, Guerineau M. Biochem Biophys Res Commun. 1972;48:950.
132. Deniss IS, Morgan AR. Nucleic Acids Res. 1976;3:315.
133. Drlica K, Franco RJ. Biochemistry. 1988;27:2253.
134. McCann J, Choi E, Yamasaki E, Ames BN. Proc Natl Acad Sci U S A. 1976;73:950.
135. Burger AM, Double JA, Konopa J, Bibby MC. Br J Cancer. 1996;74:1369.
136. Dziegielewski J, Skladanoski A, Konopa J. Ann Oncol. 1996;7 Suppl 1:56.
137. Skladanoski A, Plisov SY, Konopa J, Larsen AK. Mol Pharmacol. 1996;49:772.
138. Augustin E, Wheatley DN, Lamb J, Konopa J. Cancer Chemother Pharmacol. 1996;38:39.
139. Burger AM, Jenkins TC, Double JA, Bibby MC. Br J Cancer. 1999;81:367.

Chapter 2
Ruthenium Polypyridyl Metallointercalators

Nikita Orkey, Paul Wormell, and Janice Aldrich-Wright

2.1 Introduction

Understanding how a molecule finds a unique binding location on DNA is one of the most significant chemical or biochemical questions. This intensive area of research, at the junction between biology and chemistry, is a challenge, as the fundamental principles by which DNA discriminates are not well understood. Investigating the biological functions of DNA necessitates probing interactions at the molecular level. As a result, there have been extensive research efforts to use transition metal complexes, particularly of ruthenium, to investigate the principles involved in DNA recognition [1–24].

In the early 1950s Dwyer observed and reported the differential biological activity of the enantiomers of the *tris*-phenanthroline complexes of transition metals [1, 2, 4]. He recognised the suitability of these complexes as models from which structural information about biological molecules could be obtained [1, 2, 4], explaining that "since stable complex cations can only produce their effects by physical means, a correlation of their more important physical properties with their biological activity should provide a great deal of information concerning the physicochemical characteristics of the biological systems with which they interact. Since the size, charge distribution, stereochemistry, redox potential and other physical properties of the metal chelates can be varied readily during chemical synthesis, these substances would seem to be ideal pharmacological tools with which to investigate many functional systems in the living cell." [9]

Interest in the synthesis of ruthenium(II) complexes with polypyridyl ligands was further provoked when Paris and Brandt [25] reported that the complex [Ru (bpy)$_3$]$^{2+}$ (bpy = 2,2′-bipyridine) had luminescent properties. The unique combination of chemical stability, redox properties, excited state reactivity, luminescence emission and excited state lifetime has attracted the attention of many researchers.

J. Aldrich-Wright (✉)

University of Western Sydney, School of Biomedical & Health Sciences, Penrith South DC New South Wales, Sydney, Australia
e-mail: J.Aldrich-Wright@uws.edu.au

The structural variation is only limited by the researcher's imagination, and there are now several hundred derivatives of the original molecules that initiated this interest, [Ru(bpy)$_3$]$^{2+}$ and [Ru(phen)$_3$]$^{2+}$ (phen = 1,10-phenanthroline).

The soundness of Dwyer's insight is shown by the number of metalloprobe studies still undertaken after more than half a century. In this chapter we discuss studies that have exploited the distinctive characteristics of ruthenium complexes to contribute to our understanding of DNA structure and recognition, and describe some synthetic strategies that can be used. There have been several recent reviews with other emphases, such as anticancer properties [26–51], photoreactions [52–57], electron transfer through DNA [52, 58–65] and chiral metal tetradentates [66–70].

2.2 Modes of DNA Binding

Inert transition metal complexes interact reversibly with highly charged DNA by three significantly different non-covalent modes which include electrostatic attraction, groove binding and intercalation (Fig. 2.1). Electrostatic binding occurs as a result of interactions between cations and the negatively charged phosphate backbone at the exterior of the DNA helix. Ruthenium(II) polypyridyl complexes can bind by direct interactions in either the major or minor groove of DNA due to their great diversity in overall shape, size, hydrogen-bonding potential, polarizability of ligands and charge. The topology of the grooves also differs significantly in size, hydration and electrostatic potential, which depends in part on the position of hydrogen-bonding sites that provide various opportunities for binding. Ruthenium complexes with the ability to hydrogen-bond appear to favour major-groove binding. Examples include Λ-[Ru(TMP)$_3$]$^{2+}$ (TMP = 3,4,7,8-tetramethyl-1,10-phenanthroline; ligand structures are shown in Figs. 2.3 and 2.4) [71], and dinuclear helicates such as [Ru$_2$(bpy)$_4$((*NE,N′E*)-4,4′-methylene-*bis*(*N*-(pyridin-2-ylmethylene)aniline))]$^{4+}$ [51].

Intercalation is distinguished by the insertion of generally planar polycyclic aromatic systems between the stacked base pairs of DNA. This interaction is stabilised by the overlap of the π-clouds of the intercalator and the nearby nucleobases [72] and can occur from either the major [73] or the minor [74] groove. Intercalation increases the separation of adjacent base pairs, and the resulting helix distortion is compensated by adjustments in the sugar-phosphate backbone and, generally, by an unwinding of the duplex. Association constants are reported to be of the order of 10^5–10^6 for mononuclear complexes [75]. Intercalation is not restricted to square planar complexes; tetrahedral and octahedral complexes such as [Co(phen)$_2$]$^{2+}$ [76, 77], [Ru(bpy)$_2$(ppz)]$^{2+}$ (ppz = 4,7-phenanthroline[6,5-*b*]-pyrazine) [78–80], [Ru(phen)$_2$(HAT)]$^{2+}$ (HAT = 1,4,5,8,9,12-hexaazatriphenylene) [53, 81–84], [Ru(phen)$_2$(dppz)]$^{2+}$ (dppz = dipyrido[3,2-*a*:2′,3′-*c*] phenazine) [4, 65–68], and [Ru(phen)$_2$(dpq)]$^{2+}$ (dpq = dipyrido-[3,2-*d*:2,3-*f*]-quinoxaline) [23, 74] have also been reported to intercalate. Intercalation anchors the metal complex
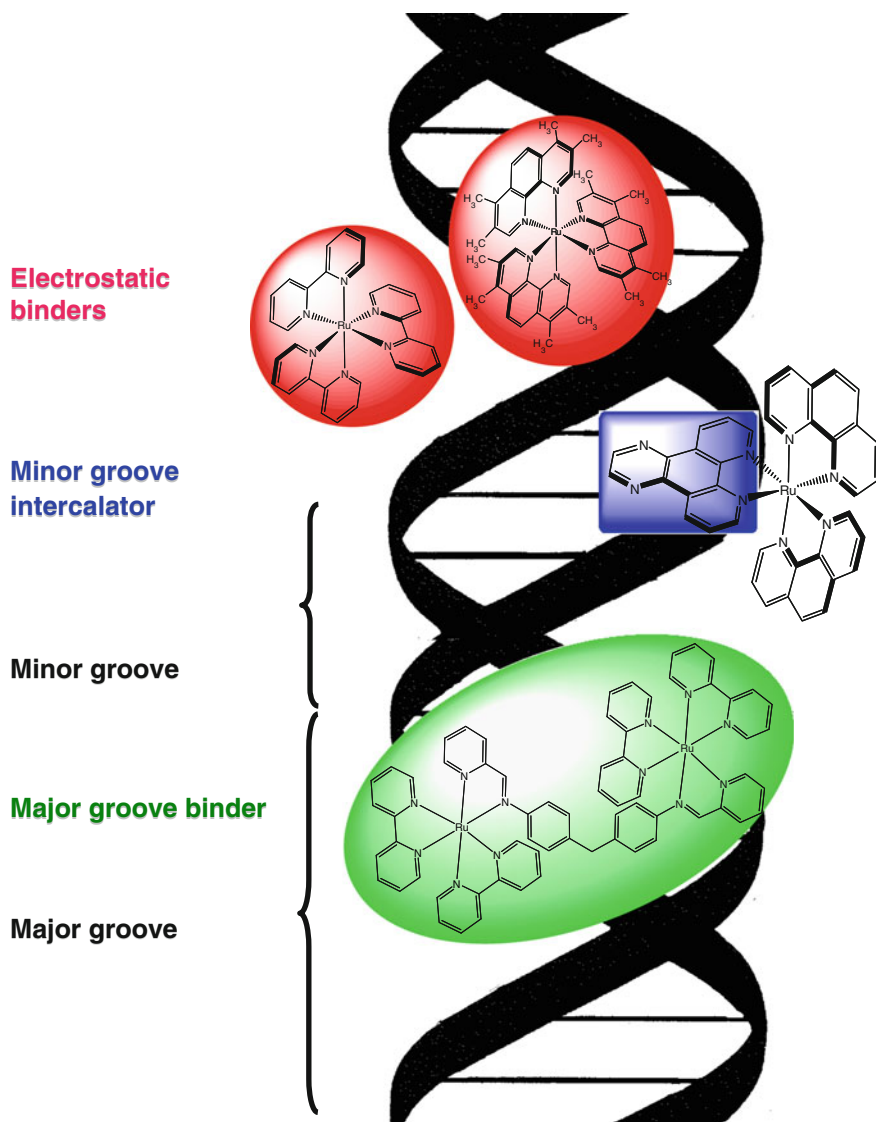
Fig. 2.1   Non-covalent DNA binding modes with electrostatic groove binders [Ru(bpy)$_3$]$^{2+}$ and [Ru (TMP)$_3$]$^{2+}$, a minor groove intercalator [Ru(phen)$_2$(dpq)]$^{2+}$ and a major groove binder [Ru$_2$(bpy)$_4$ ((*NE,N′E*)-4,4′-methylene-*bis*(*N*-(pyridin-2-ylmethylene)aniline))]$^{4+}$

with a well-defined orientation within the intercalation site. Modulation of ancillary ligands allows more specific interactions to occur with the functional groups of DNA.

Although binding modes are described in specific terms, some compounds have more than one type of interaction, or classically defined binding modes cannot be

clearly discerned. In these cases the ambiguity has caused some difficulty in uniquely characterising their interactions. It is perhaps expedient to remember that non-covalent interactions are transient and one form of binding does not preclude another.

2.3   Ruthenium Complexes as DNA Probes

2.3.1   Tris(1,10-Phenanthroline)Ruthenium(II)

The significance of optical isomerism in metal complexes was demonstrated in toxicity studies carried out on mice in 1952 [3], which showed a difference in the biological activity of Λ- and Δ-[Ru(phen)$_3$]$^{2+}$. *In vivo* testing in mice established the minimum toxic dose when administered by intraperitoneal injection. Mice that were fed five times the intraperitoneal toxic dose showed no obvious effects, but inspection of their faeces revealed that the Λ- and Δ-[Ru(phen)$_3$]$^{2+}$ complexes were excreted intact. From this observation, it was hypothesized that the interaction of these complexes with the biological system was physical, not chemical, and that the biological effect must be due to the overall three-dimensional shape of the complex, rather than simply the constituent ligands [85]. This conclusion was reached and published before the structure of DNA was made known in 1953 [86]. The potential of ruthenium(II) complexes in biological chemistry was confirmed with the report of their bacteriostatic and antitumour activity in the late 1960s [85].

With the development of spectroscopic techniques for studying transition metal complexes in biological systems, more comprehensive investigations were made. Ruthenium(II) complexes were reported to interact with DNA, although these interactions vary depending on the type of ligands coordinated and the concentrations used for the binding studies. Spectroscopic experiments to elucidate the type, strength, location and geometry of binding of mononuclear ruthenium(II) complexes to DNA were the focus of research in the late 1980s and 1990s [10–15, 52, 53, 66–70, 73, 78, 79, 81, 87–114].

Despite extensive nuclear magnetic resonance (NMR) and other spectroscopic studies, the enantioselectivity and DNA binding modes of chiral ruthenium(II) complexes were the subject of much debate over many years. For [Ru(phen)$_3$]$^{2+}$, intercalation as well as groove binding was proposed from the results of binding studies using optical [21] and ^{1}H NMR [10, 97, 101] spectroscopy, but definitive evidence for a precise binding mode was not found. The major unanswered questions were the location of the binding interaction, and whether it occurred in the major or minor groove through intercalation by one of the phenanthroline ligands. Barton [16, 20–22, 91] suggested that binding of [Ru(phen)$_3$]$^{2+}$ could occur by two possible modes: intercalation and surface interaction. In contrast, studies by Nordén [10, 12, 14] brought the binding mechanism proposed by Barton into question. Linear dichroism (*LD*) and circular dichroism (*CD*) studies suggested that both

isomers of [Ru(phen)$_3$]$^{2+}$ do not intercalate [10] and showed no clear specificity for any part of the DNA.

In an effort to provide some irrefutable evidence, sophisticated two-dimensional NMR techniques such as nuclear Overhauser effect spectroscopy (NOESY) were employed. ^{1}H NMR experiments with [Ru(phen)$_3$]$^{2+}$ and the decanucleotide, d(CGCGATCGCG)$_2$ provided evidence for minor-groove binding [13]. Intermolecular NOE cross peaks from the protons of the metal complex to protons located in the minor groove of DNA were observed, with a preference for the AT base pairs. No cross peaks were observed between the complex and the protons in the DNA major groove, confirming that both the Δ- and Λ- enantiomers of [Ru(phen)$_3$]$^{2+}$ bind in the minor groove of the decanucleotide under these conditions. Rapid exchange on the NMR time scale indicates that [Ru(phen)$_3$]$^{2+}$ does not bind by intercalation, although the Δ-enantiomer associated more strongly than the Λ-enantiomer [14].

Further investigations of the binding conditions were undertaken. Using *CD*, *LD* and computer modelling experiments, at low metal complex to DNA base ratios, Λ-[Ru(phen)$_3$]$^{2+}$ was shown to partially intercalate from the major groove of DNA whereas Δ-[Ru(phen)$_3$]$^{2+}$ binds on the surface of the minor groove [13]. This indicates that [Ru(phen)$_3$]$^{2+}$ may exhibit different binding modes, depending on the chirality of the enantiomer of the complex, the DNA sequence and, for the Δ-enantiomer, the concentration of the complex. This model is consistent with the published results of Eriksson for Δ-[Ru(phen)$_3$]$^{2+}$ but it was reported that other binding modes, up to ~30%, may also occur [115]. This may account for the discrepancies between the conclusions previously reported by Barton and Nordén. At high metal complex to DNA ratios, the minor groove is saturated by surface-bound complexes, whereas the major groove is partly filled in a partially inter-calative geometry.

2.3.2 Mononuclear Ruthenium(II) Tris(polypyridyl) Complexes

Many structural analogues of Δ-[Ru(phen)$_3$]$^{2+}$ have been constructed in an effort to obtain more effective compounds for interacting with DNA and probing its tertiary structure. Since [Ru(phen)$_3$]$^{2+}$ has only limited aromatic overlap between the phen ligand and the base pairs, intercalating ligands with larger aromatic surface areas were investigated. One of the first complexes to be evaluated was [Ru(phen)$_2$(dppz)]$^{2+}$, where the intercalating ligand incorporated two additional aromatic rings when compared with phen [14]. Other extended intercalator ligands included dpq [89], dpqC (dipyrido[6,7-*d*:2′,3′-*f*]6,7,8,9-tetrahydrophenazine) [24] and, more recently, *o*-npip (2-(4-nitrophenyl)imidazo[4,5-*f*]-1,10-phenanthroline) [23] and 2-(4-benzothiazolyl)phenylimidazo[4,5-*f*]1,10-phenanthroline [116] as shown in Fig. 2.4. Ruthenium(II) complexes such as [Ru(phen)$_2$(dppz)]$^{2+}$ [97] and [Ru(bpy)$_2$(dppz)]$^{2+}$ showed great promise, with association constants greater than 10^6 [89]. Upon intercalation with DNA they became much more strongly luminescent, leading to their description as "molecular light switches" for DNA [95].

DNA binding experiments using NMR spectroscopy were conducted on the interaction of Δ- and Λ-[Ru(phen)$_2$(dppz)]$^{2+}$ with the hexanucleotide d(GTCGAC)$_2$ [89]. Although NMR data gave evidence that both isomers intercalate, in agreement with luminescence studies [73, 117], exact DNA binding geometry and direction of insertion (major or minor groove) were not confirmed. A few intermolecular NOE contacts suggested that the dppz ligand intercalates from the major groove, but no NOE contacts were observed between the major groove protons and the phen ligands [89]. Selective deuteration of the phen ligands (Δ-[Ru(phen-d_8)$_2$(dppz)]$^{2+}$) [89] simplified the NMR spectrum of the DNA-complex, and this was also used in an attempt to reveal the precise binding geometry [117]. Photophysical evidence from luminescence titrations of Δ- and Λ-[Ru(phen)$_2$(dppz)]$^{2+}$ with various types of DNA indicated that intercalation occurs via the minor groove [73]. In conjunction with the luminescence studies, *LD* experiments probed the binding with respect to transition moment directions and mutual overlap of absorption bands. The data allowed for the determination of the precise DNA binding geometry [118, 119].

Intercalating complexes with moderate binding affinity, such as [Ru(phen)$_2$(dpq)]$^{2+}$, were also investigated using NMR binding experiments with the hexanucleotide d(GTCGAC)$_2$ and dodecanucleotide d(TCGGGATCCCGA)$_2$ [23, 120]. The resulting NMR data indicated that the complex bound to d(GTCGAC)$_2$ with some preference for GA/TC sites, and when bound to d(TCGGGATCCCGA)$_2$ displayed a preference for GG/CC sites. It was concluded that the ruthenium(II) complexes with a dpq intercalator exhibited preference for purine–purine sequences, although the specific binding model could not be determined. To overcome the exchange broadening problems seen with [Ru(phen)$_2$(dpq)]$^{2+}$, a new strategy was developed. Methyl groups were included on the non-intercalating ligand, producing complexes such as [Ru(2,9-Me$_2$phen)$_2$(dpq)]$^{2+}$, (2,9-Me$_2$phen = 2,9-dimethyl-1,10-phenanthroline; Fig. 2.3) these were expected to make NOE cross peaks between the complex and the DNA groove into which the complex inserted [23]. The resulting cross peaks between the complex and the oligonucleotide suggested that both the Δ- and Λ- enantiomers of [Ru(2,9-Me$_2$phen)$_2$(dpq)]$^{2+}$ intercalate from the minor groove, and the bound Δ- enantiomer is more deeply inserted than the Λ [23]. As this strategy had proved to be useful, [Ru(2,9-Me$_2$phen)$_2$(dpqC)]$^{2+}$ and [Ru(2,9-Me$_2$phen)$_2$(dppz)]$^{2+}$ were investigated in a similar manner. Significant exchange broadening of the resonances in the bound Δ-[Ru(phen)$_2$(dpqC)]$^{2+}$ spectra precluded full elucidation of the binding model. However, the changes in observed ^{1}H NMR chemical shifts indicated that the dpqC complex binds from the DNA minor groove [23]. For the [Ru(2,9-Me$_2$phen)$_2$(dppz)]$^{2+}$ complex the NOE cross-peaks between the Me$_2$phen and hexanucleotide minor-groove protons were observed in NOESY spectra. NOE cross peaks between the protons at the end of the dppz ligand and the hexanucleotide major-groove protons were also observed. The observed broadening of the resonances from the metal complex and the selective upfield shifts of the dppz resonances when coupled with the NOE data indicate that Δ-[Ru(2,9-Me$_2$phen)$_2$(dppz)]$^{2+}$ intercalates from the minor groove of d(GTCGAC)$_2$ as illustrated in Fig. 2.2 [23].
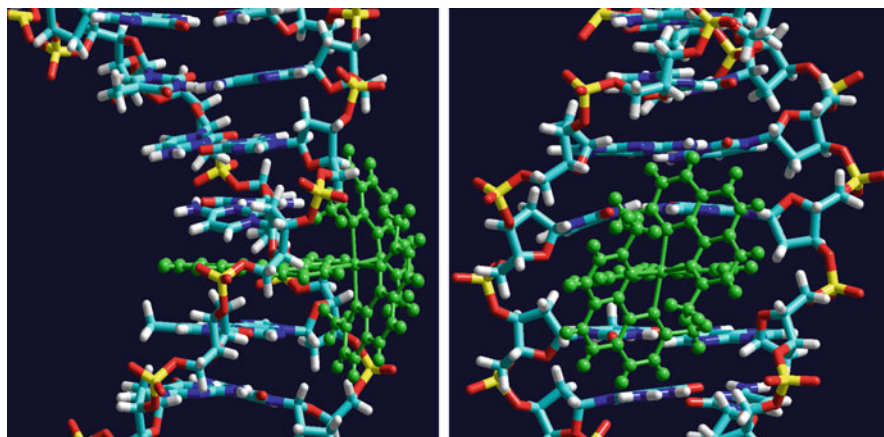
Fig. 2.2 A HyperChem model illustrating the intercalative binding of Δ-[Ru(2,9-Me$_2$phen)$_2$dppz]$^{2+}$ between the G4A5 residues and the T2C3 residues of the complementary strand of the hexanucleotide d(GTCGAC)$_2$ [74]
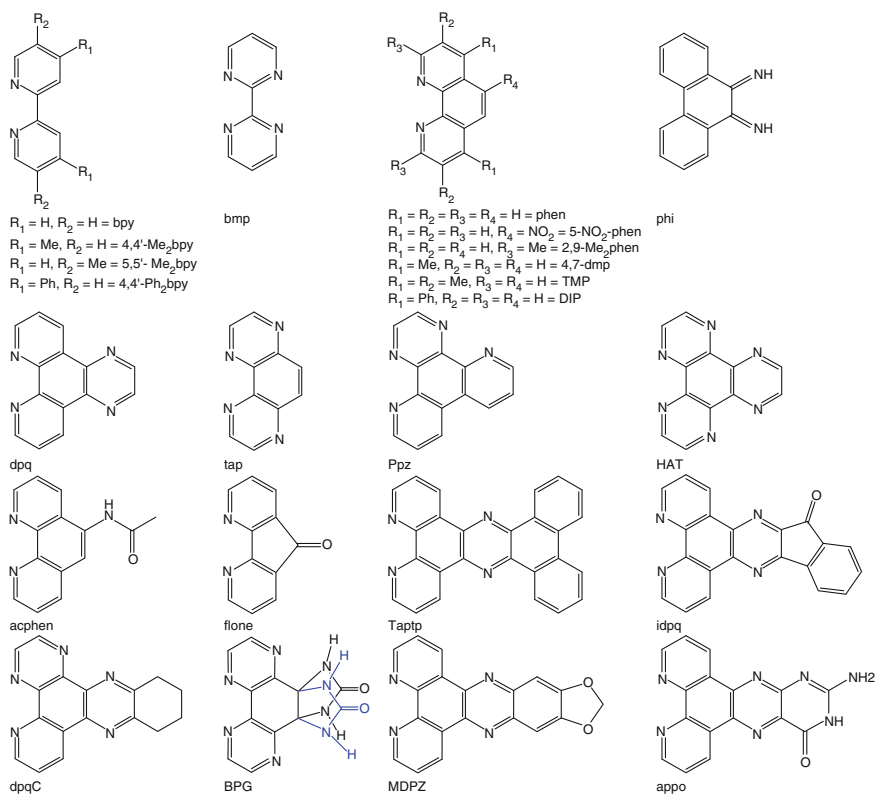

R$_1$ = H, R$_2$ = H = bpy
R$_1$ = Me, R$_2$ = H = 4,4'-Me$_2$bpy
R$_1$ = H, R$_2$ = Me = 5,5'- Me$_2$bpy
R$_1$ = Ph, R$_2$ = H = 4,4'-Ph$_2$bpy

bmp

R$_1$ = R$_2$ = R$_3$ = R$_4$ = H = phen
R$_1$ = R$_2$ = R$_3$ = H, R$_4$ = NO$_2$ = 5-NO$_2$-phen
R$_1$ = R$_2$ = R$_4$ = H, R$_3$ = Me = 2,9-Me$_2$phen
R$_1$ = Me, R$_2$ = R$_3$ = R$_4$ = H = 4,7-dmp
R$_1$ = R$_2$ = Me, R$_3$ = R$_4$ = H = TMP
R$_1$ = Ph, R$_2$ = R$_3$ = R$_4$ = H = DIP

phi

dpq   tap   Ppz   HAT

acphen   flone   Taptp   idpq

dpqC   BPG   MDPZ   appo

Fig. 2.3 Structures of the ligands mentioned in the text

dptap

R = H = Im
R = Me = MeIm

Phehat

R = H = dppz
R = Me = dppzMe$_2$

IP

R$_1$ = R$_2$ = R$_3$ = H = pip
R$_1$ = NO$_2$, R$_2$ = R$_3$ = H = o-npip
R$_1$ = OCH$_3$, R$_2$ = R$_3$ = H = mopip
R$_1$ = R$_2$ = H, R$_3$ = OH = hpip
R$_1$ = OH, R$_2$ = OCH$_3$, R$_3$ = H = mhpip

MCMIP

pmip

bpid

R = NO$_2$ = mitatp
R = OCH$_3$ = nitatp

HNAIP

pyip

PIPSH

PAIDH

PYNI

Tbz

MPyTPP

BPIP

POQ-Nmet
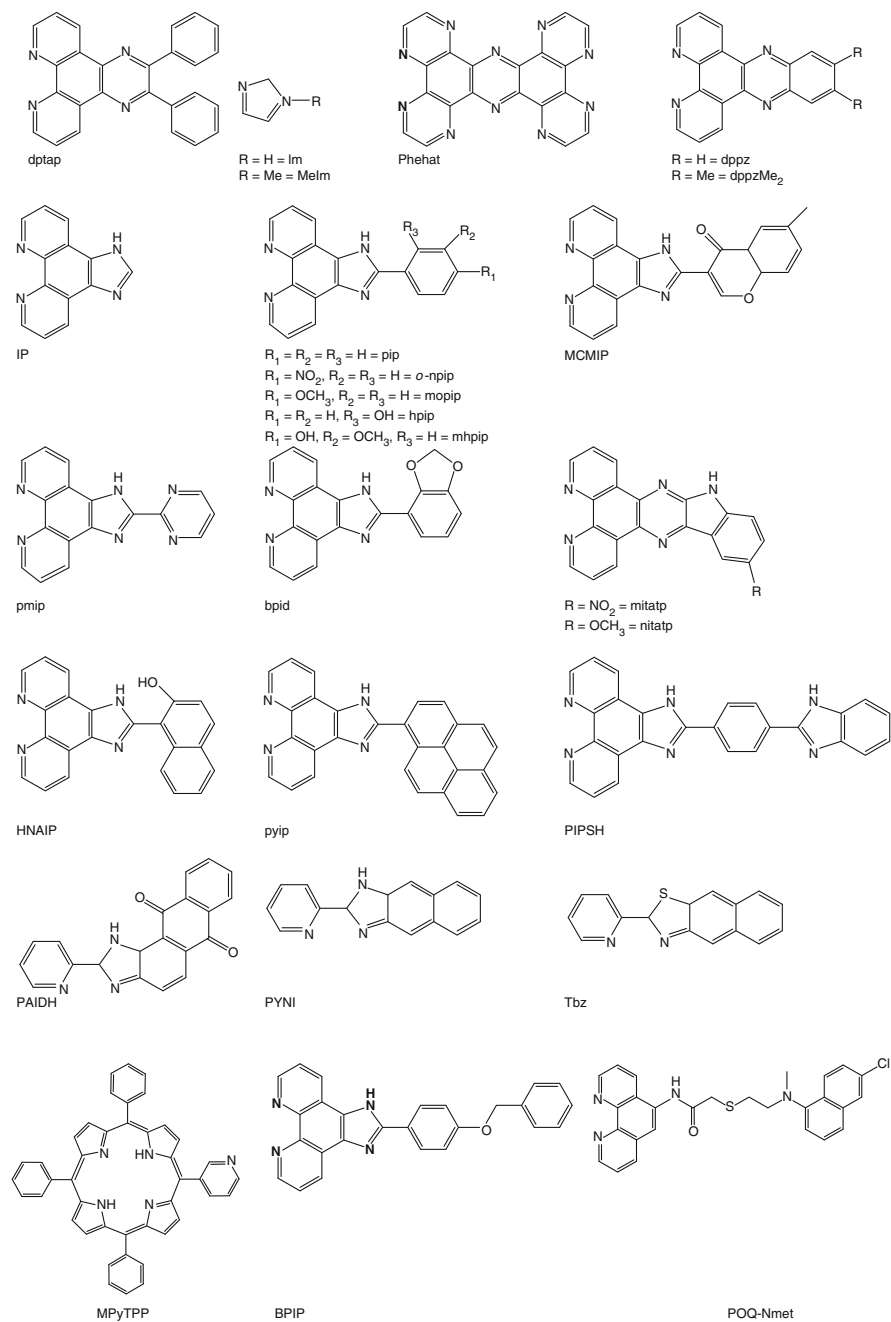
Fig. 2.3 (continued)

Further evidence for minor-groove binding and a preference for purine–purine bases was provided by electrospray ionisation mass spectroscopy using competitive binding experiments involving distamycin and daunomycin, and $[Ru(phen)_2(dpq)]^{2+}$, $[Ru(phen)_2(dpqC)]^{2+}$, $[Ru(phen)_2(dppz)]^{2+}$ and $[Ru(phen)_2(dpqMe_2)]^{2+}$ ($dpqMe_2$ = 2-methyldipyrido[3,2-f:2′,3′-h]-quinoxaline) [121, 122]. The results showed the displacement of distamycin molecules by $[Ru(phen)_2(dpqC)]^{2+}$, $[Ru(phen)_2(dppz)]^{2+}$ or $[Ru(phen)_2(dpqMe_2)]^{2+}$, suggesting that these complexes share at least some of the same binding sites as daunomycin.

Recently, differential quenching studies with minor- and major-groove quenchers and time-resolved luminescence studies reported that $[Ru(phen)_2(dppz)]^{2+}$ binds DNA by intercalation from the minor-groove side, ejecting the mismatched bases into the major groove, indicating that there is further utility for ruthenium complexes for probing small local distortions in the structure of DNA [123]. Luminescence data show a similar correlation with mismatch instability, suggesting that $[Ru(bpy)_2(dppz)]^{2+}$ may bind via insertion of the dppz ligand from the minor groove in a similar fashion. This may cause one or both bases to be ejected into the major groove. The luminescence produced through interactions with these mismatched sites is most likely because insertion into the minor groove allows for deeper binding. In the presence of a DNA mismatch, Δ-$[Ru(phen)_2(dppz)]^{2+}$ shows an increase in the long-lived excited-state lifetime. This observation is consistent with binding through intercalation in the smaller minor groove, where the complex is expected to be more deeply held and more protected. For Λ-$[Ru(phen)_2(dppz)]^{2+}$, little difference is evident with the mismatch.

2.3.3 Achieving Sequence Selectivity and High Affinity

A wide range of complexes has been synthesised, where the intercalator and other ligands have been varied in the pursuit of complexes that have high binding affinity and sequence selectivity. Trends in binding constants, K_b, for ruthenium(II) complexes are reported in Table 2.1. Small variations in K_b are apparent when different spectroscopic techniques have been used for the same compound. Salt concentration has a significant effect on the binding affinity: low salt concentrations (0–20 mM) are applicable for complexes that have a low affinity, exhibiting almost purely electrostatic interactions. Higher salt concentrations (50–100 mM) are required to measure binding constants that range from ~10^5 to 10^8. The constants will also show some temperature dependence, but temperatures have not been consistently cited in the literature, in many cases this can only be assumed to be ambient as no details are given, this has thermodynamic implications and is one likely reason for the variation in binding constants.

To achieve greater sequence selectivity a number of research groups has attached single amino acids and short peptides to metal complexes. The complex,

Table 2.1 Binding constants for ruthenium complexes

Complex	$K_b \times 10^4$	Technique	DNA	Buffer	Ref.
rac-[Ru(bpy)₂(phen)]²⁺	0.06	Absorption	Calf thymus	10 mM Tris, 50 mM NaCl, pH 7.0 at 25 °C	[130]
rac-[Ru(bpy)₂(acphen)]²⁺	0.064	Absorption	Calf thymus	10 mM Tris, 50 mM NaCl, pH 7.0 at 25 °C	[130]
rac-[Ru(bpy)₃]²⁺	0.07	Dialysis	Calf thymus	5 mM Tris, 50 mM NaCl, pH 7.5 at 25 °C	[131]
rac-[Ru(bpy)₂(phen)]²⁺	0.07	Dialysis	Calf thymus	5 mM Tris, 50 mM NaCl, pH 7.5 at 25 °C	[131]
rac-[Ru(bpy)₂(DIP)]²⁺	0.17	Dialysis	Calf thymus	5 mM Tris, 50 mM NaCl, pH 7.5 at 25 °C	[131]
rac-[Ru(bpy)₂(acphen)]²⁺	0.71	Luminescence	Calf thymus	10 mM Tris, pH 7.0 at 25 °C	[131]
rac-[Ru(bpy)₂(phen)]²⁺	0.84	Luminescence	Calf thymus	10 mM Tris, pH 7.0 at 25 °C	[130]
rac-[Ru(4,7-dmp)(bdip)]²⁺	1.15	Absorption	Calf thymus	5 mM Tris, 50 mM NaCl, pH 7.2 at r.t.	[132]
rac-[Ru(bpy)₂(POQ-Nmet)]²⁺	1.32	Absorption	Calf thymus	10 mM Tris, 50 mM NaCl, pH 7.0 at 25 °C	[130]
rac-[Ru(4,4-dmb)₂(MCMIP)]²⁺	2.0	Absorption	Calf thymus	5 mM Tris, 50 mM NaCl, pH 7.2 at r.t.	[133]
rac-[Ru(bpy)₂(pmip)]²⁺	2.03	Absorption	Calf thymus	5 mM Tris, 50 mM NaCl, pH 7.2 at r.t.	[134]
rac-[Ru(bpy)₂(BPIP)]²⁺	2.97	Absorption	Calf thymus	5 mM Tris, 50 mM NaCl, pH 7.2 at r.t.	[135]
rac-[Ru(bpy)₂(bdip)]²⁺	3.25	Absorption	Calf thymus	5 mM Tris, 50 mM NaCl, pH 7.2 at r.t.	[132]
rac-[Ru(bpy)₂(dptatp)]²⁺	3.8	Absorption	Calf thymus	5 mM Tris, 50 mM NaCl, pH 7.0 at r.t.	[136]
rac-[Ru(bpy)₂(dptatp)]²⁺	3.8	Absorption	Calf thymus	5 mM Tris, 50 mM NaCl, pH 7.0 at r.t.	[137]
rac-[Ru(bpy)₂(dpq)]²⁺	4.7	Absorption	Calf thymus	5 mM Tris, 50 mM NaCl, pH 7.2 no temp given	[138]
rac-[Ru(bpy)₂(phi)]²⁺	4.8	Absorption	Calf thymus	5 mM Tris, 50 mM NaCl, pH 7.5 at 25 °C	[131]
rac-[Ru(bpy)₂(dpq)]²⁺	5.9	Luminescence	Calf thymus	20 mM phosphate, 10 mM NaCl, pH 7.85 no temp given	[60]
rac-[Ru(bpy)₂(atatp)]²⁺	7.6	Absorption	Calf thymus	5 mM Tris, 50 mM NaCl, pH 7.2 at r.t.	[137]
rac-[Ru(bpy)₂(HNAIP)]²⁺	8.4	Absorption	Calf thymus	5 mM Tris, 50 mM NaCl, pH 7.2 at r.t.	[139]
rac-[Ru(bpy)₂(dpqC)]²⁺	8.5	Luminescence	Calf thymus	20 mM phosphate, 10 mM NaCl, pH 7.85 no temp given	[60]
rac-[Ru(bpy)₂(POQ-Nmet)]²⁺	11.3	Luminescence	Calf thymus	10 mM Tris, pH 7.0 at 25 °C	[130]
rac-[Ru(bpy)₂(phi)]²⁺	16.0	Dialysis	Calf thymus	5 mM Tris, 50 mM NaCl, pH 7.5 at 25 °C	[131]
rac-[Ru(bpy)₂(taptp)]²⁺	17	Absorption	Calf thymus	5 mM Tris, 50 mM NaCl, pH 7.0 at r.t.	[136]
rac-[Ru(bpy)₂(taptp)]²⁺	17	Absorption	Calf thymus	5 mM Tris, 50 mM NaCl, pH 7.0 at r.t.	[137]
rac-[Ru(bpy)₂(PIP)]²⁺	47	Absorption	Calf thymus	5 mM Tris, 50 mM NaCl, pH 7.2 at r.t.	[139]
rac-[Ru(bpy)₂(pmip)]²⁺	51.3	Absorption	Calf thymus	5 mM Tris, 50 mM NaCl, pH 7.0 at r.t.	[140]
rac-[Ru(bpy)₂(PAIDH)]²⁺	51.9	Absorption	Calf thymus	5 mM Tris, 50 mM NaCl, pH 7.0 at r.t.	[141]
Λ-[Ru(bpy)₂(pyip)]²⁺	82	Absorption	Calf thymus	5 mM Tris, 50 mM NaCl, pH 7.0 at r.t.	[142]
rac-[Ru(bpy)₂(pyip)]²⁺	87	Absorption	Calf thymus	5 mM Tris, 50 mM NaCl, pH 7.0 at r.t.	[142]
rac-[Ru(bpy)₂(appo)]²⁺	100	Absorption	Calf thymus	5 mM Tris, 50 mM NaCl, pH 7.0 at r.t.	[143]

rac-[Ru(bpy)₂(dppz)]²⁺	>100	Luminescence	Calf thymus	20 mM phosphate, 10 mM NaCl, pH 7.85 no temp given	[60]
rac-[Ru(bpy)₂(dppz)]²⁺	>100	Absorption	Calf thymus	5 mM Tris, 50 mM NaCl, pH 7.1 at 25 °C	[89]
rac-[Ru(bpy)₂(idpq)]²⁺	170	Absorption	Calf thymus	5 mM Tris, 50 mM NaCl, pH 7.0 no temp given	[144]
rac-[Ru(bpy)₂(MDPZ)]²⁺	210	Absorption	Calf thymus	5 mM Tris, 50 mM NaCl, pH 7.2 at r.t.	[145]
rac-[Ru(bpy)₂(PIPSH)]²⁺	230	Absorption	Calf thymus	5 mM Tris, 50 mM NaCl, pH 7.0 no temp given	[116]
rac-[Ru(4,4-dmb)₂(dppz)]²⁺	450	Absorption	Calf thymus	50 mM Tris, 50 mM NaCl, pH 7.2 at r.t.	[146]
rac-[Ru(bpy)₂(dppz)]²⁺	500	Absorption	Calf thymus	5 mM phosphate, 50 mM NaCl, pH 7.2 at r.t.	[146]
rac-[Ru(bpy)₂(mitatp)]²⁺	838	Absorption	Calf thymus	5 mM Tris, 50 mM NaCl, pH 7.0 at r.t.	[147]
rac-[Ru(bpy)₂(dppMe₂)]²⁺	880	Luminescence	Calf thymus	20 mM phosphate, 10 mM NaCl, pH 7.85 no temp given	[60]
rac-[Ru(bpy)₂(PIPNH)]²⁺	930	Absorption	Calf thymus	5 mM Tris, 50 mM NaCl, pH 7.0 no temp given	[116]
rac-[Ru(bpy)₂(nitatp)]²⁺	1,070	Absorption	Calf thymus	5 mM Tris, 50 mM NaCl, pH 7.0 at r.t.	[147]
rac-[Ru(HAT)₂(phen)]²⁺	0.56	Luminescence	Calf thymus	10 mM Tris, 50 mM NaCl, pH 7.0 at r.t.	[148]
rac-[Ru(DIP)₂(phen)]²⁺	1.01	Dialysis	Calf thymus	5 mM Tris, 50 mM NaCl, pH 7.5 at 25 °C	[131]
rac-[Ru(phi)₂(bpy)]²⁺	1.76	Dialysis	Calf thymus	5 mM Tris, 50 mM NaCl, pH 7.5 at 25 °C	[131]
rac-[Ru(phi)₂(bpy)]²⁺	2.42	Absorption	Calf thymus	5 mM Tris, 50 mM NaCl, pH 7.5 at 25 °C	[131]
rac-[Ru(bpy)(BPG)₂]²⁺	2.87	Absorption	Calf thymus	5 mM phosphate, 50 mM NaCl, pH 7.2 at 25 °C	[149]
rac-[Ru(dpq)₂(BPG)]²⁺	3.14	Absorption	Calf thymus	5 mM phosphate, 50 mM NaCl, pH 7.2 at 25 °C	[149]
rac-[Ru(dppz)₂(BPG)]²⁺	6.19	Absorption	Calf thymus	5 mM phosphate, 50 mM NaCl, pH 7.2 at 25 °C	[149]
rac-[Ru(phen)(BPG)₂]²⁺	9.14	Absorption	Calf thymus	5 mM phosphate, 50 mM NaCl, pH 7.2 at 25 °C	[149]
rac-[Ru(NH₃)₅(dppz)]²⁺	18	Absorption	Calf thymus	5 mM phosphate, pH 7.2 at 25 °C	[150]
rac-[Ru(HAT)₂(phen)]²⁺	24	Luminescence	Calf thymus	10 mM Tris, pH 7.0 at r.t.	[148]
rac-[Ru(HAT)₂(phen)]²⁺	38	Luminescence	[poly(dA-dT)]₂	10 mM Tris, pH 7.0 at r.t.	[148]
rac-[Ru(tbz)₂(dppz)]²⁺	210	Absorption	Calf thymus	5 mM Tris, 50 mM NaCl, pH 7.0 at r.t.	[151]
rac-[Ru(phen)₂(MPyTPP)]	302	Absorption	Q-d(TTAGGG)	20 mM Tris, 100 mM KCl, pH 7.5 at r.t.	[152]
rac-[Ru(phen)₃]²⁺	0.55	Absorption	Calf thymus	5 mM Tris, 50 mM NaCl, pH 7.5 at 25 °C	[131]
rac-[Ru(phen)₃]²⁺	0.62	Dialysis	Calf thymus	5 mM Tris, 50 mM NaCl, pH 7.1 at r.t.	[21]
rac-[Ru(phen)₃]²⁺	0.79	Absorption	Calf thymus	5 mM Tris, 50 mM NaCl, pH 7.1 at r.t.	[153]
rac-[Ru(phen)₃]²⁺	0.31	Dialysis	Calf thymus	5 mM Tris, 50 mM NaCl, pH 7.5 at 25 °C	[131]
Δ-[Ru(phen)₃]²⁺	0.97	Luminescence	Calf thymus	5 mM Tris, 50 mM NaCl, pH 7.0 at 20 °C	[97]
Δ-[Ru(phen)₃]²⁺	4.9	Luminescence	Calf thymus	5 mM Tris, 10 mM NaCl, pH 7.1 at 20 °C	[97]
Δ-[Ru(phen)₃]²⁺	5.5ᵇ	DNA Melting	Calf thymus	2 mM phosphate, 0.25 mM EDTA, pH 7	[101]
Λ-[Ru(phen)₃]²⁺	1.07	Luminescence	Calf thymus	5 mM Tris, 50 mM NaCl, pH 7.0 at 20 °C	[97]

(continued)

Table 2.1 (continued)

Complex	$K_b \times 10^4$	Technique	DNA	Buffer	Ref.
Λ-[Ru(phen)$_3$]$^{2+}$	2.8	Luminescence	Calf thymus	5 mM Tris, 10 mM NaCl, pH 7.1 at 20 °C	[97]
Λ-[Ru(phen)$_3$]$^{2+}$	6.7^b	DNA Melting	Calf thymus	2 mM phosphate, 0.25 mM EDTA, pH 7	[101]
rac-[Ru(5-NO$_2$-phen)$_3$]$^{2+}$	0.10	Dialysis	Calf thymus	5 mM Tris, 50 mM NaCl, pH 7.5 at 25 °C	[131]
rac-[Ru(phen)$_2$(flone)]$^{2+}$	0.21	Dialysis	Calf thymus	5 mM Tris, 50 mM NaCl, pH 7.5 at 25 °C	[131]
rac-[Ru(phen)$_2$(bpy)]$^{2+}$	0.24	Dialysis	Calf thymus	5 mM Tris, 50 mM NaCl, pH 7.5 at 25 °C	[131]
rac-[Ru(phen)$_2$(DIP)]$^{2+}$	0.25	Dialysis	Calf thymus	5 mM Tris, 50 mM NaCl, pH 7.5 at 25 °C	[131]
rac-[Ru(phen)$_2$(phendo)$_2$]$^{2+}$	0.29	Absorption	Calf thymus	5 mM Tris, 50 mM NaCl, pH 7.1 at r.t.	[153]
rac-[Ru(phen)$_2$(BPG)]$^{2+}$	0.39	Absorption	Calf thymus	5 mM phosphate, 50 mM NaCl, pH 7.2 at 25 °C	[149]
rac-[Ru(phen)$_2$(bpy)]$^{2+}$	0.46	Absorption	Calf thymus	5 mM Tris, 50 mM NaCl, pH 7.5 at 25 °C	[131]
rac-[Ru(2,9-Me$_2$phen)$_2$(MCMIP)]$^{2+}$	0.54	Absorption	Calf thymus	5 mM Tris, 50 mM NaCl, pH 7.2 at r.t.	[133]
rac-[Ru(phen)$_2$(DIP)]$^{2+}$	1.12	Absorption	Calf thymus	5 mM Tris, 50 mM NaCl, pH 7.5 at 25 °C	[131]
rac-[Ru(2,9-Me$_2$phen)$_2$(pmip)]$^{2+}$	1.17	Absorption	Calf thymus	5 mM Tris, 50 mM NaCl, pH 7.2 at r.t.	[134]
rac-[Ru(phen)$_2$(p-MOPIP)]$^{2+}$	2.0	Absorption	Calf thymus	5 mM Tris, 50 mM NaCl, pH 7.0 at r.t.	[154]
rac-[Ru(phen)$_2$(dptatp)]$^{2+}$	2.0	Absorption	Calf thymus	5 mM Tris, 50 mM NaCl, pH 7.0 at r.t.	[137]
rac-[Ru(2,9-Me$_2$phen)$_2$(PYNI)]$^{2+}$	2.73	Absorption	Calf thymus	5 mM Tris, 50 mM NaCl, pH 7.2 no temp given	[155]
rac-[Ru(phen)$_2$(MHPIP)]$^{2+}$	3.4	Absorption	Yeast tRNA	5 mM Tris, 50 mM NaCl, pH 7.0 at r.t.	[156]
rac-[Ru(phen)$_2$(BPIP)]$^{+}$	3.96	Absorption	Calf thymus	5 mM Tris, 50 mM NaCl, pH 7.2 at r.t.	[135]
rac-[Ru(phen)$_2$(phi)]$^{2+}$	4.6	Dialysis	Calf thymus	5 mM Tris, 50 mM NaCl, pH 7.5 at 25 °C	[131]
rac-[Ru(phen)$_2$(phi)]$^{2+}$	4.68	Absorption	Calf thymus	5 mM Tris, 50 mM NaCl, pH 7.5 at 25 °C	[131]
rac-[Ru(phen)$_2$(PYNI)]$^{2+}$	5.35	Absorption	Calf thymus	5 mM Tris, 50 mM NaCl, pH 7.2 no temp given	[155]
rac-[Ru(phen)$_2$(pmip)]$^{2+}$	5.70	Absorption	Calf thymus	5 mM Tris, 50 mM NaCl, pH 7.2 at r.t.	[134]
rac-[Ru(phen)$_2$(taptp)]$^{2+}$	6.4	Absorption	Calf thymus	5 mM Tris, 50 mM NaCl, pH 7.0 at r.t.	[137]
rac-[Ru(phen)$_2$(p-HPIP)]$^{2+}$	6.9	Absorption	Calf thymus	5 mM Tris, 50 mM NaCl, pH 7.0 at r.t.	[154]
rac-[Ru(phen)$_2$(atatp)]$^{+}$	8.8	Absorption	Calf thymus	5 mM Tris, 50 mM NaCl, pH 7.2 no temp given	[157]
rac-[Ru(phen)$_2$(p-NPIP)]$^{2+}$	15.6	Absorption	Calf thymus	5 mM Tris, 50 mM NaCl, pH 7.0 at r.t.	[154]
rac-[Ru(2,9-Me$_2$phen)$_2$ (PAIDH)]$^{2+}$	17.3	Absorption	Calf thymus	5 mM Tris, 50 mM NaCl, pH 7.0 at r.t.	[141]
rac-[Ru(phen)$_2$(PAIDH)]$^{2+}$	20.3	Absorption	Calf thymus	5 mM Tris, 50 mM NaCl, pH 7.0 at r.t.	[141]
rac-[Ru(phen)$_2$(HPIP)]$^{2+}$	65	Absorption	Calf thymus	5 mM Tris, 50 mM NaCl, pH 7.2 at r.t.	[139]
rac-[Ru(phen)$_2$(pmip)]$^{2+}$	66.4	Absorption	Calf thymus	5 mM Tris, 50 mM NaCl, pH 7.0 at r.t.	[140]
rac-[Ru(phen)$_2$(dpqMe$_2$)]$^{2+}$	130	Luminescence	Salmon sperm	50 mM Tris, pH 7.1 no temp given	[158]
Λ-[Ru(phen)$_2$(dppz)]$^{2+}$	170	Luminescence	Calf thymus	5 mM Tris, 50 mM NaCl, pH 7.1 at 20 °C.	[107]

rac-[Ru(2,9-Me$_2$phen)$_2$(dppz)]$^{2+}$	230	Absorption	Calf thymus	50 mM Tris, 50 mM NaCl, pH 7.2 at r.t.	[146]
Δ-[Ru(phen)$_2$(phehat)]$^{2+}$	250	Absorption	Calf thymus	1 mM Tris, 10 mM NaCl, pH 7 at r.t.	[62]
rac-[Ru(phen)$_2$(dpqMe)]$^{2+}$	260	Luminescence	Salmon sperm	50 mM Tris, pH 7.1 no temp given	[158]
Δ-[Ru(phen)$_2$(dppz)]$^{2+}$	320	Luminescence	Calf thymus	5 mM Tris, 50 mM NaCl, pH 7.1 at 20 °C.	[107]
rac-[Ru(phen)$_2$(idpq)]$^{2+}$	400	Absorption	Calf thymus	5 mM Tris, 50 mM NaCl, pH 7.0 no temp given	[144]
rac-[Ru(phen)$_2$(dpq)]$^{2+}$	410	Luminescence	Salmon sperm	50 mM Tris, pH 7.1 no temp given	[158]
[Ru(Im)$_4$(dppz)]$^{2+}$	250	Absorption	Calf thymus	55 mM Tris, 50 mM NaCl, pH 7.2 no temp given	[159]
[Ru(MeIm)$_4$(dpq)]$^{2+}$	1.2	Absorption	Calf thymus	5 mM Tris, 50 mM NaCl, pH 7.2 no temp given	[138]
[Ru(MeIm)$_4$(dppz)]$^{2+}$	110	Absorption	Calf thymus	5 mM Tris, 50 mM NaCl, pH 7.2 no temp given	[159]
rac-[Ru(phen)(dppz)(bpy-GYA^a)]$^{2+}$	300	Luminescence	Calf thymus	10 mM phosphate, 100 mM NaCl, pH 7 no temp given	[129]
rac-[Ru(phen)(dppz)(bpy-KAK^a)]$^{2+}$	500	Luminescence	Calf thymus	10 mM phosphate, 100 mM NaCl, pH 7 no temp given	[129]
rac-[Ru(phen)(dppz)(bpy-KYK^a)]$^{2+}$	900	Luminescence	Calf thymus	10 mM phosphate, 100 mM NaCl, pH 7 no temp given	[129]
rac-[Ru(IP)2(dppz)]$^{2+}$	2,100	Absorption	Calf thymus	5 mM Tris, 50 mM NaCl, pH 7.0 at r.t.	[146]

^{a}GYA, KAK, KYK are conjugated peptides

^{b}Note that these values are slightly higher than the binding constants determined by more traditional methods at room temperature, a finding consistent with our conclusion that the binding enthalpy is of positive sign and small in magnitude

[Ru(terpy)4-CO$_2$H-4′-Mebpy-Gly-*L*-His-*L*-LysCONH$_2$)Cl]$^+$, synthesised on solid phase [50, 65, 94, 103, 124–129], was reported to be highly soluble in water, with the chloro group being displaced by water after several hours. Interactions of the complex with DNA were studied, and the results demonstrated that the complex bound coordinatively to DNA, preferring guanine and cytosine residues [125].

Following comprehensive investigation of mononuclear metal complexes, it is evident that improved DNA sequence specificity and binding affinity can only be achieved through the synthesis of multinuclear molecules. The exploitation of intermolecular interactions will also be a crucial factor in the design LD new complexes that can target longer sequences of DNA.

2.3.4 *Dinuclear Ruthenium(II) Complexes*

Multinuclear complexes of ruthenium(II) and (III) have been studied comprehensively as a consequence of their electrochemical and spectroscopic properties [139]. These are examples of the increasing numbers of dinuclear complexes that can be used as DNA probes [36, 41, 59, 87, 111, 160–175]. For example, dimers of rhodium (III) complexes such as [Rh(bpy)$_2$(phi)]$^{3+}$ (phi = 9,10-phenanthrenequinone diimine) and[Rh(phi)$_2$(bpy)]$^{3+}$ have also been found to show some DNA recognition. Dimers of Δ-[Rh(4,4′-diphenylbpy)$_2$(phi)]$^{3+}$ (4,4′-diphenylbpy = 4,4′-diphenyl-2,2′-bipyridine) specifically targeted the palindromic DNA sequence 5′-CTCTAGAG-3′ [98, 102, 104]. These rhodium(III) complexes demonstrated the significance of shape complementarity for specific binding between the octahedral complexes and DNA. Complexes with sterically bulky methyl or phenyl groups on the non-intercalating ligands showed sequence preferences [98, 102, 104].

The DNA binding affinities of dinuclear ruthenium(II) complexes of the type [{(phen)$_2$Ru}$_2$μ-(Mebpy-4-(CH$_2$)$_n$-4-bpyMe)]$^{4+}$ (Mebpy = 4′-methyl-2,2′-bipyridyl, n = 5, 7, 10, Fig. 2.5), have been examined using photophysical techniques (Table 2.2) [176–178] The mononuclear equivalent, [Ru(bpy)$_2$(4,4′-Me$_2$bpy)]^2 binds weakly to DNA even at low ionic strength, mostly through electrostatic interactions. The dinuclear complexes bind appreciably more strongly, even at high ionic strength [176]. In subsequent work, the terminal bpy ligands were replaced with phen, producing [{(phen)$_2$Ru}$_2$μ-(Mebpy-4-(CH$_2$)$_n$-4-bpyMe)]$^{4+}$ (n = 5, 7, 10), shown in Fig. 2.5 [177]. As a result the binding constant increased about 50-fold compared to the mononuclear complex, and the length of the linking chain was found to be optimal for this series at n = 7 [178].

There have also been investigations of two dinuclear complexes derived from [Ru(phen)$_2$(dppz)]$^{2+}$, namely [{Ru(phen)$_2$}$_2$μ-(11,11′-didppz)$_2$]$^{4+}$ (11,11′-didppz = 11,11′-*bis*-(dipyrido[3,2-*a*:2′,3′-*c*]phenazinyl)), [{Ru(phen)$_2$}$_2$μ-C4(cpdppz)$_2$]$^{4+}$, (C4(cpdppz)$_2$ = *N,N′*-*bis*-(cpdppz) and cpdppz = 12-cyano-12,13-dihydro-11H-8-cyclopenta[*b*]dipyrido[3,2-*h*:2′,3′-*j*]phenazine-12-carbonyl). As shown in Fig. 2.4, the ruthenium ions are joined through the intercalator [179–184]. Using *CD, LD* and

Table 2.2 Binding constants for dinuclear ruthenium complexes

Complex	$K_b \times 10^4$	Technique	DNA	Buffer	Ref
ΔΔ-[{Ru(bpy)₂}₂μ-(11,11'-didppz)₂]⁴⁺	~10⁸	LDTᵃ	Calf thymus	5 mM Tris, 1 mM cacodylate, pH 7.22 at r.t.	[179]
ΛΛ-[{Ru(bpy)₂}₂μ-(11,11'-didppz)₂]⁴⁺	~10⁸	LDT	Calf thymus	5 mM Tris, 1 mM cacodylate, pH 7.22 at r.t.	[179]
ΔΔ-[{Ru(phen)₂}₂μ-(11,11'-didppz)₂]⁴⁺	~10⁸	LDT	Calf thymus	5 mM Tris, 1 mM cacodylate, pH 7.22 at r.t.	[179]
ΛΛ-[{Ru(phen)₂}₂μ-(11,11'-didppz)₂]⁴⁺	~10⁸	LDT	Calf thymus	5 mM Tris, 1 mM cacodylate, pH 7.22 at r.t.	[179]
ΔΔ-[{Ru(phen)₂}₂μ-C4(cpdppz)₂]⁴⁺	1.7 × 10⁶	LDT	Calf thymus	5 mM Tris, 1 mM cacodylate, pH 7.22 at 20 °C	[186]
ΔΔ-[{Ru(phen)₂}₂μ-C4(cpdppz)₂]⁴⁺	8.0 × 10⁶	LDT	Calf thymus	5 mM Tris, 1 mM cacodylate, pH 7.22 at 20 °C	[186]
ΔΔ-[{Ru(phen)₂}₂μ-C4(cpdppz)₂]⁴⁺	4.8 × 10³	LDT	[poly(dA-dT)]₂	5 mM Tris, 1 mM cacodylate, pH 7.22 at 20 °C	[186]
ΛΛ-[{Ru(phen)₂}₂μ-C4(cpdppz)₂]⁴⁺	7.7 × 10⁴	LDT	Calf thymus	5 mM Tris, 1 mM cacodylate, pH 7.22 at 20 °C	[186]
Δ-[Ru(phen)₂(dppz)]²⁺	3.2 × 10²	LDT	Calf thymus	5 mM Tris, 1 mM cacodylate, pH 7.22 at 20 °C	[186]
Λ-[Ru(phen)₂(dppz)]²⁺	1.7 × 10⁴	LDT	Calf thymus	5 mM Tris, 1 mM cacodylate, pH 7.22 at 20 °C	[186]
ΔΔ-[{Ru(Me₂bpy)₂}₂(μ-bpm)]⁴⁺	0.1	NMR	r(CCGGAAUUCCGG)₂	10 mM phosphate, 20 mM NaCl, 0.1 mM EDTA, pH 7.0 at 25 °C	[174]
ΛΛ-[{Ru(Me₂bpy)₂}₂(μ-bpm)]⁴⁺	0.1	NMR	r(CCGGAAUUCCGG)₂	10 mM phosphate, 20 mM NaCl, 0.1 mM EDTA, pH 7.0 at 25 °C	[174]
ΔΔ-[{Ru(Me₂bpy)₂}₂(μ-bpm)]⁴⁺	6	NMR	Bulge r(CCGAGAAUUCCGG)₂	10 mM phosphate, 20 mM NaCl, 0.1 mM EDTA, pH 7.0 at 25 °C	[174]
ΛΛ-[{Ru(Me₂bpy)₂}₂(μ-bpm)]⁴⁺	6	NMR	Bulge r(CCGAGAAUUCCGG)₂	10 mM phosphate, 20 mM NaCl, 0.1 mM EDTA, pH 7.0 at 25 °C	[174]
rac-[{Ru(bpy)₂}₂(μ-btb)]⁴⁺	7.5	Absorption	Calf thymus	5 mM Tris, 50 mM NaCl, pH 7.2 no temp given	[164]
rac-[{Ru(bpy)₂}₂(μ-btapb)]⁴⁺	48	Absorption	Calf thymus	5 mM Tris, 50 mM NaCl, pH 7.2 no temp given	[164]
rac-[{Ru(bpy)₂}₂(μ-bdptb)]⁴⁺	76	Absorption	Calf thymus	5 mM Tris, 50 mM NaCl, pH 7.2 no temp given	[164]
rac-[Ru(bpy)₂(4,4'-Mebpy)]⁴⁺	0.91	Luminescence	Salmon testes	10 mM Phosphate, pH 6.92 no temp given	[176]
rac-[{Ru(bpy)₂}₂(Mebpy-4-(CH₂)₅-4-Mebpy)]⁴⁺	150	Luminescence	Salmon testes	10 mM phosphate, pH 6.92 no temp given	[176]
rac-[{Ru(bpy)₂}₂(Mebpy-4-(CH₂)₇-4-Mebpy)]⁴⁺	78	Luminescence	Salmon testes	10 mM phosphate, pH 6.92 no temp given	[176]
rac-[Ru(phen)₂(4,4'-Mebpy)]⁴⁺	7.5	Luminescence	Salmon testes	10 mM phosphate, pH 6.92 no temp given	[177]
rac-[{Ru(phen)₂}₂(Mebpy-4-(CH₂)₅-4-Mebpy)]⁴⁺	240	Luminescence	Salmon testes	10 mM phosphate, pH 6.92 no temp given	[177]

(*continued*)

Table 2.2 (continued)

Complex	$K_b \times 10^4$	Technique	DNA	Buffer	Ref
rac-[{Ru(phen)$_2$}$_2$(Mebpy-4-(CH$_2$)$_7$-4-Mebpy)]$^{4+}$	360	Luminescence	Salmon testes	10 mM phosphate, pH 6.92 no temp given	[177]
rac-[{Ru(phen)$_2$}$_2$(Mebpy-4-(CH$_2$)$_{10}$-4-Mebpy)]$^{4+}$	300	Luminescence	Salmon testes	10 mM phosphate, pH 6.92 no temp given	[177]
rac-[Ru(dpq)$_2$(phen)]$^{2+}$	5.1	Luminescence	Calf thymus	10 mM phosphate, 100 mM NaCl, 1 mM EDTA, pH 7.02 no temp given	[160]
rac-[{Ru(dpq)$_2$}$_2$(phen-3-SOS-3-phen)]$^{4+}$	3.2×10^3	Luminescence	Calf thymus	10 mM phosphate, 100 mM NaCl, 1 mM EDTA, pH 7.02 no temp given	[160]
rac-[{Ru(dpq)$_2$}$_2$(phen-4-SOS-4-phen)]$^{4+}$	6.3×10^3	Luminescence	Calf thymus	10 mM phosphate, 100 mM NaCl, 1 mM EDTA, pH 7.02 no temp given	[160]
rac-[{Ru(dpq)$_2$}$_2$(phen-5-SOS-5-phen)]$^{4+}$	5.9×10^3	Luminescence	Calf thymus	10 mM phosphate, 100 mM NaCl, 1 mM EDTA, pH 7.02 no temp given	[160]

[a]Luminescence Dilution Titrations
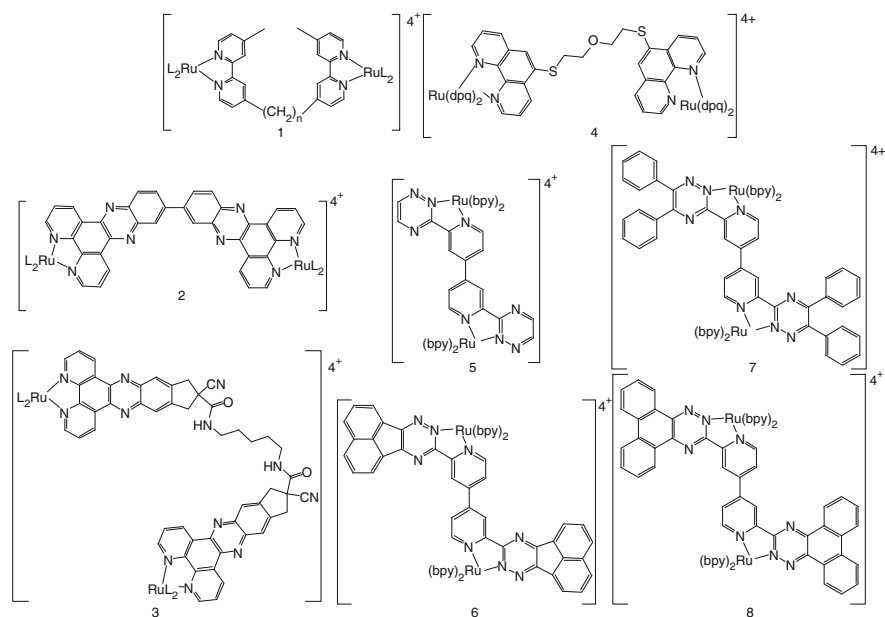
Fig. 2.4 Dinuclear ruthenium complexes (1) [{Ru(L)$_2$}$_2$(μ-Mebpy-4-(CH$_2$)$_n$-4-bpyMe)]$^{4+}$ (where L = bpy or phen and n = 5, 7 or 10), (2) [{Ru(L)$_2$}$_2$μ-(11,11′-didppz)$_2$)]$^{4+}$, (3) [{Ru(L)$_2$}$_2$μ-C4 (cpdppz)$_2$]$^{4+}$, (4) [{Ru(dpq)$_2$}$_2$(phen-5-SOS-5-phen)]$^{4+}$ (5) [{Ru(bpy)$_2$}$_2$(μ-btb)]$^{4+}$, (6) [{Ru(bpy)$_2$}$_2$(μ-bdapb)]$^{4+}$, (7) [{Ru(bpy)$_2$}$_2$(μ-bdptb)]$^{4+}$ and (8) [{Ru(bpy)$_2$}$_2$(μ-btpb)]$^{4+}$

luminescence spectroscopy, all three stereoisomers of [{Ru(phen)$_2$}$_2$-(11,11′-didppz)$_2$)]$^{4+}$, ΔΔ-, ΛΛ- and *meso-* (ΔΛ/ΛΔ-), have been shown to form groove-bound associations with ct-DNA, initially [182]. Binding subsequently reorganises slowly, taking almost a day to reach equilibrium, before intercalation takes place by threading one of the Ru(phen)$_2$ moieties through the DNA [183]. Binding constants were found to be extremely high, ~10^{12} (Table 2.2). The results suggest the following order of binding constants: ΛΛ-bpy ≈ ΔΔ-bpy > ΔΔ-phen > ΛΛ-phen at ~5 × 10^{11} [179, 182]. The subsequent complexes based on [{Ru(phen)$_2$}$_2$μ-C4 (cpdppz)$_2$]$^{4+}$ [179, 182] have been described as threading *bis*-intercalating dimers [180, 183], which exhibit very high DNA binding affinities (Table 2.2) [185]. They act like "molecular staples", with both of the dppz moieties inserted between the base pairs in the same groove of DNA [180].

Dinuclear ruthenium(II) complexes, [{Ru(bpy)$_2$}$_2$(μ-BL)]$^{4+}$, have been prepared using the bridging ligands (BL) 2,2′-*bis*(1,2,4-triazin-3-yl)-4,4′-bipyridine (btb), 2,2′-*bis*(1,2,4-triazino[5,6-f]acenaphthylen-3-yl)-4,4′-bipyridine (btapb), 2,2′-*bis*(5,6-diphenyl-1,2,4-triazin-3-yl)-4,4′-bipyridine (bdptb) [164–166, 187]. These complexes have been shown to intercalate and have binding affinities of from 10^4 to 10^5 (Table 2.2). The ΛΛ-isomer of [{Ru(bpy)$_2$}$_2$(μ-bdptb)]$^{4+}$ exhibited a strong enantiopreference for DNA over the ΔΔ-isomer [165, 187].

Di- and trinuclear helicates have been shown to groove-bind with DNA, and the iron helicate [Fe$_2$L$_3$]$^{4+}$ (where L is (*NE,N′E*)-4,4′-methylene-*bis*(*N*-(pyridin-

2-ylmethylene)aniline)) induces intra-molecular coiling of the DNA [188]. Upon crystallization this helicate was found at the centre of a DNA three-way junction, a finding confirmed by NMR studies [188]. Ruthenium bisazopyridine complexes, [RuL$_2$Cl$_2$], are reported to be very active against cancer cell lines [189]. Other multinuclear mixed-valence complexes of ruthenium and osmium have been synthesised [36], initially for probing the stereochemical influences on intervalence charge transfer transitions [161], but more recently they have been investigated as DNA probes [59, 170]. NMR studies indicate that [{Ru(4,4′-Me$_2$bpy)$_2$(μ-bpm)]^4 (bpm = 2,2′-bipyrimidine) (Fig. 2.2 and Table 2.2) binds in the grooves of B-DNA [190], and displays modest affinity for bulge sites [190] with enantioselectivity [170].

2.3.5 Ruthenium(II)-Arene Anticancer Complexes

Ruthenium(II)-arene complexes are being explored for use in cancer treatment. Ru(II)-arene complexes of the general type [(η^6-arene)Ru(X)(Y)(Z)] have been synthesised and are being studied to elucidate their biological interactions. The general structure of these complexes represents a "piano-stool" configuration with the arene ligand being the seat of the stool and L (neutral chelating ligand/s which can be either mono- or bidentate) being the two legs of the stool (Fig. 2.5). Z is the monoanionic ligand which in most cases [43, 191]. The arene and the X-Y ligands confer stability to the complex while the Z ligand, being a good leaving group, allows complex activation, providing a good binding site for biological molecules. Ruthenium(II) has advantages as it would bring in a different affinity to the binding interaction as compared to the ruthenium(III) complex NAMI-A (NAMI = new anti-tumour metastasis inhibitor; the suffix A denotes the first of a series).
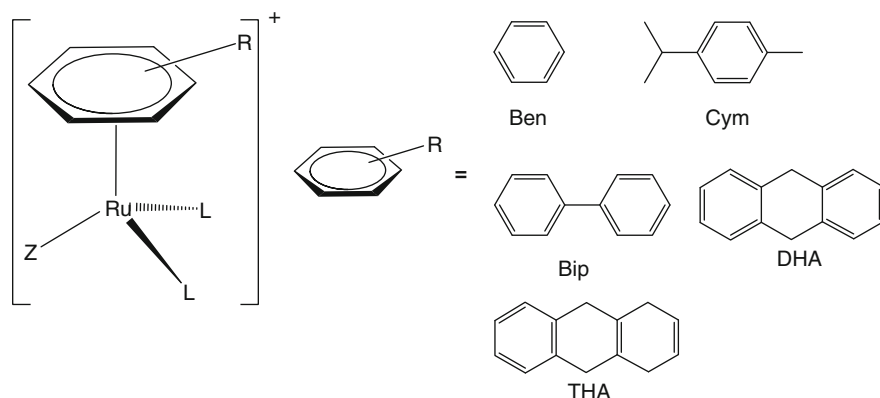
Fig. 2.5 The general chemical "piano-stool" structure of a Ru(II)-arene complex and the different arene molecules that can be complexed to the metal core to alter biological activity

Various Ru(II)-arene complexes, such as [Ru(η^6-cymene)(PTA)(C$_2$O$_4$)] (PTA = 1,3,5-triaza-7-phosphatricyclo[3.3.1.1]decane), [Ru(η^6-cymene)(PTA)(C$_2$H$_6$O$_4$)], [Ru (η^6-cymene)(RAPTA)(Cl$_2$)]   (RAPTA = 1,3,5-triaza-7-phosphatricyclo[3.3.1.1]-decane), [Ru(η^6-benzene)(en)(Cl)]$^+$, (en = 1,2-diaminoethane), [Ru(η^6-p-cymeme) (azpy)Cl]PF$_6$ (azpy = 2-(phenylazo)pyridine), [(η^6-p-cymene)Ru(azpy-NMe$_2$)(Cl)] PF$_6$, [Ru(η^6-bip)(azpy)(Cl)]PF$_6$ (bip = biphenyl) and [Ru(benzene)(DMSO)(Cl$_2$)], have been synthesised [31, 51, 191–193]. These complexes are water soluble and intensely coloured owing to their metal-to-ligand charge-transfer (d^6–π^*) and intraligand (π–π^*) transitions occurring in the visible region (ε of 5,000–63,700 M^{-1} cm^{-1}) [31, 191].

Studies of the biological effects of the Ru(II)-arene complexes have shown [Ru (η^6-benzene)(en)(Cl)]$^+$ to be highly selective towards the TS/A mouse adenocarcinoma cancer cell line, and effective against secondary lung tumours in mice [193]. The complex, [Ru(η^6-benzene)(en)(Cl)]$^+$, however, has its shortcomings as it quickly hydrolyses and therefore needs to be given in a saline solution to overcome the loss of chloride ligands. Hydrolysis is disadvantageous as the by-products formed can be difficult to characterise, and interfere with the clinical evaluation of the complexes. The two PTA analogues [Ru(η^6-cymene)(PTA)(C$_2$O$_4$)] and [Ru(η^6-cymene)(PTA) (C$_2$H$_6$O$_4$)] have overcome this problem, as they are highly soluble in water, relatively stable and do not easily hydrolyse. More importantly their biological activity is not much altered as they too inhibit cancer cell metastases and display similar DNA binding characteristics to their [Ru(η^6-benzene)(en)(Cl)]$^+$ counterpart [27].

Gopal et al. have reported that [Ru(η^6-benzene)(DMSO)(Cl)$_2$] completely inhibits the activity of topoisomerase II by binding bi-directionally to DNA and topoisomerase II to form a metal-cleavage complex [194]. They postulated that the interaction of the metal complex with the biological molecules was similar to that of 2,2′-bipyridyl complexes of ruthenium(II). This was further explained by pointing out that intercalation was not possible as the benzene ring (arene ligand) which is bound to the ruthenium metal is prevented from π-stacking. They have also suggested that the metal may interact directly with DNA through covalent bonding with the nucleotide bases.

Studies conducted by the Sadler group have shown that in the A2780 human ovarian cancer cell line, the complex [Ru(η^6-benzene)(en)(Cl)]$^+$ displayed anticancer activity. The anticancer activity of the complex was improved as the size of the arene was increased in the order benzene <p-cymene (Cym) <biphenyl (bip) <dihydroanthracene (DHA) <tetrahydroanthracene (THA) [31, 51, 191].

The Ru(II)-arene complex of [Cl(terpy)(Me$_4$phen)Ru]$^+$ (terpy = 2,2′;6′,2″-terpyridine and Me$_4$phen = 3,4,7,8-tetramethylphenanthroline has been seen to bind to DNA purine bases and inhibit cell proliferation [108, 192]. The lability of the chloride ion allows the complex to be hydrolysed and plays a part in its antitumour activity. A suggested mechanism of action for the Ru(II)-arene type molecules is via the hydrolysis of the chloro ligand. Studies have suggested that the aqua (–OH$_2$) ligand is more reactive than the hydroxo (–OH) ligand. These complexes favour purine over pyrimidine bases. Hydrolysis or aquation allows the complex to bind rapidly to the 5′-phosphate on the DNA helix followed by a rearrangement to give N7-, N1- or N3-bound products [38]. As previously mentioned,

the Sadler group has found that increasing the size of the arene increases anticancer activity of the complex. This suggests that N7 binding is favoured and it happens because of hydrophobic interactions. This shows that the arene ligand, the chloride leaving group and the neutral non-chelating ligands each play an essential part in the function of the molecule.
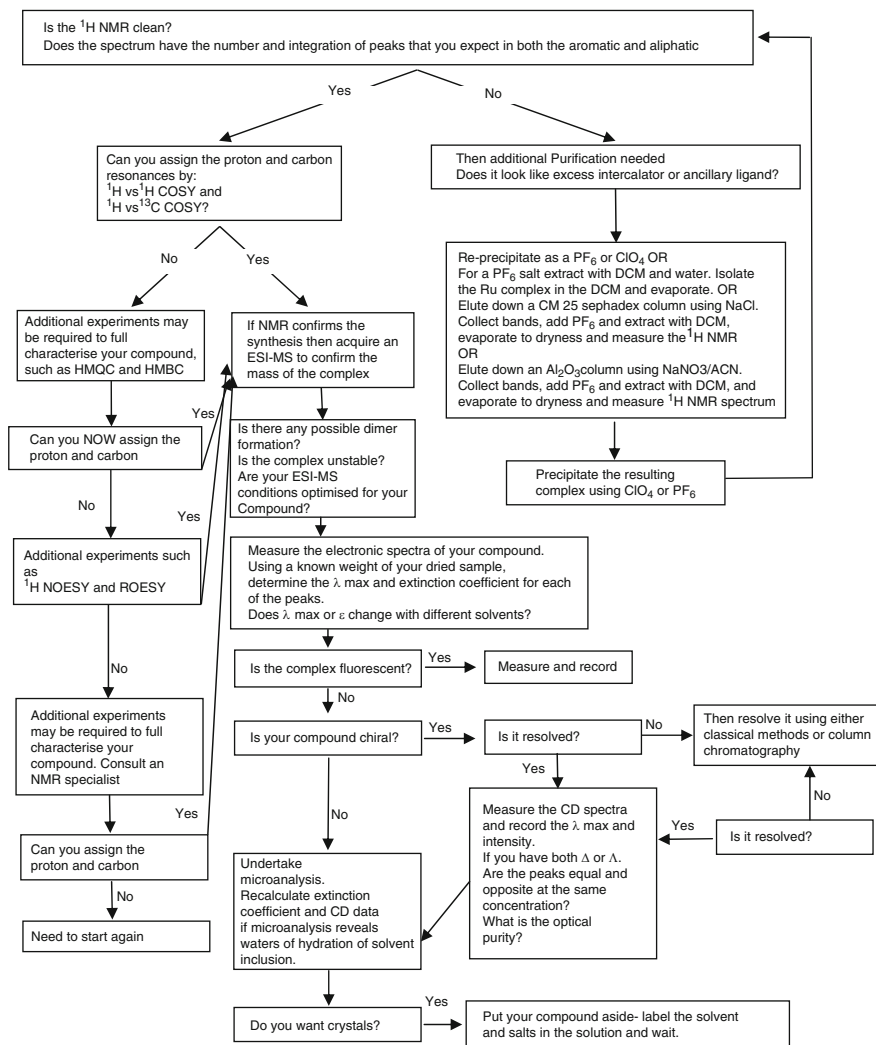
2.4 Synthesis

Ruthenium chemistry has been studied for many potential applications, such as DNA oxidation/reduction agents [38], electron transfer models [96, 195–198], potential chemotherapeutic agents [4, 26–42, 44–49, 51, 169, 175, 191, 199], catalysts for organic reactions [200–205], kinase inhibition [39, 40, 199, 206–219] and for probing DNA [63, 64, 100, 110, 117, 120, 160, 166, 170, 172, 175–178, 190, 220, 221]. Many methods are available for the synthesis, separation and resolution of the stereoisomers of mono-, di- and multinuclear ruthenium complexes. A general process for synthesis, purification and characterisation is shown in Scheme 2.1.

2.4.1 Synthesis of Racemic Mononuclear cis-[Ru(pp)$_2$Cl$_2$]·2H$_2$O Complexes

Mononuclear ruthenium(II) complexes containing bidentate polypyridyl (pp) ligands often use a *cis*-[Ru(pp)$_2$Cl$_2$] precursor which can be isolated in good yield by four general methods. The simplest and most widely used method for the preparation of *cis*-[Ru(pp)$_2$Cl$_2$]·2H$_2$O is by Sullivan et al. [222]. In general the method requires that the polypyridyl ligand and RuCl$_3$.3H$_2$O are refluxed in DMF (*N,N'*-dimethylformamide) in a "one pot" reaction. The "ruthenium blue" method of Togano et al. [99], later modified by Anderson et al. [223], reduces *cis*-[Ru(pp)$_2$Cl$_2$]Cl·2H$_2$O to *cis*-[Ru(pp)$_2$Cl$_2$]·2H$_2$O, forming a blue intermediate during the synthesis. The DMF method of Hua et al. [109]. usually produces a lower yield, but the purity is excellent. Lastly, reactions based on *cis*-[Ru(DMSO)$_4$(Cl)$_2$] [224], in which the polypyridyl ligands are added under mild conditions, are used predominantly when making [Ru(pp)$_3$]Cl$_2$, [Ru(pp)(DMSO)$_2$Cl$_2$] or [Ru(N$_4$-tetradentate)Cl$_2$].

2.4.1.1 Method 1: Sullivan

Polypyridyl ligand (8.6 mmol), RuCl$_3$.3H$_2$O (4.3 mmol) and LiCl (0.47 mol) were combined in DMF (10 mL) and heated at reflux for 48 h. The solution was allowed to cool to room temperature, acetone (500 mL) was added and the solution left to cool in the freezer overnight. The resulting black solid was then collected, washed

Synthetic Scheme 2.1 Synthesis, purification and characterisation protocol for $[Ru(I_L)_2(A_L)]$ precipitated with ClO_4 or PF_6

with acetone, H_2O, ethanol and diethyl ether (each ~50 mL). The resulting product was air dried and then oven dried [222]. Yield ~90%.

2.4.1.2   Method 2: "Ruthenium Blue"

$RuCl_3.3H_2O$ (8.4 mmol) was dissolved in ethanol/H_2O (3:2, 75 mL) and the mixture heated at reflux until a shiny black residue appeared on the surface of the flask and the solution appeared blue (~4 h). The colour of the solution should

change from dark brown to deep blue, via dark green. The solution may stop at dark green without the blue solution being generated. The polypyridyl ligand (21.5 mmol) dissolved in ethanol/HCl (14:1, 110 mL) was added to the hot blue solution and the resulting mixture heated at reflux overnight. The solution was reduced to ~50 mL and filtered. The brown solid was washed with acetone and diethyl ether (each ~50 mL), before being resuspended in HCl (3 M, 1.25 L). $SnCl_2 \cdot 2H_2O$ (1.6 mmol) was added to the mixture and the mixture was boiled for 2.5 h. Upon cooling with ice the brown solid $[Ru(pp)_2Cl_2]$ precipitated, and was collected by filtration, washed with cold H_2O and air dried [99, 223]. Yield ~70%.

2.4.1.3 Method 3: Hua

$RuCl_3 \cdot 3H_2O$ (8.25 mmol) and polypyridyl ligand (13.57 mmol) were refluxed in DMF (65 mL) for 6 h. Solvent volume was reduced to ~30 mL under reduced pressure. Acetone (60 mL) was added and the solution stored at $-20\,^{\circ}C$ overnight. The dark purple precipitate was collected *via* filtration. The solid was dissolved in a 1:1 H_2O/ethanol mixture (270 mL) and refluxed for 1 h. The solution was filtered, and LiCl (0.78 mol) was added to the filtrate. Ethanol was removed by distillation, and the residue was cooled to $0\,^{\circ}C$. The resulting black crystals were collected *via* filtration and washed with cold water (40 mL) [109]. Yield ~40%.

2.4.1.4 Method 4: via cis-[Ru(DMSO)$_4$(Cl)$_2$] [224]

$RuCl_3 \cdot 3H_2O$ (20 mmol) was refluxed in dimethyl sulfoxide (5 mL) for 5 min. The volume was then reduced (2 mL) by rotary evaporation. A yellow precipitate formed upon the addition of acetone (20 mL) which was collected by filtration, washed with acetone and diethyl ether (each ~5 mL), and vacuum dried. Yield ~70%.

A hot mixture of *cis*-[Ru(DMSO)$_4$]Cl$_2$ (1.44 mmol) and polypyridyl ligand (4.3 mmol) in water (200 mL) and ethanol (100 mL) was stirred with heating for 48 h. A saturated solution of ClO_4^- (2 mL) was added to the orange solution and left to stand for 24 h until an orange solid appeared. The product was filtered, washed with water, ethanol and diethyl ether (each ~2 × 20 mL) and recrystallized from a solution of water/acetone (30/70, 200 mL) to yield an orange solid. Yield ~73%.

2.4.2 Synthesis of Racemic Mononuclear Complexes of the Type [Ru(pp)$_2$(pp′)]Cl$_2$·2H$_2$O

In general, the third ligand (pp′) is added to *cis*-[Ru(pp)$_2$Cl$_2$]·2H$_2$O at a 1:1 molar ratio in methanol, ethanol or water. The mixture is heated to reflux until the solution changes colour (often to orange/red) or until the reaction is

completed. TLC testing is ideal for monitoring the progress of the reaction. The product is isolated from the solution by precipitation with PF_6, ClO_4^- or similar counterion.

In a typical experiment, $[Ru(pp)_2Cl_2]$ (0.45 mmol) and pp′ (0.42 mmol) were dissolved in methanol (40 mL) and refluxed for 24 h. The solvent was removed under reduced pressure and redissolved in H_2O (100 mL). The resulting suspension was filtered. Saturated potassium hexafluorophosphate solution (5 mL) was added to the filtrate to induce precipitation. The solution was cooled over ice and filtered. The solid collected was washed with cold H_2O (60 mL). The solid was resuspended in H_2O (50 mL) and stirred over Amberlite IRA-400 (Cl) exchange resin until it had dissolved. The solution was filtered and the solvent removed under reduced pressure, yielding a dark red solid (~85%).

2.4.3 Purification Techniques

Additional purification is sometimes needed to isolate a pure compound. Below are two techniques that we have found to be useful.

2.4.3.1 Extraction with Organic Solvents

$[Ru(pp)_2(pp')](PF_6)_2$ can be extracted with CH_2Cl_2 from water (5 × 200 mL), and the combined extracts dried over anhydrous Na_2SO_4. The resulting solution can then be evaporated to dryness to yield a product purified from water-soluble impurities [225].

2.4.3.2 Column

The crude product of $[Ru(pp)_2(pp')](PF_6)_2$ can be purified on silica gel using eluent solution (89% CH_3CN, 1% saturated KNO_3 solution, 10% H_2O). The fractions containing pure $[Ru(pp)_2(pp')](PF_6)_2$ can be identified by TLC and confirmed by ^1H NMR, combined and extracted with CH_2Cl_2, dried over anhydrous Na_2SO_4, and then evaporated. The isolated $[Ru(pp)_2(pp')](PF_6)_2$ was dissolved in acetone and then precipitated by the addition of H_2O. The complex was collected, isolated by filtration, washed with diethyl ether and air-dried. If required the complex can be subsequently purified by column chromatography on alumina, eluting with CH_3CN. The single fraction is usually collected and evaporated to dryness to yield the product as an orange solid [225].

2.4.4 Characterisation Techniques

NMR spectroscopy is used to determine the structure of almost all organic, inorganic and biological molecules by using the magnetic properties of nuclei of the elements contained within these molecules. Rabi et al. first reported the use of NMR in 1938 [226] followed by Bloch and Purcell who shared the Nobel Prize in 1952 for adapting NMR spectroscopy for deducing the chemical structures of compounds. NMR spectroscopy can be used not only to determine the chemical structures of molecules, but also to deduce their purity. NOESY, COSY (correlation spectroscopy) and ROESY (rotating-frame Overhauser effect spectroscopy) are examples of two-dimensional NMR spectroscopic methods that are used to further characterise a molecule based on the coupling patterns between neighbouring nuclei (see Chap. 5).

2.4.4.1 NMR Spectroscopy

In the case of ruthenium complexes confirmation of coordination is monitored using proton NMR spectroscopy, at least initially. The corresponding chemical shifts and coupling constants for some simple systems are presented in Table 2.3. As might be expected, the spectra for the various ligands are very similar. Resonances attributed to the hydrogen atoms of phen can be assigned with relative ease. Resonances for atoms H(2), H(3) and H(4) are observed at 8.59, 7.85, and 9.14 ppm, respectively, with vicinal coupling constants $J_{2,3} = 4.1$, $J_{3,4} = 8.1$ and $J_{2,4} = 1.7$, respectively. The rest of the ligands can be characterised by the same process, and for each diimine the number of signals is characteristic of the ligand. For example, dpq displays three doublets with a singlet at 9.13 ppm, dppz has five doublets within the 7.90–9.51 ppm range and dppzMe$_2$ displays one fewer aromatic resonance than dppz due to the methyl proton at 2.52 ppm.

The simplicity of the spectrum of each metal complex cation can be attributed to its dihedral (D_3 or C_2) symmetry. This aspect of the complexes' structures allows easy comparisons both between the complexes and with the free ligands. The H(2) proton of phen is displaced upfield from 8.59 to 8.09 ppm upon coordination. This is the only proton that demonstrates any substantial chemical shift. For all of the complexes, the H(2) proton is the most vulnerable to shielding by the relative positioning of the aromatic ring of the other coordinated diimines, leading to a characteristic upfield shift. The assignment of the protons of dppz is more difficult, as five multiplets are seen in the spectrum of the ligand and the ruthenium complex. These multiplets can be attributed to an [AB]$_2$ four-spin system. This type of multiplet pattern is common in fused-ring systems where there are two pairs of protons with the same chemical shifts but different coupling constants J_{AB}, $J_{AA'}$, $J_{AB'}$ and J_{BB}. Their J couplings are insufficiently different to allow unequivocal assignment of chemical shifts. Here a ^{1}H COSY is required to confirm the coupling of these peaks [74].

Table 2.3 ¹H NMR data for the ligands phen, phendo, dpq, dppz and dppzMe₂ and the simple [RuL₃] complexes

Protons	phen L	phen RuL₃	phendo L	phendo RuL₃	dpq L	dpq RuL₃	dppz L	dppz RuL₃	dppzMe₂ L	dppzMe₂ RuL₃
CH₃									2.52 (s,2H)	2.66 (s,2H)
H(3)	7.85ᵃ (ddᵈ,2H)	7.78 (dd,2H)	7.68 (dd,2H)	7.85ᵃ (dd,2H)	7.92 (dd,2H)	7.92 (dd,2H)	7.90 (dd,2H)	7.95ᵃ (dd,2H)	7.91 (dd,2H)	7.89 (dd,2H)
H(11)							8.02 (sm, 2H)	8.19 (sm, 2H)	8.13 (s, 2H)	8.20 (s, 2H)
H(10)					9.13 (s, 2H)	9.38 (s, 2H)	8.35 (sm, 2H)	8.51 (sm, 2H)		
H(5)	8.06 (s,2H)	8.39 (s,2H)								
H(2)	8.59 (d,2H)	8.09ᵉ (d,2H)	8.89 (d,2H)	7.98 (d,2H)	9.22 (d,2H)	8.33 (d,2H)	9.18 (d,2H)	8.38 (d,2H)	9.18 (d,2H)	8.37 (d,2H)
H(4)	9.14 (d,2H)	8.78 (d,2H)	8.39 (d,2H)	8.55 (d,2H)	9.43 (d,2H)	9.55 (d,2H)	9.51 (d,2H)	9.65 (d,2H)	9.52 (d,2H)	9.53 (d,2H)
J Couplings										
$J_{3,4;2,3}$	8.1, 4.4	8.2, 5.2	7.8, 4.7	7.9, 5.7	8.2, 4.4	8.3, 5.8	8.1, 4.4	8.3, 5.5	10.0, 4.4	8.3, 5.4
$J_{7,8;8,8'}$							6.5, 3.4	6.6, 3.4		
$J_{2,3;2,4}$	4.4, 1.7	5.2, 1.1	4.6, 1.8	5.6, 1.3	4.4, 1.8	5.3, 1.2	4.4, 1.8	5.3, 1.1	6.2, 2.2	5.4, 1.3
$J_{3,4;2,4}$	8.1, 1.7	8.2, 1.2	7.8, 1.8	7.9, 1.3	8.2, 1.8	8.3, 1.2	8.1, 1.8	8.3, 1.1	10.6, 2.6	8.3, 1.3

ᵃChemical shifts are in ppm (±0.01) relative to TMS as an internal standard and coupling constants are in Hz (±0.1), ᶜthe solvent was d_6-DMSO in all cases, ᵈs = singlet, d = doublet, dd = doublet of doublets, sm = symmetrical multiple, ᵉthe italicized values illustrate the effect on the H(2) by coordination.

phen

phendo

dpq

R = H = dppz
R = CH₃ = dppz
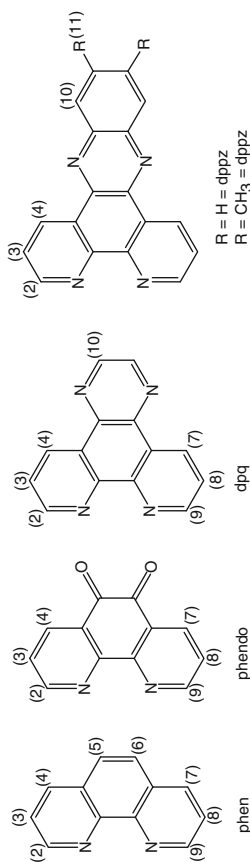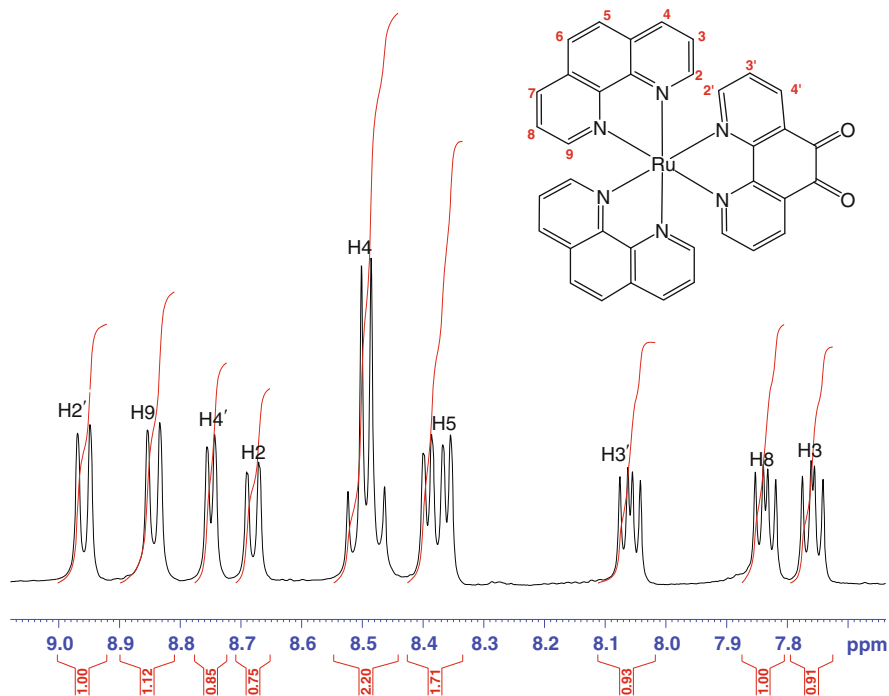
Fig. 2.6 The ^{1}H NMR spectrum of [Ru(phen)$_2$(phendo)](PF$_6$)$_2$ in d_6-acetone

For more complicated structures the method of assignment follows a similar process. As expected, the ^{1}H NMR spectrum of [Ru(phen)$_2$(phendo)](PF$_6$)$_2$ (phendo = 1,10-phenanthroline-5,6-dione) in d_6-acetone shows nine different signals corresponding to the protons in the complex. Since the complex is symmetrical, and some protons are in identical environments, nine signals are produced (Fig. 2.6). A 2D NOESY spectrum (Fig. 2.7) was recorded so that the nine signals could be assigned. From the NOESY spectrum, it can be seen that the protons labelled H2′, H9, H4′ and H2 are doublets as they neighbour only one other proton. Also these signals integrate to 1, confirming that they indeed are single protons.

As expected, the ^{1}H NMR spectrum of [Ru(phen)$_2$(dpq)](PF$_6$)$_2$ in d_6-DMSO shows eight signals corresponding to the protons in the complex (Fig. 2.8). Since this complex is also symmetrical, eight signals are produced. However, some signals (H4, H5/6, H8, H9) integrate to two, showing that these protons are identical in nature. To further assign the protons on the complex, a 2D NOESY spectrum (Fig. 2.9) was recorded. From the NOESY spectrum, it can be seen that protons labelled H4′ and H2′ are doublets as they neighbour only one other proton. The peak at ~9.4 ppm is a singlet and does not give a NOE cross peak, thus allowing us to assign it as H10.
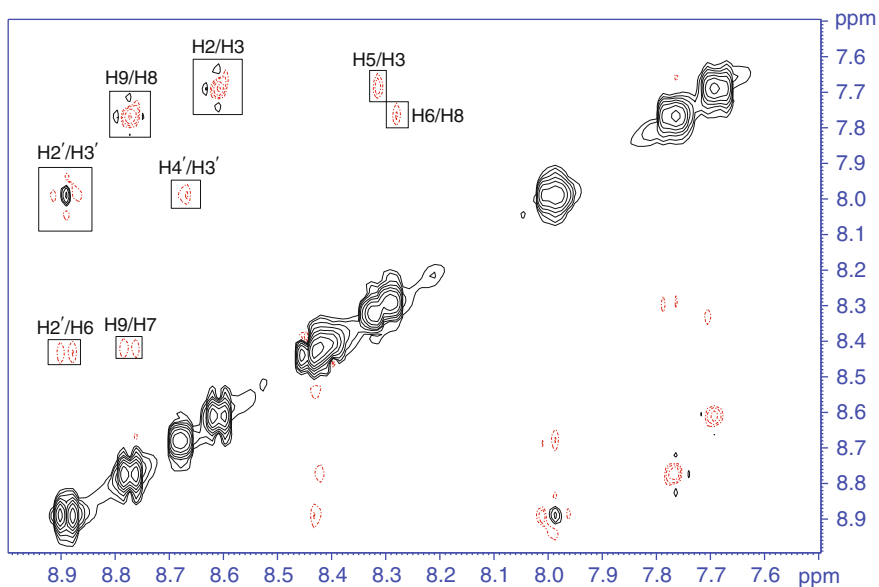
Fig. 2.7 The NOESY spectrum of [Ru(phen)$_2$(phendo)](PF$_6$)$_2$ in d_6-acetone
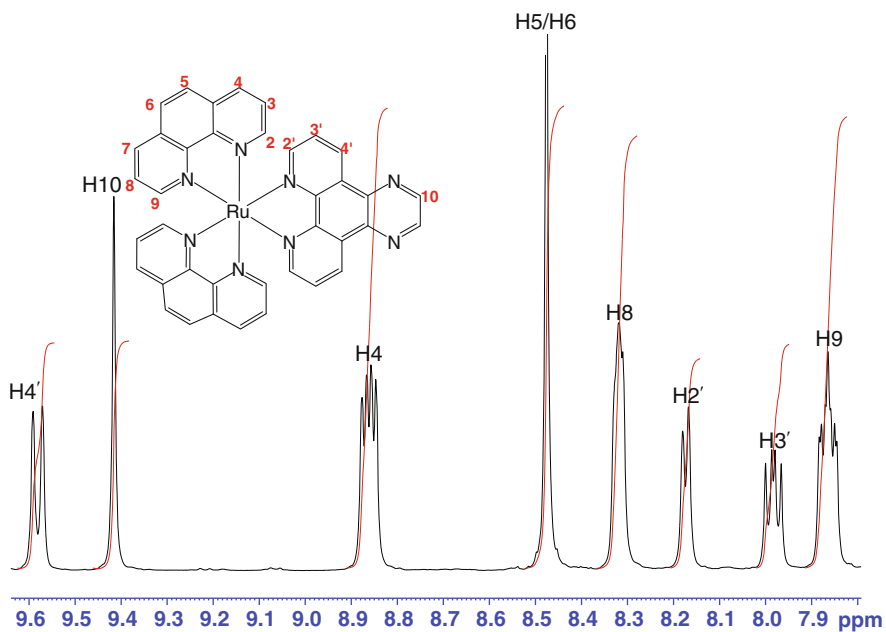
Fig. 2.8 The ^{1}H NMR spectrum of [Ru(phen)$_2$(dpq)](PF$_6$)$_2$ in d_6-DMSO
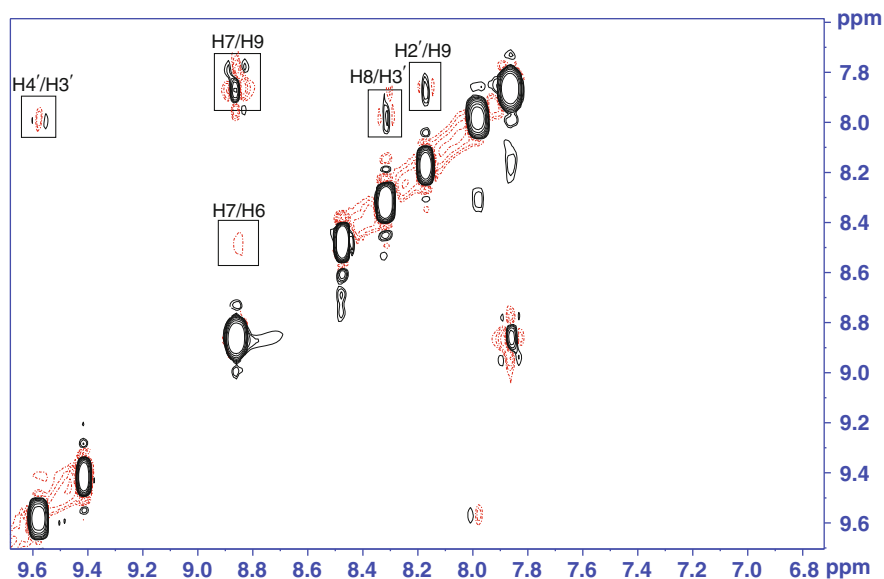
Fig. 2.9 The NOESY spectrum of [Ru(phen)$_2$(dpq)](PF$_6$)$_2$ in d_6-DMSO

2.4.4.2 Crystal Structure Determination

There are many ruthenium polypyridyl structures in the literature, and often the complexes have been isolated by evaporation of an aqueous solution. In some cases the reported structures can be used to confirm that coordination has occurred. For example, the two related structures [Ru(2,9-Me$_2$phen)$_2$(dppz)](PF$_6$)$_2$ [74] and [Ru (phen)$_2$(dpq)](PF$_6$)$_2$ [74] crystallize in the monoclinic space groups $P2_1/n$ and $P2_1/c$, respectively (Fig. 2.10). The crystal structure analysis confirmed that coordination of two 2,9-Me$_2$phen ligands and the dpqz ligand is possible but there is significant steric strain arising from the bulk introduced by the methyl substituents. For instance, the Ru-N(2,9-Me$_2$phen)[2.092(3)–2.125(3) Å] and Ru-N(dpqz)[2.082 (3)–2.084(3) Å] bond lengths are significantly longer than the Ru-N(phen)[2.065 (6)–2.073(6) Å] and Ru-N(dpq)[2.043(5)–2.063(5) Å] bond lengths. In addition, the Me$_2$phen ligands are significantly bowed as a result of interactions between the methyl groups and the nitrogen donor atoms of adjacent ligands.

2.4.4.3 Spectroscopic Techniques

Electronic spectra of ruthenium polypyridyl complexes have been reported in many synthetic and computational papers and a review by Juris et al. [227]. The photochemical and photophysical properties of these complexes have been further reviewed by Campagna et al. [55]. Absorption, *LD*, *CD* and luminescence spectra
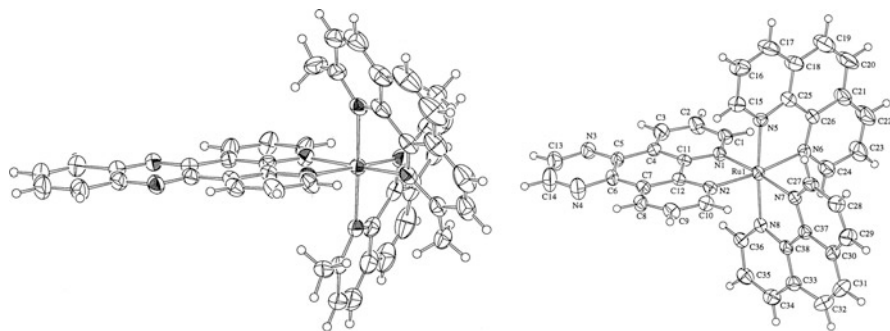
Fig. 2.10 ORTEP diagrams of the two related structures [Ru(2,9-Me$_2$phen)$_2$(dppz)](PF$_6$)$_2$ [74] on the *left* and [Ru(phen)$_2$(dpq)](PF$_6$)$_2$ on the *right* [74]

may provide information about molecular structures, chemical environment (including different modes of DNA binding), and binding constants as shown in Table 2.1 above. Some electronic absorption and *CD* data for a range of complexes are presented in Table 2.4, and a detailed explanation of the experimental methods is given in Chap. 5. Use of the corresponding luminescence spectra is described in Chap. 5.

The absorption spectra of the archetypal complexes [Ru(bpy)$_3$]$^{2+}$ and [Ru (phen)$_3$]$^{2+}$ are shown in Fig. 2.10. The band systems in these spectra have been assigned to electronic transitions that are predominantly metal-centred (MC), ligand-centred (LC) or metal-to-ligand charge-transfer (MLCT) in character. Octahedral Ru(II) complexes are low-spin d^6, corresponding to a $t_{2g}{}^6 e_g{}^0$ configuration ($^1A_{1g}$ symmetry) in the ground electronic state. The first two MC transitions involve excited states of $^1T_{1g}$ and $^1T_{2g}$ symmetry, respectively, giving weak absorption bands at 529 and 386 nm, in [Ru(H$_2$O)$_6$]$^{2+}$, and 390 and 310 nm in [Ru(NH$_3$)$_6$]$^{2+}$ [228, 229]. In symmetric tris-chelate complexes, the ligand environment has D_3 symmetry, and the degeneracy of the t_{2g} orbitals is removed as shown in Fig. 2.12, where they are labelled $\pi_M e$ (doubly degenerate) and $\pi_M a_1$ [227, 230]. The ground electronic state has A_1 symmetry, and the $^1T_{1g}$ and $^1T_{2g}$ excited states are each split into E and A states. In practice, the spectroscopically accessible states are a near-degenerate set of A_2 and E (denoted E_a) states (centred on 370 nm for [Ru(en)$_3$]$^{2+}$) and a higher-energy E (denoted E_b) state (around 348 nm for [Ru(en)$_3$]$^{2+}$) [231]. There is significant mixing between the E_a and E_b states. These states influence the luminescent properties of some complexes, and may produce weak bands in some absorption or *CD* spectra of ruthenium(II) complexes. However, the MC bands of many complexes are typically dominated by more intense LC and MLCT systems that are associated with the polypyridyl. [Ru(en)$_3$]$^{2+}$ is pale-yellow in colour, and the smaller polypyridyl ligands such as phen and bpy are colourless, but as Fig. 2.10 shows, polypyridyl complexes of Ru(II) can have strong and distinctive colours, owing to MLCT transitions.

Polypyridine ligands have filled π-bonding and empty π^*-antibonding orbitals, and σ-type n-orbitals associated with the heteroatoms. The free ligands have a large number of possible electronic transitions at wavelengths above 200 nm, comprising

Table 2.4 Spectrophotometric and optical parameters of Ru(II) complexes

Complex	λ_{max}(MLCT) nm ($\varepsilon M^{-1}cm^{-1}$)[a]	CD Spectra λ nm ($\Delta\varepsilon$ $M^{-1}cm^{-1}$)[a]	Ref
Δ-[Ru(bpy)$_3$]$^{2+}$	451 (14,000)	240 (24), 257 (-12), 278 (149), 292 (-331), 323 (21), 358 (12), 418 (23), 469 (-18)	[237, 238]
Λ-[Ru(bpy)$_3$]$^{2+}$		240 (-23), 257 (12), 278 (-147), 292 (347), 323 (-20), 358 (-12), 418 (-22), 469 (18).	
Δ-[Ru(bpy)$_2$(phen)]$^{2+}$	452 (14,900)	380 (58), 457 (-56)	[237]
Λ-[Ru(bpy)$_2$(phen)]$^{2+}$		380 (-59), 457 (55)	
Δ-[Ru(bpy)$_2$(dpq)]$^{2+}$	449 (14,500)	400 (79), 461 (-67)	[237]
Λ-[Ru(bpy)$_2$(dpq)]$^{2+}$		400 (-81), 461 (66)	
Δ-[Ru(bpy)$_2$(dpqC)]$^{2+}$	451 (16,200)	412 (62), 468 (-54)	[237]
Λ-[Ru(bpy)$_2$(dpqC)]$^{2+}$		412 (-64), 468 (54)	
Δ-[Ru(bpy)$_2$(dppz)]$^{2+}$	448 (16,400)	395 (64), 461 (-58)	[237]
Λ-[Ru(bpy)$_2$(dppz)]$^{2+}$		395 (-70), 461 (58)	
Δ-[Ru(4,4′-DMB)$_3$]$^{2+}$	450 (17,000)	231 (54), 260 (-7), 277 (142), 292 (-351), 328 (18), 367 (11), 424 (21), 477 (-17)	[227, 237]
Λ-[Ru(4,4′-DMB)$_3$]$^{2+}$		231 (-55), 260 (4), 277 (-141), 292 (357), 328 (-18), 367 (-11), 424 (-21), 477 (19)	
Δ-[Ru(bpm)$_3$]$^{2+}$	454 (8,600),	235 ($+51$), 254 ($+45$), 268 (-210), 320 (-19), 411 ($+22$), 468 (-14)	[237, 238]
Λ-[Ru(bpm)$_3$]$^{2+}$	418 (8,200)	235 (-48), 254 (-40), 268 ($+200$), 320 ($+19$), 411 (-21), 468 ($+14$)	
Δ-[Ru(4,4′-DMB)$_2$(phen)]$^{2+}$	456 (14,100)	400 (53), 465 (-54)	[237]
Λ-[Ru(4,4′-DMB)$_2$(phen)]$^{2+}$		400 (-59), 457 (56.5)	
Δ-[Ru(4,4′-DMB)$_2$(dpq)]$^{2+}$	439 (13,900)	415 (53.6) 476 (-38.8)	[237]
Λ-[Ru(4,4′-DMB)$_2$(dpq)]$^{2+}$		415 (-54), 476 (40)	
Δ-[Ru(4,4′-DMB)$_2$(dpqC)]$^{2+}$	452 (15,200)	386 (51), 464 (-46)	[237]
Λ-[Ru(4,4′-DMB)$_2$(dpqC)]$^{2+}$		386 (-60), 464 (46)	
Δ-[Ru(4,4′-DMB)$_2$(dppz)]$^{2+}$	443 (16,300)	390 (63), 467 (-51)	[237]
Λ-[Ru(4,4′-DMB)$_2$(dppz)]$^{2+}$		390 (-70), 467 (51)	
Δ-[Ru(phen)$_3$]$^{2+}$	453 (14,700)	227 (-19), 234 (33), 259 (437), 268 (-602), 296 (-72), 385 ($+7$), 419 (15), 464 (-22)	[227, 237]
Λ-[Ru(phen)$_3$]$^{2+}$		227 (10), 234 (-33), 259 (-430), 268 (582), 296 (87), 385 (-7), 419 (-15), 464 (23)	
Δ-[Ru(HAT)$_3$]$^{2+}$	436 (14,180),	232 ($+8$), 250 (-15), 262 ($+4$), 282 (-6), 314 ($+48$), 406 (-13), 462 ($+12$)	[237]
Λ-[Ru(HAT)$_3$]$^{2+}$	414 (sh)	232 (-8), 250 ($+15$), 262 (-2), 282 ($+7$), 314 (-45), 406 ($+14$), 462 (-11)	
Δ-[Ru(phen)$_2$(dpq)]$^{2+}$	446 (17,300)	396 (30), 452 (-52)	[237]
Λ-[Ru(phen)$_2$(dpq)]$^{2+}$		396 (-33), 456 (51)	
Δ-[Ru(phen)$_2$(dpqC)]$^{2+}$	448 (14,300)	407 (40), 467 (-54)	[237]
Λ-[Ru(phen)$_2$(dpqC)]$^{2+}$		407 (-43), 467 (58)	

Table 2.4 (continued)

Complex	λ_{max}(MLCT) nm $(\varepsilon M^{-1}cm^{-1})^a$	CD Spectra λ nm $(\Delta\varepsilon\ M^{-1}cm^{-1})^a$	Ref
Δ-[Ru(phen)$_2$(dppz)]$^{2+}$	439 (16,300)	405 (41), 458 (−49)	[237]
Λ-[Ru(phen)$_2$(dppz)]$^{2+}$		405 (−55), 458 (61)	
Δ-[Ru(dpq)$_3$]$^{2+}$	452 (15,335)	410 (15.1), 465 (−17.6)	[239]
Λ-[Ru(dpq)$_3$]$^{2+}$		410 (−13.6), 465 (19.0)	
Δ-[Ru(phen)$_2$(phendo)]$^{2+}$	438 (16,750)	440 (63.1),490 (−53.4)	[118, 239]
Λ-[Ru(phen)$_2$(phendo)]$^{2+}$		440 (−63.2), 490 (55.3)	
Δ-[Ru(phen)$_2$(dpqMe$_2$)]$^{2+}$	448 (16,531)	383 (100.2), 461(−114.6)	[239]
Λ-[Ru(phen)$_2$(dpqMe$_2$)]$^{2+}$		383 (−104.2), 461(115.5)	
Δ-[Ru(phen)$_2$(phiMe$_2$)]$^{2+}$	537 (27,657)	401 (181.2), 467 (−147.2)	[239]
Λ-[Ru(phen)$_2$(phiMe$_2$)]$^{2+}$		401 (−170.9), 467 (148.5)	
Δ-[Ru(2,9-Me$_2$phen)$_2$(dpq)]$^{2+}$	438 (9,700)	385 (112.2), 502 (−27.3)	[239]
Λ-[Ru(2,9-Me$_2$phen)$_2$(dpq)]$^{2+}$		385 (−110.3), 502 (27.2)	
Δ-[Ru(2,9-Me$_2$phen)$_2$(dpqC)]$^{2+}$	439 (10,307)	375 (108.8), 463 (−26.5)	[239]
Λ-[Ru(2,9-Me$_2$phen)$_2$(dpqC)]^{2}		375 (−105.1), 463 (24.5)	
Δ-[Ru(2,9-Me$_2$phen)$_2$(dpqMe$_2$)]$^{2+}$	438 (8,931)	373 (69.4),460 (−24.3)	[239]
Λ-[Ru(2,9-Me$_2$phen)$_2$(dpqMe$_2$)]$^{2+}$		373 (−68.5),460 (23.2)	
Δ-[Ru(2,9-Me$_2$phen)$_2$(dppz)]$^{2+}$	448 (11,483)	417 (71.7), 475 (−56.7)	[239]
Λ-[Ru(2,9-Me$_2$phen)$_2$(dppz)]$^{2+}$		417 (−70.7), 475 (56.5)	
Δ-[Ru(tmphen)$_2$(dpq)]$^{2+}$	427 (16,626)	390 (63.8), 465 (−63.9)	[239]
Λ-[Ru(tmphen)$_2$(dpq)]$^{2+}$		390 (−60.6), 465 (63.2)	

^{a}Visible and CD spectra measured in CH_3CN

$n \rightarrow \pi^*$ transitions that are typically weak and disappear in aqueous systems owing to hydrogen-bonding, and $\pi \rightarrow \pi^*$ transitions that range in absorption strength from unobservably weak to very strong. These are the basis of the LC bands in the spectra of Ru(II) polypyridine complexes. In practice most absorption spectra are dominated by a small number of $\pi \rightarrow \pi^*$ transitions; see the spectra in Fig. 2.11. As shown in Fig. 2.11, the empty ligand-π^* orbitals (denoted π_L^*) are available to accept electrons from the metal π_M orbitals, and the transition energies correspond to visible or UV wavelengths. A number of different although near-degenerate transitions are possible. As they involve metal-to-ligand charge transfer, they are denoted as MLCT transitions. The absorption bands, reported in Table 2.4, are fairly strong, typically with $\varepsilon > 10,000$ M^{-1} cm^{-1}. Spectra are readily measured between 200 and 300 nm for the free ligands and complexes, but the bands may be overlapped or obscured by DNA absorption during binding studies. However, longer-wavelength LC bands may be accessible for study, and the complexes in Fig. 2.11 and Table 2.4 have MLCT absorption bands in the 400–500 nm (visible) region. These bands appear to have at least two components, and this is confirmed by the corresponding CD spectra (see Fig. 2.12 below). Bands of this type may be associated with a cluster of excited MLCT states, leading to temperature- and solvent-dependence of the luminescence from some complexes; for example, DNA binding of some complexes may greatly enhance their
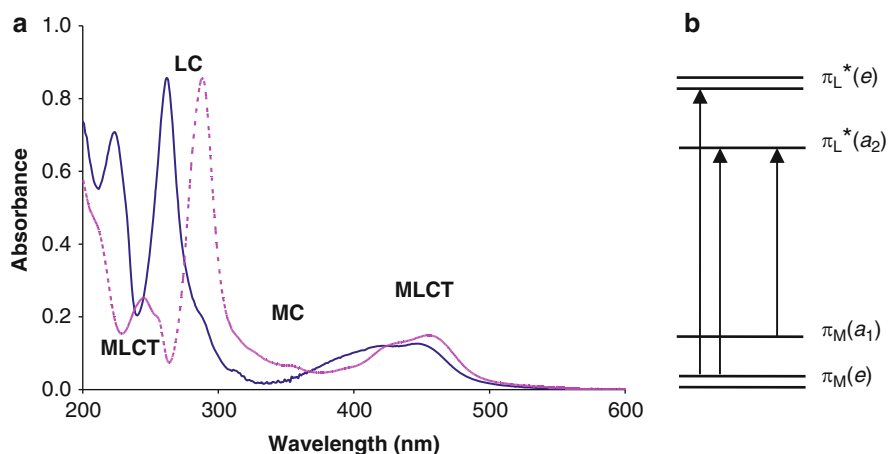
Fig. 2.11 (**a**) Electronic absorption spectra of [Ru(bpy)$_3$]$^{2+}$ (*dashed lines*) and [Ru(phen)$_3$]$^{2+}$ in water solution (band assignments for [Ru(bpy)$_3$]$^{2+}$ after Campagna et al. [56]). (**b**) Simplified orbital energy-level diagrams for the MLCT transitions of a Ru(III) polypyridine complex of D_3 symmetry
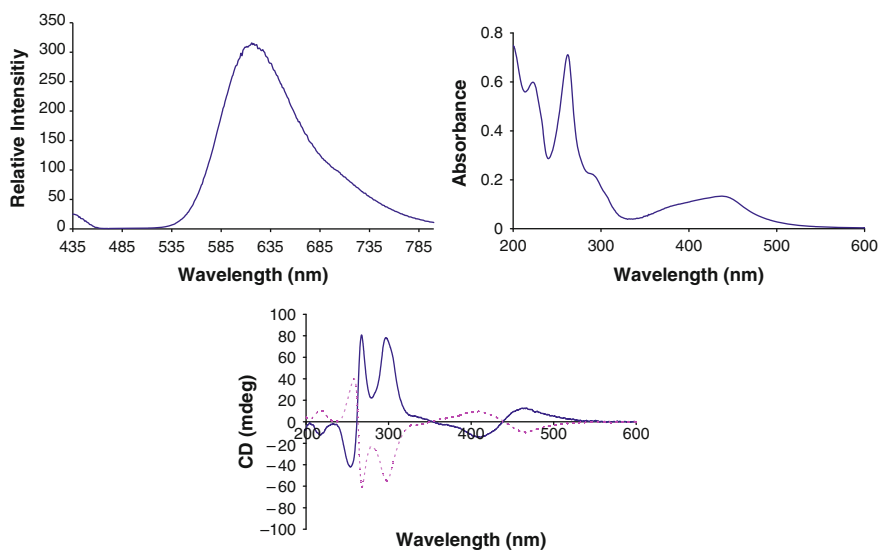

Fig. 2.12 UV absorption and *CD* spectra for Δ- (*dashed lines*) and Λ-[Ru(phen)$_2$(phendo)]$^{2+}$ (*continuous line*)

luminescence intensities; these complexes are often described as "light-switches" [232]. Their intensity, sensitivity to chemical environment, and lack of overlap with DNA absorption bands, allows Ru(II) polypyridine complexes to serve as valuable spectroscopic probes of DNA binding [10].

Typically the LC and MLCT transitions may be identified by comparison with the electronic spectra of the free ligand (either neutral or protonated), noting that complexes may contain more than one ligand type, and there are often excitonic interactions between ligands, leading to strong and distinctive sigmoidal structure in the *CD* bands; for example, in the 250–300 nm regions for Ru(bpy)$_3$]$^{2+}$ and [Ru (phen)$_3$]$^{2+}$ [230, 233, 234]. In some cases it may be useful to analyse the absorption spectra of the free ligands, to allow a comprehensive analysis of the absorption, *CD* and *LD* (if available) spectra of the complex, which in turn may be useful when studying the binding of the complex to DNA. Spectra of the ligands, and indeed of the complexes themselves, can be modelled computationally at various levels of theory, using semiempirical methods such as CNDO/S-CI and INDO [235] as well as more sophisticated *ab initio* and density-functional theory (DFT) methods [236].

These computations may be used to predict approximate band energies and absorption intensities, including weak transitions that are typically not seen in solution-phase absorption spectra, but that might influence *CD* spectra; they can also predict the direction of the electronic transition moment, and hence the band polarizations that would be seen in *LD* spectra if the ligand could be oriented [227]. In some cases a ligand will have clearly discernible long and short axes; for example, 1,10-phenanthroline and tpphz. When these molecules are oriented, *LD* spectra may obtained by subtracting the absorbances recorded using plane-polarized light. See Sect. 9.2.2 for experimental detail. However, other ligands such as dpq are too symmetric to be readily oriented. This problem may be overcome if the ligand is substituted with a long side-chain, as in the case of *rac*-[Ru(phen)$_2$(dpq-PyPyPy)]$^{2+}$. Similarly, Ru(II) complexes of these ligands may be too symmetric to be oriented readily but *LD* spectra may be recorded when they bind to DNA [115]; see Sect. 9.3.1 for *LD* spectra of a DNA-bound bis iron tris-chelate helicate.

Chiral chromophores may preferentially absorb left or right circularly polarized light or UV, giving rise to a *CD* spectrum. An achiral ligand, or a racemic mixture of a chiral ligand or chiral complex, will not produce a *CD* spectrum. However, the *CD* spectra of resolved tris-chelate complexes are well known: for example, [Ru (en)$_3$]$^{2+}$, [Ru(bpy)$_3$]$^{2+}$ and [Ru(phen)$_3$]$^{2+}$ [231, 233, 234]. Figure 2.12 compares the *CD* spectra for Δ- and Λ-[Ru(phen)$_2$(phendo)]$^{2+}$. The spectra of the enantiomers are not perfect mirror images, as the samples could not be perfectly resolved. However, they show the typical sigmoidal behaviour of the MLCT band near 450 nm, as well as excitonic behaviour around 260 nm. As reported above, the low-energy MLCT bands are often associated with a cluster of excited electronic states (three in the case of [Ru(bpy)$_3$]$^{2+}$) [227], the corresponding luminescence spectra may be sensitive to temperature and chemical environment.

Owing to the presence of the heavy ruthenium atom, spin–orbit coupling produces excited states of mixed spin multiplicity, but the lowest MLCT state for [Ru (bpy)$_3$]$^{2+}$ is predominantly triplet in character. It is often referred to as ^{3}MLCT, and like other triplet states its luminescence may be affected by the presence of O$_2$ [240]. The luminescence spectrum of [Ru(phen)$_2$(phendo)]$^{2+}$ is shown in Fig. 2.12. Given the approximate mirror-image relationship between the absorption and luminescence spectra, and the relatively short emission lifetimes (typically in the

microsecond range), luminescence spectra of these complexes are often treated experimentally in the same way as fluorescence spectra. Some experimental techniques are reported in Chap. 10.

2.4.5 Resolution

Techniques are available for the resolution of inorganic complexes using resolving agents and recycle column chromatography, but no single technique or resolving agent can be successfully applied to every complex. A number of techniques have been successfully employed for the resolution of ruthenium(II) polypyridyl complexes. Classical techniques include fractional recrystallization or differential precipitation by diastereomeric salt formation [6, 13, 109, 111, 237, 241]. Column chromatography employing chiral eluents and stationary phases [106, 111, 117, 120, 237] has also been effective, and an example of this is shown in Fig. 2.13. Capillary electrophoresis [242, 243], affinity chromatography, DNA-HPLC [106], cyclodextrin-HPLC [244, 245] and paper chromatography [246, 247] have also been used. A new resolving agent, TRISPHAT ([(*tris*-(tetrachlorocatecholato)phosphate(V)]⁻), has shown promise for the resolution of ruthenium(II) polypyridyl complexes, and has been used for ion-pair chromatography [248], enantioselective extraction [249] and as an NMR shift agent.
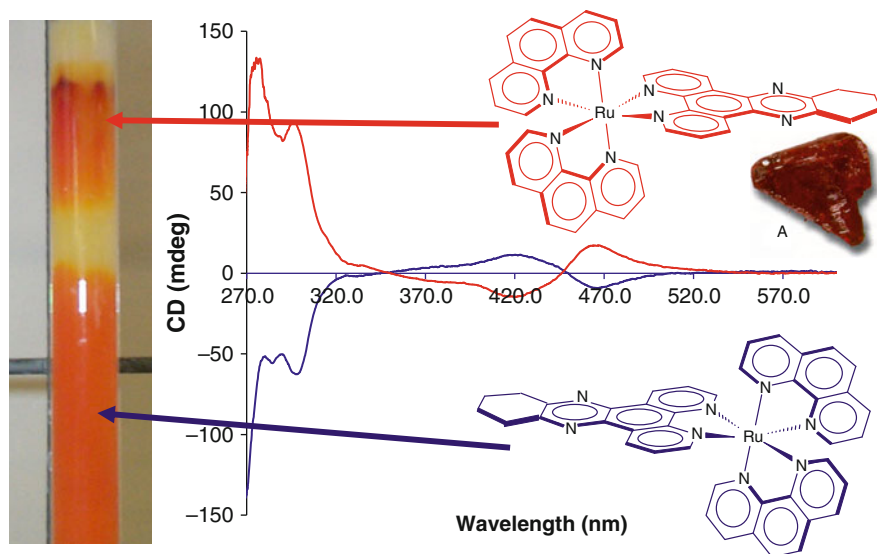
Fig. 2.13 Results of a recycled column chromatography resolution; the image of the column shows the separation of the two bands. The crystal identified as A is Λ-[Ru(bpy)$_2$(py)$_2$](2,3-dibenzoyltart)$_2$, classical resolution and identified by CD

References

1. Dwyer FP, Gyarfas EC. J Proc Roy Soc NSW. 1950;83:170.
2. Dwyer FP, Gyarfas EC, O'Dwyer MF. Nature. 1951;167:1036.
3. Dwyer FP, Gyarfas EC, Rogers WP, Koch JH. Nature. 1952;170:190.
4. Dwyer FP, Mayhew E, Roe EMF, Shulman A. Br J Cancer. 1965;19:195.
5. Dwyer FP, Reid IK, Shulman A, Laycock GM, Dixson S. Aust J Expt Biol Med Sci. 1969;47:203.
6. Bosnich B, Dwyer FP. Aust J Chem. 1966;19:2229.
7. Koch JH, Gyarfas EC, Dwyer FP. Aust J Biol Sci. 1956;9:371.
8. Koch JH, Rogers WP, Dwyer FP, Gyarfas EC. Aust J Biol Sci. 1957;10:342.
9. Mellor DP. Proc Roy Aust Chem Inst. 1970;37:199.
10. Hiort C, Nordén B, Rodger A. J Am Chem Soc. 1971;1990:112.
11. Nordén B, Patel N, Hiort C, Graeslund A, Kim SK. Nucleosides Nucleotides. 1991;10:195.
12. Eriksson M, Leijon M, Hiort C, Nordén B, Graeslund A. J Am Chem Soc. 1992;114:4933.
13. Hiort C, Lincoln P, Nordén B. J Am Chem Soc. 1993;115:3448.
14. Eriksson M, Leijon M, Hiort C, Nordén B, Graslund A. Biochemistry. 1994;33:5031.
15. Nordén B, Kurucsev T. J Mol Recognit. 1994;7:141.
16. Barton JK. J Biomol Struct Dyn. 1983;1:621.
17. Barton JK. Chem Eng News. 1983;61:32.
18. Barton JK. Comments Inorg Chem. 1985;3:321.
19. Barton JK. Science. 1986;15:8.
20. Barton JK, Basile LA, Danishefsky A, Alexandrescu A. PNAS. 1984;81:1961.
21. Barton JK, Danishefsky AT, Goldberg JM. J Am Chem Soc. 1984;106:2172.
22. Barton JK, Goldberg J, Kumar CV, Turro NJ. J Am Chem Soc. 2081;1986:108.
23. Collins JG, Sleeman AD, Aldrich-Wright JR, Greguric I, Hambley TW. Inorg Chem. 1998;37:3133.
24. Collins JG, Aldrich-Wright JR, Greguric ID, Pellegrini PA. Inorg Chem. 1999;38:5502.
25. Paris JP, Brandt WW. J Am Chem Soc. 1959;81:5001.
26. Alessio E, Mestroni G, Bergamo A, Sava G. Met Ions Biol Syst. 2004;42:323.
27. Ang WH, Daldini E, Scolaro C, Scopelliti R, Juillerat-Jeannerat L, Dyson PJ. Inorg Chem. 2006;45:9006.
28. Bratsos I, Jedner S, Gianferrara T, Alessio E. Chimia. 2007;61:692.
29. Bruijnincx PCA, Sadler PJ. Curr Opin Chem Biol. 2008;12:197.
30. Casini A, Guerri A, Gabbiani C, Messori L. J Inorg Biochem. 2008;102:995.
31. Dougan SJ, Sadler PJ. Chimia. 2007;61:704.
32. Gossens C, Tavernelli I, Rothlisberger U. Chimia. 2005;59:81.
33. Hannon MJ. Pure Appl Chem. 2007;79:2243.
34. Hartinger Christian G, Jakupec Michael A, Zorbas-Seifried S, Groessl M, Egger A, Berger W, et al. Chem Biodivers. 2008;5:2140.
35. Heffeter P, Jungwirth U, Jakupec M, Hartinger C, Galanski M, Elbling L, et al. Drug Resist Updat. 2008;11:1.
36. Holtze ACG, Kariuki BM, Hannon MJ. Angew Chem, Int Ed. 2006;45:4839.
37. Keppler BK, Jakupec MA, In: Proceedings of the European conference on chemistry for life sciences, 2nd. Wroclaw, Poland, Sept 4–8, 2007; 2007: 21.

38. Kostova I. Curr Med Chem. 2006;13:1085.
39. Maksimoska J, Feng L, Harms K, Yi C, Kissil J, Marmorstein R, et al. J Am Chem Soc. 2008;130:15764.
40. Maksomiska J, Williams DS, Atilla-Gokcumen GE, Smalley KSM, Carroll PJ, Webster RD, et al. Chem Eur J. 2008;14:4816.
41. McDonnell U, Kerchoffs JMCA, Castineiras RPM, Hicks MR, Hotze ACG, Hannon MJ, Rodger A. Dalton Trans. 2008:667.
42. Ott I, Gust R. Arch Pharm. 2007;340:117.
43. Pizarro AM, Sadler PJ. Biochimie. 2009;91:1198.
44. Pluim D, van Waardenburg RCAM, Beijnen JH, Schellens JHM. Cancer Chem Pharm. 2004;54:71.
45. Rademaker-Lakhai JM, Van Den Bongard D, Pluim D, Beijnen JH, Schellens JHM. Clin Can Res. 2004;10:3717.
46. Reedijk J. Platinum Met Rev. 2008;52:2.
47. Reisner E, Arion VB, Eichinger A, Kandler N, Giester G, Pombeiro AJL, et al. Inorg Chem. 2005;44:6704.
48. Reisner E, Arion VB, Guedes da Silva MFC, Lichtenecker R, Eichinger A, Keppler BK, et al. Inorg Chem. 2004;43:7083.
49. Reisner E, Arion VB, Keppler BK, Pombeiro AJL. Inorg Chim Acta. 2008;361:1569.
50. Robillard MS, Bacac M, van den Elst H, Flamigni A, van der Marel GA, van Boom JH, et al. J Comb Chem. 2003;5:821.
51. Yan YK, Melchart M, Habtemariam A, Sadler PJ. Chem Commun. 2005:4764
52. Mesmaeker AK-D, Lecomte J-P, Kelly JM. Top Curr Chem. 1995;27:177.
53. Mesmaeker AK-D, Orellana G, Barton JK, Turro NJ. Photochem Photobiol. 1990;52:461.
54. Baranoff E, Barigelletti F, Bonnet S, Collin J-P, Flamigni L, Mobian P, et al. Struct Bond. 2007;123:41.
55. Campagna S, Puntoriero F, Nastasi F, Bergamini G, Balzani V. Top Curr Chem. 2007; 280:117.
56. Campagna S, Puntoriero F, Nastasi F, Bergamini G, Balzani V. In: Photochemistry and photophysics of coordination compounds I. 2007. pp. 117.
57. Lemercier G, Bonne A, Four M, Lawson-Daku LM. C R Chim. 2008;11:709.
58. Barton JK, Kumar CV, Turro NJ. J Am Chem Soc. 1986;108:6391.
59. Brodkorb A, Mesmaeker AK-D, Rutherford TJ, Keene FR. Eur J Inorg Chem. 2001:2151.
60. Delaney S, Pascaly M, Bhattacharya PK, Han K, Barton JK. Inorg Chem. 1966;2002:41.
61. Mesmaeker AK-D, Moucheron C, Boutonnet N. J Phys Org Chem. 1998;11:566.
62. Moucheron C, Kirsch-De Mesmaeker A, Choua S. Inorg Chem. 1997;36:584.
63. Stemp EDA, Arkin MR, Barton JK. J Am Chem Soc. 1997;2921:119.
64. Stemp EDA, Holmlin RE, Barton JK. Inorg Chim Acta. 2000;297:88.
65. Wagenknecht H-A, Stemp EDA, Barton JK. J Am Chem Soc. 2000;122:1.
66. Anderson MA, Richards JPG, Stark AG, Stephens FS, Vagg RS, Williams PA. Inorg Chem. 1986;25:4847.
67. Goodwin TJ, Williams PA, Vagg RS. Inorg Chim Acta. 1982:133.
68. Vagg RS. J Pro Royal Soc NSW. 1984;117:99.
69. Vagg RS, Williams PA. Inorg Chimica Acta. 1981;51:61.
70. Vagg RS, Williams PA. Pro Roy Aust Chem Inst Inorg Div Nat Conf, Melb. 1986
71. Mei HY, Barton JK. PNAS. 1988;85:1339.
72. Lerman LS. J Mol Biol. 1961;3:18.
73. Dupureur CM, Barton JK. J Am Chem Soc. 1994;116:10286.
74. Greguric A, Greguric ID, Hambley TW, Aldrich-Wright JR, Collins JG. Dalton Trans. 2002:849
75. Neidle S, Abraham Z. Crit Rev Biochem. 1984;17:73.
76. Marshall LE, Graham DR, Reich KA, Sigman DS. Biochemistry. 1981;20:244.
77. Thederahn TB, Kuwabara MD, Larsen TA, Sigman DS. J Am Chem Soc. 1989;111:4941.

78. Baker AD, Morgan RJ, Strekas TC. J Am Chem Soc. 1991;113:1411.
79. Baker AD, Morgan RJ, Strekas TC. J Chem Soc, Chem Commun. 1992:1099.
80. Morgan O, Wong S, Bae J, Baker AD, Strekas TC, Engel R. Book of Abstracts, 212th ACS National Meeting, Orlando, FL. August 25–29 1996, ORGN.
81. De Buyl F, Kirsch-De Mesmaeker A, Tossi A. Kelly JM J Photochem Photobiol A. 1991;60:27.
82. Mesmaeker AK-D, Jacquet L, Masschelein A, Vanhecke F, Heremans K. Inorg Chem. 1989;28:2465.
83. Tossi AB, Kelly JM. Photochem Photobiol. 1989;49:545.
84. Tysoe SA, Kopelman R, Schelzig D. Inorg Chem. 1999;38:5196.
85. White DO, Harris AW, Cheyne IM, Shew M. Aust J Expt Biol Med Sci. 1969;47:81.
86. Watson JD, Crick FHC. Nature. 1953;171:737.
87. Cathey CJ, Constable EC, Hannon MJ, Tocher DA, Ward MD. J Chem Soc, Chem Commun. 1990:621.
88. Chow CS, Barton JK. J Am Chem Soc. 1990;2839:112.
89. Friedman AE, Chambron JC, Sauvage JP, Turro NJ, Barton JK. J Am Chem Soc. 1990; 112:4960.
90. Pyle AM, Chiang MY, Barton JK. Inorg Chem. 1990;29:4487.
91. Rehmann JP, Barton JK. Biochemistry. 1990;29:1701.
92. Friedman AE, Kumar CV, Turro NJ, Barton JK. Nucleic Acids Res. 1991;19:2595.
93. Morgan RJ, Chatterjee S, Baker AD, Strekas TC. Inorg Chem. 1991;30:2687.
94. Peek BM, Ross GT, Edwards SW, Meyer GJ, Meyer TJ, Erickson BW. Int J Pept Protein Res. 1991;38:114.
95. Hartshorn RM, Barton JK. J Am Chem Soc. 1992;114:5919.
96. Kurimura Y, Sairenchi Y, Nakayama S. Makromol Chem Macromol Symp. 1992;59:199.
97. Satyanarayana S, Dabrowiak JC, Chaires JB. Biochemistry. 1992;31:9319.
98. Sitlani A, Long EC, Pyle AM, Barton JK. J Am Chem Soc. 1992;114:2303.
99. Togano T, Nagao N, Tsuchida M, Kumakura H, Hisamatsu K, Howell FS, et al. Inorg Chim Acta. 1992;195:221.
100. Murphy CJ, Barton JK. Meth Enzymol. 1993;226:576.
101. Satyanarayana S, Dabrowiak JC, Chaires JB. Biochemistry. 1993;32:2573.
102. Sitlani A, Dupureur CM, Barton JK. J Am Chem Soc. 1993;115:12589.
103. Sardesai NY, Zimmermann K, Barton JK. J Am Chem Soc. 1994;116:7502.
104. Sitlani A, Barton JK. Biochemistry. 1994;33:12100.
105. Aldrich-Wright J, Greguric I. In: The National Conference of Inorganic Chemistry Division, RACI, Adelaide, S.A. Australia. 1995: p. 30.
106. Aldrich-Wright JR, Greguric I, Vagg RS, Vickery K, Williams PA. J Chromatogr A. 1995;718:436.
107. Haq I, Lincoln P, Suh D, Nordén B, Chowdhry BZ, Chaires JB. J Am Chem Soc. 1995;117:4788.
108. Helms JB, Huang L, Price R, Sullivan BP, Sullivan BA. Inorg Chem. 1995;34:5335.
109. Hua X, von Zelewsky A. Inorg Chem. 1995;34:5791.
110. Kato M. Kagaku. 1995;50:314.
111. Rutherford TJ, Quagliotto MG, Keene FR. Inorg Chem. 1995;34:3857.
112. Sardesai NY, Lin SC, Zimmermann K, Barton JK. Bioconjug Chem. 1995;6:302.
113. Vagg RS, Williams PA. Inorg Chimina Acta. 1981;52:69.
114. Vagg RS, Williams PA. Inorg Chim Acta. 1982:101.
115. Coggan DZM, Haworth IS, Bates PJ, Robinson A, Rodger A. Inorg Chem. 1999;38:4486.
116. Sun B, Guan J-X, Xu L, Yu B-L, Jiang L, Kou J-F, et al. Inorg Chem. 2009;48:4637.
117. Dupureur CM, Barton JK. Inorg Chem. 1997;36:33.
118. Lincoln P, Broo A, Nordén B. J Am Chem Soc. 1996;118:2644.
119. Tuite E, Lincoln P, Nordén B. J Am Chem Soc. 1997;119:239.
120. Greguric I, Aldrich-Wright JR, Collins JG. J Am Chem Soc. 1997;119:3621.

121. Beck JL, Gupta R, Urathamakul T, Williamson NL, Sheil MM, Aldrich-Wright JR, Ralph SF. Chem Commun. 2003:626.
122. Urathamakul T, Beck JL, Sheil MM, Aldrich-Wright JR, Ralph SF. Dalton Trans. 2004: 2683.
123. Lim MH, Song H, Olmon ED, Dervan EE, Barton JK. Inorg Chem. 2009;48:5392.
124. Robillard MS, Valentijn ARPM, Meeuwenoord NJ, van der Marel GA, Van Boom JH, Reedijk J. Angew Chem, Int Ed. 2000;39:3096.
125. Karidi K, Garoufis A, Hadjiliadis N, Reedijk J. Dalton Trans. 2005:728.
126. Myari A, Hadjiliadis N, Garoufis A. Eur J Inorg Chem. 2004:1427.
127. Hastings CA, Barton JK. Biochemistry. 1999;38:10042.
128. Copeland KD, Fitzsimons MP, Houser RP, Barton JK. Biochemistry. 2002;41:343.
129. Copeland KD, Lueras AMK, Stemp EDA, Barton JK. Biochemistry. 2002;41:12785.
130. Pierard F, Del Guerzo A, Kirsch-De Mesmaeker A, Demeunynck M, Lhomme J. PCCP. 2001;3:2911.
131. Pyle AM, Rehmann JP, Meshoyrer R, Kumar CV, Turro NJ, Barton JK. J Am Chem Soc. 1989;111:3051.
132. Li-Feng T, Sheng Z, Hui C, Kang-Cheng Z, Fang W, Yue X, et al. Helv Chim Acta. 2007;90:1786.
133. Liu Y-J, He J-F, Yao J-H, Mei W-J, Wu F-H, He L-X. J Coord Chem. 2009;62:665.
134. Xu H, Zheng K-C, Deng H, Lin L-J, Zhang Q-L, Ji L-N. New J Chem. 2003;27:1255.
135. Tan L-F, Wang F, Chao H, Zhou Y-F, Weng C. J Inorg Biochem. 2007;101:700.
136. Zhen Q-X, Ye B-H, Zhang Q-L, Liu J-G, Hong L, Ji L-N, et al. J Inorg Biochem. 1999;76:47.
137. Zhen Q-X, Ye B-H, Liu J-G, Zhang Q-L, Ji L-N, Wang L. Inorg Chim Acta. 2000;303:141.
138. Chen L-M, Liu J, Chen J-C, Shi S, Tan C-P, Zheng K-C, et al. J Mol Struct. 2008;881:156.
139. Liu J-G, Ye B-H, Li H, Zhen Q-X, Ji L-N, Fu Y-H. J Inorg Biochem. 1999;76:265.
140. Shi S, Xie T, Yao T-M, Wang C-R, Geng X-T, Yang D-J, et al. Polyhedron. 2009;28:1355.
141. Yuan Y, Wang Y, Jiang L, Gao F, Liang S, Su C, et al. Aust J Chem. 2008;61:732.
142. Shuo S, Tian-Ming Y, Xiao-Ting G, Ling-Feng J, Jie L, Qing-Yuan Y, et al. Chirality. 2009;21:276.
143. Gao F, Chao H, Zhou F, Chen X, Wei Y-F, Ji L-N. J Inorg Biochem. 1050;2008:102.
144. Liu X-W, Xu L-C, Li H, Chao H, Zheng K-C, Ji L-N. J Mol Struct. 2009;920:163.
145. Tan L, Chao H, Fei J, Su G, Zhang S, Xia Y, et al. Aust J Chem. 2008;61:376.
146. Liu JG, Zhange QL, Shi XF, Ji LN. Inorg Chem. 2001;40:5045.
147. Yu H-J, Huang S-M, Li L-Y, Jia H-N, Chao H, Mao Z-W, et al. J Inorg Biochem. 2009;103:881.
148. Blasius R, Nierengarten H, Luhmer M, Constant J-F, Defrancq E, Dumy P, et al. Chem Eur J. 2005;11:1507.
149. Deshpande MS, Kumbhar AA, Kumbhar AS, Kumbhakar M, Pal H, Sonawane UB, et al. Bioconjug Chem. 2009;20:447.
150. Nair RB, Teng ES, Kirkland SL, Murphy CJ. Inorg Chem. 1998;37:139.
151. Shi H-J, Chen Y, Gao F, Yu H-J, Li G-Y, Chao H, et al. J Mol Struct. 2008;892:485.
152. Mei W-J, Wei X-Y, Liu Y-J, Wang B. Transit Met Chem. 2008;33:907.
153. Arounaguiri S, Easwaramoorthy D, Ashokkumar A, Dattagupta A, Maiya BG. Proc Indian Acad Sci (Chem Sci). 2000;112:1.
154. Liu J, Mei WJ, Lin LJ, Zheng KC, Chao H, Yun FC, et al. Inorg Chim Acta. 2004;357:285.
155. Liu Y-J, Mei W-J, Lu J-Z, Zhao H-J, He L-X, Wu F-H. J Coord Chem. 2008;61:3213.
156. Xu H, Deng H, Zang Q-L, Hunag Y, Liu J-H, L-N Ji. Inorg Chem Commun. 2003;6:766.
157. Zhen Q-X, Zhang Q-L, Liu J-G, Ye B-H, Ji L-N, Wang L. J Inorg Biochem. 2000;78:293.
158. O'Donoghue KA, Penedo JC, Kelly JM, Kruger PE. Dalton Trans. 2005:1123.
159. Chen L-M, Liu J, Chen J-C, Tan C-P, Shi S, Zheng K-C, et al. J Inorg Biochem. 2008;102:330.
160. Aldrich-Wright JR, Brodie C, Glazer EC, Luedtke NW, Elson-Schwab L, Tor Y. Chem Commun. 2004:1018.
161. D'Alessandro DM, Kelso LS, Keene FR. Inorg Chem. 2001;40:6841.

162. de Tacconi NR, Lezna RO, Konduri R, Ongeri F, Rajeshwar K, MacDonnell FM. Chem Eur J. 2005;11:4327.
163. Guckian AL, Doering M, Ciesielski M, Walter O, Hjelm J, O'Boyle NM, Henry W, Browne WR, McGarvey JJ, Vos JG. Dalton Trans. 2004:3943.
164. Jiang C-W. Eur J Inorg Chem. 2004:2277.
165. Jiang C-W. J Inorg Biochem. 2004;98:497.
166. Jiang C-W, Chao H, Hong X-L, Li H, Mei W-J, Ji L-N. Inorg Chem Commun. 2003;6:773.
167. Malina J, Hannon MJ, Brabec V. Chem Eur J. 2008;14:10408.
168. McDonnell U, Hicks MR, Hannon MJ, Rodger A. J Inorg Biochem. 2052;2008:102.
169. Pascu GI, Hotze ACG, Sanchez-Cano C, Kariuki BM, Hannon MJ. Angew Chem, Int Ed. 2007;46:4374.
170. Patterson BT, Collins JG, Foley FM, Keene FR. Dalton. Trans. 2002:4343.
171. Patterson BT, Keene FR. Inorg Chem. 1998;37:645.
172. Smith JA, Collins JG, Patterson BT, Keene FR. Dalton Trans. 2004:1277.
173. Smith JA, Keene FR. Chem Commun. 2006:2583.
174. Spillane CB, Smith JA, Buck DP, Collins JG, Keene FR. Dalton Trans. 2007:5290.
175. van der Schilden K, Garcia F, Kooijman H, Spek AL, Haasnoot JG, Reedijk J. Angew Chem, Int Ed. 2004;43:5668.
176. O'Reilly F, Kelly J, Kirsch-De Mesmaeker A. Chem Commun. 1996:1013.
177. O'Reilly FM, Kelly JM. New J Chem. 1998;22:215.
178. O'Reilly FM, Kelly JM. J Phys Chem B. 2000;104:7206.
179. Lincoln P, Nordén B. Chem. Commun. 1996:2145.
180. Önfelt B, Lincoln P, Nordén B. J Am Chem Soc. 1999;121:10846.
181. Westerlund F, Wilhelmsson LM, Nordén B, Lincoln P. J Am Chem Soc. 2003;125:3773.
182. Westerlund F, Wilhelmsson LM, Nordén B, Lincoln P. J Phys Chem B. 2005;109:21140.
183. Wilhelmsson LM, Esbjoerner EK, Westerlund F, Nordén B, Lincoln P. J Phys Chem B. 2003;107:11784.
184. Wilhelmsson LM, Westerlund F, Lincoln P, Nordén B. J Am Chem Soc. 2002;124:12092.
185. Önfelt B, Gostring L, Lincoln P, Nordén B, Onfelt A. Mutagenesis. 2002;17:317.
186. Olson EJC, Hu D, Hoermann A, Jonkman AM, Arkin MR, Stemp EDA, et al. J Am Chem Soc. 1997;119:11458.
187. Jiang C-W. Inorg Chim Acta. 2005;358:1231.
188. Hannon MJ, Moreno V, Prieto MJ, Erlend M, Sletten E, Meistermann I, et al. Angew Chem, Int Ed. 2001;40:879.
189. Aneta O, Alexandre GB, Roeland B, Isabel U, Joan A, Alison R, et al. Angew Chem, Int Ed. 2006;45:1834.
190. Foley FM, Keene FR, Collins JG. Dalton Trans. 2002:2968.
191. Dougan SJ, Melchart M, Habtemariam A, Parsons S, Sadler PJ. Inorg Chem. 2006;45:10882.
192. Clarke MJ. Coord Chem Rev. 2003;236:209.
193. Scolaro C, Bergamo A, Brescacin L, Delfino R, Cocchietto M, Laurenczy G, et al. J Med Chem. 2005;48:4161.
194. Gopal YNV, Jayaraju D, Kondapi AK. Biochemistry. 1999;38:4382.
195. Creutz C, Kroger P, Matsubara T, Netzel TL, Sutin N. J Am Chem Soc. 1979;101:5442.
196. Ito T, Hamaguchi T, Nagino H, Yamaguchi T, Kido H, Zavarine IS, et al. J Am Chem Soc. 1999;121:4625.
197. Rau H, Frank R, Greiner G. J Phys Chem. 1986;90:2476.
198. Robinson EA, Earley JE. Inorg Chem. 1999;38:4128.
199. Smalley KSM, Contractor R, Haass Nikolas K, Kulp Angela N, Atilla-Gokcumen GE, Williams Douglas S, et al. Cancer Res. 2007;67:209.
200. Arends IWCE, Kodama T, Sheldon RA. Top Organomet Chem. 2004;11:277.
201. Chatani N. Top Organomet Chem. 2004;11:173.
202. Derien S, Monnier F, Dixneuf PH. Top Organomet Chem. 2004;11:1.
203. Marciniec B, Pietraszuk C. Top Organomet Chem. 2004;11:197.

204. Nagashima H. Ruthenium Org Synth. 2004;36:333.
205. Nishiyama H. Top Organomet Chem. 2004;11:81.
206. Bregman H, Williams DS, Atilla GE, Carroll PJ, Meggers E. J Am Chem Soc. 2004;126:13594.
207. Zhang L, Carroll P, Meggers E. Org Lett. 2004;6:521.
208. Bregman H, Williams DS, Meggers E. Synthesis 2005:1521.
209. Williams DS, Atilla GE, Bregman H, Arzoumanian A, Klein PS, Meggers E. Angew Chem, Int Ed. 2005;44:1984.
210. Atilla-Gokcumen GE, Williams DS, Bregman H, Pagano N, Meggers E. Chembiochem. 2006;7:1443.
211. Bregman H, Carroll PJ, Meggers E. J Am Chem Soc. 2006;128:877.
212. Bregman H, Meggers E. Org Lett. 2006;8:5465.
213. Debreczeni JE, Bullock AN, Atilla GE, Williams DS, Bregman H, Knapp S, et al. Angew Chem, Int Ed. 2006;45:1580.
214. Meggers E, Atilla-Gokcumen GE, Bregman H, Maksimoska J, Mulcahy SP, Pagano N, Williams DS. Synlett 2007:1177.
215. Pagano N, Maksimoska J, Bregman H, Williams DS, Webster RD, Xue F, et al. Org Biomol Chem. 2007;5:1218.
216. Atilla-Gokcumen GE, Pagano N, Streu C, Maksimoska J, Filippakopoulos P, Knapp S, et al. Chembiochem. 2008;2933:9.
217. Anand R, Maksimoska J, Pagano N, Wong EY, Gimotty PA, Diamond SL, et al. J Med Chem. 2009;52:1602.
218. Atilla-Gokcumen GE, Pagano N, Streu C, Maksimoska J, Filippakopoulos P, Knapp S, et al. Chembiochem. 2009;10:198.
219. Xie P, Streu C, Qin J, Bregman H, Pagano N, Meggers E, et al. Biochemistry. 2009;48:5187.
220. Liu J-G, Ji L-N. Wuji Huaxue Xuebao. 2000;16:195.
221. Nozaki K. Kokagaku. 2001;32:2.
222. Sullivan BP, Salmon DJ, Meyer TJ. Inorg Chem. 1978;17:3334.
223. Anderson PA, Anderson RF, Furue M, Junk PC, Keene FR, Patterson BT, et al. Inorg Chem. 2000;39:2721.
224. Evans IP, Spencer A, Wilkinson G. Dalton Trans. 1973;2/1710:204
225. Brodie C. PhD thesis, University of Western Sydney (Campbelltowm), 2006.
226. Rabi II, Zacharias JR, Millman S, Kusch P. Phys Rev. 1938;53:318.
227. Juris A, Balzani V, Barigelletti F, Campagna S, Belser P, Zelewsky AV. Coord Chem Rev. 1988;84:85.
228. Bernhard P, Lehman H, Ludi A. Comments Inorg Chem. 1983;2:145.
229. Matsubara T, Efrima S, Metiu HI, Ford PC. J Chem Soc, Faraday Trans. 1979;75:390.
230. Mason SF. Quart Rev (London) 1963:17.
231. Elsbernd H, Beattie JK. Inorg Chem. 1969;8:893.
232. Sun Y, Lutterman DA, Turro C. Inorg Chem. 2008;47:6427.
233. Bosnich B. Inorg Chem. 1968;7:2379.
234. Bosnich B. Acc Chem Res. 1969;2:266.
235. Broo A, Lincoln P. Inorg Chem. 1997;36:2544.
236. Fan J, Autschbach J, Ziegler T. Inorg Chem. 2010;49:1355.
237. Rutherford TJ, Pellegrini PA, Aldrich-Wright J, Junk PC, Keene FR. Eur J Inorg Chem. 1998:1677.
238. Rillema DP, Allen G, Meyer TJ, Conrad D. Inorg Chem. 2002;22:1617.
239. Greguric I. PhD thesis, University of Western Sydney (Sydney), 1999.
240. Sasso MG, Quina FH, Bechara EJH. Analyt Biochem. 1986;156:239.
241. Burstall FH. J Chem Soc Abstr. 1936:173.
242. Holder E, Trapp O, Trapp G, Marin V, Hoogenboom R, Schubert US. Chirality. 2004;16:363.
243. Kane-Maguire NAP, Wheeler JF. Coord Chem Rev. 2001;211:145.

244. Sun P, Krishnan A, Yadav A, MacDonnell FM, Armstrong DW. J Mol Struct. 2008;890:75.
245. Sun P, Krishnan A, Yadav A, Singh S, MacDonnell FM, Armstrong DW. Inorg Chem. 2007;46:10312.
246. Hannon MJ, Meistermann I, Isaac CJ, Blomme C, Rodger A, Aldrich-Wright JR. Chem Commun. 2001:1078.
247. Pellegrini P, Aldrich-Wright JR. Dalton Trans. 2003:176
248. Lacour J, Torche-Haldimann S, Jodry JJ. Chem Commun. 1998:1733.
249. Lacour J, Goujon-Ginglinger C, Troche-Haldimann S, Jordry JJ. Angew Chem, Int Ed. 2000;39:3695.

Chapter 3
The Synthesis of Platinum(II) Intercalators

Anwen M. Krause-Heuer, Madhura Manohar, K. Benjamin Garbutcheon-Singh, Dianne M. Fisher, and Janice Aldrich-Wright

3.1 Introduction

The pharmacological properties of any drug are largely dependent on binding interactions with biomolecules. The investigation of such interactions is essential to gain some understanding of the mechanisms of drug action, and to determine which structural characteristics influence the pharmacological properties. Of particular interest are the interactions between anticancer agents and DNA, as DNA is considered to be the major cellular target for a large number of compounds that are effective in the treatment of various types of cancers [1–11]. It has been reported that the binding of such drugs to DNA can inhibit cellular processes such as DNA replication and transcription, which are vital for the proliferation of cells [12, 13]. The inhibition or prevention of cell division is the primary objective for drug design as it most markedly affects rapidly dividing cells such as tumour cells, and ultimately prevents their spread throughout the body.

3.1.1 Cisplatin and Cisplatin Analogues

Since the 1960s, there has been extraordinary interest in the development of platinum-based anticancer agents as a result of the clinical success of [*cis*-diammi-nedichloroplatinum(II)] (cisplatin, **1**, Fig. 3.1) [5, 13–19]. Cisplatin is highly effective against a number of cancer types, chiefly testicular, ovarian, cervical, head and neck, oesophageal and small-cell lung cancers [20]. Cisplatin reacts with a wide range of biomolecules, such as proteins, but it is generally accepted that its tumour-inhibiting properties result from targeting nuclear DNA [3, 13, 17, 21–24]. When the drug is administered into the bloodstream, the high chloride concentration

J. Aldrich-Wright (✉)

University of Western Sydney, School of Biomedical & Health Sciences, Penrith South DC New South Wales, Sydney, Australia
e-mail: J.Aldrich-Wright@uws.edu.au
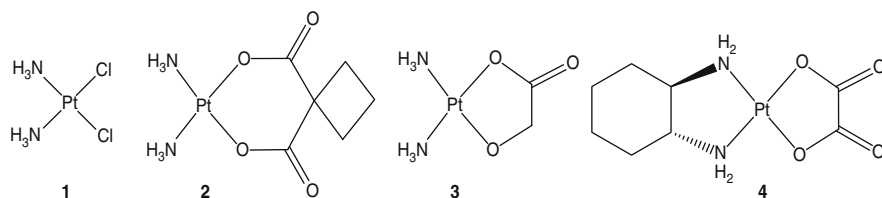
Fig. 3.1 Platinum(II) chemotherapeutic compounds, (**1**) cisplatin and the second-and third-generation cisplatin analogues: (**2**) carboplatin, (**3**) nedaplatin and (**4**) oxaliplatin
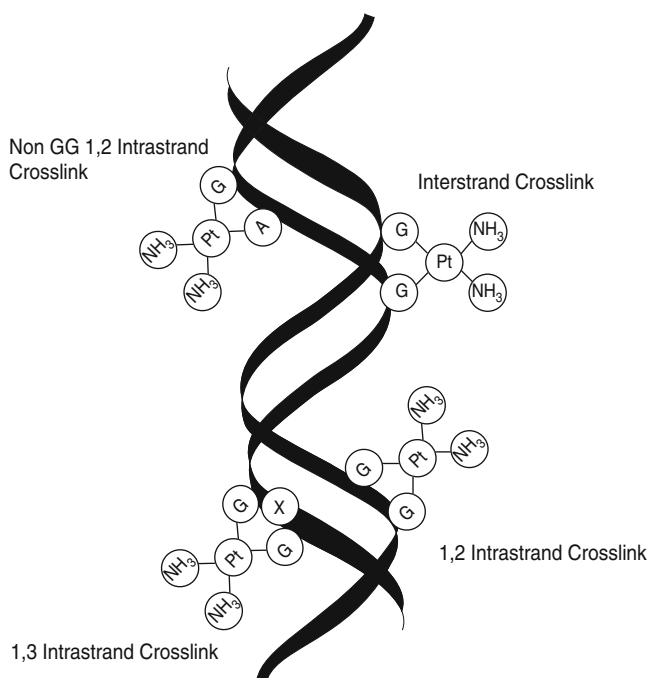
Fig. 3.2 DNA adduct formation with cisplatin adapted with permission from Boulikas et al., *Cancer Therapy*. 2007: 5; 537 [19]

(100 mM) suppresses the hydrolysis of the compound. Once inside the cell, the cisplatin encounters a significantly lower chloride concentration (4–20 mM) which facilitates hydrolysis, forming the species $[Pt(NH_3)_2Cl(OH_2)]^+$ which reacts readily with DNA [25]. The most common DNA-drug adduct, is where the platinum atom binds to the N7 atoms of two adjacent guanine residues on the same DNA strand forming 1,2-intrastrand crosslinks (Fig. 3.2) [3, 13, 21, 26]. Other platinum-DNA adducts such as 1,3-intrastrand crosslinks on non-adjacent bases, as well as monofunctional DNA adducts can also be formed [27–29]. The formation of these crosslinks can cause three-dimensional changes in the structure of DNA such as

localised bending and unwinding [21, 30, 31]. These distortions can obstruct, or inhibit the cellular processes involving DNA [3, 21, 22, 24, 32] such as DNA replication and transcription [22, 24, 33], which prevents further growth and proliferation of cancer cells [14] and in some cases leads to programmed cell death (apoptosis) [5].

Despite its clinical success there are disadvantages associated with the use of cisplatin. Such disadvantages include low solubility in aqueous solutions (which results in protracted intravenous drug administrations with hydration and diuresis required to minimise nephrotoxicity) [3, 24, 25], significant toxicity which limits patient doses [15], severe side effects such as nausea and neurotoxicity [16, 17] and intrinsic or acquired resistance against the drug in some cancer types [18, 25].

Cisplatin analogues have been developed to overcome some of the clinical disadvantages. Carboplatin, ([*cis*-diammine(1,1-cyclobutandicarboxylato)platinum(II)], **2**, Fig. 3.1) is less toxic than cisplatin and it does not induce nephrotoxicity [22, 33] and is clinically used for the treatment of ovarian cancer [21, 22]. Nedaplatin, ([*cis*-diammineglycolatoplatinum(II)], **3**, Fig. 3.1) has received clinical approval in Japan for treatment of a variety of cancer types, including testicular and cervical cancers [34–36]. The mechanism of action of carboplatin and nedaplatin is very similar to that of cisplatin [37], and they are used for the treatment of cancers with limited or no response to cisplatin. However, some cisplatin resistant cancers have been found to be cross resistant to carboplatin and nedaplatin [24, 35, 38–40]. Oxaliplatin, [(1*R*,2*R*)-diaminocyclohexane)oxalatoplatinum(II)], **4**, Fig. 3.1) is a third-generation platinum complex that is not cross resistant with cisplatin [41, 42]. It has been widely utilised in the treatment of colorectal and ovarian cancers after cisplatin or carboplatin has failed, or when the cancer has relapsed [28, 33]. Oxaliplatin is more water-soluble than cisplatin, lacks the nephrotoxicity of cisplatin and has less haematological toxicity than carboplatin at therapeutic doses [35, 39, 40].

3.1.2 Other Platinum-Based Chemotherapeutic Complexes

Over the years, thousands of platinum-based complexes have been designed, synthesised, characterised and examined for their antitumour activity [21], but of these only 33 compounds have made their way into clinical trials and only a few are not cisplatin analogues [22, 32, 33, 43, 44]. From the thousands of cisplatin analogues a number of structural requirements were considered to be necessary for activity against tumours. These structural requirements include: (1) platinum(II) oxidation state; (2) coordination of the metal ion to two protonated N donor atoms (such as NH_3 or ligands containing stable primary or secondary amine groups); (3) two anionic leaving groups (for coordination to the DNA); (4) square-planar geometry with *cis*-coordination of the anionic leaving groups; and (5) an overall neutral charge [35, 45]. Recently researchers have developed new platinum anticancer drugs that break with these conventions [3, 41, 46].
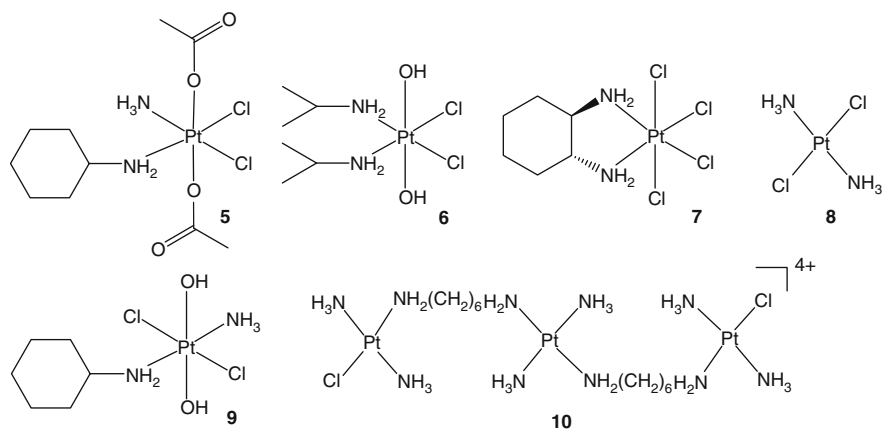
Fig. 3.3 Platinum(IV)-based cancer complexes: (**5**) satraplatin, (**6**) iproplatin, (**7**) tetraplatin, and *trans*-coordinated platinum complexes: (**8**) transplatin (**9**) JM335 and the multinuclear platinum coordination complex, (**10**) BBR3464

Platinum(IV) complexes with octahedral geometry (Fig. 3.3) are believed to be reduced to platinum(II) *in vivo* [47]. Some platinum(IV) complexes lack cross resistance with cisplatin, exhibit lower toxicity and are suitable for oral administration [21, 47]. Satraplatin ((*OC*-6-43)-*bis*(acetato)amminedichloro(cyclohexylamine)platinum **5**, JM216) is the most successful of the platinum(IV) complexes; iproplatin (*cis*-dichloro-*trans*-dihydroxy-*bis*-isopropylamine platinum(IV), **6**) and tetraplatin (1,2-diaminocyclohexane tetrachloroplatinum(IV), **7**) [43] are also undergoing clinical development. Although transplatin (*trans*-diamminedichloroplatinum(II), **8**) was found to be inactive against tumours, substitution of the am(m)ine ligands has produced a number of active antitumour *trans*-coordinated complexes [48]. The *trans*-platinum(IV) complex, JM335 (*trans*-ammine (cyclohexylaminedichlorodihydroxo) platinum(IV), **9**) has demonstrated higher antitumour activity than its *cis*-isomer, JM149, in human ovarian carcinoma cells [24].

A number of multinuclear platinum complexes have also been developed [3, 49–56], some of which have shown activity in both cisplatin-sensitive and cisplatin-resistant cell lines [5]. The most well-studied is BBR3464 [26] (**10**, Fig. 3.3) which exhibits a higher potency than cisplatin *in vitro*, while *in vivo* studies have shown it to be effective towards human xenograft tumours with intrinsic or acquired resistance to cisplatin [27–31]. In phase II clinical trials, **10** was reported to have 100 times the cytotoxicity of cisplatin [14]; however, only partial responses have been observed with cisplatin-resistant ovarian and non small cell lung cancers [3]. Further phase II studies have shown **10** to have minimal antitumour activity against gastric carcinomas, with significant haematological toxicities encountered by patients [32]. Most of the platinum(II) complexes developed have had no major advantage over cisplatin or carboplatin. They have been ineffective against cisplatin-resistant tumours although chemotherapy-related side effects have been reduced and as a result anticancer drug design has shifted towards the development

of platinum complexes that challenge conventional structural models, target different biological molecules and receptors, are not composed of platinum (for example ruthenium- and gold-based drugs) [33, 44] and/or act by a different mechanism [5].

3.1.3 Alternate DNA Binding Modes

Previous platinum-based complexes, such as cisplatin, effected their therapeutic action by covalently coordinating to the base pairs of DNA; however, this is not the only mode by which small platinum complexes can interact with DNA. Positively-charged small molecules can also bind to negatively-charged DNA *via* a range of non-covalent, reversible binding modes such as electrostatic, groove-binding and intercalation.

Electrostatic binding occurs when ions or molecules bind electrostatically to the DNA [57]. Examples include $[Pt(en)_2]^{2+}$ (en = 1,2-diaminoethane), Na^+ and $^+H_3NCH_2CH_2CH_2NH_3^+$ [57]. Groove-binding agents are molecules that bend to fit into the curvature of the groove of the DNA [58]. The binding of these molecules is generally stabilised by a mixture of hydrophobic, electrostatic, hydrogen-bonding and van der Waals interactions [57, 59, 60]; these interactions causes little change to the overall structure of DNA. Examples of groove-binding molecules include Hoechst 33258 (Fig. 3.4), netropsin and **10** before hydrolysis [57, 58, 61, 62].

Molecules that bind via intercalation generally contain a planar, heteroaromatic moiety which inserts between DNA base pairs [38, 59]. This binding is stabilised by π–π stacking and dipole–dipole interactions between the intercalator and DNA base pairs [58, 59]. Examples of intercalating molecules include ellipticine (Fig. 3.4),
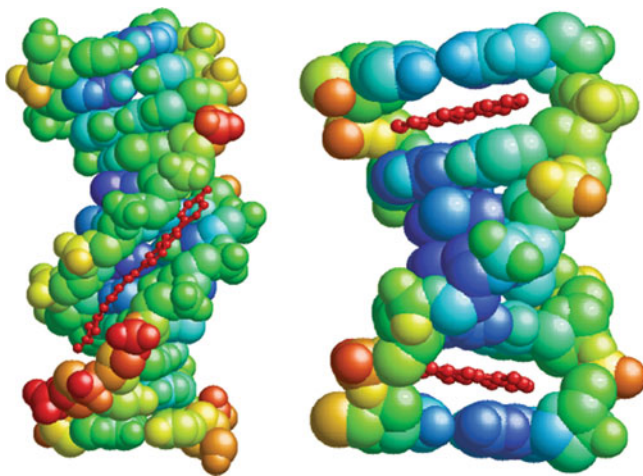
Fig. 3.4 Non-covalent DNA binding modes minor groove with Hoechst 33258 (*left*) [63] and the intercalator ellipticine (*right*) [64]. Both compounds are bound to B-DNA

daunomycin and [Pt(en)(dpq)]$^{2+}$ (where dpq is dipyrido[3,2-d:2',3'-f]quinoxaline) [57, 65–67]. The interaction between intercalating molecules and DNA is strong but reversible [36, 57, 68] and occurs on a millisecond timescale [39]. These unique properties make this non-covalent mode of binding an attractive alternative mechanism for potential anticancer agents to bind to DNA.

3.1.4 Structural Requirements for Intercalation

Investigations into intercalating compounds have shown that these molecules must contain an intercalating moiety consisting of three or four aromatic rings, or have a planar surface area of approximately 28 Å [40] and they must be positively charged so that electrostatic interactions can occur between the intercalating molecule and the negatively charged DNA [69, 70]. Organic molecules such as 1,10-phenanthroline (**11**, phen) or 2-(2'-pyridyl)quinoxaline **12** are unlikely to intercalate DNA because they are neutral. They will, however, intercalate into DNA when either a charged side chain is attached such as in the case of mitoxantrone **13** or aclacinmycin **14**, or when they are coordinated to a metal as part of a charged complex, such as [Pt(bpy)(en)]$^{2+}$ [(2,2'-bipyridine)(1,2-diaminoethane)platinum(II)] **15** and [Pt(en)(phen)]$^{2+}$ [(1,2-diaminoethane)(1,10-phenanthroline)platinum(II)] (**16**, Fig. 3.5) [46].

Methylated phenanthroline derivatives increase the viscosity of DNA solutions to varying extents, depending on the positioning of the methyl substituents [71]. It has been proposed that these compounds intercalate with DNA in a non-classical manner, causing lengthening and bending of the DNA [71, 72]. X-ray
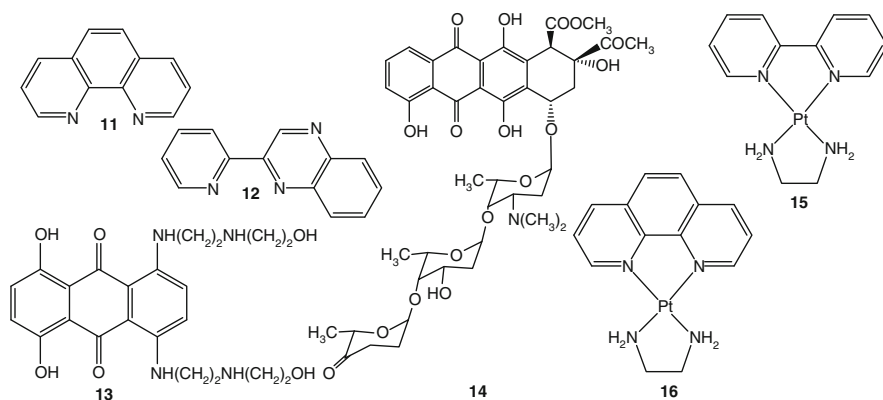
Fig. 3.5 Examples of neutral organic intercalator such as (**11**) phen and (**12**) 2-(2'-pyridyl) quinoxaline; charged organic intercalators such as (**13**) mitoxantrone and (**14**) aclacinmycin, and charged metal complex incorporating an intercalator such as (**15**) [Pt(bpy)(en)]$^{2+}$and (**16**) [Pt(en) (phen)]$^{2+}$

crystallographic studies of ethidium derivatives with bulky substituents, such as ethyl and phenyl groups show that these compounds also bend DNA [73].

3.1.5 The Biological Effects of Intercalating Drugs

Changes in the topology of DNA after insertion of an intercalator are recognised to influence biological activity [36, 40, 49–51, 69, 74]. Intercalation into the base pairs of DNA has been shown to inhibit the synthesis of DNA and RNA, as well as other intracellular processes [36, 69, 74] and leave the cells more susceptible to the normal cellular defence mechanisms [72]. The effects of intercalative drugs are more evident with rapidly proliferating cells, with compounds often exhibiting antibacterial, antiparasitic and antitumour activity [36, 49, 50, 57, 69]. Although many intercalators have been reported to induce biological effects, they lack specificity which can result in indiscriminate toxicity [57], which can curtail their use.

3.2 Platinum(II) Metallointercalators

In 1974, the intercalative binding of platinum(II) complexes containing the bidentate ligands 2,2′-bipyridine (bpy) and phen were investigated using X-ray diffraction and electrophoresis. The complexes **15** and **16** were observed to intercalate and unwind DNA [52–54]. Following this work the concept of metallointercalation was extended with the subsequent development of various octahedral intercalating complexes [46, 55, 56, 75–77]. A series of chiral *tris*(phenanthroline) octahedral complexes using zinc [56], iridium [78, 79], iron [77, 80, 81], cobalt [80, 82, 83], osmium [84–87], rhodium [85, 87–99] and ruthenium [46, 56, 75–77, 82, 85, 87–89, 98–114] metal centres were synthesised and their interactions with DNA investigated. The inclusion of a metal centre into the design of intercalating compounds gives rise to a greater range of geometric diversity and structural flexibility than any purely organic molecules can achieve [89].

Since the 1970s, numerous platinum(II) metallointercalators have been constructed [52–54, 70, 115–138], however, there have been limited investigations into the mechanism of action. The pharmacological properties of platinum metallointercalators have only been reported for a small number of complexes [116–118, 134, 137, 138]. A series of related platinum(II) compounds containing bpy, phen and 3,4,7,8-tetramethyl-1,10-phenathroline (3,4,7,8-Me$_4$-phen) intercalating ligands (Fig. 3.6), were tested against the L1210 murine leukaemia cell line to assess their cytotoxicity; these results are reported in Table 3.1 [116]. These achiral compounds were reported to be active, with [Pt(3,4,7,8-Me$_4$-phen)(en)]$^{2+}$ being the most active, followed by [Pt(3,4,7,8-Me$_4$-phen)(1,3-pn)]$^{2+}$(1,3-pn = 1,3-diaminopropane) and [Pt(phen)(en)]$^{2+}$, having IC$_{50}$ values of 0.7, 1 and 2 μM, respectively. However, the complexes [Pt(bpy)(1,4-bn)]$^{2+}$ and [Pt(phen)(1,4-bn)]$^{2+}$
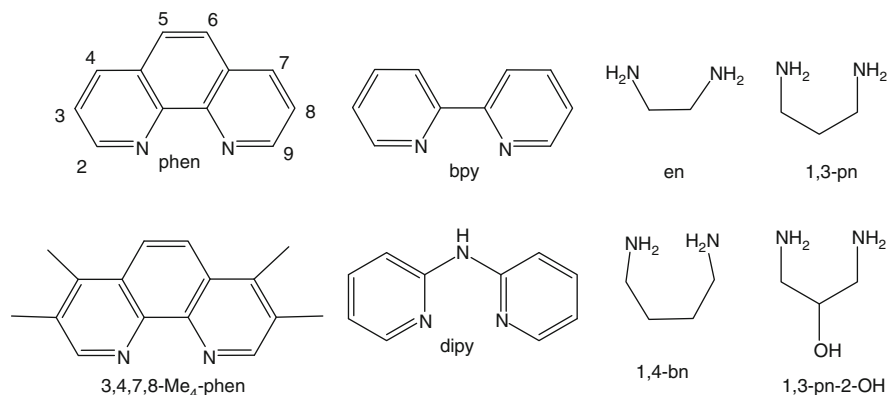
Fig. 3.6 The structure of the intercalating and ancillary ligands used for the synthesis of platinum complexes assessed in Table 3.1

Table 3.1 The IC$_{50}$ values in the L1210 cell line of platinum(II) complexes containing phen, bpy or 3,4,7,8-Me$_4$-phen as the intercalating ligand and various achiral ancillary ligand

Compound	L1210 (μM) [116]
Cisplatin	0.5–1.0
[Pt(bpy)(en)]Cl$_2$ 15	33
[Pt(bpy)(1,4-bn)]Cl$_2$	>500
[Pt(bpy)(1,3-pn-2-OH)]Cl$_2$	43
[Pt(bpy)(1,3-pn)]Cl$_2$	9
[Pt(phen)(en)]Cl$_2$ 16	2
[Pt(phen)(1,4-bn)]Cl$_2$	110
[Pt(phen)(1,3-pn-2-OH)]Cl$_2$	11
[Pt(phen)(1,3-pn)]Cl$_2$	14
[Pt(3,4,7,8-Me$_4$-phen)(en)]Cl$_2$	0.7
[Pt(3,4,7,8-Me$_4$-phen)(1,4-bn)]Cl$_2$	50
[Pt(3,4,7,8-Me$_4$-phen)(1,3-pn-2-OH)]Cl$_2$	5
[Pt(3,4,7,8-Me$_4$-phen)(1,3-pn)]Cl$_2$	1

(1,4-bn = 1,4-diaminobutane) were inactive in the L1210 cell line, having IC$_{50}$ values of >500 and 110 μM, respectively [116]. These results suggest that the combination of intercalator and ancillary ligand coordinated to the platinum has a significant effect on the biological activity of these complexes [116]. As a result of the cytotoxicity displayed by [Pt(phen)(en)]$^{2+}$ and [Pt(3,4,7,8-Me$_4$-phen)(en)]$^{2+}$ in the L1210 cell line [116], *in vivo* investigations were conducted, although, neither complex showed significant anticancer activity in mice bearing murine leukaemia [116]. Further *in vitro* testing were conducted with conflicting results and are discussed in Sect. 3.2.2. The broad spectrum of cytotoxicity results obtained with the limited number of intercalator and ancillary ligand combinations necessitated further investigation. In order to improve the cytotoxic effects of metallointercalators, a systematic approach was undertaken to explore the consequences of varying

the ancillary ligand, and separately, changing the intercalator [117, 139]. In the sections that follow we highlight some of the significant changes to the activity of platinum(II) intercalators when both the ancillary and intercalating ligands are varied.

3.2.1 Variation of the Ancillary Ligand

One of the earliest studies into the structure-activity relationships of platinum(II) intercalators involved changes to the ancillary ligand included compounds of the type $[Pt(I_L)(A_L)]^+$, where I_L = bpy, phen or 2,2′-dipyridylamine (dipy) and A_L = amino acids (Fig. 3.7) [140–142]. The cytotoxicity in the murine lymphocytic leukaemia cell line, P338, was determined and these results are reported in Table 3.2. Most complexes displayed similar or less activity than cisplatin, with the most active compound of the series reported was [Pt(dipy)(Ala)]Cl with a IC_{50} value of 1.2 μM. The complexes containing phen were less active than those containing bpy for all compounds tested. Changing the counter-ion of the complexes $[Pt(phen)(A_L)]^+$ from chloride to nitrate resulted in a reduction in activity, for all compounds tested. The results indicate that increased solubility increases the cytotoxicity of these compounds.

Other ancillary ligands investigated include chiral diamines such as 2,3-butane-diamine (2,3-bn) in the form of $[Pt(phen)(A_L)]^{2+}$ where A_L = 2R,3R-, 2S,3S- and 2R,3S-bn (Fig. 3.8) [115]. Here the cytotoxicity in a number of human carcinoma cell lines were assessed and compared with $[Pt(phen)(en)]^{2+}$ and cisplatin [118]. The inclusion of the chiral 2,3-bn ligand into the complexes increased the cytotoxicity for each cell line tested (Table 3.3). The complexes, $[Pt(phen)(R,R-bn)]^{2+}$ and $[Pt(phen)(S,S-bn)]^{2+}$ were also assessed against L1210 and the cisplatin-resistant

R = H = Gly
R = CH₃ = Ala
R = CH₂(CH)(CH₃)₂ = Leu
R = (CH)(CH₃)₂ = Val
R = CH₂CH₂SCH₃ = Met
R = CH₂-Ph = Phe
R = CH₂OH = Ser
R = CH₂-Ph-OH = Tyr
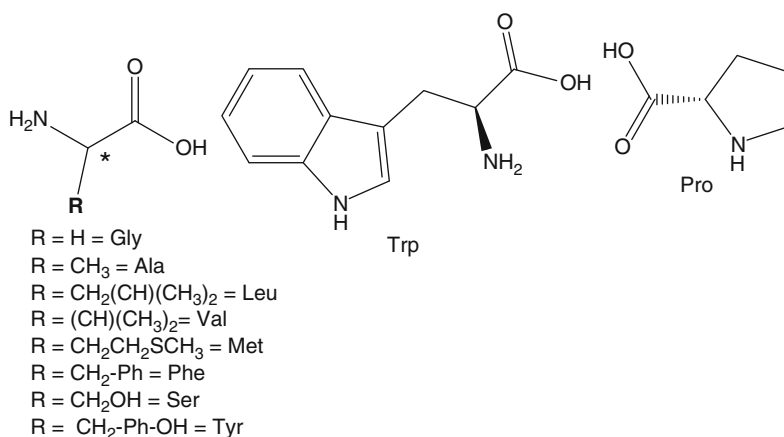
Fig. 3.7 The structure of the amino acids coordinated as ancillary ligands, as assessed in Table 3.2

Table 3.2 The cytotoxicity in the P338 cell line of platinum(II) complexes containing amino acids as the ancillary ligand

Compound	IC$_{50}$ P388 (μM)	Compound	IC$_{50}$ P388 (μM)
Cisplatin	16–17	[Pt(phen)(Leu)]Cl [143]	36
[Pt(bpy)(Ala)]Cl [142]	15	[Pt(phen)(Leu)]NO$_3$ [143]	57
[Pt(bpy)(Asn)]Cl [142]	39	[Pt(phen)(Pro)]Cl [143]	36
[Pt(bpy)(Gly)]NO$_3$ [142]	>43	[Pt(phen)(Ser)]Cl [143]	36
[Pt(bpy)(Leu)]Cl [142]	17	[Pt(phen)(Trp)]NO$_3$ [143]	35
[Pt(bpy)(Met)]Cl [142]	14	[Pt(phen)(Tyr)]Cl [143]	33
[Pt(phen)(Ala)]Cl [143]	34	[Pt(phen)(Tyr)]NO$_3$ [143]	77
[Pt(phen)(Ala)]NO$_3$ [143]	>100	[Pt(phen)(Val)]Cl [143]	15
[Pt(phen)(Gly)]Cl [143]	12	[Pt(dipy)(Ala)]Cl [144]	1.2
[Pt(phen)(Gly)]NO$_3$ [143]	86	[Pt(dipy)(Gly)]Cl [144]	>100

L1210 cell line, L1210cis^R, 2008 (human ovarian carcinoma), C13*5 (human ovarian carcinoma cell line with acquired resistance to cisplatin) and SKOV-3 (7 days) (human ovarian carcinoma cell line with intrinsic resistance to cisplatin). [Pt(phen)(R,R-bn)]$^{2+}$, was more active than [Pt(phen)(S,S-bn)]$^{2+}$ and both were more active than [Pt(phen)(en)]$^{2+}$, but less active than cisplatin in all cell lines [139].

The activities of [Pt(phen)(S,S-dach)]$^{2+}$ and [Pt(phen)(R,R-dach)]$^{2+}$ were determined in 12 cell lines: L1210, L1210cis^R, 5637, 2008, C13*5, SKOV-3, A-427 (human lung cancer), MCF-7 (human breast cancer), RT-4 (human bladder cancer), SISO (human cervical cancer), KYSR-70 (human oesophagal cancer) and LCLC-103H (large cell carcinoma). In these experiments S,S- was more active than the R, R-enantiomer; moreover [Pt(phen)(S,S-dach)]$^{2+}$ was more cytotoxic than cisplatin in all cell lines tested (Table 3.2) [143]. These experiments showed that the diaminocyclohexane ligand imparts greater cytotoxicity on the complex than the butanediamine ligand. Methylation of the diaminocyclohexane ligand resulted in decreasing the activity of the complexes [118].

The sterically crowded 1,3-diamino-1,2,2-trimethylcyclopentane ligand (R,S-tmcp and S,R-tmcp (Fig. 3.8)) was also used to form the complexes, [Pt(I$_L$)(A$_L$)]$^{2+}$ where I$_L$ = phen or 3,4,7,8-Me$_4$-phen, A$_L$ = R,S-tmcp or S,R-tmcp. Some differences were observed in the *in vitro* cytotoxicity experiments, with complexes having the (S, R) configuration showing higher biological activity in L1210 cells (Table 3.3) [144]. [Pt(3,4,7,8-Me$_4$-phen)(S,R-tmcp)]$^{2+}$ was the most active and showed an increase in biological activity over the non-methylated counterparts [200]. The increase in activity is significant when compared to [Pt(3,4,7,8-Me$_4$-phen)(en)]$^{2+}$ with an IC$_{50}$ of >50 μM [117].

1,2-Diphenylethanediamine (dpen) and the fluorinated derivative 1,2-*bis*(4-fluorophenyl)-1,2-ethylenediamine (bfed) (Fig. 3.8) were used to synthesise [Pt(5,6-Me$_2$-phen)(R,R-dpen)](ClO$_4$)$_2$, [Pt(5,6-Me$_2$-phen)(S,S-dpen)](ClO$_4$)$_2$, [Pt(5,6-Me$_2$-phen)(bfed)]Cl$_2$, [Pt(5-Me-phen)(bfed)]Cl$_2$ and [Pt(phen)(bfed)]Cl$_2$ [145]. These ligands have been used to mimic the synthetic estrogens diethylstilbestrol and

Table 3.3 The cytotoxicity against identified cell lines of selected platinum(II) complexes containing 1,10-phenanthroline and various ancillary ligands

Compound	IC$_{50}$ (µM)												
	L1210	L1210 cis^R	5637	2008	C13*5	SKOV-3 (7 days)	A-427	MCF-7	RT-4	SISO	RT-112	KYSR-70	LCLC-103H
[Pt(phen)(en)]Cl$_2$ [117, 143]	9.65	–	23.7	–	–	–	15.1	21.8	–	9.47	49.1	–	41.2
Cisplatin	0.5–1.0	6.90	0.43	0.60	10	3	1.969	1.43	3.42	0.19	1.47	1.18	1.44
[Pt(phen)(2R,3S-bn)]Cl$_2$ [118]	–	–	0.72	–	–	–	0.92	–	–	–	–	–	1.07
[Pt(phen)(2S,3S-bn)]Cl$_2$ [118]	3.4	6.65	0.98	9.1	25.3	10.3	1.35	–	–	–	–	–	2.39
[Pt(phen)(2R,3R-bn)]Cl$_2$ [118]	1.5	2.2	0.43	3.1	7.1	3.17	0.54	–	–	–	–	–	0.78
[Pt(phen)(rac-bn)](ClO$_4$)$_2$ [118]	–	–	0.95	–	–	–	0.67	–	–	–	–	–	1.06
[Pt(phen)(Me$_2$-R,R-dach)](ClO$_4$)$_2$ [118]	>40	>40	23.6	–	–	–	>40	–	–	–	–	–	–
[Pt(phen)(Me$_2$-S,S-dach)](ClO$_4$)$_2$ [118]	>40	>40	55.6	–	–	–	>40	–	–	–	–	–	–
[Pt(phen)(1S,2S-dach)Cl$_2$ [143, 154, 155]	0.13 and 0.19	0.28 and 0.20	0.091	0.41	0.72	0.37	0.11	0.15	0.88	0.14	0.11	0.14	–
[Pt(phen)(1R,2R-dach)Cl$_2$ [143, 154, 155]	–	–	0.54	3.2	7.15	3.45	1.19	0.25	2.95	0.34	0.51	1.75	–
[Pt(phen)(1R,2R-dach)(ClO$_4$)$_2$ [143, 154, 155]	1.5	4.4	–	–	–	–	–	–	–	–	–	–	–
[Pt(phen)(R,S-tcmp)Cl$_2$ [144]	13.2	–	–	–	–	–	–	–	–	–	–	–	–
[Pt(phen)(S,R-tcmp)Cl$_2$ [144]	11.2	–	–	–	–	–	–	–	–	–	–	–	–
[Pt(3,4,7,8-Me$_4$-phen)(R,S-tcmp) Cl$_2$ [144]	11.5	–	–	–	–	–	–	–	–	–	–	–	–
[Pt(3,4,7,8-Me$_4$-phen)(S,R-tcmp) Cl$_2$ [144]	8.5	–	–	–	–	–	–	–	–	–	–	–	–
[Pt(5,6-Me$_2$-phen)(R,R-dpen)] (ClO$_4$)$_2$ [145]	–	–	1.22	–	–	–	2.52	1.56	8.47	6.26	–	–	–
[Pt(5,6-Me$_2$-phen)(S,S-dpen)] (ClO$_4$)$_2$ [145]	–	–	2.96	–	–	–	2.46	2.67	11.59	5.1	–	–	–
[Pt(phen)(rac-bfed)]Cl$_2$ [145]	–	–	10.86	–	–	–	>20	>20	>20	–	–	–	15.7
[Pt(5,-Me-phen)(rac-bfed)]Cl$_2$ [145]	–	–	5.45	–	–	–	>20	>20	>20	–	–	–	6.96
[Pt(5,6-Me$_2$-phen)(rac-bfed)]Cl$_2$ [145]	–	–	2.11	–	–	–	3.07	7.97	11.88	–	–	–	1.75
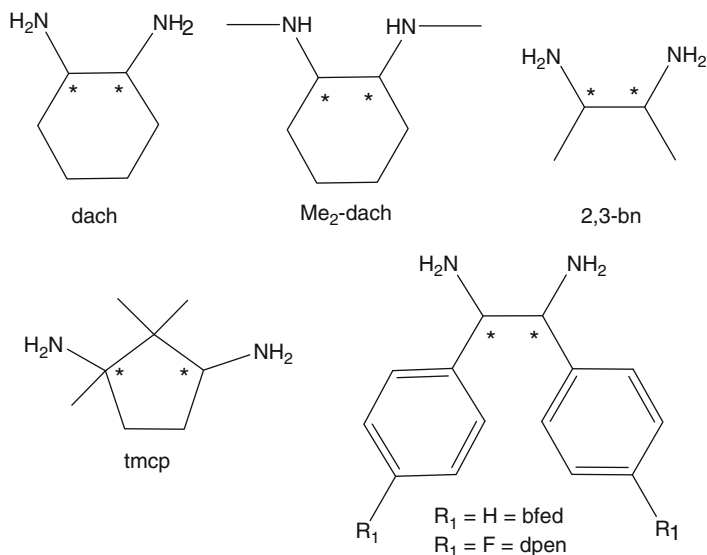
Fig. 3.8 The structure of the various ancillary ligands coordinated to platinum, with the cytotoxicity assessed in Table 3.3

hexestrol in an attempt to target the oestrogen receptor system [146–149]. 1,2-Diarylethanediamine platinum(II) compounds have displayed activity in a number of hormone dependent (MCF-7) and independent (MDB-MB 231) breast cancer cell lines [150–152]. The most active of these, the *meso* and racemic derivatives of [(1,2-*bis*(4-fluorophenyl)-1,2-ethylenediamine)sulfatoplatinum(II)] [150] have been reported to have *in vitro* activity, although these compounds did not display significant activity *in vivo* [153]. As such, it was of interest to determine whether the addition of a phenanthroline intercalating ligand to the molecule would produce a more cytotoxic compound. When 1,10-phenanthroline was added to [Pt(bfed)Cl$_2$], the resulting complex was less active than [Pt(bfed)Cl$_2$]. The cytotoxicity of these compounds was much less than [Pt(5,6-Me$_2$-phen)(en)]Cl$_2$ or cisplatin [145].

3.2.2 Variation of the Intercalating Ligand

The affect of the intercalator was investigated by comparing the cytotoxicity of different methyl-substitution on the phenanthroline of [Pt(I$_L$)(en)]$^{2+}$ complexes [117], where I$_L$ = phen [53], 4-Me-phen, 5-Me-phen, 4,7-Me$_2$-phen, 5,6-Me$_2$-phen and 3,4,7,8-Me$_4$-phen [116] (Fig. 3.9) with cisplatin in the L1210 cell line (Table 3.4). The *in vitro* experiments, reported by McFadyen et al., for [Pt(phen)(en)]$^{2+}$ and [Pt(3,4,7,8-Me$_4$-phen)(en)]$^{2+}$ (Table 3.1) had been reported at 2 and 0.7 μM, respectively [116], but when repeated, by Brodie et al., the IC$_{50}$

R3, R4, R6, R7, R8 = H, R5 = NO2 = 5-NO2-phen
R3, R4, R6, R7, R8 = H, R5 = NH2 = 5-NH2-phen
R3, R4, R6, R7, R8 = H, R5 = Me = 5-Me-phen
R3, R4, R6, R7, R8 = H, R5 = Cl = 5-Cl-phen
R3, R5, R6, R7, R8 = H, R4 = Me = 4-Me-phen
R3, R4, R7, R8 = H, R5, R6 = Me = 5,6-Me2-phen
R3, R5, R6, R8 = H, R4, R7 = Me = 4,7-Me2-phen
R5, R6 = H, R3, R4, R7, R8 = Me = 3,4,7,8-Me4-phen
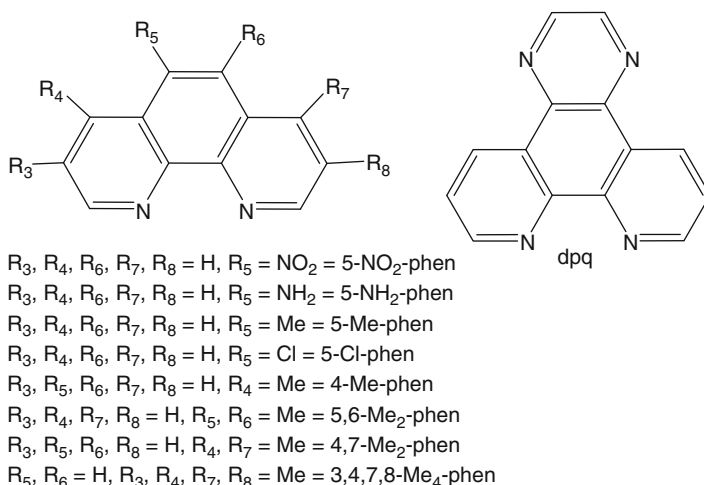
Fig. 3.9 The structure of the various intercalating ligands used in Table 3.4

Table 3.4 The cytotoxicity of platinum(II) complexes of ethylenediamine and derivatives of 1,10-phenanthroline against identified cell lines

Compound	IC_{50} (µM)						
	L1210	5637	A-427	MCF-7	SISO	KYSE 520	LCLC-103H
Cisplatin	0.5	0.31	3.95	1.43	0.19	6.63	1.44
[Pt(phen)(en)]Cl2 [117, 143]	9.65	23.7	15.1	21.8	9.47	49.1	41.2
[Pt(5,6-Me2phen)(en)]Cl2 [117]	1.5	–	–	–	–	–	–
[Pt(5-Me-phen)(en)]Cl2 [117]	2.8	–	–	–	–	–	–
[Pt(4-Me-phen)(en)]Cl2 [117]	>50	–	–	–	–	–	–
[Pt(4,7-Me2-phen)(en)]Cl2 [117]	>50	–	–	–	–	–	–
[(Pt(3,4,7,8,-Me4-phen)(en)Cl2 [117]	>50	–	–	–	–	–	–

values of $[Pt(phen)(en)]^{2+}$ and $[Pt(3,4,7,8-Me_4-phen)(en)]^{2+}$ were 9.65 and 50 mM, respectively [117]. No reason was given for the discrepancy although any residual free platinum in the complex could account for increased activity. These experiments did show that methyl substitution on specific endocyclic carbon atoms of phen can affect the biological activity of a complex. The order of activity is 5,6-Me2-phen > 5-Me-phen > phen > 4-Me-phen = 4,7-Me2-phen = 3,4,7,8-Me4-phen [116].

NMR studies revealed that they all insert into the hexanucleotide d(GTCGAC)2 from the minor groove, predominantly between the T_2A_5 and C_3G_4 base pairs [117]. The NMR evidence also indicated that the intercalator is inserted into the DNA with the en in the minor groove. It is probable that the observed enhancement

Table 3.5 The cytotoxicity of platinum(II) complexes of diaminocyclohexane and derivatives of 1,10-phenanthroline against identified cell lines

Compound [156]	IC$_{50}$ (μM)	
	L1210	5637
Cisplatin	0.5–1.0	0.43
[Pt(5,6-Me$_2$-phen)(*S,S*-dach)]Cl$_2$	0.0092	0.082
[Pt(4,7-Me$_2$-phen)(*S,S*-dach)]Cl$_2$	0.13	0.043
[Pt(5-Me-phen)(*S,S*-dach)]Cl$_2$	0.033	0.046
[Pt(5-Cl-phen)(*S,S*-dach)]Cl$_2$	0.25	–
[Pt(5-NH$_2$-phen)(*S,S*-dach)]Cl$_2$	0.32	–
[Pt(5-NO$_2$-phen)(*S,S*-dach)]Cl$_2$	0.32	–
[Pt(3,4,7,8-Me$_4$-phen)(*S,S*-dach)]Cl$_2$	0.87	0.143
[Pt(5,6-Me$_2$-phen)(*R,R*-dach)]Cl$_2$	0.46	0.171
[Pt(5-Me-phen)(*R,R*-dach)]Cl$_2$	1.2	–
[Pt(5-Cl-phen)(*R,R*-dach)]Cl$_2$	1.1	–
[Pt(5-NH$_2$-phen)(*R,R*-dach)]Cl$_2$	1.2	–
[Pt(5-NO$_2$-phen)(*R,R*-dach)]Cl$_2$	1.7	–
[Pt(dpq)(*R,R*-dach)]Cl$_2$	1.1	–
[Pt(dpq)(*S,S*-dach)]Cl$_2$	0.25	–

in biological activity is due to favourable hydrogen bonding or steric interactions. For the complexes [Pt(4-Me-phen)(en)]$^{2+}$, [Pt(4,7-Me$_2$-phen)(en)]$^{2+}$ and [Pt(3,4,7,8-Me$_4$-phen)(en)]$^{2+}$, results from DNA-NMR binding experiments suggest that the hydrogens of the methyl groups on C4 and C7 are close to the base pairs and possibly interacting unfavourably and this may result in the reduced biological activity of these complexes [117]. In addition, it is possible that the methyl groups interact with phosphodiester groups of the sugar-phosphate backbone, affecting the depth of intercalation. The overall binding interaction however is dependent upon the overall structural characteristics of the metallointercalator, the type of DNA and the ionic strength of the binding environment.

Further changes were assessed with fourteen complexes of the type [Pt(I$_L$)(A$_L$)]$^{2+}$ (I$_L$ = 5-chloro-1,10-phenanthroline (5-Cl-phen), 5-methyl-1,10-phenanthroline (5-Me-phen), 5-amino-1,10-phenanthroline (5-NH$_2$-phen), 5-nitro-1, 10-phenanthroline (5-NO$_2$-phen) or dipyrido[3,2-*d*:2′,3′-*f*]quinoxaline and A$_L$ = en, *S,S*-dach or *R,R*-dach) were synthesised and their cytotoxicities determined in the L1210 cell line (Table 3.5). The most cytotoxic complexes are those that contain *S,S*-dach ancillary ligands and 5-Me-phen intercalating ligands, with [Pt(5-Me-phen)(*S,S*-dach)]Cl$_2$ displaying a five to tenfold increase in cytotoxicity compared to cisplatin.

3.2.3 Intercalating and Intercalating/Covalent Complexes

Other platinum-based complexes where the intercalating ligand and an aromatic achiral ligand are coordinated to platinum or an intercalator is attached via a linker or tethered to the platinum have also been developed, (Fig. 3.10) [131, 157–161].
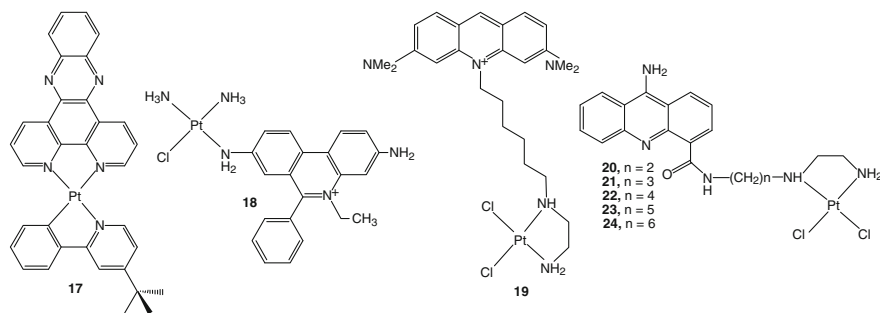
Fig. 3.10 Second-generation platinum(II) metallointercalators: (**17**) $[Pt(dppz)(4-tBu-2-phpy)]^{2+}$ [131], and metal-linked metallointercalators (**18**) linked [157] or (**19–24**) tethered [160]

$[Pt(dppz)(4-tBu-2-phpy)]^{2+}$ is potent with an IC_{50} value 1.7 µM compared to cisplatin at 22.1 µM in KB-3-1 human carcinoma cells lines. This compound is also fluorescent and has the potential to be used to probe cellular interaction using the confocal microscope. Dichloroplatinum complexes tethered intercalators such as ethidium and acridines make the most of the both intercalative and coordinate binding opportunities. Examples include 9-aminoacridine-4-carboxamides, which are cytotoxic with IC_{50} values of 3.2, 0.56, 2.8, 1.8 and 0.67 µM for compounds 20, 21, 22, 23 and 24, respectively, when compared with cisplatin (0.30 µM) in the same P338 cell line [132, 160–164].

3.3 Synthesis

The coordination of platinum(II) to N-donor ligands is well reported in the literature [34, 162–185]. Many of the reported complexes are structural analogues of cisplatin or transplatin, in that they are square planar but increasingly there are more examples with new structural motifs. Here synthetic schemes and details of different metallointercalators are provided with the primary references. In the schemes, phenanthroline and ethylenediamine have been used to represent the intercalating and ancillary ligands, respectively. A generic procedure for synthesis, purification and characterisation for platinum intercalators and this is shown in Scheme 3.1. We have used the synthesis of $[Pt(phen)(en)]Cl_2$ as an exemplar. There are several different approaches for synthesising the intermediates, $[Pt(phen)Cl_2]$ and $[Pt(en)Cl_2]$, these are detailed in Sects. 3.3.1.1–3.3.1.5 and 3.3.2.1–3.3.2.2, respectively, and illustrated in Scheme 3.2. Isolation of the complex, [Pt(phen) (en)]Cl_2 is synthesised from two intermediates, $[Pt(phen)Cl_2]$ and $[Pt(en)Cl_2]$, in Sect. 3.3.3.1–3.3.3.3 and 3.3.4.1–3.3.4.3, respectively, and this is depicted in Scheme 3.3. The characterisation of platinum intercalator complexes are discussed to illustrate techniques used.
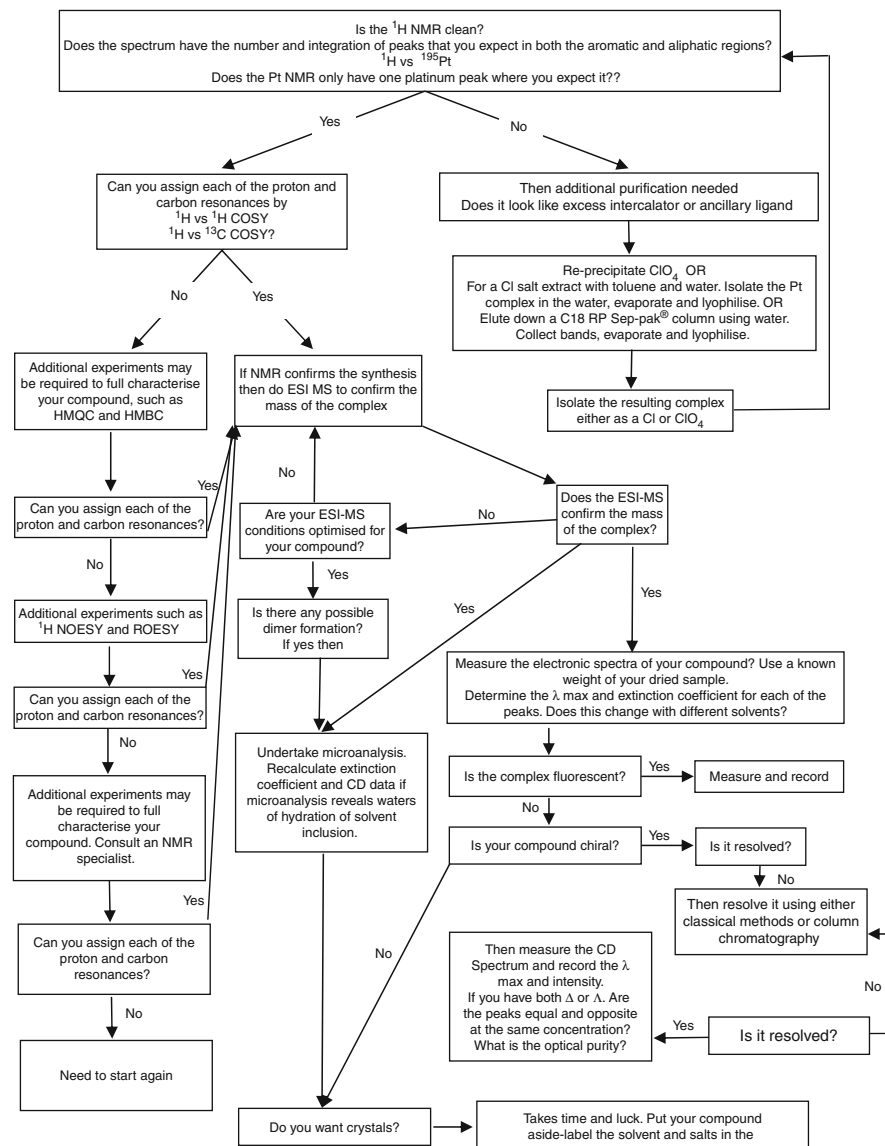
Synthetic Scheme 3.1 Synthesis, purification and characterisation protocol for $[Pt(I_L)(A_L)]Cl_2$ or precipitated with ClO_4

3.3.1 Reaction of $K_2[PtCl_4]$ to Produce of $[Pt(I_L)Cl_2]$, Scheme 3.2

3.3.1.1 Isolation of *cis*-[Pt(DMSO)$_2$Cl$_2$] [186]

$K_2[PtCl_4]$ (1 equiv.) was dissolved in H_2O (~20 mL). The red solution was filtered to remove any insoluble impurities. DMSO (~2–3 equiv.) was added slowly and the
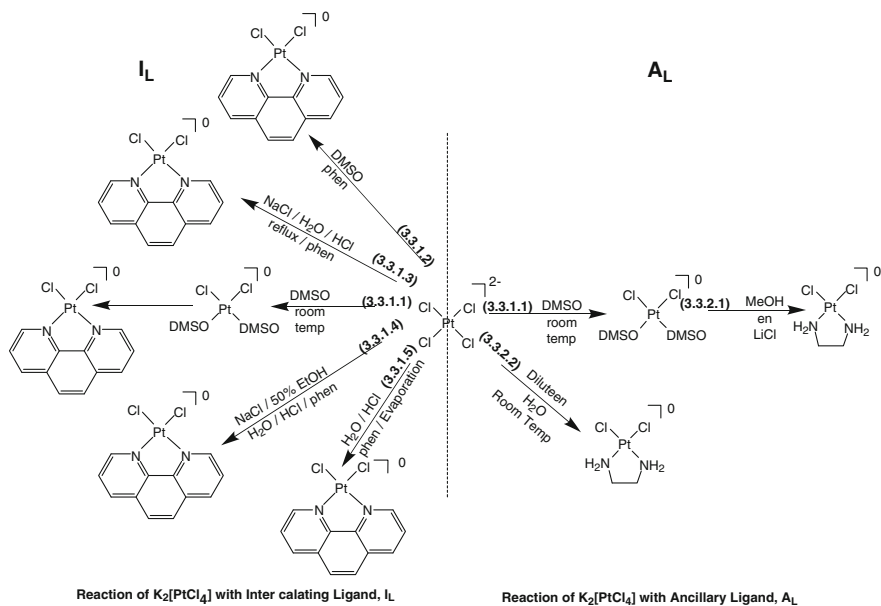
Synthetic Scheme 3.2 An overview of the reactions of $K_2[PtCl_4]$ with the ancillary ligand, A_L and the intercalating ligand, I_L
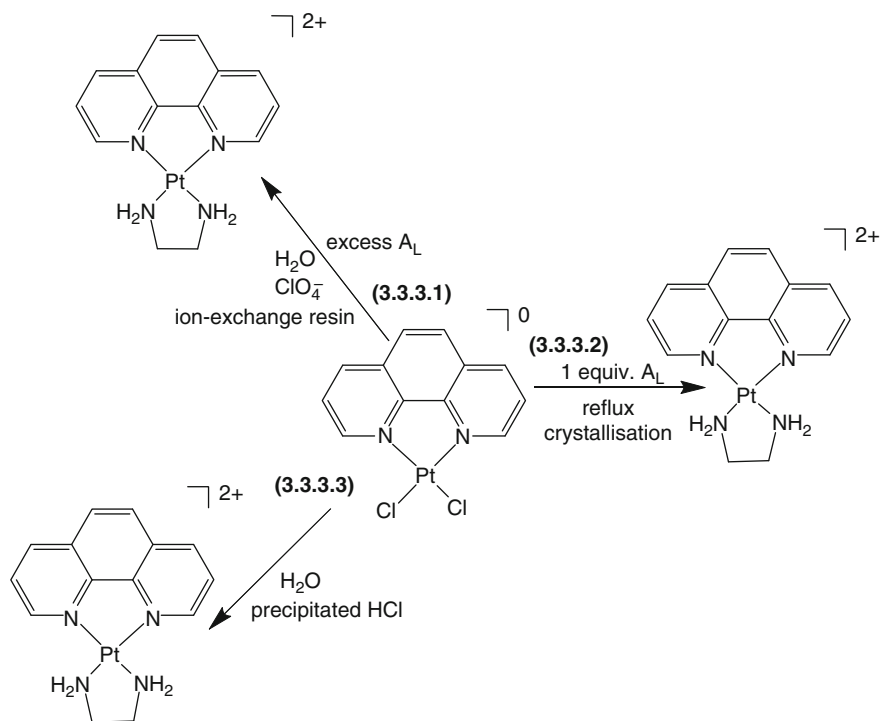
Synthetic Scheme 3.3 Reaction of $[Pt(I_L)Cl_2]$ with ancillary ligand

solution stirred (2 h). Yellow needles of *cis*-[Pt(DMSO)$_2$Cl$_2$] precipitated overnight and were filtered and washed with a minimum volume of H$_2$O (4 °C), ethanol and diethyl ether and dried under vacuum. Yield ~95%.

3.3.1.2 Synthesis of [Pt(I$_L$)Cl$_2$] from DMSO [116]

The intercalating ligand (I$_L$ = phen and phen derivatives, 1 equiv.) was dissolved in DMSO (10 mL) with gentle heating and stirring. To the solution, K$_2$PtCl$_4$ (1 equiv.) was dissolved in H$_2$O/DMSO (or DMSO [187]) (1:3, 4 mL) was added. The solution was removed from the heat and then cooled slowly to room temperature (1–2 h). The resultant crystals were filtered and washed (chilled HCl (1 M), water, ethanol, and diethyl ether [117]) before being dried under vacuum (100 °C). Yield ~75–90%.

3.3.1.3 Synthesis of [Pt(I$_L$)Cl$_2$] from Water [188]

K$_2$PtCl$_4$ (1 equiv.) and NaCl (0.01 mmol) were dissolved in warm water (350 mL). To the solution I$_L$ (I$_L$ = phen, 5-NO$_2$-phen, 5-Cl-phen or dpq, 1 equiv.) dissolved in HCl (10 M, 2 mL) was added and the mixture heated (100 °C) for 4 h. The flocculant precipitate was filtered, washed with ice-cold water and dried under vacuum. Yield ~25–60%.

3.3.1.4 Synthesis of [Pt(I$_L$)Cl$_2$] from Water–Ethanol and Other Mixed Solvents [189]

K$_2$PtCl$_4$ (1 equiv.) and NaCl (1 equiv.) were dissolved in a mixture of warm water/ethanol (2 L). To the solution I$_L$ (I$_L$ = phen, 5-NO$_2$-phen, 5-Cl-phen or dpq, 1 equiv.) dissolved in HCl (10 M, 2 mL) was added and the mixture allowed to stand for 3 h. The yellow precipitate was filtered, washed with ice-cold water and dried under vacuum. Yield ~95%. Other solvents such as methanol, acetone or acetonitrile can be used in place of ethanol. The only drawback is that solvents such as ethanol and methanol can cause reduction of platinum.

3.3.1.5 Large Scale Synthesis of [Pt(I$_L$)Cl$_2$] from HCl Solution by Evaporation [189]

K$_2$PtCl$_4$ (1 equiv.) and I$_L$ (1.2 equiv.) were dissolved in H$_2$O (1.5 L) containing a small amount of HCl, and the solution stirred (100 °C, 20 h). The mixture was either filtered hot [190], or allowed to cool to room temperature before filtration. The solid was washed with hot water, and dried under vacuum. Yield ~90%.

3.3.2   Reaction of K$_2$[PtCl$_4$] with Ancillary Ligand, Scheme 3.2

3.3.2.1   Synthesis of [Pt(A$_L$)Cl$_2$] from *cis*-[Pt(DMSO)$_2$Cl$_2$] [145, 187]

A suspension of *cis*-[Pt(DMSO)$_2$Cl$_2$] (1 equiv.) in methanol (40 mL) was added to a mixture of A$_L$ (1 equiv.) in methanol (20 mL). The mixture was stirred until clear (1 h), stored at 4 °C (12 h) and then filtered. The filtrate volume was reduced by rotary evaporation to afford a viscous residue which was then dissolved in warm H$_2$O (20 mL) and ethanol (20 mL). The solution was filtered, and poured onto an excess of LiCl (~0.5 g). The volume was then reduced by half on a steam bath, before being cooled over ice. Fine pale-yellow needles were collected at the pump, washed with cold water and air-dried. Yield 67%.

3.3.2.2   Synthesis of [Pt(A$_L$)Cl$_2$] from Water [156]

K$_2$PtCl$_4$ (1 equiv.) was dissolved in water (10 mL) with stirring and A$_L$ (1 equiv.) was added and the solution stirred (45 min). The resultant crystalline solid was filtered, washed with ice-cold water and ethanol. To the filtrate, a second equivalent of A$_L$ was added and the solution was stirred (45 min), obtaining extra product. Yield 75–86%. This synthetic method was the only one that could be used to successfully synthesise [Pt(5-NO$_2$-phen)(en)]Cl$_2$ [156].

3.3.3   Reaction of [Pt(I$_L$)Cl$_2$] with Ancillary Ligand, Scheme 3.3

3.3.3.1   Synthesis of [Pt(I$_L$)(A$_L$)]Cl$_2$ via the Perchlorate Salt [156]

[Pt(I$_L$)Cl$_2$] (1 equiv.) and A$_L$ (2–8 equiv.) [117, 144] were dissolved in water (40 mL) and heated under reflux until the solution became clear (prolonged refluxing causes oxidation to Pt(0) which is observed as a black precipitate in the reaction solution). The solution was then cooled to room temperature, filtered and reduced in volume (~5 mL). A saturated solution of ClO$_4^-$ (Na$^+$ or Li$^+$, 5 mL) was added and the mixture cooled (4 °C, 1 h). The resultant precipitate was collected and washed with chilled HCl (1 M), water, ethanol and diethyl ether then dried under vacuum. [Pt(I$_L$)(A$_L$)](ClO$_4$)$_2$ was converted to the chloride salt by dissolving in water and stirring with anion-exchange resin (Dowex$^®$ [156] or Amberlite [117, 143]) overnight. The resin was removed via filtration. Often liquid-liquid extraction with toluene was required to remove organic impurities, with the product isolated from the aqueous phase by evaporation under reduced pressure or lyophilisation. Yield 50–90%.

When synthesising [Pt(I$_L$)(en)]Cl$_2$ [117] or [Pt(I$_L$)(tmcp)]Cl$_2$ [144], 6 and 8 equiv. of the ancillary ligand, respectively, were required. [Pt(I$_L$)(py)]$^{2+}$ can be

isolated with NH_4PF_6 [120]. This method could not be used to prepare [Pt(dpq)(S,S-dach)]Cl_2 or [Pt(dpq)(R,R-dach)]Cl_2 [156].

3.3.3.2 Crystallisation of [Pt(phen)(en)]Cl_2. Method [119]

Similar to the method in Sect. 3.3.3.1, [Pt(I_L)Cl_2] (1 equiv.) and A_L (1 equiv.) were dissolved in water (40 mL) and refluxed (10 h). A second equivalent of A_L was added and the solution heated at reflux overnight. The clear yellow solution was filtered, evaporated to dryness, and recrystallised from water. Yield 25%.

3.3.3.3 Synthesis of [Pt(I_L)(A_L)]Cl_2 via Acid Precipitation Method [144]

[Pt(I_L)Cl_2] was heated with A_L (2–8 equiv.) (~60 °C for en [190] and at reflux for tmcp [144]) in H_2O until the solution went clear. The solution was concentrated, and the compound was precipitated with HCl (1 M). The compound was often recrystallised from water [190] or washed with cold HCl and acetone. Yield 80–88%.

3.3.4 Reaction of [Pt(A_L)Cl_2] with Intercalating Ligand

3.3.4.1 Synthesis of [Pt(dpq)(A_L)]Cl_2 via Silver Nitrate Method [156]

[Pt(A_L)Cl_2] (1 equiv.) was dissolved in DMF, (forming the reactive intermediate [Pt(A_L)(DMF)$_2$](NO_3)$_2$) followed by the addition of $AgNO_3$ (2 equiv.) in DMF. The resultant solution was stirred overnight in the dark. The insoluble AgCl was removed by filtration, yielding a clear yellow filtrate containing [Pt(A_L)(NO_3)$_2$]. I_L (I_L = dpq, 1 equiv.) was dissolved in DMF and added to the filtrate, which was stirred overnight in the dark. The product was precipitated with diethyl ether, and the solution cooled before the product [Pt(A_L)(I_L)](NO_3)$_2$ was collected by filtration. The product was converted to the water-soluble chloride salt by stirring in water with Dowex® ion-exchange resin. Extraction with toluene was often useful to remove organic impurities. The product was isolated from the aqueous phase (Scheme 3.4).

3.3.4.2 Synthesis of [Pt(I_L)(A_L)](ClO_4)$_2$ in Water [119]

[Pt(A_L)Cl_2] (1 equiv.) and I_L (9,10-phenanthrenequinone diimine, phi, ~2.6 equiv.) were refluxed vigorously in water (~30 mL) in the dark (4 h). The mixture was filtered to remove excess I_L, and excess concentrated $NaClO_4$ was added to the filtrate, which was refrigerated overnight. The product was filtered and
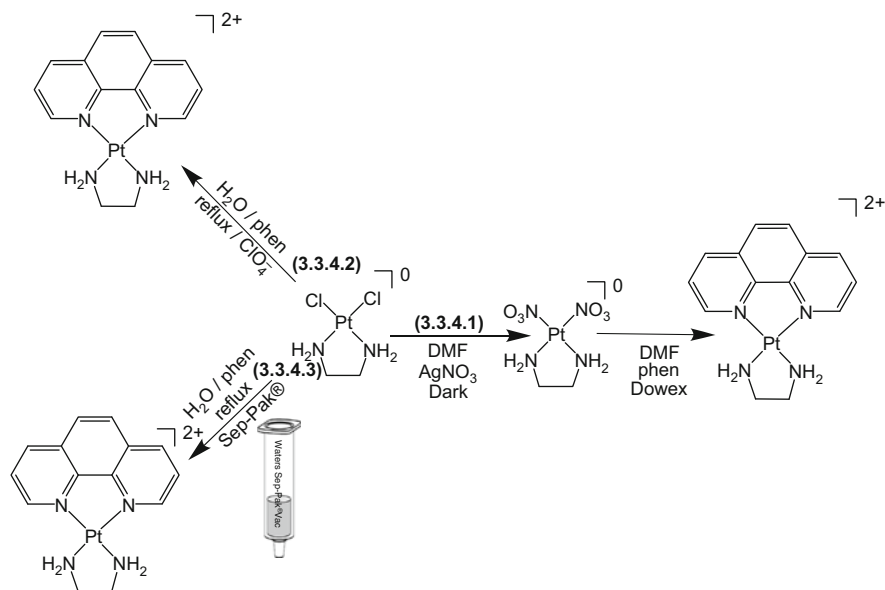
Synthetic Scheme 3.4 Reaction of [Pt(A$_L$)Cl$_2$] with intercalating ligand

recrystallised from water. The dark yellow product was converted to the chloride salt using IRA 400 (Cl) Amberlite®. The resulting orange solution was evaporated to dryness and then washed with methanol and ether. Yield ~20%.

3.3.4.3 Synthesis of [Pt(I$_L$)(A$_L$)]Cl$_2$ Using the Sep-pak® Method [155]

In a method similar to that of Sect. 3.3.4.2, [Pt(A$_L$)Cl$_2$] (1 equiv.) and I$_L$ (~1.2 equiv.) were refluxed in H$_2$O (~100–400 mL) until the solution became clear (~24 h). The solution was filtered to remove any oxidised platinum or undissolved I$_L$ and then the filtrate was reduced in volume (~20–50 mL). A Waters (2 g) C18-reverse phase Sep-Pak® column was activated by first washing with methanol (10 mL) followed by water (20 mL). The metal complex solution was then loaded onto the head of the column, with the yellow band of the metal complex eluted with water (~40 mL), leaving an orange-black band on the head of the column. The column was washed with acetonitrile/H$_2$O (1:1), with this fraction collected and eluted on a clean Sep-Pak® column. The column was cleaned with acetonitrile/H$_2$O/trifluoroacetic acid (90:9:1) and then washed with water. The aqueous fractions were combined and evaporated to dryness. Occasionally, due to the presence of unreacted I$_L$, the compound required redissolving in minimum H$_2$O and re-elution on the Sep-Pak®. Yield 80–90%. This method does not work when the A$_L$ is also aromatic I$_L$; eg. dpen [145].

3.4 Characterisation Techniques

3.4.1 NMR Spectroscopy

NMR spectroscopy is used to confirm the structure of the complexes. Knowledge of the NMR spectrum of the starting materials is useful when trying to assign resonances and evaluate changes to the chemical shifts of the protons of the ligand as a result of coordination. The NMR spectrum can inform about the chemical structure, as well as the chemical and isomeric purity of the complex. Both one and two dimensional NMR techniques such as ^{1}H, ^{13}C, ^{195}Pt, NOESY, COSY and ROESY are often used to characterise a complex. Chapter 5 includes further discussion about NMR techniques.

The confirmation of coordination, for platinum complexes, is monitored using proton and platinum NMR spectroscopy. The NMR spectra of related intercalators can be compared with that of the complex and resonance attributed to the hydrogen atoms of the 1,10-phenanthroline ligand, for example can be easily assigned. The number of resonances is characteristic of the ligand as are the vicinal coupling constants. A coordinated intercalator, such as phen can also be characterised using the resonances and vicinal coupling constants (Table 3.6). The H2 proton of phen, however is displaced upfield, from 8.59 to 9.25 ppm upon coordination. This proton demonstrates the most significant; chemical shift and this change holds true for other phen derivatives (Table 3.6).

Characterisation of [Pt(5,6-Me$_2$-phen)(R,R-dpen)](ClO$_4$)$_2$ [191] as an example is detailed below. The ^{1}H NMR (Fig. 3.11) contains nine resonances in total: five aromatic, two broad singlets consistent with NH$_2$ groups, one benzylic singlet and one aliphatic singlet. These resonances were assigned based on the peak frequency, spin multiplicity and two-dimensional COSY and NOESY intermolecular connectivities.

In the NOESY spectrum (Fig. 3.12), the CH$_3$ of the 5,6-Me$_2$-phen ligand appears upfield as a singlet at 2.83 ppm. This resonance gives a NOE cross-peak to the doublet of the H4/H7 at 9.24 ppm, which gives a NOE to the multiplet of the H3/H8 at 8.21 ppm. The H3/H8 gives a cross-peak to the doublet of the H2/H9 at 9.18 ppm. The H1″ of the diphenylethylenediamine ligand appears downfield as a singlet at 4.48 ppm. The high frequency of this resonance is a consequence of the proton being in the benzylic position combined with being in close proximity to the nitrogen atom. The H1′ gives a cross-peak to the H2′/H6′ resonance at 7.50 ppm, which gives a cross peak to the H3′/H4′/H5′ proton resonance at 7.32 ppm. The H4′ exists in a very similar chemical environment to the H3′/H5′, and as such these protons appear as a single multiplet. In the COSY spectrum (Fig. 3.13) the H4/H7 resonance gives a cross peak to the H3/H8 resonance, which in turn gives a cross peak to the H2/H9 resonance. The H2′/H6′ resonance of the diphenylethylenediamine ligand gives a cross peak to the H3′/H4′/H5′ resonance.

In the ^{13}C NMR spectrum of [Pt(5,6-Me$_2$-phen)(R,R-dpen)](ClO$_4$)$_2$ (Fig. 3.14) there are ten resonances from aromatic carbons, one resonance from a benzylic

Table 3.6 ¹H NMR data for the phen and $[Pt(I_L)(A_L)]^{2+}$ complexes
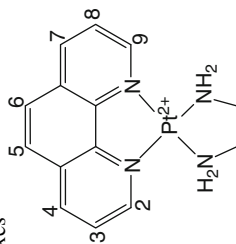
Protons	phen	$[Pt(phen)(en)]^{2+}$	$[Pt(5\text{-Me-phen})(en)]^{2+}$	$[Pt(5,6\text{-Me}_2\text{-phen})(en)]^{2+}$	$[Pt(4,7\text{-Me}_2\text{-phen})(en)]^{2+}$	$[Pt(3,4,7,8\text{-Me}_4\text{-phen})(en)]^{2+}$
CH_3			2.86 (s, 3H)	3.06 (s, 6H)	2.92 (s, 6H)	2.58, 2.77 (s, 6H, 6H)
H(2)	8.59^{ab} (d, 2H, $J_{2,3} = 4.4$ Hz)	9.37 (d, 2H, $J_{2,3} = 4.8$ Hz)	9.28 (d,1H, $J_{2,3} = 5.4$ Hz)	9.25 (d, 2H, $J_{2,3} = 5.2$ Hz)	9.09 (d, 2H, $J_{2,3} = 5.6$ Hz)	9.14 (s, 2H)
H(3)	7.85 (dd, 2H, $J_{3,4;2,3} = 8.1$, 4.4 Hz)	8.30 (dd, 2H, $J_{3,4;2,3} = 8.8$, 5.5 Hz)	8.26 (dd, 1H, $J_{3,4;2,3} = 8.5$, 5.4 Hz)	8.22 (dd, 2H, $J_{3,4;2,3} = 8.6$, 5.2 Hz)	8.08 (d, 2H, $J_{2,3} = 5.4$ Hz)	
H(4)	9.14 (d, 2H, $J_{3,4} = 8.1$ Hz)	9.20 (d, 2H, $J_{3,4} = 8.0$ Hz)	9.15 (d, 1H, $J_{3,4} = 8.5$ Hz)	9.17 (d, 2H, $J_{3,4} = 8.7$ Hz)		
H(5)	8.06 (s, 2H)	8.39 (s, 2H)	8.12 (s, 1H)		8.40 (s, 2H)	8.30 (s, 2H)
H(6)			8.99(d, 1H,			
H(7)			$J_{7,8} = 8.4$ Hz			
H(8)			8.19 (dd, 1H, $J_{3,4;2,3} = 8.3$, 5.4 Hz)			
H(9)			9.20 (d, 1H, $J_{8,9} = 5.4$ Hz)			
NH_2		7.39 (bs, 4H)	7.22 (bs, 4H)	7.30 (bs, 4H)	7.07 (bs, 4H)	7.14 (bs, 4H)
CH_2		2.82 (s, 4H)	2.74 (s, 4H)	2.71 (s, 4H)	2.72 (s, 4H)	2.74(s, 4H)

a Chemical shifts are in ppm and coupling constants are in Hz (±0.1)
b The solvent was D_6-DMSO in all cases

s singlet, d doublet, dd doublet of doublets, bs broad singlet
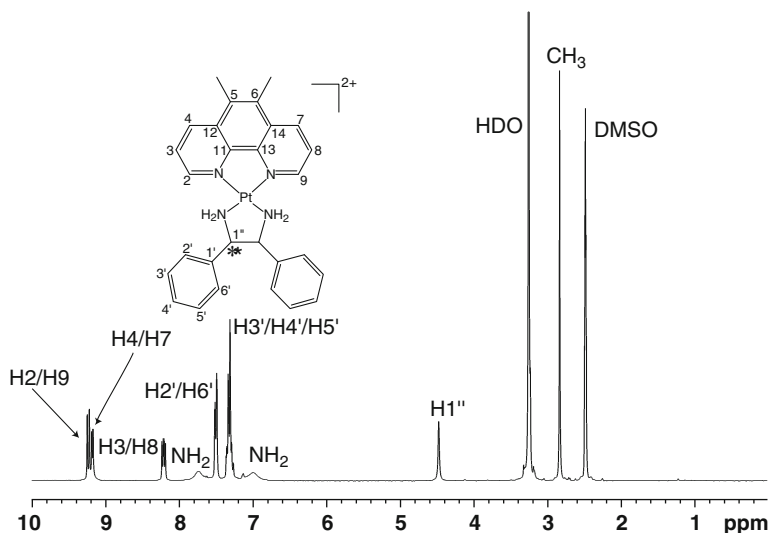
Fig. 3.11 The ^{1}H NMR spectrum of [Pt(5,6-Me$_2$-phen)(R,R-dpen)](ClO$_4$)$_2$ in d$_6$-DMSO showing the assignment of all proton resonances
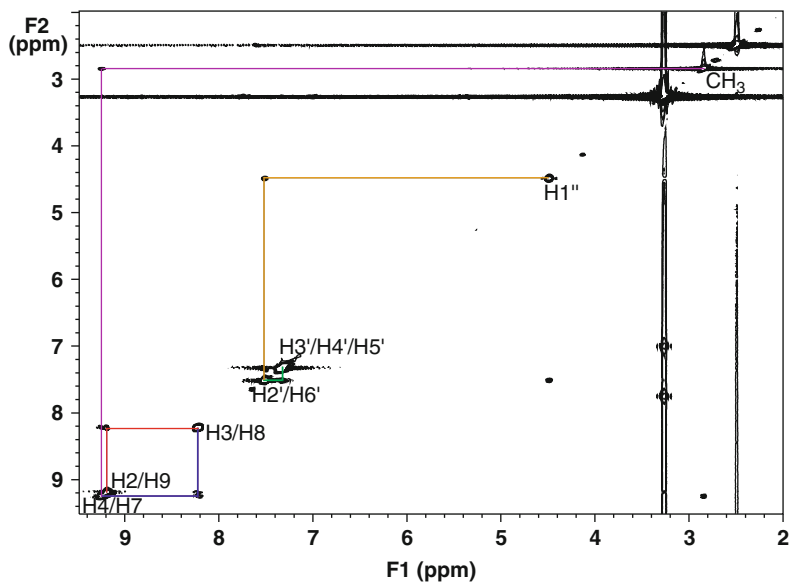
Fig. 3.12 The NOESY spectrum of [Pt(5,6-Me$_2$-phen)(R,R-dpen)](ClO$_4$)$_2$ showing the intramolecular connectivities

carbon and one resonance from an aliphatic carbon. The number and type of resonances observed is consistent with the number of resonances predicted from the structure of the molecule.
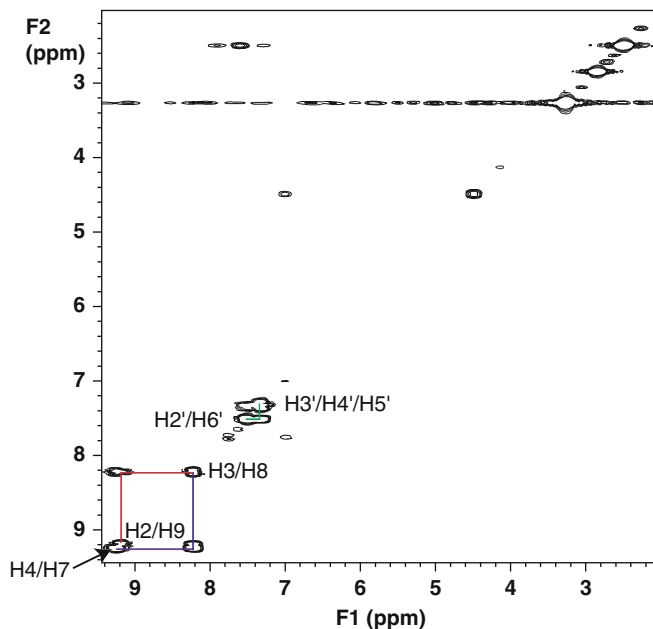
Fig. 3.13 The COSY spectrum of [Pt(5,6-Me$_2$-phen)(R,R-dpen)](ClO$_4$)$_2$ showing the intramolecular connectivities
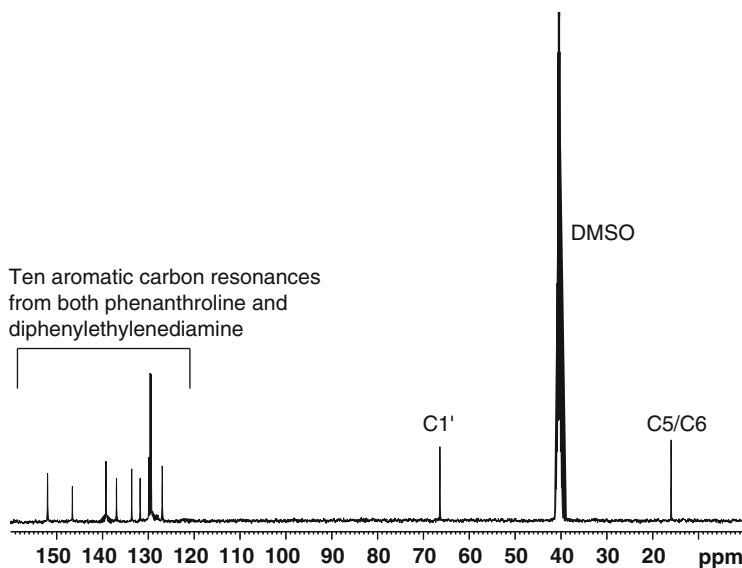
Fig. 3.14 The ^{13}C NMR spectrum of [Pt(5,6-Me$_2$-phen)(R,R-dpen)](ClO$_4$)$_2$. The assignment of the carbon resonances is indicated
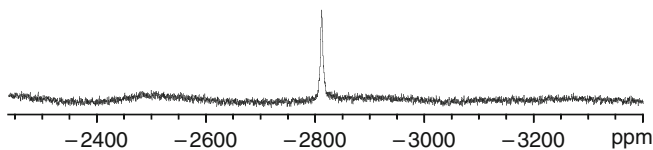
Fig. 3.15 The ^{195}Pt NMR spectrum of 56MERRdpen
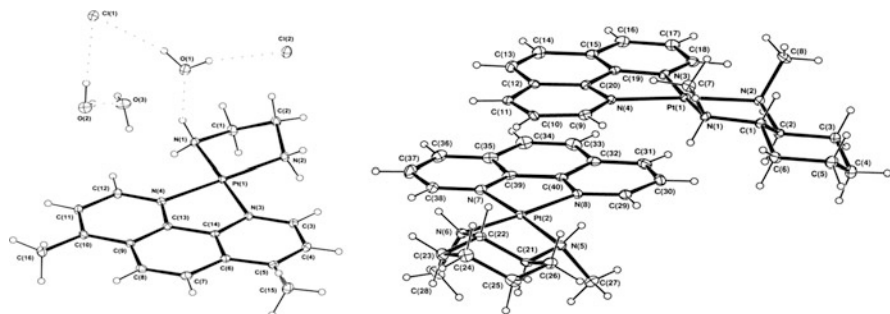
Fig. 3.16 An ORTEP representation of the [Pt(4,7-Me$_2$-phen)(en)]Cl$_2$ and [Pt(phen)(Me$_2$-S,S-dach)](ClO$_4$)$_2$

The ^{195}Pt spectrum of [Pt(5,6-Me$_2$-phen)(R,R-dpen)](ClO$_4$)$_2$ (Fig. 3.15) shows one peak at $-2{,}811$ ppm, indicating that there is one type of platinum atom in the molecule. For the ^{195}Pt spectrum of the starting material, [PtCl$_4$]$^{2-}$ a peak should appears at $-1{,}635$ ppm, the absence of this peak confirming that coordination was successful.

3.4.2 Crystal Structure Determination

Crystal structures of several platinum intercalators have been reported in the literature [23, 54, 144, 145, 174, 178, 179, 185, 187, 192–208] and these crystals have been isolated by a variety of techniques including slow evaporation of the aqueous solution. Examples of these crystal structures include [Pt(4,7-Me$_2$-phen)(en)]Cl$_2$.3D$_2$O [208], from D$_2$O, and [Pt(phen)(Me$_2$-S,S-dach)](ClO$_4$)$_2$.1.5H$_2$O [143] which have been determined to crystallise in the monoclinic, space group P2$_1$/c and P2$_1$2$_1$2$_1$, respectively (Fig. 3.16). The structural features present in both complexes are the square planar coordination sphere around the platinum(II) with nitrogen donor atoms, and the expected planarity of the intercalators 4,7-Me$_2$-phen and phen. The molecules are π stacked, and the intermolecular spacing between the two intercalators is estimated to be approximately 3.4 Å. An interplanar spacing of 3.66 Å (measured between the phen ligands) was previously reported for [Pt(phen)(R,R-dach)](PF$_6$)$_2$ where it was suggested that the spacing had been expanded to accommodate the larger PF$_6^-$ counter-ion [209].

References

1. Kelland L. Nat Rev Cancer. 2007;7:573.
2. Rosell R, Martinez-Balibrea E, Abad A, Cobo M, Isla D, Sanchez JJ, Sanchez-Ronco M, Taron M, Ramirez JL. Met Compd Cancer Chemother. 2005:269.
3. Farrell NP. Semin Oncol. 2004;31:1.
4. Nieto Y, Jones RB. Cancer Chemother Biol Response Modif. 2002;20:197.
5. Fuertes MA, Castilla J, Alonso C, Perez JM. Curr Med Chem: Anti-Cancer Agents. 2002;2:539.
6. Natile G, Coluccia M. Top Biol Inorg Chem. 1999;1:73.
7. Hartmann M, Keppler BK. Comment Inorg Chem. 1995;16:339.
8. Khatsiliades N, Markopoulos I. Chem Chron, Genike Ekdosis. 1977;42:30.
9. den Engelse L, van Benthem J, Scherer E. Mutat Res. 1990;233:265.
10. Hannon MJ, Moreno V, Prieto MJ, Moldrheim E, Sletten E, Meistermann I, et al. Angew Chem, Int Ed. 2001;40:880.
11. Hurley LH. Nat Rev Cancer. 2002;2:188.
12. Waring MJ. Drugs Exptl Clin Res. 1986;12:441.
13. Waring MJ. Annu Rev Biochem. 1981;50:159.
14. Boulikas T, Vougiouka M. Oncol Rep. 2003;10:1663.
15. Chabner BA, Allegra CJ, Curt GA, Calabresi P. In: Hardman JG, Limbird LE, Gilman AG, editors. Goodman and Gilman's the pharmacological basis of therapeutics, 9th Intern. edn. New York; McGraw-Hill: 1996.
16. Hayes D, Cvitkovic E, Golbey R, Scheiner E, Krakoff IH. Proc Am Assoc Cancer Res. 1976;17:169.
17. Loehrer PJ, Einhorn LH. Ann Intern Med. 1984;100:704.
18. Kelland LR. Drugs Exptl Clin Res. 2000;59:1.
19. Boulikas T, Pantos A, Bellis E, Christofis P. Cancer Ther. 2007;5:537.
20. Giaccone G. Drugs Exptl Clin Res. 2000;59:9.
21. Wong E, Giandomenico CM. Chem Rev. 1999;99:2451.
22. Reedijk J. Proc Natl Acad Sci USA. 2003;100:3611.
23. Bierbach U, Hambley TW, Roberts JD, Farrell N. Inorg Chem. 1996;35:4865.
24. Kelland LR, Barnard CFJ, Mellish KJ, Jones M, Goddard PM, Valenti M, et al. Cancer Res. 1994;54:5618.
25. Jamieson ER, Lippard SJ. Chem Rev. 1999;99:2467.
26. Farrell N. In: Sigel A., Sigel H, editors. Metal ions in biological systems, vol. 42. New York; Marcel Dekker: 2004.
27. Roberts JD, Peroutka J, Beggiolin G, Manzotti C, Piazzoni L, Farrell N. J Biol Inorg Chem. 1999;77:47.
28. Perego P, Caserini C, Gatti L, Carenini N, Romanelli S, Supino R, et al. Mol Pharmacol. 1999;55:528.
29. Perego P, Gatti L, Caserini C, Supino R, Colangelo D, Leone R, et al. J Inorg Biochem. 1999;77:59.
30. Pratesi G, Perego P, Polizzi D, Righetti SC, Supino R, Caserini C, et al. Brit J Cancer. 1999;80:1912.

31. Manzotti C, Pratesi G, Menta E, Domenico RD, Cavalletti E, Fiebig HH, et al. Clin Cancer Res. 2000;6:2626.
32. Jodrell DI, Evans TRJ, Steward W, Cameron D, Prendiville J, Aschele C, et al. Eur J Cancer. 2004;40:1872.
33. Kopf-Maier P, Kopf H. Chem Rev. 1987;87:1137.
34. Appleton TG, D'Alton CJ, Hall JR, Mathieson MT, Williams MA. Can J Chem. 2008;1996:74.
35. Pasini A, Zunino F. Angew Chem, Int Ed. 1987;26:615.
36. Gale EF, Cundliffe E, Reynolds PE, Richmond MH, Waring MJ. The molecular basis of antibiotic action. London: Wiley; 1972. p. 173.
37. Alberts DS, Fanta PT, Running KL, Adair Jr LP, Garcia DJ, Liu-Stevens R, et al. Cancer Chemother Pharm. 1997;39:493.
38. Lerman LS. J Mol Biol. 1961;3:18.
39. Saenger W. Principles of nucleic acid structure. New York: Springer; 1984.
40. Pindur U, Haber M, Sattler K. J Chem Edu. 1993;70:263.
41. Tashiro T, Kawada Y, Sakurai Y, Kidani Y. Biomed Pharmacother. 1989;43:251.
42. Kraker AJ, Moore CW. Cancer Res. 1988;48:9.
43. Lebwohl D, Canetta R. Eur J Cancer. 1998;34:1522.
44. Clarke MJ, Zhu F, Frasca DR. Chem Rev. 1999;99:2511.
45. Reedijk J. Pure Appl Chem. 1987;59:181.
46. Barton JK. J Biomol Struct Dyn. 1983;1:621.
47. Hall MD, Hambley TW. Coord Chem Rev. 2002;232:49.
48. Perez JM, Fuertes MA, Alonso C, Navarro-Ranninger C. Crit Rev Oncol Hematol. 2000;35:109.
49. Schwartz HS. Adv Cancer Chemother. 1979;1:1.
50. Denny WA. AntiCancer Drug Des. 1989;4:241.
51. Werner MH, Gronenborn AM, Clore GM. Science. 1996;271:778.
52. Howe-Grant M, Wu KC, Bauer WR, Lippard SJ. Biochemistry. 1976;15:4339.
53. Lippard SJ, Bond PJ, Wu KC, Bauer WR. Science. 1976;194:726.
54. Jennette KW, Gill JT, Sadownick JA, Lippard SJ. J Am Chem Soc. 1976;98:6159.
55. Nordén B, Tjerneld F. FEBS Lett. 1976;67:368.
56. Barton JK, Dannenberg JJ, Raphael AL. J Am Chem Soc. 1982;104:4967.
57. Blackburn GM, Gait MJ. Nucleic acids in chemistry and biology. 2nd ed. New York: Oxford University Press; 1996.
58. Kim SK, Nordén B. FEBS Lett. 1993;315:61.
59. Long EC, Barton JK. Acc Chem Res. 1990;23:271.
60. Friedman AE, Kumar CV, Turro NJ, Barton JK. Nucleic Acids Res. 1991;19:2595.
61. Eriksson M, Leijon M, Hiort C, Nordén B, Graeslund A. J Am Chem Soc. 1992;114:4933.
62. Coury JE, Anderson JR, McFail-Isom L, Williams LD, Bottomley LA. J Am Chem Soc. 1997;119:3792.
63. Yang XL, Wang AHJ. Pharmacol Therapeut. 1999;83:181.
64. Palchaudhuri R, Hergenrother PJ. Curr Opin Biotech. 2007;18:497.
65. Waring MJ. J Mol Biol. 1965;13:269.
66. Cohen G, Eisenberg H. Biopolymers. 1969;8:45.
67. Chow CS, Barton JK. J Am Chem Soc. 1990;112:2839.
68. Sundquist WI, Lippard SJ. Coord Chem Rev. 1990;100:293.
69. Berman HM, Young PR. Ann Rev Biophys Bioeng. 1981;10:87.
70. Odani A, Sekiguchi T, Okada H, Ishiguro S-I, Yamauchi O. Bull Chem Soc Jpn. 1995;68:2093.
71. Gabbay EJ, Scofield R, Baxter CS. J Am Chem Soc. 1973;95:7850.
72. Wilson WD, Jones RL. Adv Pharmacol Chemother. 1981;18:177.
73. Sobell HM, Reddy BS, Bhandray KK, Jain SC, Sakore TD, Seshadri TP. Cold Spring Harbor Symposia on quantitative biology. Cold Spring Harbor, New York: Cold Spring Harbor Lab; 1977.

74. Neidle S. Prog Med Chem. 1979;16:151.
75. Barton JK, Danishefsky AT, Goldberg JM. J Am Chem Soc. 1984;106:2171.
76. Barton JK, Basile LA, Danishefsky A, Alexandrescu A. Proc Natl Acad Sci USA. 1984;81:1961.
77. Barton JK, Raphael AL. J Am Chem Soc. 1985;106:2466.
78. Stinner C, Wightman MD, Kelley SO, Hill MG, Barton JK. Inorg Chem. 2001;40:5245.
79. Stodt R, Gencaslan S, Frodl A, Schmidt C, Sheldrick WS. Inorg Chim Acta. 2003;355:242.
80. Carter MT, Rodriguez M, Bard AJ. J Am Chem Soc. 1989;1989:8901.
81. Yoshioka MN, Inoue H. J Inorg Biochem. 1999;77:239.
82. Barton JK, Paranawithana SR. Biochemistry. 1986;25:2205.
83. Arounaguiri S, Maiya BG. Inorg Chem. 1996;35:4267.
84. Holmlin RE, Barton JK. Inorg Chem. 1995:7.
85. Arkin MR, Stemp EDA, Holmlin RE, Barton JK, Hoermann A, Olson EJC, et al. Science. 1996;273:475.
86. Holmlin RE, Yao JA, Barton JK. Inorg Chem. 1999;38:174.
87. Erkkila KE, Odom DT, Barton JK. Chem Rev. 1999;99:2777.
88. Johann TW, Barton JK. Philos Trans R Soc Lond Sect A. 1996;354:299.
89. Pyle AM, Chiang MY, Barton JK. Inorg Chem. 1990;29:4487.
90. Krotz AH, Kuo KC, Barton JK. Inorg Chem. 1993:5963.
91. Krotz AH, Kuo LY, Shields TP, Barton JK. J Am Chem Soc. 1993;115:3877.
92. Krotz AH, Barton JK. Inorg Chem. 1994:1940.
93. Sitlani A, Barton JK. Biochemistry. 1994;33:12100.
94. Trebrueggen RH, Barton JK. Biochemistry. 1995;34:8227.
95. Kelley SO, Arkin MA, Stemp EDA, Barton JK. J Inorg Biochem. 1995;59:136.
96. Hudson BP, Barton JK. J Am Chem Soc. 1998;120:6877.
97. Odom DT, Parker CS, Barton JK. Biochemistry. 1999;38:5155.
98. Sorasaenee K, Dunbar KR. ChemTracts. 1999;12:870.
99. Nunez ME, Barton JK. Curr Opin Chem Bio: Bio-inorg chem. 2000;4:199.
100. Pyle AM, Barton JK. Prog Inorg Chem. 1990;38:413.
101. Friedman AE, Chambron J, Sauvage J, Turro NJ, Barton JK. J Am Chem Soc. 1990;112:4960.
102. Hartshorn RM, Barton JK. J Am Chem Soc. 1992;114:5919.
103. Jenkins Y, Friedman AE, Turro NJ, Barton JK. Biochemistry. 1992;31:10809.
104. Turro C, Bossmann SH, Jenkins Y, Barton JK, Turro NJ. J Am Chem Soc. 1995;117:9026.
105. Dupureur CM, Barton JK. Inorg Chem. 1997;36:33.
106. Lim AC, Barton JK. Biochemistry. 1998;37:9138.
107. Lincoln P, Nordén B. J Phys Chem B. 1998;102:9583.
108. Murphy-Poulton SF, Vagg RS, Vickery KA, Williams PA. Met-Based Drugs. 1998;5:225.
109. Zhen Q-X, Ye B-H, Zhang Q-L, Liu J-G, Li H, Ji L-N, et al. J Inorg Biochem. 1999;76:47.
110. Zhen Q-X, Zhang Q-L, Liu J-G, Ye B-H, Ji L-N, Wang L. J Inorg Biochem. 2000;78:293.
111. Gisselfalt K, Lincoln P, Nordén B, Jonsson M. J Phys Chem B. 2000;104:3651.
112. Ambroise A, Maiya BG. Inorg Chem. 2000;39:4264.
113. Patel KK, Plummer EA, Darwish M, Rodger A, Hannon MJ. J Inorg Biochem. 2002;91:220.
114. Aldrich-Wright JR, Fenton RF, Greguric ID, Hambley TW, Williams PA. Dalton Trans. 2002:4666.
115. Bulluss GH. Honours thesis, The University of Sydney (Sydney). 1999.
116. McFadyen DW, Wakelin LPG, Roos IAG, Leopold VA. J Am Chem Soc. 1985;28:1113.
117. Brodie CR, Collins JG. Aldrich-Wright JR. Dalton Trans. 2004:1145.
118. Fenton RR, Aldrich-Wright J, (The University of Sydney, Australia). Application: WO: 2002; p. 26.
119. Collins JG, Rixon RM, Aldrich-Wright JR. Inorg Chem. 2000;39:4377.
120. Cusumano M, Letizia M, Giannetto A. Inorg Chem. 1999;38:1754.
121. Cusumano M, Petro MLD, Giannetto A, Nicolo F, Rotondo E. Inorg Chem. 1998;37:563.

122. Fisher DM. Honours thesis, University of Sydney (Sydney). 2000.
123. Lippard SJ. Acc Chem Res. 1978;11:211.
124. Wang AHJ, Nathans J, van der Marel G, van Boom JH, Rich A. Nature. 1978;276:471.
125. Vijay-Kumar S, Sakore TD, Sobell HM. J Biomol Struct Dyn. 1984;2:333.
126. Masuda H, Yamauchi O. Inorg Chim Acta. 1987;136:L29.
127. Odani A, Shimata R, Hideki M, Yamauchi O. Inorg Chem. 1991;30:2133.
128. Kato M, Kosuge C, Yano S, Kimura M. Acta Crystallogr C. 1997;53:838.
129. Arena G, Scolaro LM, Pasternack RF, Romeo R. Inorg Chem. 1995;34:2994.
130. Liu H-Q, Peng S-M, Che CM. J Chem Soc, Chem Commun. 1995:509.
131. Che C-M, Yang M, Wong K-H, Chan H-L, Lam W. Chem Eur J. 1999;5:3350.
132. McCoubrey A, Latham HC, Cook PR, Rodger A, Lowe G. FEBS Lett. 1996;380:73.
133. Cusumano M, Giannetto A. J Inorg Biochem. 1997;65:137.
134. Lowe G, Droz AS, Vilaivan T, Weaver GW, Park JJ, Pratt JM, et al. J Med Chem. 1999;42:3167.
135. Cusumano M, Di Pietro ML, Giannetto A, Romano F. Inorg Chem. 2000;39:50.
136. Romeo R, Scolaro LM, Plutino MR, Albinati A. J Organomet Chem. 2000;593–594:403.
137. Chan H-L, Ma D-L, Yang M, Che C-M. Chem Bio Chem. 2003;4:62.
138. Ma D-L, Che C-M. Chem Eur J. 2003;9:6133.
139. Bulluss GH. PhD thesis, University of Sydney (Sydney). 2004.
140. Kumar L, Kandasamy NR, Srivastava TS, Amonkar AJ, Adwankar MK, Chitnis MP. J Biol Inorg Chem. 1984;23:1.
141. Mital R, Srivastava TS, Parekh HK, Chitnis MP. J Biol Inorg Chem. 1991;41:93.
142. Paul AK, Mansuri-Torshizi H, Srivastava TS, Chavan SJ, Chitnis MP. J Biol Inorg Chem. 1993;50:9.
143. Fisher DM, Bednarski PJ, Grunert R, Turner P, Fenton RR, Aldrich-Wright JR. ChemMedChem. 2007;2:488.
144. Jaramillo D, Buck DP, Collins JG, Fenton RR, Stootman FH, Wheate NJ, Aldrich-Wright JR. Eur J Inorg Chem. 2006:839.
145. Krause-Heuer AM, Gruenert R, Kuehne S, Buczkowska M, Wheate NJ, Le Pevelen DD, et al. J Med Chem. 2009;52:5474.
146. Bednarski PJ, Gust R, Spruss T, Knebel N, Otto A, Farbel M, et al. Cancer Treat Rev. 1990;17:221.
147. Bednarski PJ. Biochemistry. 1995;60:1.
148. Schertl S, Hartmann RW, Batzl-Hartmann C, Bernhardt G, Spruß T, Beckenlehner K, et al. Arch Pharm. 2004;337:349.
149. Reile H, Spruss T, Mueller R, Gust R, Bernhardt G, Schoenenberger H, et al. Arch Pharm. 1990;323:301.
150. Ott I, Gust R. Anticancer Agents Med Chem. 2007;7:95.
151. Jennerwein M, Wappes B, Gust R, Schönenberger H, Engel J, Seeber S, et al. Res Clin Oncol. 1988;114:347.
152. Wappes B, Jennerwein M, Von Angerer E, Schöenenberger H, Engel J, Berger M, et al. J Med Chem. 1984;27:1280.
153. Schertl S, Hartmann RW, Batzl-Hartmann C, Bernhardt G, Spruss T, Beckenlehner K, et al. Arch Pharm. 2004;337:335.
154. Fisher DM, Fenton RR, Aldrich-Wright JR. Chem Commun. 2008:5613.
155. Wheate NJ, Taleb RI, Krause-Heuer AM, Cook RL, Wang S, Higgins VJ, Aldrich-Wright JR. Dalton Trans. 2007:5055.
156. Kemp S, Wheate NJ, Buck DP, Nikac M, Collins JG, Aldrich-Wright JR. J Biol Inorg Chem. 2007;101:1049.
157. Sundquist WI, Bancroft DP, Chassot L, Lippard SJ. J Am Chem Soc. 1988;110:8559.
158. Bowler BE, Hollis LS, Lippard SJ. J Am Chem Soc. 1984;106:6102.
159. Whittaker J, McFadyen WD, Baguley BC, Murray V. Anticancer Drug Des. 2001;16:81.

160. Holmes RJ, McKeage MJ, Murray V, Denny WA, McFadyen WD. J Inorg Biochem. 2001;85:209.
161. Wickham G, Wakelin L, Palmer B, Lee H, Johnson P, Baguley B, Denny W, McFadyen D. Platinum Other Met Coord Compd Cancer Chemother [Proc. Int. Symp.], 6th 1991: 51.
162. Appleton TG. Cisplatin. 1999:363.
163. Appleton TG, Hall JR, Kennard CHL, Mathieson MT, Neale DW, Smith G, et al. J Organomet Chem. 1993;453:299.
164. Appleton TG, Hall JR, Ralph SF. Inorg Chem. 1985;24:673.
165. Appleton TG, Hall JR, Ralph SF, Thompson CSM. Inorg Chem. 1984;23:3521.
166. Appleton TG, Berry RD, Davis CA, Hall JR, Kimlin HA. Inorg Chem. 1984;23:3514.
167. Appleton TG, Hall JR. J Chem Soc, Chem Commun. 1983:911.
168. Appleton TG, Bennett MA. J Organomet Chem. 1973;55:C88.
169. Appleton TG, Hall JR. Inorg Chem. 1972;11:124.
170. Hall JR, Appleton TG. Inorg Chem. 1971;10:1717.
171. Appleton TG, Hall JR. Inorg Chem. 1970;9:1807.
172. Appleton TG, Hall JR. Inorg Chem. 1970;9:1800.
173. New EJ, Roche C, Madawala R, Zhang JZ, Hambley TW. J Inorg Biochem. 2009;103:1120.
174. Diakos CI, Zhang M, Beale PJ, Fenton RR, Hambley TW. Eur J Med Chem. 2009;44:2807.
175. Giannikopoulos G, Teo C-L, Hall MD, Fenton RR, Hambley TW. Aust J Chem. 2003;56:685.
176. Hambley TW, Ling ECH, Munk VP, Davies MS. J Biol Inorg Chem. 2001;6:534.
177. Ling ECH, Allen GW, Vickery K, Hambley TW. J Inorg Biochem. 2000;78:55.
178. Munk VP, Fenton RR, Hambley TW. Polyhedron. 1999;18:1039.
179. Bierbach U, Hambley TW, Farrell N. Inorg Chem. 1998;37:708.
180. Natile G, Intini FP, Pacifico C, Cisplatin. 1999:429.
181. Bierbach U, Sabat M, Farrell N. Inorg Chem. 2000;39:3734.
182. Bierbach U, Sabat M, Farrell N. Inorg Chem. 2000;39:2960.
183. Farrell N, Roberts JD, Hacker MP. J Inorg Biochem. 1991;42:237.
184. Hoeschele JD, Farrell N, Turner WR, Rithner CD. Inorg Chem. 1988;27:4106.
185. Farrell N, Carneiro TMG, Einstein FWB, Jones T, Skov KA. Inorg Chim Acta. 1984;92:61.
186. Price JH, Williamson AN, Schramm RF, Wayland BB. Inorg Chem. 1972;11:1280.
187. Fanizzi FP, Natile G, Lanfranchi M, Tiripicchio A, Laschi F, Zanello P. Inorg Chem. 1996;35:3173.
188. Palocsay FA, Rund JV. Inorg Chem. 1969;8:524.
189. Hodges KD, Rund JV. Inorg Chem. 1975;14:525.
190. Hall JR, Plowman RA. Aust J Chem. 1956;9:143.
191. Krause-Heuer AM. Honours thesis, University of Western Sydney (Sydney). 2007.
192. Marques-Gallego P, den Dulk H, Brouwer J, Kooijman H, Spek AL, Roubeau O, et al. Inorg Chem. 2008;47:11171.
193. van der Schilden K, Garcia F, Kooijman H, Spek AL, Haasnoot JG, Reedijk J. Angew Chem, Int Ed. 2004;43:5668.
194. Graves BJ, Hodgson DJ, Van Kralingen CG, Reedijk J. Inorg Chem. 1978;17:3007.
195. Mackay FS, Woods JA, Moseley H, Ferguson J, Dawson A, Parsons S, et al. Chem Eur J. 2006;12:3155.
196. McGowan G, Parsons S, Sadler PJ. Inorg Chem. 2005;44:7459.
197. Bales JR, Mazid MA, Sadler PJ, Aggarwal A, Kuroda R, Neidle S, Gilmour DW, Peart BJ, Ramsden CA. Dalton Trans. 1985:795.
198. Bales JR, Coulson CJ, Gilmour DW, Mazid MA, Neidle S, Kuroda R, Peart BJ, Ramsden CA, Sadler PJ. J Chem Soc, Chem Commun. 1983:432.
199. Neidle S, Ismail IM, Sadler PJ. J Inorg Biochem. 1980;13:205.
200. Ren T, Bancroft DP, Sundquist WI, Masschelein A, Keck MV, Lippard SJ. J Am Chem Soc. 1993;115:11341.

201. Bowler BE, Ahmed KJ, Sundquist WI, Hollis LS, Whang EE, Lippard SJ. J Am Chem Soc. 1989;111:1299.
202. Hollis LS, Lippard SJ. Inorg Chem. 1983;22:2600.
203. Hollis LS, Lippard SJ. J Am Chem Soc. 1981;103:6761.
204. Teo C-L, Fenton RR, Turner P, Hambley TW. Aust J Chem. 1998;51:977.
205. Xiao H, Lawrance GA, Hambley TW. Aust J Chem. 1998;51:871.
206. Fenton RR, Easdale WJ, Er HM, O'Mara SM, McKeage MJ, Russell PJ, et al. J Med Chem. 1997;40:1090.
207. Fontes APS, Oskarsson A, Loevqvist K, Farrell N. Inorg Chem. 2001;40:1745.
208. Brodie CR, Turner P, Wheate NJ, Aldrich-Wright JR. Acta Crystallogr E. 2006;E62:m3137.
209. Koshiyama T, Kato M. Acta Crystallogr C. 2003;C59:m446.

Chapter 4
Platinum(II) Intercalating Complexes Based on 2,2':6',2''-Terpyridine

Benjamin W.J. Harper, Marcelis van Holst, and Janice Aldrich-Wright

4.1 Introduction

New complexes with similar structures to cisplatin very rarely offer any significant benefits to those analogues already in clinical use [1]. This has caused considerable interest in other platinum complexes, particularly metallointercalators as it is believed these complexes could display a different spectrum of anticancer activity due to their different mode of binding [2].

4.1.1 Square-Planar Metallointercalators

Coordination complexes capable of interacting with biomolecules have been extensively studied due to a consistently expanding range of potential applications. One group of coordination complexes is based on 2,2':6',2''-terpyridineplatinum(II) which has received considerable attention due its binding affinity towards DNA and proteins, often in a selective manner. The synthesis of 2,2':6',2''-terpyridineplatinum(II) complexes such as chloro(2,2':6',2''-terpyridine)platinum(II), (**1**, [Pt(terpy)(Cl)]$^+$) was first reported in 1934 [3]. Investigations into the chemical and biological properties of 2-hydroxyethanethiolato(2,2':6',2''-terpyridine)platinum(II), (**2**, [Pt(terpy)(HET)]$^+$, HET = S(CH$_2$)$_2$OH)) were not undertaken until the late 1970s using UV-vis spectroscopy, viscosity, circular dichroism (CD), fluorescence displacement and unwinding experiments [4]. [Pt(terpy)(HET)]$^+$ was shown to bind reversibly to ct-DNA, increasing the helical length and DNA stability [4, 5]. [Pt(terpy)](HET)]$^+$ binds to DNA with a binding constant in the order of 2×10^5 M^{-1}, which is comparable to that of ethidium bromide (3.9×10^5 M^{-1}) [4]. A series of new cationic terpyridineplatinum(II) complexes coordinated with

J. Aldrich-Wright (✉)
University of Western Sydney, School of Biomedical & Health Sciences, Penrith South DC New South Wales, Sydney, Australia
e-mail: J.Aldrich-Wright@uws.edu.au
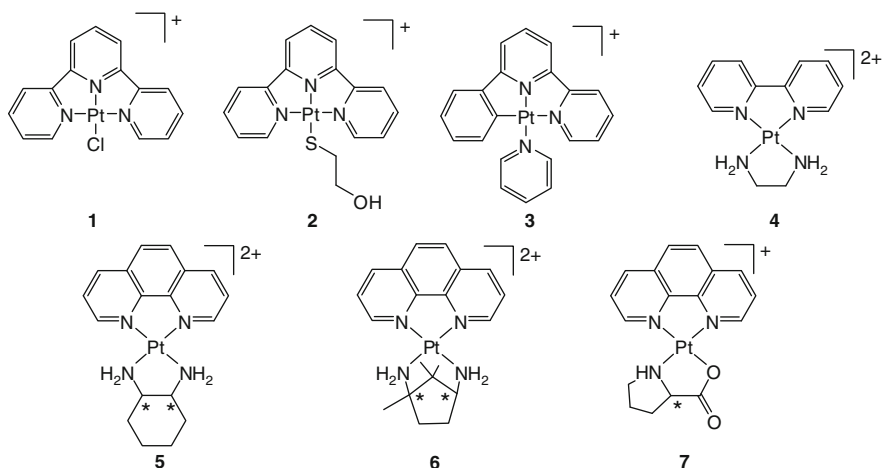
Fig. 4.1 Some examples of square planar metallointercalators showing platinum(II) complexes coordinated to terpyridine (**1** and **2**), 6-phenyl-2,2′-bipyridine (**3**), bpy (**4**) and phen (**5**, **6** and **7**), where the symbol *asterisk* indicates a chiral centre (*R* or *S*)

sulfur donor ligands with various functional components was later prepared as a means of evaluating the effects of charge, polarity and steric hindrance on the process of DNA intercalation (Fig. 4.1). The conjugation of two or more such species was also performed using well established organic synthetic techniques. Other ligands consisting of π-electron rich planar ring systems have also been shown to intercalate DNA, including 2,2′-bipyridine (bpy), when coordinated to form a square-planar platinum complex [6]. Molecules of this type show a strong DNA sequence selectivity for 5′-GpC sites [7] because of their higher dipole moment. Most platinum(II) intercalators binding with constants in the range of 10^4–10^7 M^{-1} [7–10]. Variance in binding strength appears to be due to differences in the charge and extent of the aromatic system of individual molecules, with the general trend being 1,10-phenanthroline (phen) > terpy > bpy [7].

Square planar metallointercalators have displayed the ability to bind DNA with a number of orientations, including major or minor groove binding, or by partial intercalation. For example, the crystal structure of **2** bound to the dinucleotide (CpG) showed the platinum intercalator interacting with the major groove [11]. Platinum(II) complexes of 6-phenyl-2,2′-bipyridine [12] **3** and bpy [13] **4** also intercalate. In contrast it has been shown by 2D NMR studies that platinum intercalators containing phen **5** and phenanthrene-9,10-diimine (phi) bind to the oligonucleotide d(GTCGAC)$_2$ from the DNA minor groove [14]. Additionally it has been shown that bulky ancillary ligands may prevent full insertion of the intercalating ligand into the DNA helix. The inclusion of the chiral ligand 1,3-diamino-1,2,2-trimethylcyclopentane (*R,S*- and *S,R*-tmcp, **6**) was shown to prevent the full insertion of the methylated phenanthroline ligand into the DNA helix [15]. The metallointercalators instead bind by partial intercalation in a "side-on" fashion [15]. The activity of metallointercalators containing phen and amino acids as ligands has also been investigated in Chap. 3.

Table 4.1 The cytotoxicity of selected platinum(II) complexes illustrated in Fig. 2.1, against identified cell lines

Metallointercalator	Cell line	IC$_{50}$ (µM)	Standard	IC$_{50}$ standard (µM)	Reference
1	L1210	450	Cisplatin		[13]
2	L1210	5	Cisplatin		[13]
3	HL60	1.0	Cisplatin	4.2	[12]
4	L1210	33	Cisplatin		[13]
5a, *S,S*-dach	L1210	0.13	Cisplatin	0.5	[16]
5b, *R,R*-dach	L1210	1.5	Cisplatin	0.5	[16]
6	L1210	11.2	Cisplatin	0.5	[15]
7	Molt-4	9.8	Cisplatin	1.7	[17]

The cell lines are: L1210 (murine lymphocytic leukaemia), HL60 (human leukaemia) and Molt-4 (human leukaemia).

4.1.2 The Biological Activity of Square-Planar Metallointercalators

Metallointercalators where the intercalating ligand was coordinated through a methylene chain to cisplatin have been synthesised and investigated. Others where the intercalator such as phen; bpy; 3,4,7,8-tetramethyl-1,10-phenanthroline (3,4,7,8-Me$_4$phen) and terpy, are directly attached to the platinum(II) moiety have also been studied and their cytotoxicity in murine leukaemia cell lines determined (Table 4.1) [13].

4.2 Terpyridineplatinum(II) Based Intercalators

4.2.1 Platinum(II) Terpyridine Mono-Intercalators

The first terpyridineplatinum(II) compound produced was ([Pt(terpy)Cl]$^+$ **1**, Fig. 4.1) which was shown to bind to ct-DNA [4]. These binding studies revealed that two binding modes included: covalent binding (platination) and intercalation [18, 19]. It was determined that **1** initially intercalated via the aromatic terpy ligand, inserting between the base pairs, leading to modifications in the structure and properties of the ct-DNA [18, 20, 21]. **1** subsequently formed covalent bonds to the base pairs in DNA *via* the loss of the labile chloride ligand, which acts as a good leaving group, allowing the covalent binding of the [Pt(terpy)H$_2$O]$^{2+}$ to base pairs of DNA [4, 19]. In order to determine the effect of intercalation, over the well studied chemical interaction of covalent binding to DNA, substitution of the chloride ion with a ligand that has a much slower rate of substitution was investigated.

The substitution of the reactive chloride ion in **1** produced **2** (Fig. 4.1) which was the prototype for a family of terpyridineplatinum(II) intercalating complexes. Since then various functional groups have been use to synthesise a range of analogous complexes. The properties of the resulting complexes can be tailored by the specific choice of the group coordinated to the $[Pt(terpy)]^{2+}$ moiety, which affects the structure activity relationships, self-stacking [22], photophysical properties and interaction with biomolecules, including proteins and DNA.

4.2.2 Ring Substitution and Attached Groups

The potential of terpyridineplatinum(II) complexes as anticancer drugs was indicated by the reported cytotoxicity of several complexes against human ovarian carcinoma cell lines and cell lines resistant to cisplatin [23–25]. Linear dichroism studies and unwinding ligation studies showed that the complexes bound to ct-DNA by intercalation, whereas circular dichroism and fluorescence spectroscopy (ethidium bromide displacement) experiments were used to determine the binding constant [23, 26]. It was evident that $[Pt(terpy)]^{2+}$ complexes form a covalent bond with DNA base pairs by nucleophilic substitution of the fourth coordinate ligand [27, 28]. Terpyridineplatinum(II) complexes have been shown to bind preferentially to GC-residues in nucleotides such as quadruplex DNA at the end of telomeres, giving a potential target for selective drugs to interact. Platination is not limited to G-residues in DNA, and ligand substitution of the functional groups of thiols and the imidazoles on proteins can also occur to produce cell death [9, 29]. The different mode of action compared to cisplatin may explain the biological activity and indicates that a new class of platinum antitumour agents has been found with little to no cross-resistance to cisplatin.

Terpyridineplatinum(II) complexes with chloro, hydroxy and picoline ligands coordinated at the fourth position are particularly susceptible to nucleophilic substitution [23]. The rigid tridentate geometric arrangement of the 2,2′:6′,2″-terpyridine ligand forces the middle pyridine to form a shorter bond to the platinum, this in turn forces the ligand *trans* to the middle pyridine to have a slightly weaker and longer bond making it much more susceptible to substitution [26]. It was shown that variation of the ligand to include sulphur groups produces relatively inert complexes due to the high affinity of sulphur for Pt(II) [18, 29] which subsequently does not undergo nucleophilic substitution. Interactions with the DNA can therefore be attributed to intercalation alone and not platination.

The effect of substituents at the 4′-position was evaluated with derivatives of complex **10** against the human ovarian cell lines (4′-position = X, Fig. 4.2 and Table 4.2). Complexes of this structural type showed a significant loss of activity due to the large electron-donating substituents in the 4′-position, whereas the introduction of a 4′-chloro group increased activity (Table 4.2) [23]. Complex **10** (where X = H) was shown to intercalate strongly with DNA with a binding
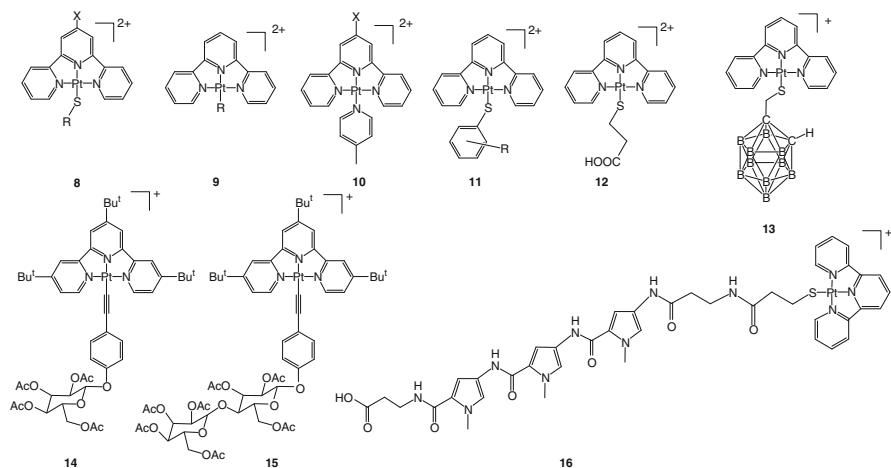
Fig. 4.2 The chemical structures of a range of platinum(II) terpyridine monointercalating complexes

constant in the order of $2 \times 10^7 \ M^{-1}$, more than two orders of magnitude greater than ethidium bromide and complex **1** [9, 27].

A series of terpyridineplatinum(II) complexes with various fourth coordinate ligands (fourth coordinate ligands = R, in Fig. 4.2) have been prepared to investigate the effect of the ligand on anticancer activity. Compounds **8a** and **b** have reduced anticancer activity when compared with compound **1** (IC_{50} values reported in Table 4.2). Derivatives of complex **9** were found to be more effective than carboplatin but not cisplatin in the human ovarian cancer cell lines including CHI, CHIcis[R], CHIdox[R], A2780, A2780cis[R] and SKOV3 (also shown in Fig. 4.2 and Table 4.2). Substituents on the pyridine ligand of complex **9**, had a small effect on the cytotoxicity of the complex [23]. Complex **9**, where R = NH$_3$, also displays strong antiprotozoal activity *in vitro* against *Leishmania donovani*, *Trypanosoma cruzi*, and *Trypanosoma brucei*, the causative organisms of the tropical diseases leishmaniasis and trypanosomiasis [26, 30]. This feature is of importance because the therapies involved in treating these diseases have variable efficacy, have toxic side effects and a poor therapeutic index, that could be improved with the development of new drugs [26].

The effect of replacing the coordinated chloride of [Pt(terpy)Cl]$^+$ with an aromatic thiol was evaluated with derivatives of complex **11** (Fig. 4.2 and Table 4.2). This produced active compounds which exert their effects rapidly with widespread cell lysis revealed under microscopic examination [13]. The incorporation of a terpyridineplatinum(II) unit into a sequence selective polyamide was explored using (3-mercaptopropionic)terpyridineplatinum(II) [Pt(terpy)(MPA)]$^{2+}$, **12**, and solid phase synthesis. The aim was to produce complexes like **16** that exhibit DNA sequence specificity [31, 32].

Table 4.2 Reported cytotoxicity of platinum(II) complexes illustrated in Fig. 4.2 against selected cell lines

Metallointercalator	Cell line	IC_{50} (μM)[a]	Standard	IC_{50} standard (μM)	Reference
8a, R = C_4H_9, X = H	L1210	14	Not reported		[21]
8b, R = 4-pyridyl, X = Cl	NCH89	2.5	Not reported		[29]
9a, R = 4-Me-C_5H_4N	CH1	14	Cisplatin/carboplatin	0.4/6.2	[23]
9b, R = 4-Br-C_5H_4N	CH1	2.1	Cisplatin/carboplatin	0.4/6.2	[23]
9c, R = 4-MeCO-C_5H_4N	CH1	2.2	Cisplatin/carboplatin	0.4/6.2	[23]
9d, R = 4-Me_2N-C_5H_4N	CH1	6.1	Cisplatin/carboplatin	0.4/6.2	[23]
9e, R = 2-F-C_5H_4N	CH1	15.5	Cisplatin/carboplatin	0.4/6.2	[23]
9f, R = 3-F-C_5H_4N	CH1	17	Cisplatin/carboplatin	0.4/6.2	[23]
9g, R = thiazole	CH1	17	Cisplatin/carboplatin	0.4/6.2	[23]
9h, R = imidazole	CH1	16.5	Cisplatin/carboplatin	0.4/6.2	[23]
9i, R = MeCN	CH1	18	Cisplatin/carboplatin	0.4/6.2	[23]
9j, R = (HO-CH_2)C_5H_4N	CH1	14	Cisplatin/carboplatin	0.4/6.2	[23]
9k, R = C_5H_5N	CH1	17.5	Cisplatin/carboplatin	0.4/6.2	[23]
9l, R = H_2O	CH1	12	Cisplatin/carboplatin	0.4/6.2	[23]
9m, R = NH_3	CH1	5.2	Cisplatin/carboplatin	0.4/6.2	[23]
9o, R = Cl	CH1	6.6	Cisplatin/carboplatin	0.4/6.2	[23]
9p, R = thionaphtholate	L1210	5	Cisplatin	0.4/6.2	[13]
10a, R = $N(CH_2CH_2OH)_2$	CH1	19.5	Cisplatin/carboplatin	0.4/6.2	[23]
10b, R = $NMeCH_2CH_2OH$)	CH1	>100	Cisplatin/carboplatin	0.4/6.2	[23]
10c, R = Cl	CH1	6.35	Cisplatin/carboplatin	0.4/6.2	[23]
10d, R = Br	CH1	5.4	Cisplatin/carboplatin	0.4/6.2	[23]
10e, R = OMe	CH1	15.5	Cisplatin/carboplatin	0.4/6.2	[23]
10f, R = 4-Me-C_6H_4	CH1	7.2	Cisplatin/carboplatin	0.4/6.2	[23]
10g, R = 4-Br-C_6H_4	CH1	5.0	Cisplatin/carboplatin	0.4/6.2	[23]
10h, R = $N(CH_2CH_2)_2$	CH1	16	Cisplatin	0.4/6.2	[23]
10i, R = $NHNH_2$	CH1	65	Cisplatin	0.4/6.2	[23]
10j, R = $NMeNH_2$	CH1	4.6	Cisplatin	0.4/6.2	[23]
10k, R = 4-OH	HeLa	24.31	Cisplatin	39.85	[55]
10l, R = 4-NH_2	HeLa	32.30	Cisplatin	39.85	[55]
10m, R = $NHCOCH_3$	HeLa	32.33	Cisplatin	39.85	[55]
11a, R = 4-H	L1210	6	Not reported		[13]

11b, R = 2-OCH$_3$	L1210	10	Not reported		[13]
11c, R = 3-OCH$_3$	L1210	4	Not reported		[13]
11d, R = 4-OCH$_3$	L1210	9	Not reported		[13]
11e, R = 4-NO$_2$	L1210	13	Not reported		[13]
11f, R = 4-F	L1210	13	Not reported		[13]
11g, R = 4-Cl	L1210	9	Not reported		[13]
11h, R = 4-Br	L1210	9	Not reported		[13]
11i, R = 4-CH$_3$	L1210	12	Not reported		[13]
11j, R = 4-NH$_3$	L1210	32	Not reported		[13]
12	L1210	>50	Cisplatin	0.5	[31, 32]
13	L1210cis^R	1.6/0.9	Cisplatin/carboplatin	0.5/6.9	[13]
14	HeLa	0.1	Cisplatin	11.6	[39]
15	HeLa	0.09	Cisplatin	11.6	[39]

[a]IC50's values with significant figures as reported in original reference. The cell lines are L1210 (murine lymphocytic leukaemia), L1210cis^R (cisplatin resistant), HL60 (human leukaemia), Molt-4: (human leukaemia), NCH89 (Glioma), HeLa (cervical cancer cells taken from Henrietta Lacks) and CH1 (Human ovarian cancer).

Platinum(II) terpyridine complexes containing *bis*-(thioalkyl)-dicarba-*closo*-dode-caborane(12) (carborane) ligands, such as complex **13** (Fig. 4.2), are synergistic intercalators [33]. They combine the effects of metallointercalators with carborane cages, which are used in radiation therapy. Although high cytotoxicity in the absence of thermal radiation is not expected, complex **13** is cytotoxic in the L1210 and ovarian cancer cell lines [33, 34]. It shows comparable cytotoxicity to cisplatin in the L1210 cell line and eight times greater cytotoxicity than cisplatin in the resistant cell line L1210cis^R (Table 4.2) [33].

Aryl and alkynyl terpyridineplatinum(II) complexes have received much attention in recent times partly due to the stability of the strong Pt-C bond which slows hydrolysis and the luminescent properties of terpyridineplatinum(II) complexes with a range of acetylide ligands which exhibit long lived emission states [35–38]. A series of these complexes have been synthesised, two of which are shown in Fig. 4.2 (**14** and **15**). In more recent studies by Che and co-workers terpyridineplatinum(II) complexes with glycosylated acetylide and arylacetylide ligands have been shown to bind to DNA. They were shown to be luminescent and therefore have useful properties to be considered as biological probes. The results of cell line testing against five human cell carcinoma lines showed a potency of up to 100 times greater than that of the current clinical drug, cisplatin, for killing human cancer cell lines. (Table 4.2) [39].

4.2.3   Bisintercalators: Rigid and Flexible Linkers

Bisintercalating compounds consisting of two intercalating moieties joined by a linking chain or spacer were developed to improve cytotoxicity [40]. Bisintercalating compounds may have higher affinities due to their increased charge and ability to span a greater number of DNA base pairs unobtainable by monointercalators [40]. By spanning a larger number of DNA base pairs bisintercalators may elicit more information and target specific sequences of DNA [2]. This coupled with the potential for more effective DNA-drug associations due to increased affinity should result in clinically relevant cytotoxicity profiles. In addition, the resulting drug/DNA adducts may be more difficult to repair because of larger/novel induced conformational changes in DNA that hinder DNA repair mechanisms. As a result, dinuclear platinum bisintercalating complexes have been synthesised that utilise substituted terpyridine ligands as their major intercalating component which are linked by a variety of rigid and flexible linkers with hydrophobic and hydrophilic chains of varying length (Fig. 4.3) [23, 29, 41, 42].

Lowe and co-workers synthesised a large range of terpyridineplatinum(II) bisintercalators such as **17**, **20–24** and **28** (Fig. 4.3), with rigid and flexible linkers. These were examined in a panel of six human ovarian cancer cell lines; two that are sensitive to cisplatin (CH1, A2780), two with resistance to cisplatin (CH1cis^R, A2780cis^R), one with resistance to doxorubicin (CH1dox^R) and the highly cisplatin resistant cell line SKOV-3 [23, 40]. The cytotoxicity of the complexes was reported
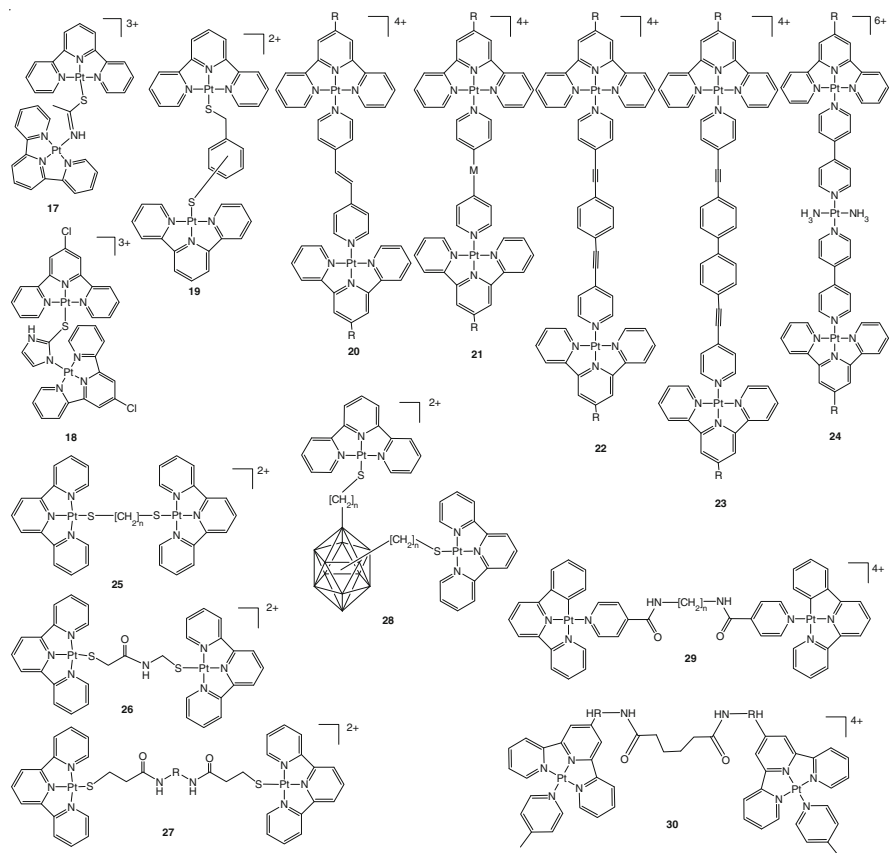
Fig. 4.3 Some examples of terpyridineplatinum(II) based bisintercalating complexes with flexible and inflexible linking chains

to depend on three variables; linker length, charge density and counter ions [23]. Complexes with shorter linkers displayed higher activity than those with longer linkers. For example, the activity of complexes **21a–d** is improved when M = no linker or when M = *trans*-CH=CH- (Table 4.3) [23]. The more highly charged complexes were also more cytotoxic [23, 40]. The high charge density and greater electrostatic stress of the shorter linked complexes is believed to increase the platination of DNA, which leads to their greater cytotoxicity [23]. Moreover, the tetrafluoroborate salts of the complexes were more active than their corresponding water-soluble nitrate salts. For example, the activity of complex **21d** is increased when the counter ion is BF_4^- compared with **21c** where the counter ion is NO_3^- (Table 4.3) [23]. All of the bisintercalators displayed little or no cross-resistance in matched cell lines [23].

Complex **19** contains a rigid 1,3-benzenedimethanethiol linker (Fig. 4.3) and binding affinity of its 1,4-benzenedimethanethiol linked analogue were examined

Table 4.3 The reported cytotoxicity of selected bisintercalating platinum(II) complexes illustrated in Fig. 4.3 against identified cell lines

Metallointercalator	Cell line	IC$_{50}$(μM)*	Standard	IC$_{50}$standard(μM)	Ref.
Rigid					
17	NCH89	2.5	Not reported		[29]
18	Not reported		Reported		[29]
19a, 1,3-	Not reported		Reported		[43]
19b, 1,4-	Not reported		Reported		[43]
20a, R = H-, NO$_3$$^-$	CHI	2.05	Cisplatin	0.4/6.2	[24]
20b, R = H, BF$_4$$^-$	CHI	1.35	Cisplatin	0.4/6.2	[24]
20c, R = Cl, BF$_4$$^-$	CHI	15.0	Cisplatin	0.4/6.2	[24]
20d, R = –BrC$_6$H$_4$, BF$_4$$^-$	CHI	2.0	Cisplatin	0.4/6.2	[24]
21a, R = H, M = no linker	CHI	1.55	Cisplatin/carboplatin	0.4/6.2	[23]
21b, R = Cl, M = no linker	CHI	0.59	Cisplatin/carboplatin	0.4/6.2	[23]
21c, R = H, M = *trans*-CH=CH–, NO$_3$$^-$	CHI	2.05	Cisplatin/carboplatin	0.4/6.2	[23]
21d, R = H, M = *trans*-CH=CH–, BF$_4$$^-$	CHI	0.73	Cisplatin/carboplatin	0.4/6.2	[24]
21e, R = H, M = *butadiyne*	CHI	1.3	Carboplatin	0.4/6.2	[23]
21f, R = Cl, M = *butadiyne*	CHI	1.55	Cisplatin/carboplatin	0.4/6.2	[23]
22a, R = H, M = 1,4-diethynylbenzene	CHI	2.15	Cisplatin/carboplatin	0.4/6.2	[23]
22b, R = Cl, M = 1,4-diethynylbenzene	CHI	2.5	Cisplatin/carboplatin	0.4/6.2	[23]
23, R = Cl	CHI	2.5	Cisplatin/carboplatin	0.4/6.2	[24]
24a, R = H	CHI	1.4	Cisplatin/carboplatin	0.4/6.2	[23]
24b, R = Cl	CHI	0.55	Cisplatin/carboplatin	0.4/6.2	[23]
28a, 1,2- sub, n = 1	L1210/L1210cis^R	0.9/0.8	Cisplatin/carboplatin	0.5/6.9	[33]
Flexible					
25a, n = 4	L1210	2	Not reported		[21]
25b, n = 5	L1210	5	Not reported		[21]
25c, n = 6	L1210	5	Not reported		[21]
25d, n = 7	L1210	5	Not reported		[21]
25e, n = 8	L1210	4	Not reported		[21]
25f, n = 9	L1210	3	Not reported		[21]
25g, n = 10	L1210	2	Not reported		[21]
26	L1210	10	Cisplatin	0.5	[31]

28b, 1,7- sub, n = 1	L1210/L1210cis^R	7.4/10	Cisplatin/carboplatin	0.5/6.9	[33]
28c, 1,12- sub, n = 1	L1210/L1210cis^R	24.5/26.5	Cisplatin/carboplatin	0.5/6.9	[33]
28d, 1,12- sub, n = 3	L1210/L1210cis^R	5.3/7	Cisplatin/carboplatin	0.5/6.9	[33]
29a, n = 3, CF$_3$SO$_3$$^-$	HL60	>350	Cisplatin	4.2	[12]
29b, n = 4, CF$_3$SO$_3$$^-$	HL60	350	Cisplatin	4.2	[12]
29c, n = 6, Cl	HL60	32	Cisplatin	4.2	[12]
30a, R = H	CH1	48	Cisplatin/carboplatin	0.4/6.2	[23]
30b, R = Me	CH1	48	Cisplatin/carboplatin	0.4/6.2	[23]

The cell lines are: L1210 (murine lymphocytic leukaemia), L1210cis^R (cisplatin-resistant), HL60 (human leukaemia), NCH89 (Glioma), HeLa (cervical cancer cells taken from Henrietta Lacks) and CH1 (human ovarian cancer).

by UV, CD and DNA melting temperature [43]. The 1,3- linked complex showed a greater DNA affinity than the 1,4- linked complex, as the DNA melting temperature was greater (82.5 °C compared to 78.0 °C) [43]. Examination of the interactions of rigid linked bisintercalators with DNA revealed that they derived their anticancer activity from non-classical DNA intercalation mechanisms [23, 40]. A study of complex **20** with the oligonucleotide d(CGTACG)$_2$ revealed that the complex could undergo ligand substitution by the oligonucleotide [23]. Nucleophillic substitution by nucleobases is well established with cisplatin, however the degree of lability of the linking chain in complex **20** was unexpected [23]. In this study the linking group was slowly displaced, producing a reactive electrophilic platinum species in solution that formed an irreversible coordinate covalent adduct through the N7 position of the terminal G residue [23, 27]. These complexes inhibit TrxR, which is a key component in the metabolism of human tumours [29]. It was proposed that these complexes act simultaneously on DNA and TrxR, producing an increased activity when compared to cisplatin [29, 40]. It was also proposed that transport of these complexes by human serum albumin might be a reason for their higher activity [30, 40].

A series of platinum terpyridine intercalators linked by a variety of carboranes have been synthesised in an attempt to enhance existing radiation oncology [33, 34, 44, 45]. This family of complexes includes mononuclear platinum complexes coordinated with an intercalating terpyridine ligand and bisintercalating linked by variable length thioalkyl chains through 1,2- 1,7- and 1,12-carborane, such as complex **28**. These complexes are designed to be inactive without the presence of thermal radiation, which would otherwise inhibit the uptake of sufficient levels of ^{10}B nuclei within cells. They do, however, display activity in ovarian cancer cell lines [34], depending on the length of the linker and the stereochemistry of the carborane cage, which is directly related to the aqueous solubility of the compounds. This was made apparent in a cytotoxicity study against the human ovarian carcinoma cell line 2008, where decreasing activity corresponds with the order of decreasing solubility in water. Incidentally, all of the compounds display relatively poor solubility in water and other polar solvents, which can be increased by the addition of a pendant glycerol group to the carborane chain [45]. In this case complexes with shorter thioalkyl linkers are more cytotoxic than their longer counterparts [34], though in this case it is directly due to the decrease in water solubility that occurs as the hydrophobic component is extended and not due to any bifunctional interaction between the complex and DNA. The successful intercalation of the platinum-terpyridine moiety has been observed by DNA-UV experiments [44]. Recent developments in this work have involved the synthesis of multinuclear intercalating species linked to one or more carborane cages. The effect on the cytotoxicity tends to increase as the thioalkyl linker length increases to the extent that the compound [{Pt(terpy)}$_2$μ-{*closo*-1,2-carborane}]$^{2+}$ is as cytotoxic as cisplatin in the L1210 cell line, and eight times more cytotoxic than cisplatin in the resistant L1210cis^R cell line [33]. The cytotoxicity is also highly dependent upon the position of the carborane cage, with 1,2- being most active [33].

McFadyen and co-workers synthesised a range of platinum(II) terpyridine bisintercalators, complex **25** (Fig. 4.3), which contain flexible alkane linkers of the type HS-[CH$_2$]n-SH where n = 4–10 [19]. DNA binding studies using equilibrium dialysis showed that the linkers with n = 5, 6 and 7 functioned as bisintercalators, while those with n = 8 and 10 bond to DNA by both mono- and bifunctional modes [19]. Complexes can readily form a one base pair "sandwich", where intercalation occurs at an adjacent base pair site or a two base pair "sandwich" where intercalation across two base pairs occurs leaving an empty intercalating site as shown in Fig. 4.4d. Depending on the properties of the linking chain, the binuclear ends have the ability to "staple" DNA, at various sites between base pairs, producing different conformational changes in DNA with the possibility of limiting or bypassing the DNA repair mechanisms [19, 21]. These complexes also showed enhanced DNA affinities, where DNA binding constants for n = 5 and n = 10, were 8 and 23 times larger than that of the mono-intercalating species [19]. Although the mono-intercalating species showed a distinct selectivity for GC sites in DNA, the bisintercalators (n = 5 and 10) did not [13, 19]. The cytotoxicity of the complexes was reported to be 2–5 μM in L1210 with no observable trend [21]. They are less active than cisplatin in L1210
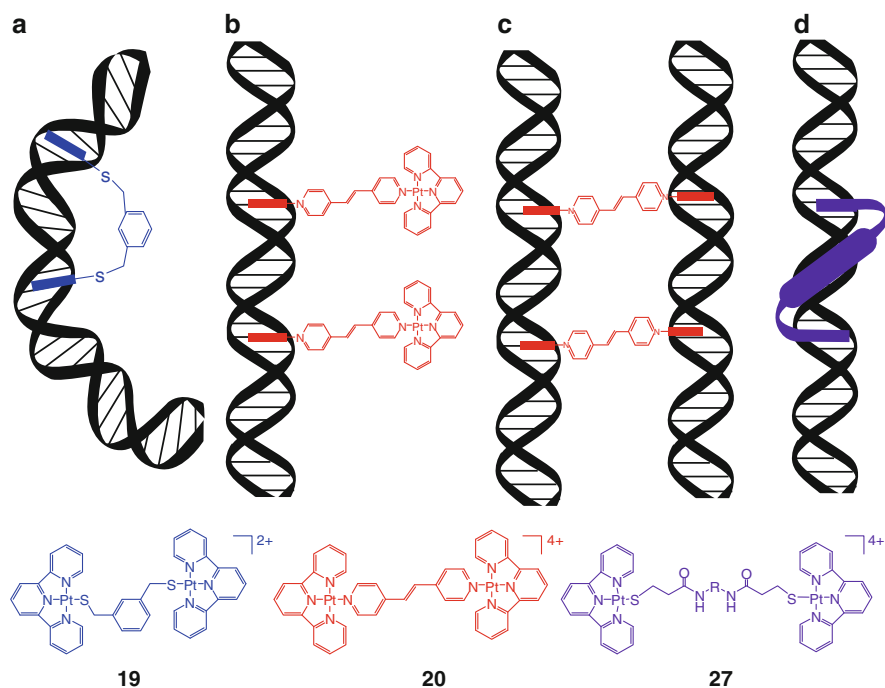
Fig. 4.4 Proposed binding modes of rigid and flexible bisintercalators. Complex **19** binds by model a, **20** can bind by model b or c and **27** can bind bisintercalate forming a base pair "sandwich", d

(reported elsewhere) and several rigid complexes, such as **20b**, **21a**, **21b**, **21d**, **21e**, **21f**, **24a** and **24b** [16].

Chan and co-workers have synthesised 6-phenyl-2,2′-bipyridine platinum(II) bisintercalating complexes such as **29**, with flexible alkane linkers of the type CONH-[CH$_2$]$_n$-NHOC (where n = 3, 4, and 6), which were examined in the human cancer cell line HL60 (Fig. 4.3) [12]. Complexes of this type possess photoluminescent properties, including vibrational absorbance and emissions characteristic of intra-ligand transitions and those of metal-to-ligand charge transfer [46] which can be utilised to probe biomacromolecules. These complexes were reported to have enhanced DNA affinities compared to the mono-intercalating species, where the DNA binding constants were in the order of 10^7 M^{-1}, more than two orders of magnitude higher than ethidium bromide and the mono-intercalating species, as expected due to the contribution of the increased charge [12, 47]. It was also shown that both mono- and bisintercalative (**29**) complexes intercalate into DNA causing conformational change and cytotoxicity, however, results showed that the bisintercalating complexes exhibited higher cytotoxicity than the monointercalative complexes [12, 47]. Unlike the results reported by Lowe, these bisintercalators were found to have increasing cytotoxicity with increasing linker length (Table 4.3) [12]. For example, the complex **29a** (n = 3) had an IC$_{50}$ value too large to be determined, while n = 6 showed the greatest activity [12] due to the capability to form various long range intercalating sites [48, 49]. This trend was not observed for compounds of the type **25** with the activity comparable to those constructed from rigid linkers.

The results from these investigations show that bisintercalators with rigid linkers had the lowest IC$_{50}$ and were the most effective against cisplatin resistant cell lines. This indicates that platination is not the major source of the biological activity and that intercalation plays the predominant role in the observed cytotoxicity [23]. Large electron donating groups at the 4′-position showed a reduction of biological activity; while bisintercalators joined by a flexible linker at the 4′-position also showed relatively reduced cytotoxicity [23, 26].

4.2.4 Proposed Mechanisms of Bisintercalator Binding

The length and flexibility of the linking group has drastic effects on the potential mechanism by which bisintercalators interact with DNA [43, 52–54]. Four DNA intercalating mechanisms are depicted in Fig. 4.4 where the type of flexible linker and its position of attachment play a role in the binding mode. For example, if the linker is short, rigid and the intercalators are in adjacent positions then bisintercalation that bends DNA may occur as depicted in Fig. 4.4a. If the instead the intercalators are separated by some distances then either monointercalation or bisintercalation can occur as depicted in Fig. 4.4b, c. If however a flexible linker connects the two intercalators then a base pair "sandwich" can be created, as shown in Fig. 4.4d [19, 21, 52, 54].

4.2.5   Probing DNA's Structure with Luminescent Complexes

The absorption and subsequent emission of terpyridineplatinum(II) complexes is of interest for its potential for spectroscopic visualisation in biological systems. It has been shown that the luminescence of platinum complexes in the presence of DNA can change according to the interaction of the complex. External binding to the DNA has been shown to lead to luminescence enhancement while intercalation leads to decreased luminescence intensity [56]. These luminescence properties can be tuned by incorporating various ligands with different functional groups. One direction of current research is photoluminescence, whereby a molecule absorbs energy and re-emits it at a longer wavelength. Photoluminescence can be broken down into two categories; luminescence in which emission is short-lived (in the nanosecond time-scale) and phosphorescence that lasts much longer. These spectroscopic and luminescence properties are primarily shown to be due to the d^8–d^8 metal–metal interactions and the π–π interactions of the terpyridyl ligands [57]. Previous spectroscopic work on terpyridineplatinum(II) complexes showed high-energy absorption bands assigned as intra-ligand transitions, with low-energy absorptions assigned as metal-to-ligand charge transfer transitions [35]. Variation of ligand substituents on the fourth position of monointercalating complexes and the nature of the linking chain in bisintercalating complexes has the potential to produce an abundance of different complexes capable of varied biological activity.

Luminescent terpyridineplatinum(II) complexes with acetylide ligands have been synthesised and reported to exhibit long lived emission states (**31**, Fig. 4.5) [37, 58, 59]. The energy of these emissions were shown to change with the substituents on the phenyl ring, more electronegative groups produced higher emission energy. These results are consistent with the triplet metal–ligand charge transfer [35]. Studies carried out on the binding of positively charged alkynylplatinum(II) terpyridyl complexes to negatively charged single-stranded nucleic acids via electrostatic interactions, have been shown to induce helical self-assembly of

25 min   Enlargement
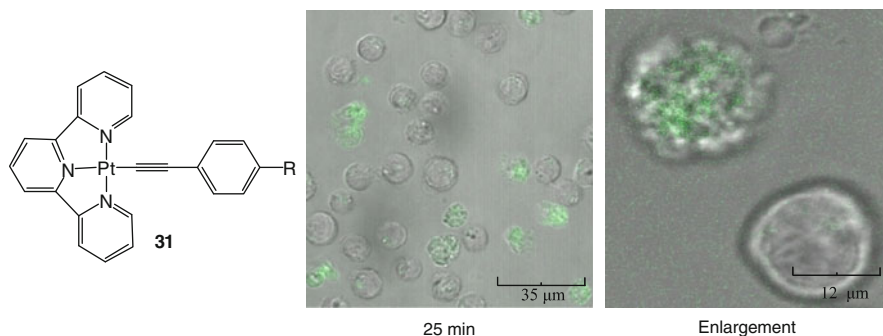
Fig. 4.5 The luminescent terpyridyl acetylide platinum(II) complex **31**. Confocal images of L1210 cells treated with [Pt(terpy)AET-fluorescein]Br and an expansion of two of these cells, where the uptake of [Pt(terpy)AET-fluorescein]Br can clearly be visualised

metal-metal and π–π interactions [20]. Intrinsically luminescent complexes or those that have a luminescent ligand attached can be used to probe the biological activity. For example, [Pt(terpy)AET-fluorescein]$^+$ has been incubated with L1210 cells and the localisation of the complex can be seen using confocal microscopy as shown in Fig. 4.5.

4.3   Synthesis

Here synthetic schemes and details are provided with the primary references for the synthesis of [Pt(terpy)R]X. In general there is a procedure that is followed for synthesis, purification and characterisation. This is shown in the general synthetic Scheme 4.1.

4.3.1   Synthesis of [Pt(terpy)Cl]Cl

The synthesis of [Pt(terpy)Cl]Cl was first reported by Morgan and Burtstall in 1934 [3]. This method is carried out by the addition of K_2PtCl_4 to a suspension of terpyridine in water and refluxed over 6 h. The product of this reaction was the double salt [Pt(terpy)Cl]$_2$[PtCl$_4$] with [Pt(terpy)Cl]Cl being the minor product. Improvement of this method was achieved by refluxing over 4 days (Fig. 4.6, Route 2). The reaction yield was modest, producing only 65%. Since this time more efficient methods for the synthesis of [Pt(terpy)X] have been developed. One such method involves combining terpyridine and K_2PtCl_4 in CH_3CN/H_2O (1:1) and refluxing for 24 h to give the product (Fig. 4.6, Route 2) [60]. One method applied to produce [Pt(terpy)Cl]Cl is that of microwave dielectric loss heating. This method involves heating K_2PtCl_4 with terpyridine in a small volume of water using two 30 s bursts of microwave energy to yield the product in yields of up to 47%. This method is extremely efficient in terms of time and convenience [61]. Two excellent papers by Cummings [62] and Newkrome [63] present a comprehensive review of all the synthetic methods in the literature and are invaluable to anyone beginning in this area.

4.3.2   Synthesis of [Pt(terpy)(R)]X$_2$ via a DMSO Intermediate

One method that has been used effectively is the reaction of K_2PtCl_4 with DMSO and the desired four coordinate ligand at 60–70 °C producing *trans*-[Pt(DMSO)$_2$(R)Cl]]X (where R = aryl or alkyl) (Fig. 4.7, Route 1) [64]. To this a solution of 2,2′:6′,2″-terpyridine in methanol is added for as little as 20 min producing the desired [Pt(terpy)R]X product [65, 66]. The reaction of 2,2′:6′,2″-terpyridine with *trans*-[Pt(DMSO)$_2$(R)(Cl)]X in methanol for 2 h at room temperature [65, 66] or in chloroform for 24 h to produce the desired [Pt(terpy)R]Cl product with yields
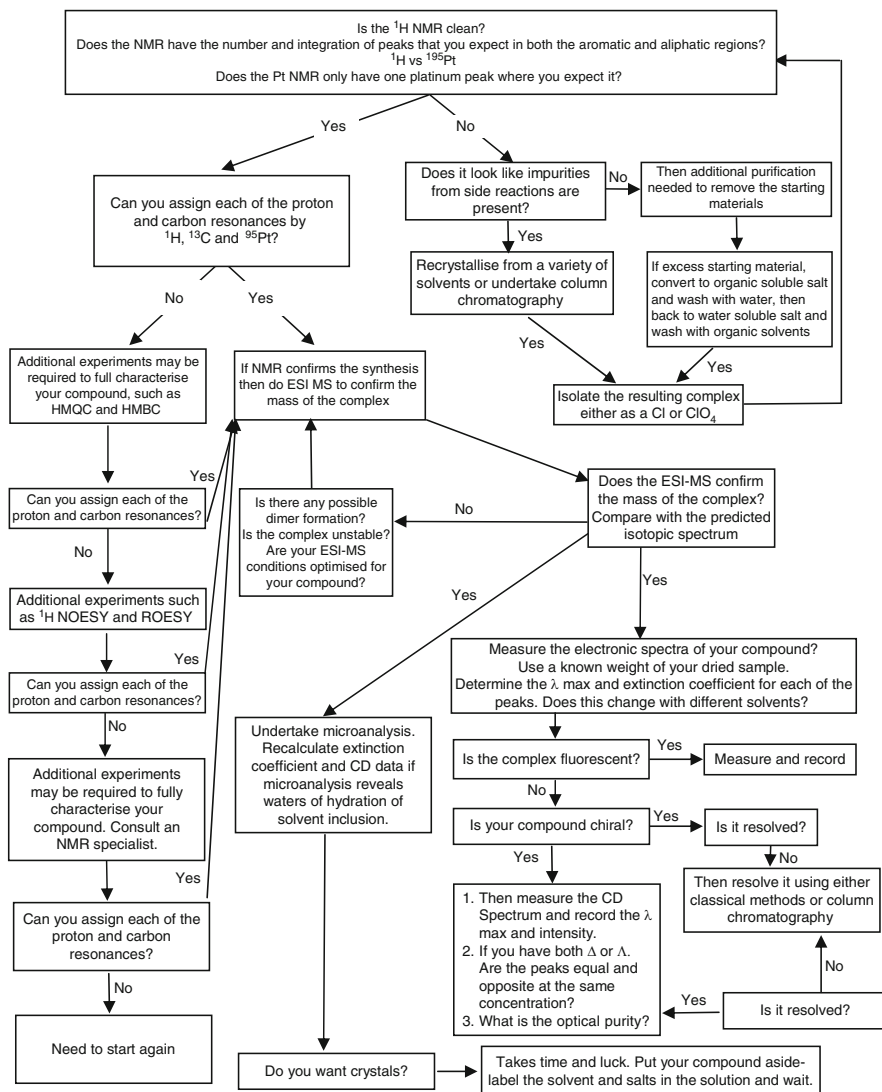
Synthetic Scheme 4.1 Synthesis, purification and characterisation protocol for [Pt(terpy)(R)]X

between 60 and 70% [67]. Alternatively, K_2PtCl_4 is initially reacted with three equivalents of DMSO in H_2O and allowed to stand at room temperature until the *cis*-[Pt(DMSO)$_2$Cl$_2$] precipitate forms [68]. 2,2′:6′,2″-Terpyridine is subsequently reacted with *cis*-[Pt(DMSO)$_2$Cl$_2$] in methanol for 2 h at room temperature producing a mixture of the double salt [Pt(terpy)Cl][Pt(DMSO)Cl$_3$] in 28% yield and [Pt(terpy) Cl]Cl·2H$_2$O in 30% yield [69]. A similar reaction using *cis*-[Pt(PhCN)$_2$Cl$_2$] with terpyridine in DMF was also shown to produce predominantly the double salt [Pt(terpy)Cl]$_2$[PtCl$_4$] (Fig. 4.6, Route 4) [69].

4.3.3 Synthesis of [Pt(terpy)(R)]X₂ via a 1,5-Cyclooctadiene Intermediate

A synthetic method reported by Annibale et al. [69]. involves initial substitution by 1,5-cyclooctadiene to produce dichloro(1,5-cyclooctadiene)platinum(II) [Pt(COD) Cl₂] (Fig. 4.6, Route 5) [60], the intermediate to [Pt(terpy)Cl]Cl. [Pt(COD)Cl₂] has been prepared using methods adapted from McDermott et al. [70]. $K_2[PtCl_4]$ is dissolved in water and filtered. To the deep red filtrate acid is added to aid in COD coordination. The reaction mixture is stirred rapidly and heated to about 90 °C on a steam bath. Over 30 min the deep red solution slowly becomes pale yellow as crystals are deposited. COD interacts with the complex through the π-orbitals of the two alkene groups. Bonds involving π–π interactions alone are weaker than typical interactions with σ-bonding ligands. This weaker interaction leads to easy displacement of the 1,5-cyclooctadiene ligand with the terpy [70, 71]. Terpy is typically added in a 1:1 ratio with a suspension of [Pt(COD)Cl₂] in H_2O and stirred with heating at 50 °C for 20 min to replace the COD ligand. Yields of up to 90% are often achieved confirming the method as extremely efficient in terms of both time and yield [69]. The [Pt(COD)Cl₂] intermediate method has also shown to be very
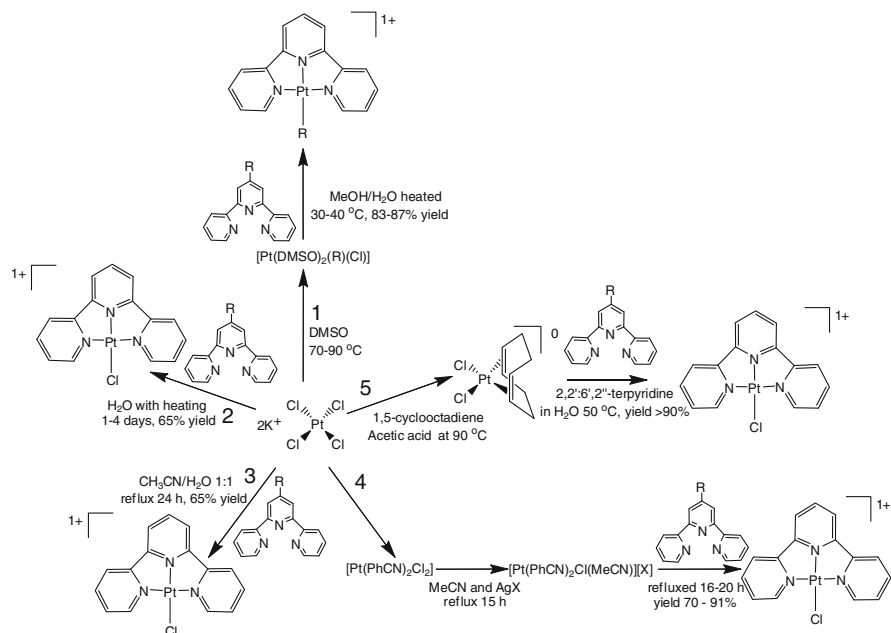
Fig. 4.6 Synthetic overview for the synthesis of [Pt(terpy)Cl]Cl or [Pt(terpy)R]Cl from: 1) [Pt (DMSO)₂(R)Cl] intermediate, 2) direct substitution in H_2O, 3) direct substitution in MeCN/H_2O, 4) [Pt(PhCN)₂Cl₂] intermediate and 5) [Pt(COD)Cl₂]
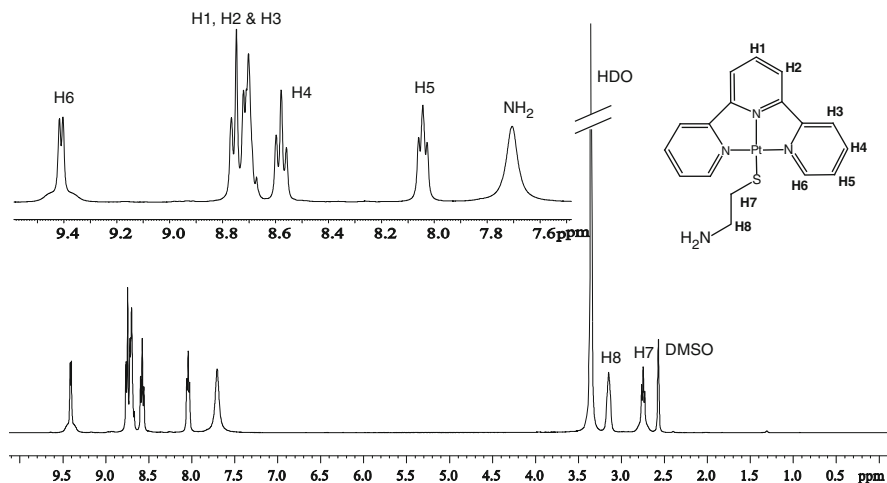
Fig. 4.7 The ^{1}H spectrum and expansion of [Pt(terpy)AET]Br in d_6-DMSO. Inset: The expansion of the aromatic region between 7.6 and 9.5 ppm

effective for 4′ substituted terpy groups including aryl [72], ethoxy, phenyl amine, and halogen substituents [23, 26, 30].

4.4 Fourth Coordination Ligand Substitution

Variation of the fourth coordination ligand on terpyridineplatinum(II) has the ability to dramatically change the solubility, stability, self-association, electro- and photochemical properties and interactions with biomolecules. [Pt(terpy)Cl] Cl·2H$_2$O is typically the precursor for the terpyridineplatinum based complexes synthesised due to its strong bond to the tridentate terpy ligand and relatively labile chloride ion which can be exchanged for the desired fourth ligand of choice. The substitution of the chloride ligand has been shown to be 10^3–10^4 times faster than that of [Pt(DETA)Cl] (DETA = diethylenetriamide) and up to 100 times faster that that of [Pt(bpy)Cl$_2$] [73]. The substitution of the chloride ligand by a plethora of nucleophilic molecules such as pseudohalides, thiols, pyridines, ketones and other halides has been reported under various reaction conditions.

4.4.1 Ligand Substitution by Halides and Pseudohalides

The substitution of the labile Cl from [Pt(terpy)Cl]Cl·2H$_2$O by both halides and pseudohalides has been shown to occur often in mild conditions. Piteri et al. showed that the reaction between either [Pt(DETA)X]$^+$ or [Pt(terpy)X]$^+$ (where X = Cl, Br

or I) with halide nucleophiles in the form LiY (where Y = Br, I or Cl) occurred by nucleophilic substitution from the monocationic platinum(II) complexes using stoichiometric amounts of LiY in warm concentrated solutions of [Pt(DETA)X]$^+$ or [Pt(terpy)X]$^+$. This mild reaction produced the halide substituted [Pt(terpy)X]$^+$ complex in 70% yield and was shown to substitute up to six orders of magnitude faster than the corresponding [Pt(DETA)X]$^+$ product due to the steric constraints imparted by the terpy ligand [74].

The substitution of [Pt(terpy)Cl]Cl·2H$_2$O by halides, pseudohalides and solvents including SCN$^-$, N$_3^-$, NO$_2^-$, CN$^-$, MeCN, −OMe, H$_2$O, and OH$^-$, has been shown under basic conditions. A comparison of the reactivity of these nucleophiles was roughly shown to coincide with the position of these ligands in the *trans* effect series where by CN$^-$>NO$_2^-$>SCN$^-$>N$_3^-$>I$^-$>Br$^-$>Cl$^-$>NH$_3^-$>OH$^-$>H$_2$O [73, 75, 76]. A study by Carr et al. showed that 4′-substituents on the terpy ligand influenced the kinetics of the fourth coordination ligand substitution. Ligand substitution on platinum(II) centres normally proceed via an associative five-coordinate transition state mechanism [77]. Carr proposed that the electron withdrawing 4′-substituuents on the terpy reduces the electron density around the platinum(II) centre and affects the rate of ligand substitution [78].

4.4.2 Ligand Substitution by Alkynes and Aryl Groups

The synthesis of terpyridineplatinum acetylide complexes typically involves the intermediate [Pt(terpy)MeCN](OTf)$_2$ formed from [Pt(terpy)Cl]Cl·2H$_2$O by refluxing in MeCN with a large equivalent of AgOTf. The highly labile MeCN in [Pt(terpy)MeCN](OTf)$_2$ can be displaced by various acetylide ligands. The typical reaction conditions used involve a mixture of two equivalents of acetylide per terpyridineplatinum, a base such as triethylamine or potassium hydroxide, typically in DMF or MeOH and copper(I) iodide as a catalyst [59, 79–82].

4.4.3 Ligand Substitution by Pyridine

As in Sect. 4.4.2, the synthesis of terpyridineplatinum pyridine complexes typically involves the intermediate [Pt(terpy)MeCN](OTf)$_2$ or [Pt(terpy)H$_2$O](NO$_2$)$_2$ by activation with AgOTf or AgNO$_2$ in either MeCN or H$_2$O, respectively. From these very reactive terpyridineplatinum complexes stoichiometric addition of the desired 4-coodinate ligand typically in acetone/H$_2$O or DMF with mild heat leads to high yields of the desired product.

The reaction of these complexes has been shown to be reversible upon addition of excess chloride to produce [Pt(terpy)Cl]Cl [83]. Pyridine bound terpyridineplatinum complexes have also been shown to be displaced by G-residues in DNA

and functional groups such as thiols and imidazoles on proteins indicating that the ligands are quite labile [9, 29]. Further fourth coordinate pyridine bound terpyridineplatinum(II) complexes have been synthesised with various substituents at the 4′-position. Large electron donating groups at the 4′-position showed a loss of biological activity, and bisintercalators joined by a flexible linker at the 4′-position also showed relatively low cytotoxicity [23, 26].

4.4.4 Ligand Substitution by Thiol

The synthesis of terpyridineplatinum thiol complexes is typically achieved by either $AgNO_3$ activation of [Pt(terpy)Cl]Cl to form [Pt(terpy)H_2O](NO_2)$_2$ or direct addition of the desired thiol linker to terpyridineplatinum with base to cause the deprotonation of the thiol group and subsequently promote the reaction of the linker with the platinum. Reactions of this type are generally carried out under strict nitrogen atmospheres in order to prevent oxidation of the sulphur. Thiols in acidic solutions are typically undissociated and the reaction with terpyridineplatinum occurs via a five-coordinate intermediate whereby the thiol proton behaves as a strong acid reacting with the chloride forming HCl. Generally thiol substituents without the ability to deprotonate, such as thioethers, are unreactive with terpyridineplatinum because the bis-cationic product cannot be stabilised by deprotonation [84, 85]. The reactivity of [Pt(terpy)Cl]Cl with biological thiols such as glutathione, L-cystine, D-penicillamine and thioglycolic acid has been shown by Petrovic et al. using a tenfold excess of ligands to [Pt(terpy)Cl]Cl in acidic MeOH/H_2O (95/5%, v/v) to prevent dimerisation and hydrolysis of the [Pt(terpy)Cl]Cl [85]. It was shown that variation of the fourth coordinate ligand to thiol groups produces relatively inert complexes due to the high affinity of sulphur to Pt(II) which subsequently do not undergo nucleophilic substitution. A kinetic study to obtain evidence of the stability was carried out by Annibale et al. whereby an excess of chloride ions was added to a thiolate terpyridineplatinum complex. The results showed that the chloride ion did not displace the thiol ligand under neutral or basic conditions and was very slow in acidic conditions with a half life greater than one day [84]. Cheng et al. reported that transition metals such as Cu(II) or Zn(II) are capable of inducing cleavage of the platinum-thiol bond in terpyridineplatinum complexes in phosphate buffer at room temperature [86]. Due to the stability of thiol ligands the interactions between terpyridineplatinum thiol complexes and DNA can be attributed to intercalation alone and not platination, leading to an interesting class of biological probes [4, 18].

The purification of terpyridineplatinum complexes, like other typical inorganic complexes, can be achieved by a variety of techniques. Column chromatography, vapour and liquid extraction, recrystallisation and ion exchange are general techniques utilised everyday in typical inorganic laboratories and can be applied to terpyridineplatinum complexes.

4.5 Spectroscopic Characterisation Techniques

The characterisation of platinum based complexes for the purpose of identity confirmation is of the upmost importance. Electronic spectra are routinely collected for all complexes synthesised. Terpyridineplatinum(II) complexes display dimer and aggregate formation in solution which can affect the absorption spectra where Beer's law is not observed in some cases in solutions as low as 15 μM [3]. An additional impediment can be the choice of solvent or in some cases counter ions, so some care needs to be taken when measuring spectra. Spectroscopic methods are the predominant tool for characterisation in modern inorganic chemistry with an array of techniques including ultraviolet/visible spectroscopy, infrared spectroscopy, X-ray spectroscopy, mass spectrometry and the most useful technique nuclear magnetic resonance spectroscopy.

4.5.1 NMR Spectroscopy

Nuclear magnetic resonance (NMR) spectroscopy is a principle characterisation method exploiting the magnetic properties of certain nuclei. One dimensional ^{1}H, (Fig. 4.8) and ^{195}Pt (Fig. 4.11) NMR are essential for characterisation, however,
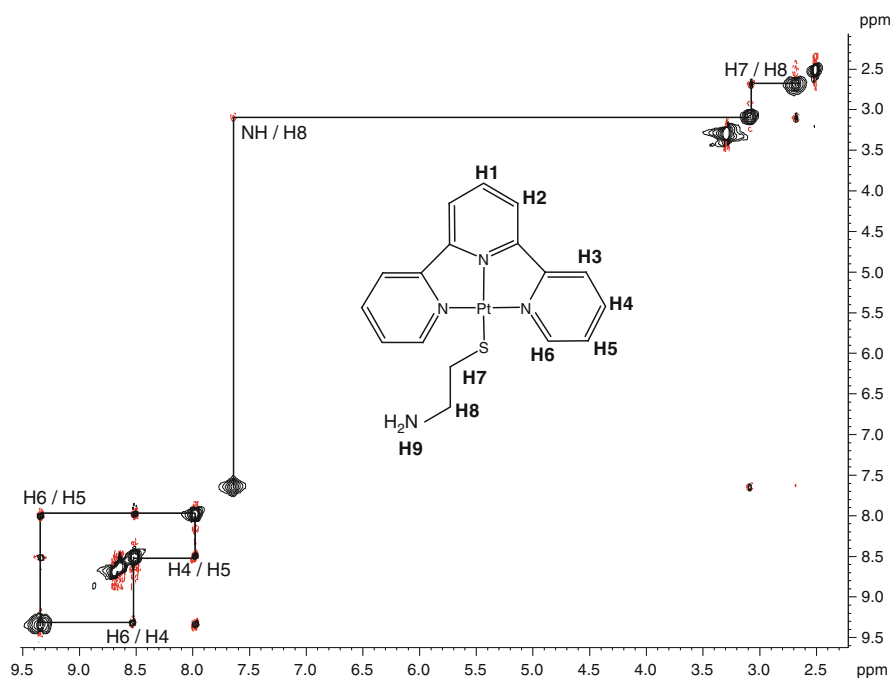
Fig. 4.8 The COSY spectrum of [Pt(terpy)AET]PF$_6$ in d_6-DMSO

increasingly multidimensional NMR are of value. The ^{1}H nucleus is ideal for NMR spectroscopy with a high selectivity and natural abundance [87, 88]. When platinum complexes contain organic skeletons it is possible to obtain simple one dimensional ^{1}H NMR and two dimensional NMR spectra by techniques such as correlation spectroscopy (COSY, Fig. 4.9), and nuclear overhauser effect spectroscopy (NOESY, Fig. 4.10), to determine the relationships of ^{1}H as separated by space and bond distances respectively [88].

2D ^{1}H NMR correlations produce spectra in which the ^{1}H chemical shifts are along two axes in order to produce a correlation between the two axes [88, 89]. The correlation between the proton resonances is often useful for structural elucidation that simple 1D NMR cannot provide, by giving the relationship of the connectivity between nuclei [88]. Typical COSY experiments can give a through bond correlation
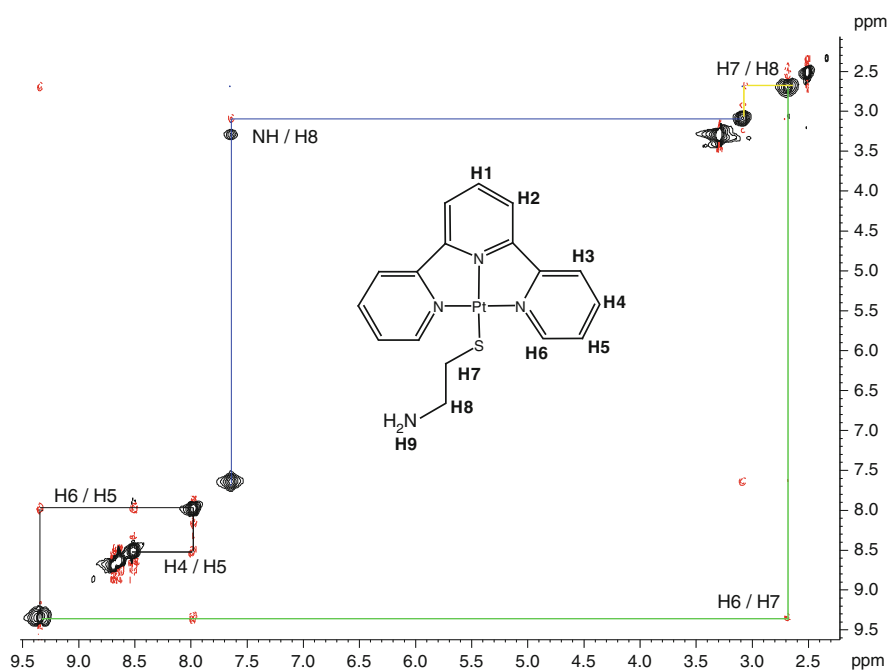
Fig. 4.9 The NOESY spectrum of [Pt(terpy)AET]PF$_6$ in d_6-DMSO
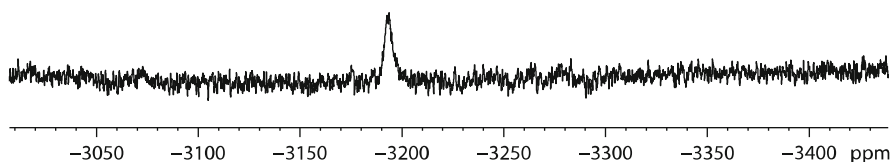
Fig. 4.10 The [195]Pt spectrum of [Pt(terpy)AET]PF$_6$ in d_6-DMSO

from a proton on one carbon, to the proton on the adjacent carbon. If a proton is coupled to more than one neighbouring proton then the cross peak will appear in more than one location and can be used to trace back the structure of the molecule as seen in Fig. 4.9. Direct comparison between the NOESY and COSY spectra can confirm the structure of the complex by determination of the connectivity and proximity of protons. As shown for [Pt(terpy)AET]PF$_6$ in Figs. 4.9 and 4.10, cross correlations are used to step around the complex until the ^{1}H NMR is fully characterised.

[195]Pt chemical shifts are highly sensitive to variations in platinum oxidation state and ligand substitution [87, 90]. Typically the [195]Pt chemical shifts for this class of compounds is between −2,600 and −3,400 ppm. The sensitive nucleus has an additive relationship of chemical shift containing various ligands with each ligand causing large shifts. The chemical shifts not only depend on the type of ligands but the type if isomer present, with *cis* isomer shifted up to 500 ppm up-field relative to a corresponding *trans* isomer. The magnetic shielding has been ordered into a magneto-chemical series according to an increasing shielding at the nucleus with I$^-$>CH$_3$>CN$^-$>Br$^-$>en>NH$_3$>Cl$^-$>NO$_2$$^-$>OH$_2$>F$^-$ showing that the chemical shift appears predictable and sensitive for varied ligands. The [195]Pt spectrum of [Pt(terpy)AET]PF$_6$ (Fig. 4.11) displayed a single peak at −3,193 ppm, confirming that a single platinum species is present. To further characterise the complex determination of the protons closest to the platinum centre can be achieved

Fig. 4.11   [195]Pt-^{1}H HMBC spectrum of [Pt(terpy)AET]PF$_6$ in d_6-DMSO

utilising ^{1}H-^{195}Pt HMQC NMR. ^{1}H-^{195}Pt NMR is a method of choice to confirm successful coordination. Figure 4.12 shows the cross correlation between the ^{195}Pt peak at −3,193 ppm with both the H6 and H7 protons.

Fig. 4.12 The unit cell of [Pt(terpy)(MeCN)](OTf)$_2$ and the stacking interaction of [Pt(terpy) (MeCN)](OTf)$_2$ involving a 90° interaction motif (*left*) and four [Pt(terpy)(MeCN)](OTf)$_2$ units as seen from above interacting in a helical fashion [92]

Fig. 4.13 The stacking interaction of {[Pt(terpy)(MPA)]Cl}$_2$ AgCl involving a head-to-head motif which is stabilised by the presence of the AgCl (*left*) and two {[Pt(terpy)(MPA)]Cl}$_2$ AgCl units interacting within the packing structure demonstrating the distance between the aromatic ligand planes (*right*). The distance between the two silver atoms is 3.0984(8) Å [31]

4.5.2 Crystal Structure Determination

There are examples of crystal structures of terpyridineplatinum(II) complexes in the literature [18, 31, 42, 46, 91, 92]. Studies have revealed that counter ions play a role in the aggregation of the complexes and produce dramatic colour changes as well as emission enhancement in the near infra-red region [20, 35]. Variation of the temperature, type and length of the linker between dinuclear terpyridine platinum(II) complexes can effected the extent of spontaneous self-association in solution-state [20]. The tendency of terpyridineplatinum(II) complexes to aggregate in solution is usually influenced by strong π–π and metal–metal interactions as shown in Figs. 4.12 and 4.13.

References

1. Alderden RA, Hall MD, Hambley TW. J Chem Educ. 2006;83:728.
2. Collins JG, Wheate NJ. J Inorg Biochem. 2004;98:1578.
3. Morgan GT, Burstall FH. J. Chem. Soc. 1934: 1498.
4. Jennette KW, Lippard SJ, Vassiliades GA, Bauer WR. Proc Natl Acad Sci USA. 1974;71:3839.
5. Barton JK, Lippard SJ. Biochemistry. 1979;18:2661.
6. Nordén B. Inorg Chim Acta. 1978;31:83.
7. Howe-Grant M, Lippard SJ. Biochemistry. 1979;18:5762.
8. Erkkila KE, Odom DT, Barton JK. Chem Rev. 1999;99:2777.
9. McCoubrey A, Latham HC, Cook PR, Rodger A, Lowe G. FEBS Lett. 1996;380:73.
10. Che CM, Yang MS, Wong KH, Chan HL, Lam W. Chem Eur J. 1999;5:3350.
11. Wang AH, Nathans J, van der Marel G, van Boom JH, Rich A. Nature. 1978;276:471.
12. Chan HL, Ma DL, Yang M, Che CM. J Biol Inorg Chem. 2003;8:761.
13. McFadyen WD, Wakelin LPG, Roos IAG, Leopold VA. J Med Chem. 1985;28:1113.
14. Collins JG, Rixon RM, Aldrich-Wright JR. Inorg Chem. 2000;39:4377.
15. Jaramillo D, Buck DP, Collins JG, Fenton RR, Stootman FH, Wheate NJ, et al. Eur J Inorg Chem. 2006;4:839.
16. Fisher DM, Bednarski PJ, Grunert R, Turner P, Fenton RR, Aldrich-Wright JR. ChemMedChem. 2007;2:488.
17. Jin VX, Ranford JD. Inorg Chim Acta. 2000;304:38.
18. Jennette KW, Gill JT, Sadownick JA, Lippard SJ. J Am Chem Soc. 1976;98:6159.
19. McFadyen WD, Wakelin LPG, Roos IAG, Hillcoat BL. J Biochem. 1987;242:177.
20. Yu C, Chan KH, Wong KM, Yam VW. Proc Natl Acad Sci USA. 2006;103:19652.
21. McFadyen WD, Wakelin LPG, Roos IAG, Hillcoat BL. J Biochem. 1986;238:757.
22. Gillard RD, Sengül A. Transit Met Chem. 2001;26:339.
23. Lowe G, Droz AS, Vilaivan T, Weaver GW, Park JJ, Pratt JM, et al. J Med Chem. 1999;42:3167.
24. Lowe G. (Isis Innovation Limited, UK). Application: WO, 2000:65.
25. Lowe G. (Isis Innovation Ltd., UK; Lowe, Gordon). Application: WO, 1997:62.

26. Lowe G, Droz A, Vilaivan T, Weaver GW, Tweedale L, Pratt JM, et al. J Med Chem. 1999;42:999.
27. Lowe G, Vilaivan T. J Chem Soc. 1996: 1499.
28. Wee S, O'Hair RAJ, McFadyen WD. Rapid Commun Mass Sp. 2005;19:1797.
29. Becker K, Herold-Mende C, Park JJ, Lowe G, Schirmer RH. J Med Chem. 2001;44:2784.
30. Bonse S, Richards JM, Ross SA, Lowe G, Krauth-Siegel L. J Med Chem. 2000;43:4812.
31. van Holst M, Le Pevelen D, Aldrich-Wright J. Eur J Inorg Chem. 2008: 4608.
32. van Holst M, Le Pevelen D, Aldrich-Wright J. Eur J Inorg Chem. 2009: 691.
33. Woodhouse SL, Ziolkowski EJ, Rendina LM. Dalton Trans. 2005;17:2827.
34. Todd JA, Turner P, Ziolkowski EJ, Rendina LM. Inorg Chem. 2005;44:6401.
35. Yam VW, Chan KH, Wong KM, Zhu N. Chemistry. 2005;11:4535.
36. Yam VW-W, Tang RP-L, Wong KM-C, Cheung K-K. Organometallics. 2001;20:4476.
37. Yam VWW, Tao CH, Zhang L, Wong KMC, Cheung KK. Organometallics. 2001;20:453.
38. Yam VW-W, Tang RP-L, Wong KM-C, Lu X-X, Cheung K-K, Zhu N. Chem Eur J. 2002;8:4066.
39. Ma D-L, TY-T. Shum, F. Zhang, C.-M. Che, M. Yang, Chem Commun. 2005; 37; 4675
40. Wheate NJ, Brodie CR, Collins JG, Kemp S, Aldrich-Wright JR. MiniRev Med Chem. 2007;7:627.
41. Lowe G, Droz AS, Park JJ, Waever GW. Bioorg Chem. 1999;27:477.
42. Lowe G, Ross SA, Probert M, Cowley A. Chem Commun. 2001: 1288.
43. Kurosaki H, Yamakawa N, Sumimoto M, Kimura K, Goto M. Bioorg Med Chem Lett. 2003;13:825.
44. Todd JA, Rendina LM. Inorg Chem. 2002;41:3331.
45. Crossley EL, Caiazza D, Rendina LM. Dalton Trans. 2005: 2825.
46. Tzeng B-C, Fu W-F, Che C-M, Chao H-Y, Cheung K-K, Peng S-M. Dalton Trans. 1999: 1017.
47. Chan H-L, Ma D, Yang M, Che C-M. Chembiochem. 2003;4:62.
48. Chen TK, Fico R, Canellakis ES. J Med Chem. 1977;21:868.
49. Denny WA, Atwell GJ, Baguley BC, Wakelin LPG. J Med Chem. 1985;28:1568.
50. Howe-Grant M, Wu KC, Bauer WR, Lippard SJ. Biochemistry. 1976;15:4339.
51. Peyratout CS, Aldridge TK, Crites DK, McMillin DR. Inorg Chem. 1995;34:4484.
52. Carpenter ML, Lowe G, Cook PR. Nucleic Acids Res. 1996;24:1594.
53. Hannon MJ. Chem Soc Rev. 2007;32:280.
54. Mullins ST, Annan NK, Cook PR, Lowe G. Biochemistry. 1992;31:842.
55. Lo Y-C, Ko T-P, Su W-C, Su T-L, Wang Andrew HJ. J Inorg Biochem. 2009;103:1082.
56. Puntoriero F, Campagna S, DI Pietro ML, Giannetto A, Cusumano M. Photochem Photobio Sci. 2006;6:357.
57. Yam VW, Chan KH-Y, Wong KM-C, Chu BW-K. Angew Chem Int Edit. 2006;45:6169.
58. Tam AY-U, Wong KM-C, Wang G, Yam VW. Chem Commun. 2007: 2028.
59. Wong KM-C, Tang W-S, Lu X-X, Zhu N, Yam VW. Inorg Chem. 2004;44:1492.
60. Lai S-W, Chan M, Cheung K-K, Che C-M. Inorg Chem. 1999;38:4262.
61. Baghurst DR, Cooper SR, Greene DL, Mingos DMP, Reynolds SM. Polyhedron. 1990;9:893.
62. Cummings SD. Coordin Chem Rev. 2009;253:449.
63. Eryazici I, Moorefield CN, Newkome GR. Chem Rev. 1834;2008:108.
64. Eaborn C, Kundu K, Pidcock A. J Chem Soc Dalton. 1981: 933.
65. Arena G, Calogero G, Campagna S, Scolaro M, Ricevuto V, Romeo R. Inorg Chem. 1998;37:2763.
66. Arena G, Scolaro M, Pasternack RF, Romeo R. Inorg Chem. 1995;34:2994.
67. Chakraborty S, Wadas TJ, Hester H, Flaschenreim C, Schmehl R, Eisenberg R. Inorg Chem. 2005;44:6284.
68. Price JH, Williamson AN, Schramm RF, Wayland BB. Inorg Chem. 1972;11:1280.
69. Annibale G, Brandolisio M, Pitteri B. Polyhedron. 1995;14:451.
70. McDermott JX, White JF, Whitesides GM. J Am Chem Soc. 1976;98:6522.
71. Mureinik RJ, Bidani M. Inorg Nucl Chem Lett. 1977;13:625.

72. Michalec JF, Bejune SA, Cuttlee DG, Summerton GC, Gertenbach JA, Field JS, et al. Inorg Chem. 2001;40:2193.
73. Mureinik RJ, Bidani M. Inorg Chim Acta. 1978;29:37.
74. Pitteri B, Marangoni G, Cattalini L, Bobbo T. J Chem Soc Dalton. 1995: 3853.
75. Aldridge TK, Stacy EM, McMillin DR. Inorg Chem. 1994;33:722.
76. Basolo F, Gray A, Pearson R. J Am Chem Soc. 1960;82:4200.
77. Paeloso A. Coord Chem Rev. 1973;10:123.
78. Carr CA, Richards JM, Ross SA, Lowe G. J Chem Res. 2000: 566.
79. Wong KM, Yam VW. Coord Chem Rev. 2007;251:2477.
80. Guo F, Sun W. Inorg Chem. 2005;44:4055.
81. Yang Q, Wu L, Wu Z, Zhang L, Tung C. Inorg Chem. 2002;41:5653.
82. Lam SC, Yam VW, Wong KM, Cheng EC, Zhu N. Organometallics. 2005;24:4298.
83. Pitteri B, Marangoni G, Viseutim FV, Cattalini L, Bobbo T. Polyhedron. 1998;17:475.
84. Annibale G, Brandolisio M, Bugarcic Z, Cattalini L. Transit Met Chem. 1998;23:715.
85. Petrovic BV, Djuran MI, Bugarcic ZD. Met Based Drugs. 1999;6:355.
86. Cheng C, Lu Y. Chem Commun. 1998: 253.
87. Vinje J, Sletten E. Anti Cancer Agent Me. 2007;7:35.
88. Nelson JH. Nuclear magnetic resonance spectroscopy, Upper Saddle River. 2003.
89. Balaram P, Bothner-By A, Dadok J. J Am Chem Soc. 1972;94:4015.
90. Still BM, Kumar PGA, Aldrich-Wright JR, Price WS. Chem Soc Rev. 2006;36:665.
91. Ross SA, Lowe G, Watkin DJ. Acta Crystallogr. 2001;C57:275.
92. Harper BWJ. Honours thesis, University Of Western Sydney (Sydney): 2009.

Chapter 5
Introduction to Nuclear Magnetic Resonance

Allan M. Torres and William S. Price

5.1 Introduction

Nuclear Magnetic Resonance (NMR) spectroscopy is a powerful non-invasive analytical method that is gaining popularity in recent years due to its wide range of applications in various fields of research [1, 2]. Of all the analytical techniques in chemistry, NMR has been proven to be superior and extremely useful for the characterisation of complex mixtures, biomolecular structures and dynamics, molecular interactions and aggregations.

The popularity of NMR spectroscopy is due mainly to the development of novel analytical NMR techniques coupled with the rapid advancement of instrumental technology [3, 4]. NMR spectrometers now incorporate much stronger magnets and stronger magnetic field gradients coupled to more sophisticated electronics, probes and computers. In conjunction with this, the introduction of pulsed Fourier transform has led to revolutionary developments of complex and diverse NMR methods engineered to characterise specific molecular properties or interactions.

This chapter provides an overview of the principles of the NMR technique and the observable parameters that can be useful in a variety of studies such as those presented in Chaps. 6 and 7 on the investigation of the interaction of metal complexes with DNA. The descriptions given here are not comprehensive and readers are advised to refer to references cited for more detailed discussion information and recent developments.

A.M. Torres (✉)
Nanoscale Organisation and Dynamics Group, School of Biomedical and Health Sciences, College of Health and Science, University of Western Sydney, Sydney, NSW 2751, Australia
e-mail: A.Torres@uws.edu.au

5.2 Basic Principles

Like most spectroscopic techniques, NMR is an absorption spectroscopy and involves specific excitation energies causing transitions between the ground or equilibrium state and a higher energy state. In NMR, the relevant states are the magnetic nuclear spin states which acquire different energies in the presence of a static magnetic field. All elements which comprise organic or biological molecules have at least one stable isotope that is NMR-active and thus they can be studied by NMR.

In a standard one-dimensional (1D) experiment, an NMR sample placed in a strong magnetic field is subjected to a radio-frequency (RF) pulse after which an RF response or signal from the sample in the form of an induced current referred to as the free induction decay (FID) is recorded (see Fig. 5.1a). A 1D NMR spectrum is then obtained after Fourier transformation of the FID. An NMR spectrum can be characterised by many peaks with different resonance positions or frequencies.

Quantum mechanics and, specifically, the density matrix formalism, is the natural language to completely describe NMR experiments [5], however, for simpler experiments it is possible to explain experimental outcomes by appealing to a vector model of the magnetisation dynamics during an NMR experiment. For completeness we note that product operators provide a more tractable but yet rigorous method for following the evolution of NMR pulse sequences – although the effects of relaxation (vide infra) are neglected. Just prior to the application of the RF pulse, the spins have a very slight bias in their alignment either with or against

Fig. 5.1 A simple NMR experiment. (**a**) Pulse acquire, FID, NMR spectra (**b**) *z*-magnetisation, RF pulse, *xy*-magnetisation

the magnetic field, which is conventionally assigned to the positive z-axis. There will be an excess of spins aligned with the magnetic field so that the net or bulk magnetisation would be aligned along the z-axis (Fig. 5.1b).

Application of the RF pulse causes the magnetic vector to be rotated towards the xy or transverse plane. In a standard 1D NMR experiment, a time delay corresponding to signal detection causes the net magnetisation to precess around the z-axis according to its respective resonance frequency which in turn induces an RF signal corresponding to the FID. Depending on the molecule, there could be many spins with different resonance frequencies so that the resulting FID can be complicated. To increase the amount of signal, the experiment can be repeated provided enough time is allowed for the spins to align themselves along the z-axis thereby building up the z-(or longitudinal) component of the magnetisation.

The FID is of the form of a decaying oscillating voltage versus time (t), which for a single resonance can be expressed as

$$S(t) = M_0 \exp(i\omega_0 t) \exp(-\lambda t) \tag{5.1}$$

where M_0 is the equilibrium magnetisation, ω_0 is the resonance (or Larmor) frequency (rad s^{-1}) and $\lambda = 1/T_2$ is the spin–spin relaxation rate and T_2 is the spin–spin relaxation rate constant. Taking the Fourier transform of this signal we obtain the two lineshape components of the spectrum, a (real) absorption part, $A(\omega)$ and a (complex) dispersive part $D(\omega)$,

$$
\begin{aligned}
F(\omega) &= \int_0^\infty S(t) e^{-i\omega t} dt \\
&= \frac{\lambda_0}{(\omega_0 - \omega)^2 + \lambda_0^2} + \frac{i(\omega_0 - \omega)}{(\omega_0 - \omega)^2 + \lambda_0^2} \\
&= A(\omega) + iD(\omega).
\end{aligned}
\tag{5.2}
$$

An NMR spectrum is normally presented using the real absorptive part $A(\omega)$ which is characterised by a typical Lorentzian lineshape. $A(\omega)$ has the notable and widely used property that the linewidth at half-height (measured in Hz) is related to the spin–spin relaxation rate constant by,

$$v_{\frac{1}{2}} = \frac{1}{\pi T_2}. \tag{5.3}$$

An NMR spectrum is usually characterised by many peaks with different resonance positions or frequencies. The resonant frequency of a nucleus, v, is proportional to the applied magnetic field and is influenced by the nature of its local electronic environment. This can be represented by the general equation

$$v = \frac{\gamma}{2\pi} B_0 (1 - \sigma) \tag{5.4}$$

where γ is the magnetogyric ratio, B_0 is the magnitude static magnetic field and σ is the shielding parameter. An increase in B_0 leads to higher v values which eventually equates to increased sensitivity and larger dispersion of signals leading to better resolution between resonances. This is the reason why stronger magnets are always preferred for studying dilute samples and those that contain complex biomolecules with many observable nuclei. The magnetic shielding parameter σ determines the exact resonance position and characterises the electronic environment of the nucleus.

5.3 NMR Effects and Interactions

The versatility of NMR is mainly due to numerous NMR effects and interactions that can be observed and utilised to provide useful information about chemical and physical properties of the sample. Some of these important effects and the corresponding type of information that can be obtained from them is summarised in Table 5.1. The following sections provide brief descriptions of these effects.

5.3.1 Chemical Shift

The positional variation of resonances in an NMR spectrum is due to the difference in effective magnetic field that each nucleus experiences. This is mainly caused by the nature of the electronic environment around the nucleus which provides shielding or deshielding from the external magnetic field. The magnetic field shielding effect of electrons is commonly referred to as chemical shift. Chemical shift values are conventionally expressed relative to the frequency of a standard resonance (v_{ref}) divided by the centre frequency of the spectrometer (v_0) and because of the very small values involved, this is normally presented in parts per million (ppm) viz

$$\delta = \frac{(v - v_{ref}) \times 10^6}{v_0} \quad \text{(ppm)}. \tag{5.5}$$

Table 5.1 Useful NMR effects and interactions

Effect or interaction	Information provided
Chemical shift	Local environment, structure
Spin–spin coupling	Local structure, through bond connectivity
Dipolar coupling	Spatial proximity, through space connectivity
Spin–lattice relaxation	Reorientational motion
Spin–spin relaxation	Reorientational motion
Magnetic field gradient	Translational diffusion

Expressing δ in this dimensionless manner has the added benefit of making the values "machine independent" thereby facilitating comparison of NMR spectral data obtained at different static magnetic field strengths.

It is a convention in NMR spectroscopy that spectra are plotted going to higher ppm from right-to-left. Anachronistically, harking back to the days of continuous wave NMR spectrometers, going towards low ppm is termed "high field" and, conversely, going to high ppm is termed "low field". Importantly, all modern spectrometers acquire information on all measurable frequencies of the observed nucleus in one go and generate the resulting spectra through Fourier transformation.

The chemical shift effect is essential in NMR studies as it provides information about the local environment around a nucleus as well as the overall structure of the molecule. For example, methyl hydrogens are shielded more than methylene hydrogens while aromatic hydrogens are shielded least. Thus, in an unknown sample, the position of hydrogen resonances will reveal the type of hydrogen present and this ultimately helps in identifying the molecule(s) present. Much of the information content of NMR spectra requires that the spectral resonances can be assigned to various nuclei in the molecule. In many cases it is too difficult to assign the 1D spectrum directly and multidimensional spectra (vide infra) must be used. A 1D ^{1}H NMR spectrum of the platinum complex 56MESS in D_2O with hydrogen peak assignments is presented in Fig. 5.2.

In protein NMR, chemical shift values play an important role in the determination of secondary structures as backbone hydrogens of amino acids in a helical conformation have chemical shifts that differ significantly from those in β-sheets. Chemical shift information can actually be used as parameter constraints in three dimensional structure calculations.

Fig. 5.2 1D ^{1}H NMR spectrum of 56MESS (20 mM in D_2O). Inset: 56MESS structure and expanded region showing peak splitting due to spin–spin coupling

5.3.2 Spin–Spin Coupling

Nuclear spins can interact with other spins via bonding electrons often leading to symmetrical splitting of the signals. This interaction is transmitted by bonding electrons and is commonly referred to as *J*-coupling or spin–spin interactions. The magnitude of this splitting is independent of the magnetic field strength but is dependent on the nature and number of the chemical bonds that separates the two interacting nuclei. Spin–spin coupling can occur between nuclei separated by one bond (direct coupling) or two or more bonds (long-range coupling).

Spin–spin coupling is important in structure elucidation as it produces splitting patterns that reflect the number or type of neighbouring nuclei (Fig. 5.2 inset). A single nucleus interacting with two identical nuclei would result in a triplet signal for the nucleus and in a similar manner this single nucleus would create a doublet signal for the two identical nuclei. The magnitude of spin–spin coupling, on the other hand, decreases with the number of bonds separating the interacting nuclei. It also provides a measure of the relative orientation of other nuclei and bonds.

Spin–spin coupling can also be used to transfer magnetisation from one spin to another spin through the use of various pulse sequences. This feature can provide means to correlate spins with one another and help in assigning resonances to particular nuclei. NMR methods that utilise spin–spin coupling include two-dimensional (2D) experiments such as correlated spectroscopy (COSY) [6], total correlation spectroscopy (TOCSY) [7], heteronuclear multiple-quantum correlated spectroscopy (HMQC) [8] and heteronuclear multiple bond correlated spectroscopy (HMBC) [9].

COSY is perhaps the simplest and most popular 2D correlation NMR method. A COSY spectrum of 56MESS with selected cross-peaks labelled is shown in Fig. 5.3. 2D COSY spectra contained two types of peaks, the diagonal and non-diagonal peaks which are commonly referred to as cross-peaks. The projection of all peaks along the *x*-axis or *y*-axis corresponds to the normal [1]H 1D spectrum and each peak in the 2D spectrum is characterized by two chemical shift values, one for *x*-axis and another for the *y*-axis. The diagonal peaks have identical chemical shift values for *x*- and *y*-axis and are due ^{1}H nuclei that did not undergo magnetisation transfer. This type of peak is not normally useful in resonance assignment. The non-diagonal cross-peaks, on the other hand, have two different chemical values and arise from magnetisation transfer between two neighbouring ^{1}H nuclei that are separated by two to three chemical bonds. Cross-peaks in COSY 2D spectra are useful since one can determine which ^{1}H nucleus is correlated to another ^{1}H nucleus by noting the corresponding chemical shift values along *x*- and *y*-axis. For example, in 56MESS case, assuming that the resonance assignments of aromatic protons H3 and H8 are known to be equivalent at ~8 ppm, one can deduce that peaks at ~9 ppm are due to pairs H4/H7 and H2/H9 since cross-peaks are present at ~8 and 9 ppm.

Other nuclei such as ^{13}C, ^{15}N, and [195]Pt, on other hand, can be correlated to ^{1}H using HMQC and HMBC. The information provided by the 2D spectra of the two methods complement each other; HMQC yields direct or one-bond correlations while HMBC mainly shows indirect or two or more bond correlations. [13]C HMQC

Fig. 5.3 ^{1}H COSY spectrum of 56MESS (20 mM in D$_2$O) acquired at 400 MHz. Non-diagonal cross-peaks indicate connectivities or correlations between neighbouring hydrogens. *Arrows* indicate aromatic hydrogen cross-peaks in 56MESS

and HMBC spectra of 56MESS are presented in Fig. 5.4. In contrast to the COSY 2D spectrum in Fig. 5.3, these spectra have one-axis dedicated to ^{13}C and have no diagonal peaks.

Besides their usefulness in correlating peaks, HMQC and HMBC are usually preferred over the simple 1D method in indirectly observing insensitive nuclei (non-^{1}H) such as ^{13}C and ^{195}Pt. This advantage is realised because, during the NMR pulse experiment, the more sensitive ^{1}H magnetisation is utilised for spin excitation and detection. A ^{195}Pt HMBC acquired in 2 h on a 20 mM 56MESS is shown in Fig. 5.5. A ^{195}Pt 1D of the same sample would require at least 10 hours experimental time.

5.3.3   Dipolar Coupling

Nuclear spin interaction can also occur without the intervening bonding electrons through the mechanism referred to as direct dipolar coupling. This interaction can

Fig. 5.4 HMQC and HMBC spectra of 56MESS (20 mm in D_2O). Cross peaks in HMQC indicate correlations due to hydrogens directly bonded to carbons while cross peaks in HMBC indicate correlations due to hydrogens separated by two or more bonds to carbons

Fig. 5.5 [195]Pt HMBC spectrum of 56MESS showing correlations between aromatic hydrogens and platinum

be likened to the magnetic interaction between two bar magnets separated in space. The magnitude of this "through space" interaction is dependent on the distance that separates the two nuclei and is represented by the dipole–dipole coupling constant D_{IS} defined by

$$D_{IS} = \frac{\mu_0 \hbar}{4\pi} \frac{\gamma_I \gamma_s}{r_{IS}^3} \qquad (5.6)$$

where γ_I and γ_S are the magnetogyric ratios of the two interacting spins, r_{IS} is the distance of the two spins, $\mu_0 = 4\pi \times 10^{-7}$ H m^{-1}, and $\hbar = 1.0546 \times 10^{-34}$ J s. Dipolar coupling is useful for determining the relative position of spins and is therefore valuable in elucidating the three-dimensional structure of a molecule.

In a case where the resonance of a particular spin is perturbed by continuous RF irradiation, this may cause some enhancement of spectral intensities of resonances of neighbouring spins through a special dipolar interaction pathway that is commonly referred to as nuclear Overhauser enhancement or NOE. This would be observed in the popular 1D NOE experiment which is routinely used to identify nuclei which are close to each other. Two-dimensional versions of nuclear Overhauser enhancement spectroscopy such as 2D NOESY [10] and rotational Overhauser enhancement spectroscopy 2D ROESY [11] operate in a similar fashion and have been used extensively in characterising three-dimensional (3D) structures of molecules of various sizes. NOESY is more applicable to high molecular weight

biomolecules such as proteins and DNA while ROESY is more appropriate for relatively low molecular weight compounds such as peptides, organic compounds and simple molecules.

The NOESY and ROESY spectra of 56MESS are presented in Fig. 5.6. The cross-peaks obtained in these spectra represents dipolar cross relaxation between two neighbouring nuclei separated by 5 Å or less while cross-peaks intensities are proportional to the distance that separates them. Several cross peaks with quantified intensities may be collected and then converted to a list of distance-constraints. This can then be used as input to a distance-geometry program to create a 3D model that satisfies the 2D NOESY spectrum.

5.3.4   Relaxation

Besides the resonance positions and coupling interactions, there are other useful observable NMR parameters that can provide valuable information about the properties of biomolecules and their interaction with others. For example, the rate of build-up of z-magnetisation upon application of magnetic field and the rate of decay of the NMR signal or transverse magnetisation, can yield information on molecular motion that includes reorientation, vibration and translational diffusion of a certain nucleus or spin.

The build-up or decay of longitudinal or z-magnetisation is referred to as spin–lattice or longitudinal relaxation while transverse magnetisation decay is commonly referred to as spin–spin or transverse relaxation. T_1 and T_2 values specifically denote the exponential time constants (expressed in seconds) for longitudinal and transverse relaxation, respectively, which are inversely proportional to the build-up or decay rates. Longitudinal relaxation is related to the efficiency of energy transfer between the spins and environment (the "lattice") in order for the system to achieve the thermal equilibrium distribution of the spin population. It is important in determining the optimum repetition rate of each NMR experiment and is measured using the inversion recovery experiment [12]. Transverse relaxation, on the other hand, affects the broadness of the peaks and is responsible for the characteristic exponential decay shape of the FID. It is measured from either the peak linewidth or more accurately through the use of Carr-Purcell-Meiboom-Gill (CPMG) sequence [13, 14]. There are many interactions that can result in relaxation and these include dipolar coupling, chemical shift anisotropy, spin–rotation, spin–spin coupling, etc. Among these, the dipolar coupling interaction is a major relaxation contributor especially for ^1H nuclei in solution. The reorientation of the molecule, which is characterised by the reorientational correlation time τ_c, modulates the dipolar interaction that causes relaxation. Large molecules which are tumbling or reorientating relatively slowly (long τ_c) have short T_2 values while small molecules which are reorientating relatively fast (short τ_c) have $T_2 \approx T_1$.

For the case of intramolecular dipole–dipole (DD) relaxation between two identical spins separated by a distance r we have,

Fig. 5.6 ^{1}H NOESY and ROESY spectra of 56MESS (20 mM in D$_2$O). Cross-peaks indicate correlations between hydrogens separated by 5 Å or less

$$R_1^{DD} = \frac{1}{T_1^{DD}} = \frac{2}{5}\left(\frac{\mu_0}{4\pi}\right)^2 \frac{\gamma^4\hbar^2 I(I+1)}{r^6}\left(J(\omega_0) + 4J(2\omega_0)\right) \tag{5.7}$$

and

$$R_2^{DD} = \frac{1}{T_2^{DD}} = \frac{1}{5}\left(\frac{\mu_0}{4\pi}\right)^2 \frac{\gamma^4\hbar^2 I(I+1)}{r^6}\left(3J(0) + 5J(\omega_0) + 2J(2\omega_0)\right) \tag{5.8}$$

where R_1^{DD} and R_2^{DD} are the rate constants for the longitudinal relaxation and transverse relaxation, respectively, and I is the spin quantum number. The spectral density functions are defined as

$$J(\omega_0) = \frac{\tau_c}{1 + \omega_0^2\tau_c^2}. \tag{5.9}$$

In the case of small molecules in solution, it is usually the case that the condition $\omega_0\tau_c \ll 1$ (normally referred to as the extreme narrowing condition) holds. In this case, (5.7) and (5.8) simplify to give

$$R_1^{DD} = \frac{1}{T_1^{DD}} = 2\left(\frac{\mu_0}{4\pi}\right)^2 \frac{\gamma^4\hbar^2 I(I+1)}{r^6}\tau_c$$

$$R_2^{DD} = \frac{1}{T_2^{DD}} = 2\left(\frac{\mu_0}{4\pi}\right)^2 \frac{\gamma^4\hbar^2 I(I+1)}{r^6}\tau_c. \tag{5.10}$$

5.3.5 Magnetic Field Gradient

Translational diffusion of molecules can be studied in NMR by the use of spin-echo or stimulated-echo based experiments that incorporate pulsed-magnetic field gradients [15]. The schematic diagram of the pulsed gradient spin-echo sequence (PGSE) is shown in Fig. 5.7.

In NMR diffusion experiments, the pulsed-magnetic field gradients provide a way of labelling the spin positions in the direction of the gradient. Spins belonging to molecules that have moved during the delay Δ separating the gradient pulses lose phase coherence resulting in a decrease in total signal. The decrease in NMR signal E can be related to the diffusion coefficient D and is given by

$$E = \frac{S}{S_{g=0}} = \exp\left(-\gamma^2 g^2 D\delta^2\left(\Delta - \delta/3\right)\right) \tag{5.11}$$

where $S/S_{g=0}$ is the normalised detected signal amplitude, g is the (magnetic-field) gradient pulse strength, and δ is the gradient pulse duration. As the diffusion

Fig. 5.7 Schematic representation of the PGSE sequence for measuring translational diffusion. The 90° RF pulse, 180° RF pulse and the detection period are separated by delay τ while the two magnetic-field gradient pulses of duration δ are separated by delay Δ

coefficient is related to the size of the molecules, this type of NMR experiment can be used in studying molecular interactions, such as binding and aggregation as illustrated in Chap. 7.

References

1. Levitt MH. Spin dynamics: basics of nuclear magnetic resonance. West Sussex: Wiley; 2001.
2. Teng Q. Structural biology: practical NMR applications. New York: Springer; 2005.
3. Derome AE. Modern NMR techniques for chemistry research. Oxford: Pergamon; 1987.
4. Keeler J. Understanding NMR spectroscopy. 2nd ed., Hoboken, NJ: Wiley; 2010.
5. Farrar TC. Conc in Magn Reson. 1990;2:1.
6. Rance M, Sörensen OW, Bodenhausen G, Wagner G, Ernst RR, Wüthrich K. Biochem Biophys Res Commun. 1983;117:479.
7. Bax A, Davis DG. J Magn Reson. 1985;65:355.
8. Bax A, Griffey RH, Hawkins BL. J Magn Reson. 1983;55:301.
9. Bax A, Summers MF. J Am Chem Soc. 2093;1986:108.
10. Kumar A, Ernst RR, Wüthrich K. Biochem Biophys Res Commun. 1980;95:1.
11. Bax A, Davis DG. J Magn Reson. 1985;63:207.
12. Vold RL, Waugh JS, Klein MP, Phelps DE. J Chem Phys. 1968;48:3833.
13. Carr HY, Purcell EM. Phys Rev. 1954;94:630.
14. Meiboom S, Gill D. Rev Sci Instrum. 1958;29:688.
15. Price WS. NMR studies of translational motion. Cambridge: Cambridge University Press; 2009.

Chapter 6
NMR Studies of Metallointercalator–DNA Interactions

Damian P. Buck and J. Grant Collins

6.1 Introduction

The study of the interaction between inert transition metal complexes and nucleic acids has developed from the early work of Dwyer [1], Lippard [2], Nordén [3] and Barton [4] to the point that it is now a central theme in bio-inorganic chemistry. While there has been considerable interest in metal complexes that bind nucleic acids, the interaction of metallointercalators with DNA and RNA has received the most attention [5, 6]. Square-planar platinum(II) complexes have demonstrated significant anticancer activity [7], and octahedral ruthenium(II) and rhodium(III) complexes have been used as probes of nucleic acid structure and as a means to study electron transfer reactions mediated by the heteroaromatic bases [5, 6]. While a range of techniques is available to study the nucleic acid binding of metal complexes, NMR spectroscopy (particularly ^{1}H NMR) has proven to be the most useful. NMR spectroscopy can provide a detailed, atom level resolution, picture of the metal complex binding, and if the quality of the data is sufficient, a three-dimensional structure of the metal complex bound to the oligonucleotide can be determined. The strategies used to assign the ^{1}H NMR spectrum of an oligonucleotide [8–10], the extension of these methods to study the interaction of metal complexes with DNA and the use of molecular modelling will be presented in this chapter.

J.G. Collins (✉)

School of Physical, Environmental and Mathematical Sciences, University College, University of New South Wales, Australian Defence Force Academy, Canberra, ACT 2600, Australia
e-mail: g.collins@adfa.edu.au

6.2 NMR Analysis of DNA

6.2.1 Sample Preparation and NMR Spectroscopy

Oligonucleotides, obtained from a commercial source, are converted to the sodium salt using a CM-25 Sephadex® column after residual impurities from the synthesis have been removed by elution through a C-18 Sep-Pak. The oligonucleotide is then dissolved in 600–700 μL of phosphate buffer (10 mM, pH 7.0) containing 20 mM NaCl and 0.1–1 mM EDTA. For experiments carried out in D_2O, the oligonucleotide sample is repeatedly freeze dried from D_2O before being made up in 99.96% D_2O. The oligonucleotide concentration is estimated from the A_{260} absorbance using an extinction coefficient of 6,600 M^{-1} cm^{-1} per nucleotide. Oligonucleotide concentrations in the range of 1–3 mM are typically used to study the binding of a metallointercalator. The exact metal complex to oligonucleotide duplex ratio is determined by integration of the respective ^{1}H resonances.

Although water-soluble chemical shift standards can be added to the oligonucleotide solution (e.g., DSS), chemical shift values are often measured relative to the residual HDO peak at a given temperature. Phase-sensitive NOESY and DQFCOSY two-dimensional NMR spectra are generally recorded using 2048 data points in t_2 for 256 t_1 values with a pulse delay of between 1.5 and 3 s, and with mixing times ranging from 50 to 300 ms. Short mixing times provide more accurate distance information, whereas, long mixing times (>200 ms) provide stronger NOE cross-peaks. Accumulation times for the two-dimensional experiments typically range from 16 to 48 h.

6.2.2 Assignment of the ^{1}H NMR Spectrum of DNA

In most NMR studies of the interaction of a metallointercalator with DNA an oligonucleotide of 6–12 base-pairs is used. Hexanucleotides are long enough to form a stable duplex, as evidenced by the observation of imino resonances and a range of diagnostic intraduplex NOEs (see below). A dodecanucleotide represents just over one turn (360°) of the duplex structure, and the spectral resolution of ^{1}H resonances is reasonable, even at relatively low magnetic fields.

Figure 6.1 shows the ^{1}H NMR spectrum of an oligonucleotide. The aromatic base resonances appear between 7.0 and 8.5 ppm, the cytosine H5 and sugar H1′ resonances 5.2–6.5 ppm, the sugar H3′ resonances 4.8–5.2 ppm, the sugar H4′/H5′/H5″ resonances 3.8–4.8 ppm and the sugar H2′/H2″ and thymine methyl resonances 1.4–3.0 ppm. The base resonances are usually well resolved, and their assignment to an adenine, guanine, cytosine or thymine is relatively straightforward. The adenine H8 resonances are generally found furthest downfield, due to experiencing only small ring current shifts from neighbouring bases. Guanine H8 resonances appear upfield (7.7–8.0 ppm), while cytosine and thymine H6 resonances appear

Fig. 6.1 [1H] NMR spectrum of an icosanucleotide showing the various spectral regions for the base aromatic and sugar protons

still further upfield (7.1–7.7 ppm) with the cytosine H6 resonances spin coupled (J ~7.5 Hz) to the cytosine H5 proton. Adenine H2 resonances can be assigned from spin–lattice relaxation time experiments, as they have a significantly longer T_1 than the other base protons. The assignment of each resonance to a particular base in the oligonucleotide sequence, and the confirmation of the type of base, is determined from two-dimensional NOESY and DQFCOSY experiments. In addition, the resonances from the sugar protons are also assigned in the two-dimensional experiments by well-established methods [8–10].

For a "standard" B-type duplex, each base H8/H6 proton should exhibit an NOE to the H1′ proton on the attached sugar residue as well as to the H1′ proton of the sugar in the 5′-direction (see Table 6.1 for typical distances and Fig. 6.2). The distance to the H1′ proton of the sugar of the 3′-residue is greater than 5 Å, the maximum distance for which NOEs are generally observed. An expansion of a NOESY spectrum that gives the aromatic base to sugar H1′ proton NOEs is shown in Fig. 6.3, with the so-called "sequential walk" between bases highlighted. In a similar fashion, the sugar H2′/H2″ resonances can be assigned, as each base H8/H6 proton exhibits an NOE to both the H2′/H2″ resonances on its own sugar residue and those on its 5′-flank.

While NOE cross-peaks from each H8/H6 proton to their own sugar H3′ and H4′/H5′/H5″ resonances are generally observed, the sequential walk strategy does not work with these protons. However, NOE cross-peaks between the H2′/H2″ and

Table 6.1 Typical inter-atomic proton distances based on canonic DNA structures

	Proton	H6/8	H1'	H2'	H2''	H3'	H4'	H5'	H5''	AH2	TCH$_3$	CH5
Intranucleotide ^{1}H distances(Å)	**H1'**	**3.7**										
	H2'	**2.5**	**3.1**									
	H2''	**3.5**	**1.8**	**1.8**								
	H3'	4.1	4.0	**2.4**	**3.0**							
	H4'	4.7	**3.7**	4.1	**3.9**	**2.6**						
	H5'	4.3	5.1	4.3	5.0	**2.9**	**2.3**					
	H5''	3.4	4.4	4.3	4.8	**3.7**	**2.6**	**1.8**				
	AH2	6.3	4.3	7.0	5.9	8.3	7.3	8.7	7.4			
	TCH$_3$	**3.0**	6.2	5.2	6.2	7.0	7.5	6.8	5.6			
	CH5	**2.4**	5.4	4.6	5.5	6.4	6.8	6.2	5.0			
5'-nucleotide ^{1}H distances(Å)	**H6/8**	4.8	7.9	7.3	8.3	8.3	7.9	6.8	5.5	8.7	**3.5**	**3.6**
	H1'	**2.9**	4.9	4.8	5.4	5.0	4.2	3.4	1.7	7.0	4.3	**3.8**
	H2'	**3.4**	7.0	5.5	6.8	6.3	6.6	5.1	4.3	9.0	**3.0**	**3.1**
	H2''	**2.2**	5.4	4.2	5.3	4.7	4.9	**3.6**	**2.6**	7.9	**3.4**	**3.1**
	H3'	5.0	8.2	6.5	7.9	6.5	6.7	4.6	4.4	11	5.4	5.4
	H4'	6.0	8.2	7.5	8.4	6.9	6.1	4.2	**3.9**	11	6.7	6.6
	H5'	7.0	10	9.0	10	8.7	8.2	6.3	5.8	12	7.0	7.1
	H5''	6.8	9.3	8.8	9.8	8.8	8.0	6.4	5.5	11	6.5	6.5
	AH2	5.4	4.6	6.8	6.2	7.3	5.6	6.4	4.8	**3.9**	6.3	5.8
	TCH$_3$	5.8	8.7	8.3	9.1	9.7	9.6	8.8	7.4	9.0	4.7	4.9
	CH5	6.1	8.8	8.7	9.4	9.9	9.4	8.6	7.1	8.5	4.3	4.4

Methyl proton distances are averaged. Distances longer than 4.5 Å are italics in text, while distances shorter than 4.0 Å are in bold. The source of such canonic structures are crystalline, and therefore the intensities of NOEs recorded in solution do not strictly reflect all of the values shown. Most of the strong sequential NOEs useful for assigning proton resonances are predicted. Exceptions are NOEs observed between AH2 with the H1' of the residue in the 3' direction (7.0 Å, not shown) or to the H1' of the nucleotide in the 5' direction on the opposite strand (7.7 Å). Also useful are the H1' NOEs to neighboring cytosine H5 protons in the 3' direction (3.8 Å).

Fig. 6.2 Schematic showing the atom numbering of an oligonucleotide segment and the distance between the H8 of the adenine residue to its own H1' proton and to the H1' of the 5'-nucleotide

Fig. 6.3 NOESY spectrum of Δ-[Ru(5,6-Me$_2$phen)$_2$dpq]$^{2+}$ bound to d(GTCGAC)$_2$ by intercalation [20]. NOEs between the metal complex and the hexanucleotide are denoted by MC-DNA

H3′ protons and the H1′ and H4′ protons can be used to assign the H3′ and H4′ respectively. The assignment of the H3′ and H4′ resonances is confirmed in DQFCOSY or TOCSY experiments, which rely on spin-coupling for the generation of cross-peaks. The value of the coupling constant is a measure of the various torsion angles within the deoxyribose ring. The H1′–H2″ and H2′–H3′ coupling is relatively strong (6–9 Hz) and insensitive to the geometry of the sugar ring, while the H1′–H2′, H2″–H3′ and H3′–H4′ vary considerably (0–10 Hz) [11], with the consequent corresponding variability of the cross-peak intensity. Assignment of the H5′/H5″ protons is hindered by the large degree of overlap in the H4′/H5′/H5″ region of the spectrum. The H5′/H5″ may be assigned through NOE connectivities via the H1′ and H3′ protons [12].

The assignment of the exchangeable (with water) imino resonances is also important, as the observation of these resonances indicates a stable, hydrogen-bonded, base-pair. Generally, an imino resonance is observed for all base-pairs except the terminal residues for a free oligonucleotide. Imino resonances are easily observed in spectra of samples dissolved in 90% H$_2$O and 10% D$_2$O, using standard HDO peak suppression pulse sequences such as WATERGATE [13]. Assignment of each imino resonance to a particular thymine or guanine residue is established from NOESY spectra. NOE cross-peaks should be observed between TH3 and the amino and H2 resonances of the base-paired adenine residue, while NOEs are detected between the GH1 and the GNH$_2$ and base-paired CNH$_2$ protons. In addition, NOEs can be detected between imino resonances from adjacent nucleotide residues.

6.2.3 Solution Conformation

Although under most circumstances an oligonucleotide will adopt a B-type DNA structure, the solution conformation can be easily confirmed through the analysis of the relative intensities of various NOE cross-peaks in short mixing time NOESY experiments [8–10]. The intensity of an NOE is proportional to $1/r^6$, where r = the distance between the two protons; consequently, a larger NOE will be observed for a shorter inter-proton distance.

For a right-handed helix (A- or B-type DNA), purine H8 and pyrimidine H6 protons will exhibit NOEs to their own H1′, H2′ and H2″ protons as well as to the corresponding protons on the flanking 5′-sugar, but not to the H1′, H2′ and H2″ protons on the adjacent 3′-sugar. The B-type conformation can then be established from the relative H8/H6–H2′ cross-peak intensities. For a B-type helix, the distance between H8/H6 protons and their own H2′ proton is approximately 2 Å while the distance to the H2′ on the 5′-sugar is approximately 4 Å. For an A-type conformation, the relative H8/H6-H2′ distances are reversed with the shorter distance to the H2′ on the 5′-sugar. Furthermore, for a B-type structure the distance between a H8/H6 proton and the various H2′/H2″ protons increases in the order: H2′ of own sugar; H2″ of 5′-sugar; H2″ of own sugar; and H2′ of 5′-sugar.

The deoxyribose ring conformation is generally considered to be an equilibrium of rapidly inter-converting C2′-endo and C3′-endo geometries [11]. In B-type DNA, the C2′-endo geometry dominates, with pyrimidine nucleotides 75–90% and purine nucleotides 90–100% C2′-endo [11]. The relative proportion of the C2′-endo geometry can be estimated from various ^3J coupling constants, in particular $J_{2″-3′}$ and $J_{3′-4′}$ [12]. The glycosidic torsion angle can be determined from the intra-nucleotide H8/H6-H1′ distance in NOESY experiments, 3.5–3.6 Å for the *anti* geometry and about 2.7 Å for the *syn* geometry in B-type DNA.

6.2.4 Solution Structure

The full solution structure of an oligonucleotide can be generated using molecular dynamics simulations that are constrained by proton-proton distances from NOESY spectra and torsion angles obtained from through-bond coupling constants. As would be expected, the quality of such a structure is dependent upon the number and type of the experimental constraints and the potential functions used in the simulations [14, 15]. However, regardless of the quality of the NMR data, DNA structures are generally less well defined than small proteins. Most NOE constraints are from neighboring nucleotides or base-pairs, as oligonucleotide duplexes have little or no tertiary structure. By comparison, proteins often have a well-defined tertiary structure that allows the observation of NOEs between protons on amino acid residues that are far apart in the primary structure. The introduction of ^{13}C and ^{15}N labeling, which allow the determination of many additional torsion angles, has resulted in improved structures, but again, primarily only the local conformation [16, 17].

The ability to obtain accurate DNA global, rather than local, structure has been greatly aided by the development of techniques to measure and utilise residual dipolar couplings [15, 18, 19]. Residual dipolar couplings are a function of both distance and orientation between two nuclei, and hence, are an excellent source of additional structural data [15]. The residual couplings average to zero in isotropic solutions; however, techniques have been developed that induce anisotropic rotational diffusion of the oligonucleotide that allows the measurement of the residual couplings.

6.3   Metallointercalator–DNA Interactions

There are many examples of NMR spectroscopy being used to study the binding of a metallointercalator with an oligonucleotide [7, 20–28]. Optimally, the NMR data may be used to obtain a detailed, atomic level model of the metal complex bound to the oligonucleotide. However, the quality of the molecular model is highly dependent upon the degree of binding site selectivity and the rate of exchange between the free and DNA-bound forms.

6.3.1   Exchange Rate

The line width of the ^{1}H NMR resonances from the metal complex and oligonucleotide is dependent upon the rate of exchange between the free and DNA-bound forms. For slow exchange, where the difference in the chemical shift between the free and DNA-bound form for a particular resonance is significantly greater than the rate of exchange, separate peaks will be observed for the protons of the free and bound species. Consequently, if the metal complex is titrated into an oligonucleotide solution and an NMR spectrum recorded at each titration point, the intensity of the resonances from the free oligonucleotide will decrease and resonances for the bound oligonucleotide will concomitantly increase. However, if the rate of exchange between the free and bound forms is similar to the difference in the chemical shift in Hz (i.e., magnetic field dependent) of the individual resonances, the resonances will be in the intermediate regime. This results in only one broad resonance being observed for each metal complex and oligonucleotide proton, with the chemical shift being the weighted average of the chemical shifts of the free and bound forms, as given by (6.1).

$$\delta_{obs} = \chi_f \delta_f + \chi_b \delta_b \qquad (6.1)$$

Where δ_{obs} is the observed chemical shift of the metal complex or oligonucleotide resonances, χ_f and χ_b are the mole fractions of free and bound metal complex or oligonucleotide and δ_f and δ_b are the chemical shifts of the resonances of the free and bound metal complex or oligonucleotide. Fast exchange kinetics is observed if the rate of exchange between the free and bound forms is significantly greater than

the difference in the chemical shift of the corresponding individual resonances. The chemical shift of the resonances is still given by (6.1), but the resonances show little or no exchange broadening.

In general, metallointercalators have been shown to bind to oligonucleotides with intermediate exchange kinetics [7, 20, 24]. The resultant exchange broadening of all the resonances hinders the full assignment of the ^{1}H NMR spectrum and reduces the intensity of the intermolecular NOEs which can be used to obtain a detailed binding model. However, in some cases slow exchange kinetics has been observed [23, 25], and if coupled with high binding site selectivity (see below) allows for a detailed binding model to be developed.

6.3.2 Binding Site Selectivity

The other major determinant of the quality of the NMR data is the degree of DNA binding site selectivity exhibited by the metallointercalator. In general, the intercalating moiety per se does not show a high degree of site selectivity. Consequently, if the metal complex binding is in the intermediate exchange time scale, the resonances will represent a weighted average for all the binding sites. As a result, NOE cross-peaks may be observed from one metal complex proton to a range of oligonucleotide protons that are separated by more than 5 Å.

Hudson and Barton reported the best (to date) example of an NMR study that allowed the generation of a high quality solution structure of a metallointercalator with an oligonucleotide [25]. The metallointercalator Δ-α-[Rh[(R,R)-Me$_2$-trien] phi]$^{3+}$ [(RR)-Me$_2$trien = 2R,9R-diamino-4,7-diazadecane; phi = 9,10-phenanthrenequinone diimine] bound to d(GAGTGCACTC)$_2$ selectively at the 5'-TGCA-3' site and exhibited slow exchange kinetics. The inert rhodium(III) complex achieved the selectivity through both specific hydrogen bonding (to the guanine O6) and van der Waals contacts (to the TMe), while the insertion of the aromatic planar phi ligand between the 5'-GC-3' bases provided the main thermodynamic driving force.

Collins et al. reported a more typical NMR study, intermediate exchange kinetics and multiple binding sites, where Δ-[Ru(phen)$_2$dpq]$^{2+}$ (phen = 1,10-phenanthroline; dpq = dipyrido[3,2-d:2',3'-f]quinoxaline) bound the hexanucleotide d(GTCGAC)$_2$ [24]. Although a reasonable number of metal complex-oligonucleotide NOEs were observed in this study, no one qualitative binding model could be obtained to satisfy all the distance constraints.

6.3.3 Determination of Binding Site

A range of techniques, including NMR spectroscopy, can be used to confirm the intercalative binding mode of a metal complex with DNA; however, NMR spectroscopy can also be used to obtain information on the precise binding site.

Although, NOE data provides the most definitive information on the metal complex binding site, analysis of selective resonance broadening and changes in chemical shift can also be indicative of the binding site.

Generally, the metal complex is titrated into the oligonucleotide solution, with one-dimensional spectra obtained at each titration point and two-dimensional spectra recorded at the final binding ratio, usually 1:1 or 2:1. At low metal complex to oligonucleotide duplex ratios, the metallointercalator will exhibit its highest selectivity for binding sites. Consequently, observation of selective changes in chemical shift among the well-resolved base proton resonances is indicative of the intercalation site. Furthermore, selective changes in chemical shift of resonances from protons located in either the major or minor groove is indicative of which groove the metal centre binds from. The base H8/H6/H5, TMe, sugar H2′, H2″ and H3′ protons are located in the major groove, while the AH2 and sugar H1′, H4′ and H5′/H5″ are located (or most accessible from) in the minor groove. As with selective changes in chemical shift, the observation of selective broadening of specific resonances can also provide significant binding site information.

6.3.3.1   Selective Changes of Chemical Shift of Metal Complex upon Binding

In a similar fashion to changes in chemical shift for oligonucleotide resonances upon metal complex binding, selective shifts of the resonances from the metal complex can be used an indicator of binding mode. Typically, large upfield shifts (0.5–1 ppm) are observed for resonances from protons that are placed between the stacked bases of the oligonucleotide upon intercalation. For example, in the study by Brodie *et al.* of the binding of $[Pt(4\text{-Mephen})(en)]^{2+}$ (en = 1,2-diaminoethane; 4-Mephen = 4-methyl-1,10-phenanthroline) to the hexanucleotide d(GTCGAC)$_2$, the 4-Mephen protons shifted upfield by 0.42–1.01 ppm, whereas, the en resonances only shifted 0.08 ppm upfield upon binding [7]. Furthermore, the magnitude of the upfield shift for the resonances from the ligand that intercalates can be used as an indication of the proton's position within the stacked base-pairs. A larger upfield shift is generally indicative of the proton being positioned more towards the centre of the bases at the binding site.

6.3.3.2   NOESY Spectra of the Metallointercalator-Bound Oligonucleotide

As previously mentioned, if the metallointercalator binds selectively and with slow exchange kinetics, high quality NOE data can be obtained that will provide the necessary distance constraints to obtain a detailed picture of the binding site and binding orientation. For an example see the study by Hudson and Barton of Δ-α-[Rh [(*R,R*)-Me$_2$-trien]phi]$^{3+}$ bound to d(GAGTGCACTC)$_2$ [25]. As the intercalating ligand stacks into the DNA duplex, the separation of the base-pairs at the binding site increases from 3.4 to 6.8 Å, and consequentially, a loss in the inter-nucleotide sequential walk should be observed.

Alternatively, if the metallointercalator binds non-selectively and with intermediate exchange kinetics it will not be possible to obtain a quantitative binding model. However, the observation of metal complex-oligonucleotide NOEs (for an example see Fig. 6.3) can still be used to obtain a qualitative binding model. The observed inter-molecular NOEs can be used to confirm the tentative conclusions drawn from changes in chemical shift and line broadening of selective oligonucleotide resonances. For an example see the study by Brodie *et al.* of [Pt(4-Mephen) (en)]$^{2+}$ bound to d(GTCGAC)$_2$ [7].

6.4 Molecular Modelling

Molecular modelling is useful for interpreting NMR spectra of metallointercalator interactions with DNA. Models can confirm whether or not the specific interactions detected in the NMR spectra reflect specific DNA binding modes envisaged in the design of the metal complex. This in turn can be used to guide the synthesis of more specific DNA metallointercalators.

6.4.1 Modelling DNA

A molecular mechanical model is the most suitable strategy for modelling biological macromolecules such as DNA. It uses a program known as a "forcefield", which consists of a number of equations, each designed to emulate the amount of energy inherent in a particular conformational feature, and sums the energies. Molecular mechanics approaches chemical bonding states and electronic states as static, which greatly reduces the computational requirements of large biomolecules. The bonds of an atom to its neighbours are used to determine the "atom type". The atom type invokes its properties or "parameters", but not an approximation of the charge on the atom. These must be added separately, and in the case of DNA atoms, they can be downloaded quickly in the form of nucleotide templates. Templates also include data such atom types, a 3D generic crystal-like or "canonic" structure, and additional nucleotide-specific parameters for a variety of forcefields. The forcefield Amber [29] (Assisted Model Building and Energy Refinement) is suitable for emulating the conformational behaviour of DNA in solution without explicitly treating the water molecules (i.e., "in vacuo"). At present we use the *Hyperchem* suite of programs [30], which has various forcefields including different editions of Amber, and combines them with a selection of energy optimization algorithms, such as the Polak-Ribiere, into a graphics interface allowing model "manipulation" as well as text-based inputs. Other packages popular in DNA research include InsightII [31] (Accelerys, formerly BIOSYM/Molecular Simulations) for Linux and Irix platforms, and the freely available XPLOR-NIH [32, 33] (National Institute of Health, Bethesda, Maryland) for Mac and Linux platforms, often aided by the more graphic oriented development VMD-XPLOR [34].

The strength of hydrogen bonds is not represented accurately by molecular mechanics forcefields like Amber, because the charge mobility is lacking and complex to emulate. Earlier editions of Amber retain a separate hydrogen bonding equation, but the resulting models were sometimes not representative. Other editions of Amber incorporate the hydrogen bonding component into the equation for non-bonded interactions. This treats the interaction between base-pairs as a shallow energy well at just shorter than 2 Å. This treatment is sufficient for emulating the inter-atomic distances of duplex DNA hydrogen bonds. However, the optimization algorithm may be unable to locate these small energy minima if the duplex is disrupted for any reason during the optimization. This is because of the large size of the energy landscape. If the NMR spectra indicate that a B-type duplex is predominant, then applying energy restraints between the hydrogen bond participants during the optimization is appropriate to reflect this. Any modest energy value is sufficient to guide the optimization to the energy wells representing hydrogen bonds. However, before optimizing certain DNA interactions, it may be necessary to select, name and then restrain every hydrogen bond member of the duplex. The restraints should be turned off to complete the optimization, to ensure that the resulting conformation reflects a local energy minimum.

Molecular dynamics simulations (MD or MDS) are more exhaustive modelling treatment of DNA. Simulations can be performed at more physiologically relevant temperatures to assess conformational behaviour over time. Energy restraints can be applied to represent observed DNA NOEs (rMDS). Such simulations effectively explore sub-optimal DNA solution conformations that are nonetheless readily formed at physiological temperatures, as this flexibility is considered important for DNA recognition in biology [35].

For the purpose of drug design, such impressive modelling exercises provide difficult targets. In the majority of cases, however, NMR data suggest target DNA sequences assume at least localized right handed B-type DNA features much of the time, even when a minority of non-duplex structures are present in the oligonucleotide sequences (such as unpaired bases, or "bulges"). So while MDS may be useful to explain specific DNA interactions with DNA-binding proteins, in terms of drug design, a simple, static optimized DNA conformation derived from a canonic form usually represents a valid and easily presented target.

6.4.2 Modelling Metal Complexes

The semi-empirical quantum mechanical method ZINDO1 [36] produces plausible charge approximations for Ru(II) complexes. This quantum mechanical program calculates molecular orbitals, but has been modified to reflect some of the observed properties of second row transition metals, hence the expression "semi-empirical" method. It can be used in conjunction with an optimization algorithm in a similar manner to the molecular mechanical methods, although even modestly sized complexes are likely to take many hours to "converge". The resulting charges, just as in

the DNA modelling, are assumed not to alter significantly with conformation. This assumption can be tested by repeating the ZINDO1 optimization of the metallointercalator in the presence of immobile DNA after the Amber optimization to assess charge distribution and structure for alterations.

The charges of platinum complexes can be approximated from literature values, as there is no semi-empirical method commercially available to approximate the Pt (II) molecular orbitals. Molecular mechanical studies of Pt(II) complexes have been used to derive forcefield parameters that are consistent with NMR and crystal structures [37]. Point charges can be entered manually using *Hyperchem* and come into force during optimizations using the Amber forcefield.

Metallointercalator ligands can often be modelled using atom types assigned automatically by Amber, but the type and the bond parameters it entails should be checked for its appropriateness. If required, the atom type can be manually changed to any of the other atom types available in the forcefield. Notes on the atom types, including the macromolecule the atom type is designed to emulate, are provided as text files among the program runfiles at the "front end" of *Hyperchem* and are useful for assessing suitability.

Ligand bond length parameters can be taken from literature regarding the solution or crystal structures of similar compounds. These can be entered as text using the "front end" runfiles provided by *Hyperchem*, and they come into force after the type rules are compiled and the forcefield parameter file is compiled. Typing rules are the set of rules used to make forcefields assign atom types automatically, which may be useful in some metallointercalator ligand atoms, but the main reason for compiling type rules is so that that the additional atom types appear on the list of types available in the forcefield, and can therefore be entered manually using the graphic interface. The new parameters should be tested by measuring the optimised equilibria, because "back end" equilibrium parameters replace entered parameters without notification in the case of a conflict.

The metallointercalator itself is likely to require additional atom types, along with parameters for them derived from the literature. These are required because the *cis*, *trans* and orthogonal coordinate atoms cannot be distinguished using a single atom type, and all four or six bonds cannot be modelled using only one bond angle, since there are two, 90° and 180°. The parameters of the extra types are duplicates, except that extra bond angle parameters are included to specify their relationship to each other around the metal nucleus. Square planar models require one extra coordinate atom type, to make a total of two, and octahedral coordinate atoms require two extra types to make a total of three. The extra types are assigned to the coordinate atoms manually for technical reasons.

6.4.3 Modelling DNA–Metallointercalator Interaction

Rigid metallointercalators can technically be modelled as rigid and the DNA optimized around it using Amber, thus eliminating the need to approximate such

parameters as bond stretches and angle bending terms. This is because all of the non-bonded properties, charge, radius and "hardness", are retained while not selected in the *Hyperchem* graphic interface. This approach is inadequate when aliphatic ligands are introduced, however. Some of the complex can be treated as rigid, while the aliphatic ligands are allowed to interact with the DNA during optimization using Amber parameters. However, optimizations are most efficient when the extra atom types are used to enable square-planar and octahedral complexes to be modelled interactively.

"Manual docking" is an expression for bringing model DNA-binding complexes to within the van der Waals distance of a DNA model. The orientation and site are essentially contrived to fulfil a preconceived account of how the complex and DNA interact to produce the observed NMR spectra. Therefore all conceivable interactions should be explored and optimized separately for comparison. The procedure can be assisted by inter-atomic restraints reflecting observed intermolecular NOEs.

As an alternative, optimizations of a range of starting geometries can be examined, also with observed intermolecular NOEs imposed as energy restraints. This serves in the main part to test for interactions not excluded by the NMR data and also not anticipated in the study. It also serves as a more limited way of testing whether a deceptive local energy minimum is obscuring a more global minimum from the optimization algorithm.

6.4.4 Modelling DNA Intercalation Sites

The base-pairs that flank DNA intercalation sites have a doubled rise that is unwound by about 20° from the canonic form. Such a site can be described by a lengthy list of bond torsion angles that deviate from the canonic forms provided in the Amber database. Technically, these unusual torsion angles can be specified as the rest of the nucleotide template is downloaded. This process is lengthy and can be overruled by the "back end" of the program, and is therefore suitable only for replication of published results rather than emulation. One alternative reported is to create two duplexes with such an orientation that the rise and unwinding between them is the same as an occupied intercalation site. The two duplexes are then covalently joined and the new bond lengths and torsions between the nucleotide base-pair stacks are optimized to produce a plausible intercalation pocket in duplex DNA [25].

A fast, effective method is to insert a model intercalator into the putative intercalation site regardless of the high energy of the start conformation. The following optimization suffers at first from "bad contacts" as the proximity of atoms falls at the steep part of the non-bonded energy curve below 1.8 Å, but the flexibility of the bonds according to Amber and the imposition of restraints to reflect H-bonds ensures that the Amber optimization arrives quickly at a plausible conformation.

For bulky intercalators, a smaller intercalator model such as ethidium can be used to create the intercalation pocket. Ethidium's electronic structure has been studied [38], so an approximation in Amber can be easily created, and inserted between two stacked, canonic nucleotides using the graphic interface to form a high energy starting point. After some optimization, the metallointercalator model can be superimposed on the ethidium model, and the ethidium deleted. The metallointercalator remains in the intercalation pocket. The additional bulk of the metallointercalator can then be assessed for model feasibility. In some cases, aliphatic moieties can be rotated away from "bad contacts". If not, there is a reasonable chance that the optimization process will tolerate a high energy resumption point for the metallointercalator in the same manner that it tolerates a high energy starting point for the ethidium intercalation. The resulting optimum is likely to acquire even more conformational properties that are not typical to B-type DNA. This does not make the model inherently implausible, but it does make it easier to assess in terms of experimental evidence.

References

1. Shulman A, Dwyer FP. Metal chelates in biological systems. In: Dwyer FP, Mellor DP, editors. Chelating agents and metal chelates. New York: Academic; 1964. and references therein.
2. Jennette KW, Lippard SJ, Vassiliades GA, Bauer WR. Proc Natl Acad Sci USA. 1974;71:3839.
3. Nordén B, Lincoln P, Akerman B, Tuite E. DNA interactions with substitution-inert transition metal ion complexes. In: Sigel A, Sigel H, editors. Metal ions in biological systems, vol. 33. New York: Marcel Dekker; 1996. p. 177.
4. Pyle AM, Barton JK. Probing nucleic acids with transition metal complexes. In: Lippard SJ, editor. Progress in inorganic chemistry. New York: Wiley; 1990. p. 413.
5. Zeglis BM, Pierre VC, Barton JK. Chem Commun. 2007: 4565.
6. Erkkila KE, Odom DT, Barton JK. Chem Rev. 1999;99:2777.
7. Brodie CR, Collins JG, Aldrich-Wright JR. Dalton Trans. 2004: 1145.
8. Scheek RM, Boelens R, Russo N, van Boom JH, Kaptein R. Biochemistry. 1984;23:1371.
9. Feigon J, Leupin W, Denny WA, Kearns DR. Biochemistry. 1983;22:5943.
10. Patel DJ, Shapiro L, Hare D. J Biol Chem. 1986;261:1223.
11. Searle MS. Prog NMR Spectroscopy. 1993;25:403.
12. Weisz K, Shafer RH, Egan W, James TL. Biochemistry. 1992;31:7477.
13. Piotto M, Saudek V, Sklenar V. J Biomol NMR. 1992;2:661.
14. Zhou H, Vermeulen A, Jucker FM, Pardi A. Biopolymers. 1999;52:168.
15. Vermeulen A, Zhou H, Pardi A. J Am Chem Soc. 2000;122:9638.
16. Vanwijk J, Huckriede BD, Ippel JH, Altona C. Method Enzymol. 1992;211:286.
17. Zimmer DP, Marino JP, Griesinger C. Magn Reson Chem. 1996;34:S177.
18. Tjandra N, Bax A. Science. 1997;278:1111.
19. Tjandra N, Tate S-I, Ono A, Kainosho M, Bax A. J Am Chem Soc. 2000;122:6190.
20. Collins JG, Aldrich-Wright JR, Greguric I, Pellegrini PA. Inorg Chem. 1999;38:5502.
21. Eriksson M, Lejion M, Hiort C, Nordén B, Graslund A. Biochemistry. 1994;33:5031.
22. Dupureur CM, Barton JK. J Am Chem Soc. 1994;116:10286.
23. Shields TP, Barton JK. Biochemistry. 1995;34:15049.

24. Collins JG, Sleeman AD, Aldrich-Wright JR, Greguric I, Hambley TW. Inorg Chem. 1998;37:3133.
25. Hudson BP, Barton JK. J Am Chem Soc. 1998;120:6877.
26. Franklin SJ, Barton JK. Biochemistry. 1998;37:16093.
27. Proudfoot EM, Mackay JP, Karuso P. Biochemistry. 2001;40:4867.
28. Cordier C, Pierre VC, Barton JK. J Am Chem Soc. 2007;129:12287.
29. Case DA, Pearlman DA, Caldwell JW, Cheatham III TE, Ross WS, Simmerling CL, et al. AMBER 6. San Francisco: University of California; 1999.
30. Hypercube, Hyperchem Release 7.5, Hypercube, Inc.; 2002, Gainesville, Florida, USA.
31. InsightII, User's Guide, Molecular Simulation Inc., 1997
32. Schwieters CD, Kuszewski JJ, Tjandra N, Clore GM. J Magn Res. 2003;160:66.
33. Schwieters CD, Kuszewski JJ, Clore GM. Progr NMR Spectroscopy. 2006;48:47.
34. Schweiters CD, Clore GM. J Mag Res. 2001;149:239.
35. Alleman RK, Egli M. DNA recognition and bending. Chem Biol. 1997;4(9):643–50.
36. Anderson JP, Cundari TR, Zerner MC. Int J Quantum Chem. 1991;39:31.
37. Hambley TW, Jones AR. Coord Chem Rev. 2001;212:35.
38. Luedtke NW, Liu Q, Tor Y. Chem Eur J. 2005: 495

Chapter 7
Pulsed Gradient Spin-Echo NMR

Gang Zheng, Anwen M. Krause-Heuer, and William S. Price

7.1 Introduction

Translational diffusion (also referred to as self-diffusion, Brownian motion, or random walks) plays a vital role in all sorts of molecular dynamics in biological systems (e.g., ligand–DNA interactions, lipid–macromolecule interactions, and macromolecule aggregation). Due to its non-invasive nature, pulsed gradient spin-echo (PGSE) NMR has become a method of choice for the study of molecular dynamics and structural details of biological systems [1, 2]; in combination with magnetic resonance imaging (MRI), it allows (localised) *in vivo* diffusion measurements.

In this chapter, the fundamentals of translational diffusion and PGSE NMR diffusion measurements and the solutions of the common artefacts in PGSE experiments (such as background gradients, huge solvent (e.g., water) signal, and thermal convection) are discussed and the practical issues of PGSE measurements (inculding sample preparation, selection of pulse sequences, and parameter settings) are considered; the fundamentals of the application of PGSE NMR to the study of ligand–macromolecule interactions and supramolecular assembly are examined.

7.1.1 Translational Diffusion

Translational diffusion is the random movement of molecules or small particles resulting from thermal energy [3–6]. Self-diffusion for an isotropic unrestricted system can be characterised by the isotropic self-diffusion coefficient (D, $m^2\ s^{-1}$).

W.S. Price (✉)

Nanoscale Organisation and Dynamics Group, College of Health and Science, University of Western Sydney, Locked Bag, Penrith, NSW 2751, Australia

e-mail: w.price@uws.edu.au

Self-diffusion of molecules and small particles is affected by many factors including temperature, molecular weight, and solvent viscosity. Using the Stokes–Einstein (also referred to as Stokes–Einstein–Sutherland) equation [7–9], the diffusion coefficient at infinite dilution can be related to the factors mentioned above [7–9]

$$D = \frac{kT}{f},$$ (7.1)

where k is the Boltzmann constant, T is temperature, and f is the friction coefficient. Although the friction coefficient takes different forms depending on the shape of the diffusing particle [10], for a spherical molecule with a Stokes radius (i.e., effective hydrodynamic radius) r_s, which normally increases with increasing molecular weight (Mw), in a solvent of viscosity η, the friction factor is given by

$$f = 6\pi\eta r_s.$$ (7.2)

It can be inferred from (7.1) and (7.2) that D decreases in proportion to the inverse of the cube root of Mw.

7.1.2   Diffusion Measurements

Although there are numerous methods for measuring diffusion such as light scattering [11], fluorescence [12], capillary [13] and nuclear magnetic resonance (NMR) [14]; NMR based methods outperform the others due to their non-invasive nature and not affecting the thermodynamics of a system. In general, NMR based diffusion measurements can be classified into relaxation based methods (e.g., [15]) and pulsed field gradient spin-echo (PGSE) methods (e.g., [16]). The relaxation based methods measure the molecular reorientation occurring in the picosecond to nanosecond range, while the PGSE methods measure translational motion occurring on the timescale of milliseconds to seconds (e.g., [17]).

The application of relaxation based analysis relies on a number of assumptions [17]: the relaxation mechanism of the probe species being known, being able to separate inter- and intramolecular contributions to the relaxation, the type of reorientational motion (e.g., the motion of a spherical model could be characterised by a single correlation time), that the probe molecules see the solvent as being continuous, and the Stokes radius of the probe molecules being known. These assumptions may or may not be justified depending upon the system being studied. In contrast to the relaxation based method, the PGSE method works without any assumptions. However, analysis of PGSE data requires the diffusion propagator (i.e., the solution of the diffusion equation with the appropriate boundary and initial conditions) be known. A PGSE experiment generally includes three steps: first,

a pulsed magnetic field gradient (or a group of pulsed gradients) is applied to the sample to encode the position of each diffusing particle (i.e., nuclear spin); secondly, a delay (i.e., observation time or diffusion time) is given for observing the diffusion of the encoded particles; and finally, at the end of the delay, another identical pulsed magnetic field gradient (or group of such pulses) is applied so that the position of each particle can be decoded (i.e., inversely encoded). Without diffusion, a complete decoding can be achieved, while diffusion leads to an incomplete decoding and thus an attenuation of the observed NMR signal. The value of the signal attenuation is directly related to the value of the diffusion coefficient and thus can be used for diffusion measurements.

7.1.3   Fundamentals of PGSE NMR

Nuclear spin phase shifts caused by the application of magnetic field gradients are analysed to determine the effects of diffusion on the spin phase shift distribution along the direction of the applied gradients. The correlation between the diffusion coefficient and the spin-echo attenuation follows Stejskal and Tanner's analysis [18] based on solving the Bloch–Torrey equations [19]. For a single spin, the cumulative phase shift caused by a single magnetic field gradient oriented along (typically) the z-direction at time t is (e.g., [17])

$$\phi(t) = \gamma p(t') \left(B_0 + \int_0^t g(t')z(t')dt' \right), \tag{7.3}$$

where $p(t')$ is the coherence level (with a value of -1, 0, or 1) in one of the selected coherence pathways at time t'. For a multiple quantum (MQ) coherence, $\gamma p(t')$, in (7.3), should be replaced by $\gamma \mathrm{eff}(t')(p(t')/|p(t')|)$.

By evaluating (7.3) over the first τ period of the original Hahn spin-echo PGSE sequence (Fig. 7.1a), the phase shift of a spin i with a single quantum coherence in a spin ensemble at time t is (e.g., [17]),

$$\phi_i(t) = \underbrace{\gamma B_0 \tau}_{\text{static field}} + \underbrace{\gamma g \int_{t_i}^{t_i+\delta} z_i(t)dt}_{\text{applied gradient}} \tag{7.4}$$

where the first term is the phase shift due to B_0, and the second is due to the gradient. At the end of the first τ period, the coherence level is changed from 1 to –1 by the application of a π radiofrequency (RF) pulse and thus, based on (7.3), if there is no
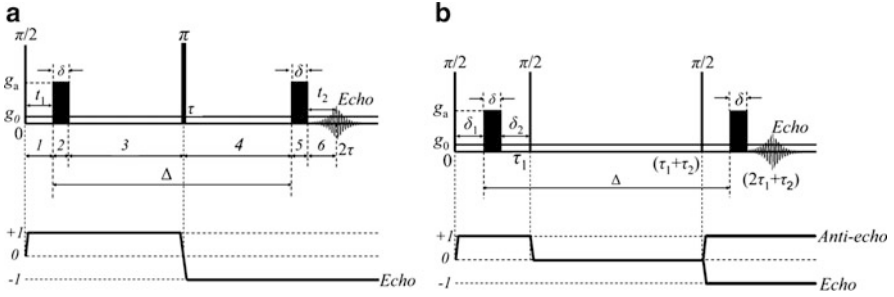
Fig. 7.1 (**a**) The Hahn spin-echo PGSE sequence and (**b**) the stimulated echo-based PGSE sequence (STE-based PGSE). $\pi/2$ and π are radiofrequency pulses. For the Hahn spin-echo PGSE sequence, two pulsed gradients of duration δ and magnitude g_a are inserted into each τ delay; for the STE-based PGSE sequence, two pulsed gradients of duration δ and magnitude g_a are applied in the two encoding intervals, (0 to τ_1) and ($\tau_1 + \tau_2$ to $2\tau_1 + \tau_2$), which are separated by the phase storage period (τ_2). The background gradient has a magnitude of g_0. The separation between the leading edges of the pulsed gradients is denoted by Δ (i.e., the observation time or diffusion time). The applied gradient is along the z-axis (the direction of the static magnetic field, B_0). The Hahn spin-echo-based PGSE sequence can be divided into six intervals according to the variation of the net magnetic gradients. Only the second half of the echo is digitized and used as the free induction decay (FID). The coherence pathways are also shown here. The STE-based PGSE sequence only captures half of the theoretical maximum magnetization

diffusion, the phase shift generated by the first gradient pulse is completely cancelled by the phase shift generated by the second gradient pulse. However, if the spin does diffuse between the two gradients, the net phase shift experienced by spin i at the end of the sequence is given by [17]

$$
\phi_i(2\tau) = \left(\gamma B_0 \tau + \gamma g \int_{t_1}^{t_1+\delta} z_i(t)dt \right) - \left(\gamma B_0 \tau + \gamma g \int_{t_1+\Delta}^{t_1+\Delta+\delta} z_i(t')dt' \right)
$$

$$
= \gamma g \int_{t_1}^{t_1+\delta} z_i(t)dt - \gamma g \int_{t_1+\Delta}^{t_1+\Delta+\delta} z_i(t')dt'. \tag{7.5}
$$

For an ensemble of diffusing nuclei, the intensity of the echo signal at $t = 2\tau$ is given by (e.g., [17])

$$
S(2\tau) = S^{t=0} \exp\left(-\frac{2\tau}{T_2} \right) \int_{-\infty}^{\infty} P(\phi, 2\tau)e^{i\phi}d\phi. \tag{7.6}
$$

where $S^{t=0}$ is the signal immediately after the first $\pi/2$ pulse (i.e., initial excitation in the PGSE sequence) and $P(\phi, 2\tau)$ is the (relative) phase-distribution function.

Similarly for the STE-based PGSE sequence, the result is

$$S(2\tau_1 + \tau_2) = \frac{S^{t=0}}{2} \exp\left(-\frac{2\tau_1}{T_2}\right) \exp\left(-\frac{\tau_2}{T_1}\right) \int\limits_{-\infty}^{\infty} P(\phi, 2\tau_1 + \tau_2)e^{i\phi}d\phi, \quad (7.7)$$

where T_1 and T_2 are the longitudinal and transverse relaxation times, respectively.

Comparing (7.6) and (7.7) and considering $\tau \gg \tau_1$, it is clear that the STE-based PGSE sequence is less susceptible to the attenuation due to transverse relaxation than the Hahn spin-echo PGSE sequence, which makes it suitable for NMR diffusion experiments on samples with fast transverse relaxation (e.g., macromolecules such as proteins and DNA). It will be shown in the following discussions that the STE-based PGSE sequence also suffers less attenuation due to background gradients which is discussed in detail in Sect. 7.3.1.

However, it is also shown in Fig. 7.1 and by comparing (7.6) and (7.7) that the STE-based PGSE sequence captures only half of the total magnetization while the Hahn spin-echo PGSE sequence captures all. Therefore, in practice there is always a trade-off between the signal loss due to the use of the STE based sequence itself and the signal loss due to relaxation and background gradients.

The spin-echo attenuation caused by diffusion can be calculated via the Stejskal–Tanner equation (neglecting relaxation processes) [18],

$$\ln\left[\frac{S^{t=acq}}{S^{t=0}}\right] = -D\int\limits_0^t F^2(t'')dt'', \quad (7.8)$$

where F (rad m^{-1}) is the spin dephasing given by

$$F(t'') = \int\limits_0^{t''} \gamma_{\text{eff}}(t')\frac{p(t')}{|p(t')|}g(t')dt', \quad (7.9)$$

$S^{t=acq}$ is the echo signal, $S^{t=0}$ is the signal immediately after the first $\pi/2$ pulse (i.e., initial excitation in the PGSE sequence), t (s) is the time at which the signal acquisition begins, and g (T m^{-1}) is the net gradient (the sum of all magnetic gradients existing in the system). As shown in Fig. 7.1a, the Hahn spin-echo-based PGSE sequence can be divided into six intervals according to the variation of g. Equation 7.8 is evaluated over each period of a pulse sequence. As an example, for the Hahn spin-echo PGSE sequence shown in Fig. 7.1a, the spin-echo attenuation in the presence of background gradients is derived as

$$\ln\left[\frac{S^{t=acq}}{S^{t=0}}\right] = -D\left[\int_0^{t_1}\gamma^2\left(\int_0^{t''}(-g_0)dt'\right)^2 dt''\right.$$

$$+ \int_{t_1}^{t_1+\delta}\gamma^2\left(\int_0^{t_1}(-g_0)dt' + \int_{t_1}^{t''}(-g_0-g_a)dt'\right)^2 dt'' + \cdots$$

$$+ \int_{\Delta+t_1+\delta}^{2\tau}\gamma^2\left(\int_0^{t_1}(-g_0)dt' + \cdots + \int_{\Delta+t_1}^{\Delta+t_1+\delta}(g_0+g_a)dt' + \int_{\Delta+t_1+\delta}^{t''}g_0dt'\right)^2 dt''\left.\right]$$

$$= -\gamma^2\left[\underbrace{g_a^2\delta^2\left(\Delta-\frac{\delta}{3}\right)}_{g_a-only-term} + \underbrace{g_ag_0\delta\left[2\tau^2 - t_1^2 - t_2^2 - \delta(t_1+t_2) - \frac{2}{3}\delta^2\right]}_{cross-term}\right.$$

$$\left. + \underbrace{\frac{2\tau^3}{3}g_0^2}_{g_0-only-term}\right]D = -bD, \tag{7.10}$$

where b is normally called the attenuation factor.

Similarly for the STE-based PGSE sequence (Fig. 7.1b), the result is

$$\ln\left[\frac{S^{t=acq}}{S^{t=0}}\right] = -\gamma^2\left\{\underbrace{g_a^2\delta^2\left(\Delta-\frac{\delta}{3}\right)}_{g_a-only-term} + \underbrace{g_0^2\tau_1^2\left(\tau_2 + \frac{2}{3}\tau_1\right)}_{g_0-only-term}\right.$$

$$\left. + \underbrace{g_ag_0\delta\left[2\tau_1\tau_2 + 2\tau_1^2 - \frac{2}{3}\delta^2 - \delta(\delta_1+\delta_2) - \left(\delta_1^2+\delta_2^2\right)\right]}_{cross-term}\right\}D. \tag{7.11}$$

In practice, $S_{g=0}^{t=acq}$ (i.e., the echo signal with zero gradient strength) is measured instead of $S^{t=0}$. When the effects of background gradients can be neglected, the spin-echo attenuation is given by

$$\ln[E] = \ln\left[\frac{S^{t=acq}}{S_{g=0}^{t=acq}}\right] = -\gamma^2 D g_a^2\delta^2\left(\Delta - \frac{\delta}{3}\right), \tag{7.12}$$

where E is the normalized echo attenuation.

7.2 Performing PGSE Experiments

7.2.1 Sample Preparation and the Deleterious Effects of Background Gradients

In a medium, the magnetic flux density $\mathbf{B}$ (T), which is usually referred to as the magnetic field in NMR experiments, established by an applied magnetic field $\mathbf{H}$ (A m^{-1}) can be calculated by (e.g., [20–22])

$$\begin{aligned} \mathbf{B} &= \mu_0(1 + \chi)\mathbf{H} \\ &= (1 + \chi)\mathbf{B}_0, \end{aligned} \tag{7.13}$$

where μ_0 is the magnetic permeability of free space ($4\pi \times 10^{-7}$ H m^{-1}) and χ (dimensionless) is the magnetic susceptibility which expresses how readily the medium develops a magnetic moment on exposure to an external magnetic field. χ is zero for a vacuum and for materials it may take positive (for paramagnetic materials) or negative (for diamagnetic materials) values. Hereafter, $\mathbf{B}$ is referred to as the magnetic field. A paramagnetic sample tries to pull the magnetic field into the material resulting in a stronger magnetic field than the applied magnetic field while a diamagnetic sample tries to push the magnetic field out of the material leading to a weaker magnetic field.

From (7.13), it can be realized that the differences in the magnetic susceptibility creates spatial magnetic field variations (background gradients) in the sample [23]. As shown in Fig. 7.2, background gradients are generated around a diamagnetic object in vacuum due to the difference in the magnetic susceptibility. In some cases, the amplitude of the background gradients can be of the order of T m^{-1}, which is similar to the strength of applied magnetic field gradients in PGSE diffusion experiments. For example, it is estimated that red blood cells have gradients up to 2×10^{-2} T m^{-1} due to the large difference in the magnetic susceptibility between
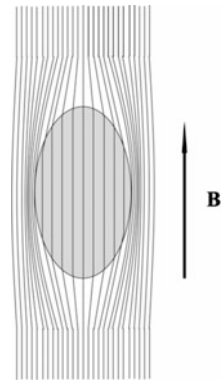
Fig. 7.2 A conceptual diagram of the magnetic field distortion resulting from an object with a negative magnetic susceptibility ($\chi < 0$) in vacuum. The distortion has been greatly exaggerated for the sake of clarity
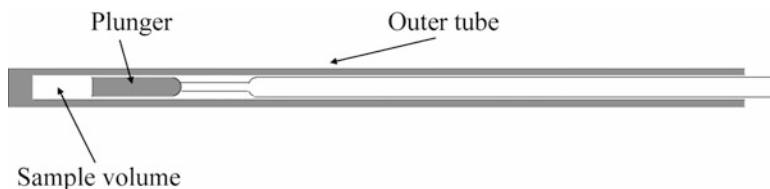
Fig. 7.3 A schematic diagram of a Shigemi tube set which is made of glass that has been matched to the susceptibility of a particular solvent

the inside and outside of the cells [24, 25]; in metal hydride samples, such background gradients can be of the order of 0.5 T m^{-1} because of differences in magnetic susceptibility between different materials [26]. These samples, containing significant susceptibility inhomogeneity, are referred to as magnetically inhomogeneous samples. Even in a glass tube containing a homogeneous sample such as water, background gradients occur due to the difference in magnetic susceptibility between the water and the air that surrounds the sample and tube [27].

The existence of background gradients can cause erroneous diffusion determination (e.g., [28]). The first step to avoid the deleterious effects of background gradients is to avoid susceptibility interfaces such as by using susceptibility matched NMR tubes (e.g., Shigemi tubes) (Fig. 7.3) whenever possible. The use of Shigemi tubes have a few significant merits over the use of standard NMR tubes: (a) no background gradients are generated at the interface between a solvent and glass of the same magnetic susceptibility; and thus the use of a plunger avoids the existence of solvent–air interface, at which background gradients are normally generated; (b) the sample length is restricted within the size of RF coil (e.g., ~1 cm) and therefore the effects of B_1 (i.e., RF irradiation) inhomogeneity can be avoided; and (c) the sample is contained within the constant region of the applied magnetic field gradient.

If inhomogeneous samples are encountered, PGSE sequences with background gradient suppression must be used. A detailed discussion on background gradient suppression in PGSE experiments can be found in a recent review by Zheng and Price [28].

7.2.2 Selection of Pulse Sequence: Hahn Spin-Echo PGSE Versus STE PGSE

When the resonances of long T_2 species (e.g., ligands) are of interest, Hahn spin-echo PGSE sequences [18] are preferred. For example, in studies of ligand–macromolecule interactions, the Hahn spin-echo based PGSE sequence can act as a T_2 filter, which leaves the resonances of interest (i.e., ligand resonances) intact while filtering out the macromolecule resonances with short T_2's.

When the resonances of short T_2 species (e.g., macromolecules) are of interest, STE based PGSE sequences [29] are preferred due to their reduced sensitivity to transverse relaxation. Furthermore, the phase distortions caused by J-coupling (i.e., the coupling between two nuclear spins mediated by chemical bonds, including hydrogen bonds) can also be reduced by the use of STE based PGSE sequences, which contain much shorter transverse periods compared to Hahn spin-echo based sequences (e.g., [30]).

7.2.3   Echo Time Settings

For an AX spin system, the echo time (i.e., TE or 2τ) in Hahn spin-echo based experiments should be set to n/J ($n = 1, 2, 3, \ldots$) to avoid J-evolution effects according to the evolution equation

$$I_x \xrightarrow{\pi J_{IS} TE 2I_z S_z} I_x \cos(\pi J_{IS} TE) + 2I_y S_z \sin(\pi J_{IS} TE), \qquad (7.14)$$

where I_x is the in-phase x-magnetization, $2I_z S_z$ is the longitudinal two-spin order, $2I_y S_z$ is the anti-phase y-magnetization, and J_{IS} is the J-coupling constant.

7.2.4   Solvent Signal Suppression in PGSE NMR Diffusion Experiments

In many PGSE experiments (especially biomolecular PGSE experiments), without appropriate measures the presence of a huge water resonance makes diffusion determination impossible. As shown in Fig. 7.4, without solvent signal suppression the intense (protonated) solvent resonances not only overlap with the (much weaker) resonances of interest, but also saturate the NMR receiver causing many other complications such as base-line distortions and phase roll. If the receiver gain is set very low to enable acquisition of the large solvent resonances, the weak solute resonances are inadequately digitized resulting in poor spectra.

Here, we recommend two PGSE sequences with water suppression: PGSE–WATERGATE and PGSTE–WATERGATE. As shown in Fig. 7.5a, the PGSE–WATERGATE sequence is quite similar to the original Hahn spin-echo based PGSE sequence except that the PGSE–WATERGATE sequence contains a selective π pulse, which inverts all resonances except the water resonance, instead of a hard π pulse as in the original Hahn spin-echo based PGSE sequence. During the PGSE–WATERGATE sequence, the resonances of interest experience diffusive attenuation while the water resonance is completely dephased by the two pulsed gradients. The starting gradient strength must be high enough to suppress the water

Fig. 7.4 (a) ^{1}H 500 MHz
spectrum of 2 mM lysozyme
in 90% ^{1}H$_2$O and 10% ^{2}H$_2$O
using one scan and a very low
receiver gain; (**b**) Same
spectrum as (**a**) but with the
vertical scale expanded ~900
times (with permission from
[31])
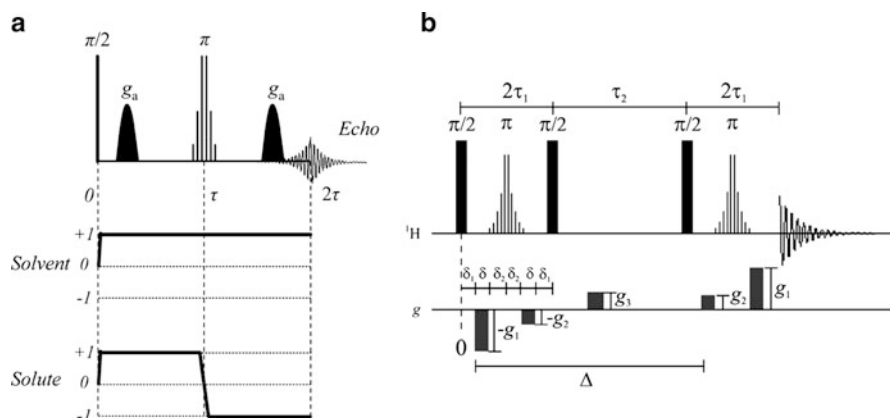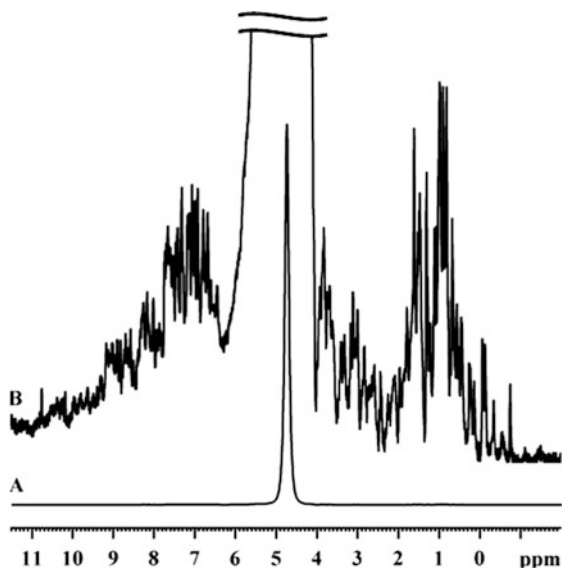
Fig. 7.5 (**a**) The PGSE–WATERGATE pulse sequence. The bar grouping represents a binomial
(chemical-shift) selective π pulse, which inverts the solute magnetization only (with permission
from [31]) (**b**) The PGSTE–WATERGATE sequence (with permission from [31])

resonance sufficiently (e.g., 0.1 T m^{-1}) to achieve consistent water suppression
through all the experiments.

   As shown in Fig. 7.5b, the PGSTE–WATERGATE sequence contains two
selective π pulses and two pairs of asymmetric bipolar gradients. By the use of
PGSTE–WATERGATE, both the resonances of interest and the water resonance
are attenuated by diffusion but the water resonances are much more strongly
attenuated.

Some important points in setting up PGSTE–WATERGATE experiments are:

1. g_1 should be always larger than g_2
2. At the start of a PGSTE–WATERGATE experiment, the g_1 and g_2 values should be set large enough to suppress the solvent signal with $g_1–g_2 = 0.005$ T m^{-1} (e.g., $g_1 = 0.105$ T m^{-1}, $g_2 = 0.1$ T m^{-1}, diffusion time $= 100$ ms, and $\delta = 4$ ms)
3. If the molecules of interest have short T_2 relaxation times, δ should be short and g_1 and g_2 should be large
4. After reaching the desired solvent suppression level, g_2 should be kept constant and g_1 should be increased with suitable increments to obtain the attenuation curve (e.g., $g_1 = 0.105, 0.155, \ldots, 0.505, 0.555; g_2 = 0.1$ T).

7.2.5   Compensation of Thermal Convection in PGSE NMR Diffusion Experiments

Convection is a very common problem when diffusion experiments are performed with low viscosity solvents above or below ambient temperature. As shown in Fig. 7.6b, no acceptable diffusion coefficient can be obtained by fitting the attenuation equation to the data obtained with a relatively long diffusion time (e.g., $\Delta = 0.3$ s) at 37 °C.

A simple way to determine the existence of convection artefacts is to repeat the same diffusion experiment with differing values of Δ. Convection artefacts may exist if the determined diffusion coefficient varies as Δ varies.

For species with relatively long T_2's, the CONVEX sequence can be used for convection compensation [33]. As shown in Fig. 7.7, the CONVEX sequence is based on a double spin-echo sequence and contains two selective π pulses and two pairs of bipolar gradients at different strength. This sequence affords both
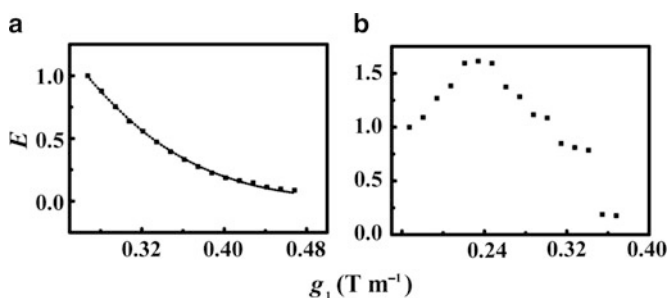
Fig. 7.6 Representative ^{1}H PGSE NMR diffusion attenuation plots for lysozyme obtained with the standard STE based PGSE sequence with $\Delta = 0.1$ s (**a**) and 0.3 s (**b**) at 37 °C. The *dotted lines* represent non-linear least square regression of the relevant attenuation equation (i.e., Eq. 9 in ref [32].) onto the data [32] (with permission from [32])
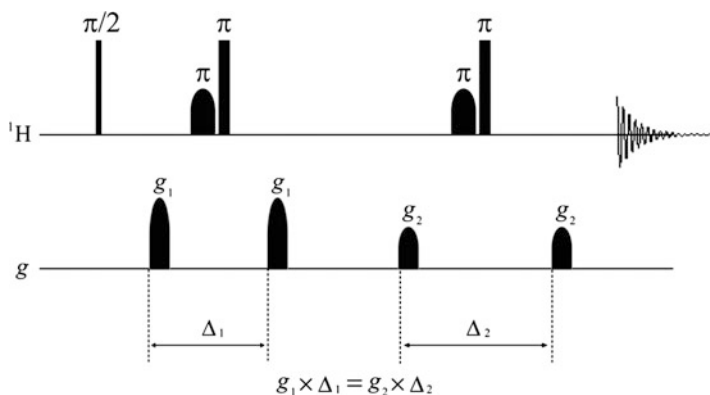
Fig. 7.7 The CONVEX sequence [33]
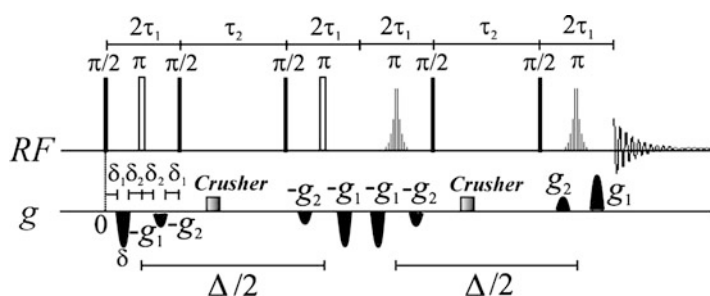
Fig. 7.8 The double echo PGSTE–WATERGATE sequence with half sine shaped gradients. The *black bars* and *white rectangles* represent $\pi/2$ and π rf pulses (with permission from [32])

convection compensation and water suppression. To achieve convection compensation, $\Delta_1/\Delta_2 = g_2/g_1$.

For species with relatively short T_2's, the double-PGSTE sequence is preferred [34]. Recently, Zheng and Price [32] proposed the double echo PGSTE–WATERGATE sequence for simultaneous convection compensation and solvent suppression (Fig. 7.8).

7.2.6 Ligand–Macromolecule Interactions Studied by PGSE Experiments

The simple two-site model is commonly used for ligand binding studies. It is assumed that a ligand L can bind to any of the n identical independent binding sites on a macromolecule P and the equilibrium of this process can be described by (see [35])

$$PL \overset{K_d}{\leftrightarrow} P + L \tag{7.15}$$
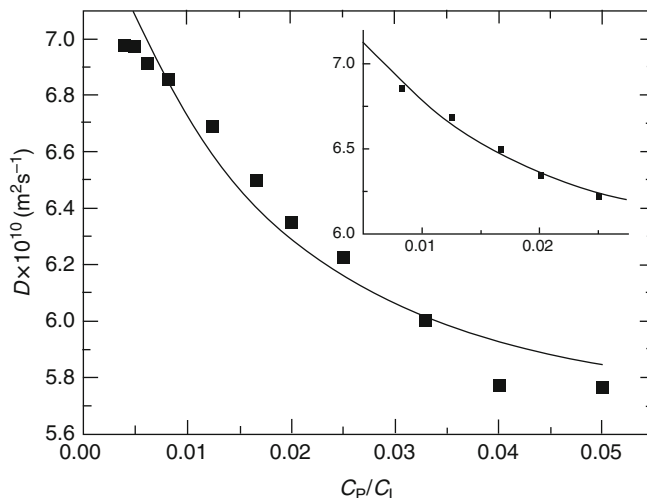
Fig. 7.9 Diffusion of salicylate as a function of C_P/C_L. The curve was obtained by regressing the two-site model (7.16) on to the data. From the systematically poor fit of the model to the data, it is evident that this model is too simplistic and does not truly describe the molecular reality of salicylate binding to BSA. The sample with the highest salicylate concentration was excluded from the analysis. If only a small subset of the concentration range is used in the regression, a deceptively good fit to the data is obtained, as shown in the inset (with permission from [36])

The determined ligand diffusion coefficient, D, is the population-weighted average of the free (D_f) and bound (D_b) ligand diffusion coefficients,

$$D = (1 - P_b)D_f + P_bD_b \qquad (7.16)$$

with the bound population given by

$$P_b = \alpha - \sqrt{\alpha^2 - \beta} \qquad (7.17)$$

where $\alpha = (C_L + nC_P + K_d)/2C_L$, $\beta = nC_P/C_L$ and C_L and C_P are the total concentrations of ligand and macromolecule, respectively. D_b and D_f can be determined by measuring the diffusion of pure macromolecule and pure ligand solutions, respectively. Providing the macromolecule is large, D_b is to a very good approximation identical with the diffusion coefficient of the pure macromolecule, D_P. Clearly, diffusion modulation of the observed ligand diffusion coefficient will only be suitable for probing binding when there is sufficient exchange between the two binding sites. However, this method can still be used to tell if ligands bind in slow-exchange systems.

Price et al [36]. studied the binding of the anti-inflammatory drug salicylate to bovine serum albumin (BSA) in water by the use of PGSE–WATERGATE and the above mentioned two-site model. Fitting of the two-site model on to the diffusion data of salicylate gave the estimates $K_d = 0.030 \pm 0.004$ M with $n = 33 \pm 3$ (Fig. 7.9).

7.3   Applications

The applications of diffusion NMR spectroscopy are far-reaching, as the technique allows the monitoring of interactions between various components within a single measurement one experiment allows the individual diffusion coefficients of multi-component systems to be measured simultaneously. From these diffusion coefficients, detailed insights about the interactions between the components can be gained. One of the most useful applications of diffusion NMR spectroscopy is in the area of supramolecular chemistry. The term "supramolecular" was coined by Nobel Laureate Jean–Marie Lehn, describing it as "chemistry beyond the molecule" [37]. More specifically, supramolecular chemistry describes the structures and functions of two or more molecular aggregates, held together by non-covalent intermolecular forces, such as van der Waals forces, hydrogen bonding, π–π stacking and hydrophobic effects. In addition, as diffusion NMR spectroscopy is a non-invasive technique, it is also well suited to biological and physiological applications.

The solution-phase diffusion of supramolecular complexes containing metallointercalators is most important in the field of drug delivery. Drug transport and uptake can mediate the binding of drugs to macromolecules and affect plasma circulation lifetimes. In addition, tumour vasculature has enhanced permeability to macromolecules [38], which may have a positive effect on the uptake of platinum complexes in cancerous tissues. As such, diffusion NMR spectroscopy is a valuable technique for such investigations.

In this section we provide general methods and procedures to follow when conducting PGSE NMR experiments. We also focus on the specific applications and current uses of diffusion NMR, specifically PGSE NMR, to the field of metallointercalators. This work is relatively recent, as the implementation of diffusion NMR spectroscopy to the studies of supramolecular chemistry began less than 20 years ago [39]. The majority of studies have focussed on gaining preliminary insight into the molecular interactions between platinum(II)-intercalating complexes and host compounds, such as cucurbit[n]urils, cyclodextrins, calix[n]arenes and dendrimers. PGSE diffusion NMR has also been used recently to probe the self-aggregation of intercalating molecules.

7.3.1   Experimental Procedures

In the following section we provide a general description on conducting ^{1}H diffusion NMR experiments. The emphasis here is not on the mathematics or theoretical workings and background of the spectrometer (covered in Sect. 7.1 and 7.2), instead it covers practical aspects of conducting these experiments.

7.3.1.1 Sample Preparation

The preparation of samples of known concentration is of particular importance when performing PGSE experiments, as the diffusion coefficient platinum(II) complexes has been shown to be concentration dependent [2]. In our studies, the lower limit of sample concentration is 0.5 mM.

7.3.1.2 Parameters

There are a number of important parameters to consider when performing PGSE experiments. A brief explanation is given below as to how to determine the optimum parameters for an experiment.

(a) Recycle delay

To ensure accurate diffusion coefficient determination a recycle delay of $>= 5 \times T_1$ should be used, although it is sometimes possible to use a shorter delay [40]. T_1 values for platinum metallointercalators are usually <1 s, and as such, a recycle delay of ~5 s is usually sufficient. Measurement of the T_1 for individual compounds should be made to ensure full longitudinal relaxation.

(b) Diffusion time

Perhaps the two most important parameters to optimise when running a PGSE diffusion experiment are Δ (i.e., diffusion time) and δ. As shown in Fig. 7.1, Δ is the duration between the leading edges of the two gradient pulses (e.g., ~10–100 ms), and δ is the length of each gradient pulse (e.g., ~1–5 ms). Each diffusion experiment may require different values of Δ and δ in order to obtain appropriate signal attenuation (e.g., killing ~80% of the echo signal). An initial "test" experiment is often performed with a lower number of scans and only 2 gradient values (e.g., 0.01 and 0.59 T m^{-1}) to determine whether the values chosen for Δ and δ are appropriate. These values are then modified until appropriate attenuation is obtained. For a more detailed discussion on setting up these parameters, please consult [41].

(c) Number of scans and number of gradient strength increments

The number of scans chosen for each diffusion experiment set needs to be enough to ensure there is an adequate signal-to-noise (S/N) ratio. Increasing the number of scans will improve the signal-to-noise ratio of the spectrum, but at the expense of longer experimental running times. The S/N ratio accumulated by adding together n transients is a factor of $n^{1/2}$ larger than the S/N ratio for a single transient. (e.g., [42]) Typically, for measuring the diffusion of small molecules using ^{1}H PGSE NMR, 16 individual experiments are performed, with the gradient increasing from 0 to 0.5 T m^{-1}.

7.3.1.3 Results

The resulting PGSE spectra must be appropriately phased before signal intensities (or integrals) can be determined. If the data set is good, the phase parameters determined for the first spectrum should be applicable to all of the other spectra. If not there is a strong possibility of eddy current problems or other technical issues (e.g., [41]). A set of spectra obtained in a diffusion experiment of 56MESS are shown in Fig. 7.10a, with the signal attenuation decreasing with increasing gradient strength. For the experiment with lowest gradient strength, the peak of interest is integrated (most often this integral is set to 1.0). This region is then integrated in each of the following experiments, with respect to the first experiment.

7.3.1.4 Data Processing

As shown in Fig. 7.10b, the diffusion coefficient can be obtained by fitting (7.12) to the experimental data using a nonlinear least square algorithm.

7.3.2 Intercalator Self-aggregation

It is widely accepted that complexes which contain fused aromatic rings are capable of forming dimers in aqueous solvents [43]. The dimerisation of platinum(II) complexes has been shown using electronic spectroscopy and chemical shift
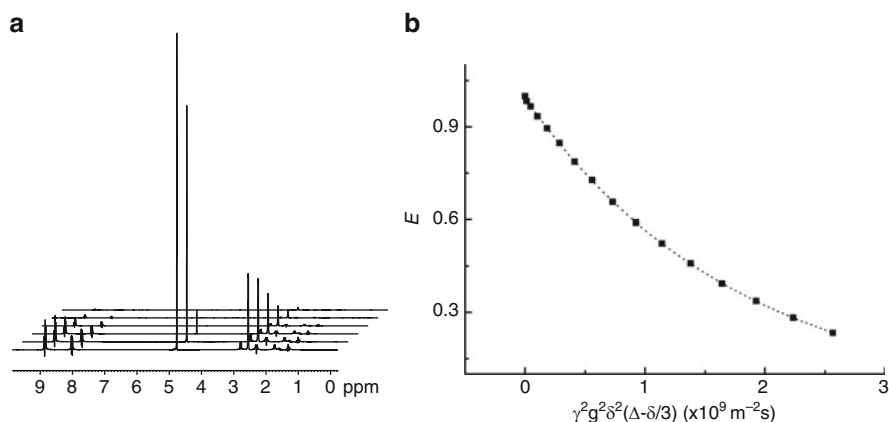
Fig. 7.10 (**a**) A series of 400 MHz ^{1}H PGSE spectra of a sample of **56MESS** in D_2O at 298 K. The signal attenuates as the gradient strength increases from 0 to 0.4 T m^{-1} in equal increments. (**b**) A plot of E versus $\gamma^2 g^2 \delta^2 (\Delta - \delta/3)$. The *dotted line* shows nonlinear least square fitting of (7.12) to the data. The diffusion coefficient was determined to be 5.62×10^{-10} m^{2}s^{-1} for **56MESS**
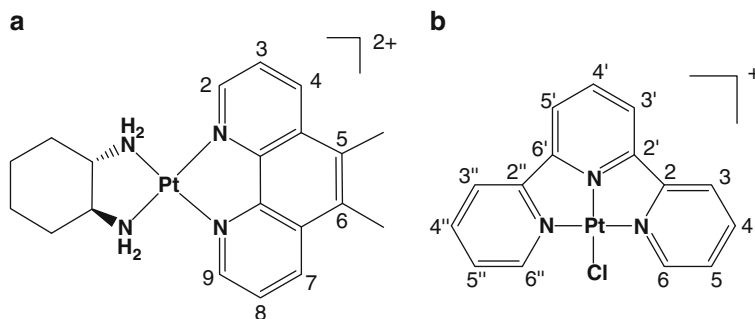
Fig. 7.11 The chemical structure of (**a**) **56MESS** and (**b**) [Pt(terpy)Cl]$^+$

changes in ^{1}H NMR spectra [43–46]; however, the formation of higher order aggregates has not been well demonstrated. It has been recently discovered that the platinum (II)-based DNA intercalators [(5,6-dimethyl-1,10-phenanthroline)(1S,2S-diaminocyclohexane)platinum(II)]$^{2+}$ (**56MESS**, Fig. 7.11a) and [(2,2′:6′,2″-terpyridine)chloroplatinum(II)]$^+$ ([Pt(terpy)Cl]$^+$) (Fig. 7.11b) self-stack in solution, forming nanorods [2]. Pulsed gradient spin-echo measurements were used to show that the diffusion coefficient of **56MESS** and [Pt(terpy)Cl]$^+$ is concentration dependent, with a reduction in the diffusion coefficient observed with increasing metal complex concentration. The lengths of the macromolecules formed were then estimated from the diffusion coefficients, by modelling the macromolecules as ellipsoids.

The simple model of an ellipsoid was employed in order to determine the length of the macromolecule. The observed diffusion coefficient for each experiment (e.g., at varying concentration and/or temperature) was substituted into the Stokes–Einstein equation (7.19).

For an oblate ellipsoid the friction coefficient is given by [47, 48]

$$f_O = \frac{\sqrt{1 - p^2}}{p^{1/3} \tan^{-1}(\sqrt{1 - p^2}/p)} \tag{7.18}$$

where $p = b/c < 1$ and $R = (b^2 c)^{1/3}$, where b is the semi major axis and c is the semi minor axis.

For a prolate ellipsoid the friction coefficient is given by [47, 48]

$$f_P = \frac{\sqrt{p^2 - 1}}{p^{1/3} \tanh^{-1}(\sqrt{p^2 - 1}/p)} \tag{7.19}$$

where $p = b/c > 1$ and $R = (c^2 b)^{1/3}$.

The equation for the friction coefficient [initially the oblate model, (7.18)] was also substituted into the Stokes–Einstein equation, (7.1). The value of c was estimated as 0.75 nm (radial diameter ~ 1.5 nm) for **56MESS** and 0.50 nm (radial diameter ~1.0 nm) for [Pt(terpy)Cl]$^+$ based on measurements from X-ray

crystal data. The value of b was then modified until the calculated diffusion coefficient was in agreement with the experimentally observed value. If the calculated diffusion coefficient could not be reduced to that of the experimental value with $b < c$, the prolate model was used, by substituting the friction coefficient for the prolate ellipsoid (7.19) into the Stokes–Einstein equation. The number of molecules in the aggregate was estimated assuming a standard π–π stacking distance of 0.34 nm.

At 25 °C, the diffusion coefficients of **56MESS** and [Pt(terpy)Cl]$^+$ decrease monotonically with increasing concentration (Fig. 7.12), indicating the formation of larger particles. At the lowest concentration examined (1 mM) the **56MESS** macromolecule contains ~2–3 molecules, creating a nanorod that is only 0.6 nm in length. At 25 mM, there are ~3–4 molecules in the nanorod, with a length of 1.0 nm (Fig. 7.13a). [Pt(terpy)Cl]$^+$, however, appears to self-stack to a much greater extent than **56MESS**, with nanorods 0.7–2.9 nm (~3–10 molecules) in length formed as
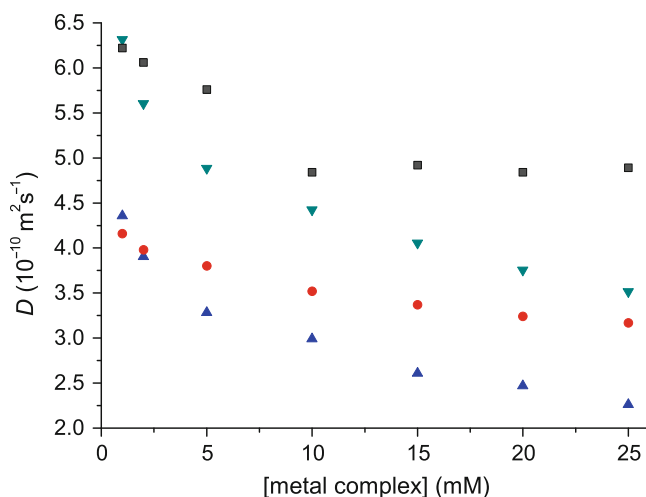
Fig. 7.12 The diffusion coefficient of **56MESS** (*Solid square* 37 °C, *Bullet* 25 °C) and [Pt(terpy) Cl]$^+$ (*Inverted triangle* 37 °C, *Upward triangle* 25 °C) with increasing concentration
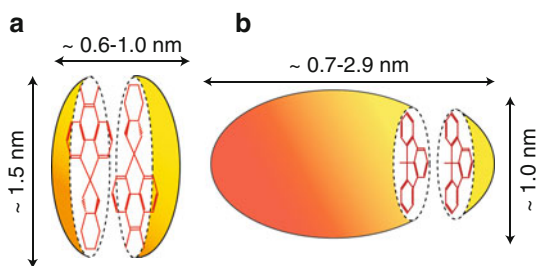
Fig. 7.13 A schematic representation of the head-to-tail stacking at 25 °C of (**a**) the oblate (*disk-like*) model of 56MESS and (**b**) the prolate (*rod-like*) model of [Pt(terpy) Cl]$^+$

the concentration is increased up to 25 mM (Fig. 7.13b). At high concentrations (15–25 mM) the ^{1}H NMR resonances of [Pt(terpy)Cl]$^+$ also experience a greater degree of broadening, supporting this finding of aggregation.

The aggregation of both complexes was also examined at 37 °C. The higher temperature reduces the size of the aggregates formed; at the lowest concentration (1 mM) **56MESS** does not appear to undergo stacking. Between 2 and 10 mM the reduction in the diffusion coefficient suggests that some stacking does occur; however, it does not change between 10 and 25 mM, with the maximum nanorod formed consisting of ~2–3 molecules, with length 0.5 nm. [Pt(terpy)Cl]$^+$ does not appear to have the same upper limit on the size of the nanorod formed, with the diffusion coefficient continuing to decrease with increasing concentration (up to 25 mM). The nanorods formed are also longer than those of **56MESS**, consisting of a maximum of ~4–5 molecules, with a length of 1.2 nm. These results may have implications in the delivery and transport of DNA intercalating drugs, particularly platinum(II)-based drugs, in disease treatment.

Despite 40 years of research, the mechanism by which platinum drugs (like cisplatin and carboplatin) are transported into cells is still not clear. Cisplatin complexes are neutrally charged (although they can become slightly cationic (1+ or 2+) upon hydrolysis within the cell) and may only interact weakly with negatively charged cell membranes. Both [Pt(terpy)Cl]$^+$ and **56MESS** nanorods, however, are more cationic (4+ to 12+) at physiological temperature, and so may have stronger electrostatic interactions with cell surfaces. In addition, the nanorods formed by **56MESS** and [Pt(terpy)Cl]$^+$ are of similar diameter to some biomolecules (e.g., insulin ~3.0 nm and cytochrome C ~4.0 nm) [49]. Tumour vasculature is known to have enhanced permeability to macromolecules [38], which may have a positive effect on the uptake of **56MESS** in cancerous tissues.

Overall, these results have implications not just in the delivery of platinum-based DNA intercalating agents, but for all small molecule drugs that contain fused aromatic ring systems, such as doxorubicin and daunorubicin, which are routinely used in the treatment of human breast cancers. These results are also extremely relevant in the investigations of bis-intercalating compounds and the interactions of these aggregates with biomolecules. They also highlight the usefulness of PGSE NMR in the measurement of aggregation of intercalating complexes.

7.3.3   Cucurbit[n]uril Encapsulation of Platinum Complexes

Cucurbit[*n*]urils, (CB[*n*]) where $n = 5, 6, 7, 8$, or 10, are a family of macrocycles made from the condensation of glycoluril and formaldehyde under strongly acidic conditions [49, 50]. CB[*n*]s have an internal hydrophobic cavity which is accessible through two symmetrical ureido-carbonyl lined portals [51, 52]. The internal cavity of CB[*n*] is able to partially or fully encapsulate a range of small molecules: such binding is stabilized through hydrophobic effects within the cavity and/or ion–dipole or dipole–dipole interactions between the guest and the CB[*n*] portals [51].
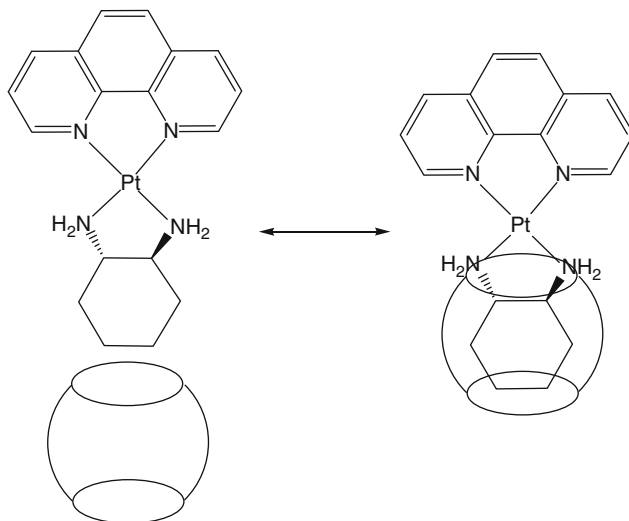
Fig. 7.14 A schematic diagram showing the exchange process between a free platinum(II)-based DNA intercalator (**PHENSS**) and where it is encapsulated over the ancillary ligand by a CB[6] molecule. Anions and charges have been omitted for clarity [55]

The host–guest interactions of CB[n] give rise to a range of applications, including drug delivery [51–53]. In many of these applications, the interactions of CB[n] with guests, solvent, and other solutes play a part in their recognition and binding properties [54–57].

It has been shown that CB[n] is able to bind to a variety of platinum-based complexes [58, 59], including intercalators [55]. In the case of intercalators of the form $[Pt(A_L)(I_L)]^{2+}$ (where A_L is the ancillary ligand and I_L is an intercalating ligand), encapsulation by CB[n] occurs predominantly over the ancillary ligand of the complex (Fig. 7.14). This encapsulation has varying effects on cytotoxicity that are dependent on the individual metal complex and the type of CB[n] used [55, 57]. Encapsulation also reduces the reactivity of the metal complex to L-glutathione [54]. In a recent preliminary study, PGSE experiments have been conducted on the free CB[n] macrocycles, with the diffusion coefficient dependent on the concentration (Fig. 7.15) [60, 61]. This indicates that some degree of self-association occurs between the CB[n] molecules.

7.3.4 Cyclodextrin Encapsulation of Platinum Complexes

Cyclodextrins (n-CD) are a water soluble family of cyclic oligosaccharides that are composed of α-D-glucose units joined by α-1,4-linkages [62]. The three most common n-CDs consist of 6, 7, or 8 monomers and are named α-, β-, and γ-cyclodextrin, respectively. n-CDs have a toroidal basket shape with a
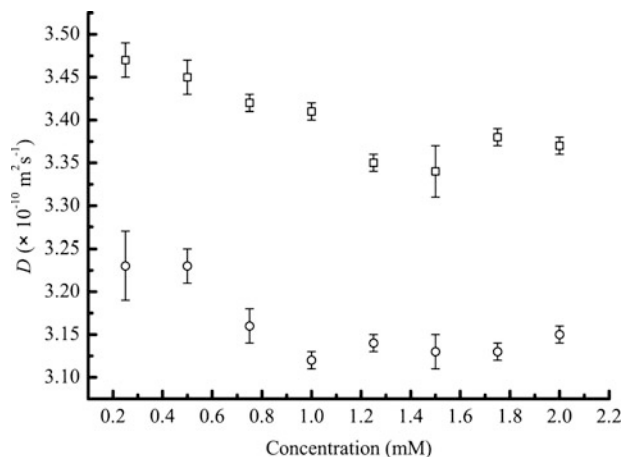
Fig. 7.15 The concentration dependence of the diffusion coefficient CB[6] (*square*) and CB[7] (*circle*) [61]

hydrophobic internal cavity, allowing them to form noncovalent encapsulation complexes with a variety of compounds [62, 63]. A large family of chemically modified cyclodextrins has been developed, and factors such as the degree of substitution, the size of the functional groups, and the charge on the molecules have been shown to influence significantly the formation of host–guest complexes in drug delivery [64].

The encapsulation of the platinum(II)-based DNA intercalators **56MESS**, [(5,6-dimethyl-1,10-phenanthroline)(1*R*,2*R*-diaminocyclohexane)platinum(II)]$^{2+}$ (**56MERR**) and [(5,6-dimethyl-1,10-phenanthroline)(ethylenediamine)platinum (II)]$^{2+}$ (**56MEEN**) with a charged cyclodextrin derivative (carboxylated-β-CD, c-β-CD) have been recently investigated. c-β-CD forms a 1:1 inclusion complex with the metal complexes, with the cyclodextrin cavity bound over the phenanthroline portion of the molecule (7.16a). This complex exists in fast-exchange on the ^{1}H NMR timescale. This encapsulation significantly slowed the reaction of the metal complex with *L*-glutathione, whilst not affecting the cytotoxicity of **56MESS** against the LoVo (human colorectal cancer) cell line. PGSE diffusion measurements were used to confirm the encapsulation of the metal complexes, with a reduction in the diffusion coefficient of the metal complex upon encapsulation (Fig. 7.16b) [65]. The diffusion coefficient of the c-β-CD (2 mM) was found to be 2.3×10^{-10} m^{2}s^{-1}, which is consistent with previous diffusion studies on cyclodextrins and their encapsulation complexes [66].

7.3.5 *Calix[*n*]arene Encapsulation of Platinum Complexes*

Calix[*n*]arenes (CX[*n*]) are cyclic oligomers of repeating phenolic units joined via methylene bridges where the number of monomers is 4, 6 or 8 [67]. Unsubstituted
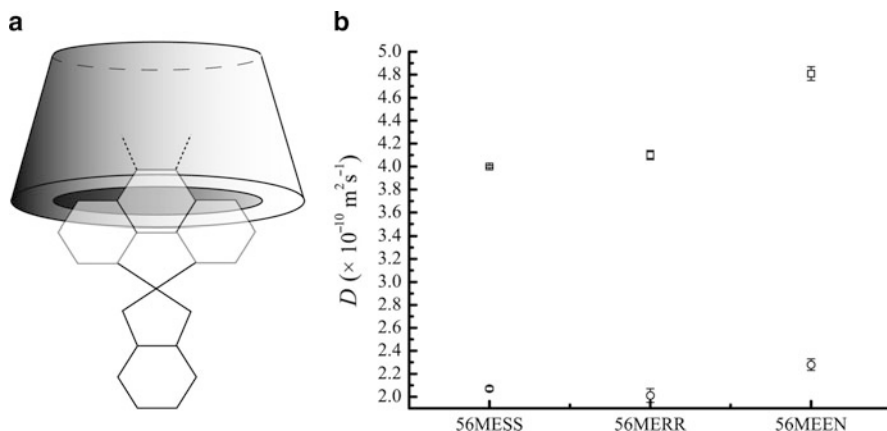
Fig. 7.16 (**a**) A diagrammatic representation of the 1:1 host–guest complexes formed by the metal complexes with c-β-CD. Anions have been omitted for clarity. (**b**) The diffusion coefficients of the metal complexes (2 mM) in the absence (*square*) and presence (*circle*) of an equimolar concentration of c-β-CD

CX[*n*]s are not water soluble, and as such, research utilizing this group of molecules as drug delivery vehicles has focused on substituted CX[*n*], particularly the *p*-sulfonatocalix[*n*]arenes (s-CX[*n*]), as they possess the highest solubility of commercially available CX[*n*] derivatives [68]. The interior surface and sulfonate groups provide association sites for both hydrophobic and hydrophilic molecules, respectively.

The encapsulation of **56MESS**, **56MERR** and **56MEEN** by s-CX[4] has been investigated, with the formation of a 2:2 host-guest complex proposed. As the metal complex was titrated into a solution of s-CX[4], This complex exists in intermediate-slow exchange on the ^{1}H NMR timescale, and it consists of two intercalator molecules stacked head-to-tail with one another, with an s-CX[4] molecule "capping" the intercalators at either end (Fig. 7.17a). The diffusion coefficient of free s-CX[4] (0.5 mM) was determined to be 3.21×10^{-10} m^{2}s^{-1}, which was significantly reduced when combined with an equimolar concentration of metal complex (Fig. 7.17b).

7.3.6 Estimation of Size and Type of Supramolecular Complex

The measurement of the diffusion coefficient can provide information about the size and type (e.g., 1:1, 2:2, 2:1) of supramolecular complex formed. The 1:1 complexes formed by c-β-CD (Sect. 7.3.4) and the 2:2 complexes formed by s-CX[4] (Sect. 7.3.5) have approximate molecular weights of 2,500 Da and 2,800 Da, respectively. The similar diffusion coefficients for the encapsulation complexes of each with the metal complexes (2.0×10^{-10} m^{2}s^{-1} to 2.6×10^{-10} m^{2}s^{-1},
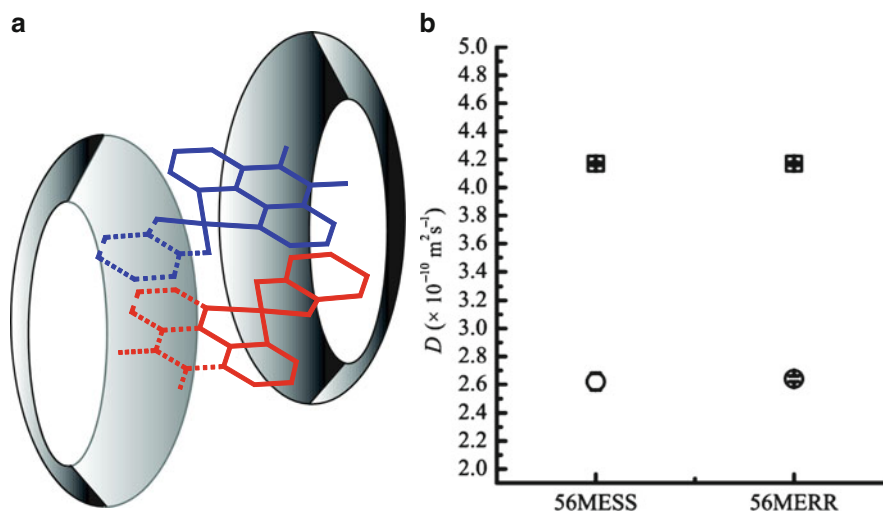
Fig. 7.17 (a) A diagrammatic representation of the 2:2 host–guest complex of **56MESS**–s-CX[4] where two metal complex molecules associate in a head-to-tail fashion, with one s-CX[4] molecule encapsulated over either end. (**b**) The diffusion coefficients of the metal complexes in the absence (*square*) and presence (*circle*) of an equimolar concentration of s-CX[4] (0.5 mM) in D_2O

Fig. 7.16b and Fig. 7.17b) support the formation of host–guest complexes with similar effective molecular weights, and, therefore, the formation of a 2:2 complex with s-CX[4]. These results show that diffusion NMR is useful for comparisons of different types of supramolecular complexes.

The trinuclear platinum complex *trans*-[{Pt-$(NH_3)_2(dpzm)_2$}]$^{2+}$ (tri-Pt) [69] has been shown to form 1:1 and 2:1 inclusion complexes with CB[7] [58, 59]. Free tri-Pt (2 mM) was observed to have a diffusion coefficient of $2.88 \times 10^{-10}\,m^2s^{-1}$. The diffusion coefficient is reduced to $2.43 \times 10^{-10}\,m^2s^{-1}$ and $1.90 \times 10^{-10}\,m^2s^{-1}$ when encapsulated by one and two CB[7] molecules, respectively [60]. The observed diffusion coefficients are directly related to the effective molecular weight of the inclusion complex. Although this complex is not an intercalator, these results still highlight the usefulness of PGSE NMR to determine the formation of inclusion complexes with CB[*n*], and also to provide evidence for the type of inclusion complex formed (e.g., 2:1 host : guest).

7.3.7 Dendrimer Encapsulation of Platinum Complexes

Dendrimers are highly branched polymeric molecules that are capable of associating with guest molecules on their outer surface or within their large inner cavities. Recently there have been studies conducted on the interactions between anionic
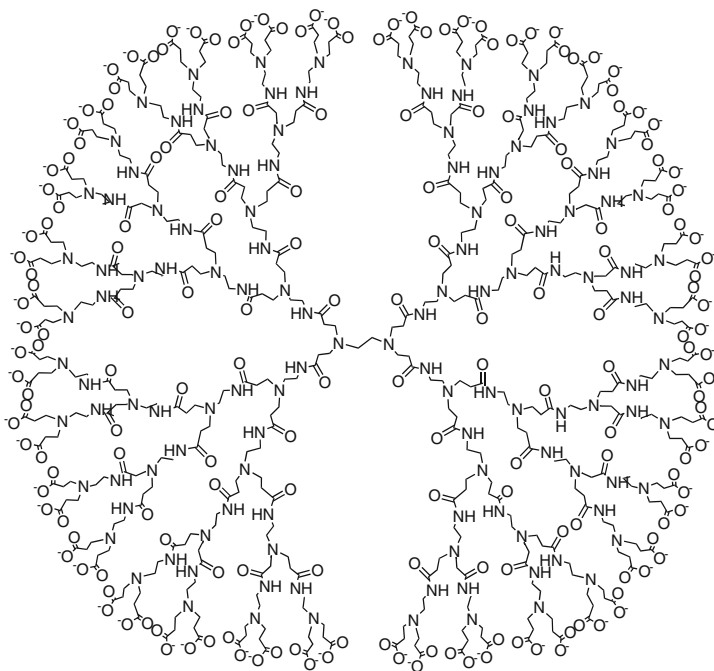
Fig. 7.18 The chemical structure of a generation 3.5 PAMAM dendrimer

half-generation poly(amidoamine) (PAMAM) dendrimers (Fig. 7.18) and **56MESS** [54]. By monitoring the ^{1}H chemical shift changes during the titration of metal complex in dendrimer, it was found that the metal complex was binding to the surface of the dedrimers through electrostatic interactions. PGSE diffusion NMR was used to examine the size of the free dendrimer, and the dendrimer when combined with **56MESS** at maximum loading.

The hydrodynamic radius of each dendrimer was calculated from the diffusion coefficient, using the Stokes–Einstein equation. The hydrodynamic radius includes the dendrimer and all other associated molecules, such as solvents and water molecules in the hydration shell. The diameters calculated for the half-generation dendrimers [70] are larger than that of the consecutive full-generation (Table 7.1) [71]. This is possibly due to a greater degree of hydrogen-bonding occurring between the anionic dendrimer and the solvent molecules, resulting in a larger hydration shell, and therefore a larger hydrodynamic radius compared to the uncharged full generation dendrimers. The size of the dendrimer is very sensitive to changes in the solvent environment, such as pH and ionic strength.

In all cases, the size of the free dendrimer increases with generation size (decreased diffusion coefficient), and the size increases when **56MESS** is added to each dendrimer (Table 7.1). There appears to be no relationship between the generation and the magnitude of the size increase, with the size increasing in

Table 7.1 The diffusion coefficient D and radii of the dendrimers with **56MESS** at maximum binding [70, 71]

Dendrimer generation	Max. binding 56MESS (eq.)	D_f ($\times 10^{-11}$ m^{2}s^{-1})	D_b ($\times 10^{-11}$ m^{2}s^{-1})	Diameter free (nm)	Diameter bound (nm)
3.5	28	6.1	3.3	7.2	13.2
4.0	–	–	–	4.0	–
4.5	36	5.6	3.7	7.8	11.8
5.0	–	–	–	5.3	–
5.5	72	3.9	3.0	11.2	14.5
6.0	–	–	–	6.7	–
6.5	96	3.3	2.2	13.4	20.0
7.0	–	–	–	8.0	–

Maximum binding is defined as the number of metal complex equivalents required to saturate dendrimer binding

the order G3.5 > G4.5 > G6.5 > G5.5. In any case, the large increase in the diameter strongly supports the hypothesis that the majority of the metal complex molecules are associating at the dendrimer surface rather than inside the core. In addition, the association of the metal complex may cause localised charge neutralisation, and promote the aggregation of the dendrimers, causing larger sized particles. This work highlights the usefulness of PGSE NMR in determining associations between metallointercalators and dendrimers.

References

1. Price WS. NMR studies of translational motion. 1st ed. Cambridge: Cambridge University Press; 2009.
2. Krause-Heuer AM, Wheate NJ, Price WS, Aldrich-Wright JR. Chem Commun. 2009: 1210.
3. Jost W. Diffusion in solids, liquids, gases. New York: Academic; 1960.
4. Berg HC. Random walks in biology. Princeton: Princeton University Press; 1983.
5. Truskey GA, Yuan F, Katz DF. Transport phenomena in biological systems. Upper Saddle River: Pearson Prentice Hall; 2004.
6. Green PF. Kinetics, transport, and structure in hard and soft materials. Boca Raton, FL: Taylor & Francis; 2005.
7. Stokes GG. Trans Cambridge Philos Soc. 1856;9:8.
8. Einstein A. Annalen der Physik (Leipzig). 1905;17:549.
9. Sutherland W. Philos Mag. 1905;9:781.
10. Macchioni A, Ciancaleoni G, Zuccaccia C, Zuccaccia D. Chem Soc Rev. 2008;37:479.
11. Van der Meeren P, Bogaert H, Stastny M, Vanderdeelen J, Baert L, Colloid Interface J. Science. 1993;160:117.
12. Lellig C, Wagner J, Hempelmann R, Keller S, Lumma D, Hartl W. J Chem Phys. 2004;121:7022.
13. Molenat J. J Electroanal Chem. 1987;216:89.
14. Momot KI, Kuchel PW. Concepts Magn Reson. 2006;28A:249.
15. Woessner DE. Concepts Magn Reson. 1996;8:397.
16. Stilbs P. Prog Nucl Magn Reson Spectrosc. 1987;19:1.
17. Price WS. Concepts Magn Reson. 1997;9A:299.

18. Stejskal EO, Tanner JE. J Chem Phys. 1965;42:288.
19. Torrey HC. Phys Rev. 1956;104:563.
20. Bleaney BI, Bleaney B. Electricity and magnetism. London: Oxford University Press; 1976.
21. Purcell EM. Electricity and magnetism. 2nd ed. New York: McGraw-Hill Book Co; 1985.
22. Cowan B. Nuclear magnetic resonance and relaxation. Cambridge: Cambridge University Press; 1997.
23. Kuchel PW, Chapman BE, Bubb WA, Hansen PE, Durrant CJ, Hertzberg MP. Concepts Magn Reson. 2003;18A:56.
24. Endre ZH, Kuchel PW, Chapman BE. Biochim Biophys Acta. 1984;803:137.
25. Kuchel PW, Bulliman BT. NMR Biomed. 1989;2:151.
26. Williams WD, Seymour EFW, Cotts RM. J Magn Reson. 1978;31:271.
27. Price WS, Stilbs P, Jönsson B, Söderman O. J Magn Reson. 2001;150:49.
28. Zheng G, Price WS. Concepts Magn Reson. 2007;30A:261.
29. Tanner JE. J Chem Phys. 1970;52:2523.
30. Torres AM, Zheng G, Price WS. Magn Reson Chem. 2010;48:129.
31. Zheng G, Price WS. Prog Nucl Magn Reson Spectrosc. 2010;56:267.
32. Zheng G, Price WS. J Biomol NMR. 2009;45:295.
33. Momot KI, Kuchel PW. J Magn Reson. 2004;169:92.
34. Jerschow A, Müller N. J Magn Reson. 1997;125:372.
35. Luo RS, Liu ML, Mao XA. Spectrochim Acta A. 1897;1999:55.
36. Price WS, Elwinger F, Vigouroux C, Stilbs P. Magn Reson Chem. 2002;40:391.
37. Lehn J-M. Angew Chem Int Ed. 1988;27:89.
38. Hambley TW. Aust J Chem. 2008;61:647.
39. Cohen Y, Avram L, Frish L. Angew Chem Int Ed. 2005;44:520.
40. Stait-Gardner T, Anil Kumar PG, Price WS. Chem Phys Lett. 2008;462:331.
41. Price WS. Concepts Magn Reson. 1998;10:197.
42. Levitt MH. Spin dynamics: basics of nuclear magnetic resonance. 2nd ed. Hoboken: John Wiley Sons; 2008.
43. Arena G, Monsú Scolaro L, Pasternack RF, Romeo R. Inorg Chem. 1995;34:2994.
44. Yu C, Chan KH-Y, Wong KM-C, Yam VW-W. Proc Natl Acad Sci USA. 2006;103:19652.
45. Yam VW-W, Wong KM-C, Zhu N. Chem-Eur J. 2005;11:4353.
46. Yam VW-W, Wong KM-C, Zhu N. J Am Chem Soc. 2002;124:6506.
47. Koenig SH. Biopolymers. 1975;14:2421.
48. Perrin F. J Phys Radium. 1934;5:497.
49. Esfand R, Tomalia DA. Drug Discov Today. 2001;6:427.
50. Kim J, Jung I-S, Kim S-Y, Lee E, Kang J-K, Sakamoto S, et al. J Am Chem Soc. 2000;122:540.
51. Lagona J, Mukhopadhyay P, Chakrabarti S, Isaacs L. Angew Chem Int Ed. 2005;44:4844.
52. Kim K, Selvapalam N, Ko YH, Park KM, Kim D, Kim J. Chem Soc Rev. 2007;36:267.
53. Wheate NJ. Aust J Chem. 2006;59:354.
54. Kemp S, Wheate NJ, Pisani MJ, Aldrich-Wright JR. J Med Chem. 2008;51:2787.
55. Wheate NJ, Taleb RI, Krause-Heuer AM, Cook RL, Wang S, Higgins VJ, Aldrich-Wright JR. Dalton Trans. 2007: 5055.
56. Jeon WS, Kim E, Ko YH, Hwang IH, Lee JW, Kim SY, et al. Angew Chem Int Ed. 2005;44:87.
57. Kemp S, Wheate NJ, Wang S, Collins JG, Ralph SF, Day AI, et al. J Biol Inorg Chem. 2007;12:969.
58. Wheate NJ, Buck DP, Day AI, Collins JG. Dalton Trans. 2006;3:451.
59. Wheate NJ, Day AI, Blanch RJ, Arnold AP, Cullinane C, Collins JG. Chem Commun. 2004:1424.
60. Wheate NJ, Kumar PGA, Torres AM, Aldrich-Wright JR, Price WS. J Phys Chem B. 2008;112:2311.
61. Grant MP, Wheate NJ, Aldrich-Wright JR, J Chem Eng Data. 2009;54:323.

62. Bender ML, Kominyama M. Cyclodextrin chemistry. Berlin: Springer; 1978.
63. Szejtli J. Cyclodextrins and their inclusion complexes. Budapest: Akademiai Kiado; 1982.
64. Wenz G. Angew Chem Int Ed. 1994;33:803.
65. Krause-Heuer AM, Wheate NJ, Tilby MJ, Pearson DG, Ottley CJ, Aldrich-Wright JR. Inorg Chem. 2008;47:6880.
66. Avram L, Cohen Y. J Org Chem. 2002;67:2639.
67. Gutshe CD. The characterisation and properties of calixarenes. Cambridge: The Royal Society of Chemistry; 1989.
68. Arduini A, Pochini A, Reverberi S, Ungaro R. J Chem Soc, Chem Commun. 1984:981.
69. Wheate NJ, Broomhead JA, Collins JG, Day AI. Aust J Chem. 2001;54:141.
70. Pisani MJ, Wheate NJ, Keene FR, Aldrich-Wright JR, Collins JG. J Inorg Biochem. 2009;103:373.
71. Svenson S, Tomalia DA. Adv Drug Delivery Rev. 2005;57:2106.

Chapter 8
Mass Spectrometric Studies of Non-Covalent Binding Interactions Between Metallointercalators and DNA

Thitima Urathamakul, Jihan Talib, Jennifer L. Beck, and Stephen F. Ralph

8.1 Introduction

Over the past 2 decades there has been increasing interest in metal complexes that bind non-covalently to DNA, driven in part by a host of potential applications for molecules that can accomplish this task with high affinity and selectivity. As a result many workers have used a wide variety of experimental techniques, several of which are discussed in other chapters of this book, to unravel the details of the precise intermolecular interactions involved. Here we discuss one of the most recent additions to the armory of techniques used by chemists to interrogate metal complex/ DNA interactions. For the majority of its existence mass spectrometry (MS) has proven to be of enormous advantage to chemists by virtue of its ability to provide the molecular weights of compounds as well as structural information via fragmentation patterns. However, the high energies associated with many earlier MS techniques which result in fragmentation of covalent bonds, prevent its application for studying weaker intermolecular interactions. The advent of soft ionisation methods such as matrix assisted laser desorption ionisation (MALDI) and electrospray ionisation (ESI) has revolutionised mass spectrometric analysis of biomolecules, by allowing these normally fragile molecules to be introduced into the gas phase for analysis with minimal, if any, fragmentation. It was then recognised that ESI–MS, in particular, might be suitable for investigating non-covalent interactions between small molecules and either proteins or nucleic acids. This was confirmed by a number of early studies involving organic intercalators and minor groove binding ligands, prompting our interest in evaluating ESI–MS as a tool for studying non-covalent interactions between metal complexes and DNA. This chapter contains a discussion of the basic principles behind ESI–MS that enable it to introduce representative samples of solutions containing metal complexes and DNA into the gas phase for analysis. This will be followed by a discussion of the results that can be obtained using this method, drawing heavily on studies performed in our laboratory. The advantages

S.F. Ralph (✉)
School of Chemistry, University of Wollongong, Northfields Avenue, NSW, Australia
e-mail: sralph@uow.edu.au

and disadvantages of using ESI–MS in comparison to other techniques for investigating these types of systems will be addressed throughout, and some final comments made concerning how mass spectrometry may enable other questions concerning metal complex/DNA interactions to be addressed in the near future.

8.2   The Electrospray Ionisation Process

The history of ESI–MS dates back to the pioneering work of Dole and co-workers in the late 1960s [1]. It was, however, 2 decades before the potential of the technique for analysis of biomolecules was fully demonstrated by Fenn and his group, who used ESI–MS to measure the molecular mass of a number of proteins, including insulin, lysozyme, α-amylase, conalbumin and cytochrome c [2]. During the ESI process, small charged droplets containing the analyte are initially formed at the tip of a capillary, which is typically subjected to a potential of 1–4 kV. As a result, molecular ions with multiple positive or negative charges are generated. In the case of positive ion mass spectra, ionisation occurs when protons are transferred from electrolyte ions present among solvent molecules on the surface of the droplets to basic functional groups on analyte molecules (e.g., lysine or arginine residues of proteins). Conversely, in negative ion ESI mass spectra negatively charged ions are produced when protons are transferred from acidic functional groups present on analyte molecules to basic electrolyte ions. Since the phosphate groups present on the backbone of DNA are deprotonated at physiological pH values, most ESI–MS studies of DNA and its non-covalent complexes with small organic or inorganic molecules have been conducted using negative ion mode.

   As the droplets formed by the ESI process pass through the region between the capillary tip and the cone they are exposed to a warm stream of nitrogen gas, which aids in evaporating the solvent and reducing the size of the droplets (Fig. 8.1). Although the size of the droplets decreases, the overall charge remains the same, resulting in an increase in repulsive Coulombic forces. Eventually the repulsive forces present within a droplet reach a critical point (Rayleigh limit) where they exceed the surface tension of the liquid, resulting in fission into several smaller droplets. This process is repeated many times until the point where either an analyte ion desorbs from the droplet (ion-evaporation model) [3], or all solvent molecules have been removed to leave behind a droplet containing only charged analyte ion(s) [4]. There has been considerable debate over the relative importance of these processes, and it is likely that both play a role depending on the nature of the analyte [5–8]. Irrespective of how they are formed, the solvent-free ions pass through an electrical potential and pressure gradient until they reach the analyser which is contained in a high vacuum system. ESI sources are now coupled to a wide range of analysers, including ion trap, quadrupole, triple quadrupole, time of flight (ToF) and quadrupole-ToF mass analysers.
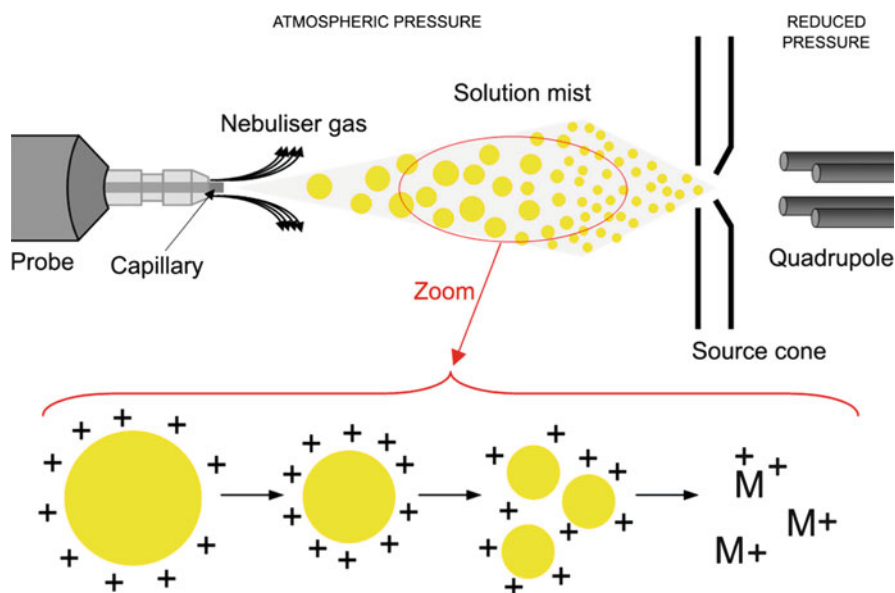
Fig. 8.1 Schematic illustration of ion formation during the ESI process

The gentle nature of the ESI process generally leaves covalent bonds intact. Furthermore experimental and instrumental conditions can be found where non-covalent complexes are retained using ionisation. This has enabled ESI–MS to be widely used for analysis of a large range of non-covalent complexes. In contrast, the other soft ionisation method widely used today in biochemical research, MALDI, has received less attention for examining formation of non-covalent complexes between biomolecules, or between biomolecules and small organic or inorganic compounds. This is because in MALDI the sample of interest must first be dissolved in an organic matrix, which is often acidic (e.g., cinnamic acid), and subsequently dried, which does not provide the ideal environment for maintaining non-covalent interactions. The application of both ESI–MS and MALDI–MS to the analysis of biomolecular interactions has been reviewed several times recently [9–13].

8.3 Mass Spectrometry of DNA

8.3.1 Duplex DNA

Over the years, researchers investigating the non-covalent DNA binding properties of metal complexes have made extensive use of calf thymus DNA (ct-DNA) owing to its low cost and ready availability. An inherent assumption in these studies was

that ct-DNA is representative of DNA in general, and provides the full range of possible binding sites. A considerable amount of information has been obtained from these studies, including average binding constants and binding site sizes, information on the selectivity of the binding process, and the mechanism(s) by which binding occurs. One disadvantage of using ct-DNA in studies of this type, however, is that its heterogeneous nature makes it unsuitable for X-ray crystallographic or nuclear magnetic resonance (NMR) spectroscopic studies designed to provide precise details about the nature of individual metal/DNA binding interactions. The heterogeneous nature of ct-DNA also makes it unsuitable for mass spectrometric investigations owing to the large number of different ions observed. As a consequence most, if not all, mass spectrometric investigations of DNA and its binding interactions with other molecules have used discrete oligonucleotide sequences generally containing six or more bases or base pairs.

One of the first applications of ESI–MS for studying oligonucleotides was reported in 1988 by Henion and co-workers, who examined a synthetic single-stranded dodecanucleotide [14]. However, it was not until 1993 that the first reports of ESI mass spectra of duplex DNA appeared [15, 16]. Ganem and co-workers reported ion-spray mass spectra of solutions containing the self-complementary oligonucleotides 5′-CCCCGGGG-3′ and 5′-GGTCGACC-3′, after they were annealed in 10 mM ammonium acetate solution [15]. The annealing process consisted of heating the oligonucleotide solutions at 95°C for 5 min, and then allowing them to cool slowly to room temperature. Ions attributable to dsDNA were observed in both cases, however these were of much lower abundance than those arising from single stranded DNA. Even weaker ions assigned to dsDNA were observed when a mass spectrum was obtained of a solution prepared by annealing equimolar amounts of 5′-TTTTTTTT-3′ and 5′-AAAAAAAA-3′. This was attributed to the presence of only two hydrogen bonds between the nucleotides in each of the AT base pairs, whereas the previous dsDNA molecules contained GC base pairs in which the nucleotides are held together by three hydrogen bonds. In more recent experiments where dsDNA has been analysed by ESI–MS, the spray solution has been 100 mM ammonium acetate [17]. Under these conditions and where the temperature of the ionisation source has been kept low ($< 80°C$), almost all of the DNA was present as dsDNA in negative ion mass spectra. While modern ESI instruments provide the user with the ability to "soften" ionisation conditions in order to minimise dissociation of dsDNA (e.g., by optimising/minimising sample cone voltage), it is still important to carefully select the length and base sequence of the oligonucleotides to be used in order to ensure their stability in the source of the mass spectrometer.

Another problem relating to assignment of ions as arising from ssDNA or dsDNA occurs when self-complementary oligonucleotide sequences, such as 5′-CCCCGGGG-3′, are used in mass spectrometric studies. This is because of a fundamental aspect of the ESI process in which multiply charged ions are formed. Mass spectrometers analyse samples on the basis of their mass to charge ratios (m/z). In the case of a single strand of 5′-CCCCGGGG-3′, each ion (1-, 2-, 3- etc.) has the same m/z ratio as the duplex with twice the charge (2-, 4-, 6- *etc*.). This makes it

very difficult in some cases to determine whether specific ions are due to single-stranded DNA (ssDNA) or duplex DNA (dsDNA), or some combination of both, although the absence of odd-numbered ions is highly suggestive that only ssDNA has been detected. It is for this reason that many workers choose to work with duplex DNA prepared by annealing two complementary DNA molecules with different base sequences, and therefore different molecular masses. For example, in their pioneering work, Light-Wahl and co-workers prepared and analysed dsDNA obtained by annealing 5′-CCTTCCTCCCTCTCTCCTCC-3′ (M_r 5826.9) with 5′-GGAGGAGAGAGGGAGGAAGG-3′ (M_r 6410.3) [16]. A low capillary-skimmer interface voltage, and low capillary temperature were used to minimise dissociation of annealed dsDNA molecules. The resulting mass spectrum is shown in Fig. 8.2, and contains ions of medium to high abundance attributable only to dsDNA, as well as other ions of lower abundance from ssDNA. Further analysis of the spectrum showed there were no ions from duplex DNA molecules formed through non-specific homo-dimerisation of a single DNA strand. The absence of such signals was noteworthy, as it provided further evidence that the ESI process was faithfully sampling the analytes present in solution, rather than non-specific complexes formed in the ionisation source.
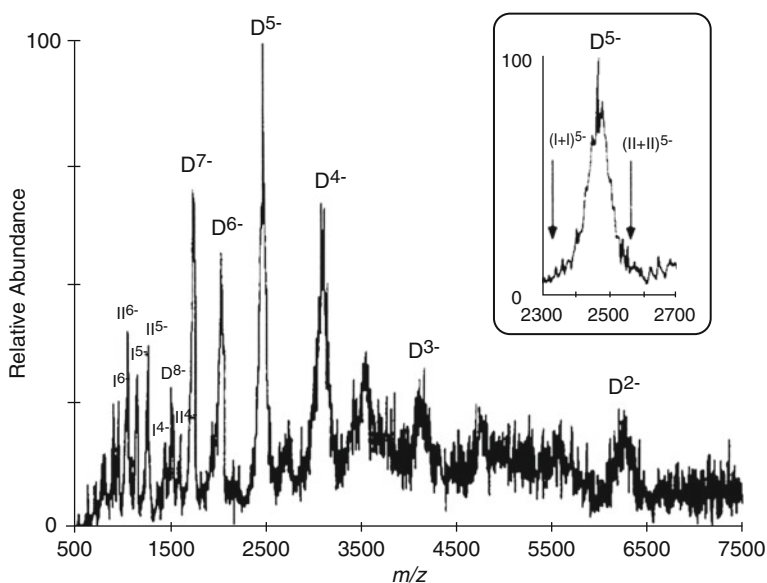
Fig. 8.2 Negative ion ESI mass spectrum of dsDNA prepared by annealing two complementary 20mer ssDNA molecules with different molecular masses. Ions labelled with a D are dsDNA, while ions marked I or II are ssDNA. The *inset* is an expanded view of the spectrum in the vicinity of D^{5-}, showing the absence of ions arising from non-specific homo-dimerisation of ssDNA. Reprinted in part with permission from Light-Wahl KJ, et al., J Am Chem Soc. 1993: 115; 803–804. Copyright 1993 American Chemical Society

The production of several ions corresponding to multiple charge states of the same analyte is an important property of ESI–MS, as it enables quick and accurate estimation of the molecular mass of large biomolecules. However, in the case of the spectrum shown in Fig. 8.2, a molecular mass of $12{,}297 \pm 10$ Da was obtained for the dsDNA molecule, which was considerably higher than the calculated molecular mass of 12,237 Da. This difference was attributed to incomplete desolvation of dsDNA ions formed during the ESI process, or to formation of intermolecular aggregates between the dsDNA and cations present in solution. Both possible explanations serve to illustrate the importance of choosing the correct conditions for preparing and obtaining spectra of dsDNA.

One of the first questions that must be addressed when attempting to acquire high quality ESI spectra of dsDNA is what is the most appropriate buffer to use. Most buffers used in biochemical studies (e.g., phosphate, HEPES, Tris) consist of non-volatile components that are not compatible with mass spectrometry. This problem is now generally overcome through the use of aqueous ammonium acetate solutions, which can be adjusted to the desired pH (typically between 7.0 and 7.5) through addition of either ammonia or acetic acid. The use of aqueous solutions of ammonium acetate has been shown to provide an appropriate amount of electrostatic stabilisation to ensure that dsDNA remains in the duplex form, and to enable efficient generation of both negative and positive ions through proton transfer reactions involving the ammonium and acetate ions. It is essential to choose a concentration of ammonium acetate that enables the structure of dsDNA to be maintained on transfer from solution to the gas phase, but does not result in large quantities of non-specific adducts in which the ammonium cations are bound electrostatically to the negatively charged phosphate groups along the DNA backbone. For the same reason, care must be taken during sample preparation to minimise the concentration of other cations, such as Na^+, K^+, Mg^{2+} and Ca^{2+}, in the DNA sample. This is because the mass spectrometer will detect and provide a separate signal for DNA molecules with different numbers of adducted cations, thereby resulting in a broad envelope of signals instead of a single peak. In addition, the presence of a number of different salt adducts of DNA, instead of just the DNA by itself, effectively reduces the concentration of the species being detected, and therefore results in lower sensitivity.

There are also a number of instrumental parameters which must be optimised to enable the detection of signals arising from free DNA and non-covalent complexes formed with either organic or inorganic molecules. These may vary from instrument to instrument, but generally include the sampling cone voltage and desolvation temperature. Prior to commencing a detailed investigation of non-covalent systems, it is necessary to systematically examine the effect of each of the above parameters to obtain optimum conditions. The conditions selected must be sufficiently energetic to generate a uniform stream of droplets, completely desolvate analyte ions, and minimise formation of non-specific associations between molecules. However, the conditions must not be so energetic that the relatively weak bonds holding together the DNA duplex, or enabling non-covalent binding of drug molecules to DNA, are broken. Fig. 8.3 illustrates the ESI mass spectrum of
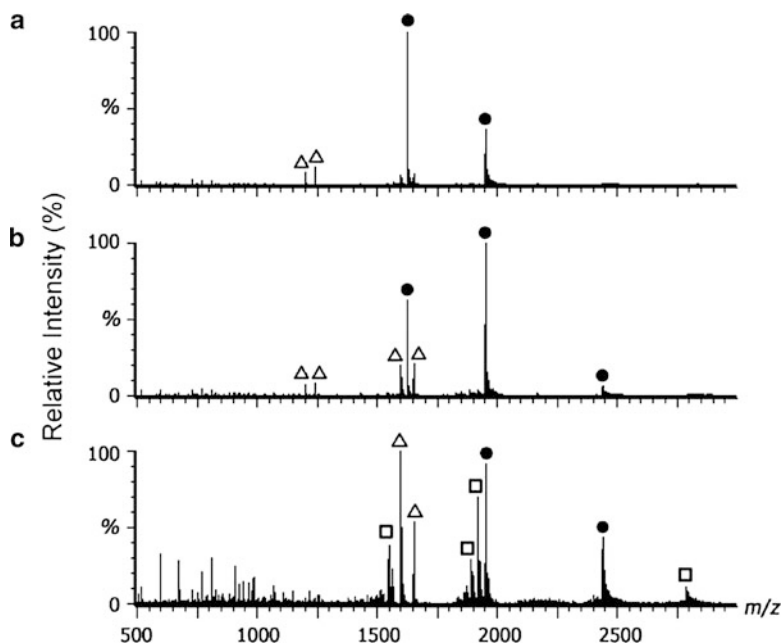
Fig. 8.3 Effect of altering ionisation conditions on the appearance of the negative ion ESI mass spectrum of a solution containing a 16mer dsDNA molecule. Spectra were obtained using a Waters QToF Ultima™ ESI mass spectrometer and the following conditions: (**a**) capillary voltage 2.3 kV, cone voltage 35 V, RF lens 1 voltage 63 V, source temperature 25°C, desolvation temperature 80°C; (**b**) capillary voltage 2.3 kV, cone voltage 150 V, RF lens 1 voltage 63 V, source temperature 25°C, desolvation temperature 80°C; (**c**) capillary voltage 2.3 kV, cone voltage 150 V, RF lens 1 voltage 63 V, source temperature 45°C, desolvation temperature 200°C. (*Bullet*) dsDNA; (*Triangle*) ssDNA; (*Square*) ssDNA – guanine or dsDNA – guanine

a 16mer dsDNA molecule obtained under optimised conditions using a modern ESI–QToF mass spectrometer, as well as the changes to the spectrum caused by altering the ionisation conditions. In Fig. 8.3a the two most abundant ions are the 5- and 6- charge states of the DNA duplex. Two ions of much lower abundance are also present at lower m/z that are assigned to the constituent single strands. These are present either as a result of incomplete annealing of the two strands prior to mass spectral analysis, or due to a small amount of denaturation of the duplex within the mass spectrometer. Increasing the cone voltage from 35 to 150 V (Fig. 8.3b) resulted in a reversal of the relative abundances of the two ions from dsDNA. Furthermore ions of very low abundance attributable to the 4- charge state of the duplex are now also apparent, as well as additional ions from ssDNA. The appearance of the latter ions resulted in a significant decrease in the overall percentage of ions assigned to dsDNA. Fig. 8.3c shows this was exacerbated by further increasing the desolvation temperature to 200°C and also raising the source temperature from 25 to 45°C, with ions assigned to ssDNA now of comparable

abundance to those arising from dsDNA. In addition, new ions are also present in
the spectrum as a result of loss of guanine from either ssDNA or dsDNA molecules.

8.3.2 Quadruplex DNA

Chromosomal DNA is now known to contain a variety of structures in addition to
the well-known B-form double helix. These structures include Z-DNA, hairpins,
bulge regions and quadruplexes [18, 19]. In recent years quadruplex DNA struc-
tures formed from guanine rich sequences (G-quadruplex DNA), such as those in
telomeres have attracted increasing attention. Telomeres are regions found at the
end of chromosomes that do not code for specific proteins, but are instead thought
to be involved in providing protection against DNA damage. In normal somatic
human cells, telomeres undergo shortening every time replication and cell division
occurs. Eventually the telomeres become too short to protect the chromosome,
resulting in apoptosis and cell death. In contrast, approximately 85% of all cancer
cells are able to maintain the length of their telomeric sequences by increasing the
level of activity of the enzyme telomerase, thereby rendering these cells immortal.
It is therefore not surprising that there is growing interest in developing different
approaches to inhibiting the action of telomerase. One such approach involves
synthesising small molecules that can inhibit telomerase, for example, by binding
to and stabilising G-quadruplex DNA structures, as this is believed to affect the
activity of the enzyme [20–26].

The basic structural unit of G-quadruplex DNA is the guanine tetrad (G-tetrad),
which is comprised of four guanine bases held together in a square planar arrange-
ment by eight Höögsteen hydrogen bonds (Fig. 8.4a). Within a G-quadruplex DNA
region, several guanine tetrads are stacked on top of each other to give a structure
that is stabilised by the presence of monovalent cations such as sodium or potas-
sium. The latter coordinate to the carbonyl groups of guanines in adjacent G-tetrads,
which are directed towards the interior of the structure. In a quadruplex DNA
structure containing n G-tetrads there is therefore expected to be a total of n-1
monovalent cations. G-quadruplex structures can be formed in a variety of ways
from one, two or four DNA strands. These include the parallel tetrameric
G-quadruplex structure shown in Fig. 8.4b, and the antiparallel structure involving
two DNA strands shown in Fig. 8.4c. In addition, it is possible for quadruplex DNA
to form as a result of the folding of a single DNA strand on itself, as shown in
Fig. 8.4d.

There has been growing recognition that ESI–MS can be used to characterise
quadruplex DNA, and provide information about its interactions with potential drug
molecules. One of the first studies to describe the use of ESI–MS for examining the
interactions of small molecules with G-quadruplex DNA was that of Brodbelt and co-
workers, who compared the binding of several organic compounds, including *N,N′-
bis*(2-morpholinylpropyl)-3,4,9,10-perylenetetracarboxylic acid diimide (Tel01), dis-
tamycin A and diethylthiocarbocyanine iodide (DTC), to dsDNA and the DNA
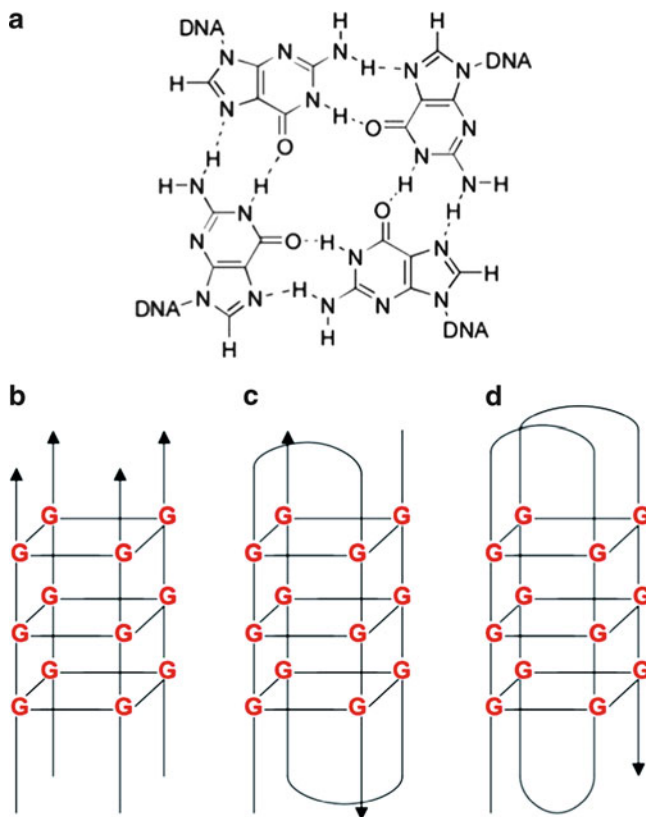
Fig. 8.4 (**a**) Structure of a G-tetrad. (**b**)–(**d**) Schematic illustrations of different G-quadruplex structures formed from four, two and one DNA strands, respectively. Reprinted under BioMed Central Open Access Charter from Nelson et al., Cell and Chromosome. 2004:3

quadruplex [d(TTGGGGGT)]$_4$ [27]. By examining dissociation patterns of ions arising from non-covalent complexes in tandem mass spectrometry experiments, evidence was obtained that supported the results of previous solution studies which suggested that Tel01 interacts with G-quadruplex DNA via stacking interactions with a G-tetrad at the end of the molecule, whereas both distamycin and DTC bind to the grooves along the sides of the quadruplex.

In order to obtain high quality spectra of four-stranded G-quadruplex DNA, we have found it is necessary to use slightly harsher conditions than those used for running dsDNA. This is achieved by increasing both the cone voltage and desolvation temperature. While this does not appear to affect the stability of the G-quadruplex itself, the use of more energetic conditions was found to place restrictions on the types of metal complexes whose binding interactions could be studied (see later). Fig. 8.5 shows the ESI mass spectra of three tetrameric parallel G-quadruplex DNA
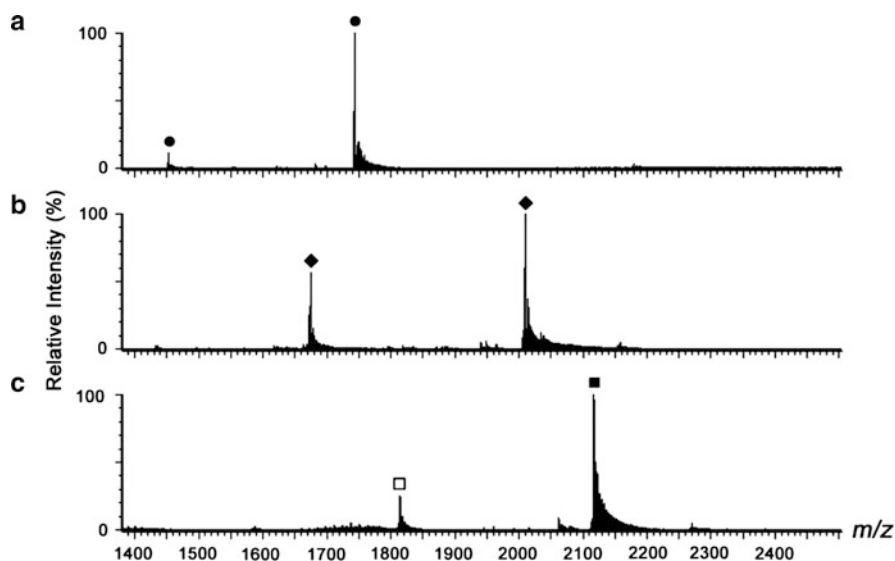
Fig. 8.5 Negative ion ESI mass spectra of quadruplex DNA obtained using a Waters QToF Ultima™ ESI mass spectrometer. (**a**) Q4; (**b**) Q5; (**c**) Q7. (*Bullet*) Q4 + 3 NH_4^+; (*Diamond*) Q5 + 4 NH_4^+; (*Square*) Q7 + 5 NH_4^+; (*Filled square*) Q7 + 6 NH_4^+

molecules with different lengths, obtained under optimal conditions. The base sequences of the three quadruplexes were: Q4 $(TTGGGGT)_4$; Q5 $(TTTGGGGGT)_4$; and Q7 $(TTGGGGGGGT)_4$.

Figure 8.5a shows the spectrum of the smallest quadruplex, Q4, consists of ions at m/z 1452.6 and 1743.4. These are assigned to $[Q4 + 3NH_4^+ - 9H^+]^{6-}$ and $[Q4 + 3NH_4^+ - 8H^+]^{5-}$, respectively. Both contain ammonium ions as a result of spectra being obtained in ammonium acetate solution, and the requirement for monovalent cations to be present within the quadruplex structure in order for it to remain stable. In contrast ESI mass spectra do not show ions from adducts in which ammonium ions are bound to dsDNA. The number of ammonium cations present in both ions is one less than the maximum number of G-tetrads. This was a generally observed phenomenon, and provides strong support for the conclusion that the quadruplex structures were successfully transferred from solution to the gas phase. For example, the most abundant ions present in the mass spectrum of Q5 (Fig. 8.5b) are assigned to $[Q5 + 4NH_4^+ - 10H^+]^{6-}$ and $[Q5 + 4NH_4^+ - 9H^+]^{5-}$. However, while the most abundant ions in the spectrum of Q7 (Fig. 8.5c) are attributable to $[Q7 + 6NH_4^+ - 12H^+]^{6-}$, there are also ions of medium abundance at m/z 1814.0 that are assigned to $[Q7 + 5NH_4^+ - 12H^+]^{7-}$, containing one less than the expected number of ammonium ions. This suggests that either one ammonium ion dissociated in the mass spectrometer or that a "slipped" structure was present in which the seven guanines in each of the four strands were not in perfect alignment [27].

8.4   Mass Spectrometry of Metallointercalators

ESI–MS is now a routine tool for characterisation of metal complexes, where it is principally employed to provide confirmation of proposed structures. This can generally be accomplished, provided the metal complex has sufficient kinetic and thermodynamic stability. It is not a coincidence that most DNA binding studies involving metallointercalators have centred on complexes of ruthenium(II), rhodium(III) and platinum(II), as the low spin d^6 and d^8 configurations of these metal ions are amongst the most kinetically stable known. Most metallointercalators also incorporate exclusively bidentate or sometimes tridentate ligands to enhance thermodynamic stability relative to complexes containing similar unidentate ligands. Much research has been devoted to altering the structure of simple bidentate ligands such as bipyridine and phenanthroline present in metal complexes, in order to confer greater affinity and/or selectivity towards DNA.

Figure 8.6 shows the positive ion ESI mass spectra of two metal complexes whose structures illustrate some of the approaches taken to modifying the structures of metal complexes in order to enhance DNA binding properties. The first of the complexes is [Ru(bpy)$_2$(dppz)](PF$_6$)$_2$ (dppz = dipyrido[3,2-a:2′,3′-c]phenazine) which contains the extended planar aromatic dppz ligand shown to enhance the ability of a metal complex to bind to duplex DNA by intercalation. The most abundant ion in the spectrum of this complex (Fig. 8.6a) is that at m/z 348.3, which is assigned to the divalent molecular ion. The only other feature of this spectrum are ions of very low
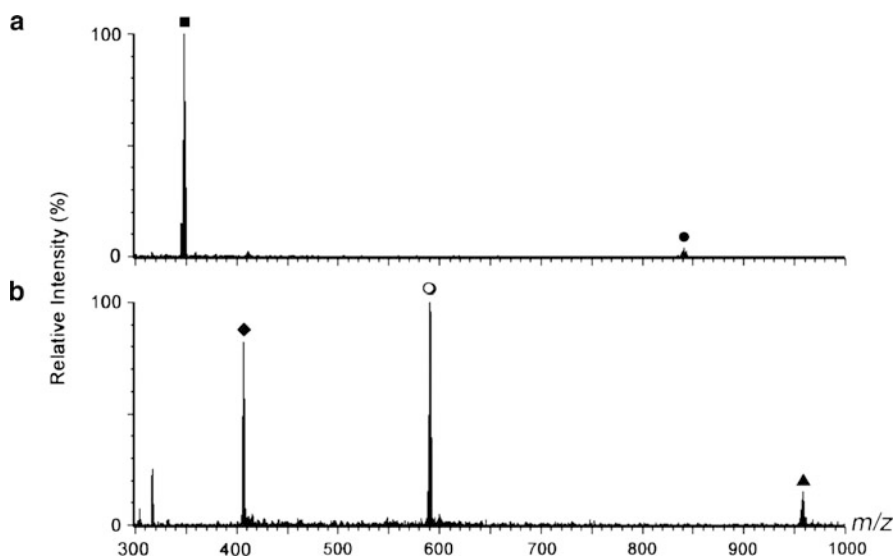
Fig. 8.6 Positive ion ESI mass spectra of: (**a**) [Ru(bpy)$_2$(dppz)](PF$_6$)$_2$ and (**b**) [{Ru(dpq)$_2$}$_2$μ-(phen-3-SOS-3-phen)](PF$_6$)$_4$. (*Square*) [Ru(bpy)$_2$(dppz)]$^{2+}$; (*Bullet*) {[Ru(bpy)$_2$(dppz)]$^{2+}$ + PF$_6^-$}$^+$; (*Diamond*) [{Ru(dpq)$_2$}$_2$μ-(phen-3-SOS-3-phen)]$^{4+}$; (*Circle*) {[{Ru(dpq)$_2$}$_2$μ-(phen-3-SOS-3-phen)]$^{4+}$ + PF$_6^-$}$^{3+}$; (*Triangle*) {[{Ru(dpq)$_2$}$_2$μ-(phen-3-SOS-3-phen)]$^{4+}$ + 2 PF$_6^-$}$^{2+}$

abundance at m/z 841.1, which are assigned to the ion pair $\{[Ru(bpy)_2(dppz)]^{2+} + PF_6^-\}^+$. Signals attributable to ion pairs are common features of ESI mass spectra of metal complexes containing large anions such as PF_6^-, ClO_4^- and $CF_3SO_3^-$, and in many cases are present in significant abundance. This is further exemplified by the spectrum of the diruthenium complex $[\{Ru(dpq)_2\}_2\mu\text{-(phen-3-}SOS\text{-3-phen)}](PF_6)_4$ (dpq = dipyrido[3,2-d:2′,3′-f]quinoxaline) shown in Fig. 8.6b. The most abundant ions present in this spectrum are those at m/z 590.7, which are assigned to the ion pair $\{[\{Ru(dpq)_2\}_2\mu\text{-(phen-3-}SOS\text{-3-phen)}]^{4+} + PF_6^-\}^{3+}$. This spectrum also contains ions of low abundance at m/z 958.3 assigned to another ion pair, $\{[\{Ru(dpq)_2\}_2\mu\text{-(phen-3-}SOS\text{-3-phen)}]^{4+} + 2PF_6^-\}^{2+}$, as well as ions of high abundance at m/z 406.8 assigned to $[\{Ru(dpq)_2\}_2\mu\text{-(phen-3-}SOS\text{-3-phen)}]^{4+}$. Dinuclear complexes have attracted increasing interest in recent years, as researchers look for new ways to enhance affinity and selectivity for different DNA structures [28–33].

In general we have observed that metallointercalators containing ruthenium(II), platinum(II) or nickel(II) centres undergo very little fragmentation either when they are free in solution or bound to dsDNA. However, ESI mass spectra of solutions containing dsDNA and iron(II) or zinc(II) metal complexes show evidence of significant fragmentation as a result of the lower stability of their metal-nitrogen bonds.

8.5 Interactions Between Metallointercalators and Duplex DNA

To the best of our knowledge, the first report of the use of ESI–MS for examining the binding of metallointercalators to duplex DNA was that of Gross and co-workers [34]. These authors prepared both 6mer and 12mer duplexes using self-complementary DNA molecules, with different sequences (AT-rich or GC-rich) chosen in order to enable molecules with different binding mechanisms to exhibit their preferred modes of interaction. While most of the compounds examined in this study were classical organic minor groove binding agents or intercalators, the metal complexes shown in Fig. 8.7 were also examined. These include several sterically-hindered metalloporphyrins and $[Ru(12S4)(dppz)]^{2+}$ (12S4 = 1,4,7,10-tetrathiate-tradecane). All were shown to have mixed binding modes and form non-covalent complexes with DNA that could be characterised by ESI–MS.

Experiments performed using five 6mer duplexes with different base sequences demonstrated that the metalloporphyrins shown in Fig. 8.7 exhibit a preference for AT-rich DNA [34]. This result suggests that the metalloporphyrins were functioning as minor groove binding agents. In contrast, it was revealed that $[Ru(12S4)(dppz)]^{2+}$ had a clear preference for binding to the sequence $d(GCGCGC)_2$ over other duplex 6mers with two or more AT base pairs. This suggests that the preferred mode of DNA binding for the ruthenium complex is intercalation. Each of the above studies was performed using a dsDNA:drug ratio of 1:2, which resulted in many cases in relatively low overall levels of non-covalent complex formation. Competition experiments involving a single dsDNA molecule and two different

X = Cu^{2+}, Fe^{2+} or Mn^{2+}
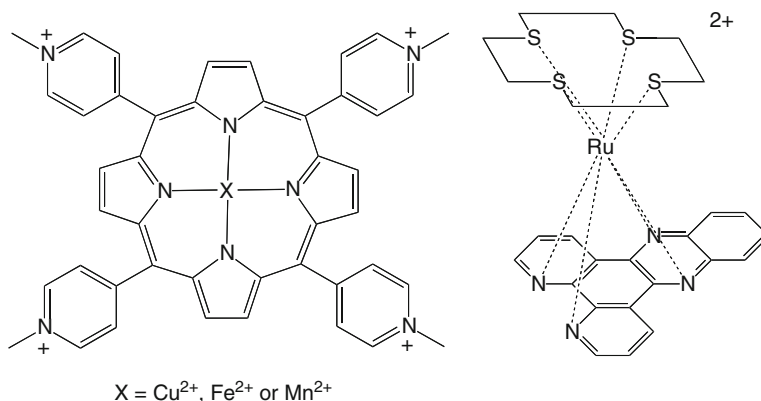
Fig. 8.7 Structures of metal complexes whose DNA binding properties were investigated using ESI–MS by Gross and co-workers [34]

[Ru(phen)$_3$]$^{2+}$ [Ru(phen)$_2$(dpq)]$^{2+}$ [Ru(phen)$_2$(dpqC)]$^{2+}$ [Ru(phen)$_2$(dppz)]$^{2+}$
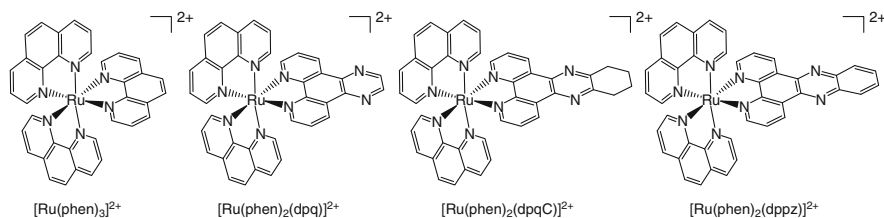
Fig. 8.8 Structures of some ruthenium metallointercalators

metal complexes were also performed, and shown to be a potential method for assessing the relative DNA binding affinities.

The dppz ligand is the best-known member of a family of heterocycles that have been incorporated into octahedral and square planar metal complexes in order to modify their DNA binding properties. The parents of this family of ligands are 2,2′-bipyridine (bpy) and 1,10-phenanthroline (phen), while other members include dpqC (dipyrido[3,2-*a*:2′,3′-c](6,7,8,9-tetrahydro)phenazine), terpy (2,2′:6′,2″-terpyridine) and phi (phenanthrenequinone). It was shown in the early 1970s that square planar platinum(II) complexes containing the terpy ligand could act as intercalators [35], while the tetrahedral [Cu(phen)$_2$]$^{2+}$ participated in groove binding interactions [36]. Subsequently an enormous amount of work has been published examining the DNA binding properties of octahedral complexes of inert metal ions such as ruthenium(II) [37–39]. In view of the large amount of comparative data available from studies performed using other techniques, it was decided to initially use ESI–MS to examine the DNA binding properties of the ruthenium complexes shown in Fig. 8.8.

Since each of the complexes had a similar overall charge, size and shape, as well as two identical phenanthroline ligands, it was expected that the degree to which

they were attracted to the negatively charged phosphate backbone of DNA would also be similar. Any differences in DNA binding affinity that were detected would then be attributable to the variation in the third ligand present in the coordination sphere. We also set out to determine whether the mass spectrometric technique could potentially reveal differences in binding mode by examining the interactions of each metal complex with the three different DNA molecules (D1 - D3) shown below. It was anticipated that the greater GC content of D1 and D2 would make them more attractive to metal complexes which prefer to bind to DNA by intercalation, whereas the AT-rich D3 would facilitate binding by those complexes that prefer to bind in the DNA minor groove [28–33].

D1 d(CCTCGGCCGGCCGACC/GGTCGGCCGGCCGAGG)
D2 d(CCTCATGGCCATGACC/GGTCATGGCCATGAGG)
D3 d(CCTCAAAATTTTGACC/GGTCAAAATTTTGAGG)

In our initial studies we obtained negative ion ESI mass spectra of solutions containing a wide range of metal:DNA ratios. Fig. 8.9 shows the results obtained using solutions containing $[Ru(phen)_2(dpq)]^{2+}$:D2 ratios ranging from 1:1 up to 30:1. Fig. 8.9a shows the spectrum of a solution containing equimolar quantities of the ruthenium complex and D2. The most abundant ions in this spectrum are those at m/z 1626.5 and 1951.9, which are assigned to $[D2-6H]^{6-}$ and $[D2-5H]^{5-}$, respectively, suggesting that there is still a large amount of free DNA in solution. In addition, ions of lower abundance are present at m/z 1750.9 and 2100.4, which are attributable to a non-covalent complex consisting of a single intact $[Ru(phen)_2(dpq)]^{2+}$ bound to D2. Increasing the Ru:D2 ratio to 5:1 resulted in the abundance of these ions increasing, and the appearance of new ions attributable to a non-covalent complex (or complexes) consisting of two $[Ru(phen)_2(dpq)]^{2+}$ bound to D2. Fig. 8.9 also shows that further raising the Ru:D2 ratio resulted in the appearance of ions assigned to non-covalent complexes containing even greater numbers of $[Ru(phen)_2(dpq)]^{2+}$ bound to D2, and the simultaneous disappearance of ions assigned to free DNA. At the highest Ru:D2 ratio examined the most abundant ions observed were those assigned to non-covalent complexes containing three and four $[Ru(phen)_2(dpq)]^{2+}$ molecules. The signal to noise ratio of Fig. 8.9e is noticeably poorer than that of the other spectra, most likely as a result of interference to the ESI process caused by the extremely high electrolyte concentration present in the original solution. It should also be noted that the high concentrations of metal complexes in some of these solutions might encourage non-specific associations in the ESI source.

One method for simply illustrating the changes in solution composition revealed by the above spectra involves the use of relative ion abundances. These are calculated by combining the absolute intensities of all ions assigned to a specific non-covalent complex in a given spectrum, and converting them to relative abundances by dividing by the combined intensity of all ions present. The resulting relative abundances are subsequently plotted as a function of metal complex:DNA ratio. Using this method the information contained in Fig. 8.9 was used to generate the plots of relative abundance shown in Fig. 8.10.
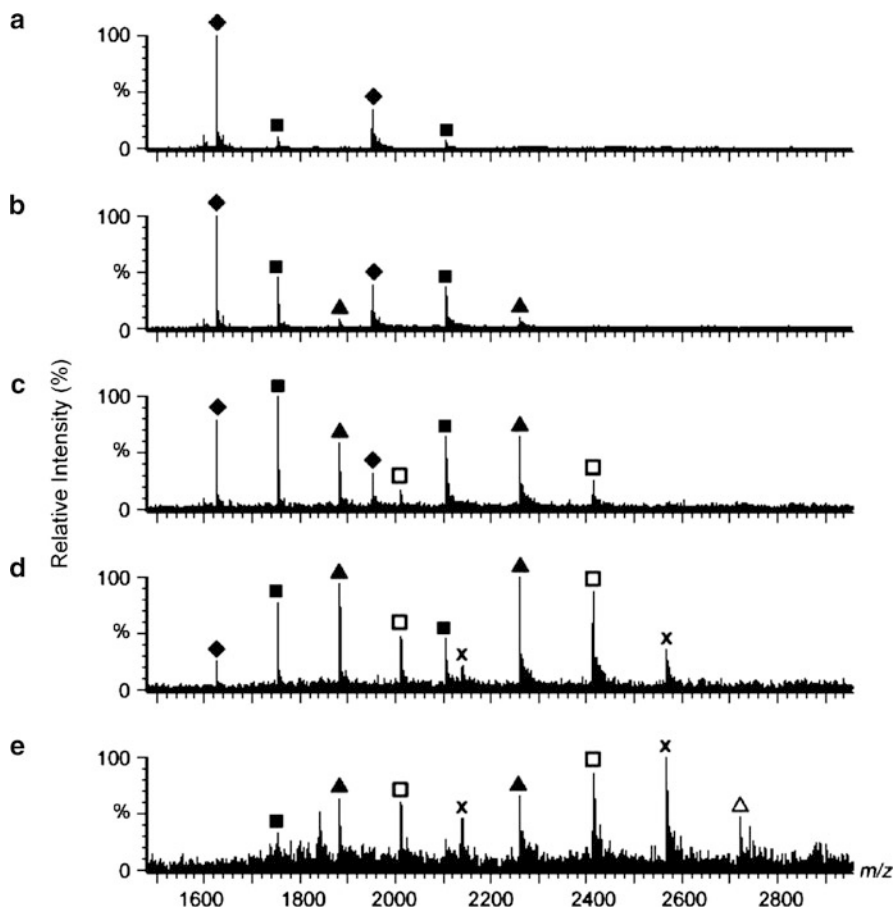
Fig. 8.9 Negative ion ESI mass spectra of solutions containing different $[Ru(phen)_2(dpq)]^{2+}$:D2 ratios: (**a**) Ru:D2 = 1:1; (**b**) Ru:D2 = 5:1; (**c**) Ru:D2 = 10:1; (**d**) Ru:D2 = 20:1; Ru:D2 = 30:1. (*Diamond*) D2; (*Filled square*) D2 + 1$[Ru(phen)_2(dpq)]^{2+}$; (*Triangle*) D2 + 2$[Ru(phen)_2(dpq)]^{2+}$; (*Square*) D2 + 3$[Ru(phen)_2(dpq)]^{2+}$; (*Times symbol*) D2 + 4$[Ru(phen)_2(dpq)]^{2+}$

Figure 8.10 clearly shows the relative abundances of individual non-covalent complexes increasing, reaching a maximum value, and subsequently decreasing as more highly substituted non-covalent complexes become dominant in solution. The variations in relative abundances illustrated in Fig. 8.10 strongly resemble concentration profiles for stepwise complex formation equilibria of transition metal complexes. This provides support for the conclusion that the ESI technique is faithfully reflecting variations in solution composition. Further support for this conclusion is provided by the significant variations in affinity towards a given DNA molecule displayed by different metal complexes such as those shown in Fig. 8.8. These can be seen by directly comparing the abundances of ions seen in spectra of solutions containing identical ratios of different metal complexes and DNA, or through an
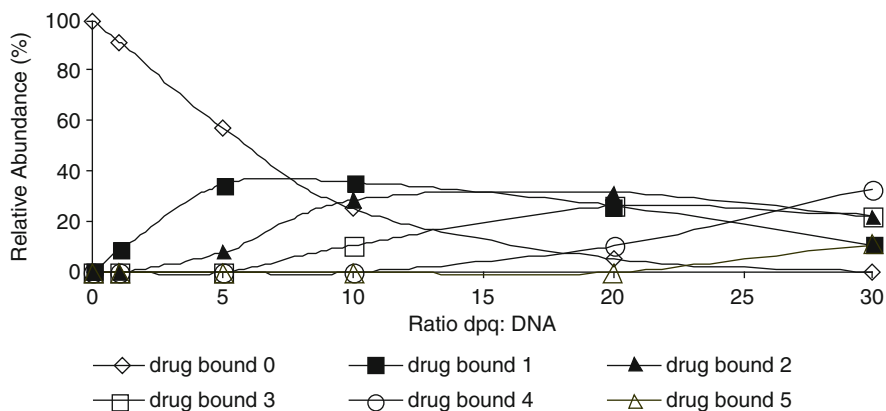
Fig. 8.10 Relative abundances of free DNA and non-covalent complexes in the spectra shown in Fig. 8.9. (*Diamond*), free D2; (*Filled Square*) D2 + 1[Ru(phen)$_2$(dpq)]$^{2+}$; (*Filled triangle*) D2 + 2 [Ru(phen)$_2$(dpq)]$^{2+}$; (*Square*) D2 + 3[Ru(phen)$_2$(dpq)]$^{2+}$; (*Circle*) D2 + 4[Ru(phen)$_2$(dpq)]$^{2+}$; (*Triangle*) D2 + 5[Ru(phen)$_2$(dpq)]$^{2+}$
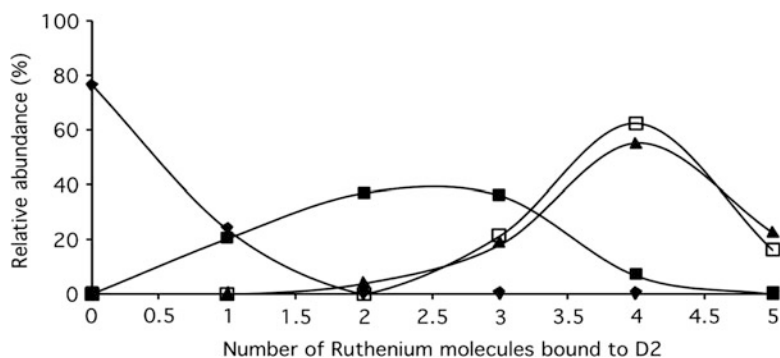
Fig. 8.11 Relative abundances of non-covalent complexes present in solutions containing a 6:1 ratio of ruthenium complexes and D2. (*Diamond*) [Ru(phen)$_3$]$^{2+}$ (*Filled square*) [Ru(phen)$_2$(dpq)]$^{2+}$ (*Triangle*) [Ru(phen)$_2$(dpqC)]$^{2+}$ (*Square*) [Ru(phen)$_2$(dppz)]$^{2+}$ [40]

examination of relative abundances derived from such spectra. For example, Fig. 8.11 shows the relative abundances of different non-covalent complexes present in solutions containing a 6:1 ratio of the ruthenium complexes shown in Fig. 8.8 and the DNA duplex D2. The Fig. 8.11 shows that the most abundant ions present in the solutions containing [Ru(phen)$_2$(dpqC)]$^{2+}$ and [Ru(phen)$_2$(dppz)]$^{2+}$ were those corresponding to non-covalent complexes consisting of four ruthenium molecules bound to D2. In contrast, the relative abundance of analogous non-covalent complexes in the spectra of solutions containing either of the other two ruthenium complexes was either very low or zero. This clearly suggests that [Ru(phen)$_2$(dpqC)]$^{2+}$ and [Ru(phen)$_2$(dppz)]$^{2+}$ have significantly higher overall

binding affinities towards D2 than either $[Ru(phen)_2(dpq)]^{2+}$ or $[Ru(phen)_3]^{2+}$. Further analysis of Fig. 8.11 reveals that the relative abundance of non-covalent complexes containing two or three ruthenium molecules bound to D2 is much greater in the case of $[Ru(phen)_2(dpq)]^{2+}$ than $[Ru(phen)_3]^{2+}$. This suggests that of these two ruthenium molecules the former has a significantly higher affinity towards D2. Relative abundances obtained from ESI mass spectra can therefore be used to derive orders of relative binding affinities for metal complexes. In the case of the ruthenium complexes shown in Fig. 8.8, overall affinity towards D2 increased in the following manner: $[Ru(phen)_3]^{2+} < [Ru(phen)_2(dpq)]^{2+} < [Ru(phen)_2(dpqC)]^{2+} \sim [Ru(phen)_2(dppz)]^{2+}$. Such a variation clearly suggests that varying the third ligand in the coordination sphere of the metal ion can have a major influence on overall binding affinity.

Further support for the conclusion that ESI–MS is a valid technique for analysing the composition of solutions containing non-covalent complexes was provided by a study which compared orders of relative DNA binding affinity determined by ESI–MS for two series of metal complexes, with those obtained using other established techniques for investigating these types of systems. Absorption spectrophotometry, circular dichroism (CD) spectroscopy and fluorescence spectroscopy have all been widely used in the past to qualitatively determine the extent of non-covalent complex formation between metal complexes and ct-DNA, and in many instances also provide overall binding constants. For example, fluorescence spectroscopy was used to obtain overall binding constants of 3.2×10^6 and $1.7 \times 10^6\,M^{-1}$ for Δ and Λ-$[Ru(phen)_2(dppz)]^{2+}$, respectively [41]. These values are significantly greater than those determined by a similar method for Δ and Λ-$[Ru(phen)_3]^{2+}$ with ct-DNA, which were 9×10^3 and $1.1 \times 10^4\,M^{-1}$, respectively [42], and therefore in accordance with our results which were obtained using racemic metal complexes.

A better comparison, however, would involve binding constants determined from experiments performed using the same DNA molecule as that used in the mass spectrometric experiments. It was therefore decided to use an absorption spectrophotometric titration method to determine overall binding constants for the interaction of nine complexes belonging to the series $[Ru(phen)_2L]^{2+}$ and $[RuL'_2(dpqC)]^{2+}$ (L and L$'$ = bidentate heterocyclic ligand) with D2 [43]. These were found to provide orders of relative binding affinity that showed a good correlation with those determined by ESI–MS. In addition, orders of binding affinity based on changes in the melting temperature of D2 caused by addition of the ruthenium complexes, and alterations to the CD spectrum of D2, were also in general agreement with those obtained by the mass spectrometric method. Further validation of the use of ESI–MS came from a comparison of the ability of analogous nickel and ruthenium complexes with the same general formula $[M(phen)_2L]^{2+}$ (M = Ni or Ru: L = phen, dpq, dpqC, dppz) to bind to D2 [44]. Both CD spectroscopy and ESI–MS showed that replacing nickel in a metal complex by ruthenium resulted in a small, but measurable, increase in binding affinity that was most evident for the complexes with L = dpqC or dppz. This conclusion was also supported by the results of transcription inhibition assays and gel electrophoresis studies performed with both series of metal complexes and different DNA molecules.

These studies show that ESI–MS can be used to provide a valid assessment of the differences in DNA binding affinities between metallointercalators. This can be done either indirectly, through comparison of mass spectral data obtained from solutions containing different metal complexes and a common DNA molecule, or directly from ESI mass spectra of solutions containing two or more metal complexes and a single type of duplex DNA. For example, Fig. 8.12 shows the mass spectrum of a solution containing a 3:3:1 ratio of $[Ru(phen)_2(dpq)]^{2+}$, $[Ru(phen)_2(dppz)]^{2+}$ and D2. The total abundance of ions assigned to non-covalent complexes consisting of one or more $[Ru(phen)_2(dppz)]^{2+}$ bound to DNA is clearly greater than that for the corresponding ions containing $[Ru(phen)_2(dpq)]^{2+}$. In addition, the spectrum also reveals the presence of non-covalent complexes containing one or more of both types of ruthenium molecules bound to D2.

ESI–MS can also be used to provide information on the DNA sequence selectivity of a specific metal complex. This can be accomplished as shown in Fig. 8.13,
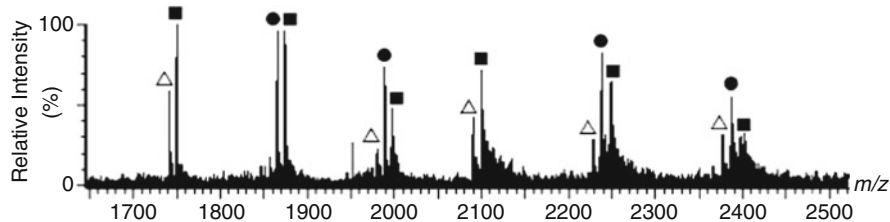
Fig. 8.12 Negative ion ESI mass spectrum of a solution containing a 3:3:1 ratio of $[Ru(phen)_2(dpq)]^{2+}$: $[Ru(phen)_2(dppz)]^{2+}$:D2. (*Triangle*) D2 + $x[Ru(phen)_2(dpq)]^{2+}$; (*Square*) D2 + $x[Ru(phen)_2(dppz)]^{2+}$; (*Bullet*) D2 + one or more of both ruthenium molecules
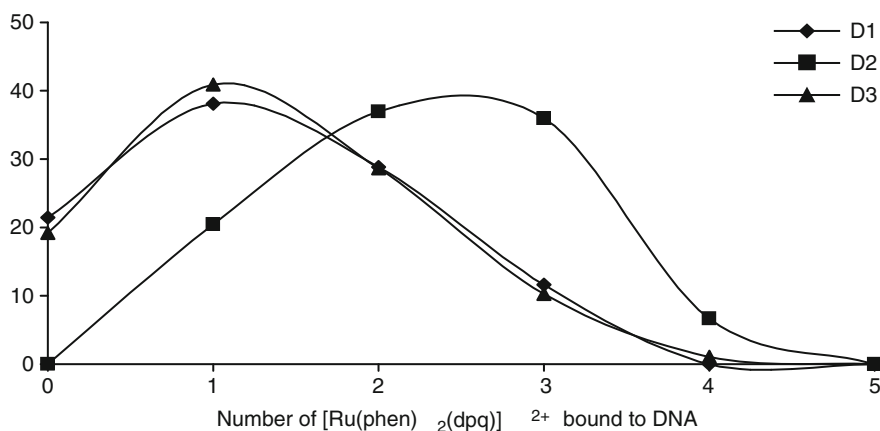
Fig. 8.13 Relative abundances of non-covalent complexes present in solutions containing a 6:1 ratio of $[Ru(phen)_2(dpq)]^{2+}$ and different oligonucleotides [40]

by plotting the relative abundances of ions from solutions containing the same ratio of the metal complex and DNA molecules with different base sequences. Figure 8.13 shows that the relative abundance of non-covalent complexes with DNA containing three bound $[Ru(phen)_2(dpq)]^{2+}$ molecules was significantly greater when the DNA duplex involved was D2, than when it was either D1 or D3. This was a somewhat surprising result, as it was anticipated that the greater number of GC base pairs in D1 might facilitate intercalative interactions with the dpq ligand. However, $[Ru(phen)_2(dppz)]^{2+}$, which contains the even more strongly intercalating dppz ligand, also did not show a preference for binding to D1, but instead showed slightly more extensive binding to D2.

There are many methods that can be used to provide information on relative DNA binding affinities for metallointercalators. However, no other technique can as readily as ESI–MS also afford the number, relative amounts, and stoichiometry of the non-covalent complexes present in solutions containing these molecules. For example, no other technique can easily provide definitive evidence for the presence of non-covalent complexes containing more than one type of metal complex bound to DNA, as is apparent after inspection of Fig. 8.12. This is because of the limited type of information most other techniques provide. For example, the absorption spectrophotometric method usually involves monitoring the effect of adding increasing amounts of DNA on peaks present in the absorption spectrum of a metallointercalator. While the position and intensity of the absorption bands may change in such a way as to provide clues as to how the metallointercalator is interacting with the duplex, there is no change in the number of absorption bands, nor is there any other change that can be readily analysed to deduce the number of non-covalent complexes present in a solution with a specific metal:DNA ratio. Similarly, fluorescence and CD spectra, which have also been widely used to examine the interactions of metallointecalators with duplex DNA, do not give multiple signals that can be assigned to specific non-covalent complexes in the same way as ESI–MS. In addition to this advantage, few techniques also offer the speed and sensitivity of mass spectrometric methods of analysis, making the latter ideal for high throughput screening of DNA-binding drugs. While there have not yet been any reports of binding constants for metallointercalator/DNA interactions determined on the basis of ESI–MS data, these have been measured for several organic compounds that bind to DNA and shown to be similar to those obtained for the same systems by fluorescence spectroscopy [45].

While there are therefore a number of advantages in using ESI–MS to examine metallointercalator/DNA systems, there are some drawbacks that the technique suffers in relation to other methods. One of these is that ESI–MS cannot directly be used to identify which of the DNA bases along a duplex DNA molecule a metallointercalator is directly interacting with. This can, however, be accomplished quite simply in the case of metal complexes that bind covalently to DNA. A number of groups have shown how it is possible to take advantage of the fact that the presence of the metal complex shields nearby phosphodiester bonds from enzymatic hydrolysis, and use various phosphodiesterases to degrade metal/DNA complexes into a series of fragments that can be identified by mass spectrometry

[46–48]. The latter include free nucleotides or nucleosides, depending on the enzymes used, as well as a fragment consisting of the metal complex still attached to one or two nucleotides or nucleosides, which can then be identified from its total mass. Unfortunately it is likely that in most cases the non-covalent interactions that bind metallointercalators to duplex DNA will not be strong enough to survive enzymatic hydrolysis, rendering this method unsuitable for identifying binding sites. One method of solving this problem would involve the use of a chemical cross-linking agent to also covalently attach the metallointercalator to nearby DNA bases. Alternatively if the metallointercalator was to bind sufficiently strongly to a DNA molecule, it might also be able to shield those nucleotides it was interacting with from enzymatic hydrolysis. Support for this idea comes from a recent study in which a large antibiotic molecule was able to shield regions of DNA to which it was non-covalently bound from enzymatic attack [49]. In this case the central aglycone region of the antibiotic participated in intercalative interactions with a duplex DNA molecule, while two trisaccharide side-chains attached to the aglycone were also involved in a number of additional non-covalent interactions, resulting in a very strong overall binding interaction.

Conventional ESI–MS also cannot distinguish whether a metal complex is bonding to duplex DNA primarily by intercalation, through a simple electrostatic mechanism, or via hydrogen bonding and other dipole–dipole interactions. In the absence of an X-ray structure, the most definitive methods for establishing whether a metal complex interacts with duplex DNA primarily by intercalation are NMR spectroscopy, and techniques that can detect the resulting lengthening of the double helical molecule, such as relative viscosity measurements [42]. Another technique that may prove to be useful for analysing the binding mode(s) used by metal complexes with duplex DNA is ion mobility mass spectrometry (IMMS).

8.6 Interactions Between Metallointercalators and Quadruplex DNA

During the past 10 years a number of research groups have used ESI–MS to investigate the binding of small organic molecules to quadruplex DNA [27, 50–55]. However, it was not until recently that the first report appeared describing the use of this technique, along with CD spectroscopy, to characterise analogous interactions involving metal complexes [56]. ESI–MS was used to examine solutions containing the tetrameric parallel quadruplex $(TTGGGGGT)_4$ (Q5), and either the octahedral ruthenium complexes shown in Fig. 8.8, or one of several square planar platinum(II) complexes including $[Pt(5,6-Me_2phen)(S,S-dach)]^{2+}$ as well as several others with the general formula $[Pt(en)L]^{2+}$, when en = 1,2-ethanediamine and L = 1,10-phenanthroline or one of several methylated phenanthroline derivatives. Both types of metal complexes formed non-covalent complexes with Q5 that

were sufficiently stable to enable their detection. In every case the resulting ions consisted of one or more intact molecules of the metal complex, and four ammonium ions, bound to DNA. The observation that four ammonium ions were always present strongly suggests that the complexation event does not affect the intrinsic G-quadruplex structure of Q5.

When solutions containing octahedral nickel(II) complexes as well as Q5 were examined, ions attributable to non-covalent complexes consisting of the intact metal complex bound to DNA were either of very low abundance or not detectable. Instead the spectra of these solutions contained ions of medium to high abundance consisting of fragments of the initial nickel complexes bound to Q5. This was a surprising result in view of the absence of any evidence for fragmentation occurring to a significant extent when spectra were obtained of solutions containing the same nickel complexes and D2 [44]. It was concluded that the combination of slightly lower thermodynamic stability of the nickel(II) complexes, compared to that of similar ruthenium(II) or platinum(II) complexes, and slightly harsher ionisation conditions employed to obtain optimal mass spectra of Q-DNA, was responsible for fragmentation occurring. Consistent with this, experiments in which non-covalent ions assigned to $\{[\text{Ni}(\text{phen})_3]^{2+} + 4 \text{ NH}_4^+ + \text{Q1}-10\text{H}^+\}^{4-}$ were subjected to collision-induced dissociation, resulted in fragmentation occurring initially through loss of a phenanthroline ligand [56]. When the experiment was performed using ions assigned to the analogous non-covalent complex containing $[\text{Ru}(\text{phen})_3]^{2+}$, dissociation was not detected until much higher collision energies were used, and was found to involve initial loss of an ammonium ion.

The above observations provide a sobering reminder that ESI–MS might not be as widely applicable as previously hoped. This was confirmed when spectra of solutions containing $[\text{Fe}(\text{phen})_3]^{2+}$ and D2 were obtained, and found to contain ions of roughly equal abundance assigned to intact iron complexes bound to duplex DNA, and those in which only fragments of the initial metal complex were non-covalently attached. In the case of solutions containing $[\text{Zn}(\text{phen})_3]^{2+}$ and D2, the only non-covalent ions detected were those containing fragments of the zinc complex [56].

Talib et al. showed that solutions containing the same ratio of different ruthenium complexes and Q5 gave spectra that were similar in appearance [56]. For example, Fig. 8.14 shows spectra of solutions containing a 40:1 ratio of several ruthenium(II) complexes and Q5, as well as of Q5 itself. For each of the solutions containing a ruthenium complex, the most abundant ions observed were those attributable to non-covalent complexes of the G-quadruplex with two bound ruthenium molecules. In addition, the abundance of ions assigned to free DNA, and non-covalent complexes containing either one or three ruthenium molecules bound to Q5, were generally very similar. The results shown in Fig. 8.14 contrast significantly with those presented in Fig. 8.11, which shows relative abundances of non-covalent complexes present in solutions containing a 6:1 ratio of the same ruthenium complexes and the DNA duplex D2. In the latter figure it is apparent that replacement of one of the phenanthroline ligands in $[\text{Ru}(\text{phen})_3]^{2+}$ by more
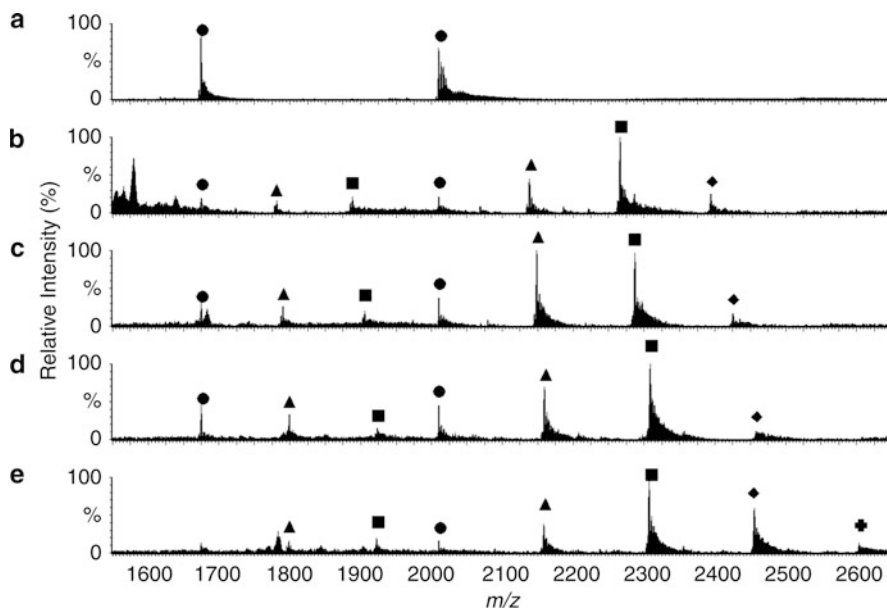
Fig. 8.14 Negative ion ESI mass spectra of Q5 and solutions containing a 40:1 ratio of different ruthenium complexes and Q5: (**a**) free Q5; (**b**) Q5 + [Ru(phen)$_3$]$^{2+}$; (**c**) Q5 + [Ru(phen)$_2$(dpq)]$^{2+}$; (**d**) Q5 + [Ru(phen)$_2$(dpqC)]$^{2+}$; (**e**) Q5 + [Ru(phen)$_2$(dppz)]$^{2+}$. (*Bullet*) free Q5; (*Triangle*) Q5 + 1 [Ru(phen)$_2$(L)]$^{2+}$; (*Square*) Q5 + 2 [Ru(phen)$_2$(L)]$^{2+}$; (*Diamond*) Q5 + 3 [Ru(phen)$_2$(L)]$^{2+}$; (*Plus*) Q5 + 4 [Ru(phen)$_2$(L)]$^{2+}$. L = phen, dpq, dpqC or dppz

extended heterocyclic ligands has a major effect on overall binding affinity. The absence of a similar effect on the overall binding affinity of the same ruthenium complexes towards Q5 therefore suggests that replacing the ligands does not significantly enhance the ability of metal complexes to interact with G-quadruplex DNA. This is consistent with a significant change in the nature of the binding interactions used by these metal complexes with the two types of DNA structures.

Comparison of Figs. 8.11 and 8.14 also strongly suggests that each of the ruthenium complexes [Ru(phen)$_2$(L)]$^{2+}$ (L = phen, dpq, dpqC, dppz) has a significantly higher binding affinity towards D2 than Q5. This is also consistent with a different combination of binding modes being used by a given ruthenium complex with the two types of nucleic acid molecules. A similar conclusion is reached after comparison of the relative abundances of non-covalent complexes in solutions containing the same ratio (10:1) of the same platinum(II) complex and either D2 or Q5. These results are presented in Fig. 8.15. The spectra of solutions containing Q5 all contain ions attributable to free DNA, whereas this is not the case for spectra of the corresponding solutions containing D2. Examining the stoichiometry of the non-covalent complexes present in the spectra provides further evidence that the affinity of each of the platinum complexes towards Q5 is less than that towards D2.
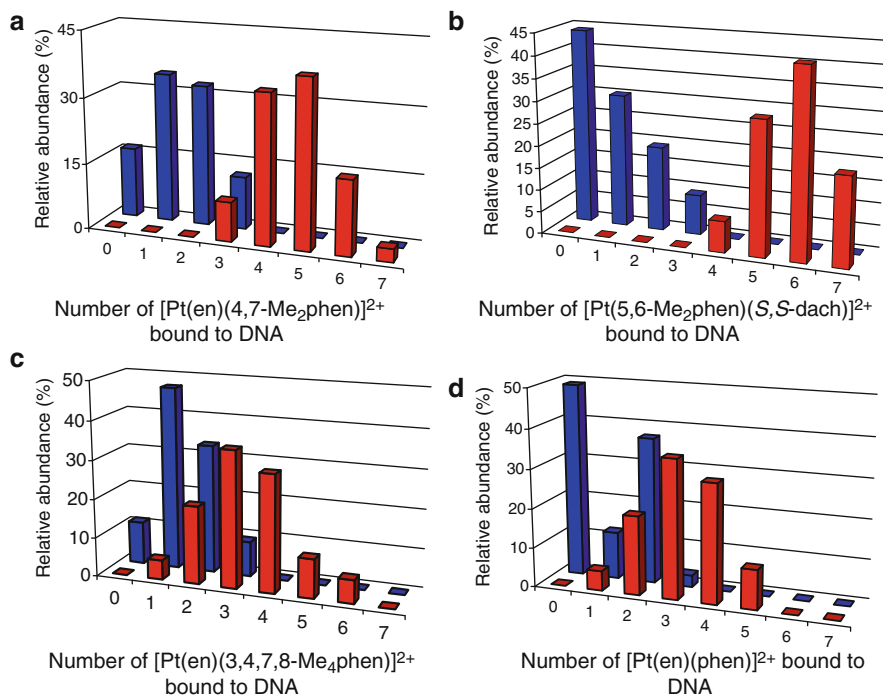
Fig. 8.15 Comparison of relative abundances of non-covalent complexes present in solutions containing a 10:1 ratio of platinum(II) complex and either D2 or Q5. *Red bar* Non-covalent complexes containing D2. *Blue bar* Non-covalent complexes containing Q5

In the case of solutions containing Q5, the most abundant non-covalent complexes present were those with either one or two intact platinum molecules. However, non-covalent complexes containing between three and six platinum molecules were the most prevalent in solutions containing D2. This suggests that these square planar platinum(II) complexes, like the octahedral ruthenium(II) complexes discussed above, interact with different regions of these duplex and quadruplex DNA molecules and/or use different binding mechanisms in those interactions.

Brodbelt and co-workers recently used ESI–MS to show that it was possible to increase the affinity of platinum(II) complexes for quadruplex DNA by incorporating ligands with extended planar structures [57]. However, increases in binding affinity were only observed with a parallel 4-stranded quadruplex and an antiparallel intramolecular quadruplex. In contrast, no significant increases in binding affinity were displayed towards two parallel intramolecular quadruplexes by any of the platinum complexes studied. These differences were attributed to variations in secondary structure between different quadruplexes, and further emphasise the role that ESI–MS can play in understanding differences between binding interactions used by potential drug molecules.

8.7 Conclusions and Future Directions

The tools of molecular biology have advanced to the point where it is now often possible to use them to pinpoint alterations to the sequence and structure of DNA that trigger the onset of cancer. This will both direct and enhance prospects for success for researchers charged with the task of finding molecules that can correct aberrant changes to our chromosomes. By using a variety of techniques, a great deal has already been learnt about how organic compounds and inorganic complexes interact with duplex DNA. Two of the most informative methods have been X-ray crystallography and NMR spectroscopy. These techniques can provide a level of information concerning interactions between small molecules and DNA that is unmatched by other methods. They are not, however, without some inherent limitations that impact on their applicability. In the case of NMR spectroscopy these include a lack of sensitivity that necessitates the use of relatively concentrated samples, and the length of time required to process spectra into a detailed picture of intermolecular contacts. X-ray crystallography on the other hand requires suitable crystals of a drug/DNA complex that may take weeks or months to obtain, if at all. In fact there are still, to the best of our knowledge, only a very small number of X-ray structures of non-covalent complexes formed between metal complexes and DNA [58, 59]. Both NMR spectroscopy and X-ray crystallography are therefore not suitable for widespread screening of families of small molecules for their suitability to act as drugs that act by selectively interacting with DNA.

Most information concerning the nature and strength of non-covalent interactions between metal complexes and DNA has come from more universally applicable techniques such as absorption spectrophotometry, circular dichroism spectroscopy and fluorescence spectroscopy. These have been widely used in binding studies using ct-DNA to provide an estimate of overall binding strength, as well as information concerning the average number of base pairs involved in binding to a specific metal complex, and clues as to the nature of the metal/DNA interaction. This information has generally been obtained through analysis of coarse changes in broad spectral features, which cannot be analysed to provide specific details of these interactions. ESI–MS, on the other hand, does provide precise information concerning the number of different types of adducts present in a solution with a known ratio of metal complex and DNA molecule of precisely defined composition. In addition, for each non-covalent complex present it is possible to readily determine how many metal complexes are bound to the nucleic acid, and if they have retained all or only some of the ligands present in their initial coordination sphere. While it is not always possible to determine easily if the loss of a ligand has been caused by fragmentation within the mass spectrometer source or a change in binding mode from non-covalent to covalent, complete retention of all of the initial coordination sphere does confirm that non-covalent binding is taking place. These are attributes of the ESI–MS method that are not shared by any other technique.

It is not possible currently to directly use ESI–MS to obtain information about the precise location of metal complexes non-covalently attached somewhere along an oligonucleotide sequence, or even whether the metal complex uses intercalation,

electrostatic bonding, or "groove-binding" as the primary means of interaction, or some combination of these methods. Future developments in mass spectrometer design and/or innovations in methods of analysing metal complex/DNA interactions may provide the means to overcome these limitations. For example, it may be possible to use cross-linking agents to covalently attach to DNA, [Ru (phen)$_2$(dppz)]$^{2+}$ molecules that are already involved in non-covalent interactions, and then employ the same enzymatic hydrolysis techniques applied previously to covalently attached platinum complexes [46–48]. This would then enable at least some of the nucleotides involved in non-covalent binding to the ruthenium molecule to be identified. Tandem mass spectrometry has the potential to accomplish the same task, without the need for enzymes or subsequent purification of the digestion mixture by HPLC. However, it will be first necessary to find ways to cleave the phosphodiester bonds holding nucleotides together in DNA without disrupting the non-covalent interactions binding the metal complex to the DNA. Alternatively, it may be possible to utilise the fact that displacement of non-covalently attached metal complexes from DNA occurs at lower in-source collision energies in ESI–MS/MS experiments than strand cleavage to identify the type of non-covalent binding interactions present. To date little attention has been directed towards these types of experiments to see, for example, if the energy required to displace metal complexes bound to dsDNA through intercalation is different to when the predominant means of interaction is either electrostatic in nature or "groove-binding". This information may also prove one day to be obtainable through the use of other newly emerging techniques. For example, non-covalent attachment of metal complexes to DNA via different mechanisms may produce changes in molecular shape and mobility that can be analysed using IMMS.

The use of ESI–MS for analysing the non-covalent interactions of metal complexes with DNA is still in its infancy, having only been applied principally to studies centred on B-DNA over the past 10 years. However, it is already obvious that ESI–MS provides information not readily afforded by more widely used methods. These unique aspects of ESI–MS, combined with its very high sensitivity and speed and ease of analysis, and the possibility of obtaining information concerning binding sites and mechanism of binding, suggest that it is a technique with the potential to become one of the most powerful in the arsenal of the bioinorganic chemist.

References

1. Dole M, Hines RL, Mack LL, Mobley RC, Ferguson LD, Alice MB. Macromolecules. 1968;1:96.
2. Fenn JB, Mann M, Meng CK, Wong SF, Whitehouse CM. Science. 1989;246:64.
3. Iribarne JV, Thomson BA. J Chem Phys. 1976;64:2287.

4. Dole M, Mack LL, Hines RL, Mobley RC, Ferguson LD, Alice MB. J Chem Phys. 1968;49:2240.
5. Kebarle P, Peschke M. Anal Chim Acta. 2000;406:11.
6. Tang L, Kebarle P. Anal Chem. 1991;63:2709.
7. Tang L, Kebarle P. Anal Chem. 1993;65:3654.
8. Kebarle P, Tang L. Anal Chem. 1993;65:972A.
9. Akashi S. Med Res Rev. 2006;26:339.
10. Bolbach G. Curr Pharm Des. 2005;11:2535.
11. Veenstra TD. Biophys Chem. 1999;79:63.
12. Rosu F, De Pauw E, Gabelica V. Biochimie. 2008;90:1074.
13. Benesch JLP, Robinson CV. Curr Opin Struct Biol. 2006;16:245.
14. Covey TR, Bonner RF, Shushan BI, Henion J. Rapid Commun Mass Spectrom. 1988;2:249.
15. Ganem B, Li YT, Henion JD. Tetrahedron Lett. 1993;34:1445.
16. Light-Wahl KJ, Springer DL, Winger BE, Edmonds CG, Camp II DG, Thrall BD, et al. J Am Chem Soc. 1993;115:803.
17. Kapur A, Beck JL, Sheil MM. Rapid Commun Mass Spectrom. 1999;13:2489.
18. Gilbert DE, Feigon J. Curr Opin Struct Biol. 1999;9:305.
19. Nelson SM, Ferguson LR, Denny WA. Cell Chromosome. 2004;3:1.
20. Han H, Langley DR, Rangan A, Hurley LH. J Am Chem Soc. 2001;123:8902.
21. Shin-ya K, Wierzba K, Matsuo K, Ohtani T, Yamada Y, Furihata K, et al. J Am Chem Soc. 2001;123:1262.
22. Minhas GS, Pilch DS, Kerrigan JE, LaVoie EJ, Rice JE. Bioorg Med Chem Lett. 2006;16:3891.
23. Anantha NV, Azam M, Sheardy RD. Biochemistry. 1998;37:2709.
24. Harrison RJ, Cuesta J, Chessari G, Read MA, Basra SK, Reszka AP, et al. J Med Chem. 2003;46:4463.
25. Han H, Cliff CL, Hurley LH. Biochemistry. 1999;38:6981.
26. Sun D, Thompson B, Cathers BE, Salazar M, Kerwin SM, Trent JO, et al. J Med Chem. 1997;40:2113.
27. David WM, Brodbelt J, Kerwin SM, Thomas PW. Anal Chem. 2002;74:2029.
28. Wilhelmsson LM, Westerlund F, Lincoln P, Nordén B. J Am Chem Soc. 2002;124:12092.
29. Brodie CR, Aldrich-Wright JR. Eur J Inorg Chem. 2007:4781.
30. Rajput C, Rutkaite R, Swanson L, Haq I, Thomas JA. Chem Eur J. 2006;12:4611.
31. Smith JA, Collins JG, Patterson BT, Keene FR. Dalton Trans. 2004:1277.
32. Morgan JL, Spillane CB, Smith JA, Buck DP, Collins JG, Keene FR. Dalton Trans. 2007:4333.
33. Smith JA, Morgan JL, Turley AG, Collins JG, Keene FR. Dalton Trans. 2006 :3179.
34. Wan KX, Shibue T, Gross ML. J Am Chem Soc. 2000;(122):300.
35. Lippard SJ. Acc Chem Res. 1978;11:211.
36. Sigman DS, Bruice TW, Mazumder A, Sutton CL. Acc Chem Res. 1993;26:98.
37. Zeglis BM, Pierre VC, Barton JK. Chem Commun. 2007:4565.
38. Metcalfe C, Thomas JA. Chem Soc Rev. 2003;32:215.
39. Keene FR, Smith JA, Collins JG. Coord Chem Rev. 2009;253:2021.
40. Beck JL, Gupta R, Urathamakul T, Williamson NL, Sheil MM, Aldrich-Wright JR, et al. Chem Commun. 2003:626.
41. Haq I, Lincoln P, Suh D, Nordén B, Chowdhry BZ, Chaires JB. J Am Chem Soc. 1995;117:4788.
42. Satyanarayana S, Dabrowiak JC, Chaires JB. Biochemistry. 1992;31:9319.
43. Urathamakul T, Waller DJ, Beck JL, Aldrich-Wright JR, Ralph SF. Inorg Chem. 2008;47:6621.
44. Talib J, Harman DG, Dillon CT, Aldrich-Wright J, Beck JL, Ralph SF. Dalton Trans. 2009:504.
45. Rosu F, Gabelica V, Houssier C, De Pauw E. Nucleic Acids Res. 2002;30:e82/1.

46. Gonnet F, Kocher F, Blais JC, Bolbach G, Tabet JC, Chottard JC, et al. Spectrom. 1996;31:802.
47. Troujman H, Chottard J-C. Anal Biochem. 1997;252:177.
48. Gupta R, Beck JL, Sheil MM, Ralph SF. J Inorg Biochem. 2005;99:552.
49. Kelso C, Tillott V, Rojas JD, Furlan RLA, Padilla G, Beck JL. Arch Biochem Biophys. 2008;477:348.
50. Rosu F, Gabelica V, Houssier C, Colson P, De Pauw E. Rapid Commun Mass Spectrom. 2002;16:1729.
51. Carrasco C, Rosu F, Gabelica V, Houssier C, De Pauw E, Garbay-Jaureguiberry C, et al. Chembiochem. 2002;3:1235.
52. Rosu F, De Pauw E, Guittat L, Alberti P, Lacroix L, Mailliet P, et al. Biochemistry. 2003;42:10361.
53. Rosu F, Gabelica V, Shin-ya K, De Pauw E. Chem Commun. 2003:2702.
54. Chen W-H, Qin Y, Cai Z, Chan C-L, Luo G-A, Jiang Z-H. Bioorg Med Chem. 2005;13:1859.
55. Gornall KC, Samosorn S, Talib J, Bremner JB, Beck JL. Rapid Commun Mass Spectrom. 2007;21:1759.
56. Talib J, Green C, Davis KJ, Urathamakul T, Beck JL, Aldrich-Wright JR, et al. Dalton Trans. 2008:1018.
57. Pierce SE, Kieltyka R, Sleiman HF, Brodbelt Jennifer S. Biopolymers. 2009;91:233.
58. Pierre VC, Kaiser JT, Barton JK. Proc Natl Acad Sci USA. 2007;104:429.
59. Kielkopf CL, Erkkila KE, Hudson BP, Barton JK, Rees DC. Nat Struct Biol. 2000;7:117.

Chapter 9
Investigating Binding Interactions Using Linear Dichroism and Circular Dichroism

Alison Rodger and Per Lincoln

9.1 Introduction

The great structural, geometrical and spectroscopic variations exhibited by metal complexes make it a challenge for biophysical studies to determine whether a putative metallointercalator does indeed bind to DNA intercalatively. In general, we require two pieces of evidence from completely different techniques that strongly suggest intercalation before we can conclude with any confidence that we do have a metallointercalator. The purpose of this chapter is to outline the information that linear dichroism (*LD*) and circular dichroism (*CD*) and also normal absorbance can provide to help us understand how a metal complex interacts with DNA. The chapter begins with an outline of what *LD* and *CD* are and why one might choose to use them to probe intercalation, then discusses how to do the experiments, and concludes with examples of typical data one might get for different types of compound, binding mode, etc.

9.2 Definitions of Spectroscopic Techniques

9.2.1 UV–Visible Absorbance Spectroscopy

The two fundamental principles that govern the absorption of light passing through a solution are that the absorption of light is exponentially related to the number of molecules of the absorbing species in the solution, and also exponentially related to the length of the light pathway through the sample. The absorbance is defined as:

$$A = \log_{10}(I_0/I), \tag{9.1}$$

A. Rodger (✉)
MOAC Doctoral Training Centre University of Warwick, Coventry, UK
e-mail: a.rodger@warwick.ac.uk

where I_0 and I are respectively the intensity of the incident and the intensity of the emergent light. We may write the Beer–Lambert law:

$$A = \varepsilon_\lambda cl, \tag{9.2}$$

where A is the absorbance, c is the concentration expressed in mol dm^{-3}, ε_λ is the extinction coefficient at wavelength λ which has units of mol^{-1} dm^3 cm^{-1} and l is the cell path length in cm. Equation (9.2) may be used to determine the concentration using the known absorbance measurements at a given wavelength. In the case of DNA, the characteristic UV absorbance band has a maximum around 260 nm (the precise position depends on the sequence of the DNA) and a minimum at 230 nm. The DNA concentration (in bases) can be calculated from the absorbance at ~260 nm. Some examples include: poly[d(A-T)$_2$] $\varepsilon_{262} = 6,600$ cm^{-1} mol^{-1} dm^3; poly[d(G-C)$_2$] $\varepsilon_{254} = 8,400$ cm^{-1} mol^{-1} dm^3; poly[d(A)] $\varepsilon_{257} = 8,600$ cm^{-1} mol^{-1} dm^3; poly[d(T)] $\varepsilon_{264} = 8,520$ cm^{-1} mol^{-1} dm^3 and calf thymus DNA $\varepsilon_{258} = 6,600$ cm^{-1} mol^{-1} dm^3. UV absorbance is also widely used for the determination of DNA purity since the absorbance ratio, A_{260}/A_{280}, should be between 1.7 and 2.0 for DNA that is free of proteins.

9.2.2 Linear Dichroism

When a molecule absorbs a photon of radiation of the correct energy to excite it from its ground state to an excited state, the electron distribution in the molecule is reorganised. The net linear direction of this change defines the polarisation of the transition. If the incident radiation does not have a component of its electric field along the transition polarisation direction then no absorption occurs. Conversely if it lines up perfectly then the maximum absorption occurs. Linear dichroism (*LD*) is a form of absorbance spectroscopy that takes advantage of this to give us information about the relative orientations of subunits of a molecular system. *LD* is the difference in absorption of light linearly polarised parallel and perpendicular to an orientation axis at a given wavelength:

$$LD_\lambda = A_{//\lambda} - A_{\perp\lambda}. \tag{9.3}$$

In this chapter we shall focus on the *LD* arising from electronic transitions. The *LD* may be analysed to give the orientation of the transitions of a molecule with respect to the polarisation of incident light [1, 2]. If one knows how the transitions are oriented within a molecule, the *LD* then tells how the molecule is oriented in the experiment. For example, if a molecule binds to an oriented piece of DNA, *LD* can be used to understand its orientation on the DNA. *LD* has been largely used for studying DNA–ligand binding systems. The reduced *LD*, which is defined as:

$$LD^r = \frac{LD}{A},$$ (9.4)

is often a useful quantity to plot for analysis.

There are two methods commonly used for orientating samples in DNA/ligand experiments: (1) film *LD* where a polymer film containing a small analyte molecule is stretched, forcing the analyte to line up with its long axis preferentially along the stretch direction, and (2) flow *LD* where a flow cell, usually of Couette design (Fig. 9.1), is used to flow-orient a long piece of DNA (typically at least 1,000 base pairs) and anything that is bound to it [1, 3–8].

9.2.3 Circular Dichroism

Circular dichroism (*CD*) is defined as the difference in absorption of left and right circularly polarised light:

$$CD = A_\ell - A_r.$$ (9.5)

The *CD* analogue of the Beer–Lambert Law (9.2) is:

$$CD = \Delta A = \Delta\varepsilon c\ell.$$ (9.6)

CD is used to study chiral or asymmetric molecules. Since chiral molecules do not have a reflection plane, the rearrangement of their electrons when radiation strikes the molecule does not have one either, therefore the interaction between the chiral molecule and the left- and right-handed photons will be different. *CD* may be used to check the chirality of a molecule or the purity of enantiomers (though to give a definitive answer the value for $\Delta\varepsilon$ needs to be known). It is also a sensitive probe of changes in biomacromolecular structure and may be used to probe DNA interactions with small molecules, especially achiral ones whose induced *CD* (*ICD*) is due solely to their interaction with DNA. For DNA, the sugar units of the backbone are responsible for providing the original chirality, but the spectroscopy observed above 180 nm is due to the coupling of the helically stacked planar bases. Many DNA binding molecules are achiral but upon binding to DNA they acquire an *ICD*
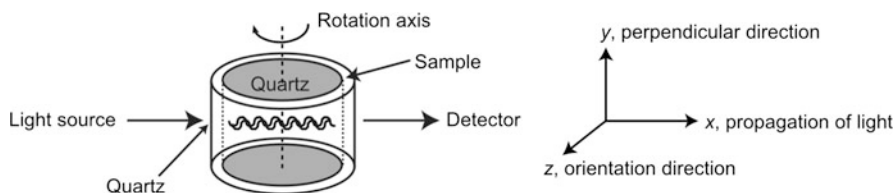
Fig. 9.1 Schematic of a Couette flow cell

that is characteristic of their interactions. The ligand also perturbs the DNA *CD* signal. However, it should be noted that metallomolecules usually have transitions that overlay the DNA signals so deductions about DNA structure based on the *CD* spectrum in the presence of a metal complex may not be reliable as one is viewing both DNA *CD* changes and metal complex *CD* changes overlaid.

9.3 Experimental Methodologies

The binding of metallointercalators to DNA usually involves a cationic metal complex binding to the anionic DNA. Before embarking on any experiment at all, it is important to check whether there is any precipitation, DNA condensation or aggregation of any kind. Another general caveat is that we like to think of one ligand binding to DNA in one mode, such as intercalation; however, the energy difference between different DNA binding modes may not be very large and so the possibility that multiple binding modes may be operative must be taken into account. On the other hand, electronic spectra, in particular *CD*, may be sensitive to perturbation by neighbouring chromophores or to DNA sequence-dependent induced *CD* signals so the changes in the distribution pattern of bound metal complexes along the DNA lattice arising under a titration may give a false impression of a binding geometry heterogeneity.

9.3.1 Linear Dichroism

9.3.1.1 Film *LD*

For a molecule to be aligned in a stretched film it must be either an integral part of the film or associated sufficiently strongly that when the film is stretched the molecule follows the film alignment axis. In practise one of two films are appropriate for most molecules: polyethylene for non-polar molecules (typically ligands that will later be bound to metals in the context of this book, though some charged metal complexes can be oriented on polyethylene) and polyvinyl alcohol for polar molecules (typically the final metal complexes).

9.3.1.2 Alignment in Polyethylene Films

Polyethylene (PE) is microcrystalline and when it is mechanically stretched along the manufacturer's stretch direction a molecular orienting environment is produced. PE is well suited for orienting non-polar molecules for spectroscopy as it has transparency in UV (above 200 nm), in the visible, and in the infrared regions. The key to success with PE film *LD* is the choice of PE and the degree of stretching.
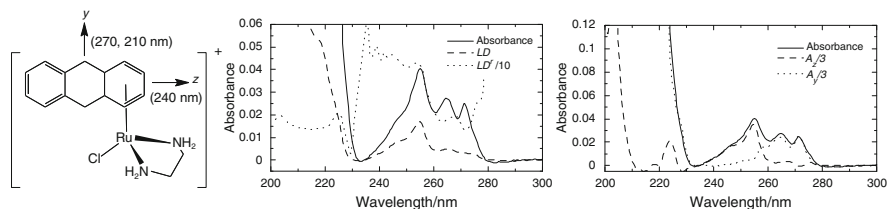
Fig. 9.2 [(η^6-dihydroanthracene)Ru(en)Cl]PF$_6$ indicting the energies and transition polarizations of the isolated dihydroanthracene transitions determined from the dihydroanthracene film UV–visible absorbance, LD and LD^r spectra in a PE stretched film [10]

A good source of PE is the plastic bags supplied with micropipette tips. However, to stretch this PE you need to have some kind of mechanical stretcher into which the film can be fixed. In the absence of a film stretcher to stretch and hold the PE, the thinner PE sometimes used for magazine wrappers can usually be stretched by hand and fixed, using bluetack, onto one wall of the sample compartment so that the light beam passes through the film. By convention the parallel direction of the polarised light is usually taken to be horizontal, so the stretch direction of the film should be aligned horizontally. It is advisable not to stretch too close to the breaking point of the polymer since the film has a tendency to become opaque and to rip suddenly. With a film stretcher a factor of ~3 is fairly straightforward for PE.

One can add molecules to the polyethylene film either before or after stretching and get the same spectrum. The most efficient protocol is, therefore, first to stretch the film, then measure the baseline spectrum (see below). After the baseline has been collected, then introduce the analyte into the stretched film either by adding droplets of a solution containing the analyte in cyclohexane or chloroform or dichloromethane to the surface of the film. Allow the solvent to evaporate between drops. Since the solvent may also enter and swell the PE and is itself aligned when the film is stretched, the baseline must be measured on a film that has been treated with solvent in the same way as the sample film will be. You should also endeavour to collect the sample spectrum on the same part of the film as the baseline. An example of the film LD of a ligand designed for a ruthenium metallointercalator is given in Fig. 9.2. Component spectra were determined by assuming that the 240 nm region is long-axis (z) polarised and the 210 nm region is short-axis (y) polarised, following the Trial and Error Method of Thulstrup et al. [9]. The degree of orientation in the film was high (LD^r(maximum) = 0.45) as expected for such a rod shaped molecule [1]. The 230–255 nm region is essentially long-axis polarised and the 200–225 nm and 260–280 nm regions are short-axis polarised.

9.3.1.3 Alignment in Polyvinyl Alcohol Films

Polyvinylalcohol (PVA) is a fairly universal host for polar molecules; the film is transparent in the UV (above 200 nm) and visible regions of the spectrum, though it

has a strong absorption over large regions of the infrared [11]. For small molecules it has to be used in a dry form (less than a few percent water). PVA films are more difficult to prepare than PE films; however, the quality of data is often better. To prepare a PVA film, one mixes well-hydrolysed commercial PVA powder in cold water (10% w/v) to make a slurry, then heats it to near boiling to form a viscous solution. The sample solution (typically ~5 mM in water, but the aim is to have the final film with an absorbance maximum between 0.1 and 1) is then added to half of the PVA solution, and the mixture is also cast onto a glass plate and left to dry [12]. The same volume of water as of sample is then added to the remainder of the solution which is then cast onto a glass plate and left to dry (this typically takes 1–3 days in a well-ventilated dust-free place) to make a film for baseline measurements. Once dry, the films are stretched by the same factor (typically ~2) at an elevated temperature by holding the films in the hot air from a hair dryer as they are being stretched. PVA films are quite brittle and one really needs to use a well-engineered film stretcher. It is also advisable to stretch a safe amount first then measure the spectra before trying a larger stretch. The greater the stretch factor the greater the *LD* signal magnitude, until of course the film breaks. An example of PVA film absorbance and *LD* spectra is given in Fig. 9.3. It is discussed further below.
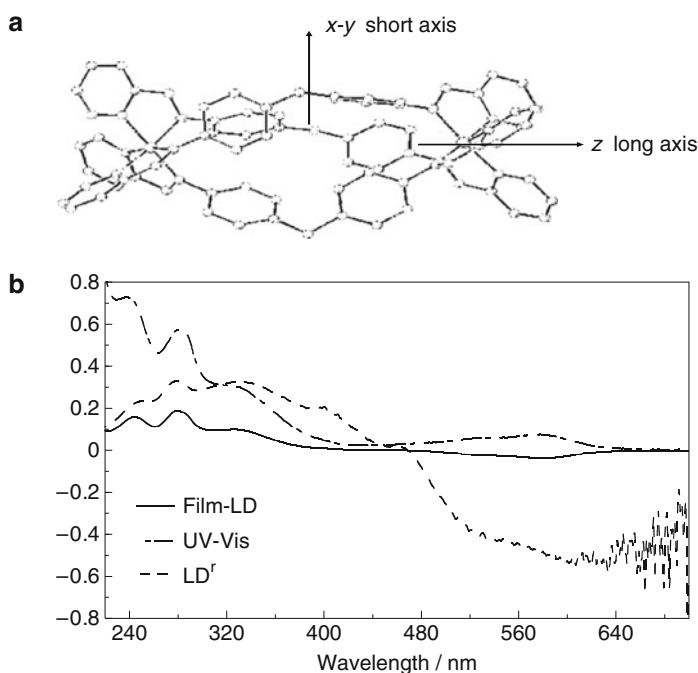
Fig. 9.3 (**a**) A bis iron tris-chelate helicate $[Fe_2L_3]^{4+}$ of empirical formula: $[Fe_2(C_{25}H_{20}N_4)_3]Cl_4$. and where L is (*NE*,*N'E*)-4,4'-methylenebis(*N*-(pyridin-2-ylmethylene)aniline). Hydrogens have been omitted for clarity. (**b**) Absorbance, *LD* and *LD^r* spectra for $[Fe_2L_3]^{4+}$ in PVA film prepared as described in the text [13]

9.3.1.4 Flow LD

The shear forces exerted on a polymeric molecule such as DNA that is dissolved in water and flowed past a stationary surface at about 1 m s^{-1} give sufficient orientation to ensure that $A_{//}$ and $A_{\perp}$ are different. If the walls are quartz then we can measure LD spectra in the visible and UV regions. The problem that arises if the shear flow is provided by a linear flow-through system such as an HPLC pump is that it is very expensive on sample. In 1964 Wada [7, 8] solved this issue with the invention of the Couette flow cell illustrated in Fig. 9.1 where the sample is endlessly flowed between two cylinders one of which rotates and one of which is stationary (Fig. 9.1). Much more recently we developed a microvolume Couette flow cell that requires less than 50 μL of sample rather than the mLs of the previous Couette cells [5]. Figure 9.4 illustrates a standard and micro-volume Couette flow cell. A standard volume cell of the kind illustrated in Fig. 9.4 may be loaded using a micropipette (usually of 1 mL volume) with sufficient sample to ensure the meniscus is above the window through which the light passes. It is then easy to add additional material such as a DNA binding ligand to measure a titration series. The microvolume option, as the name implies, requires less sample but is more difficult to ensure no air bubble is trapped in the light beam. Adding material after the initial loading is also not as straightforward as with the larger cell. A baseline spectrum needs to be subtracted before final presentation of data. With the microvolume cuvettes this can usually be collected either via stopping the Couette cell rotating or by filling it with the buffer. The standard volume design usually has slightly different baseline spectra for different orientations of the rotating quartz, so it is better to collect a rotating buffer sample.

When collecting data (for LD and CD) one must ensure that the sample absorbance is not too high since if the photomultiplier tube is not receiving many photons it becomes unreliable. The ideal absorbance is about 1 but a range from 0.1 to 2 is appropriate. The approach of ensuring that the voltage on the photomultiplier tube is less than 600 V is not always good enough if the sample scatters light. Especially at lower wavelengths when xenon lamp instruments are struggling for light
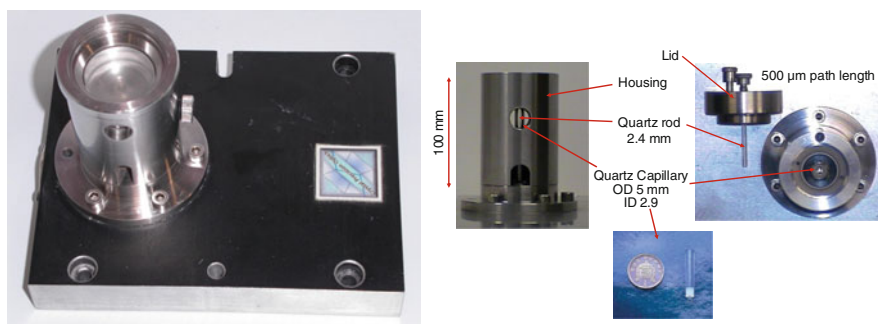
Fig. 9.4 Standard volume and microvolume Couette flow cells
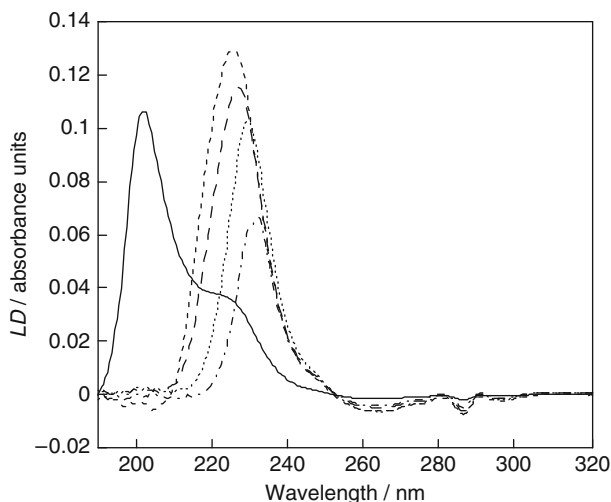
Fig. 9.5 Far UV *LD* spectra showing the apparent shift to shorter wavelength of the maximum signal as the concentration of F-actin is reduced. F-actin concentrations 93, 74, 62, 53 and 12 μM (the true spectrum, solid line) [6]

intensity, a significant percentage of the light that does reach the photomultiplier tube from a light scattering sample is often scattered light rather than light that has passed through the sample. It is important to check the Beer Lambert law is being followed by diluting the sample and checking the spectrum. False maxima are otherwise observed as illustrated in Fig. 9.5 for a polymerised protein where the effect is more obvious than for most DNA samples [6].

Light scattering may also give a contribution to the measured signal so that:

$$LD^{Observed} = LD^{Absorbance} + LD^{Scattering}. \tag{9.7}$$

If this has happened it is apparent as a sloping baseline. We usually only want the absorbance contribution. Nordh et al. [14] showed that a simple empirical correction, which is illustrated in Fig. 9.6 can often be subtracted from the observed *LD* spectrum to remove the sloping baseline: [15]

$$LD^{Scattering} = a\lambda^{-k}. \tag{9.8}$$

9.3.1.5 *LD* Instrumentation

One can use a normal absorbance spectrometer and polarizers to collect *LD* spectra; however, this requires either rotating the sample or the polarizer. It is much easier and the signal to noise is significantly better if one converts a *CD* spectropolarimeter into a *LD* instrument. One can either (1) change the data mode on a
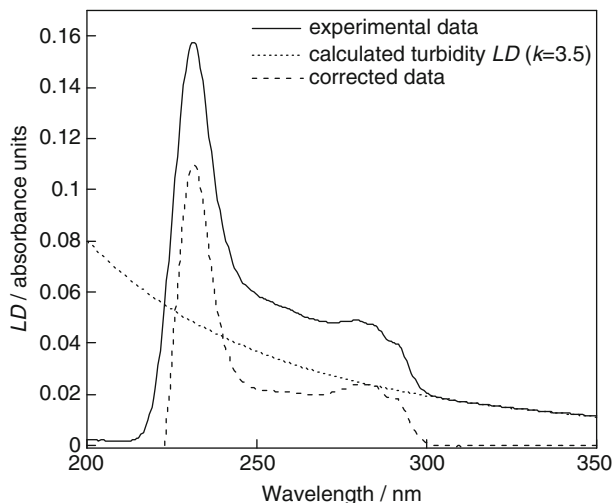
Fig. 9.6 A method of light scattering correction applied to a polymerised tubulin *LD* spectrum: the experimental data (*continuous line*); the calculated turbidity *LD*, using a *k* value of 3.5, with α determined by rescaling the curve at 320 nm where there is no intrinsic absorbance (*dotted line*); and the corrected data (*dashed line*) [15]

spectropolarimeter from *CD* to *LD* (assuming that this option is available) or (2) insert a quarter wave plate. Option (2) usually results in data being output in mdeg, so conversion to ΔA is performed by dividing by 32,980 [1].

9.3.1.6 LD Data Analysis

When a molecule is oriented in a stretched film or in flow, the molecules that are adsorbed into the film or being flowed are not all perfectly lined up as in a crystal. So the *LD* of such a molecule, even, if we make the not entirely correct assumption that the orientation is uniform about the stretch or flow direction, is for a transition polarised along the stretch direction:

$$LD = 3A_{iso}S(\theta), \qquad (9.9)$$

and for one perpendicular to the stretch direction:

$$LD = -\frac{3}{2}A_{iso}S(\theta), \qquad (9.10)$$

where A_{iso} is the absorbance of an unoriented sample. The factor of three arises because of the averaging in three dimensions of the unoriented sample. $S(\theta)$ describes the orientational distribution of the long axis of the molecules in the

film or flow. More generally, for a transition polarised at an angle α to the stretch direction:

$$LD = 3A_{iso}O(\alpha)S(\theta) = 3A_{iso}\left\{\tfrac{1}{2}(3\langle\cos^2\alpha\rangle - 1)\right\} \times \left\{\tfrac{1}{2}(3\langle\cos^2\theta\rangle - 1)\right\}. \quad (9.11)$$

To be really quantitative in our analysis we therefore need to determine S. For samples that may be considered to be uniaxially oriented, as may be assumed to be the case for certain symmetrical molecules in films and DNA in shear flow [1], the LD signal may thus be written:

$$LD = \frac{3A}{2}S(3\langle\cos^2\alpha\rangle - 1), \quad (9.12)$$

where A is the isotropic absorbance of the same sample in the same path length, $\cos^2\alpha$ is the average of the cosine square of the angle the transition moment makes with the orientation direction and S is the orientation parameter (which equals 1 for a perfectly oriented sample and 0 for an unoriented one). We usually calculate an "average" $\alpha = a\cos(\langle\cos^2\alpha\rangle\tfrac{1}{2})$, despite the fact that the measured average of the cosine squared ($\langle\cos^2\alpha\rangle$) may be substantially different from the square of the cosine of the average of α ($\cos^2\langle\alpha\rangle$) if the variance of α is large.

The film LD spectrum of a tetracationic iron triple helicate is shown in Fig. 9.3 [16]. If we assume (reasonably) that the molecule orientation axis is the long axis of the triple helix and that the orientation is uniaxial (due to the x–y degeneracy of the metal complex itself), then the negative sign of the LD from 500 to 600 nm indicates that the transitions here are predominantly short axis (i.e., $\perp$) polarised transition. By assuming it is pure $\perp$ polarised we get a lower bound on the orientation parameter. Component polarised spectra with incrementally increased orientation parameters are given in Fig. 9.7. The in-ligand transitions below 400 nm are of mixed
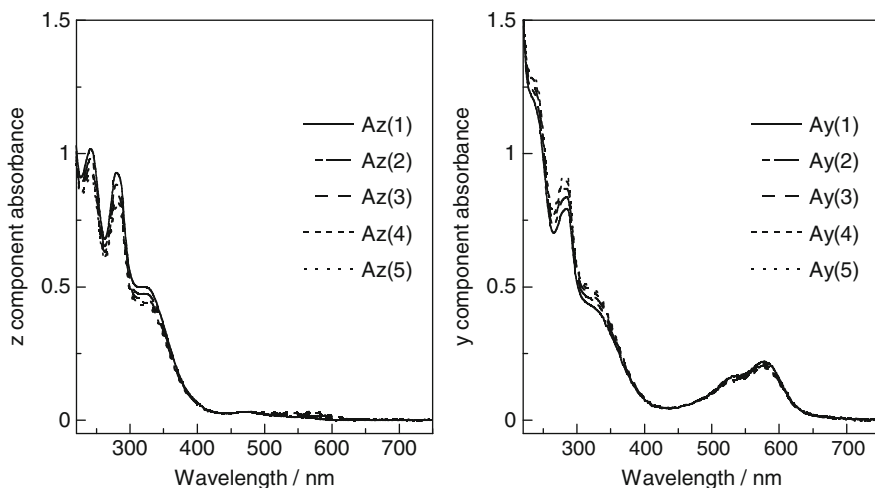
Fig. 9.7 Component spectra derived for the data of Fig. 9.3 determined as outlined in the text
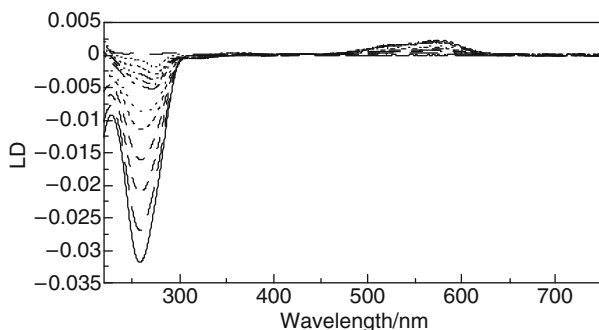
Fig. 9.8 *LD* (0.5 mm annular gap in *LD* cell making total 1 mm path length) 500 μM (in bases) calf thymus DNA in 20 mM NaCl and 1 mM Na(CH$_2$)$_2$AsO$_2$.3H$_2$O buffer pH = 6.8 with increasing concentrations of [Fe$_2$L$_3$]$^{4+}$ (where L is (*NE,N'E*)-4,4'-methylenebis(N-(pyridin-2-ylmethylene)aniline)) showing the bending of the DNA [13]

polarization since the *LD^r* magnitude never reaches twice that at 550 nm (9.9) and (9.10). More careful inspection shows that they have slightly more // than ⊥ character. The "best looking" spectra with no negative values are chosen as the component spectra.

Determining *S* is required for a quantitative analysis of *LD* spectra and is often extremely difficult. For the bases in B-DNA it is accepted [17] that ⟨α⟩ ~86°. So one can calculate *S* from the *LD* and A of a sample. Unfortunately when one is studying metallomolecules binding to DNA the metallomolecule usually absorbs at the same wavelength as the DNA, so one cannot determine the *LD* of the DNA. One is then usually left with assuming that *S* remains the same for free DNA and ligand-bound DNA. As Fig. 9.8 shows this is not always the case: in this case the *LD* signal at 260 nm decreases much more rapidly than is possible due to the addition of a positive ligand *LD* signal. Here the DNA is being bent by the di-iron triple helicate. If, by way of contrast, *S* increases this is indicative (though not conclusive) of an intercalating ligand that stiffens the DNA. The *LD* of ethidium bromide and other intercalators binding to DNA illustrates this effect most obviously in the *LD^r* spectrum since the ligand region (>300 nm) is more negative than the DNA region (~260 nm). An independent check of the DNA orientation may be made by using a small amount of a dye in the experiment, for example one can use methylene blue (MB) a known DNA intercalator [18] if its absorbance is in a window of the ligand.

9.3.2 Circular Dichroism

To measure a UV–visible *CD* spectrum of a ligand–DNA complex one requires a solution containing both species of interest (and no others that will absorb a significant percentage of the photons); a quartz cuvette of a path length that ensures the absorbance maximum in the range of interest is no more than 2; and a *CD*

spectropolarimeter. Although many *CD* spectroscopists prefer cylindrical cuvettes, for drug–DNA work rectangular cuvettes have the advantage of fitting into standard absorbance spectrometers and Peltier thermostatted cell holders. It is almost always advisable to collect absorbance data in parallel with the *CD* data. If the sample is chiral (which DNA is) and gives a good UV–visible absorbance spectrum then it is highly likely that you will get a good *CD* spectrum.

CD machines are much more expensive than standard absorbance instruments as the absorbance magnitude signal of a typical *CD* spectrum is a fraction of a percent of that observed in the normal absorbance spectrum, so the optics have to be significantly better. Another requirement due to the high energy xenon arc lamps used in most *CD* machines is that the optics of the instrument usually need to be purged with nitrogen gas to avoid ozone being created and reacting with surfaces of mirrors (and the operator). Nitrogen purging is also required for the sample compartment when running below 200 nm to avoid having O_2 absorbing the incident radiation. In practise this means a moderate nitrogen flow rate (3–5 cm^3 min^{-1}) at all times, with an increase to 10 or more cm^3 min^{-1} when collecting data below 200 nm.

A machine baseline (i.e., *CD* spectrum of air) measured on a standard *CD* spectropolarimeter will not be flat. In addition, the cuvette used for an experiment will also have its own *CD* spectrum. So it is essential to collect a baseline spectrum of the solvent/buffer under the same conditions as the sample spectrum using the same cuvette in the same orientation and same position with respect to the light beam. Subtract the baseline spectrum from the sample spectrum to produce the final *CD* plot. It is usually the case that with small *CD* signals, even when the baseline is subtracted, the *CD* is not exactly zero outside the absorption envelope. However, if the spectrum is flat outside the absorption envelope, it may be zeroed by adding or subtracting a constant. If it is not flat outside the absorbance region then there is a scattering contribution to what is being observed. With DNA metallocomplexes this is often indicative of the DNA being precipitated out of solution, so it is a warning sign that should be heeded. Thus one should always collect data from at least 20 nm on the longer wavelength side of the lowest energy band.

The parameters one selects to collect *CD* (and *LD*) data are not independent. The signal to noise ratio in a *CD* spectrum increases with: $\sqrt{n}$, (*n* is the number of accumulations that are averaged); $\sqrt{\tau}$ (*τ* is the time over which the machine averages each data point), some instruments use the label response time which is related to *τ* and $\sqrt{I}$ (*I* is the intensity of the light beam). To optimise signal to noise effects, *τ* should be selected to be as large as possible subject to $\tau \times s \leq \frac{b}{2}$ (*b* is the bandwidth and *s* the scan speed). If *τ* is too long for the chosen *s* and *b*, then maxima of peaks (both positive and negative) will be cut off and their wavelengths shifted. Scan speeds of 100 nm min^{-1}, $\tau = 1$ s, $b = 1$ nm, and a data step of 0.5 nm are typically a good starting point parameter set for most solution phase DNA–ligand experiments where the samples have the broad band shapes usually found for solution samples. If the bandwidth is fixed, the instrument will be programmed to control the slit width directly. If a number of spectra with the same parameters are to be collected, it is worth investing the time in determining whether scan speed, *τ* or *b* can be increased without affecting the resulting spectrum. If a collected spectrum
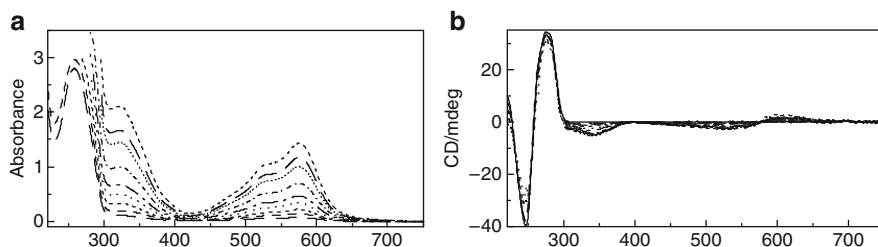
Fig. 9.9 (**a**) Absorbance (1 cm pathlength) and (**b**) *CD* (1 cm pathlength) of 500 μM (in bases) calf thymus DNA in 20 mM NaCl and 1 mM $Na(CH_2)_2AsO_2.3H_2O$ buffer pH = 6.8 with increasing concentrations of $[Fe_2L_3]^{4+}$ [13]

looks too noisy there are some post collection smoothing options but it is preferable to collect good data by increasing the number of scans, or increasing concentrations or changing other parameters.

Data from most *CD* machines are produced in millidegrees which are related to absorbance by

$$\theta/\text{millidegrees} = 32,980C\ell(\varepsilon_\ell - \varepsilon_r) = 32,980(A_\ell - A_r). \qquad (9.13)$$

With DNA–ligand systems it is not always clear which concentration one should use to normalise the data to 'per mole'. If one's focus is the DNA region, then the DNA concentration is probably the better choice. If one's focus is outside the DNA region then the ligand concentration is probably most useful. Otherwise one simply leaves the data in either absorbance or millidegrees. An example of absorbance and *CD* data for $[Fe_2L_3]^{4+}$ matching the *LD* of Fig. 9.8 are given in Fig. 9.9.

9.4 Applications of *LD* and *CD* to DNA-Metallomolecules

In this section some examples of the type of *LD* and *CD* data one can collect for metallomolecules which were designed to be intercalators and the conclusions that can be drawn are outlined. The applications include:

1. Platinum 2,2′:6′,2″-terpyridine complexes
2. Ruthenium arene complexes
3. Ruthenium substituted 2,2′:6′,2″-terpyridine complexes
4. Further methods of analysis of flow LD spectra

9.4.1 *Picoline-2,2′:6′,2″-Terpyridine–Platinum(II)*

2,2′:6′,2″-Terpyridine–platinum(II) complexes were first reported to bind to double stranded DNA by intercalation over thirty years ago, the duplex unwinding angle being comparable to that found with ethidium bromide [19]. An investigation of the
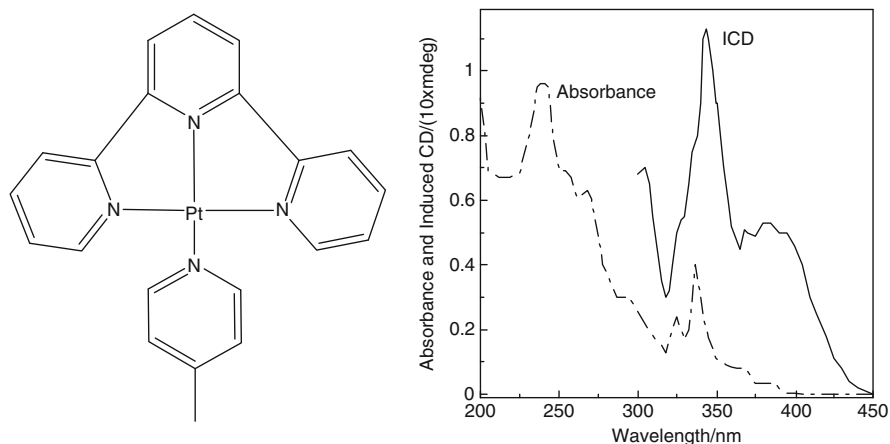
Fig. 9.10 Molecular structure of 4-picoline-2,2′:6′,2″-terpyridine–platinum(II), its absorption spectrum (20 μM) in water and its *ICD* spectrum (90 μM) when mixed with poly[(dA-dT)₂] (500 μM) in 10 mM aqueous NaCl [21]

binding of 2-hydroxyethane-thiolato(2,2′:6′,2″-terpyridine) platinum(II), [Pt(terpy) HET]²⁺, with calf thymus DNA by fiber X-ray diffraction techniques showed the platinum ions are distributed along the helix axis in accord with the nearest neighbour exclusion model, [20] which is the maximum binding density for non-metallo intercalators. The first +2 charged platinum terpy complex whose DNA binding was investigated, 4-picoline-2,2′:6′,2″-terpyridine–platinum(II) (denoted Pt-terpy), is shown in Fig. 9.10 [21]. As hoped, it unwound the DNA which was indicative (though not conclusive) of intercalation. The absorbance of Pt-terpy and *CD* spectra of Pt-terpy with poly[d(A-T)₂] are also shown in Fig. 9.10. The loss of structure in the spectrum and shifts of the bands to longer wavelength between the free Pt-terpy absorbance and the DNA-bound *CD* is also suggestive of an intercalative binding mode. A titration series of *CD* data was used [21] to calculate the binding constant to be $2 \times 10^7 \text{ M}^{-1}$ with a site size of four bases. It is the linear dichroism which confirms intercalation. Linear dichroism (LD) spectra were obtained with 200 μM DNA and 0–50 μM Pt. There is a low intensity positive LD signal for the metal to ligand charge transfer at around 440 nm, the rest of the LD spectra are negative. The sample with low concentration Pt-terpy, where most of the ligand is bound in the first binding mode has *LD*/[Pt-terpy] > *LD*/[DNA]. This indicates that the in-plane transitions of Pt-terpy are perpendicular to the DNA helix axis but also that its binding stiffens and/or lengthens the DNA. These observations, together with the unwinding assay, provide powerful (close to definitive) evidence for the intercalative mode of Pt-terpy with DNA.

In general the challenge with *CD* and *LD* of platinum complexes is that little of the spectroscopy is above 300 nm so one is always struggling with overlapping metal complex and DNA spectroscopy. A typical example is given in Fig. 9.11 for [Pt(*R,R*-dach)(4-Me-phen)]²⁺ (dach = 1*R*,2*R*-diaminocyclohexane, denoted RR4M)
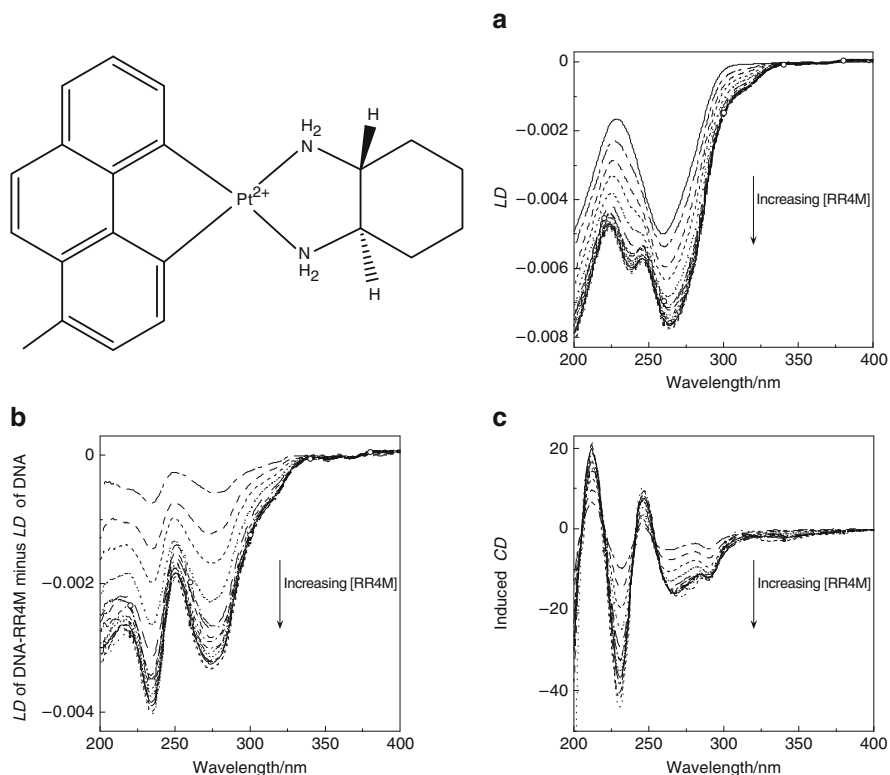
Fig. 9.11 Molecular structure of [Pt(*R*,*R*-dach)(4-Me-phen)]$^{2+}$, denoted RR4M. (**a**) *LD* spectra of RR4M (0–95 μM) with calf thymus DNA (150 μM); (**b**) *LD* of RR4M with DNA *LD* subtracted; and (**c**) ICD of RR4M (0–125 μM) with calf thymus DNA (150 μM) after subtraction of DNA *CD*

[22]. In this case the induced *LD* spectrum was calculated by subtracting the DNA *LD* spectrum by using the program of Stootman et al. [23] to first determine the main components. The negative *LD* spectrum is strongly suggestive of intercalation. This conclusion was supported by other data. A careful analysis of both the *LD* and *CD* data using data at 230 nm where the DNA has little signal and the Pt complex a significant *ICD*, showed a binding site size of 4–5 bases and binding constant of $7.0 \pm 2.8 \times 10^6$ M^{-1} [22].

9.4.2 DNA Interactions of Monofunctional Organometallic Ruthenium(II) Antitumor Complexes

Organometallic ruthenium(II) arene complexes of the type [(η^6-arene)Ru(en)Cl]PF$_6$ (en = ethylenediamine) constitute a relatively new group of anticancer compounds [24] with a mechanism of action different from the ruthenium(III) complex

{Na[*trans*-Cl$_4$Im(Me$_2$SO)Ru], Im = imidazole} currently in clinical trials [25]. A direct correlation between cytotoxicity and DNA binding was observed for several ruthenium compounds in cell cultures [26] and so Sadler et al. designed organometallic complexes with the potential to intercalate. Here we focus on the dihydroanthracene compound, Ru-DHA, illustrated in Fig. 9.2. The induced *CD* for Ru-DHA upon interaction with calf thymus DNA shows a simple positive *CD* band centred around 370–380 nm whose intensity increases with the level of DNA ruthenation. The 260 nm region of the spectrum shows an increase in positive *CD* when Ru-DHA is added to DNA and a decrease in negative intensity at 230 nm suggesting positive Ru-DHA *ICD* signals in both regions. In order to probe whether the anthracene moiety intercalated between base pairs, the film *LD* of DHA in polyethylene was measured. As shown in Fig. 9.2, 260–280 nm of DHA is short axis polarised and 250–260 nm is long axis polarised. If the DHA is intercalated between DNA base pairs upon binding of Ru-DHA to DNA both transition should give a negative contribution to the flow *LD* spectrum which would increase the apparent intensity of the DNA band. The solution phase *LD* of Ru-DHA plus calf thymus DNA, poly[(dG-dC)$_2$], and poly[(dA-dT)$_2$] is, by way of contrast, less negative than that of free DNA [10]. The DNA-Ru-DHA *LD* has, however, lost the structure of the DHA ligand which would be consistent with intercalation or some other form of π–π stacking binding mode. It is not possible to conclude how this molecule is binding to DNA, it seems to be both bending the DNA (reducing *S* and hence the intensity) and the DHA chromophore may be acquiring a positive *LD*. It may be partially intercalating, but what we can definitively conclude from the *LD* is that Ru-DHA is not binding to DNA by standard intercalation.

9.4.3 Aryl Substituted Ruthenium Bis-2,2′:6′,2″- Complexes: Intercalation and Groove Binding

Simple 2,2′:6′,2″-terpyridine ligands bound to metals are generally found to intercalate between DNA bases as discussed above. However, when the terpy has substituents on it, it may well be that the preferred position of the terpy cannot be adopted. For example, ligands composed of terpy with an attached group in the 5 position resulted in compounds that intercalated if the attached group was big enough (phenanthrenyl, anthracenyl and pyrenyl, Fig. 9.11), but where the terpy itself did not intercalate under any circumstances [27]. The smaller 4,4′-biphenyl tail did not intercalate and a naphthyl tail showed both intercalation and a non-intercalative binding even at low metal complex concentrations.

The film *LD* for the [Ru(terpyanth)$_2$]Cl$_2$ compound is shown in Fig. 9.12. The long axis terpy transitions of [Ru(terpyanth)$_2$]$^{2+}$ centred at ~310 and 330 nm have negative film *LD* signals, whereas its ~270–290 nm region is positive. The anthracene's chromophore is a long axis polarised transition (~250 nm) which aligns perpendicular to the metal complex's long axis, i.e., the anthracene, which lies across the film orientation axis so its 250 nm band is thus negative. The anthracene
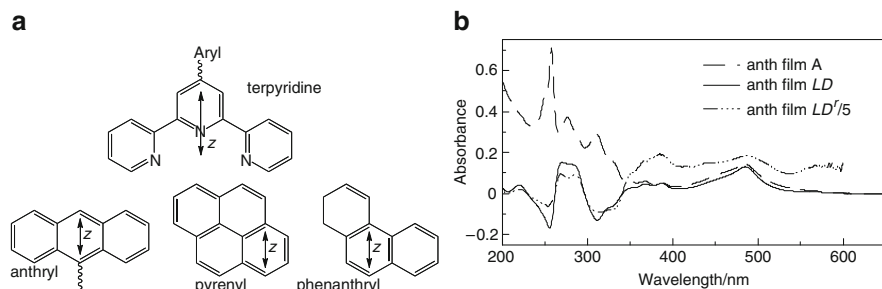
Fig. 9.12 (**a**) The general structure of the [Ru(terpyL)$_2$Cl$_2$] complexes where L = anthracene (anthryl), pyrene (pyrenyl) or phenanthrene (phenanthryl). The aryl substituent on the terpy indicates point of attachment of L to 4′ position on the 2,2′:6′,2″-terpyridine (terpy). z indicates the approximate position of the metal complex long axis in each subunit. (**b**) PE film absorbance, *LD* and *LD^r* for Ru-terpyanth (denoted anth in figure) [27]
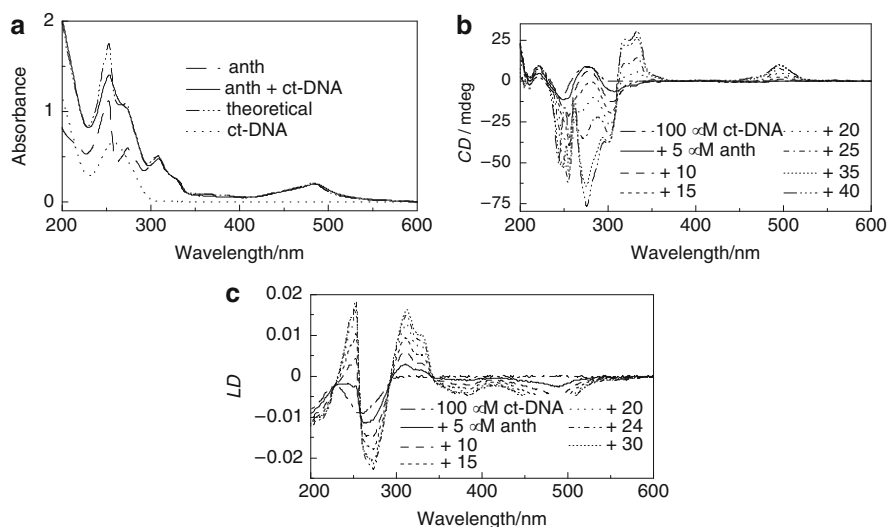
Fig. 9.13 (**a**) UV–visible absorption spectrum of [Ru(terpyanth)$_2$]$^{2+}$ (10 μM) in water; [Ru (terpyanth)$_2$]$^{2+}$ (10 μM) plus ct-DNA (100 μM) and ct-DNA (100 μM) together with the 'theoretical' sum spectrum. (**b**) *CD* spectra from a titration series of [Ru(terpyanth)$_2$]$^{2+}$ with ct-DNA (100 μM). Metal complex concentrations are indicated in the figure insert. (**c**) LD spectra from a titration series of each complex with ct-DNA (100 μM). Metal complex concentrations are indicated in the figure insert [27]

225 and 380 nm regions, which align with the anthracene short axis, are positive since they align with the metal complex short axis. The metal ligand charge transfer transitions are dominated by *z*-polarised transitions, particularly at ~500 nm where each complex has a large positive *LD^r* signal [27].

The absorption spectra of [Ru(terpyanth)$_2$]$^{2+}$ in the absence and presence of DNA (at DNA base:complex ratio of 10:1) is illustrated in Fig. 9.13. As both ct-

DNA and the ruthenium complexes have overlapping transitions below 300 nm, metal complex spectral changes can be most easily seen above this wavelength where ct-DNA has no absorbance. We see that the absorption maxima shift to longer wavelengths and the intensity is lower than expected if the spectrum were simply the sum of the component parts. This is consistent with enhanced π-stacking upon addition of the DNA which could arise either from intercalation between DNA base pairs or metal complex stacking mediated by the DNA template.

The *CD* of $[Ru(terpyanth)_2]^{2+}$ (Fig. 9.13b) has positive MLCT signals at all ratios and small signals for the long wavelength tail transitions. At the low metal complex loads the 310 nm terpy region of the spectra has negative *CD* bands and the DNA region is dominated by the DNA *CD* signal. At about 5:1 DNA base to metal complex mixing ratio, the terpy region and the DNA region take on a very different form indicating the switching on of a second binding mode. There is a large increase in signal magnitude and a non-zero isosbestic point at 310 nm. A non-zero isosbestic point indicates that the binding sites associated with mode 1 (non-zero 310 nm *CD*) are filled before mode 2 is significantly occupied. If one subtracts the mode 1 *CD* signal from a high loading spectrum, the resulting mode 2 spectrum suggests a degenerate exciton interaction (neighbouring large positive and negative signals) between terpy groups, with the zero point being the absorbance maximum. There is also probably a degenerate exciton coupling between tail groups (there is for e.g., an approximate isosbestic point at the anthracenyl maximum at ~250 nm). The magnitude of the induced *CD* signals per added metal complex at the higher loadings increases rather than being constant or decreasing as is usually the case for independent metal complexes binding – again indicative of a degenerate exciton interaction between metal complexes.

While *CD* tells us about changes in binding mode, it does not readily provide geometric data. Flow oriented *LD* (Fig. 9.13c) can be used to gain information about the relative orientation of DNA bases and bound molecules. DNA itself exhibits a negative flow *LD* signal between 200 and 300 nm, due to the transitions of its bases being approximately perpendicular to the long axis of DNA as expected. When the metal complex is added to the DNA, the DNA region and the metal complex region show *LD* signals, which means that $[Ru(terpyanth)_2]^{2+}$ binds in a specific orientation (rather than randomly along the backbone). The orientation of the DNA bases is not able to be determined in the presence of the metal complexes, since, as noted above, the metal complex absorbances overlap with those of the bases. An independent check of the DNA orientation was, therefore, made in this case [27] using a small amount of methylene blue (MB), a known DNA intercalator. For each complex at R = 20:1, DNA base to metal complex, the MB + DNA + metal complex MB *LD* signals were found to be larger in magnitude than those of the MB + DNA [27]. This suggests that at R = 20:1 the complexes are either lengthening (by unwinding due to intercalation) or stiffening the DNA. Flow *LD* titration series (Fig. 9.3) were performed and show negative MLCT region, negative anth signals from 350–400 nm, and positive terpy region between 300 and 340 nm. Although the spectra are suggestive of only a single binding orientation for each complex, there is a subtle

change in the shapes of the spectra from about R = 5:1 (where the *CD* changes). Thus the low and high loading binding modes are oriented in similar but not identical fashions. In summary the $[\text{Ru(terpyanth)}_2]^{2+}$ complex has negative *LD*^{r}s of similar magnitude for all the *z*-polarised transitions indicating they are polarised approximately perpendicular to the DNA helix axis. The two terpy groups of necessity lie perpendicular to one another in all complexes as well as perpendicular to the metal complex *z*-axis. Thus, regardless of their orientations in the x/y plane, the net *LD* signal from the two perpendicular terpy ligands will be positive if the z-axis lies perpendicular to the DNA helix. Thus these spectra are consistent with an intercalative orientation of the anthracene moiety but not of the 2,2′:6′,2″-terpyridines.

Thus the combined spectroscopic data suggest that $[\text{Ru(terpyanth)}_2]^{2+}$ (and indeed the phenanthroline and pyrene analogues) binds intercalatively until this mode is occupied or the second mode becomes energetically attractive (at mixing ratios of ~7:1). Then further $[\text{Ru(terpyanth)}_2]^{2+}$ add to the DNA in such a way as to have a similar orientation to the intercalative mode and with the tails and terpy π-systems stacked one above the other (thus giving rise to the exciton *CD* signals).

9.4.4   *Further Methods of Analysis of Flow LD Spectra*

When absorption bands of differently polarised electronic transitions overlap, the *LD*^{r} values of the individual transitions cannot directly be determined from the sloping LD/A_{iso} curves. However, in favourable cases, when the absorption bands are distinctively dissimilar and not more than two transitions overlap in the interval, the TEM procedure (Trial and Error Method) of Michl et al. [9] can frequently be used to extract the *LD*^{r} values by searching for the linear combinations of the LD and the isotropic absorption spectrum for which the characteristic features of the absorption band vanishes [28]. In particular cases, when the same chromophore can be oriented in different ways, e.g., when two enantiomers of a chiral octahedral complex have diastereomerically different DNA binding geometries, a generalised matrix inversion TEM procedure have been used to resolve three (almost) orthogonally polarised absorption components in $[\text{Ru(L)}_2\text{Y}]^{2+}$ systems [29, 30].

References

1. Nordén B, Rodger A, Dafforn T. Linear dichroism and circular dichroism: A textbook on polarized spectroscopy. Cambridge: Royal Society of Chemistry. 2010.
2. Nordén B, Kubista M, Kuruscev T. Q Rev Biophysics. 1992;25:51.
3. Rodger A. In: Riordan JF, Vallee BL, editors. Methods in enzymology, Vol. 226. San Diego: Academic 1993, p. 232.
4. Marrington R, Dafforn TR, Halsall DJ, Hicks M, Rodger A. Analyst. 2005;130:1608.
5. Marrington R, Dafforn TR, Halsall DJ, Rodger A. Biophys J. 2004;87:2002.

6. Rodger A, Marrington R, Geeves MA, Hicks M, de Alwis L, Halsall DJ, et al. PhysChem-ChemPhys. 2006;8:3161.
7. Wada A. Biopolymers. 1964;2:361.
8. Wada A. Appl Spectros Rev. 1972;6:1.
9. Thulstrup EW, Michl J, Eggers JH. J Phys Chem 1970;74:3868.
10. Novakova O, Chen H, Vrana O, Rodger A, Sadler PJ, Brabec V. Biochemistry. 2003;42:11544.
11. Matsuoka Y, Nordén B. J Phys Chem. 1982;86:1378.
12. Ismail MA, Sanders KJ, Fennel GC, Latham HC, Wormell P, Rodger A. Biopolymers. 1998;46:127.
13. Hannon MJ, Moreno V, Prieto MJ, Molderheim E, Sletten E, Meistermann I, et al. Angew Chem. 2001;40:879.
14. Nordh J, Deinum J, Nordén B. Eur Biophys J. 1986;14:113.
15. Marrington R, Seymour M, Rodger A. Chirality. 2006;18:680.
16. Rodger A, Sanders KJ, Hannon MJ, Meistermann I, Parkinson A, Vidler DS, et al. Chirality. 2000;12:221.
17. Chou PJ, Johnson JWC. J Am Chem Soc. 1993;115:1205.
18. Hiort C, Nordén B, Rodger A. J Am Chem Soc. 1990;112:1971.
19. Jennette K, Lippard SJ, Vassiliades G, Bauer W. Proc Natl Acad Sci USA. 1974;71:3839.
20. Bond R, Langridge R, Jennette KW, Lippard SJ. Proc Natl Acad Sci USA. 1975;72:4825.
21. Mc Coubrey A, Latham HC, Rodger A, Lowe G. FEBS Lett. 1996;380:73.
22. Fisher DM, PhD Thesis, Sydney University (Sydney), 2005.
23. Stootman FH, Fisher DM, Rodger A, Aldrich-Wright JR. Analyst. 2006;131:1145.
24. Aird R, Cummings J, Ritchie A, Muir M, Morris R, Chen H, et al. Br J Cancer. 2002;86:1652.
25. Sava G, Bergamo A. Int J Oncol. 2000;17:353.
26. Clarke MJ, Zhu F, Frasca DR. Chem Rev. 1999;99:2511.
27. Rodger A, Patel KK, Sanders KJ, Datt M, Sacht C, Hannon MJ. Dalton. 2002, 3656.
28. Cusumano M, Pietro MLD, Giannetto A, Nicolo F, Nordén B, Lincoln P. Inorg Chem. 2004; 43:2416.
29. Lincoln P, Broo A, Nordén B. J Am Chem Soc. 1996;118:2644.
30. Lincoln P, Nordén B. J Phys Chem B. 1998;102:9583.

Chapter 10
Applications of Fluorescence Spectroscopy and Confocal Microscopy

Anya Salih, Paul Wormell, K. Benjamin Garbutcheon-Singh, Benjamin Harper, Simon Myers, David Geny, Christopher Hammang, and Janice Aldrich-Wright

10.1   Introduction

In this chapter we describe the use of fluorescence spectroscopy and confocal microscopy to investigate the DNA binding capacity, uptake route and intracellular localisation of novel metallointercalators. Fluorescence is the property whereby some atoms or molecules absorb UV or visible light and then re-emit it at longer wavelengths after a brief interval, termed the fluorescence lifetime.

Confocal scanning laser microscopy (CSLM) is a light-based imaging technique, developed during the last 3 decades, which permits visualisation of cells and thick samples by their fluorescence. Its development rapidly overcame the popularity of conventional microscopes and led to a dramatic transformation of the study of cells and tissues in the biological and biomedical sciences. CSLM is mainly used with either fixed or living tissues and cells that have been labelled with one or several fluorescent probes. It allows one to visualise not only the external, but also the internal, cellular and tissue structure, and to do so in three-dimensional (3D) or four-dimensional (4D, time being the fourth dimension) modes.

Confocal imaging, coupled with fluorescence spectroscopy, nowadays provides us with an approach for studying dynamic cellular events in living cells at high spatial and temporal resolutions, at micro- and even at molecular scales. Paralleling the developments in imaging technologies have been the emergence of fast and low-cost computing resources, as well as advanced 3D and 4D software packages for analysing large amounts of digital information generated by bioimaging. These advances are providing a powerful stimulus in research across all life-sciences and are, perhaps, the most powerful imaging methods now available for studying biology and biomedicine.

A. Salih (✉)

School of Natural Sciences, College of Health and Science, University of Western Sydney, Penrith South, NSW, Australia

e-mail: a.salih@uws.edu.au

10.2   Fluorescence Spectroscopy

Fluorescence detection, imaging and spectroscopy are powerful, versatile and sensitive analytical techniques that are widely used in the life sciences and clinical diagnostics. The widespread application of fluorescence in the study of biological interactions can be explained by a combination of its sensitivity, ease of use, rapidity, reproducibility, and adaptability.

Fluorescence is a spectroscopic technique that studies the emission of UV or visible light following excitation at a shorter wavelength [1]. When a molecule absorbs a UV or visible photon, this typically causes an electronic transition in which a bonding or non-bonding electron is promoted to an antibonding orbital. Depending on the nature of the higher-energy orbital, and the reorganisation of electron distribution that occurs during the transition, the excitation may be localised in one part of the molecule, or more widely delocalised. For example, in a polypyridyl complex of ruthenium(II), such as many typical metallointercalators, an excitation might be localised in part of a single ligand (for some ligand-centred transitions, denoted LC), or localized on the ruthenium ion (metal-centred transitions; MC), or delocalised over a single ligand (LC), or delocalized among the other ligands (LC again), or it may involve metal-to-ligand charge transfer (MLCT) involving one or more ligands [2]. As described in Chap. 2, the lowest-energy (longest-wavelength) absorption bands of many ruthenium(II) polypyridyl complexes are MLCT in character. Electronic transitions may occur to the lowest vibrational level of an excited electronic state (corresponding to the "origin band" of the transition), or to a higher-energy vibronic level. The breadth and shape of a UV or visible absorption band depend on how many electronic transitions it contains, their relative intensities, and their vibronic profiles. These factors also affect the corresponding linear dichroism (*LD*) and circular dichroism (*CD*) spectra [3].

Figure 10.1 shows a typical energy-level diagram, often called a Jablonski diagram, for an organic molecule; for example, a polypyridyl ligand such as 1,10-phenanthroline, 2,2′-bipyridyl or dipyrido[3,2-*a*:2′,3′-*c*] phenazine (dppz). The different electronic states of a molecule are represented by bold lines, and vibrational (i.e., vibronic) states by lighter lines. In the lowest-energy or ground electronic state, all electrons are paired. The state is accordingly a singlet state; hence it is labelled as S_0. For organic molecules, in which spin-orbit coupling is weak, the selection rules for electronic transitions strongly favour the excited singlet states (S_1, S_2, S_3, etc.), and UV–visible absorption spectra are dominated by singlet–singlet transitions. However, the molecules also have accessible excited triplet states (two unpaired electrons; denoted T_1, T_2, etc.), which are typically drawn on the right-hand side of the energy-level diagrams, and that occur at lower energies than the corresponding singlet states. Very weak $S_0 \rightarrow T_1$ absorption bands may be detected for some organic ligands, but in practice the spectra are dominated by singlet–singlet absorptions, mostly of $\pi \rightarrow \pi^*$ character, although weak $n \rightarrow \pi^*$ absorptions may be seen for some compounds, especially in non-polar solvents [4]. The situation is different for many ruthenium(II) polypyridyl complexes, in which
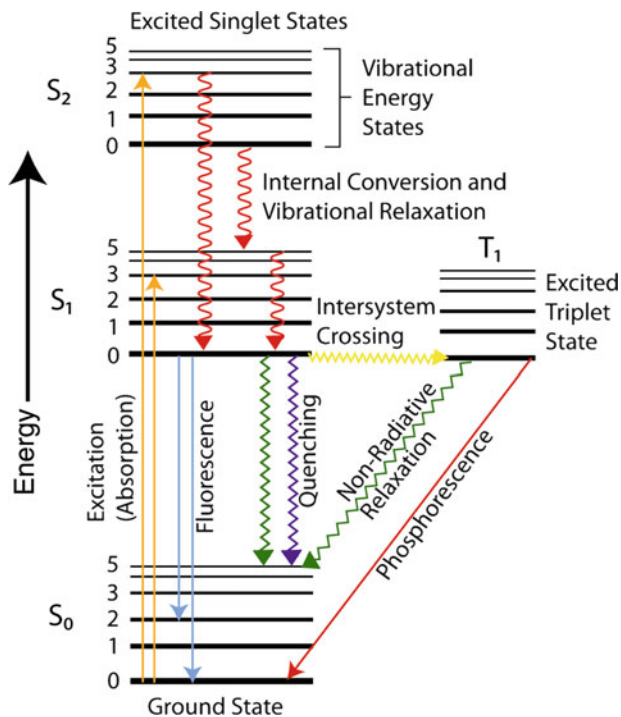
Fig. 10.1 Energy-level diagram for a fluorescent organic molecule

the lowest-energy MLCT states are dominated by triplet orbital character [2, 5], but spin-orbit coupling is large enough for them to produce quite strong visible absorption, *LD* and *CD* spectra, as shown in Chaps. 2 and 5.

When an organic molecule absorbs UV or visible light it undergoes a transition to an excited vibronic state; typically an excited vibrational state of S_1 or a higher electronic state. When the molecule is in a condensed phase (e.g., in water solution) it can rapidly lose some or all of its excitation energy as heat to its surroundings, by dropping down through its manifold of vibronic levels (vibrational relaxation) and, if necessary, moving down the higher singlet states and ending up in the S_1 state (internal conversion). For many molecules, this process continues: the molecule enters the higher S_0 vibrational states, and continues its vibrational relaxation until it is in thermal equilibrium with its surroundings. When this happens, the molecule does not radiate at UV or visible wavelengths. However, a molecule in the lowest vibronic state of S_1 may also be able to radiate its excess energy as a photon, ending up in one of the S_0 vibrational states. The relative probabilities of transitions to the different vibrational states (known as Franck-Condon factors) determine the contour of the resulting emission spectrum [1]. Figure 10.1 shows that the emission will typically have a lower energy than the corresponding absorption, although there is potential for some overlap, especially when the molecule's environment causes

inhomogeneous broadening of the absorption and emission bands; this feature is nicely shown in the spectra of Λ-[Ru(phen)$_2$(phendo)]$^{2+}$ (see Fig. 2.13). From an experimental point of view, it is important to remember that emission typically occurs at *longer* wavelengths than absorption (where the spectrum of absorption that leads to emission is often known as a excitation spectrum) [6, 7]. For molecules in condensed phases, it is very rare for emission to occur from S_2 or a higher excited state; this is summarized in Kasha's Law [8]. Accordingly, every wavelength in the excitation spectrum produces the same fluorescence spectrum, although the overall fluorescence intensity will depend on the excitation wavelength.

For an organic molecule, the lifetime of the singlet–singlet emission is short, typically of the order of nanoseconds or less. This type of emission is known as *fluorescence*, as shown in Fig. 10.1; it is one category of the more general phenomenon of *luminescence*. Fluorescence is only one of the possible pathways by which a molecule may lose its excitation energy. Internal conversion and vibrational relaxation is another (and this may dominate for many species); alternatively, spin-orbit coupling may be strong enough that molecules in the S_1 and/or higher excited singlet states may undergo intersystem crossing to a triplet state [1]; this process may be enhanced when heteroatoms such as nitrogen are present [9], as in many polypyridyl ligands. As for the excited singlet states, excitation energy may be lost through non-radiative means, and the molecule will relax to the bottom of the T_1 state. Emission, known as *phosphorescence*, may occur from this state, but on a significantly longer timescale than fluorescence, often with lifetimes of from milliseconds to seconds, or even longer. As shown in Fig. 10.1, phosphorescence occurs at longer wavelengths than fluorescence, and there may be a large wavelength gap between the excitation and phosphorescence spectra.

As indicated above, the lowest excited MLCT states of ruthenium(II) polypyridyl complexes such as [Ru(bpy)$_3$]$^{2+}$ are largely triplet in character; however, owing to the presence of the heavy ruthenium atom, they absorb quite strongly at visible wavelengths and, in appropriate chemical environments (e.g., bound to DNA) have strong emission spectra with fairly short lifetimes (typically of the order of microseconds). They can therefore be treated experimentally in the same way as the fluorescence spectra of organic ligands, hence their treatment in this particular chapter, although they are typically referred to as luminescence spectra in the literature.

The efficiency of fluorescence or luminescence is called the *quantum yield* (Φ_f), which is the ratio of the number of emitted photons to the number of absorbed photons:

$$\Phi_f = \frac{\text{Number of emitted photons}}{\text{Number of absorbed photons}} \tag{10.1}$$

Some strongly fluorescent molecules have quantum yields that approach the maximum value of 1.0. However, given the sensitivity of modern detection systems, useful data can be obtained even when the quantum yield is low: it is much

easier to detect a weak fluorescence than a weak absorption, for which the spectroscopic noise may swamp the absorption signal. Measurements can now be made at extremely low concentrations (picomolar or femtomolar) of fluorophores and even single molecules can be detected and tracked [10–12].

As explained above, and shown in Fig. 10.1, the difference between the excitation and fluorescence energy is dissipated as heat: the greater the energy difference, the greater the amount of heat per absorption event. Similarly, the lower the fluorescence quantum yield, the greater the amount of heat produced. This has practical implications for analytical techniques, such as fluorescence spectroscopy and confocal imaging. Fluorescent probes with high quantum yields are preferred, as this reduces the amount of heating that occurs for the sample, and hence the extent of photobleaching that may occur for some probes.

Many metallointercalators, such as ruthenium(II) polypyridyl complexes have been reported [13–15] and extensively studied for their luminescent properties [13–15]. Ruthenium mononuclear [16, 17] and dinuclear [18] complexes containing bipyridine ligands [19, 20] have been reported to display high quantum yields. Mixed metal ruthenium(II)-platinum(II) [18, 21] and platinum(II) compounds have also been reported to display luminescent properties. Fluorescence spectroscopy is an ideal method for measuring DNA binding constants (K_b) as it has the advantage of nanomolar detection limits. The methods are straightforward and the instrumentation is not overly expensive or exotic. There are a wide range of experimental conditions which can be varied, such as complex type, macrobiomolecule (for example, DNA), buffers, pH and ionic strength, which is simply modulated by salt concentrations. But it is the sensitivity along with the simplicity of the spectra that are the major advantages of this technique.

10.2.1   Fluorescence Quantum Yields

As explained above, quantum yield, Φ_f, is a measure of the emission efficiency of a given fluorophore. Quantum yield (Φ_f) measurements can be determined using the method of Damrauer et al. [22]. Values of Φ are reported relative to a standard, [Ru (bpy)$_3$]$^{2+}$ in CH$_3$CN ($\Phi_r = 0.062$) [23] and calculated using (10.2) [24]:

$$\Phi_{\text{metallointercalator}} = \Phi_{\text{std}} \left(\frac{I_{\text{metallointercalator}}}{A_{\text{metallointercalator}}} \right) \left(\frac{A_{\text{std}}}{I_{\text{std}}} \right) \left(\frac{\eta_{\text{metallointercalator}}}{\eta_{\text{std}}} \right)^2 \qquad (10.2)$$

where $\Phi_{metallointercalator}$ is the radiative quantum yield of a metallointercalator, Φ_{std} is the radiative quantum yield of the standard, $I_{metallointercalator}$ and I_{std} are the integrated emission intensities of a metallointercalator and [Ru(bpy)$_3$]$^{2+}$, respectively. A$_{metallointercalator}$ and A_{std} are the absorbance of a metallointercalator and [Ru (bpy)$_3$]$^{2+}$, respectively, at the wavelength of excitation (450 nm). $\eta_{metallointercalator}$ and η_{std} are the indices of refraction of a metallointercalator and [Ru(bpy)$_3$]$^{2+}$

Table 10.1 The fluorescence quantum yields and UV–Visible extinction coefficients of selected mono- and dinuclear complexes [25]

Complex	Quantum yield Φ	ε_{max} ($\times 10^5$ L mol^{-1} cm^{-1})
[Ru(dpq)$_2$(phen)](PF$_6$)$_2$	0.061	1.06
[Ru(dpq)$_2$(3-Br-phen)](PF$_6$)$_2$	0.042	1.02
[Ru(dpq)$_2$(4-Cl-phen)](PF$_6$)$_2$	0.050	1.20
[Ru(dpq)$_2$(5-Cl-phen)](PF$_6$)$_2$	0.059	1.10
[{Ru(dpq)$_2$}$_2$(μ-(phen-3-SOS-3-phen)](PF$_6$)$_4$	0.062	2.08
[{Ru(dpq)$_2$}$_2$(μ-(phen-4-SOS-4-phen)](PF$_6$)$_4$	0.053	2.05
[{Ru(dpq)$_2$}$_2$(μ-(phen-5-SOS-5-phen)](PF$_6$)$_4$	0.048	2.02

solutions, respectively. Values of η corresponding to the pure solvent are generally used; if you use the same solvent then $\eta_{metallointercalator}/\eta_{std} = 1$. The fluorescence quantum yields of some metallointercalators are reported in Table 10.1.

10.3 Fluorescence Spectroscopy Applications

The direct titration technique requires the metallointercalator, such as [Ru (phen)$_2$(dppz)]$^{2+}$ or [Ru(phen)$_2$(dpq)]$^{2+}$ (dpq = dipyrido-[3,2-d:2,3-f]-quinoxaline), to be intrinsically fluorescent. Derivatisation can be used to incorporate a fluorescent moiety and produce a fluorescent complex but it should be noted that intermolecular interactions subsequently measured may differ from the non-derivatised complex. The experimental conditions for direct titrations are quite varied (Chap. 2, Tables 2.1–2.3), so if you wish to compare binding constants of metallointercalators with literature values the experimental conditions need to be equivalent. In Chap. 2, Tables 2.1–2.3, the binding constants of many ruthenium metallointercalators are listed; the technique, type of DNA and buffer system used in each case has been included. For example, the binding affinity of rac-[Ru(phen)$_3$]$^{2+}$ while similar varies between 3.1–7.9 $\times$ 10^{-3} for the various experiments. A strongly binding metallointercalator (K_b above 10^6) would bind too effectively at low salt concentrations of ~10–50 mM, to compensate for this strong binding affinity higher salt concentrations (100 mM) are often included in the buffer. At lower salt concentrations (10 mM), the metallointercalator can bind to the DNA and precipitate out of solution. The optimum salt concentration can be determined but titrating salt into a saturated DNA–metal complex and monitoring the point at which the fluorescence is reduced by about half the intensity.

If the metallointercalator is not fluorescent then Fluorescent Intercalator Displacement experiments (FID) [26, 27] can be used. This technique requires that the DNA is initially saturated with a fluorescent molecule such as ethidium bromide (EtBr) or thiazole orange reaching a maximum fluorescence. This is then reduced as the metal complex is titrated into the solution, displacing EtBr from DNA. Experimental considerations include: the metal complex must bind more strongly to DNA than EtBr; it is assumed that the energy required for the metal complex to displace

EtBr from DNA is the same as that required for the metal complex to bind to DNA alone; and interactions between EtBr and the metal complexes can occur, which can complicate the interpretation of the data.

10.3.1   Direct Titration of $[\{Ru(dpq)_2\}_2(\mu\text{-phen-4-SOS-4-phen})]^{4+}$

Calf thymus DNA (sonicated to 2,000 base pairs in length) was acquired from Gilbco BRL and used without purification. The titrations were conducted in a phosphate buffer (10 mM sodium phosphate, pH 7.0, 100 mM NaCl and 1 mM EDTA) at 25 °C. Measurements were made on a Perkin Elmer LS 50B luminescence spectrometer using an excitation wavelength of 450 nm, and the emission intensity was recorded from 500 to 800 nm. The spectra shown in Fig. 10.2 are each an average of three scans. The emission intensity of $[\{Ru(dpq)_2\}_2(\mu\text{-phen-4-SOS-}4\text{-phen})]^{4+}$ at 10^{-8} M is small but measurable and is enhanced upon the addition of ct-DNA. The resulting emission spectra of $[\{Ru(dpq)_2\}_2(\mu\text{-phen-4-SOS-4-phen})]^{4+}$ (8.6×10^{-8} M) after small aliquots of ct-DNA (1 μL, 3.9×10^{-4} M) were titrated into the solution were measured until saturation was reached, as shown in Fig. 10.2.

The characteristic emission curve is conserved after each successive addition of ct-DNA. The small peak at 530 nm is due to Raman scattering of the light beam which occurs at a constant distance from the excitation wavelength. The emission peaks of the subsequent spectra are shifted (1–2 nm) upon the addition of ct-DNA; this shift can vary depending on the metallointercalator. The progress of the titration
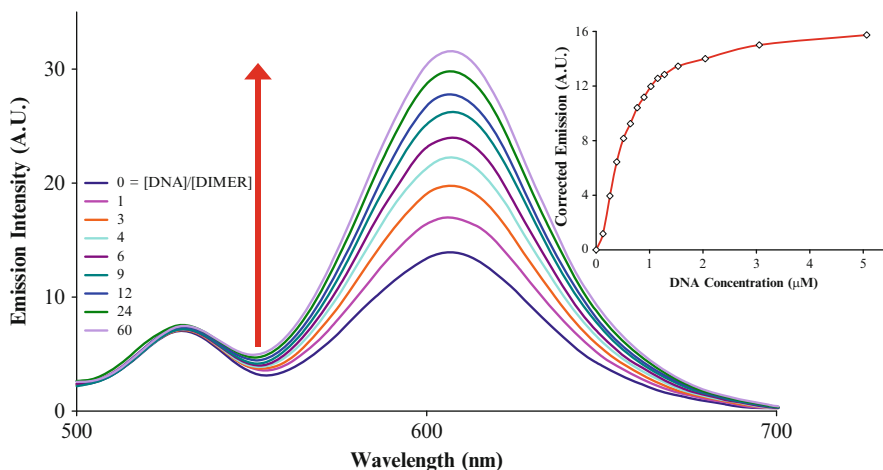
Fig. 10.2 Fluorescence emission spectra of $[\{Ru(dpq)_2\}_2(\mu\text{-phen-4-SOS-4-phen})]^{4+}$($8.6 \times 10^{-8}$ M) with increasing concentrations of ct-DNA (10 mM sodium phosphate, pH 7.0, 100 mM NaCl and 1 mM EDTA). The *arrow* indicates the direction of change in the spectral features with increasing ct-DNA concentration. The *inset* shows the response curve for the titration

was monitored through a plot of measured emission as a function of DNA concentration. The titration curve plateaus when all of the DNA binding sites are occupied, indicating the end of the titration.

The method of Rodger and Nordén offers an effective approach based upon the Scatchard method. If the association of a metallointercalator with DNA is treated as a simple equilibrium, (10.3) applies, where Met_f is a free metallointercalator, DNA_f is unbound DNA, and DNA-Met is a metallointercalator in a binding site:

$$[Met_f] + [DNA_f] \xleftrightarrow{K_b} [DNA - Met].$$ (10.3)
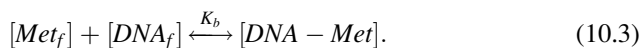
As represented in (10.4), α is a constant that changes with wavelength and is obtained from the spectrum as a result of changing the proportion of bound metallointercalator (Met_b). This relationship is a ratio of the concentration of the bound metallointercalator (Met_b), concentration of the free metallointercalator (Met_f) and the free DNA binding site concentration (DNA_f), as shown in (10.5):

$$Met_b = \alpha\rho.$$ (10.4)

$$K_b = \frac{Met_b}{DNA_f Met_f}.$$ (10.5)

If each binding event is independent of all others (i.e., there is no cooperative or non-cooperative binding), then (10.6) shows the relationship between the variation in the total DNA concentration (DNA_{tot}) and the change in emission (ρ) [3]. For these experiments, the total metallointercalator concentration (Met_{tot}) was constant while the DNA_{tot} varied. By plotting the x and y values determined using (10.7) and (10.8) (Fig. 10.3), a linear relationship with a slope of Met_{tot}/α and a y-intercept of $n\alpha$ is produced (Met_{tot} = the total metallointercalator concentration a known value, n = the number of binding sites (in base pairs) and α is used to determine Met_b.)
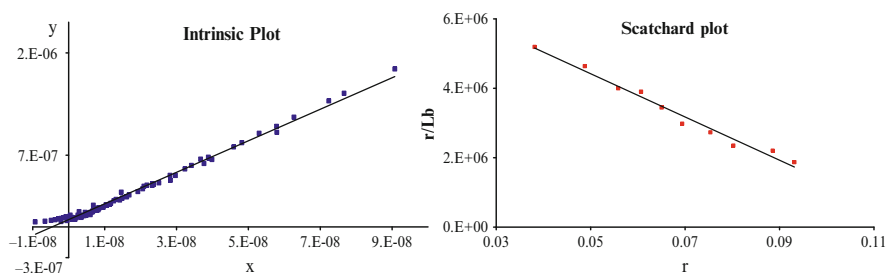
Fig. 10.3 On the *left* the intrinsic method plot of x and y as defined in (10.5) and (10.6) for [{Ru (dpq)$_2$}$_2$(μ-phen-4-SOS-4-phen)]$^{4+}$ (8.6 × 10^{-8} M) with increasing ct-DNA concentration (10 mM sodium phosphate, pH 7.0, 100 mM NaCl and 1 mM EDTA). The determined value for α, from the intrinsic plot, is used calculate Met_f to be used in (10.9) for the Scatchard plot, on the *right*

$$\frac{DNA_{tot}^k - DNA_{tot}^j}{\rho^k - \rho^j} = \frac{Met_{tot}}{\alpha} \left(\frac{\frac{DNA_{tot}^k}{\rho^k} - \frac{DNA_{tot}^j}{\rho^j}}{\rho^k - \rho^j} \right) + n\alpha \tag{10.6}$$

$$y = \frac{DNA_{tot}^k - DNA_{tot}^j}{\rho^k - \rho^j} \tag{10.7}$$

$$x = \left(\frac{\frac{DNA_{tot}^k}{\rho^k} - \frac{DNA_{tot}^j}{\rho^j}}{\rho^k - \rho^j} \right) \tag{10.8}$$

The free metallointercalator concentration (Met_f) can be determined by subtracting the bound metallointercalator concentration (Met_b) from the total metallointercalator concentration (Met_{tot}). If these values are determined for each titration aliquot and the data used to produce a Scatchard plot of r ($r = Met_b^k/DNA^k$) versus r/Met_f, then ($r/Met_f = \frac{Met_b^k/DNA}{Met_f^k}$). Met_b is calculated from $\alpha \times Met_{tot}$. The slope of $-K_b$ and the y-intercept of K_b/n are obtained from the Scatchard plot (10.9):

$$\frac{r}{Met_f} = \frac{K_b}{n} - rK_b. \tag{10.9}$$

This method does not take into account the existence of more than one binding site, and produces a non-linear Scatchard plot. In these cases the McGee and von Hippel equation can be applied to the data [28]:

$$\frac{r}{Met_f} = K_b(1 - nr) \left[\frac{1 - nr}{n - (1 - n)r} \right]^{n-1}. \tag{10.10}$$

A plot of r/Met_f versus r gives K_b as the intercept on the r/Met_f axis and n on the r axis. The McGee and von Hippel model takes into consideration the effects of cooperative ligand binding, but if cooperativity is significant then the values of K_b and n may be unreliable [28].Any method for processing the binding data has its disadvantages. On some occasions the data just cannot be processed by any model because the theory does not take into account the complexity of the particular binding event.

10.4 Confocal Microscopy

10.4.1 Principles of Confocal Microscopy

The principle of confocal imaging was patented by Marvin Minsky in 1957 [29]. By physically removing the "out-of-focus" light before the image is formed, Minsky managed to overcome some of the limitations of traditional wide-field fluorescence

microscopy [30]. In wide-field fluorescence imaging, the entire specimen is illuminated by a light source. The resulting fluorescence from the focal planes above and below the region of interest in the specimen is detected by the observer, the microscope's photo-detector or by a camera, and the observed signal is thus not specific to the region of interest. The distinctive difference of the confocal approach is that it has the ability to eliminate the "out-of-focus" fluorescence from the specimen by using a pinhole positioned in front of the detector. The term "confocal" originates from this configuration: only fluorescence that is produced from very close to the focal plane is detected. Light detection is limited to a confocal volume, as the pinhole focuses the light emitted or scattered from the specimen before it reaches the detector (Fig. 10.4). A confocal microscope provides an almost perfectly focused plane (the z-plane) with minimal contribution of light from above or below it.

The focal-plane thickness is defined by the inverse of the square of the numerical aperture (N.A.) of the objective lens, by the sample's optical properties and the index of refraction. The higher the N.A., the smaller the amount of out-of-focus light, and the greater the z-plane resolution, which therefore depends almost entirely on the objective's N.A [31]. The confocal mode gives an improved image resolution, in both the lateral and axial planes, and enables serial optical sections to be obtained from the surface down to a depth of 200 mm, a range that is much better than that of wide-field microscopes. The depth of imaging can be controlled, image degrading out-of-focus information is eliminated, and sub-surface
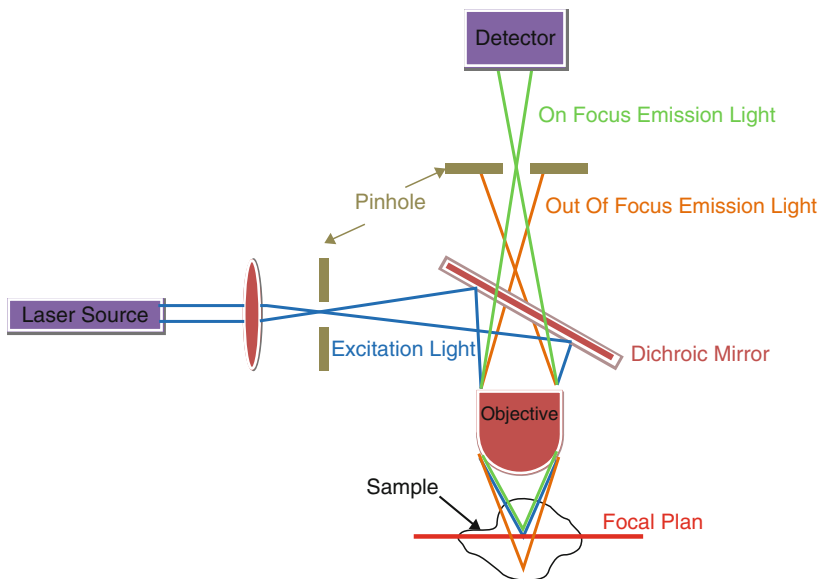
Fig. 10.4 Schematic diagram of a confocal microscope

serial optical sections from thick specimens can be collected (Fig. 10.5). However, since the pinhole blocks much of the light from sample, this increased resolution is achieved at the cost of lowered signal intensity, requiring longer exposure times.

Specimens for confocal imaging do not need to be transparent or thin. Using low magnification (e.g., a 10× objective) it may be possible to optically section several mm into transparent tissue. At higher magnification (e.g., 100× objective) the limit may be approximately 20–50 μm, depending on the density of the specimen.

Confocal imaging is usually achieved by lasers, which are designed to produce and amplify light into intense, focused monochromatic (single-wavelength) beams. Since only one point in the sample is illuminated at a time, imaging is achieved by scanning over a rectangular pattern of parallel scanning lines, i.e., raster imaging. The image is built up from the output of a photosensitive detector. Classes of detector include photomultiplier tubes (PMTs), photodiodes, and solid-state charge-coupled devices (CCDs) [32]. The output is processed in a computer imaging system and displayed on a video monitor.
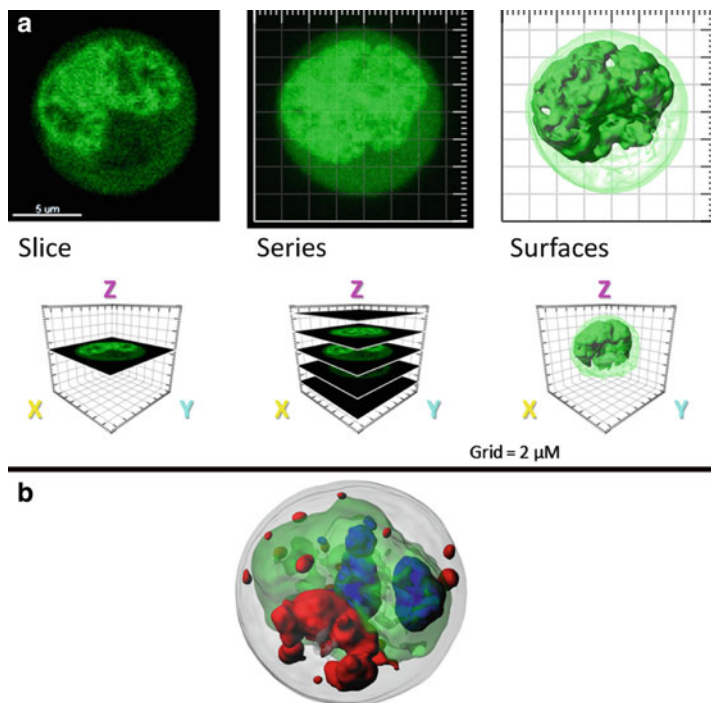
Fig. 10.5 Confocal imaging of fluorescently labelled cells in 3D. (**a**) Serial confocal imaging of L6 cell stained with SYTO - a single slice in the *xyz* plane; a series of slices reconstructed in a 3D mode, rendered to visualize nuclear DNA. (**b**) L1210 cell stained with Acridine Orange (AO) showing DNA and RNA, imaged by Leica SP5 confocal microscope: *green* emissions at 500–550 nm and *red* at 600–680 nm; rendered to represents the co-localisationof *red* and *green* fluorescence in *blue*. All serial sections reconstructed using Imaris software

10.4.2   Fluorescent Probes for Confocal Imaging

Fluorescent probes are fluorophores that bind or accumulate within a specific region of a biological specimen or respond to a specific biological stimulus. They are extremely sensitive and provide us with the ability not only to visualise cellular structures, but also to visualize, track, and quantify proteins and molecules in living cells and study their dynamic migrations and interactions. The widespread use of fluorescent probes can be explained by a combination of sensitivity, ease of use, rapidity, reproducibility and adaptability [31]. With the recent development of fluorescence and confocal methods [32], a very large number of fluorescent probes have become commercially available [33]. There are now thousands of probes available for a wide range of applications. Some fluoro-probes are constructed around synthetic organic compounds that are designed to bind with a biological macromolecule, such as a protein or a nucleic acid. Other probes are designed to localize within a specific structural region of the cell, such as the cytoskeleton, mitochondria, Golgi apparatus, endoplasmic reticulum or nucleus. A range of probes have been developed to monitor cellular integrity, distinguishing between live and dead cells, and probing apoptosis, endocytosis, exocytosis, membrane fluidity, protein trafficking, signal transduction, and enzymatic activity, with a wide range of applications in the field of molecular genetics. Other fluorophores change their emission and excitation spectra depending on the molecular environment surrounding the probe, and are used to determine local pH, ion concentration and membrane potential. The internet contains a wealth of information on many such fluorophores and there are a number of companies that have extensive web-based catalogues such as Invitrogen's Molecular Probes [33].

Metallointercalator drugs can bind to RNA, proteins, and other biomolecules, but DNA is their primary biological target [33–37]. Experimental evidence has shown that the success of platinum complexes in destroying tumour cells is largely due to their ability to form various types of adducts on DNA [35, 36]. For example, ruthenium polypyridyl complexes have been reported to bind and photo-react with DNA [38, 39].

The ability of metallointercalators to bind to DNA can be investigated using nucleic acid-binding fluorescent compounds for DNA visualisation and quantification [37]. The most efficient DNA probes for live-cell imaging are small molecules with a high affinity for DNA [40–42]. A range of DNA and RNA binding probes have been discovered since the 1950s that can be classified according to their molecular structure, the mode of binding and the class of nucleic acids to which they bind.

Hoechst, DAPI (4′6-diamidino-2-phenylindole), propidium iodide, ethidium bromide and SYTO® dyes are the most frequently used fluorescent dyes that bind strongly and preferentially to DNA. Their binding properties correlate well with their molecular structures: ethidium bromide and propidium iodide intercalate with dsDNA [43], whereas the cationic dyes Hoechst and DAPI interact with the minor groove, especially with sequences that are rich in dA/dT [44, 45]. Ethidium bromide

(excitation 535 nm/emission 617 nm) is widely used to probe the structure of DNA and alterations that occur upon interactions with drugs or proteins. Ethidium bromide (EtBr) has a high affinity for DNA and its intercalation site mainly depends upon electrostatic interactions. SYTO dyes (Fig. 10.5), such as Sytox green (excitation 504 nm/emission 523 nm), and chromomycin A3 (excitation 450 nm/emission 570 nm) bind to various nucleic acids and are cell-impermeable, thus requiring that the specimens be fixed and permeabilized [46].

Acridine orange (AO) (Fig. 10.6) is another widely used cationic fluorescent probe. Similarly to EtBr, AO binds to DNA, as it slips between adjacent base pairs
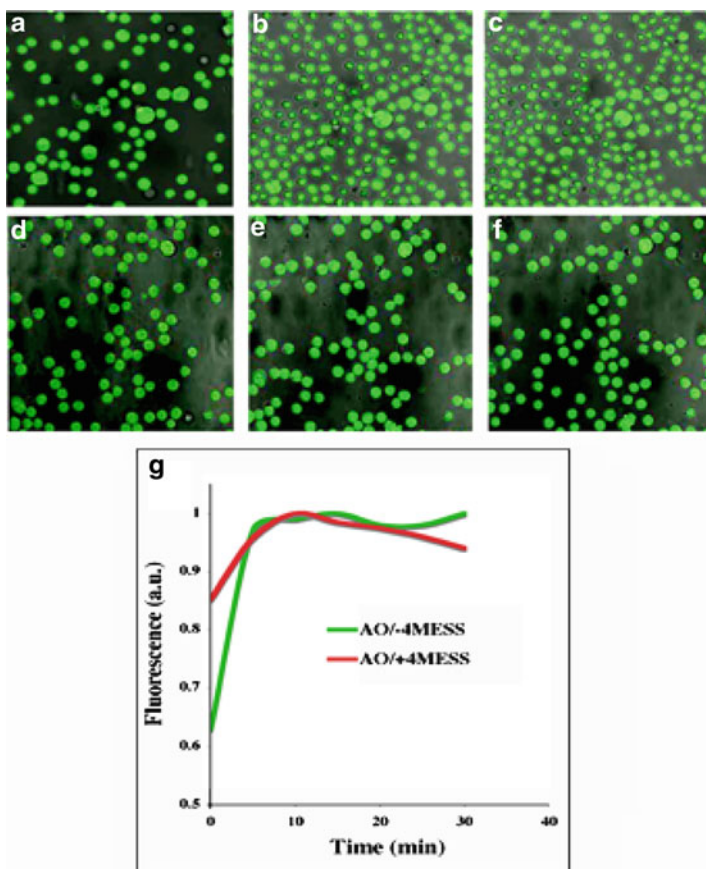
Fig. 10.6 Staining of L1210 cells by AO as part of the displacement experiment of AO by a metallointercalator non-fluorescent compound 4MESS, hypothesized to intercalate with both mitochondrial and nuclear DNA. Confocal imaging of green fluorescence of (**a–c**) control cells stained by AO (+AO/−4MESS); (**d–e**) cells stained by AO and 4MESS (+AO/+4MESS). (**f**) Fluorescence intensity of control and 4MESS cells during 40 min of exposure (at excitation by 488 nm) showing decrease of fluorescence of 4MESS treated cells indicating displacement of AO by 4MESS

of DNA. It is versatile since it can differentiate between DNA and RNA. When bound to DNA, AO fluoresces green, with an excitation and emission maxima at 502 and 525 nm, respectively. When AO binds with RNA, it fluoresces red; excitation maximum shifts to 460 nm (blue) and the emission maximum shifts to 650 nm. Another useful application of AO is its use in conjunction with EtBr to differentiate between live and apoptotic cells. A disadvantage is that acridine dyes tend to be non-permeant for cell membranes, but cells can be made permeable by treatment with a non-ionic detergent at low pH. AO staining can be done on unfixed cells and may be used as a rapid method for analysing cell ploidy levels and cell cycle status from DNA measurements, based on green fluorescence, and cell transcriptional activity from RNA staining, based on red fluorescence [47]. Thus, a wealth of structural and functional information can be obtained by exposing cells to metallointercalator drugs in combination with AO staining.

Staining by AO is an example of the displacement method when testing a novel metallointercalator compound 4MESS ([(4-methyl-1,10-phenanthroline)(1S,2S-diaminocyclohexane) platinum(II)]$^{2+}$), which is not fluorescent, and which was hypothesised to intercalate with both mitochondrial and nuclear DNA was explored (Singh et al., unpublished). The binding constant of 4MESS was known to be greater than that of AO, so that the former would displace the stain in a competitive assay. A significant decrease of AO fluorescence was recorded compared to the untreated control (+AO/−4MESS) during the first 30 min of exposure, when L1210 cells were imaged in x,y,t mode using a Leica SP5 confocal microscope with excitation by a 488-nm laser line. The decrease was attributed to the displacement of AO by 4MESS (+AO/+4MESS) by intercalating with DNA (Fig. 10.6).

For the purpose of investigating the cellular function of metallointercalators, the above mentioned fluorescent probes can also reveal the disruption of DNA interactions with other molecules, such as DNA/protein interactions. The choice of DNA fluoro-stains is dependent on the experimental requirements for imaging of live cells, especially since imaging may require relatively long periods of time, and the need to avoid photobleaching and phototoxicity. It is unfortunate that the majority of DNA fluoro-labels used in cell biology that are cell-permeant, such as DAPI, Hoechst 33342 or 33258, are excited by the ultraviolet (UV, 200–400 nm) part of the spectrum. Even relatively short irradiation periods using these wavelengths can cause extensive photodamage due to formation of free radicals and to cross-linking of DNA and DNA-associated proteins [48]. Normal cellular processes are disrupted, DNA replication fails and mitosis is compromised, leading to cell cycle arrest and death. Whilst EtBr and propidium iodide are excited by less photodamaging wavelengths, the former has limited intercalation capacity, while the latter does not effectively penetrate into cells (Fig. 10.7).

In the last decade, a number of new DNA-binding fluorophores have been developed that are cell permanent, are non-toxic and are excited at longer than UV wavelengths. One such dye, BENA435 (N'-(2,8-dimethoxy-12-methyl-dibenzo [c,h] [1, 5]naphthyridin-6-yl)-N,N-dimethyl-propane-1,3-diamine) has excitation at 435 nm and emission at 484 nm and preferentially binds to double-stranded DNA rather than RNA and intercalates between the opposite DNA strands [49]. The use
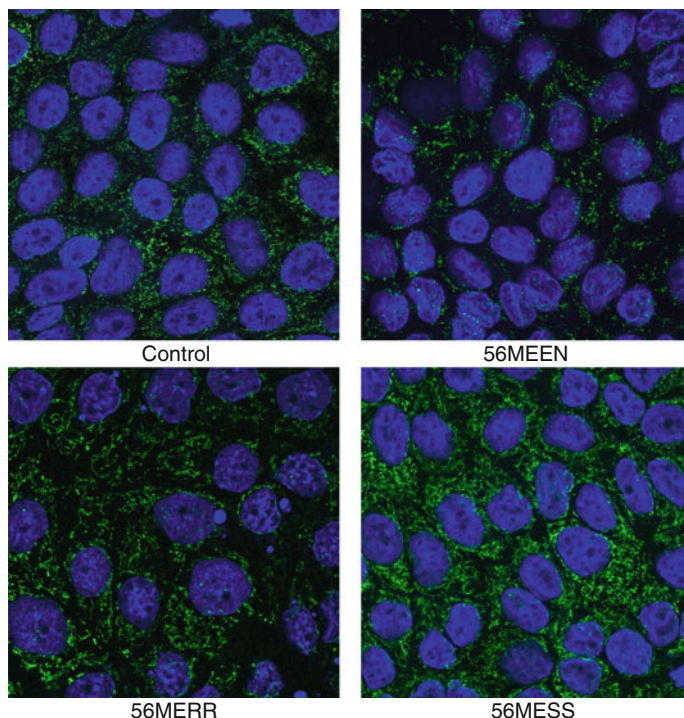
Fig. 10.7 Indirect immunofluorescence images of MDCK cells showing stained nuclei and mitochondria. MDCK cells were treated with 56MESS (2 μM), 56MERR (4 μM) and 56MEEN (5 μM) and an untreated control, where these concentrations represent the IC_{50} concentration for that drug. The MTC02 antibody was used to exhibit the mitochondria (*green*) and and DAPI was used to show the nucleus (*blue*)

of such dyes will spur the research of drug/DNA interactions and are useful in metallointercalator DNA binding studies.

Some of the metallointercalators are themselves fluorescent and can even function as sensitive fluorescent probes; for example, the synthesised ruthenium complexes. Several dipyridophenazine (dppz) complexes of Ru(II) can act as molecular "light switches", as they are almost non-fluorescent in aqueous solution, but acquire intense fluorescence when bound to DNA or when otherwise protected from water [38, 50–54]. Confocal microscopy has been used to investigate whether Ru(II) complexes (for example, $[Ru(DIP)_2(dppz)]^{2+}$, $[Ru(phen)_2(dppz)]^{2+}$ and $[Ru(bpy)_2(dppz)]^{2+}$; (DIP $=$ 4,7-diphenyl-1,10-phenanthroline) penetrate the cellular interior rather than being localized at the membrane surface [53]. The most intense fluorescence was found in the cytoplasm, possibly associated with the mitochondria and endoplasmic reticulum.

Fluorescent probes are frequently used in the determination of binding constants for non-fluorescent compounds using displacement studies, where a fluorescent intercalator (e.g., ethidium bromide or AO) binds to DNA and another molecule

displaces it from its binding site [52, 54]. Once bound to DNA, the stain would exhibit fluorescence that will decrease in intensity after treatment by a non-fluorescent drug due to the latter displacement of the stain. Displacement techniques have been used effectively to investigate the binding properties of metallointercalators, especially in cases when the latter are non-fluorescent. This non-destructive technique allows for the determination of binding constants for such non-fluorescent compounds [53–56].

The sub-cellular localisationof metallointercalators can be best revealed by co-staining experiments using organelle-specific fluorescent probes. Association with mitochondria or endoplasmic reticulum can be imaged using specific fluorescent probes [45, 57]. Common mitochondrial stains include rhodamine 123, DiOC(6) and the MitoTracker dyes (Molecular Probes) [57]. The MitoTracker dyes are cell permeable and are therefore easier to work with than non-permeable stains. Cells are labeled by adding the stain to the culture medium for a period of time during which it accumulates in the organelles. Appropriate protocols are available at Molecular Probes [33]. Since mitochondria have a large membrane potential which is negative inside, many stains have been specifically developed to monitor membrane potential due to their positive charge. DiOC6(3) (3,3′-dihexyloxacarbo-cyanine) stains mitochondria but is non-specific; it will stain other organelles as it accumulates in various intracellular membranes [57]. At low concentrations it accumulates in mitochondria, but at higher concentrations it labels the endoplasmic reticulum (ER), identified by its tubular morphology. This dye is bright (i.e., it has a high quantum yield) but it is lipophilic, which limits its solubility in water, and is not very photostable. It should be made as a 0.5 mg/mL stock solution in ethanol and stored in the dark below 0 °C. It may be diluted to 2.5 μg/mL into growth medium and used to stain living cells for 5 min. At higher concentrations, the dye begins to label cytosolic structures indiscriminately. Following labelling, samples should be mounted in PBS supplemented with 3% N-propyl gallate and imaged immediately. A number of dyes are available for staining Golgi and since these organelles are enriched with enzymes and certain lipids, such properties are used as a staining basis. The C6-NBD and BODIPY-fluorescent analogues of ceramide work well; for example, BODIPY-Cer (Molecular Probes).

The fluorescence or confocal microscopic imaging technique referred to as FISH (fluorescent in situ hybridisation) [42] is another method that may find wide application in investigating the DNA binding activity of metallointercalators. In situ hybridisation is a method that became very widespread for localizing and detecting specific mRNA sequences in tissue sections or cells by hybridizing the complementary strand of a nucleotide probe to the sequence of interest. The location and size of genomic sequences can thus be studied. DNA or RNA sequences from the selected chromosome-specific probes are labelled with fluoroprobes, which are later identified through fluorescence imaging. The labelled DNA or RNA probe is then hybridized to the metaphase chromosomes or interphase nuclei, and after washing and signal amplification the sample is imaged for reporter molecules by fluorescence or confocal microscopy, and the presence or absence of specific sequences on chromosomes is determined. When combined with an

immunofluorescence technique, it is possible to correlate the localisation of chromosomal or other DNA elements with the localisation of specific proteins. The technique becomes especially powerful with the simultaneous use of multiple fluorescent probes. Multicolour FISH can identify as many labelled features as the number of different fluorophores that have been used in the hybridization process. The technique may be used to study individual cells using fluorescence or confocal microscopy. It can do so at multiple wavelengths and multiple focal planes in each cell. There are numerous applications and practical approaches to FISH techniques, including the analysis of interphase cells for multicolour probe spot counts, immunophenotyping, determination of cell DNA content, and the characterisation of marker chromosomes, breakpoints, aberrations and nuclear architecture [58, 59]. It is expected that there will be rapid growth in the use of FISH techniques to study many of the above mentioned cellular parameters, such as the development of chromosomal abnormalities, DNA reactions, changes in nuclear architecture, various epigenetic changes, as well as elucidation of the antitumour effects of metallointercalators.

10.4.3 Green Fluorescent Protein (GFP) Technology

The dominant fluorescence technology for *in vivo* labelling, cellular assaying, imaging and detection is currently based on GFP and related GFP-type proteins [60–63]. GFP's unique properties stem from the fact that its chromophore is encoded by the primary amino acid sequence of the protein, and it forms spontaneously without the requirement for cofactors or external enzymes (Fig. 10.8). As its fluorescence is encoded by a single gene, introduction of this gene into a cell or any organism will produce fluorescence [64]. By fusing GFP to targeting peptide sequences and tissue-specific promoters, it can be directed to specific cellular compartments or tissues. It can be fused to a protein of interest by joining the DNA sequences of GFP and the studied protein.

As a consequence of its molecular characteristics, GFP caused a revolution in the study of cellular processes *in vivo*, allowing direct genetic encoding of fluorescence. It has become the most powerful microscopic, imaging and molecular tool in cell biology, medicine and biotechnology [60]. The discovery of GFP and a series of important research developments that led to its use as a tagging tool in bioscience were deemed to be so important that the 2008 Nobel Prize in Chemistry was awarded to the three scientists involved, Osamu Shimomura, Martin Chalfi, and Roger Y. Tsien. More than any other label, GFP and its related proteins aid in the study of cells, to identify what is in them, assess how they use proteins to communicate and perform various functions, and evaluate how these processes are affected by diseases and pharmacological agents. This is a powerful technology for unravelling the mechanisms of action, cellular localisation and targets of metallointercalators.
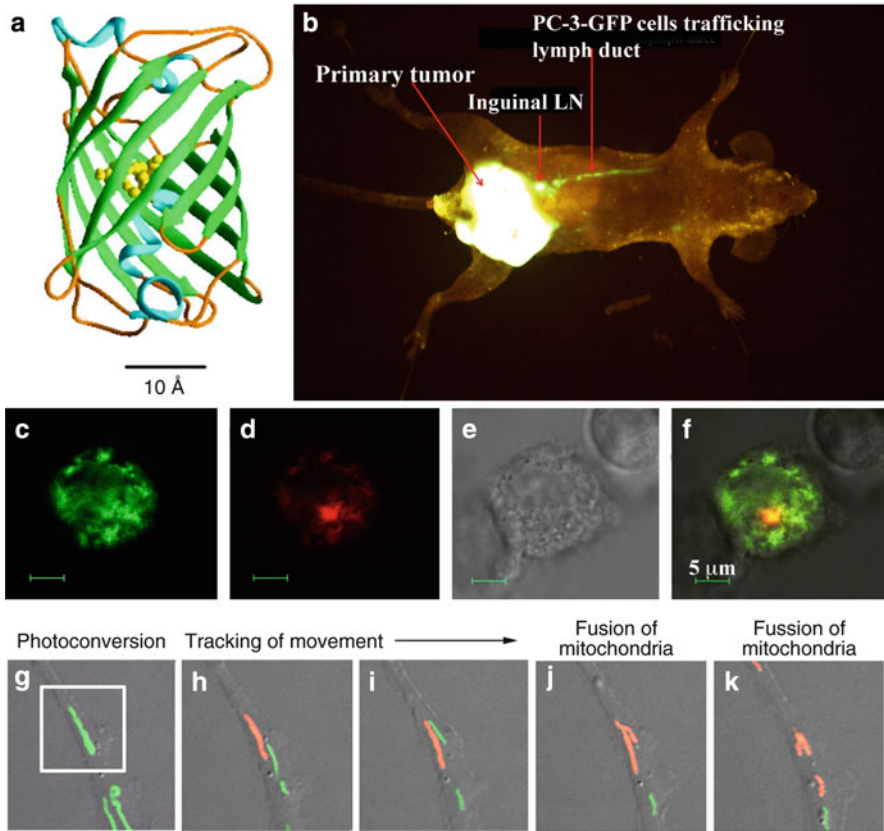
Fig. 10.8 *In vivo* labelling by GFP. (**a**) Molecular structure of GFP. (**b**) GFP-labelled human PC-3 prostate carcinoma cells orthotopically-transplanted into nude mice. The non-invasive image shows primary tumour growth and the metastatic trafficking in a lymphatic duct. Imaging by Indec FluorVivo system and image by T. Nakayama and S. Yagi, AntiCancer Japan; R. Hoffman, AntiCancer Inc. Protein and organelle tracking by a coral GFP-type protein observed by labelling mitochondria with td-EosFP, expressed in L1210 cells and confocally imaged at (**c**) excitation by 488 nm showing green emission of mitochondria; (**d**) at excitation 561 nm laser, red emissions from a small AOI, photoconverted to red by 405 nm laser irradiation; (**e**) transmitted light image of the cell; (**f**) merged images c–e. (**g–k**) A single mitochondrion was converted from green to red by 405 nm laser in the region indicated by white rectangle and its movement and fusion events tracked by red fluorescence over time. Image by M.W. Davidson (Florida State University), modified from Wiedenmann et al. 2009

A range of *in vivo* fluorescence labelling and detection technologies were originally based on a single (wild-type) GFP from a jellyfish *Aequorea victoria*. In the wild-type GFP (wt-GFP), the chromophore is formed through an autocatalytic, post-translational cyclization and oxidation of the tripeptide unit [65]. Substitutions, via mutagenesis, of one or more amino acids in close proximity to the chromophore resulted in a range of GFP mutants, with different absorption and

emission properties and, in some cases, improved emission and photostability [66]. Because of the rapidly increasing number of applications, there is a huge demand for an expanded "library" of GFP-like proteins. This has led to the development of blue (BFP), cyan (CFP) and yellow (YFP) fluorescent proteins, enabling the simultaneous multi-colour imaging of a range of proteins, genes and cells [67].

When GFP-type proteins were discovered in reef organisms in 1999 [68] a new multi-colour labelling revolution began. A range of GFP-type fluorescent proteins have been cloned from anemones and corals [69–73], in in which they are especially abundant. Their colours cover almost the full visible spectrum, and many have unique photoactive properties and biochemical characteristics that are highly useful for developing cellular and molecular biosensors [63, 68, 74]. The first red GFP-type protein, named DsRed and derived from a zoanthid, a coral-like organism [68], was soon followed by the discovery of other cyan, green, orange and red GFPs. The list of organisms with GFP-type proteins so far includes corals, sea anemones, hydrozoans, crustaceans and even amphioxus, a basic chordate animal. The fluorescence colours range from cyan to red [72, 73, 75]. The race to discover and mutagenically optimise these proteins continues, leading to a colour palette of GFP-type proteins with improved optical properties, brighter fluorescence, red-shifted colours, enhanced photostability, photoactivity, reduced oligomerisation, pH insensitivity, and faster maturation rates [63, 71, 76]. A number of companies specialize in developing various GFP-type fluorescent protein labels, derived from marine organisms, and marketing them to the research and biomedical community. For example, Evrogen and Invitrogen, are companies with an excellent range of GFP-type fluorescent protein labels, photoactive GFPs and GFP-based cellular sensors.

The major application of GFP technology is as a tagging molecule for real-time research in live cells. These probes are efficient reporters for monitoring gene expression and protein localisation after insertion of signal sequences into the gene [64]. Due to the tremendous popularity of GFP, it has been successfully targeted to almost every cell organelle. When fused to host proteins, GFP-type proteins have been exceptionally successful in marking subcellular compartments such as nuclei, mitochondria (Fig. 10.9), endoplasmic reticulum, Golgi apparatus, plasma membranes, secretory vesicles, peroxisomes and phagosomes [77].

GFP-based labelling technologies offer tremendous opportunities to identify the sites of cellular accumulation of metal complexes, their distribution and effect on cellular compartments and organelles. Metallointercalator activity inside the nucleus can be explored using cells expressing histone H2B fused with a GFP-type protein (supplied by Evrogen). Confocal imaging of chromatin and DNA-histone interactions [78] offers a valuable tool for studying the mechanism of action of antitumour drugs that target DNA. GFP-based techniques can be combined with the use of other fluorescent probes, such as those that are specific for DNA.

GFP-type proteins have become invaluable in the study of tumour cell mobility, invasion, metastasis and angiogenesis in live cells, tissues and whole organisms [79]. Using a stably transfected single or multicolour GFP variant, it is now possible to study the behaviour and anticancer and antitumour activity of metallointercallators in cancer cells, and even in whole organisms that express fluorescent proteins.
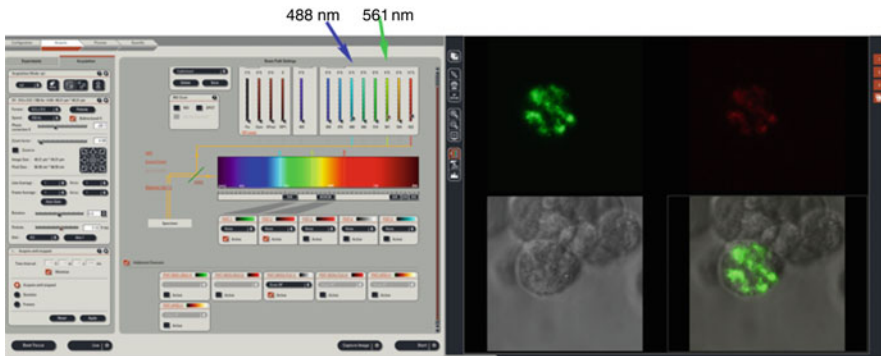
Fig. 10.9 Confocal imaging (Leica SP5, Leica Microsystems) of a coral GFP-type protein t2EosFP fused to a mitochondrial localisation signal and expressed in L1210 cells. Confocal settings showing 488 and 561 nm laser line settings and emissions directed to PMT 1-2 and 633 nm laser line transmitted line imaging (*right panel*); corresponding green emissions in PMT1, weak red emissions in PMT2; transmitted light image in PMTNOD3; and merged image

Their activity can be analyzed in real-time by tracking tumour growth and metastasis in intact animals by using, for example, transgenic mice that express GFP in all of their cells, which have been transplanted with tumour cells that express RFP (a red GFP-type fluorescent protein). The red fluorescence of the tumour cells against the green fluorescence of healthy tissue can be effectively visualised and measured in real time using fluorescence imaging [79]. When single-cell resolution is required, reversible acute skin-flaps, as well as surgically created "chronic-transparent window" models, can be used over many parts of the body such as the skin, brain, lung and liver [80].

Another new and exciting GFP-based method that emerged during the last decade is the use of GFP-type photoactivatable fluorescent proteins (PAFPs) to label cells, proteins or molecules and to reveal their dynamic movement inside cellular compartments [63, 74, 81]. After irradiation, PAFPs alter their fluorescence intensity without extensive photo-destruction or switch from one colour to another, and are referred to as photoactivatable, photoswitchable or photoconvertible proteins. Since photoactivation imaging techniques are related to other techniques for analysing dynamic events in cells, described in this chapter, the use of PAFPs is described in more detail in Sect. 10.3.4.4 below.

10.4.4 Confocal Methods to Analyse Dynamic Events and Biomolecular Interactions

The invention of GFP imaging technology revolutionised the study of live-cell protein dynamics, and was accompanied by another series of major developments that made it possible to simultaneously image the dynamics of genes, proteins and

various other molecules, and to correlate these measurements with structural changes or ligand binding. The majority of biological molecules are not freely mobile *in vivo*, but they may alternate between free states and states that are bound by their biological functions, sometimes leading to their immobilisation. Diffusion kinetics and molecular interactions can be spatially analysed using a number of fluorescence-based imaging techniques. This can be done accurately and within cellular compartments of living cells. Some of the more important techniques, useful in analysing DNA binding capacity, intracellular localisation and intracellular mobility of novel metallointercalators, are described below.

10.4.5   *Förster Resonance Energy Transfer (FRET) Imaging*

The first of these methods is known as fluorescence or FRET [82], named after the German scientist Theodor Förster, who developed the quantitative theory of molecular resonance energy transfer in the 1940s. FRET is used to measure how close two fluorophores are together [83, 84]. Using various fluorescent probes to label proteins of interest, or using GFP, GFP-type proteins or GFP mutants with different fluorescence wavelengths, FRET techniques can be used to monitor protein–protein interactions, binding and changes in conformational state.

FRET makes use of interactions between the excited electronic states of two fluorophores, and occurs when the emission spectrum of one fluorophore (the donor) overlaps the absorbance (or excitation) spectrum of a second fluorophore (the acceptor) (Fig. 10.10, left). For FRET to occur the donor fluorophore is excited by light and if an acceptor is in very close proximity, the donor's excitation energy is transferred non-radiatively (without the emission of a photon) to the acceptor fluorophore, via dipole–dipole interactions. FRET leads to a reduction in the donor's fluorescence intensity and a corresponding increase in the corresponding intensity for the acceptor. FRET is very sensitive to the distance between two fluorophores, falling off with the sixth power of the separation between them [85, 86]. In practice it occurs over very short distances, typically ranging from 10 to 100 Å, (1–10 nm).

The efficiency (E) of FRET is described by the Förster equation:

$$E = 1/[1 + (9R/R_0)^6] \qquad (10.11)$$

where R is the distance between the two fluorophores and is related to the Förster radius, R_o, which is the distance at which energy transfer is approximately 50% efficient, corresponding to 50% of the excited donors being deactivated by FRET.

The following conditions need to be satisfied for efficient FRET to occur:

- the donor and acceptor molecules must be in close proximity
- the absorption spectrum of the acceptor must overlap the fluorescence spectrum of the donor
- the donor and acceptor dipole orientations must be closely parallel.
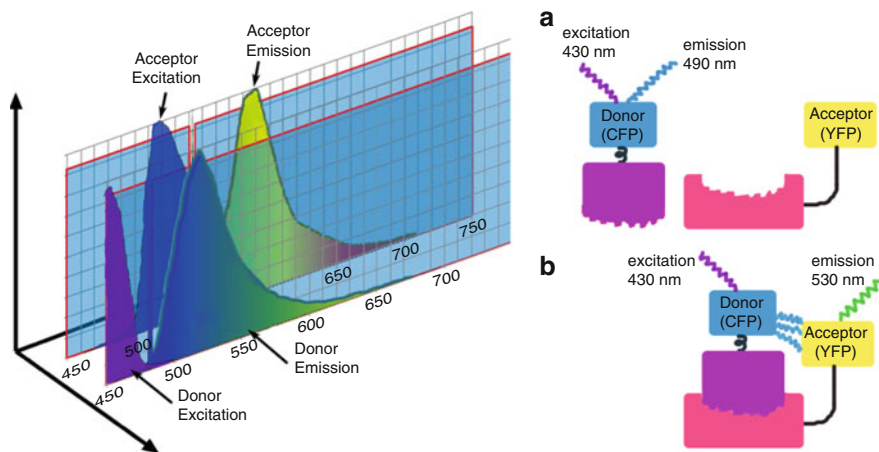
Fig. 10.10 *Left*: A representation of excitation and emission spectra of *blue* (donor) and *green* (acceptor) fluorophores which show spectral properties suitable for FRET due to donor emissions closely matching acceptor excitation. *Right*: A diagrammatic representation of a FRET-based sensor made from a donor CFP and an acceptor YFP to measure protein–protein interactions. When one studied protein (*pink*) fused with CFP and another protein (*red*), fused to YFP, do not interact, illumination with cyan (~430 nm) light results in stronger CFP fluorescence (**a**). As a result of molecular interactions between the two proteins (e.g., phosphorylation or binding), the donor CFP and the acceptor YFP are brought into close proximity, FRET occurs and donor's fluorescence is quenched as the excitation energy is transferred to the acceptor, resulting in stronger YFP fluorescence at 430 nm excitation (**b**)

FRET efficiency (E) can also be defined as the number of quanta transferred to an acceptor, divided by the total number of quanta absorbed by the donor. E is linearly proportional to the degree of molecular interaction with respect to the donor-labelled molecule, represented by the equation:

$$E = \left(\frac{E_{\max} x (DA)}{(D_{total})} \right) \tag{10.12}$$

where $E_{\max}$ is the FRET efficiency of the interacting complex, and DA and D_{total} are the concentrations of the donor–acceptor complex and total donor, respectively. FRET-based imaging analysis is now commonly performed using confocal microscopy by measuring the fluorescence intensity of the donor with and without an acceptor present.

The distance-dependent transfer of energy from an excited donor fluorophore to an acceptor fluorophore is widely used with GFP, its mutants and various multi-colour coral GFPs, as well as in combination with various cellular dyes [10]. Numerous cellular GFP-based biosensors have been developed that exploit FRET to detect protein–protein interactions and conformational changes (e.g., Fig. 10.10 right), and that allow direct visualisation and analysis of signalling cascades and protein binding. GFP-based FRET imaging methods have been instrumental in

elucidating the compartmentalisation and functional organisation of living cells, and tracing the movement of proteins inside cells. Other applications include studying the interactions between cellular components with each other and with exogenous proteins; dimer and polymer formation; enzyme–substrate binding; and DNA binding.

When selecting appropriate GFP-type proteins for FRET the most important considerations include:

- the donor and acceptor spectroscopic properties that require sufficient separation in excitation spectra for selective stimulation of the donor
- an overlap (>30%) between the fluorescence spectrum of the donor and the excitation spectrum of the acceptor to obtain efficient FRET
- sufficient wavelength separation between the fluorescence spectra of the donor and the acceptor GFPs to allow independent measurement of the fluorescence of each fluorophore.

FRET methodology provides a novel means to investigate the binding capacity of metallointercalators within nuclear compartments. For example, observed quenching of fluorescence emissions of a donor DNA-staining fluorophore following treatment with a fluorescent intercalator that acts as an acceptor fluorophore would indicate binding of the intercalator to DNA, resulting in FRET between them. Multiple intercalator donor and acceptor reagents can be assembled in a DNA duplex to achieve FRET between them and used to study nuclear processes. FRET and electron transfer along the DNA molecule has been closely studied due to the effective electron and energy transfer capacity of the stacking of π-electrons of the DNA base [87]. An example of energy transfer along DNA from the metallointercalators non-covalently bound to DNA was observed in the DNA intercalator [Ru(phen)$_2$(dppz)]$^{2+}$ which was quenched by an intercalated donor [Rh(9,10-diiminephenanthrenequinone)$_2$(phenanthrolone)]$^{3+}$. FRET and quenching was significantly reduced when DNA was modified by nonintercalating [Ru(NH$_3$)$_6$]$^{3+}$ [88]. Energy transfer via FRET has been shown between DAPI and Ru(II) complexes when both bound to poly[d(A-T)$_2$]. By evaluating the efficiency of FRET between fluorescently labelled DNA and various Ru(II) complexes it was possible to deduce the latter binding modes to DNA [89]. Another mode of unraveling the activity of metal intercalators is by analyzing FRET between metal complexes and nuclear proteins such as for example, fluorescently labelled histones and fluorescent metallointercalators. FRET-based measurements offer an exciting method to explore the local variations in nucleic acid structure and activity in response to metallointercalator binding and this can be done in living cells and in real time.

10.4.6 Fluorescence Lifetime Imaging Microscopy (FLIM)

The other method for exploiting fluorescence processes in research is to measure how quickly the excited state molecules lose their stored energy as fluorescent light,

i.e., to determine their fluorescence lifetime. When a molecule absorbs light, there is a short delay in fluorescence emission because, as described in Sect. 10.2, the molecule has to lose some energy before it reaches the lowest vibronic level of the S_1 state (Fig. 10.1), which has an inherent radiative lifetime. Fluorescence emission occurs from this level. After an initial delay at excitation, the decay follows first-order kinetics (an exponential decay curve) provided only one chemical species is involved and there is no fluorescence energy transfer via FRET. If a large number of similar molecules with similar local environments are excited by a short laser pulse the fluorescence decay function is, therefore, a single exponential. Thus, the fluorescence of these molecules is not only characterized by their quantum yield and emission spectra, but also by their lifetime. Fluorescence life-time imaging (FLIM) can be used to distinguish or identify fluorophores in cells.

The formula describing first order kinetics is:

$$\frac{I}{I_0} = e^{-kt} \tag{10.13}$$

where I is the intensity at time t, I_0 is the initial intensity, k is the fluorescence decay rate and e is the base of natural logarithms and has a value of approximately 2.13.

The fluorescence lifetime, τ, is defined as:

$$\tau = \frac{1}{k} \tag{10.14}$$

or in other words the time taken to decay to $1/e$ of the original intensity. It is approximately the same as the half-life of fluorescence.

FLIM may be implemented using either a frequency-domain or time-domain technique. Frequency-domain techniques rely on chopping (gating) the laser beam using an electro-optical modulator (EOM). The longer the lifetime, the further out of phase with the excitation pulses the detected signal will be; i.e., there is a bigger phase shift between the modulated or pulsed excitation and the emission of the sample. By controlling signal detection with a "lock in" amplifier in relation to the chopping of the incoming signal, it is possible to measure different fluorescence lifetimes. For example, Rhodamine B will be detected at 0–2 ns, and fluorescein at 3–4 ns later. Lifetime imaging can be achieved with modulated image intensifiers and wide-field microscopes, or by modulating single-channel detectors used in laser scanning microscopes, as built by Carlsson and co-workers, but with few commercial versions available [90].

The time-domain approach relies on the use of pulsed excitation, and the fluorescence decay function is recorded directly with time-correlated single photon counting (TCSPC), gating, or a streak camera. The fast pulses of a titanium sapphire (TiS) laser are commonly used, producing multiphoton excitation for TCSPC [91–94]. This is the basis of a commercial system made by Becker and Hickl, and offered by all of the major manufacturers as an accessory to their multiphoton microscopes. The TiS laser has a repetition rate of 80 MHz, which

means that the time between pulses is 12.5 ns. There will be about 200 of these pulses at each pixel as the beam scans the sample. Only one photon will be recorded for each pulse and put in a "bin" according to its time of arrival. Gradually a full lifetime histogram is acquired from the contents of the bins (Fig. 10.11). It should be cautioned, however, that two-photon lifetimes may be different from single-photon lifetimes.

The fluorescence lifetime, τ_0, is a constant for a given molecule and refraction index of the solvent. The lifetime of cellular autofluorescent molecules can be as short as 100 ps. On the other hand the lifetimes of dye aggregates or of dyes connected to metallic nano-particles are very much shorter, down to 50 ps. In contrast to measurements that are based on fluorescence intensity, the time-resolved fluorescence microscopic technique allows measurement of dynamic events at very high temporal resolution. It is an excellent technique for distinguishing cellular auto-fluorescence from the fluorescence of dyes, reagents and GFP-type proteins and can better distinguish different types of fluorophore molecules that have similar emission spectra, i.e., that fluoresce with similar colours (Fig. 10.11).

Importantly, FLIM measurements are independent of excitation intensity, unlike the fluorescence intensity-based measurements, where the strength of the signal depends on the excitation intensity and the fluorophore concentration. Lifetime measurements are also independent of fluorophore concentration. This is very important for FRET measurements, and, for this reason FLIM-based FRET analysis is becoming much more popular than fluorescence intensity-based FRET [92, 94]. Moreover, FLIM avoids the problem of the spectral bleed-through or cross-talk commonly encountered in fluorescence intensity measurements and one does not have to identify whether the imaged emission is a result of the sensitised emission or the bleed-through signal. FRET-based FLIM is probably the most widespread application of FLIM in cell biology, with applications such as analysing FRET interaction between fluorescently labelled specific proteins, lipids, enzymes, DNA and RNA, cleavage of a protein and protein conformational [92, 94]. Aside from FRET, the lifetime of a molecule is also influenced by its local environment, including the local viscosity, pH, and refractive index [95]. FLIM can therefore be used to probe the surroundings of a fluorophore.

FLIM is a highly effective method for analysing DNA binding of nuclear dyes. EtBr, AO, methylene blue and similar fluorescent compounds that are commonly used to probe DNA structure in drug-DNA and protein–DNA interactions, show an increase in lifetime upon binding to DNA and RNA by intercalation, as the molecules slip between adjacent base pairs and cause stretching of the double-helical structure. For example, the lifetime of AO increases as a function of nucleotide to dye (P/D) ratio [96]. This increase in fluorescence lifetime upon DNA binding is used as the basis of a competitive exclusion method to study the interaction of a variety of fluorescent and non-fluorescent compounds with DNA. It can, therefore, be useful in studies of non-fluorescent metallointercalators via the analysis of AO's lifetimes in exclusion studies, and can elucidate the relative extent of DNA cleavage by different metal complexes.
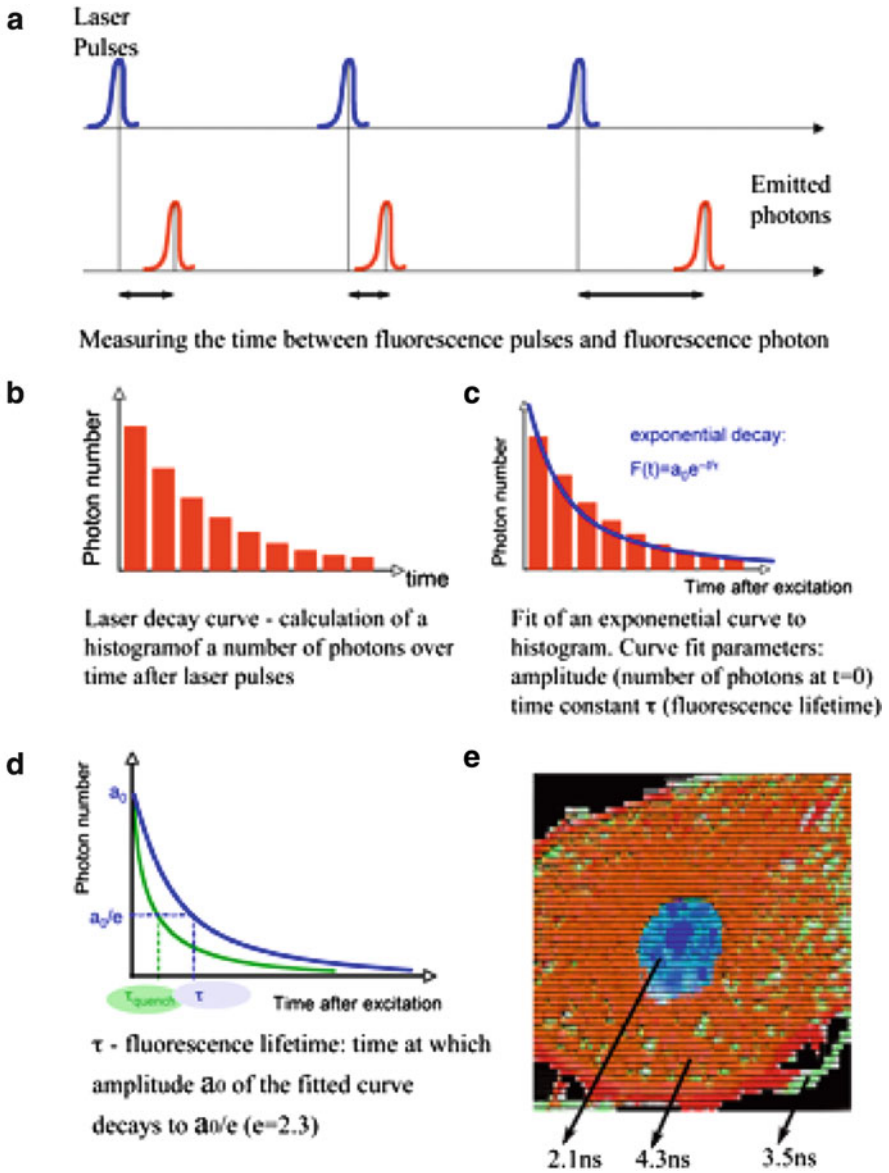
Fig. 10.11 The FLIM time-domain approach to analysing fluorescence lifetimes of fluorophores with TCSPC. (**a**) Measurement of time between pulsed excitation and the emission of photons; (**b–d**) Lifetime histogram, fit of the exponential curve to the histogram and calculation of lifetime from the fitted curve; (**e**) a FLIM image of a cell in which lifetimes are measured at each pixel and displayed as colour contrast, showing distinct lifetime differences between fluorescently labelled nucleus and other cell compartments

Metallointercalators that are themselves fluorescent can make excellent lifetime probes for probing DNA. For example, $[Ru(phen)_3]^{2+}$ and its derivatives are highly fluorescent ($\lambda_{max} = 610$ nm, lifetime $= 0.6$ ns in aerated aqueous solution). DNA intercalation leads to an increase in lifetime for the MLCT excited state. The single-photon counting experiments show a biexponential decay in emission from $[Ru(phen)_3]^{2+}$ bound to double-helical DNA. The longer-lived component (lifetime $= 2$ ns) has been assigned as the intercalated component, and the shorter-lived 0.6 ns component has been attributed to a mixture of free and groove-bound species.

FLIM has exquisite sensitivity and promises to be a valuable tool in the study of DNA–metallointercalator interactions. However, whilst quenching kinetics that affect fluorescence lifetimes can be straightforward, more commonly the analysis can be very complicated when multiple molecules, aggregates and macromolecules are involved in complex quenching kinetics. Nonetheless, the sensitivity of FLIM promises to resolve many of the structural/functional questions associated with this area of research.

10.4.7   Fluorescence Recovery After Photobleaching (FRAP)

FRAP is a technique that is most commonly used to study the location, diffusion and binding of proteins in cell-biological applications [97–100]. It can also be used to study structure and dynamics within natural and synthetic gels, solutions and mixed systems. It is a highly promising technique for studying the intracellular nuclear localisation, binding and intracellular diffusion properties of various metallointercalators.

FRAP is a relatively easy technique to perform, usually with a confocal microscope. It involves the photobleaching of autofluorescent molecules or fluorescently labelled particles within a defined area of interest (AOI) in a sample. This is achieved by irradiating the sample with a high-intensity laser, followed by monitoring the time course of the recovery of fluorescence intensity in the photobleached region (Fig. 10.12). Gradually the unbleached fluorescent molecules diffuse into the bleached AOI from the surrounding area, leading to the recovery of fluorescence. As they re-equilibrate in the cell, the extent and rate at which this occurs can be quantified and used with computer-modelling approaches to describe the kinetic parameters of a protein or a fluorescently labelled molecule. Since high laser power is used, it is extremely important to perform control experiments to evaluate the effect of photodamage, and to determine whether there is any alteration of the cell microstructure, molecular or biochemical pathways.

Depending on the protein studied, fluorescence recovery can result from the diffusion of the fluorescent molecule; its binding, dissociation or transport may also contribute to the process [99–102]. The FRAP technique is especially useful for studying the dynamics of 2D or 3D molecular mobility processes such as diffusion, transport or any other kind of movement of fluorescently labelled molecules in cells. Nowadays, confocal microscopes are specifically designed to enable
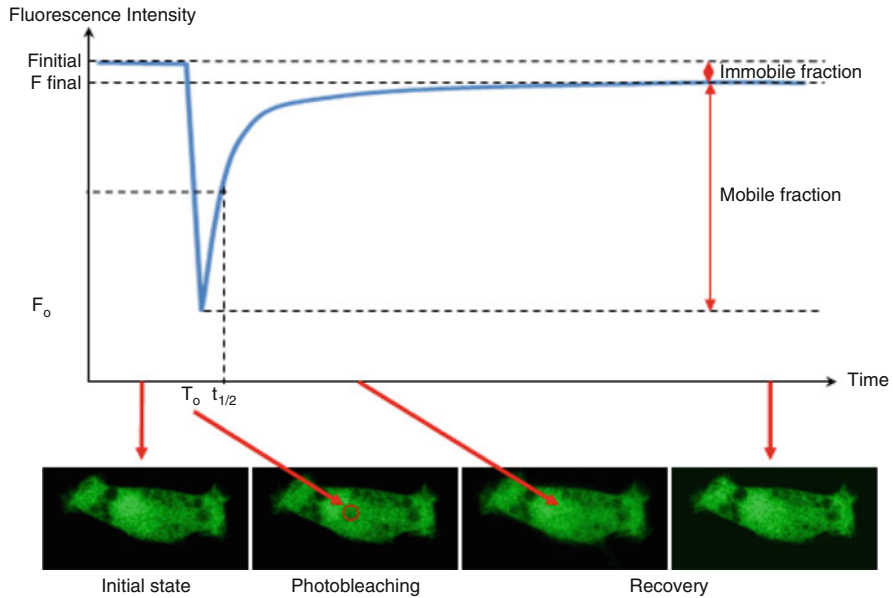
Fig. 10.12 The FRAP principle. A cell is uniformly labelled with a fluorophore (here shown expressing the EGFP-type protein) and a defined AOI is bleached using a strong laser pulse. Fluorescence recovery in AOI is monitored over time using time-lapse confocal imaging until fluorescence is restored in the bleached area

bleaching of circles, rectangles, lines or of precise areas inside cells, or of an excitation spot in an AOI. In this way, a specific cell compartment can be precisely bleached and its fluorescence intensity over time monitored, as fluorophores diffuse back into the bleached area. One of the key kinetic parameters of a protein movement studied by FRAP is the analysis of the mobile fraction, i.e., the fraction of fluorescent molecules that can diffuse into the bleached AOI during the time course of the recovery (Fig. 10.12) [99, 100, 102]. The technique provides such information as the half time of recovery ($t_{1/2}$) and the proportion of molecules that are mobile in selected cellular compartments [97]. Cells that express GFP-tagged proteins, or various other fluorophores, can be imaged at selected time intervals, ranging from nanoseconds to to many hours, providing important information about changes in the steady-state distribution of fluorescently labelled molecules over time. The time course of fluorescence recovery is monitored using a low-intensity laser, and the resulting curve is analysed to extract a diffusion coefficient, D, where $D = \ln2/t_{1/2}$. D is related to the mean squared displacement that a protein undergoes through a random migration over time, usually reported as $cm^2\ s^{-1}$ or $mm^2\ s^{-1}$ [97]. The theoretical D for a protein is related to the protein's size and its cellular environment, and deviations from this value can provide useful information about the environment of the protein. Questions such as whether the molecule of interest is freely diffusing, bound to an immobile scaffold, or undergoing binding with a protein or DNA, can be answered.

The percentage of fluorescence recovery is calculated using the formula:

$$\% \text{ recovery } = \left(\frac{F_{inital} - F_0}{F_{inital} - F_{final}}\right) \times 100 \qquad (10.15)$$

where $F_{initial}$ is the fluorescence intensity before photobleaching; F_0 is the fluorescence intensity after photobleaching; and F_{final} is the fluorescence intensity at the end of the experiment [97]. It is usual for proteins within a cellular compartment to diffuse throughout the compartment, and they are rarely immobilised unless they are bound to other proteins. In the case of fluorescent metallointercalators, the FRAP technique can be used to monitor their mobility and binding, which can be determined from the slope of the curve as shown in Fig. 10.12. The steeper the curve, the faster the recovery and, therefore, the more mobile the molecule. As stated above, the theoretical value of D is related to the fluorophore's size and its cellular environment, and deviations from this value can provide useful information about this environment. A lower D indicates slower diffusion, and a possible reason is that the fluorophore has been incorporated into an aggregate or a complex, and D is inversely proportional to the fluorophore's size. It can also indicate whether the intracellular environment encountered by the fluorophore is more viscous, or provide information about the level of interaction with fixed molecules and macromolecules. FRAP is especially useful for determining the DNA-binding kinetics of various DNA-interacting proteins, since binding to DNA causes immobilisation of the protein [103]. FRAP should prove exceptionally useful as a powerful tool for studying the mobility of fluorescently-labelled intercalating compounds and their DNA binding properties in living cells.

10.4.8 Photoactivatable GFP-Type Proteins to Monitor Molecular Kinetics and Interactions

The first photoactivatable fluorescent protein (PAFP), related to GFP-type proteins and capable of pronounced spectral changes in response to irradiation at a particular wavelength, was reported a decade ago [74, 104]. Since then, nearly every year, one or several PAFPs have been discovered in marine organisms or created mutagenetically [104–109]. The discovery of PAFPs has provided an unprecedented and minimally invasive technology for the study of protein dynamics by using optical marking, and methods of differentially highlighting and tracking cells, organelles, and fusion proteins. PAFPs now represent the second generation of GFP-based tools [74, 100, 102] as they enable direct photolabelling of molecules and cellular components. They are now replacing the more traditional FRAP technology of indirectly analysing fluorescence kinetics in or out of a photobleached region. Photoactivation allows the spatial detection of the successive translocations of proteins in a cell, and therefore, permits a visual, pulse-chase, real-time view of protein

Fig. 10.13 PAFP method by confocal imaging and time series. A cell expressing a green-to-red fluorescent protein linked to a protein of interest is irradiated by a green laser line in the nucleus, and the fluorescence intensities in green and red channels are monitored in three ROIs (in the nucleus, cytoplasm and a cytoplasmic organelle). (**b**) A spot in the nucleus irradiated by green laser line for 30 s and the protein construct in the spot is converted from green to red fluorescence; (**c**) red fluorescence of the converted protein construct spreads in the nucleus: (**d**) and is exported through the nuclear pores and cytosolic cellular compartments imaged at 180 s following irradiation
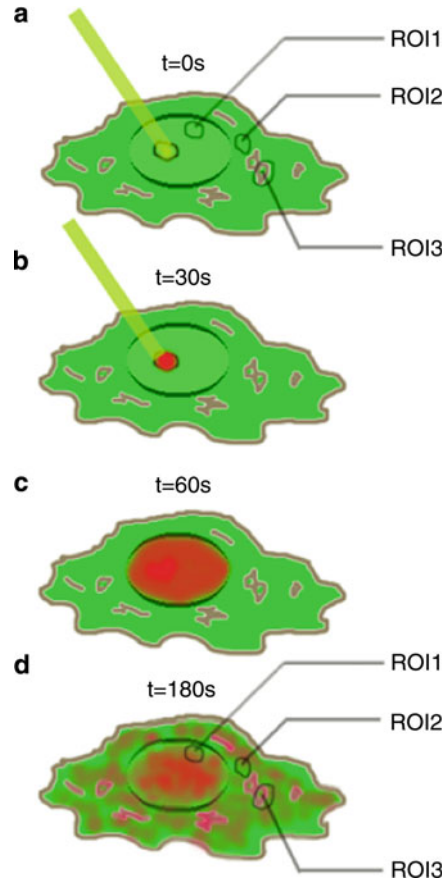
dynamics. The technique works by converting molecules to a fluorescent state by using a brief pulse of high-intensity irradiation. After fluorescently highlighting a specific population of molecules in the region of interest (ROI), as is done in FRAP, the fluorescent molecules can be followed as they re-equilibrate in the cell (Fig. 10.13). This technology promises to give profound insights into how metallointercalators enter and are retained in different membrane-bounded compartments of cells, as well as their DNA binding activity and their effects on nuclear proteins.

10.4.9   Fluorescence Correlation Spectroscopy (FCS) Imaging

In this technique, the two methods: fluorescence spectroscopy and laser confocal imaging have been combined to produce a powerful technique that can be used to address the major goals of current biological research dealing with the identification

and physico-chemical characterisation of processes at the level of individual molecules, proteins and nucleic acids. An extremely sensitive technique is required to analyse minute quantities of molecules in cellular compartments. FCS provides the required high-resolution spatial and temporal analysis of biomolecules. It is somewhat different from other fluorescence techniques in that its goal is not the measurement of fluorescence emission intensity itself. Instead, it uses the statistical analysis of spontaneous fluorescence intensity fluctuations caused by minute deviations of the small system in order to decipher dynamic molecular events, such as diffusion or conformational fluctuations. A detailed description of FCS analysis will not be presented in this chapter as there are several excellent reviews on the subject [110–113]. For beginners, outstanding tutorials and training materials can be found at the website of Professor Enrico Gratton at the Laboratory for Fluorescence Dynamics (LFD), University of California.

In simple terms, FCS is based on a correlation analysis of fluctuations in the fluorescence intensity, and all physical parameters that give rise to fluctuations in the fluorescence signal can be analysed by this technique. The large-scale fluctuations present in a system, such as chaotic system fluctuations, are ignored. In such a system, the physical parameters, such as concentrations of fluorescent molecules, are statistically averaged by the large number of molecules present and their fluctuations cannot be analysed. In FCS, the system size is limited to a tiny fraction (1 fL) of the larger system, defined by a tightly focused laser beam (Fig. 10.14). The fluorescence emitted from this minute spot arises from a small number of fluorescent molecules, and thus the fluctuations in fluorescence intensity are due to Brownian motion of these molecules, as well as the photophysical kinetics of the excitation and relaxation processes of the molecules, which occur in a sub-space defined by the optical system, i.e., the confocal volume. The number of fluorescent molecules randomly changes around the average number, and the analysis provides both the average number of fluorescent molecules and the average diffusion time of
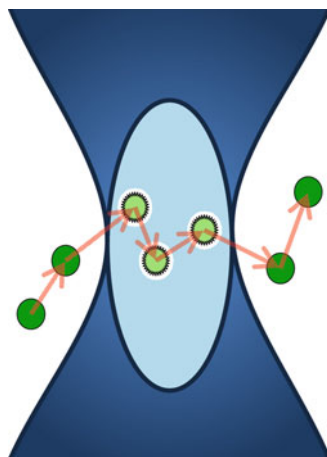
Fig. 10.14 A beam parked in a confocal volume in which molecules are moving in and out

a molecule as it passes through an optically defined space. Eventually, both the concentration and the size of the studied molecule are determined. Fluorescence intensity fluctuations measured by FCS represent changes in either the number or the fluorescence quantum yield of molecules resident in the detection volume (Fig. 10.14). Small, rapidly diffusing molecules produce rapidly fluctuating intensity patterns, whereas larger molecules produce more sustained bursts of fluorescence.

Since the method observes only a small number of molecules in a very tiny spot, it is a very sensitive analytical tool. Both parameters are very important and essential in the biochemical research, biophysics and chemistry, and more recently, in cell biology and biomedicine. In contrast to the other methods, such as HPLC analysis, FCS requires no physical separation process and has good spatial resolution, as determined by the optics. These are great advantages. Moreover, the method enables us to observe fluorescence-tagged-molecules in the biochemical pathways of intact living cells and organs. It therefore opens up a new area of study, "in situ or *in vivo* biochemistry". It is, for example, rather straightforward to determine the local concentrations, mobility coefficients or characteristic rate constants of inter- or intramolecular reactions of fluorescently labelled biomolecules in nanomolar concentrations inside living cells [109–113].

During FCS measurements, fluorescently tagged molecules pass through a strongly focused laser beam and their emitted photons are analysed using super-sensitive detectors. Confocal imaging and FCS produce a defined limit to the expansion of the observation volume along the optical axis of the confocal image plane and allow experiments in a volume under 1 fL, with concentrations in the nanomolar range, and with dynamic processes in the range from microseconds to seconds [112, 114]. This has become possible through the development of solid-state lasers, sensitive detectors, and high-resolution microscopes. FCS-based imaging methods have excellent spatial resolution in all three dimensions ~300 nm laterally and 1.5 μm along the optic axis, which far surpasses most traditional methods. The movement of the molecules leads to fluctuations of fluorescence intensity that are analysed by statistical methods (Fig. 10.15). As biological molecules alternate between free and bound states, or alter their diffusion speeds as a result of their biological functions, or are immobilised, or interact with other molecules, they can be spatially characterised by a combination of FCS imaging. Small molecules cause short fluctuations and rapidly decaying correlation functions, while large molecules or aggregates generate long fluctuations and slowly decaying correlation functions. Even higher sensitivities are possible in dual or multi-channel mode, where potential binding partners are marked with spectrally different fluorophores, and their fluorescence photons are detected in separate channels. The diffusion of doubly marked dimers creates synchronized (i.e., correlated) fluctuations, while singly marked monomers cause independent signal fluctuations.

FCS provides an unprecedented means for investigating the activity of intercalating drugs, ahead of many ultrasensitive techniques already in wide use [115]. Nucleic acid intercalators, for example, that bind specifically to dsDNA can cause its lengthening, twisting and unwinding. Such structural information can be derived
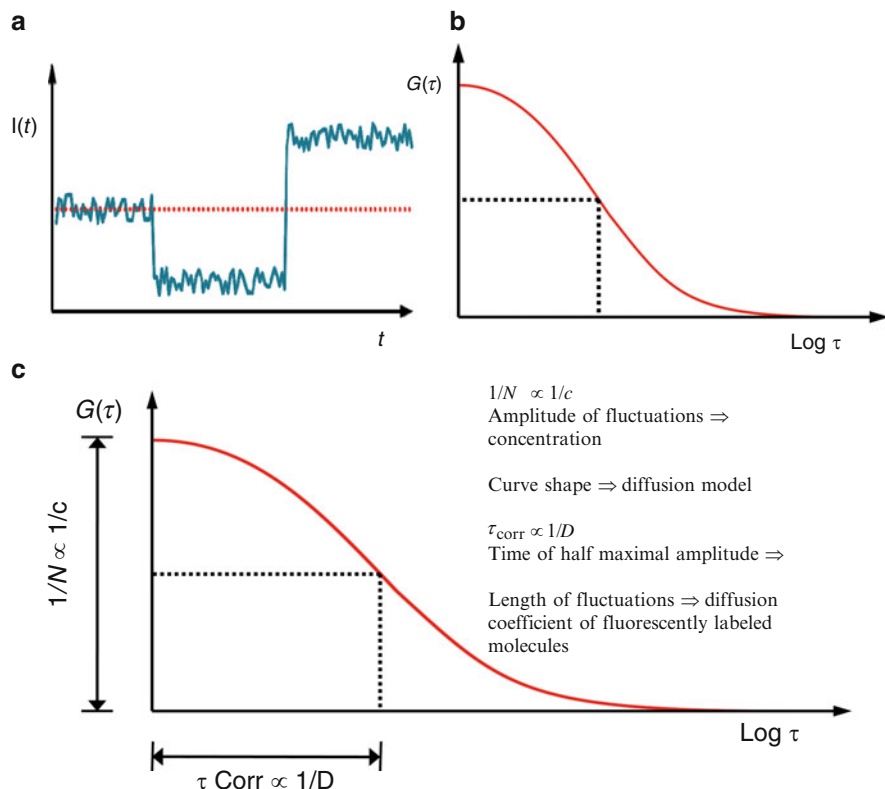
Fig. 10.15 FCS method. (**a**) Registration of intensity fluctuations as the molecules move through the confocal volume. (**b**) Fit of correlation function. (**c**) FCS curve parameters

from the mobility of molecules in solution by FCS confocal analysis, as well as cross-correlation FCS, within compartments of living cells. DNA conformation (condensation) processes in response to various drugs have been shown to differ in response to two different drugs [116–118]. These analyses provided quantitative information on molecular diffusion rates, condensation and particle number versus concentration of condensing agent.

To conclude, FCS provides an elegant and super-sensitive method for studying the flow rates, kinetic reaction constants, intracellular particle concentrations and conformational fluctuations of molecules [110–113]. By combining FCS techniques with confocal imaging, a new and very powerful technology has emerged in the last decade that provides the means to study molecules within extremely small cellular spaces. It can be used to gather fundamental information about the interactions of metallointercalators with DNA and RNA, including binding processes, rates and constants, detailed reaction stoichiometries, the mechanism and degree of DNA damage, and quantification of the amounts of free and bound complexes.

10.4.10 Super-Resolution Optical Imaging at Nano-Scales

Despite major advances in confocal microscopy, the basic optics have largely remained unchanged because the final resolution of an instrument is governed by the wavelength of light, the objective's N.A. and the properties of the specimen itself. Microscopic resolution is defined as the minimal separation between two points that results in a certain contrast between them, determined by the number of photons collected from the specimen, the signal, instrument optics and the number of picture elements (pixels) per unit area imaged. Cellular structures that are smaller than the wavelength of light, i.e., below a quarter of a micrometre, cannot be resolved, even by confocal microscopes with excellent optical elements.

In the last 6 years a range of exciting optical techniques, referred to as super-resolution (SR) imaging, have been developed. SR technology relies on nonlinear optical approaches that reduce the focal-spot size and break the diffraction limit of light, enabling resolution of structures and molecules that are smaller than the theoretical maximum resolution of 200 nm [119, 120]. Two of these techniques are photoactivation localisation microscopy (PALM) [121] and stochastic optical reconstruction microscopy (STORM) [122]. The SR imaging method uses the collection of numerous images of the specimen in which only some of the tagged molecules are made to fluoresce by being photoactivated; they are then bleached or switched off, and the activation-switching off process is repeated for several cycles. Since only a small proportion of fluorescently tagged molecules is photoactivated during each cycle, it is possible to localize these molecules in the absence of interference from the emissions of neighboring molecules. Once the series of on-off photoactivation cycles is completed, the final SR image is developed by merging all the single-molecule positions. This technique allows the visualization of cellular structures and processes at the molecular level and promises to be the technology of choice in the next decade.

We expect that we will be able to routinely image cellular structures less than 10 nm in size, and we will have an incredibly detailed view of how proteins move and interact inside living cells, and how they control cellular organisation. In the case of DNA binding by metallointercalators, it would be possible to directly visualise the binding interactions and investigate the types of covalent adducts that are formed with metallointercalator complexes. The SR technique will enable the direct visualisation of the activity of these drugs that relates to DNA modification, and that influences various nuclear activities, such as transcription, replication, and repair or disruption in complex structures.

10.5 Conclusion

The application of confocal techniques, coupled with a range of spectroscopic methods, allows greater versatility and precision in the study of metallointercalator activity within living cells. These bioimaging techniques will also shed light on the

processes by which cells develop resistance to antitumour metallointercalator drugs and provide solutions to obstacles for the clinical use of this class of drugs. Imaging in three-dimensional space in living cells and performing precise measurements at molecular scales will reveal exciting new aspects of metallointercalator research. These methods will most certainly solve important problems in cell biology and likely will lead to unexpected discoveries.

References

1. Valeur B. Molecular fluorescence: principles and applications, Chap. 3. Weinheim: Wiley VCH; 2002.
2. Campagna S, Puntoriero F, Nastasi F, Bergamini G, Balzani V. Top Curr Chem. 2007;280:117.
3. Rodger A, Nordén B. Circular dichroism and linear dichroism. Oxford: Oxford University Press; 1997.
4. Hoshi T, Inoue H, Yoshino J, Masamoto T, Tanizaki Y. Z Phys Chem Neue Folge. 1972;81:23.
5. Harriman A, Izzet G. Phys Chem Chem Phys. 2007;9:944.
6. Henry MS, Hoffman MZ. J Phys Chem. 1979;83:618.
7. Sun Y, Lutterman DA, Turro C. Inorg Chem. 2008;47:6427.
8. McNaught AD, Wilkinson A. IUPAC. Compendium of Chemical Terminology, 2nd ed. (the "Gold Book"). Oxford: Blackwell Scientific Publications; 1997.
9. Sayed MAE, Brwer RG. J Chem Phys. 1963;39:1623.
10. Chamberlain C, Hahn KM. Traffic. 2000;1:755.
11. Levi V, Ruan Q, Gratton E. Biophys J. 2005;88:2919.
12. Royer CA, Scarlata SF. In: Brand L, Johnson ML, editors. Methods in enzymology, Vol. 450. San Diego: Elsevier Academic Press; 2008. p. 80.
13. Kumar CV, Barton JK, Gould IR, Turro NJ, Houten JV. Inorg Chem. 1988;27:648.
14. Tossi AB, Kelly JM. Photochem Photobiol. 1989;49:545.
15. Anderson PA, Anderson RF, Furue M, Junk PC, Keene FR, Patterson BT, et al. Inorg Chem. 2000;39:2721.
16. Fabian RH, Klassen DM, Sonntag RW. Inorg Chem. 1980;1977:19.
17. Demas JN, Crosby GA. J Am Chem Soc. 1970;2841:93.
18. Sahai R, Baucom DA, Rillema DP. Inorg Chem. 1986;25:3843.
19. Barigelletti F, Cola LD, Balzani V, Hage R, Haasnoot J, Reedijk J, et al. Inorg Chem. 1989;28:4344.
20. Juris A, Belser P, Barigelletti F, van Zelewsky A, Balzani V. Inorg Chem. 1986;25:256.
21. Yam VW-W, Lee VW-M, Cheung K-K. J Chem Soc, Chem Commun. 1994;2075:18.
22. Damrauer NH, Boussie TR, Devenney M, McCusker JK. J Am Chem Soc. 1997;119:8253.
23. Casper JV, Meyer TJ. J Am Chem Soc. 1983;105:5583.
24. Demas JN, Crosby GA. J Phys Chem. 1971;78:991.
25. Brodie C, PhD thesis, University of Western Sydney (Campbelltowm), 2006.
26. Tse WC, Ishii T, Boger DL. Bioorg Med Chem. 2003;11:4479.

27. Morgan JL, Buck DP, Turley AG, Collins JG, Keene FR. Inorg Chim Acta. 2006;359:888.
28. McGhee JD, von Hippel PH. J Mol Biol. 1974;86:469.
29. Minsky M. Microscopy apparatus, US Patent No 3,013,467. 1961.
30. Petran M, Hadravsky M, Egger MD, Galambos R. J Opt Soc Am. 1968;58:661.
31. Murray JM. In: Spector DL, Goldman RD, editors. Basic methods in microscopy. Cold Spring Harbor: Lab Press; 2006. p. 43.
32. Spector DL, Goldman RD. Basic methods in microscopy. Cold Spring Harbor: Lab Press; 2006.
33. Haugland R. Handbook of Fluorescent Probes and Research Chemicals, 6 ed.; Molecular Probes, Inc.: Eugene, OR, 1996.
34. Reedijk J. Pure Appl Chem. 1987;59:181.
35. Johnson NP, Butour J-L, Villani G, Wimmer FL, Defais M, Pierson V, et al. Prog Clin Biochem Med. 1989;10:1.
36. Brabec V, Kasparkova J. Drug Resist Update. 2005;8:131.
37. Ott I, Gust R. Arch Pharm Chem Life Sci. 2007;340:117.
38. Friedman AE, Chambron J-C, Sauvage J-P, Turro NJ, Barton JK. J Am Chem Soc. 1990;112:4960.
39. Holmlin RE, Stemp EDA, Barton JK. Inorg Chem. 1998;37:29.
40. Jamieson ER, Lippard SJ. Chem Rev. 1999;99:2467.
41. Haugland RP. Handbook of fluorescent probes and research products. 9th ed. Eugene: Molecular Probes; 2002.
42. Ersfeld K, Stone EM. Simultaneous in situ detection of DNA and proteins. In: protein localization by fluorescence microscopy – a practical approach, Vol. New York: Oxford University Press Inc.; 2000.
43. Lerman LS. J Mol Biol. 1961;3:18.
44. Kopka ML, Yoon C, Goodsell D, Pjura P, Dickerson RE. Proc Natl Acad Sci USA. 1985;82:1376.
45. Kubista M, Akerman B, Nordén B. Biochemistry. 1987;26:4545.
46. Haugland RP. Nucleic acid detection and genomics technology. Eugene: Molecular Probes Inc.; 2002.
47. Traganos F, Darzynkiewicz Z. J Histochem Cytochem. 1977;25:46.
48. Alexander P, Moroson H. Nature. 1962;194:882.
49. Erve A, Saoudi Y, Thirot S, Guetta-Landras C, Florent JC, Nguyen C, et al. Nucleic Acids Res. 2006;34:e43.
50. Jenkins Y, Friedman AE, Turro NJ, Barton JK. Biochemistry. 1992;31:10809.
51. Olofsson J, Onfelt B, Lincoln P. J Phys Chem. 2004;108:4391.
52. Ardhammer M, Lincoln P, Nordén B. J Phys Chem. 2001;105:11363.
53. Puckett CA, Barton JK. J Am Chem Soc. 2007;129:46.
54. Tse WC, Boger DL. Acc Chem Res. 2004;37:61.
55. Yeung BKS, Tse WC, Boger DL. Bioorg Med Chem Lett. 2003;13:3801.
56. Boger DL, Fink BE, Brunette SR, Tse WC, Hedrick MP. J Am Chem Soc. 2001;123:5878.
57. Chen LB. Meth Cell Biol. 1989;29:103.
58. Trask B. Trends Genet. 1991;7:149.
59. Liehr T. Fluorescence in situ hybridization (FISH) – application guide. Berlin: Springer; 2009.
60. Tsien RY. Annu Rev Biochem. 1998;67:509.
61. Chalfie M, Kain S. Green fluorescent protein: properties, applications, and protocols. 2nd ed. Hoboken: Wiley-Interscience; 2006.
62. Day RN, Davidson MW. Chem Soc Rev. 2009;38:2887.
63. Prescott M, Salih A. In: Goldys EM, editor. Fluorescence applications in biotechnology and life sciences. Wiley-Blackwell; 2009. p. 47.
64. Chalfie M, Tu Y, Euskirchen G, Ward WW, Prasher DC. Science. 1994;263:802.
65. Cody CW, Prasher DC, Westler WM, Prendergast FG, Ward WW. Biochemistry. 1993;32:1212.

66. Shaner NC, Steinbach PA, Tsien YR. Nat Meth. 2005;12:905.
67. Heim R, Prasher DC, Tsien RY. Proc Natl Acad Sci USA. 1994;91:12501.
68. Matz MV, Fradkov AF, Labas YA, Savitsky AP, Zaraisky AG, Markelov ML, et al. Nat Biotechnol. 1999;17:969.
69. Lukyanov A. Nat Biotechnol. 1999;17:969.
70. Salih A, Larkum A, Cox G, Kuhl M, Hoegh-Guldberg O. Nature. 2000;408:850.
71. Salih A. In: Hoffman R, editor. Cancer cell signaling: methods and protocols, Vol. 218. Totowa: Humana Press Inc.; 2010.
72. Alieva NO, Konzen KA, Field SF, Meleshkevitch EA, Hunt ME, Beltran-Ramirez V, et al. PLoS ONE. 2008;3:e2680.
73. Wiedenmann J, Ivanchenko S, Oswald F, Nienhaus GU. Mar Biotechnol. 2004;6:270.
74. Lukyanov KA, Chudakov DM, Lukyanov S, Verkhusha VV. Nat Rev Mol Cell Biol. 2005;6:885.
75. Deheyn DD, Kubokawa K, Mccarthy JK, Murakami A, Porrachia M, Rouse GW, et al. Biol Bull. 2007;213:95.
76. Shaner NC, Patterson GH, Davidson MW, Cell J. Science. 2007;120:4247.
77. Ellenberg J, Lippincott-Schwartz J, Presley JF. Trends Cell Biol. 1999;9:52.
78. Wojcik K, Dobrucki JW. Cytom A. 2000;73A:555.
79. Hoffman RM. Nat Rev. 2005;5:796.
80. Yang M, Baranov E, Wang J-W, Jiang P, Wang X, Sun F-X, et al. Proc Natl Acad Sci USA. 2002;99:3824.
81. Patterson GH. Nat Biotechnol. 2004;22:1524.
82. Förster T. Ann Phys. 1948;2:55.
83. Stryer L. Ann Rev Biochem. 1978;47:819.
84. Periasamy A, Day RN. Meth Cell Biol. 1999;13:517.
85. Stryer L, Haugland RP. Proc Natl Acad Sci USA. 1967;58:719.
86. Lackowicz JR. Principles of fluorescence spectroscopy. New York: Plenum; 1986.
87. Boon E, Barton JK. Curr Opin Struct Biol. 2000;12:320.
88. Murphy CJ, Arkin MR, Jenkins Y, Ghatlia ND, Bossmann SH, Turro NJ, et al. Science. 1993;1025:262.
89. Yun BH, Kim J-O, Lee BW, Lincoln P, Nordén B, Kim J-M, et al. Phys Chem B. 2003;107:9858.
90. Carlsson K, Liljeborg A. J Microsc. 1998;191:119.
91. Becker W, Bergmann A, Hink MA, Konig K, Benndorf K, Biskup C. Micr Res Techn. 2004;63:58.
92. Becker W, Benndorf K, Bergmann A, Biskup C, König K, Tirlapur U, et al. Proc SPIE. 2001;4431:94.
93. Becker W, Bergmann A, Hink MA, Konig K, Benndorf K, Biskup C. Microsc Res Tech. 2004;63:58.
94. Becker W, Hickl H, Zander C, Drexhage KH, Sauer M, Siebert S, et al. Rev Sci Instrum. 1999;1835:70.
95. Suhling K, French PMW, Phillips D. Photochem Photobiol. 2005;4:13.
96. Kubota Y, Steiner RF. Biophys Chem. 1977;6:279.
97. Axelrod D, Koppel DE, Schlessinger J, Elson E, Webb WW. Biophys J. 1976;1055:16.
98. Houtsmuller AB, Vermeulen W. Histochem Cell Biol. 2001;115:13.
99. Klonis N, Rug M, Harper I, Wickham M, Cowman A, Tilley L. Eur Biophys J. 2002;31:36.
100. Lippincott-Schwartz J, Altan-Bonnet N, Patterson GH. Nat Cell Biol. 2003; S7
101. Lippincott-Schwartz J, Snapp E, Kenworthy A. Nat Rev Mol Cell Biol. 2001;2:444.
102. Lippincott-Schwartz J, Patterson GH. Science. 2003;300:87.
103. van Royen ME, Dinant C, Farla P, Trapman J, Houtsmuller AB. In: The nuclear receptor superfamily: methods and protocols, vol. 505. New York: Humana; 2008. p. 69.
104. Lukyanov KA, Fradkov AF, Gurskaya NG, Matz MV, Labas YA, Savitsky AP, et al. J Biol Chem. 2000;275:25879.

105. Ando R, Hama H, Yamamoto-Hino M, Mizuno H, Miyawaki A. Proc Natl Acad Sci USA. 2002;99:12651.
106. Wiedenmann J, Ivanchenko S, Oswald F, Schmitt F, Rocker C, Salih A, et al. Proc Natl Acad Sci USA. 2004;101:15905.
107. Salih A, Larkum A, Cronin T, Wiedenmann J, Szymczak R, Cox G. Proc SPIE. 2004;5329:61.
108. Habuchi S, Ando R, Dedecker P, Verheijen W, Mizuno H, Miyawaki A, et al. Proc Natl Acad Sci USA. 2005;102:9511.
109. Salih A, Matz M, Wiedenmann J, Larkum AWD, Cox G. Proc SPIE. 2006;6098:140.
110. Berland KM, So PT, Gratton E. Biophys J. 1995;68:694.
111. Rigler R, Elson ES. Fluorescence correlation spectroscopy: theory and applications. Springer series in Chemical Physics, vol 65, Springer Verlag, Eds. Berlin-New York, 2001. p. 459–476.
112. Schwüle P. Cell Biochem Biophys. 2001;34:383.
113. Haustein E, Schwule P. Methods. 2003;29:153.
114. MDIer JD, Chen Y, Gratton E. Meth Enzymol. 2003;361:69.
115. Pavski V, Le XC. Curr Opin Biotechnol. 2003;14:65.
116. Kral T, Langner M, Benes M, Baczyńska D, Ugorski M, Hof M. Biophys Chem. 2002;19:135.
117. Kral T, Hof M, Jurkiewicz P, Langner M. Cell Mol Biol Lett. 2002;7:203.
118. Clamme JP, Azoulay J, Mely Y. Biophys J. 2003;1960:84.
119. Hell SW, Dyba M, Jakobs S. Curr Opin Neurobiol. 2004;14:599.
120. Lippincott-Schwartz J, Manley S. Nat Meth. 2009;6:21.
121. Betzig E, Patterson GH, Sougrat R, Lindwasser OW, Olenych S, Bonifacino JS, et al. Science. 2006;313:1642.
122. Rust MJ, Bates M, Zhuang X. Nat Meth. 2006;3:793.

Chapter 11
Synchrotron Radiation X-Ray Spectroscopy for Investigations of Intracellular Metallointercalators: X-Ray Fluorescence Imaging and X-Ray Absorption Spectroscopy

Carolyn T. Dillon

11.1 Introduction

In an effort to determine the therapeutic feasibility of DNA metallointercalators as potential anticancer drugs it is important to confirm that they are capable of targeting DNA in cancer cells or tumours – as is the intended purpose of their design. Microprobe synchrotron radiation X-ray fluorescence (micro-SRXRF) spectroscopy is an ideal technique for investigating the cellular uptake and distribution of metallointercalators. The technique is capable of submicron elemental imaging so that samples as small as individual cells (~10 μm diameter), and the features within them, can be resolved. Consequently, the technique can ascertain whether intracellular metallointercalators colocalise with DNA; namely, in the nucleus during interphase or at the chromosomes during middle prophase to late anaphase. Metals, such as those commonly incorporated into metallointercalators (e.g., Cr, Ni, Co, Pd, Pt, Ru, Rh), are often naturally present in negligible quantities in cancer cells. This fact, together with their higher atomic number, Z, makes them ideal for *direct* probing using hard X-ray microprobes (as discussed in Sect. 11.2). There is no need for the incorporation of fluorescent tracker dyes or radioactive labels into their chemical structure. This is advantageous since it is unknown whether such chemical modifications alter the uptake kinetics of the metallointercalator [1, 2].

The detection of "introduced" C, N, and O associated with the intercalator ligands (and other organic drugs) is, however, unfeasible using micro-SRXRF due to the fact that these elements are endogenous to biological samples. Therefore, while detection of the metal is possible using micro-SRXRF, the technique does not determine whether the metallointercalator has remained intact inside the cell. Consequently, techniques such as X-ray absorption spectroscopy (XAS, Sect. 11.3) can be exploited to contribute additional information regarding the cellular uptake of the metallointercalator. XAS can be used to elucidate the coordination chemistry of the metal and,

C.T. Dillon
School of Chemistry, University of Wollongong, NSW, Australia
e-mail: carolynd@uow.edu.au

consequently, its chemical structure inside the cell/biological tissue. The technique can be used to determine whether the active form of the drug is the intact metallointercalator or whether the metal has dissociated from the ligand and coordinated to other biomolecules.

This chapter will provide a basic description of the principles of micro-SRXRF and XAS and will explain how these techniques can be used to probe intracellular metals. It will summarise micro-SRXRF and XAS studies of similar systems, explore the difficulties associated with analysing particular metals, and address the limitations of these techniques.

11.2   Synchrotron Radiation X-Ray Fluorescence Spectroscopy

X-ray emission spectroscopy is an analytical technique which involves the detection of emitted characteristic X-rays following excitation of the elements within the sample. The principal factor that determines the capabilities (both resolution and sensitivity) of the technique is the type of beam that is employed for the sample excitation. For instance, electrons, particles (protons or alpha particles), or X-rays can all be used to produce characteristic X-rays, giving rise to techniques known as energy dispersive X-ray analysis (EDXA) or energy dispersive X-ray spectroscopy (EDXS); particle-induced X-ray emission (PIXE, particle = protons or alpha particles); and synchrotron radiation X-ray fluorescence (SRXRF) also known as synchrotron radiation induced X-ray emission, (SRIXE), respectively. This section will describe the physical principles of X-ray emission spectroscopy and compare the above-mentioned techniques and their results.

11.2.1   Physical Principles

X-ray emission spectroscopy is best understood by briefly considering the fundamental quantum physics of the atom. For an element of atomic number, Z, there are Z electrons arranged in discrete energy levels, 1s, 2s, 2p, 3s, 3p, 3d, 4s, 4p, 4d, 4f, etc. [3–5]. The principal quantum number (termed n) is an integer denoting the shells. These are also conventionally defined by the terms: K ($n = 1$, 1s), L ($n = 2$, 2s, 2p,), M ($n = 3$, 3s, 3p, 3d), N ($n = 4$, 4s, 4p, 4d, 4f), etc. The angular quantum number, l, can have values of 0 to $(n - 1)$. For a K shell the only permissible value of $l = 0$. For the L shell, $l = 0$ or 1, and for the M shell $l = 0$, 1, or 2. The early optical spectrographers referred to these angular quantum numbers where $l = 0$ ('s', sharp), $l = 1$ ('p', principle), $l = 2$ ('d', diffuse), $l = 3$ ('f', fundamental) giving rise to the subshells known as: s, p, d, and f [6]. In addition to these, the third descriptor, m, is the magnetic quantum number. This takes on values of $- l$ to 0 to $+ l$. For K shell electrons, m is 0; for L shell electrons $l = 0$ or 1, so $m = 0$, $+1$, -1, etc. Finally the spin quantum number, s, only exists as $\pm\frac{1}{2}$ [6].
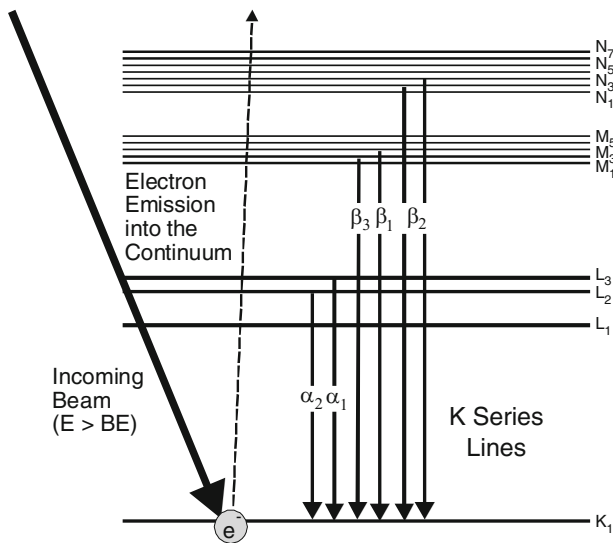
Fig. 11.1 Physical event leading to characteristic X-ray emission. Allowed electronic transitions that give rise to characteristic X-ray lines are shown. *Abbreviations: E*, energy of incoming beam, *BE* binding energy. Adapted from Williams and Carter [7]

In X-ray emission spectroscopy (Fig. 11.1), an incoming beam is used that possesses an energy high enough to excite the atoms of all the elements of interest in the sample. In order to produce the characteristic X-rays of a particular element, the beam energy must be greater than the binding energy of a core electron of that element [4, 5]. For instance, in order to analyse for Ni, a beam energy greater than 8.333 keV (the binding energy of the K electrons) is required. This beam energy is typically exceeded for all elements using a transmission electron microscope (for EDXS, ~120 keV), and a pelletron (for PIXE, 1–4 MeV) but is specifically selected for each experiment with a monochromator when using synchrotron radiation as the excitation source [4, 5, 7, 8]. When the beam strikes the sample and a core electron is ejected into the continuum, an unstable atom is produced. An electron, from an outer energy level, drops down to fill the resultant vacancy and this is accompanied by the emission of an X-ray photon. The energy of the X-ray photon is equal to the energy difference between the initial and final states of the transferred electron [4, 6].

The electron transitions obey simple selection rules. For instance, the Pauli exclusion principle states that no two electrons can have the same set of quantum numbers. In addition, the following criteria must be met:

(a) $\Delta n \geq 1$
(b) $\Delta l = 1$
(c) $\Delta j = +1, 0$ (j is equal to the vector sum of $l + s$).

Therefore, for the K series only p → s transitions are allowed producing two lines for each principal level change such that 2–6 lines are generated by electron

transitions to the K shell dependent on Z [4, 5]. For a more detailed description the reader is referred to Jenkins [4]. Finally, the energies of the characteristic X-rays increase systematically with increasing Z for each spectral series, as is described by "Moseley's Law" [4, 6]:

$$1/\lambda = K(Z - \sigma)^2, \tag{11.1}$$

where λ is the wavelength of the characteristic X-ray, K is a constant that is specific to the spectral series, Z is the atomic number of the excited element, and σ is the shielding constant with a value less than and approximately equal to unity. The wavelength is inversely proportional to the energy, E, of the photon:

$$\lambda = 12.4/E, \tag{11.2}$$

Since the differences in energy levels are discrete and characteristic for a particular element, the resultant characteristic X-rays provide a unique identification for the element [4, 5, 9]. For instance, the characteristic X-rays associated with Ni lines are $K_{\alpha 1} = 7.478$ keV; $K_{\alpha 2} = 7.460$ keV and $K_{\beta} = 8.264$ keV whereby the K_{α} lines are stronger than the K_{β} lines. Binding energies and characteristic X-rays are documented for almost all elements ($Z \leq 95$) of the periodic table [9].

Most commonly K and L lines are studied since the M and N line series are often masked by competing Auger interference [4]. The Auger effect, while not mentioned earlier, is the other of the two mechanisms that the atom undergoes in order to overcome the instability caused by the emission of a core electron into the continuum. It involves an atomic rearrangement and the emission of yet another electron from another core-level to the continuum as the initial electron vacancy is filled [10].

The number of quanta of K series (and L series) radiation emitted per ionized atom is a fixed ratio for a given atomic number [4]. This ratio is known as the fluorescent yield and is an important factor in determining elemental sensitivity. It must also be considered when comparing the intensities of various elements for elemental quantification purposes [4].

XRF spectra can be collected over an entire sample or region of a sample, and transformed into elemental maps that provide information regarding the distribution of elements of interest within a sample. Table 11.1 gives a summary of the spatial resolution and approximate sensitivity (element dependent) for the X-ray emission techniques, EDXS, PIXE and SRXRF. While it is clear that TEM theoretically provides the greatest spatial resolution (1 nm) of the X-ray emission techniques (Table 11.1), the elemental sensitivity associated with the use of an electron beam is considerably lower, by several orders of magnitude (depending on the element), than the analogous X-ray-induced technique. This stems from the broad wavelength band of radiation often referred to as the continuum or *bremsstrahlung* (decelerating) background [4, 7]. This "noise" in the XRF spectrum (Fig. 11.2) is inherently associated with the use of a charged beam, whereby the incoming electrons of the beam passing close to the atomic nucleus are decelerated by the Coulomb field of the nucleus (i.e., scattered inelastically). This releases X-ray

Table 11.1 Comparison of the spatial resolution and detection sensitivity of X-ray emission techniques

Technique	Resolution limit[a]	Detection sensitivity[b]
EDXS (typical 120 kV TEM)	1 nm	>10 ppm [4]
		~200 ppm [11]
		100–1,000 μg/g [12]
Micro-PIXE	~1 μm [13]	<10 ppm [11]
		1–10 μg/g [12]
Micro-SRXRF	0.1–0.2 μm	<ppm [14]
		1 ppb or 1 pg [4, 15]
		0.1 μg/g [12, 16]
		70 ppb ($Z \sim 35$; E = 16.1 keV) [17]

[a]For these purposes the resolution is defined by the smallest typical beam dimensions. It is important to be aware, however, that spatial resolution is related to the analysis volume which is governed by the beam–specimen interactions. It is a function of beam diameter and spreading [7]
[b]Approximate value since detection limits are dependent on and vary with respect to the atomic number, sample matrix and detection times
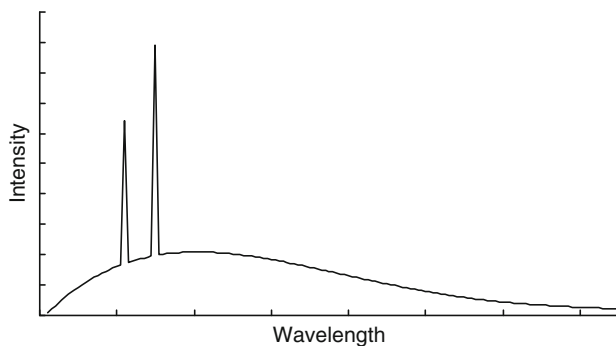
Fig. 11.2 *Bremsstrahlung* background associated with charged particle-induced X-ray emission spectroscopy [4]

energy. Since the event is random and various electrons will lose varying amounts of energy depending on their passing proximity to the atomic nucleus, a plot of the theoretical intensity vs. wavelength yields a graph similar to that shown in Fig. 11.2 [4, 5, 7, 18, 19]. As the noise is proportional to signal intensity the presence of a background *bremsstrahlung* signal gives rise to a higher level of noise and consequently lower sensitivity for characteristic peaks. Use of greater accelerating potentials (of the incoming beam) increases the intensity of the background noise and shifts the distribution of the continuum to shorter wavelengths [4].

In principle the electromagnetic interaction between any two particles can give rise to *bremsstrahlung* energy, and although a proton beam is also decelerated by interaction with matter, the deceleration should be lower due to the higher mass of the proton. This is observed as lower background signal in the characteristic X-ray region resulting in higher elemental sensitivity [8, 20].

The cross-sections of the X-ray fluorescence produced by X-ray excitation are typically 10–10^3 times higher than those generated by charged particles and the fluorescence signal to noise ratios are 10–10^5 times better when a non-charged X-ray beam is used [21, 22]. In addition to this, the brilliance of the X-ray beam typically generated by third generation synchrotrons (Sect. 11.2.2) is orders of magnitude greater than those produced in a conventional laboratory. This enables elemental sensitivities in the ppb range (element dependent) and values of 10^{-17} to 10^{-14} g have been reported with the use of a sub-micron beam [4, 23]. This, in addition to improved X-ray focusing capabilities (Sect. 11.2.2), has markedly improved the preference for micro-SRXRF over other X-ray emission techniques.

11.2.2 Instrumentation

Synchrotron radiation, is highly intense electromagnetic radiation that is generated when electrons travel at high speed (typically the speed of light) in a curved trajectory [10]. The electromagnetic spectrum generated by a synchrotron encompasses wavelengths ranging from X-rays, ultraviolet, visible, infrared through to microwave ranges [3, 10]. In addition to this, the X-rays generated by a synchrotron are divided into two groups: soft X-rays and hard X-rays. Typically soft X-rays are defined as X-rays of less than 4 keV and vacuum conditions are required for their use. Hard X-rays, are typically 4 keV up to approximately 26 keV, and are commonly used for SRXRF and XAS analysis of most metals associated with metallointercalators.

The process of X-ray production begins with an electron gun, similar to that associated with the conventional laboratory XRF source. However, the electrons are accelerated to much higher speeds using a linear accelerator and booster ring which achieve electron speeds that approach 3×10^8 m/s (the speed of light). The electrons are finally injected into a storage ring which operates under vacuum (10^{-9} to 10^{-10} torr) and acts to maintain a constant orbit primarily through the use of bending magnets (dipole magnets) that are arranged to produce a closed circular path of electrons. This gives rise to the distinctive round shape of synchrotron facilities. Quadrupole magnets are also used to focus the electron beam as it circulates around the ring, and sextupole and octupole magnets are also included to reduce chromatic aberration inherent in the quadrupolar magnetic lenses and to handle beam instabilities, respectively [10, 24]. In addition, radiofrequency cavities are used to replenish the energy lost by the beam as it circulates the storage ring [10].

Synchrotron sources, typically third generation sources that operate at energies of 7–8 GeV, produce X-ray beams that are 14–15 orders of magnitude more brilliant than conventional X-ray tube sources [3, 10]. While a number of possible X-ray sources exist, to date most of the publications of micro-SRXRF imaging studies have been generated from experiments performed at third generation sources such as the Advanced Photon Source (APS), the European Synchrotron Radiation Facility (ESRF) and the 8 GeV Synchrotron Photon ring (SPring 8) since

they are well established facilitates that provide the high brilliance X-rays [2]. More recently, a second class of third generation synchrotrons have been developed that also contain more straight sections for insertion devices such as undulators and wigglers but are smaller in size (100–200 m circumference cf. 800–1,500 m circumference of the abovementioned facilities) and run at lower energy (2–3 GeV). These machines also promise to be capable of micro-SRXRF imaging (as is evident at the newly commissioned X-ray microprobe beamline at the Australian Synchrotron).

Figure 11.3 shows the key features of the setup of a micro-SRXRF beamline. The X-ray beam is intensified by the use of an insertion device known as an undulator which is an arrangement of multiple alternating magnetic poles that oscillate the electrons in order to magnify the generated X-ray beam. The beam energy is then selected with a monochromator (commonly a Si 111 crystal) and narrowed by the use of vertical and horizontal slits prior to focusing. The high brilliance of X-rays produced by these devices, in combination with the development of revolutionary X-ray focusing devices at the beamline (Fig. 11.3), have ultimately given rise to highly intense hard X-ray sub-micron probes capable of high resolution imaging [21]. Microbeam formation of hard X-ray beams can be performed using Kirkpatrick-Baez (KB) mirrors which are capable of focusing the beam to 0.5–5 μm dimensions (typically 1–2 μm). The versatility of this device makes it the preferred choice when X-ray tunability is also required; e.g., for alternating between XRF and XAS data collection modes [21, 26]. Recently, there have been reports of the use of multi-layer mirrors bent in KB geometry
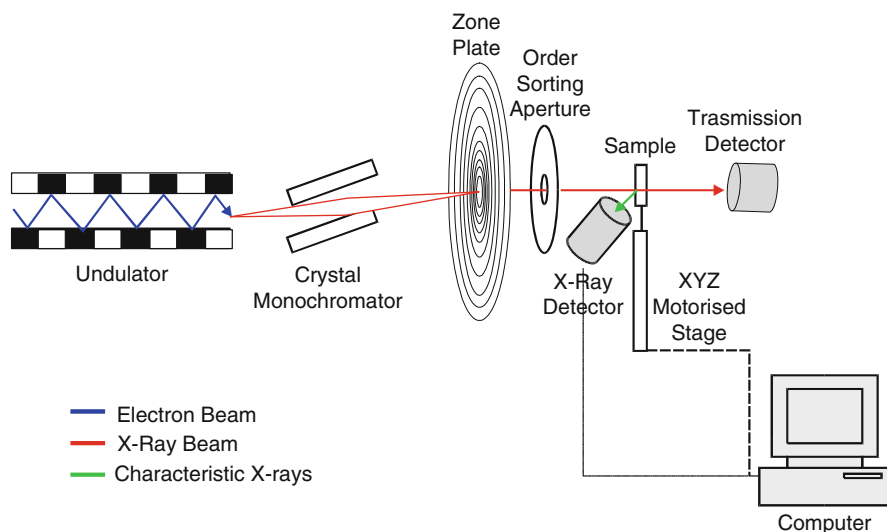
Fig. 11.3 Typical instrumentation of a microprobe synchrotron radiation X-ray fluorescence beamline. Adapted from beamline 2-ID-D at the Advance Photon Source, Argonne National Laboratory [25]

using the concept of a secondary source. This setup (at the ESRF) claims a focusing ability of a 90 nm probe and reports exceptional Pb detection capabilities [27]. Most high resolution imaging, however, employs the zone plate which is a lithography-manufactured circular diffraction grating that is capable of focusing the beam to below 0.1 μm dimensions with routinely achievable dimensions of 0.2 μm [9, 21, 26]. At the 2-ID-D beamline at APS a stacked pair of zone plates is used for optimal focusing of the X-ray beam.

Elemental imaging is performed by using a high precision XYZ motorized stage (up to 0.05 μm resolution) that scans the sample in a rastor pattern in the path of the spatially fixed beam. The sample is housed in a He atmosphere since air contains a measurable component of Ar that results in a dominant interference peak in the SRXRF spectra. During data collection the characteristic X-rays generated from the sample are detected using a multi-elemental detector. Common X-ray detectors include Si/Li detectors, Ge detectors or silicon drift detectors. Both the Si/Li and Ge detectors possess good energy resolution (150–300 eV). Unfortunately, their electronics must be cooled by regular liquid nitrogen fills. The detectors also possess a relatively large dead time that limits their count rates to about 40,000 counts per second (cps) [28]. The silicon drift detector, marketed as Vortex™, is a Peltier-cooled device that has a large active area, high energy resolution (<150 eV FWHM) and high-count rate capability (>1 Mcps) [28, 29]. It has replaced the Si/Li and Ge detectors at a number of beamlines. A CCD camera or transmission detector (located downstream of the sample) is often incorporated into the instrumental setup to assist with sample alignment. Transmission detectors provide an image of heavy elements such as those associated with the support grids (gold Finder grids). These can be compared with the light micrographs previously collected from the sample to assist in the location of regions of interest within the sample.

11.2.3 Sample Preparation

11.2.3.1 Whole Cells

Due to the high sensitivity (~10^{-14} g intracellular detections) of micro-SRXRF, it is crucial that the samples are not contaminated at any stage of their preparation or storage. Ultra-pure solutions and ultra clean containers must be used during the sample preparation and washings. The samples must be handled using appropriate and ultra clean instruments, they must not be dropped onto contaminated surfaces, and they must be stored in clean covered containers to avoid dust contamination.

Micro-SRXRF analysis of whole cells treated with metallointercalators can provide information regarding the metal distribution; although more substantial information can be gained from analysis of thin-sectioned cells. The reason for this is that the whole cell analysis provides a 2-D image of the cell with no depth

information. This reduces the experimenter's ability to clearly distinguish the organelles within the cells. However, whole cell analysis is valuable for intracellular metal quantification to determine/confirm the cellular uptake of these drugs. In addition, whole cells are appropriate for studying the integrity of the intracellular complex by XAS (Sect. 11.3). This allows the researcher to determine whether the complex has dissociated prior to uptake or how the complex has been metabolised following its uptake.

Numerous cell-lines (3,400 cell lines from 80 different countries, and more than 950 cancer cell lines [30]) of various cancer types including those that exhibit resistance, fibroblastic cell types, and suspension cells, can be obtained from Bioresource Centres [30, 31]. Two general protocols for preparation of whole cells for micro-SRXRF analysis of metal uptake have been documented: (1) cell deposition onto a substrate followed by freeze-drying [1, 14, 32–35] or (2) direct growth of the cells onto the substrate [36, 37]. Combinations and variations of these methods can be used.

The first method involves the treatment of known cell densities (grown under normal cell culture conditions) with the complex that has been freshly prepared in a solution that is isotonic and non-toxic towards the cells. Common vehicles include media (with no foetal bovine serum) or phosphate buffered saline (PBS). It is important that the metallointercalator is completely soluble in the solution and that the complex does not decompose or undergo ligand exchange reactions with potential complexing agents in the solution for the duration of the exposure time. Common exposure times include 4, 24 or 48 h. After this period the cells must be washed thoroughly (generally with PBS) to remove the extracellular complex and media. Final rinses are then performed with an isotonic solution of ammonium acetate. This ensures that the freeze-dried sample is free of salt crystals which interfere with the elemental maps (Sect. 11.2.4). It is important to minimise the time that the cells are in the ammonium acetate solution (<5 min) since this is toxic towards most cell-lines. The cell/ammonium acetate suspension (5–10 μL) is deposited onto a formvar coated Finder grid (generally gold grids are employed since the binding energies of the Au L lines are often higher than the employed beam energy, consequently reducing the interference). The grid is rapidly submerged in liquid nitrogen-cooled isopentane or Freon and then quickly transferred to a liquid nitrogen cooled sample holder (Fig. 11.4a). The sample holder shown below was custom made from aluminium since this reduces the risk of metal contamination to the sample. A brass insert within the base of the sample holder was used to maintain the cooler temperature of the holder. The grids are inserted into the numbered holes (6 mm diameter) during the freezing process. Once completed the whole apparatus is transferred to the freeze-drier and evacuated for a minimum of 12 h. Figure 11.4b shows the resultant sample sparsely covered with cells. It is important to ensure that the cells are not clumped together as this prevents successful data collection for whole cell statistical quantifications. Clumped cells also retain media contaminants. In addition, cells that are located away from the grid are preferred for analysis since this reduces scatter interference.
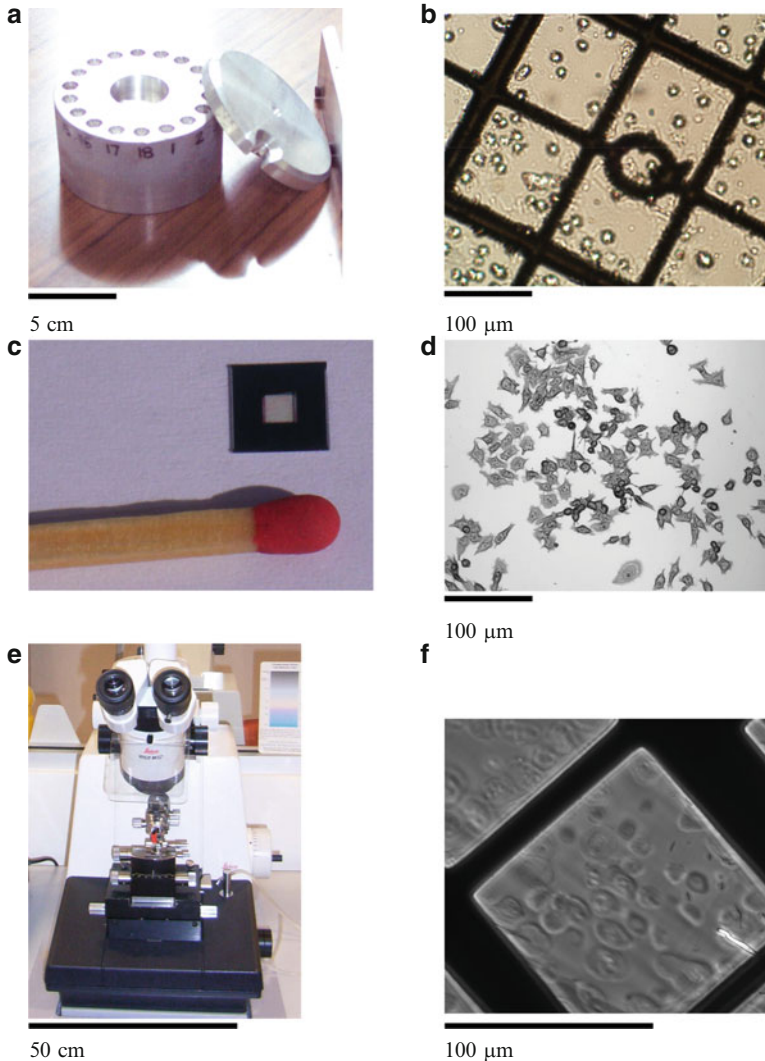
Fig. 11.4 Photograph of (**a**) the freeze-drying apparatus and (**b**) micrograph of the resultant formvar-coated 200 mesh gold Finder grid sparsely covered with freeze-dried cells. Photograph of (**c**) silicon nitride membrane, and (**d**) micrograph showing HepG2 cells growing on the membrane. Photograph of (**e**) a microtome, and (**f**) micrograph of a thin section supported by a gold finder grid showing untreated HepG2 cells

The second commonly used method for preparation of whole cells involves the growth of the cells directly onto a substrate. An ideal, but more expensive substrate is the silicon nitride membrane which is composed of elements that are "silent" in the XRF spectrum (Fig. 11.4c) [36, 37]. The membranes are placed in the wells of a 12 well plate or cell culture dishes and a suspension of cells (in media) is introduced

into the well or dish. Once the cell growth is established on the membranes, the cells can be treated with the metallointercalator for the required exposure period, washed thoroughly with PBS, immersed into ice cold methanol for fixation, and then air-dried. The resultant sample (Fig. 11.4d) enables analysis of the cells in their typical growth state. Importantly, the cells are reasonably easy to prepare by this method and result in a very clean sample (see Fig. 11.4d). In addition, the support membrane can be used for analysis across a number of techniques, namely IR spectroscopy, light microscopy, micro-SRXRF and micro-XAS.

Recent studies [38, 39] of normal and diseased tissue that were analysed intact, dried or frozen and crushed in liquid nitrogen highlight the flexibility of the sampling procedure. Importantly, however, the reported work predominantly focuses on quantification analyses and in most instances the procedures are not useful preparations for maintaining the specimen integrity for micro-SRXRF imaging.

11.2.3.2 Thin Sections

Micro-SRXRF mapping of thin-sectioned cells provides information regarding organelle and intra-organelle distribution of particular elements. Thin sections are optimally prepared using adaptations from TEM preparation procedures since these are well established protocols that aim to preserve the ultra-structure of the specimen [1, 34, 40, 41]. Following metallointercalator treatment and PBS washing (See Sect. 11.2.3(i)), the cells should be harvested and further washed with PBS by centrifugation. Fixation of the ultrastructure is best achieved by suspending the resultant pellet in glutaraldehyde (1% in PBS) for 1–2 h at room temperature with occasional inversion. Following fixation, the cells must be washed with PBS by centrifugation. While osmium tetroxide is used as a second fixative (after glutaraldehyde) and contrast agent for TEM sample preparation, this is not desirable for micro-SRXRF imaging since the Os will appear in the XRF spectrum. Dehydration is performed by incrementally increasing the ethanol (or acetone) concentrations until a final ethanol (or acetone) concentration of 100% is reached [40]. The cell pellet is then infiltrated with a 1:1 v/v ratio of dry ethanol (or acetone) and Spurrs resin overnight at room temperature, followed by $4 \times 100\%$ Spurrs resin for 6–12 h to ensure removal of all traces of water. The cell suspension contained in the Spurrs resin should be finally centrifuged to a pellet in a Beem capsule, and then cured at 60°C for 12 h. The resultant Spurrs resin block can be thin-sectioned (1 µm) using a microtome, the sections of which can be mounted onto gold Finder grids (Fig. 11.4e, f). For in-depth troubleshooting information the reader is referred to Bozzola [40]. There are, however, a few critical points to consider.

Preparation of the Specimen Block

When cells (rather than tissue) are being prepared it is essential to commence the preparation with a high number of cells ($>5 \times 10^6$) since there will be cell loss at

each of the washing, dehydration, and embedding stages. To minimise losses, long centrifugation times may be required; 1–1.5 h centrifugation is not unusual for the final embedding process.

It is important that the sample is thoroughly dehydrated to ensure proper curing of the resin and cutting of the block. The experimenter needs to be aware that Spurr's resin is affected by water vapour in the air; for instance, a humid day may play havoc. Water absorption by the resin prior to curing may lead to a brittle block which is difficult to cut.

A sticky block indicates incomplete polymerisation and may mean that an incorrect composition of the hardener or accelerator was used in the preparation of the resin. Similarly, soft blocks may indicate incomplete polymerisation. This can sometimes be overcome by increasing the curing time.

Cutting the Block

Unlike TEM analysis, micro-SRXRF imaging does not require ultrathin samples since the image is obtained in fluorescence not transmission mode. In most instances a section of approximately 1 μm is ideal for micro-SRXRF imaging of single cells (Fig. 11.4e, f) because it provides adequate thickness for measuring trace exogenous elements and at the same time is thin enough to provide the required definition of the main subcellular organelles.

Issues associated with cutting often stem from poor sample preparation. For instance, if the resin block has not been properly polymerised it is often hydrophilic and water will readily pull down behind the knife. It is extremely important to use a clean and extremely sharp glass knife to avoid knife marks in the section. This means that the knife edge should not be bumped or touched. It is also wise to use polypropylene rather than glass pipettes during the sample preparation to avoid any contamination with glass particles. Such contamination results in damage to the knife and poor sections.

Another problem that may occur during thin sectioning is "chatter" which results in horizontal marks through the section during cutting. This can be overcome by lowering the cutting speed and ensuring that there are no vibrations in the microtome bench.

This protocol has been employed for micro-SRXRF analyses of a number of cell types [1, 33–35] and tissues, including tumours [42]. Other sample preparations for micro-SRXRF analyses have involved combinations of the use of formalin-fixed paraffin embedded tissue followed by sectioning to produce thicker 10 or 20 μm sections [42, 43]. This is preferred for larger samples that do not require submicron resolution. For more fragile samples such as multi-cell layer tumour models initial embedding in agarose followed by dehydration, resin embedding and microtoming has been reported [44]. Another potentially useful procedure for tissue preparation involves embedding in OCT (optimal cutting temperature) compound, snap freezing and cryo-microtoming [45, 46].

11.2.4   Applications, Results, Analysis and Limitations

11.2.4.1   Elemental Quantifications

Elemental quantification can be performed for whole cells or regions within the cell following extraction of the spectra, background correction and curve-fitting [34, 47]. Fitting and spectral analysis programs have been developed specifically for such purposes and include MAPS [47], GNUPLOT [48] and others. Many factors need to be considered in the quantification of the XRF spectra to produce a meaningful analyte concentration. For a more accurate determination of the elemental concentrations within the sample, it is best to use an appropriately chosen internal standard incorporated into a similar matrix. However, this is challenging and certified thin film standards, such as those obtained from the National Bureau of Standards (Gaithersburg, MD, USA), are often used instead [34, 44].

There are two main factors that need to be considered within the sample: absorption effects and enhancement effects [4]. For a detailed explanation of these effects the reader is referred to Jenkins [4]. The experimenter also needs to be aware of artifacts in the spectrum including the phenomenon known as "pile-up" [7]. This occurs when the input count rate is high and the dead times are greater than 60% [7], and is associated with two photons entering the detector at exactly the same time. The simultaneously detected photons register at an energy corresponding to the sum of the two photons [7]. This is often a result of an extremely dominant element in the sample which can give rise to a peak in the spectrum at twice the energy of the characteristic line [7]. For instance, extremely high Cl concentrations (spectral peaks at $K_\alpha \sim 2.6$ and $K_\beta \sim 2.8$ keV) in the cells may give rise to peaks at 5.2–5.6 keV, which is similar in energy to the metal, Cr ($K_\alpha = 5.41$ keV and $K_\beta = 5.95$ keV). Detectors that recognize and correct for this are currently being developed.

Micro-SRXRF quantifications have been reported for whole V79 cells following exposure to Cr complexes [1]. The results showed that while Cr(V) and Cr(VI) complexes were readily taken up by cells, the potential Cr(III) metallointercalator, cis-[Cr(phen)$_2$(H$_2$O)]$^{3+}$, was less permeable [1]. It was clear from statistical analyses of these treatments that sample sizes greater than five were necessary to provide the required statistical power to discern small Cr uptake differences between the various samples. The data collection time required to perform these analyses may mean that other analytical techniques such as graphite furnace atomic absorption spectroscopy (GFAAS) of bulk sample may be a more time economical choice. This will depend on the intracellular concentrations and/or detectability of the specific metal [32, 49, 50].

Ilinski et al. [25] performed quantifications of Pt uptake by human ovarian adenocarcinoma cells that had been treated with cisplatin and Pt[N(p-HC$_6$F$_4$) CH$_2$]$_2$py$_2$. Platinum detection limits as low as 20 ag (2×10^{-17} g for Pt in a beam spot of $1 \times 0.2\ \mu m^2$ in 1 s) were reported and statistical differences were observed in resistant and non-resistant cells ($n = 3$–4 cells) for the Pt complexes tested [25].

11.2.4.2 Imaging: Whole Cells, Thin Sections and Tissue

Prior to interpreting whole cell and thin-section elemental maps it is important to be aware of some of the endogenous elements and their expected locations within organelles. Typical control mammalian cells are clearly defined by P, S, K, and Ca. Trace elements include Zn, Cu and Fe (the concentration of Fe is dependent on the cell type, e.g., blood cells). The nucleus contains the nucleolus, heterochromatin and euchromatin regions which can be differentiated by P and Zn images. Dense DNA regions such as the nucleolus and heterochromatin areas are readily defined by high P concentrations (since P is associated with the DNA backbone) and Zn concentrations (since Zn finger proteins are associated with DNA transcription) [40, 51–53]. This often gives rise to the distinct accumulation of Zn and P around the interior of the nuclear membrane indicative of heterochromatin [34]. These dense DNA regions are readily correlated with darkly stained cellular regions in light and electron microscopy images [40]. The nucleolus is evident often as a small circular region in the nucleus containing a high colocalisation of S, Zn, P and Ca. Since Ca effluxes are often indicators of cell trauma, nuclear and cytoplasmic Ca concentrations can be used to report on cell cytotoxicity [34]. The cell cytoplasm is often associated with lower Zn and P concentrations. High concentrations of S are associated with proteins and enzymes containing cysteine and methionine. When the thin sections are cut from Spurrs resin, a high concentration of Cl is observed exterior to the cells, in the surrounding resin.

Micro-SRXRF imaging of Cr(VI)-treated V79 Chinese hamster lung cells confirmed that organelle-specific localisations of Cr could be readily detected when the metal was associated with larger organelles such as the nucleus [1]. Recent studies [34] have correlated the leukemia drug, arsenite, to regions within the nucleus, namely the euchromatin.

Micro-SRXRF imaging was performed by Hall et al. [42] to investigate the uptake of Pt(II) and Pt(IV) potential anticancer agents by cancer cells. Treatment of A2780 ovarian cancer cells with the metallointercalator, *cis*-[PtCl$_2$(2-[(3-amino-propyl)amino]-9,10-anthracene-dione)(NH$_3$)], revealed a high colocalisation of Pt and P which was attributed to Pt localisation in the cell nucleus [42]. Attempts at micro-SRXRF imaging of thin sections obtained from a tumour harvested from a mouse 3 h after injection with the Pt anticancer agent, *cis*, *trans*, *cis*-[PtCl$_2$(OH)$_2$((NH$_3$)$_2$)], have also been reported [42]. The study revealed Pt and Zn colocalisation in one area of the section of tumour which appeared to be only one cell; the authors commented that identifying an appropriate sample area for imaging was an unexpected challenge [42]. Nonetheless, this could be an important area for future studies to confirm the potential clinical usefulness of metallointercalators.

XRF microtomography of bound Pt in DLD-1 human colon carcinoma spheroids has successfully monitored the depth of penetration of cisplatin and three Pt(IV) complexes after 24 h exposure [54]. While Pt intercalators were not the subject of the study, the technique amply detected 10 ppm Pt in the cancer spheroids, showing enrichment of the Pt in the outer region (corresponding to the outer proliferative region) and uniform distribution deeper within the spheroid [54]. In addition, the

study showed poorer but similar penetration profiles of Pt(IV) complexes in comparison to cisplatin [54] and represents an interesting future mechanism for studying the efficiency of Pt metallointercalator uptake by tumours.

Results of micro-SRXRF studies of metallointercalator-treated A549 human lung cancer cells are shown in Fig. 11.5. The A549 cells were treated for 4 h with: (a) cell media (control cells), (b) [Ni(phen)$_2$(dppz)]$^{2+}$ (phen = 1,10-phenanthroline, dppz = dipyrido[3,2-a:2′,3′-c]phenazine, 0.96 mM, I [55]), or (c) 56MESS (56MESS = [(5,6-dimethyl-1,10-phenanthroline)(1S,2S-diaminocyclohexane)platinum(II)]), 0.49 mM, II [56, 57]. The cells were then washed several
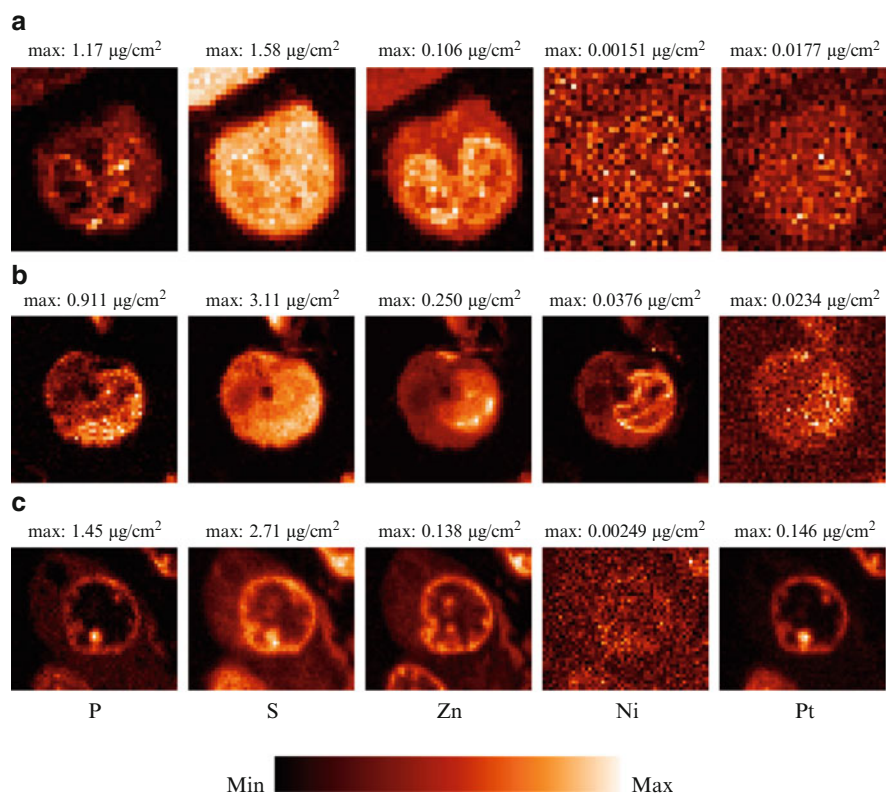
Fig. 11.5 Microprobe SRXRF elemental maps of A549 cells following treatment with: (**a**) cell media only; (**b**) [Ni(phen)$_2$(dppz)]$^{2+}$ (960 μM), or (C) 56MESS (490 μM). The elements are specified at the bottom of each column. Operating conditions include: Beam energy = 11.9 keV, Beam size = 0.2 × 0.15 μm; Stepsize = 0.3 μm; Dwell time = 3 s/pt and Scan dimensions (H × V) = (**a**) 9 × 10 μm; (**b**) 14 × 14 μm (**c**) 10 × 10 μm; (Cell samples were prepared and analysed by Dillon, Davis and Lai. Metallointercalator complexes were provided by Aldrich-Wright and Ralph) . (**a**) max: 1.17 μg/cm^2 max: 1.58 μg/cm^2 max: 0.106 μg/cm^2 max: 0.00151 μg/cm^2 max: 0.0177 μg/cm^2 . (**b**) max: 0.911 μg/cm^2 max: 3.11 μg/cm^2 max: 0.250 μg/cm^2 max: 0.0376 μg/cm^2 max: 0.0234 μg/cm^2. (**c**) max: 1.45 μg/cm^2 max: 2.71 μg/cm^2 max: 0.138 μg/cm^2 max: 0.00249 μg/cm^2 max: 0.146 μg/cm^2

times with PBS, harvested with trypsin, fixed, dehydrated, embedded and thin-sectioned (1 μm sections) as described in Sect. 11.2.3.2. Micro-SRXRF data was collected on the X-ray Operations and Research Beamline 2-ID-D at the Advanced Photon Source, Argonne National Laboratory using an 11.9 keV X-ray beam focused to 0.2 μm in the horizontal direction and 0.15 μm in the vertical direction. The XRF spectra were background corrected, element fitted and analysed using MAPS Version 1.6.3.0 (Nov, 2008 edition).

Figure 11.5a shows typical micro-SRXRF elemental maps (P, S, Zn, Ni and Pt) obtained from a control A549 cell. Each map is independently scaled, whereby a black pixel represents the minimum intensity and a white pixel represents the maximum intensity. The maximum concentration associated with each element is reported above each map. The cell is undergoing cell division which is apparent by the two distinct nuclei in the P and Zn maps. As is often the case, P and Zn are more densely localised inside the nuclei along the nuclear membrane. This region is identified as the heterochromatin region which contains densely-packed, conserved DNA. There is no significant Ni or Pt in this cell, as indicated by the low maximum concentrations, 0.00151 and 0.0177 μg/cm^2, respectively. This is important because it shows that there is negligible naturally occurring Ni or Pt in this cell-line. Furthermore, there is no evidence of contamination. In addition, the low Ni and Pt concentrations confirm that adequate background correction and fitting of the XRF spectra has been performed to remove the possibility of misleading positive signals. A typical example of spectral interference associated with these experiments would be that generated by Zn. Zn is naturally present in cells and its K_β peak is adjacent to the Pt L line in the XRF spectrum.
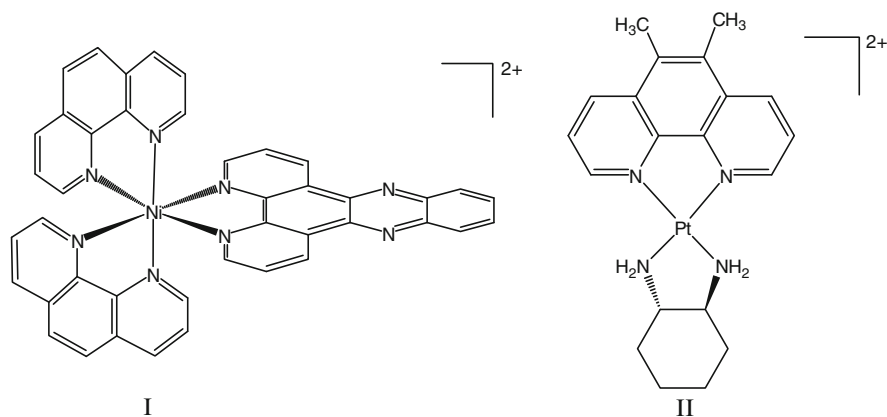
Figure 11.5b shows a [Ni(phen)$_2$(dppz)]$^{2+}$-treated cell. There is a distinct nucleus in the right side of the cell. This coincides with a significant increase in the intracellular Ni, above that observed in the control cell. The localization of Ni in the heterochromatin region places the Ni in the region of densely packed DNA material and suggests that the complex, [Ni(phen)$_2$(dppz)]$^{2+}$, has the ability to reach the DNA. The elemental maps of a 56MESS-treated cell are shown in Fig. 11.5c.

The Pt maximum concentration (0.146 μg/cm^2) is clearly above those detected in the control cell (0.0177 μg/cm^2) and the Ni-treated cell (0.0234 μg/cm^2). The P, Zn and Pt are concentrated in the nucleus which is located to the right of the cell. Further to this the Pt localisation closely follows those of P and Zn, indicating that the Pt occurs in regions of dense DNA. This result contrasts that observed for arsenite-treated cells whereby repeated experiments have shown that As accumulates in the euchromatin regions of the nucleus [34].

In conclusion, micro-SRXRF clearly shows that the Ni and Pt localise in regions of DNA following treatment with [Ni(phen)$_2$(dppz)]$^{2+}$ or 56MESS, respectively. Due to the fact that the intercalator ligands are hetero-organic with no distinguishing elements that can be probed by micro-SRXRF it is not possible to indisputably claim that the metallointercalators have remained intact solely based on micro-SRXRF experiments. Consequently, additional experiments such as electrospray ionisation-mass spectrometry (ESI-MS) stability studies of the complexes in the media should be undertaken. In this study ESI-MS indicated that the complexes were relatively stable in the cell media prior to cell uptake [58]. Additional, XAS analysis (Sect. 11.3) of the intracellular metals would be useful to establish whether the coordination spheres of the intracellular Ni or Pt remain the same as that expected for the administered metallointercalator.

11.2.5 Limitations

Micro-SRXRF imaging of particular elements such as Pt, Mo, Nb, Ru, and Rh, that present experimental challenges, will be discussed. When imaging elements such as Pt it is also imperative that the operator is aware of the coexistence of the Pt L$_{\alpha1}$ (9.442 keV) and Pt L$_{\alpha2}$ (9.362 keV) line with the Zn K$_{\beta1}$ line (9.572 keV) since Zn is an endogenous element that concentrates in the cell nucleus (Sect. 11.2.4.2). Two approaches can be undertaken to ensure sole Pt detection. The first method is to perform background subtraction and spectral fitting to minimise the Zn contribution to the Pt peak [25]. The second method is to create an ROI for Pt that detects the Pt L$_\beta$ peaks at 11.070 and 11.251 keV [42].

The characteristic X-ray energies associated with the K lines of Mo, Nb, Ru and Rh lie within 16.6–21.2 keV. This means that the corresponding binding energies and that required of the X-ray beam are 18.99–24.35 keV [9]. This poses problems when using a zone-plate whereby the optimal focusing energy is 10 keV. The experimenter could consider imaging lines of the L series; however, these occur at energies around 2.1–3.5 keV and coexist with P, S, Cl and K (2.0–3.6 keV) which are dominant intracellular elements. As such, it is unlikely that the L-lines from trace elements, such as those associated with metallointercalator exposure, would be detected. Dillon and co-workers tried to overcome these issues when studying Mo- and Nb-containing metallocenes [33]. As predicted the XRF peaks of P, S, Cl and K overshadowed those of the L lines of Mo and Nb. Micro-SRXRF data was collected at 20.5 keV to image the Mo or Nb associated with the metallocene-treated

cells. The elemental images of P, S, Cl and K were poor due to the use of such a high exciting energy. This problem was overcome by re-imaging the cells at 10 keV consequently providing maps of the endogenous elements that could be correlated with the Mo and Nb images [33].

11.3 X-Ray Absorption Spectroscopy

XAS has been demonstrated as a valuable technique for studying the structural coordination chemistry of metal or metalloid complexes [16, 59–61]. The exciting advantage of XAS is that it provides a mechanism of probing spectroscopically "quiet" metals, particularly those with either filled or empty d-shells [61]. Examples include Cu(I) and Zn(II) which are undetectable using electronic spectroscopy such as UV/Vis or microwave spectroscopy such as EPR [61]. In addition, XAS is capable of analysing numerous sample types, i.e., liquids (although often glasses are studied at low temperature to avoid X-ray damage) and solids in crystalline or amorphous form. An important advantage that stems from this is that XAS can be used to probe metals in their biological environment; for instance, dilute (millimolar) metal concentrations have been readily detected in cells and tissue.

11.3.1 Physical Principles

As Fig. 11.6 shows, XAS is based on the photoelectric effect that occurs when a tuneable X-ray beam is applied to the sample [16, 59, 61]. When the energy of the
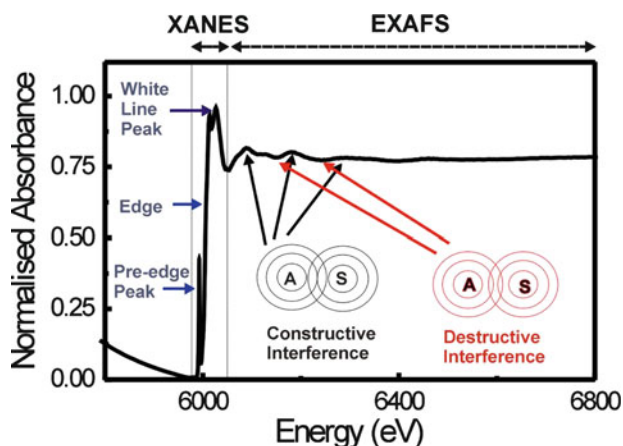
Fig. 11.6 Schematic diagram of an X-ray absorption spectrum depicting the two main regions: the X-ray absorption near edge structure (XANES), and the extended X-ray absorption fine structure (EXAFS) (adapted from Penner-Hahn [60])

incident X-ray beam exceeds the binding energy of a core electron, the electron is ejected from the atom [61]. This process results in an abrupt increase in the absorption coefficient which is observed as the absorption edge of the element in the resultant spectrum (Fig. 11.6) [59]. The spectrum derived from XAS (Fig. 11.6) can be divided into two regions: (1) the X-ray absorption near edge structure (XANES) which occurs in the immediate vicinity of the edge (from below the edge to ~0.50 eV above the absorption edge) and (2) the extended X-ray absorption fine structure (EXAFS) which is the structure above the edge, occurring from ~50 eV above the edge [16, 59–61]. Both of these spectral features result from the scattering of the ejected photoelectron. Key features of the XANES spectrum include the aforementioned edge, and the peak directly following the edge which is termed the white line peak. In some cases a peak is observed directly before the edge. This is the pre-edge peak. The EXAFS spectrum is much more subtle and is distinguished by a wavelike structure indicative of the constructive and destructive interference from which it is generated.

The XANES region is sensitive to the oxidation state, the immediate coordinating atoms, and the electronic structure of the element of interest [60]. This spectral region can be used to provide qualitative comparisons between an element of unknown chemical structure and a standard of a known chemical structure, enabling the identification of the sample [60]. Theoretical simulations of XANES can be used to determine the three dimensional structure of the absorbing site although this is difficult to achieve and spectra are often analysed qualitatively [61]. Nonetheless, typical spectral features often reflect the chemical environment of the absorber. For instance, when the coordination environment becomes less symmetric, the scattering resonances that give rise to the XANES features are broadened giving rise to a less intense white line [61]. This is often observed as a spectral difference generated by more crystalline small-molecule models compared with their protein- or peptide-bound analogues whereby the former is more symmetric [34, 61]. Typically, increases in the oxidation state are associated with increases in the energy associated with the absorption edge, since greater energy is required to eject the core electron [61]. Caution must be used when relying on the edge position to interpret the oxidation state from the spectra, however, since the coordinating atoms can also influence the edge energy. For instance, while the oxidation state does not change, a slight decrease on the local charge of the absorber element brought about by coordination to a less electron-withdrawing atom (e.g., S vs. O) would result in a lower edge energy [34, 61]. In addition, and complementary to this, the edge energy can be influenced by the metal–ligand bond distance whereby the edge energy is expected to vary inversely with the square of the metal–ligand distance [61].

While it is understood that the EXAFS arises from the electron scattering events that occur after the ejection of an electron into the continuum, it should also be noted that the ejection of the electron can be accompanied by bound state transitions that, in some instances, dominate the pre-edge structure. Weak pre-edge peaks for the K edge first row transition metals are observed from the forbidden (dipole selection rules) $1s \rightarrow 3d$ transition. It occurs for metals that have an unfilled 3d shell and provides an indicator of coordination geometry. A typical example of this

is noted for the series of Cr complexes exhibiting Cr(III) to Cr(VI) oxidation states [62, 63]. The centrosymmetric octahedral Cr(III) complex exhibits the weakest pre-edge feature. As the centrosymmetry is lost; for instance, for trigonal bipyramidal and tetrahedral complexes, the intensity of the pre-edge peak increases [62–66]. This phenomenon is due to the mixing of the 3d and 4p orbitals and direct quadrupolar coupling [61, 62]. In some instances the profile of the XANES spectra can also be contributed to by the more intense $1s \rightarrow 4p$ transition. This is observed as the rising edge in the spectrum of Cu(I) complexes, and some square planar Cu(II) and Ni(II) complexes [60].

Unlike the XANES region, the EXAFS region of the spectra can be used to provide more detailed information regarding the chemical structure of the complex. As mentioned, the EXAFS region is typically sampled from 50 eV above the edge. This is where the photoelectron has significant energy and thus has a de Broglie wavelength that approaches atomic distances. The region corresponds to the constructive and destructive interference between the outgoing and back-scattered photoelectron waves as depicted in Fig. 11.6 [61]. Briefly, the fine structure can be modelled using the EXAFS (11.3), whereby: R = distance to neighbouring atom, N = coordination number of neighbouring atom, σ^2 = mean-square disorder of neighbour distance and the scattering amplitude $f(k)$ and phase-shift $\delta(k)$ depend on the atomic number Z of the scattering atom. For a more detailed explanation refer to specialised EXAFS reviews [59–61].

$$x(k) = \sum_j \frac{N_j f_j(k) e^{-2k^2 \sigma_j^2}}{k R_j^2} \sin[2k R_j + \delta_j(k)]. \tag{11.3}$$

Analysis of the EXAFS region can provide information on bond lengths, coordination numbers, and identities of near neighbour atoms [16, 60]. The quantitative analysis involves fitting experimental data to (11.3), or similar equation, using amplitude and phase parameters that originate either from crystal structures, *ab initio* calculations or model compounds of known structures. The analysis requires fitting packages that are readily available on internet sites.

11.3.2 *Instrumentation*

XAS, contrary to X-ray emission spectroscopy, cannot be performed using a laboratory X-ray source. Instead the highly intense and tunable X-rays, generated at a synchrotron are essential for XAS [67]. XAS data can be collected in two modes: fluorescence mode or transmission mode as indicated in Fig. 11.7.

A scanning high resolution monochromator is used to tune the energy of the X-ray beam. Monochromator crystals are generally arranged in a double crystal configuration and include the Si(111), Si(220), Si(311) or Ge(111) crystals. The choice of crystal depends on the experimental requirements since the crystals
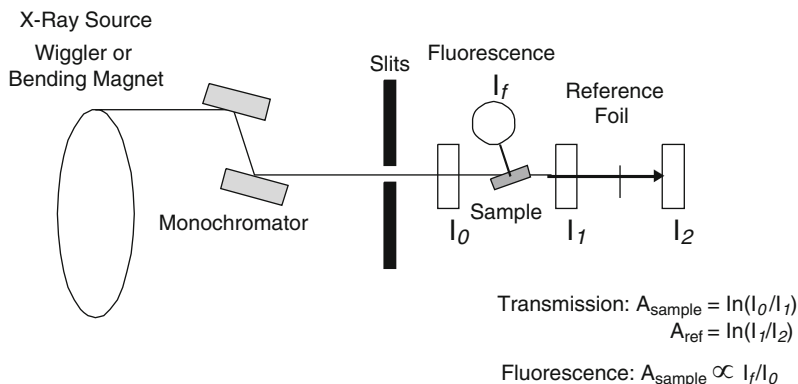
Fig. 11.7 Typical instrumentation used for XAS analysis [67]

influence the flux and energy resolution [67]. The tuned beam is fired onto the sample which is commonly housed in a cryostat, maintained at approximately 4–16 K, to reduce X-ray photodecomposition. As the energy of the beam is increased, the flux of the incident beam is measured prior to impact on the sample using an ion chamber. A further two ion chambers are positioned in the line of the sample; one directly after the sample, and the other after the reference foil. The foil is included as an internal standard and allows comparison of all spectra recorded within the study [61]. A detector is positioned at the fluorescence angle when data is collected in fluorescence mode [67]. Most spectra are collected in fluorescence mode to overcome problems associated with sample absorption [61]. Fluorescence detection also provides greater sensitivity and is often the method of data collection for analyses of metals in biological samples or proteins where the concentrations may be low.

11.3.3 Sample Preparation

Preparation of biological samples for XAS analysis is dependent on the type of analysis. As mentioned, micro-XAS can be performed on individual cells in conjunction with micro-SRXRF or, alternatively, XAS can be performed on a bulk sample of cells using a beam of millimetre dimensions. In the first instance, treated cells can be prepared by freeze-drying as described in Sect. 11.2.3.1. XAS of bulk cells can be performed more easily. It also provides detailed spectra that can be utilized for XANES component analysis and EXAFS fitting of the first coordination sphere [34, 68]. The preparation simply involves washing of treated cells to remove extracellular material followed by harvesting, further washing and finally immersion of the resultant pellet in liquid nitrogen. The sample can be stored in liquid nitrogen indefinitely and can be inserted directly into the cryostat or freeze-dried immediately prior to XAS analysis [34, 62, 68].

In addition to collection of XAS spectra of the sample, it is advisable to collect spectra of representative standards of known chemical structures using the identical experimental conditions. Standards can be prepared using a number of methods. Typically, solutions are prepared at metal concentrations of 1–5 mM with inclusion of a glassing agent (30% v/v) such as ethylene glycol or glycerine. The resultant solution can be injected into a polypropylene sample holder with a transparent window (kapton tape) that can be designed to take small volumes; typically 100–500 μL is sufficient. Powders can be prepared by grinding the solid (~1%) into boron nitride to "dilute" the sample. For recommended low temperature studies, the samples must be rapidly plunged into liquid nitrogen, and allowed to equilibrate prior to their insertion into the cryostat.

11.3.4   Results, Capabilities and Limitations

XAS analysis can be utilised for the important task of establishing the integrity of the metallointercalators in biological fluids to predict their metabolism *in vivo* and gauge their effectiveness as anticancer agents. Solutions that have been used to reproduce biological systems include simulated digestive systems and blood and its components such as serum [68]. In addition, this technique can be used to monitor the reactivity of the species in cell media prior to uptake by the ultimate target, cancer cells. Studies of this kind have been implemented for nutritional formulations such as [Cr(pic)$_3$] (pic = picolinate, 2-pyridinecarboxylato(-)) whereby extensive ligand exchange reactions have been detected [68].

There are very few reports in the literature that describe specific XAS analysis of metallointercalators in cancer cells. However, there are a number of studies that have successfully employed XAS, in particular XANES, to probe metal-containing xenobiotics (carcinogens, vitamin supplements and anticancer agents) such as Cr and Pt in the context of analysing the chemical biotransformation reactions that occur to these metals following their cellular uptake. Since both Cr and Pt are also associated with metallointercalators, the success of these studies provides incentive for studying any intracellular biotransformation reactions that may occur to analogous metallointercalators.

Most of the XANES studies of Cr compounds have been performed with an emphasis on understanding the mechanisms of carcinogenic action or to study the biotransformation reactions of chromium nutrition supplements. Dillon et al. performed the first direct XANES analyses of Cr in bulk V79 Chinese hamster lung cells (at Brookhaven National Laboratory) and showed that the predominant intracellular Cr oxidation state was Cr(III) when cells had been treated with Cr(VI) or Cr (V) [62]. Importantly, the various oxidation states of Cr are readily distinguishable, not only by the edge energy (which expectedly rises with oxidation state) but also by pre-edge features. In addition to the non-centrosymmetric nature of the Cr(V) and Cr(VI) complexes, the π bonding of the Cr=O moiety also contributes to the pre-edge features observed for these complexes [62, 64, 65]. Consequently,

an underlying knowledge of the electronic structure of the metal can lead to a wealth of knowledge regarding its biotransformation.

In addition to this capability, Ortega et al. [69, 70] reported microprobe oxidation state specific mapping (at the European Synchrotron Radiation Facility) of total Cr and Cr(VI) in single ovarian cells following their treatment with insoluble Cr(VI) particles. The results showed oxidation state specific accumulations within cells and highlight yet another capability associated with micro-XANES analyses.

Unlike chromium, the oxidation states and coordination geometries of intracellular Pt(II) and Pt(IV) complexes are not easily discerned from pre-edge peaks. Predictably the position of the edge assists in this determination (2.2 eV difference between Pt(II) and Pt(IV)), as does the ratio of the intensity of the white line peak to the post edge region, as reported by Hall et al. [35, 71]. This data was used to predict the intracellular oxidation state of Pt, and determine the ability of the cells to reduce Pt(IV) species to the potentially active Pt(II) anticancer species.

Clearly, XAS provides a direct analysis of the chemical structure of the metals in biological samples without the requirement of extensive or tedious preparation protocols. It offers the added advantage of being able to probe all metals irrespective of their oxidation state, unlike UV/Vis, EPR or NMR spectroscopy which specifically detect species based on their electronic structures or nuclear spin [61, 62]. It is apparent from studies of similar systems that XAS can provide information regarding biotransformation reactions that enable the medicinal chemist to monitor and predict the activity of the metallointercalators in cancer cells and tissue for the purposes of drug development.

The most important limitation of XAS is that it provides information regarding the average metal structure in the sample. Consequently, non-detailed analysis will only provide information regarding the most abundant species in the sample. A more thorough analysis such as that performed by multiple linear regression analysis involving simulations of spectra from feasible standards will, alternatively, provide information regarding contributions from model species [61]. Multiple linear regression analyses of XANES spectra can be performed using programs such as the DATFIT module of EXAFSPAK whereby model spectra can be fitted to spectra obtained from the metallointercalator-treated cells. Such fitting programs can be used to predict the proportion of likely metabolites, as has been performed for intracellular As and Cr complexes [34, 63, 68]. This provides some insight as to the fate of the xenobiotic. This analysis requires appropriate predictions of realistic models which may also be challenging [34, 63, 68].

Another limitation of these studies is the extraction of full chemical structural information regarding the intracellular metal species. Micro-XAS analyses of intracellular metal species are often plagued by poor signal to noise. While this is often sufficient to extract information from the XANES region of the spectrum, it is often impossible to obtain sufficient signal to noise for full EXAFS analysis from individual cells. In addition, very few microprobe XRF/XAS beamlines possess a cryostat that enables data collection at ~4 K. This restriction results in X-ray induced damage as has been reported by Ortega [72] and Dillon [34]. Often bulk

cell sample analysis, using a cryostat, provides spectra with superior signal to noise ratios that allow collection of EXAFS spectra [34, 72].

While EXAFS analyses offer the ability of fitting beyond the first atomic coordination sphere, this capability is highly reliant on appropriate models and the purity of the species being analysed. If the metallointercalator has remained chemically unchanged, then the analysis should be straightforward whereby the X-ray absorption spectrum will remain unchanged. Typically, however, biotransformation reactions occur and it is often difficult to obtain an EXAFS fit if one is not aware of the coordinating species. The experimenter needs to establish whether the coordinating species are macromolecules such as DNA or proteins, or smaller biomolecules such as glutathione or ascorbic acid. With the number of variables in mind, EXAFS analysis of intracellular species may present an insurmountable challenge and often only the first coordination sphere fitting is achieved [34, 63, 68].

11.4   Conclusions

Micro-SRXRF and XAS are powerful analytical techniques that are clearly capable of detection of extremely low concentrations of metals within mammalian cells and tissue. The physical principles of the techniques allow direct detection of the metals without the need of any enhancement agents such as the incorporation of fluorescent ligands or radioactive tracers that may interfere with the uptake kinetics of the drugs. Submicron focusing devices such as zone plates offer XRF imaging resolution that provides clear distinction of larger intracellular organelles such as the nucleus and the nucleolus. Results shown here prove that metals associated with metallointercalator-treatment of cancerous cells accumulate within the nucleus of the cells indicating their ability to target and potentially interact with DNA. Future studies using XAS should be performed to determine whether the metals remain coordinated to the organic intercalator ligand.

References

1. Dillon CT, Lay PA, Kennedy BJ, Stampfl APJ, Cai Z, Ilinski P, et al. J Biol Inorg Chem. 2002;7:640.
2. Paunesku T, Vogt S, Maser J, Lai B, Woloschak G. J. Cellular Biochemistry. 2006;99:1489.

3. Margaritondo G. Elements of synchrotron light for biology, chemistry and medical research. New York: Oxford University Press; 2002.
4. Jenkins R. X-Ray fluorescence spectrometry, Vol. 152, 2nd ed. New York: Wiley. 1999.
5. Botton G. In: Hawkes PW, Spence JCH, editors. Science of microscopy, Vol. I. New York: Springer. 2007. p. 273.
6. Williams KL. An introduction to X-ray spectrometry. London: Allen and Unwin; 1987.
7. Williams DB, Carter CB. Transmission electron microscopy. A textbook for materials science. New York: Plenum; 1996.
8. Legge GJF, Mazzolini AP. Nucl Instrum Methods Phys Res A. 1980;168:563.
9. Thompson A, Attwood D, Gullikson E, Howells M, Kim K-J, Kirz J, et al. X-ray data booklet. 2nd ed. Berkeley, CA: Lawrence Berkeley National Laboratory; 2001.
10. Winick H. Synchrotron radiation sources: a primer. Singapore: World Scientific; 1995.
11. Forslind B, Malmqvist KG, Pallon J. Scanning Microsc. 1991;5:877.
12. Ortega R. Nucl Instrum Methods Phys Res B. 2005;231:218.
13. Jamieson DN. Nucl Instrum Methods Phys Res B. 2001;181:1.
14. Bohic S, Simionovici A, Ortega R, Heymann D, Schroer C, Snigirev A. Nucl Instrum Methods Phys Res B. 2001;181:728.
15. Cholewa M, Dillon C, Lay P, Phillips DR, Talarico T, Lai B. Nucl Instrum Methods Phys Res B. 2001;181:715.
16. Bertsch PM, Hunter DB. Chem Rev. 2001;101:1809.
17. Ryan CG, Etschmann BE, Vogt S, Maser J, Harland CL, van Achterbergh E, et al. Nucl Instrum Methods Phys Res B. 2005;231:183.
18. Hawkes PW, Spence JCH. Science of microscopy, vol. 1. New York: Springer; 2007.
19. Joy DC, Romig AD (Jr), Goldstein JI. Principles of analytical electron microscopy. New York: Plenum 1986.
20. Legge GJF, McKenzie CD, Mazzolini AP. J Microsc. 1979;117:185.
21. Ice GE. X-Ray Spectrom. 1997;26:315.
22. Yun W, Pratt ST, Miller RM, Cai Z, Hunter DB, Jarster AG, et al. J. Synch. Radiation. 1998;5:1390.
23. West M, Ells AT, Kregsamer P, Potts PJ, Streli C, Van hoof C, Wobrauschek. J. Anal Atomic Spectrom. 2008; 23:1409.
24. Duke PJ. Synchrotron radiation. Production and properties. New York: Oxford Science; 2000.
25. Ilinski P, Lai B, Cai Z, Yun W, Legnini D, Talarico T, et al. Cancer Res. 2003;63:1776.
26. Dhez P, Chevallier P, Lucatorto TB, Tarrio C. Rev Sci Instrum. 1999;70:1907.
27. Carmona A, Cloetens P, Deves G, Bohic S, Ortega R. J Anal At Spectrom. 2008;23:1083.
28. Iwanczyk JS, Patt BE, Barkan S, Feng L, Tull CR. IEEE Trans Nucl Sci. 2003;50:2470.
29. Barkan S, Iwanczyk JS, Patt BE, Feng L, Tull CR. Adv X-Ray Anal. 2003;46:332.
30. ATCC. The Global Bioresource Center., http://www.atcc.org/CulturesandProducts, 2009.
31. Lonza Australia. Pty Ltd, Lonza Products and Services., http://www.lonza.com/group/en.html, 2009.
32. Harris HH, Levina A, Dillon CT, Mulyani I, Lai B, Cai Z, et al. J Biol Inorg Chem. 2005;10:105.
33. Waern JB, Harris HH, Lai B, Cai Z, Harding MM, Dillon CT. J Biol Inorg Chem. 2005;10:443.
34. Munro KL, Mariana A, Klavins A, Foster AJ, Lai B, Cai Z, et al. Chem Res Toxicol. 2008;21:1760.
35. Hall MD, Dillon CT, Zhang M, Beale P, Cai Z, Lai B, et al. J Biol Inorg Chem. 2003;8:726.
36. McRae R, Lai B, Vogt S, Fahrni CJ. J Struct Biol. 2006;155:22.
37. Liu G, Huang W, Moir RD, Vanderburg CR, Lai B, Peng Z, et al. J Struct Biol. 2006;155:45.
38. Bazhanova VV, Guljaeva LF, Krasilnikov SE, Titova VS, Shaporenko AD, Shulga Y. Nucl Instrum Methods Phys Res A. 2007;575:206.
39. Dobrowolski Z, Drewniak T, Kwiatek W, Jakubik P. Eur Urol. 2002;42:475.
40. Bozzola JJ, Russell LD. 2nd ed., Sudbury, MA: Jones and Bartlett. 1999, p. 17.

41. Munro K. Honours Thesis, University of Wollongong, 2006.
42. Hall MD, Alderden RA, Zhang M, Beale P, Cai Z, Lai B, et al. J Struct Biol. 2006;155:38.
43. Farquharson MJ, Geraki K, Falkenberg G, Leek R, Harris A. Appl Radiat Isot. 2007;65:183.
44. Modok S, Scott R, Alderden RA, Hall MD, Mellor HR, Bohic S, et al. Br J Cancer. 2007;97:194.
45. Gajda M, Banas K, Banas A, Jawien J, Mateuszuk L, Chlopicki S, et al. X-Ray Spectrom. 2008;37:495.
46. Kwiatek WM, Banas A, Banas K, Gajda M, Galka M, Falkenberg G, et al. J Alloys Compd. 2005;401:178.
47. Vogt S. J Phys IV. 2003;104:635.
48. Banas A, Kwiatek WM, Zajac W. J Alloys Compd. 2001;328:135.
49. Dillon CT, Lay PA, Bonin AM, Cholewa M, Legge GJF, Collins TJ, et al. Chem Res Toxicol. 1998;11:119.
50. Dillon CT, Lay PA, Bonin AM, Cholewa M, Legge GJF. Chem Res Toxicol. 2000;13:742.
51. Branden C, Tooze J. Introduction to protein structure. New York: Garland Publishing Inc.; 1999.
52. Quintana C, Electron J. Microsc Tech. 1991;18:411.
53. Quintana C, Olmedilla A, Antoine N, Ollacarizqueta A. Biol Cell. 1987;61:115.
54. Alderden RA, Mellor HR, Modok S, Hall MD, Sutton SR, Newville MG, et al. J Am Chem Soc. 2007;129:13400.
55. Talib J, Harman DG, Dillon CT, Aldrich-Wright J, Beck JL, Ralph SF. Dalton Trans. 2009;3:504.
56. Krause-Heuer AM, Wheate NJ, Tilby MJ, Pearson DG, Ottley CJ, Aldrich-Wright JR. Inorg Chem. 2008;47:6880.
57. Wheate NJ, Taleb RI, Krause-Heuer AM, Cook RL, Wang S, Higgins VJ, Aldrich-Wright JR. Dalton Trans. 2007;43:5055.
58. Davis KJ. Honours Thesis, Bachelor of Science (Advanced), University of Wollongong, 2009.
59. Penner-Hahn JE. Coord Chem Rev. 1999;190–192:1101.
60. Penner-Hahn JE. In: McCleverty JA, Meyer TJ, editors. Comprehensive coordination chemistry II, Vol. 2. Amsterdam: Elsevier. 2004, p. 159.
61. Penner-Hahn JE. Coord Chem Rev. 2005;249:161.
62. Dillon CT, Lay PA, Cholewa M, Legge GJF, Bonin AM, Collins TJ, et al. Chem Res Toxicol. 1997;10:533.
63. Levina A, Harris HH, Lay PA. J Am Chem Soc. 2007;129:1065.
64. Weeks C, Levina A, Dillon CT, Turner P, Fenton RR, Lay PA. Inorg Chem. 2004;43:7844.
65. Levina A, Codd R, Foran GJ, Hambley TW, Maschmeyer T, Masters AF, et al. Inorg Chem. 2004;43:1046.
66. Levina A, Foran GJ, Pattison DI, Lay PA. Angew Chem Int Ed. 2004;43:462.
67. Ascone I, Meyer-Klaucke W, Murphy L. J Synchrotron Rad. 2003;10:16.
68. Nguyen A, Mulyani I, Levina A, Lay PA. Inorg Chem. 2008;47:4299.
69. Ortega R, Deves G, Fayard B, Salome M, Susini J. Nucl Instrum Methods Phys Res B. 2003;210:325.
70. Ortega R, Fayard B, Salome M, Deves G, Susini J. J Phys IV France. 2003;104:289.
71. Hall MD, Foran GJ, Zhang M, Beale PJ, Hambley TW. J Am Chem Soc. 2003;125:7524.
72. Bacquart T, Deves G, Carmona A, Tucoulou R, Bohic S, Ortega R. Anal Chem. 2007;79:7375.

Chapter 12
The Use of Calorimetry to Study Ligand–DNA Interactions

Nichola C. Garbett

12.1 Introduction

Calorimetry monitors heat changes accompanying biological or chemical processes. As applied to the study of ligand–DNA interactions, calorimetry can be used to monitor processes including the isothermal titration of DNA targets with putative DNA binding ligands; as well as, the thermal denaturation of DNA in the absence and presence of binding ligands. By monitoring the small heat changes accompanying these events calorimetry can directly provide thermodynamic information which is invaluable for understanding the basis of how molecules interact with each other. In this chapter, the use of calorimetric approaches to the study of ligand–DNA interactions will be discussed. The chapter will begin with an overview of the information that can be obtained from calorimetric measurements and their utility for the study of ligand–DNA interactions. It will then provide an introduction to calorimetry and important experimental details and concerns when carrying out calorimetric studies. The chapter will end with the presentation of some notable examples from the literature demonstrating the application of calorimetric approaches to the study and rational design of binding ligands.

12.2 What Information Can Be Obtained from Calorimetric Measurements?

Before beginning an in-depth discussion about binding thermodynamics it is important to introduce the key parameters and their meaning at the molecular level. The interaction of a ligand with its target macromolecule is defined by the

N.C. Garbett
Biophysical Core Facility, James Graham Brown Cancer Center, University of Louisville, Louisville, KY, USA
e-mail: nichola.garbett@louisville.edu

Gibbs free energy change (ΔG) under a particular set of reaction conditions. ΔG is a crucial parameter as this shows the direction in which the reaction will proceed. A negative value means that a binding reaction will proceed spontaneously and the absolute value is indicative of the position of the molecular equilibrium. Conversely, a positive value indicates the amount of energy that would be required to drive the reaction towards product(s). For a simple reversible ligand–DNA binding system represented by:

$$D + L \rightleftharpoons DL, \tag{12.1}$$

the Gibbs free energy change describing the binding reaction is:

$$\Delta G = \Delta G^o + RT \ln \frac{[DL]}{[D][L]}, \tag{12.2}$$

where the standard Gibbs free energy (ΔG^o) represents the Gibbs free energy change under standard conditions of 1 M reactant concentrations at pH 7 and 25 °C; R is the gas constant which is equal to 8.314 J/K · mol, T is the temperature in kelvin and [DL], [D] and [L] represent the concentration of ligand–DNA complex, DNA, and unbound ligand, respectively. ΔG^o is defined by the following equation:

$$\Delta G^o = -RT \ln K_a, \tag{12.3}$$

where K_a is the equilibrium binding constant. In this way, ΔG^o can be accessed through the measurement of binding constants.

ΔG is determined by opposing enthalpy (ΔH) and entropy (ΔS) changes according to the equation:

$$\Delta G = \Delta H - T\Delta S. \tag{12.4}$$

The enthalpy change is a measure of the heat taken up or released during a binding reaction, reflecting differences in heat energy between reactants and products resulting from bond formation or bond breakage. Negative enthalpy values indicate that the product of the binding reaction is of a lower energy level than the starting components. This is a result of bond formation where there is a net release of heat energy during the binding reaction. The entropy change reflects the ease with which the energy can be distributed between various molecular energy levels. Positive entropy values indicate an increase in the disorder of the system at the end of the binding reaction through bond breakage, such as the disruption of solvent interactions and the release of previously bound water molecules to bulk solvent. Conversely, negative entropy values indicate an increase in the order of a system, for example, through conformational restrictions in the ligand–DNA complex compared with the free binding partners.

Enthalpy values can be determined directly from calorimetry measurements or indirectly from the temperature-dependence of equilibrium constants using the van't Hoff equation:

$$\Delta H_{vH} = -R \frac{\delta \ln K_a}{\delta(1/T)}. \tag{12.5}$$

The use of both calorimetric and van't Hoff enthalpies, ΔH_{vH}, will be discussed in a later section. A comparison of calorimetric and van't Hoff enthalpies can reveal important information about the mechanism of a reaction. However, it is important to understand that van't Hoff enthalpies must be considered with caution. The van't Hoff approximation assumes that ΔH does not change with temperature (i.e., that there is no heat capacity change associated with the reaction; see later); in reality this is rarely the case and significant discrepancies between calorimetric and van't Hoff enthalpies have been reported because of undetected curvature in van't Hoff plots resulting from a non-zero heat capacity change [1–4].

Along with ΔG, ΔH and ΔS, determination of the heat capacity change, ΔC_p, completes the thermodynamic profile of a binding reaction. ΔC_p can be easily determined from the temperature-dependence of ΔH values (at constant pressure) according to:

$$\Delta C_p = \left(\frac{\delta \Delta H}{\delta T} \right)_P. \tag{12.6}$$

A negative heat capacity change indicates that the complex has a lower heat capacity than the free binding partners. This, along with a positive entropy, have been proposed to indicate the formation of hydrophobic interactions in the binding complex [4]. If non-zero heat capacity changes are observed, this must be accounted for in the expressions for ΔG, ΔH and ΔS:

$$\Delta H(T) = \Delta H(T_R) + \Delta C_p(T - T_R)$$
$$\Delta S(T) = \Delta S(T_R) + \Delta C_p \ln\left(\frac{T}{T_R}\right)$$
$$\Delta G(T) = \Delta H(T_R) - T\Delta S(T_R) + \Delta C_p \left\{ (T - T_R) - T \ln\left(\frac{T}{T_R}\right) \right\}, \tag{12.7}$$

where T is the temperature of interest and T_R represents an appropriate reference temperature.

Attempts have been made to parse the free energy change associated with ligand–DNA interactions in terms of the molecular forces involved in complex formation [3, 5–7]. Ladbury and Chowdhry have discussed the types of molecular forces involved as two molecules change from being free in solution to interacting in a binding complex [8]. The observed free energy (ΔG_{obs}) is

considered to contain at least five contributions as shown by the following expression:

$$\Delta G_{obs} = \Delta G_{conf} + \Delta G_{r+t} + \Delta G_{hyd} + \Delta G_{pe} + \Delta G_{mol}. \qquad (12.8)$$

The first two terms relate to entropic penalties resulting from formation of a ligand–DNA complex. It is estimated that restriction of the binding partners within the complex results in a free energy penalty of approximately +0.6 kcal/mol per restricted bond rotation as a result of conformational changes (ΔG_{conf}) and up to +15 kcal/mol for the restriction of rotational and translational motions (ΔG_{r+t}) [3]. The free energy associated with the hydrophobic transfer of ligand from an aqueous environment to the DNA binding site (ΔG_{hyd}) is typically large and favourable (i.e., negative ΔG contribution). ΔG_{hyd} can be estimated from heat capacity changes or estimates of changes in solvent accessible surface area [9, 10]; as an example, a value of -26.4 kcal/mol has been estimated for the groove binder Hoechst 33258 [5]. Favourable binding free energy is also derived from the polyelectrolyte contribution to the free energy of binding (ΔG_{pe})based on Manning and Record's counterion condensation model. This contribution is thought to be much smaller, in the range of 0 to -4 kcal/mol. The final free energy contribution shown by (12.8) refers to the formation of noncovalent molecular interactions between ligand and DNA (ΔG_{mol}); these include hydrogen bonding, van der Waals interactions and electrostatic interactions. It has been difficult to define ΔG_{mol} because of the lack of consensus of the contribution of each type of molecular interaction to the binding free energy and the difficulty in determining the number and type of binding interactions, both broken and formed, during complex formation. Although somewhat tentative, the exercise of parsing the free energy of binding into different types of molecular forces involved in complex formation can lend itself to the rational drug design process. For example, the engineering of rigid bonds into a ligand to reduce the free energy penalty associated with the restriction of bond motion within the DNA binding site or the design of ligands to enhance molecular interactions within the binding site will thereby improve the binding free energy of ligand drug candidates.

Having provided a brief introduction to important thermodynamic parameters and their meaning at the molecular level, it is important to address the utility of such thermodynamic measurements for the study of ligand–DNA interactions.

12.3   Why Is Calorimetry Useful for Ligand–DNA Studies?

Differential scanning calorimetry (DSC) and isothermal titration calorimetry (ITC) are powerful techniques for the determination of the thermodynamics of ligand–DNA interactions. Calorimetry permits the direct measurement of energetic parameters of biomolecular interactions and yields a complete thermodynamic profile of the reaction. Measurements are performed in the solution state without need for

crystallisation, immobilisation or chemical modification. The methods are also amenable to a range of molecular sizes, shapes and chemical composition. The importance of measuring energetic parameters was demonstrated by Chaires who determined the binding energetics of two related anthracycline antibiotics, doxorubicin and daunorubicin, to calf thymus DNA [11]. Doxorubicin and daunorubicin are structurally very similar, possessing an anthraquinone ring structure with a daunosamine moiety. They differ in only a single hydroxyl group at the C-14 position, which is present in doxorubicin and absent in daunorubicin. Despite their structural similarity they exhibit very different binding energetics. Daunorubicin binding measured at $20\,°C$ is entirely enthalpically-driven ($\Delta H = -9.0 \pm 0.8$ kcal/mol) with an unfavourable entropic contribution ($T\Delta S = -1.1$ kcal/mol) resulting in a favourable binding interaction ($\Delta G = -7.9 \pm 0.3$ kcal/mol). In contrast, doxorubicin binds with nearly one order of magnitude greater affinity ($\Delta G = -8.9 \pm 0.3$ kcal/mol), with both favourable entropic ($T\Delta S = +1.5$ kcal/mol) and enthalpic components ($\Delta H = -7.4 \pm 0.6$ kcal/mol). Despite the significant difference in binding energetics, structural determination via X-ray crystallography revealed almost identical structures for the two ligand–DNA complexes. This illustrates quite clearly the importance of considering both structural and energetic information in the study of ligand–DNA interactions.

In terms of a rational drug design approach, the value of measuring a complete energetic profile is being realised. Measurement of binding affinity is a common first step in assessing potential drug candidates because this provides access to a value for the free energy of binding; binding will only occur if there is a release of free energy. However, binding affinities and free energies alone are often not sufficient in terms of discriminating potential binders. A review of the application of calorimetric methods to the study of ligand–protein interactions highlighted a study where ligands based on a common pharmacophore bound with similar free energies to a common protein binding site but with disparate thermodynamic parameters [12]. Moreover, binding affinities and free energies do not provide information on the nature of the binding interactions. In fact, similar binding free energies can mask significant differences in binding mode. A number of reports appear in the literature concerning the observation of the somewhat controversial enthalpy–entropy compensation phenomenon [13–19]. Chaires recently assembled a thermodynamic dataset of 26 ligand–DNA interactions that revealed distinct thermodynamic signatures for groove-binding and intercalating ligands [20]. Intercalation was found to be enthalpically driven and opposed by entropy, whereas groove binding was largely entropically-driven with an unfavourable or a small, favourable enthalpic contribution. A complete explanation of the observed trend is not entirely understood but some general conclusions can be drawn upon consideration of the molecular basis of the binding modes. Intercalation results in the insertion of a planar ring system between DNA base pairs forming enthalpically-favourable molecular interactions, with an entropic penalty resulting from perturbation of the DNA structure to form the intercalation pocket. In contrast, groove binders are typically crescent-shaped, matching the curvature of the minor groove, and, as such, result in negligible perturbation of the DNA structure and

consequently little entropic penalty. The greater possible molecular motion of groove binders compared with intercalators within their binding sites should also minimise the entropic penalty associated with groove binding. The positively charged nature of both intercalators and groove binders results in entropically favourable contributions to binding from the release of condensed cations from the DNA. A further entropic gain results from the release of bound water molecules to the bulk solvent upon formation of the binding complex. An examination of ligand–DNA binding interactions in this way demonstrates the utility of the measurement of thermodynamic parameters, providing a fuller picture of ligand–DNA interactions than consideration of binding affinities or free energies alone.

An understanding of the energetic basis of ligand–DNA interactions is critical for rational drug design approaches. In the case of daunorubicin and doxorubicin, a complete thermodynamic profile revealed a nearly one order of magnitude tighter binding of doxorubicin, perhaps because of differences in solvent and ion contributions to binding, observations that would not be so apparent using purely structure-based techniques [3]. The intent of this chapter is to present calorimetric strategies to obtain energetic information that describes ligand–DNA interactions. This will be illustrated using examples from the literature that demonstrate the utility of these approaches.

12.4   Introduction to Calorimetry

Two principal calorimetric techniques are typically applied to the study of ligand–DNA interactions: DSC and ITC. DSC monitors extremely small heat differences between a sample cell and a reference cell occurring as a function of a precisely-controlled temperature change. The sample cell contains a relatively dilute DNA solution (micromolar to millimolar) or a pre-formed ligand–DNA complex and the reference cell is filled with an equal volume of the solvent (usually buffer) in which the DNA or ligand–DNA sample is dissolved. Most modern DSC instruments work in a differential power compensation mode. In this mode, sensors continually monitor the temperature difference between the sample and reference cells as the cells are electrically heated or cooled at a precisely-controlled constant rate. Heaters on the cell surface apply compensating power to keep the cells in thermal balance. It is this differential power signal that is recorded by the instrument as raw data and provides a direct monitor of thermal events occurring in the sample cell. For example, if the sample undergoes an endothermic event, such as the thermal denaturation of DNA, then the sample cell will take up heat creating a thermal imbalance with the reference cell. This will require the application of compensating power until the thermal balance of the cells is restored and the result will be a positive differential power signal recorded by the instrument which will then return to a baseline value following the thermal event. The differential power is a direct measure of the heat capacity differences between the biomolecule solution in the sample cell and its solvent in the reference cell as a function of temperature. The differential power signal (W) can be easily converted into a heat capacity term (J/°C or cal/°C) after normalisation of the

instrument heating (or cooling) rate. For instance, since $1 J \equiv 1 W \cdot s$, then differential power can be converted from units of W into units of J/s. Assuming a scan rate of $1 °C/min$, or $1/60 °C/s$, it then follows that $1 J/s \equiv 60 J/°C$ or $14.3 cal/°C$ (since $1 cal = 4.184 J$). After appropriate baseline subtraction and normalisation for the number of moles of material in the sample cell, it is possible to calculate the denaturation or renaturation enthalpy (in J/mol or cal/mol) directly from the integrated area of the DSC profile. Although such interconversions are typically performed behind the scenes by the manufacturer-supplied software, it is important to understand the basis of the values reported from DSC measurements. More details on the design of current DSC instruments have been provided by Spink in a recent review [21].

Like DSC, ITC also monitors the heat difference between a sample and a reference cell, providing raw data in the form of the differential power required to maintain the thermal balance of the cells. However, the events that are monitored are different. For ligand–DNA interactions, DSC monitors the thermally-induced denaturation or renaturation of DNA and pre-formed ligand–DNA complexes; whereas, ITC reports on the energetics of the isothermal interaction of two molecules, ligand and DNA. As will be discussed later, this provides different thermodynamic information. In an ITC experiment, one of the molecular species (typically the ligand) is titrated into a stirred sample cell containing the second molecule (typically DNA). Heat changes occurring in the sample cell as a result of an interaction between the molecules are reported as a differential power signal relative to the reference cell. If a detectable heat change is associated with a binding event, then each aliquot of titrant added to the sample cell will result in a deflection of the differential power signal from a steady-state baseline value before returning to the baseline value. After baseline subtraction and normalisation for the amount of added titrant, the area of the power deflection directly yields the heat change for each addition. It is then possible to construct a binding isotherm in the form of the heat change of each addition of titrant as a function of ligand:DNA ratio. Points at the beginning of the binding isotherm represent conditions of excess binding sites where all added titrant will be completely bound and the heat change represents the binding enthalpy. As more titrant is added and the binding sites become saturated the heat change for each addition will decrease. The rate of change of the heat of binding around the saturation point represents the binding affinity. At the end of the titration all of the binding sites will be saturated and any heat signal results from the dilution of titrant into the sample cell.

Having provided a brief overview of the techniques of DSC and ITC it is now appropriate to discuss experimental approaches by which thermodynamic data are obtained and their utility for ligand–DNA studies.

12.5   General Experimental Considerations

Due to the high sensitivity of modern calorimeters, precise matching of the buffer composition in the reference and sample cells is essential. To achieve this, DNA samples are prepared in the buffer of choice and then subjected to extensive buffer

exchange to achieve complete buffer equilibrium between the sample buffer and the exchange buffer. This can be achieved through the use of buffer exchange columns or by dialysis. Whichever method is used, a portion of the final exchange buffer (either from the final dialysis step or that used to thoroughly equilibrate the buffer exchange column) is retained for use as the calorimetric reference buffer, for sample dilution and for dissolution of low molecular weight binding ligands that cannot be subjected to buffer equilibrium alongside the DNA samples. In this way there is precise matching of solution conditions for all calorimetric samples.

A further important technical detail is to determine the concentrations of all samples with the highest possible degree of accuracy. For DSC measurements, ΔH and ΔS determinations are made directly from the integrated area of the DSC profile after normalisation for the number of moles of sample in the calorimeter cell. The calorimeter cell volume is fixed and precisely determined during the manufacture of the instrument; however, any inaccuracy in the determination of sample concentration will directly impact determination of ΔH and ΔS and propagate into the calculation of ΔG. Errors in sample concentration will not affect the position of the DSC profile and therefore will not affect the determination of T_{max} values; however, errors in ligand concentration will affect the calculation of binding affinities. For ITC measurements, the determination of the titrant concentration affects the integrated areas of each point in the binding isotherm, directly affecting values of ΔH. Errors in both titrant and titrate concentration will affect the binding stoichiometry, n, and can result in non-integral values. The sources of error in ITC experiments was discussed by Tellinghuisen [22–24]. Absorbance measurements are typically an accurate and convenient method to determine the concentration of DNA and ligand samples from knowledge of an appropriate extinction coefficient. Extinction coefficients for DNAs can be found in the literature, calculated, or determined experimentally [25–29]. Ligand extinction coefficients can also be found in the literature or can be easily measured through the absorbance measurement of a series of accurately-prepared ligand solutions and the application of the Beer–Lambert law.

Samples must be degassed with stirring prior to loading into the calorimeter; this is particularly important for solutions that have been stored at low temperature for a long period of time as the solubility of air is higher at low temperature. A degassing system is supplied by instrument manufacturers. Samples should be filtered before degassing to remove any undissolved solutes or particulates. Degassing systems should operate without significant evaporation of solvent; however, if this is suspected, the sample concentration should be re-measured. There is typically a small dilution of sample solutions during sample loading since the cell is usually pre-rinsed with sample buffer. This dilution is typically only a few percent and can either be determined experimentally from an absorbance measurement after loading or a manufacturer-determined dilution factor can be applied. If material permits, the sample cell can be rinsed with sample to avoid any dilution. For DNA and ligand solutions, typically no complications result from the degassing procedure; however, for proteins, where degassing might cause precipitation or denaturation. If degassing affects sample integrity, alternative

strategies include using a lower vacuum, shorter degassing time or preparing sample solutions directly in degassed buffer.

Other experimental concerns, including appropriate DNA concentrations and solution conditions for both DSC and ITC studies, are discussed by Pilch and Buurma and Haq [30, 31]. Having discussed sample preparation issues that are common to both DSC and ITC, more detailed information related to data collection and analysis will now be provided for each technique.

12.6   DSC Studies

12.6.1   Data Collection

Readers are referred to the manufacturers' guidelines for detailed experimental procedures for instrument operation and the collection of raw calorimetric data. A discussion of some important concerns will now follow.

Calorimeter cells are precision engineered to be closely matched in terms of cell dimensions and thermal properties; however, it is impossible to exactly match the sample and reference cells in a given instrument. For this reason, a DSC instrument baseline is measured prior to loading the sample. The instrument baseline is recorded by loading buffer into both the sample and reference cells and recording a so-called buffer–buffer scan under identical scanning conditions as the sample scan (i.e., sample in the sample cell and buffer in the reference cell). The instrument baseline will reflect small differences in the thermal properties of the sample and reference cells over the temperature range of interest and will be subtracted from subsequent sample scans.

A further important consideration for DSC measurements is to collect scans under identical conditions. Selecting identical scanning parameters may seem obvious but it is also important for the scans to be collected with the same thermal history of the instrument. The thermal history refers to the precise thermal conditions the cells experience prior to a scan (i.e., starting temperature, equilibration time, scanning rate, final temperature, elapsed time and temperature profile between subsequent scans) which all impact the baseline response. For instance, if the instrument has remained idle for a period of time before a set of experiments is performed, the first scan will always appear different from subsequent scans. Once the instrument has been cycling through the same scanning procedure, identical scans should be obtained. It is typical to record a number of buffer–buffer scans until a consistent scan profile is observed before loading the sample. Samples should be loaded in an efficient and reproducible manner to avoid affecting the thermal history of the instrument. Typically this is achieved by setting the instrument to continually scan and loading the sample while the instrument is cooling to the scan start temperature; a consistent loading temperature (close to room temperature and just above the scan start temperature) and loading procedure should be employed.

12.6.2 Data Analysis

Having collected raw calorimetric data there are three steps to be performed before
obtaining a normalised sample DSC scan:

1. Subtraction of an instrument (buffer–buffer) baseline
2. Normalisation for sample amount
3. Selection of a sample baseline

These steps are shown graphically in Fig. 12.1. A number of convenient
macros are incorporated into the manufacturer-supplied data analysis software
that permits rapid and straightforward data processing; however, thoughtful
consideration at each step of the data analysis process is important in obtaining
reliable data.
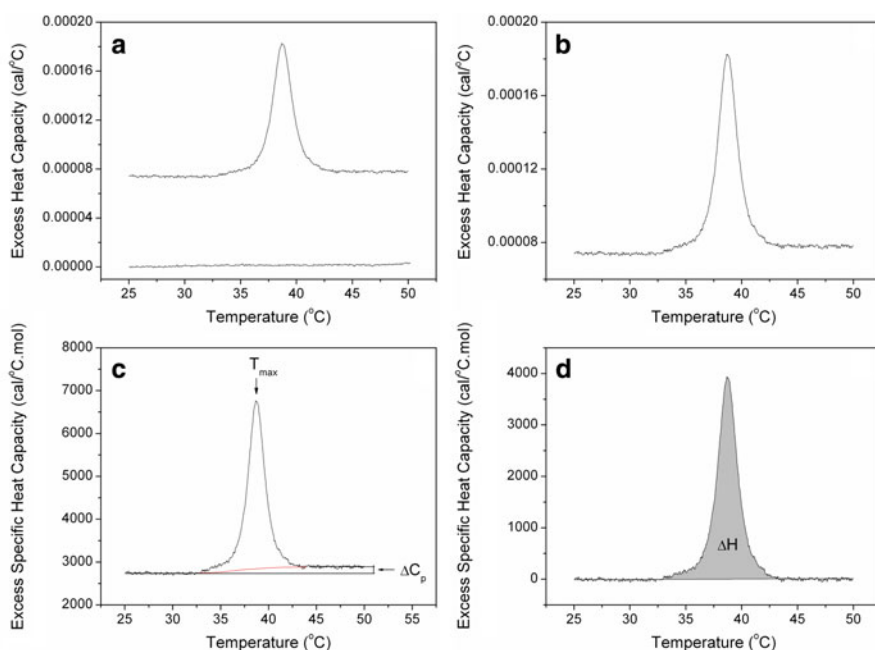
Fig. 12.1 Representative DSC data and processing steps. (**a**) Representative raw DSC data.
Lower scan is the instrumental baseline scan of buffer vs. buffer. Upper scan is the raw DNA
sample scan. (**b**) DNA sample scan after subtraction of the instrumental baseline scan. (**c**)
Normalisation of the DNA sample scan for the amount of sample in the calorimetric cell; note
that the calorimetric signal is now expressed as excess specific heat capacity in units of cal/°C · mol.
The temperature of the maximum of the heat capacity profile represents T_{max} and the difference
between the pre- and post-transition baselines reflects ΔC_p. The red line represents the selection of
a sample baseline for subsequent subtraction. (**d**) Final DNA sample scan after subtraction of the
sample baseline. The integrated area of the DSC profile directly yields ΔH. Transformation of the
final DSC profile into the form of $\Delta C_p^{ex}/T$ and integrating this new profile directly yields ΔS

Collection of an appropriate instrument baseline has been discussed in the previous section. The final buffer–buffer scan before loading the sample or, more rigorously, the average of a number of consistent buffer–buffer scans, is selected for use as the instrument baseline and is easily subtracted from a sample scan to achieve the first step in data analysis. It is typical to convert the raw power signal (W) to units of J/°C or cal/°C, as discussed earlier. This is achieved seamlessly by the data analysis software. At this point, data is in the form of excess heat capacity, ΔC_p^{ex}, the heat capacity of the sample in excess of that of the buffer.

The calorimetric signal is then normalised in terms of the number of moles of sample present in the calorimeter cell by input of sample concentration combined with a manufacturer determined cell volume. This renders the data in the form of an excess specific heat capacity. In this form, the pre-transition baseline represents the excess specific heat capacity of the native sample, the post-transition baseline represents the excess specific heat capacity of the denatured sample and the transition peak corresponds to the excess specific heat capacity of the denaturation process. The change from the pre-transition to the post-transition baseline reflects the heat capacity change accompanying the denaturation process. For DNA, changes in heat capacity are typically small (on the order of 100 cal/°C · mol [base pairs]) and determining ΔC_p can be challenging [21].

The last step in obtaining a final DSC profile is to select an appropriate sample baseline that describes the data. This is not always straightforward. The sample baseline should accurately describe the heat capacity of the sample in the absence of the transition at each temperature point of the scan. It is necessary to describe how the baseline changes as the relative proportions of native and denatured species change with temperature. A number of different mathematical functions can be applied to estimate this change; for instance, linear, cubic, progress and step functions are included in the data analysis software supplied by MicroCal instruments (MicroCal, LLC, Northampton, MA), now part of TA Instruments. Cooper et al. have reviewed in some detail concerns in selecting an appropriate sample baseline [32]. Some time should be spent comparing the data obtained using different baselines and the effect these have on the values of the resulting parameters. The nature of the sample baseline can have a significant effect on transition shape and area; generally, the choice of sample baseline translates into only small differences in T_{max} values but can result in more significant errors in ΔH, ΔH_{vH} and ΔS. The step baseline function in the MicroCal software is useful for an estimation of ΔC_p at the melting temperature.

Once the sample baseline has been selected, the thermodynamic parameters describing the transition can be determined. The enthalpy is determined directly from the integrated area of the excess specific heat capacity profile using (12.9):

$$\Delta H = \int_{T_o}^{T} C_p^{ex} \mathrm{d}T, \tag{12.9}$$

where T_o refers to the temperature at the onset of the transition and T to the temperature at the completion of the transition. The temperature of the maximum

of the excess specific heat capacity profile is defined as T_{max}. This is distinct from the temperature at the transition midpoint, T_m or $T_{1/2}$, which represents the temperature at which 50% of the sample has denatured. For a simple, two-state transition these values are identical. The entropy can be determined from (12.10):

$$\Delta S = \int_{T_o}^{T} \frac{C_p^{ex}}{T}\, dT. \tag{12.10}$$

This is calculated directly from the experimental data by dividing each point in the excess specific heat capacity profile by the temperature at that point and then integrating the new profile.

Having determined ΔH and ΔS, the Gibbs free energy change, ΔG, can be calculated from (12.4). For a two-state system, $\Delta G = 0$ at equilibrium, i.e., at T_m or $T_{1/2}$, and ΔS can be alternatively determined from (12.11):

$$\Delta S = \frac{\Delta H}{T_m}. \tag{12.11}$$

Although this provides a rapid and easy determination of ΔS, it is recommended that ΔS be determined from (12.10) since this is a direct, model-independent determination that does not require any knowledge of the nature of the system under study; until a two-state process has been verified, (12.11) should not be used.

With the determination of ΔH and ΔS directly from the experimental data and the subsequent calculation of ΔG from these values, a thermodynamic profile exists for the system under study determined in the absence of the assumption of any type of model. However, it is informative to compare the model-independent calorimetric enthalpy, ΔH_{cal}, with the model-dependent van't Hoff enthalpy. ΔH_{vH} can be determined from knowledge of ΔH_{cal}, T_{max} and the maximum of the excess specific heat capacity profile, C_p^{max}, using (12.12):

$$\Delta H_{vH} = 4RT_{max}^2 \frac{C_p^{max}}{\Delta H_{cal}}. \tag{12.12}$$

ΔH_{vH} is model-dependent, usually referring to a two-state model, and therefore a comparison of ΔH_{cal} and ΔH_{vH} can provide information about the mechanism of the denaturation process. ΔH_{vH} represents the enthalpy per mole of cooperative unit and the ratio $\Delta H_{vH}/\Delta H_{cal}$ is typically used to comment on the cooperativity of the process. For a two-state process, ΔH_{cal} and ΔH_{vH} should be identical and $\Delta H_{vH}/\Delta H_{cal}$ will be equal to 1. If $\Delta H_{vH}/\Delta H_{cal}$ is less than 1, this suggests the presence of intermediate states; and if $\Delta H_{vH}/\Delta H_{cal}$ is greater than 1, cooperativity is indicated. However, such comparisons should not be relied upon too heavily as any factors that might affect the shape of the DSC profile would lead to an incorrect determination of ΔH_{cal} and ΔH_{vH} [32]. Spink has recently discussed approaches to model the cooperativity of DNA denaturation [21].

The discussion so far has related to the extraction of thermodynamic parameters for the denaturation or renaturation of DNA samples. For the study of ligand–DNA complexes, the denaturation of DNA is characterised in the absence and presence of binding ligand. Thermodynamic parameters for these interactions do not directly yield parameters for ligand binding but this can be easily calculated using Hess's law as outlined below. Assuming saturating amounts of ligand are added to form a ligand–DNA complex, the three reactions of interest are as follows:

$$\text{duplex} \longleftrightarrow \text{single strands} \qquad \Delta H_1$$
$$\text{duplex - ligand} \longleftrightarrow \text{single strands + ligand} \qquad \Delta H_2$$
$$\text{duplex - ligand} \longleftrightarrow \text{duplex + ligand} \qquad \Delta H_3. \qquad (12.13)$$
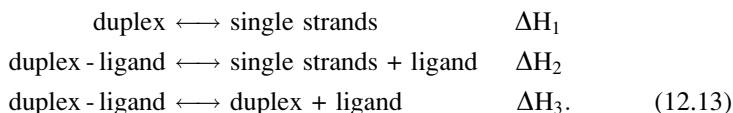
ΔH_1 and ΔH_2 are directly determined in DSC experiments. ΔH_3 can then be calculated as $\Delta H_2 - \Delta H_1$. ΔH_3 refers to the dissociation of a ligand–DNA complex to its components, i.e., the dissociation of ligand from DNA as opposed to the binding of ligand to DNA. The binding enthalpy therefore refers to the reverse reaction and the sign of ΔH_3 can simply be changed to reflect this. One final step in calculating the binding enthalpy is to normalise for the amount of bound ligand based on the binding site size of the ligand [33]. For ligands that have poor aqueous solubility, Leng et al. developed a "solid-shake" protocol for the determination of binding enthalpies using the Hess's law approach [34].

In situations where there is a less than saturating amount of ligand present, multiphase denaturation profiles will be obtained which will require deconvolution to extract binding thermodynamics. A number of approaches have been developed to deconvolute the effects of ligand binding on the biomolecule denaturation profile. A detailed discussion of these theories and the procedures involved in obtaining binding information is lengthy and beyond the scope of this article; readers are referred to the relevant literature [32, 35–41]. The methods developed by Brandts and Lin allowed the determination of ultratight binding constants of up to $10^{40} \, \text{M}^{-1}$ [36]. Cooper provides a convenient spreadsheet approach for simulating the effects of ligand binding on protein stability, the principles of which can be easily adapted to ligand–DNA systems [32]. McGhee and Crothers provided the most useful approaches to describe the melting of ligand–DNA complexes [38–41].

12.7   ITC Studies

12.7.1   Experimental Planning

A number of different ITC experimental approaches exist. The most commonly reported is a saturation experiment. In this case, a more concentrated titrant solution (~20-fold) is added in small aliquots to the titrate solution. An example of the raw

data obtained from this type of approach is illustrated in Fig. 12.2. This approach enables the determination of the binding enthalpy (ΔH_b), the binding stoichiometry (*n*) and the binding affinity (K_a) from a single experiment (after correction for appropriate control experiments). A second type of experiment is a so-called
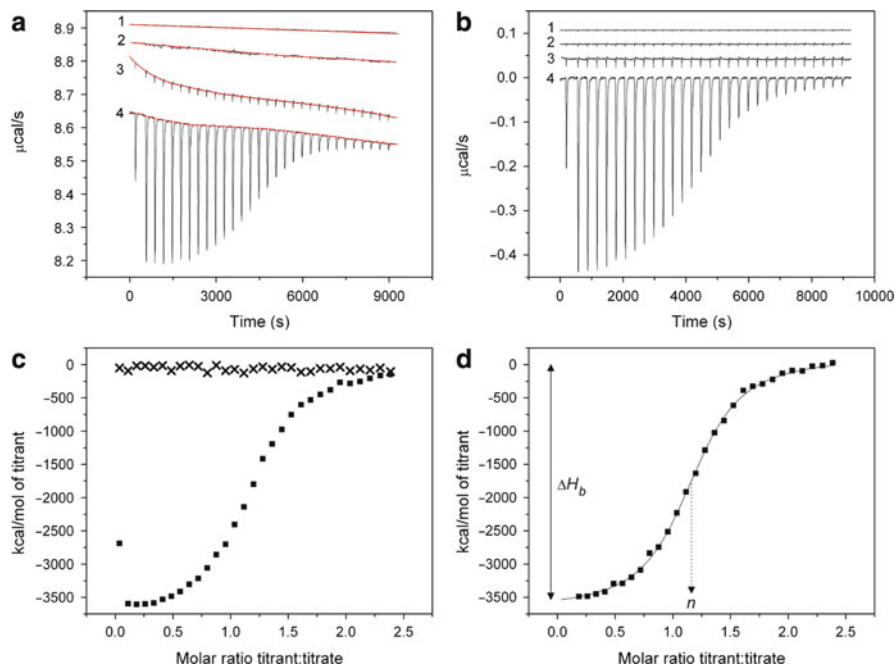
Fig. 12.2 Representative ITC data and processing steps. (**a**) Representative raw ITC data from a saturation experiment. The ITC binding experiment and all three control experiments are shown: instrument control experiment (curve 1; buffer into buffer); titrate dilution (curve 2; buffer into titrate); titrant dilution (curve 3; titrant into buffer); and binding experiment (curve 4; titrant into titrate). Integration baselines for all four datasets are shown by the *red lines*. Data were arbitrarily vertically translated for clarity. (**b**) Binding and control experiments after subtraction of the integration baseline. Note the anomalously small first injection peak for curve 4 that is discarded during subsequent analysis. This can be attributed to diffusion of titrant solution across the tip of the syringe during the pre-run equilibration period or backlash in the syringe plunger mechanism. Data were arbitrarily vertically translated for clarity. (**c**) Integration of each titration peak, normalisation for titrant and titrate amounts, and transformation of the data into the form of heat per injection vs. the molar ratio of titrant-to-titrate. Shown are data from the binding experiment (squares) and the titrant dilution experiment (crosses). The instrument control and titrate dilution experiments yield data close to zero and have been omitted for clarity. (**d**) Final binding experiment data after correction for all control experiments. ΔH_b can be determined directly from the integrated areas of the initial titration peaks and *n* can be obtained from the molar ratio of titrant: titrate at the midpoint of the binding isotherm. A model-independent, or excess sites, experiment represents operating in the low molar ratio plateau region of the binding isotherm under conditions of excess binding sites. In this scenario, each addition of titrant is completely bound and a robust determination of ΔH_b can be obtained from the area of each titration peak. Also shown is a fit using a model for one set of identical non-interacting binding sites (solid line) that will yield model-dependent values of ΔH_b, K_a and *n*

model-independent or excess sites approach [6, 42]. In this approach, similar concentrations of titrate and titrant are used such that the experiment is performed under conditions of excess binding sites where each addition of titrant is completely bound. This represents operating in the low molar ratio plateau region of Fig. 12.2 and provides a robust determination of ΔH_b. It should be noted that the first injection peak is commonly significantly smaller than subsequent peaks in both a saturation and excess sites experiment. This is typically attributed to the diffusion of titrant solution across the tip of the syringe during the pre-run equilibration period such that the actual amount delivered during the first injection is significantly smaller than expected. It is standard practice to set a very small first injection volume to avoid wasting sample as this first data point is typically discarded during analysis. However, Tellinghuisen and colleagues have recently shown that the anomalous first injection in fact arises from backlash in the syringe plunger mechanism and can be avoided by moving the plunger down a small amount after loading the syringe [24].

Before running an ITC experiment, effort should be invested in planning appropriate experimental parameters. For an uncharacterised system there is no way to predict the magnitude of the heat signal that will be obtained and therefore it may be difficult to decide what appropriate reactant concentrations and titrant volumes should be. There are, however, some established rules-of-thumb that can guide the design of an initial experiment and the results of the initial experiment can then be used to fine tune subsequent experiments. Freyer and Lewis recently discussed in some detail the planning of ITC experiments and the simulation of expected experimental data [43]. For an accurate determination of ΔH_b, the size of injection peaks in a model-independent experiment and the size of the initial peaks in a saturation experiment should be at least 10 µcal. To meet this requirement in a model-independent experiment, concentrations of titrant and titrate should be approximately the same and on the order of 10^{-4} M. For a saturation experiment, the choice of titrant and titrate concentration must also be selected by considering the shape of the binding isotherm. Wiseman et al. first defined the so-called "c-value" which defines the shape of the binding isotherm [44]. The c-value is the product of the interaction stoichiometry, the binding constant and the total molar concentration in the sample cell (M_{tot}), defined by (12.14), where the optimal range of c-values is considered to be 10–500 (or perhaps more realistically 10–100 in terms of a practical molar sample concentration, with c = 30 being ideal).

$$c = n \times K_a \times [M_{tot}]. \tag{12.14}$$

The ability to accurately define the slope of the binding isotherm is critical for a reliable determination of K_a. If the binding affinity is very high then the slope will be too sharp and defined by too few data points to accurately determine K_a. Very weak binding will result in very small changes in the slope of the binding isotherm, requiring extremely high sample cell concentrations to approach a useable c-value. Such high concentrations would be unrealistic in terms of the amount of material required as well as resulting in potentially complicating events, such as aggregation. It is this consideration of binding isotherm shape that defines an

effective range of binding affinity of 10^3–10^9 M^{-1} that is accessible from a typical ITC experiment.

Although consideration of the c-value may be useful for experiment design, little information may exist concerning an expected binding affinity or stoichiometry (determination of these parameters is, after all, the purpose of the experiment) and an appropriate sample cell concentration for an initial experiment may be very speculative. If a model-independent experiment has already been performed, then a sample cell concentration appropriate for obtaining initial peak areas of 10 μcal (from a reasonable injection volume, typically 3–10 μL) would provide a useful starting point. The sample cell concentration must also be considered in the context of an appropriate titrant concentration. For a saturation experiment, a typical titrant concentration is selected to yield a titrant:titrate ratio of ~2 or higher at the end of the experiment. With these parameters in mind, adjustments of the relative concentrations of both titrant and titrate could be considered in terms of the impact this would have on the initial peak areas (remembering that peak area is a function of the amount of added titrant and the binding enthalpy) and titrant:titrate ratios. The two leading ITC manufacturers have programs to aid in the planning of ITC experiments: BindWorks from CSC (Calorimetry Sciences Corporation, Lindon, UT), now part of TA Instruments and ITC-Expert from MicroCal. A final experimental parameter that should be considered before starting the experiment is the interval between injections. This should be sufficient to ensure a reasonable amount of baseline exists before and after a titration peak in order to obtain accurate peak integration during analysis. A larger interval is required earlier in the experiment as larger peaks result in a greater deflection from the baseline value. It is generally advisable to select a relatively long injection interval to account for the initial injection peaks; the injection interval can then be adjusted "on-the-fly" during the experiment or adopted for the entire experiment. For a model-independent experiment, all injections are equivalent and the injection interval need not be adjusted. Typical values of injection interval are in the range of 5–8 min. Depending on the binding parameters of the particular system under study, a large amount of material may be required for ITC experiments. This is generally considered worthwhile given the information content of ITC studies. Moreover, all material can be recovered at the end of the experiment and the DNA sample restored to its original state if the binding ligand can be effectively dissociated from the DNA, using a method such as dialysis, and if the sample is uncompromised by the effect of either experiment time, temperature or stirring.

12.7.2 Data Collection

Readers are referred to the manufacturers' guidelines for detailed experimental procedures for instrument operation and the collection of raw calorimetric data. A discussion of some important concerns will now follow.

Similar to DSC measurements, it is necessary to correct the raw experimental data before calculating thermodynamic information for the system of interest. There are three control datasets that must be collected in addition to the actual ITC binding experiment:

1. Instrument control (titration of buffer into a buffer-filled sample cell)
2. Heat of dilution of titrate (titration of buffer into a titrate-filled sample cell)
3. Heat of dilution of titrant (titration of titrant into a buffer-filled sample cell)

Recall that an ITC experiment records the heat difference between a sample cell and a buffer-filled reference cell as titrant is incrementally added to a stirred sample cell under isothermal conditions. The instrument control experiment in this case is the heat change associated with the titration of buffer into a buffer-filled sample cell. Similarly to the DSC instrument baseline, this will record any small differences in the thermal properties between the sample and reference cells. Unlike DSC, the instrument baseline experiment is performed under isothermal conditions and as a function of the addition of aliquots of titrant (in this case, buffer) under stirring. If the matched buffer strategy is employed for the preparation of both titrant and titrate solutions then identical buffer will be used for the preparation of titrant and titrate solutions and the correction should be virtually zero, reflecting only the heat associated with stirring and titrant (buffer) addition. The second control experiment involves the injection of (matched) buffer into a titrate-filled sample cell. Aliquots of added titrant (in this case, buffer) are small (3–10 μL) compared with the volume of the sample cell (~1.4 mL) and the heat associated with this dilution is typically negligible. By far the most significant control experiment is the heat of dilution of titrant. The injection of a small volume of titrant into the much larger sample cell volume results in a significant dilution of titrant, this might be particularly relevant if the titrant is highly concentrated (as in a saturation binding experiment). Correction for titrant dilution can be non-trivial in cases where there is a significant heat signal associated with the break-up of molecular self-association when a concentrated titrant solution is diluted into the sample cell [6]. If self-association is a significant complicating factor in the analysis of ITC data, it might be useful to assess this independently using other techniques, such as analytical ultracentrifugation.

12.7.3   Data Analysis

For a saturation experiment, at the beginning of the experiment each addition of titrant is completely bound by the titrate and the area under the peak represents ΔH_b. As more titrant is added, the binding sites become occupied and the heat change associated with each addition is correspondingly reduced. The rate of change in binding heat in the middle of the experiment represents the binding affinity, K_a, and the midpoint is the stoichiometry of the interaction, n. At the end of the titration all binding sites are saturated and the final titrant additions represent dilution of titrant. In theory, these final titrant additions should be identical to the

titrant dilution control experiment and could be used for the titrant dilution correction. In reality, this is not always the case. The final additions of titrant in the binding experiment are made into a solution containing ligand–DNA complex compared with the control experiment where titrant additions are made into buffer only. These represent different solution environments with different viscosities. Correction for titrant dilution is a particular problem in the case of ligand self-association, as discussed earlier. There is no clear resolution to this issue, with investigators reporting corrections using both a separate titrant dilution experiment as well as the final additions of a saturation experiment. Where titrant dilution is small there is not a significant difference between these approaches. This issue should be addressed on a case-by-case basis. With the determination of ΔH_b, K_a and n from a saturation experiment, the binding affinity can be used to calculate ΔG and with knowledge of ΔG and, ΔH, (12.4) can be used to calculate ΔS.

In the model-independent (or excess sites) approach the area of each peak provides an independent determination of ΔH_b and a rigorous determination of binding enthalpy can be made by averaging the peak areas of a number of peaks (20–40 injections). A binding enthalpy determined in this way is simply a direct calculation from the peak area and does not require the adoption of any models. In contrast, a saturation experiment requires the selection of a model. A model-independent experiment is recommended as a first experiment with an uncharacterised system as this will provide a robust determination of ΔH_b that can be used as a fixed parameter in the fitting of a saturation experiment. The determination of ΔH_b can also be used to calculate the size of the initial titration peaks of a saturation experiment which can guide the selection of appropriate concentrations of binding partners.

Although an optimal "c-value" is often discussed, there are other approaches that have been successfully employed to study systems outside the typical experimental range. High affinity binding ligands have been studied by means of a displacement ITC experiment described by Sigurskjold [45]. In this approach, a competitive binding model is used to fit the binding isotherm of a high affinity ligand in the presence of a pre-formed low affinity ligand–macromolecule complex. A displacement approach has also been used for low-affinity binding systems [46]. Despite the generally accepted experimental c-value range of 10–500, Turnbull and Daranas have determined reliable thermodynamic parameters for a low affinity system ($\sim 10^2$ M^{-1}) at c-values between 0.01 and 10 by extending the receptor saturation past the usual 2:1 ratio [47].

As previously discussed, additional thermodynamic information can be obtained from the temperature dependence of the binding enthalpy which yields the heat capacity change accompanying the binding interaction according to (12.6). The operating range of current ITC instruments is 2–80°C, allowing the determination of binding enthalpies over a significant temperature range including physiological temperature. If a model-independent approach is used for the determination of binding enthalpies, then the heat capacity change will also be model-independent. If a heat capacity change exists, this can be exploited by adjusting the temperature of ITC experiments to optimise the magnitude of the observed binding enthalpy;

however, when selecting experimental temperatures it is important to ensure that the biomolecules are in their native state, something that can be assessed by DSC studies.

One of the major strengths of ITC, and calorimetry in general, is that it is considered a "universal detector", monitoring heat changes that accompany most biological or chemical events. However, it is important to remember that this can also be a complicating factor as the heat signal will reflect ALL events occurring in the sample cell. One important illustration of this is the contribution from changes in protonation state as binding occurs. Any release or uptake of protons will be exchanged with the buffer solution and the observed enthalpy change, ΔH_{app}, will contain contributions from both the actual binding enthalpy, ΔH_b, and the buffer ionisation enthalpy, ΔH_{ion}, according to (12.15):

$$\Delta H_{app} = \Delta H_b + [\Delta H_{ion} \times n_{H+}], \tag{12.15}$$

where n_{H+} is the number of protons released or taken up during binding.

This observation can actually be very useful. Studies at the same pH in buffers of different ionisation enthalpies can be used to determine if there is any change in protonation state and, if there is, the number of protons involved. A plot of ΔH_{app} vs. ΔH_{ion} should yield a straight line with a slope equal to n_{H+} and a y-intercept of ΔH_b. Also, if proton uptake or release accompanies a binding interaction, judicious selection of buffer composition can be used to enhance or reduce the observed heat signal. If investigating changes of protonation state are not of interest and complicating effects on ΔH_{app} are to be avoided, then buffers should be selected with $\Delta H_{ion} \sim 0$. Good examples are phosphate and acetate. Buffers with large ΔH_{ion} values include tris. A recent comprehensive review of buffer ionisation enthalpies can be found in the literature [48]. When selecting an appropriate buffer, consideration should also be given to the volatility of the buffer which might be problematic during degassing; for example, formic acid and acetic acid are relatively volatile.

It has previously been discussed that ΔH_b can be determined directly from the peak area of each titrant addition in a model-independent experiment. For a saturation experiment, ΔH_b can also be determined directly (and model-independently) from the integrated areas of the initial peaks of the experiment. The stoichiometry can also be determined in a model-independent manner as it corresponds to the molar ratio of titrant:titrate at the midpoint of the binding isotherm. However, the binding affinity cannot be determined directly from the binding isotherm and recourse to binding models is required. In actuality, all three parameters are generally determined from the application of a binding model. A more robust approach would be to use model-independent values for ΔH_b (from a model-independent experiment) and, perhaps, n (from a saturation experiment) as fixed parameters in a subsequent model-dependent fit for K_a. A number of different binding models are conveniently available with the supplied instrument software (for example, Bind-Works supplied with instrumentation from TA Instruments and Origin (OriginLab Corporation, Northampton, MA) supplied with instrumentation from MicroCal) from the simplest one-site binding model to models for two sets of independent binding

sites, cooperativity, dissociation and competitive binding. It is also possible to include user-generated binding models within these software packages. Freyer and Lewis have recently discussed in detail model fitting using a number of the common binding models as well as more complex models, including a discussion of error analysis and the statistical significance of the best-fit parameters [43]. The models available in the instrument supplied software are somewhat limited; Buurma and Haq have recently discussed data analysis of more complex equilibria [31].

Having introduced DSC and ITC, the practical aspects of collecting and analysing calorimetric data, the type of information that can be obtained from calorimetric measurements and the importance of thermodynamic parameters, it is now appropriate to illustrate the application of calorimetric approaches to the analysis of ligand–biomolecule systems with selected examples from the literature.

12.8 Application of DSC and ITC Approaches to the Analysis of Ligand–Biomolecule Systems

12.8.1 Case Study: Monointercalating Ru^{II} Complexes as DNA Structural Probes

Ruthenium(II) complexes have received much focus because of their unique photophysical properties and their application as probes of DNA structure. A host of spectroscopic and viscometric techniques have been applied to determine binding mode, stoichiometry and binding affinity of these ligands with different DNA structures, including duplex and quadruplex forms [49, 50]. ITC was applied specifically to parse the binding free energy into enthalpic and entropic components. Haq et al. used a model-independent approach to determine the binding enthalpies of two isomers, Δ- and Λ-[Ru(phen)$_2$(dppz)]$^{2+}$, to duplex DNA [49]. In this approach, calf thymus DNA was placed in the ITC sample cell at ~2.3 mM (base pairs) and was titrated with ligand solution at ~0.7 mM such that the DNA was always in excess and all ligand was bound after each addition of titrant. Fifteen titrant additions each gave a model-independent determination of ΔH_b which were then averaged to give a final value. ITC studies were challenging because of the significant heat of dilution of the ligands when titrated into buffer. However, binding enthalpies were determined to be +0.2 kcal/mol for the Δ isomer and +2.9 kcal/mol for the Λ isomer. This determination of an entirely entropically driven binding mechanism was an extremely unexpected result given the fact that both isomers were found to bind in an intercalation binding mode, which is typically enthalpically driven and opposed by an unfavourable, negative entropy term. At the time of these studies, considerable attention had been given to the photophysical properties and structure of these ligand–DNA complexes but little was known about their energetics of binding. The observation of an entirely entropically driven binding mode was similar to that of the intercalator actinomycin D.

The Ru(II) complexes and actinomycin D share similar structural features of an intercalating aromatic ring system to which bulky substituents are attached. It was thought that fitting the bulky hydrophobic side groups of the Ru(II) complexes into the DNA grooves resulted in significant energetic costs that offset the significant favourable enthalpy normally associated with intercalative stacking interactions. Positive entropy contributions would then arise from hydrophobic interactions resulting from the burial of nonpolar groups within the DNA grooves and concomitant release of bound water from either the ligand and/or DNA. ITC studies of this system demonstrated the importance of thermodynamic measurements alongside more commonly-used spectroscopic studies. Enthalpy measurements were invaluable to the study of these systems, revealing an unusual, entirely entropically-driven binding mechanism that could not have been discerned from spectroscopic studies alone. In this way, an understanding of the basis of the molecular interactions involved in binding emerges which can be utilised to probe the nature of the target DNA structure and ultimately to aid in the design of novel complexes to target different DNA structural forms.

12.8.2 Case Study: Measurement of Ultratight Binding Interactions

Chaires and co-workers designed bis-intercalators based on the daunorubicin scaffold [51–53]. From high-resolution structures, they observed a 2:1 hexanucleotide complex where a daunorubicin monomer intercalated at either end of the DNA with the daunosamine moieties laying tail-to-tail in the minor groove separated by only 7 Å. The design strategy was to link the two daunorubicin molecules via a flexible linker of appropriate length and steric properties to form a bis-anthracycline. The increased binding site size was anticipated to confer greater sequence selectivity and enhanced binding affinity to yield greater efficacy. The binding constant of such a ligand was expected to be close to the square of the monomer binding constant, which was on the order of 10^7 M^{-1}. Measurement of binding affinities of ~10^{14} M^{-1} using spectroscopic techniques are precluded because of the need to operate in a concentration regime close to the reciprocal of the binding constant in order to ensure the presence of 10% or more of unbound ligand [33]. The approach adopted by Chaires and co-workers to characterise the binding thermodynamics of the newly designed bis-anthracycline molecules was to combine DSC and spectroscopic approaches. DSC was employed to measure the melting enthalpies of DNA in the absence and presence of saturating amounts of bis-anthracyclines and hence to calculate the binding enthalpy through the application of Hess's law. From a combination of a spectroscopically-determined shift in melting temperature and the DNA melting enthalpy it was possible to calculate a binding constant for the bis-anthracyclines at the melting temperature. Through the application of the van't Hoff equation this binding constant was extrapolated to a temperature of 20 °C which allowed the calculation of a binding free energy at that temperature.

Along with the DSC-determined binding enthalpy, it was possible to complete the thermodynamic profile through the calculation of the binding entropy. This approach revealed that the bis-anthracyclines exhibited a 1.5–2-fold increase in binding free energy over the daunorubicin monomer. Significantly enhanced binding enthalpies were offset by a large, unfavourable binding entropy that was close to zero for the daunorubicin monomer. It was thought that the unfavourable entropy was derived from the restricted rotation of the flexible linker joining the two daunorubicin monomers within the ligand-DNA complex. Improvements to the design of these bis-anthracycline molecules therefore lay in the incorporation of a restricted linker group of an appropriate geometry for insertion into the DNA minor groove. The design of these next generation bis-intercalators, with even greater enhancement in binding affinity, further illustrates the necessity of a calorimetric-based approach for the measurement of such ultratight binding affinities and the realisation of a complete thermodynamic characterisation.

12.8.3 Case Study: Drug Design Optimisation of HIV-1 Protease Inhibitors

One final illustration of the utility of calorimetric measurements comes from the area of HIV-1 protease inhibitors. These studies demonstrate the application of a calorimetry-driven rational drug design approach to the optimisation of ligand–protein interactions, approaches which can easily be translated to ligand–DNA systems. HIV-1 protease plays an important role in the maturation of the AIDS virus and inhibitors of this protein therefore have obvious relevance to AIDS therapeutics. Unfortunately, the efficacy of HIV-1 protease inhibitors has been significantly limited by the rapid appearance of viral resistance and a new generation of more effective inhibitors is sought. Freire and co-workers have played a pivotal role in understanding the molecular basis of inhibitor activity through the thermodynamic characterisation of protease inhibitors in current clinical use [54, 55]. The approach adopted by the Freire group involved the application of ITC to determine ΔG, ΔH and ΔS using a saturation experiment approach. All the inhibitors exhibited strong binding affinities and free energies. Parsing the free energy into component binding enthalpies and entropies revealed that binding was entropically-driven and in most cases was opposed by an unfavourable, positive enthalpy change. The large entropic gain upon binding stemmed principally from the solvation entropy gain associated with the hydrophobic transfer of the inhibitor from bulk solvent into the protease binding site. This was offset by an entropic penalty resulting from the ordering of two conformationally flexible surface loops of the free enzyme with only a small entropic penalty incurred for inhibitor binding because of the design of a conformationally constrained inhibitor structure preshaped to the geometry of the binding site. The drug design approach of tailoring shape complementarity and conformational rigidity to fit the binding site is commonly used for optimising binding interactions and specificity. In the case of the HIV-1 protease inhibitors,

observed viral resistance resulted from the inflexibility in inhibitor conformation that could not accommodate the conformational consequences of amino acid mutations in the protease. The consequence was reduced binding affinity and therefore inhibitor efficacy. Based on their thermodynamic analysis of inhibitor binding, Freire and co-workers proposed matching conformational flexibility of the inhibitor with highly mutateable protease sites to combat drug resistance. They realised that the most important step was to maximise inhibitor–protease interactions and developed a rapid screening approach based on ITC analysis to identify enthalpically-favourable lead compounds for subsequent optimisation. This study highlights the critical role that thermodynamics can play in the drug design process.

12.9   Conclusions

Calorimetry provides access to a wealth of thermodynamic information which is essential in the molecular characterisation of binding interactions. DSC and ITC enable a complete thermodynamic profile to be obtained for a binding interaction: Gibbs free energy (ΔG), enthalpy (ΔH), entropy (ΔS) and heat capacity change (ΔC_p). The values of these parameters indicate the probability that a particular process will occur and the nature of the energetic driving forces. It is possible to dissect the interaction energy into different types of molecular forces within the binding complex. For ligand–DNA interactions, favourable enthalpic contributions to binding arise from noncovalent molecular interactions such as hydrogen bonding, van der Waals interactions and electrostatic interactions. Additionally, favourable entropic contributions arise from the desolvation of ligand molecules and their hydrophobic transfer from an aqueous environment to the binding site, as well as from the polyelectrolyte contribution. Favourable contributions to binding are offset by unfavourable interaction forces such as conformational restrictions in the binding complex compared with the free binding partners, and entropic penalties resulting from perturbation of the DNA structure in forming the binding complex. There is a delicate balance of forces that define the nature of complex formation. These forces are not apparent from structural techniques, such as X-ray crystallography, which illustrates the essential role that thermodynamics must play in understanding molecular interactions. The ability to define the nature of the molecular forces within a binding complex allows the optimisation of binding interactions through the rational drug design process.

A major advantage of DSC and ITC methods lies in the direct monitoring of heat changes accompanying denaturation or binding events. This permits the direct measurement of energetic parameters of biomolecular interactions rather than their calculation from indirect measurements such as spectroscopic data. Moreover, calorimetric measurements are performed in the solution state without need for crystallisation, immobilisation or chemical modification. The methods are also amenable to a range of molecular sizes, shapes and chemical compositions. To fully realise the utility of calorimetric methods, careful experimental design, data collection and analysis are required. Several experimental approaches were outlined

in this chapter, along with a discussion of appropriate experimental design, data collection and data analysis. With a thorough understanding of the experimental challenges of calorimetric studies and suitable strategies for data collection and analysis, the reader should be equipped with the necessary information to perform independent calorimetric measurements and thermodynamic characterisation of their own systems.

The examples presented in this chapter illustrate how calorimetry can be employed to provide thermodynamic characterisation of ligand–biomolecule systems. The first example applied an excess sites ITC approach to define an unusual entropically-driven intercalation binding mechanism of ruthenium(II) complexes. The binding of these DNA structural probe molecules was similar to the mechanism of actinomycin D-DNA binding, where accommodation of bulky hydrophobic substituents within the DNA grooves results in significant energetic costs that offset the favourable intercalative enthalpic contributions. Favourable entropic contributions were provided by hydrophobic interactions of the nonpolar substituents and release of bound water. The second example illustrated the use of DSC to measure ultratight binding interactions that are not accessible through the use of traditional spectroscopic methods. Successful measurement of sub-picomolar binding of two bis-anthracycline bis-intercalators allowed access to a complete thermodynamic profile. This profile revealed a large, unfavourable binding entropy resulting from restricted rotation around a flexible linker region, which provided crucial information for the improved design of next generation bis-anthracycline molecules. The final example was a calorimetry-driven rational drug design approach for improved HIV-1 protease inhibitors. Thermodynamic characterisation of the binding mechanism of protease inhibitors in current clinical use revealed that the basis of clinically observed rapid viral resistance stemmed from the conformationally-constrained structure of the inhibitor molecules. Such conformational constraints are often an intentional drug design approach to tailor shape complementarity and conformational rigidity to fit the binding site and optimise binding interactions and specificity. However, in the case of the HIV-1 protease inhibitors such structural inflexibility could not accommodate the conformational consequences of amino acid mutations in the protease and resulted in reduced binding affinity and therefore inhibitor efficacy. Based on the thermodynamic analysis of inhibitor binding, an approach was proposed based on maximising inhibitor–protease interactions through matching conformational flexibility of the inhibitor with highly mutateable protease sites to combat drug resistance. A rapid screening ITC method was designed to identify enthalpically favourable lead compounds for subsequent optimisation. The three examples presented illustrate the importance of thermodynamic characterisation of ligand–biomolecule interactions and the utility of calorimetric measurements to provide this information.

The intent of this chapter was to demonstrate the utility of calorimetric studies for the characterisation of ligand–biomolecule interactions and to provide enough practical information and inspiration to encourage the reader to embark on the calorimetric characterisation of their own systems.

References

1. Chaires JB. Biophys Chem. 1997;64:15.
2. Naghibi H, Tamura A, Sturtevant JM. Proc Natl Acad Sci U S A. 1995;92:5597.
3. Chaires JB. Annu Rev Biophys. 2008;37:135.
4. Holdgate GA, Ward WHJ. Drug Discov Today. 2005;10:1543.
5. Chaires JB. Biopolymers. 1997;44:201.
6. Ren J, Jenkins TC, Chaires JB. Biochemistry. 2000;39:8439.
7. Haq I, Jenkins TC, Chowdhry BZ, Ren J, Chaires JB. Methods Enzymol. 2000;323:373.
8. Ladbury JE, Chowdhry BZ. Chem Biol. 1996;3:791.
9. Record MT, Ha J-H, Fisher MA. Methods Enzymol. 1991; 208.
10. Spolar RS, Record MT. Science. 1994;263:777.
11. Chaires JB. In: Demeunynck M, Bailly C, Wilson WD, editors. Small molecule DNA and RNA binders: from small molecules to drugs, Vol. 2. Weinheim, Germany: Wiley-VCH. 2003, p. 461.
12. Weber PC, Salemme FR. Curr Opin Struct Biol. 2003;13:115.
13. Eftink M, Biltonen R. Biochemistry. 1983;22:3884.
14. Dunitz JD. Chem Biol. 1995;2:709.
15. Breslauer KJ, Remeta DP, Chou W-Y, Ferrante R, Curry J, Zaunczkowski D, et al. Proc Natl Acad Sci U S A. 1987;84:8922.
16. Sharp K. Protein Sci. 2001;10:661.
17. Cooper A, Johnson CM, Lakey JH, Nollmann M. Biophys Chem. 2001;93:215.
18. Lumry R, Rajender S. Biopolymers. 1970;9:1125.
19. Krug R, Hunter W, Grieger R. Nature. 1976;261:566.
20. Chaires JB. Arch Biochem Biophys. 2006;453:24.
21. Spink CH. In: Correia JJ, Detrich HW, editors. Methods in Cell Biology Vol. 84: Biophysical tools for biologists: volume 1, *in vitro* techniques. San Diego, CA: Academic. 2008, p. 115.
22. Tellinghuisen J. Anal Biochem. 2004;333:405.
23. Tellinghuisen J. Anal Biochem. 2003;321:79.
24. Mizoue LS, Tellinghuisen J. Anal Biochem. 2004;326:125.
25. Plum GE. In: Bergstrom DE, editor. Current protocols in nucleic acid chemistry, Vol. 2. New York: Wiley. 2000, p. 7.3.1.
26. Kallansrud G, Ward B. Anal Biochem. 1996;236:134.
27. Henderson JT, Benight AS, Hanlon S. Anal Biochem. 1992;201:17.
28. Cavaluzzi MJ, Borer PN. Nucleic Acids Res. 2004;32:e13.
29. Tataurov AV, You Y, Owczarzy R. Biophys Chem. 2008;133:66.
30. Pilch DS. In: Bergstrom DE editor. Current protocols in nucleic acid chemistry, Vol. 2. New York: Wiley. 2000, p. 7.4.1.
31. Buurma NJ, Haq I. Methods. 2007;42:162.
32. Cooper A, Nutley MA, Wadood A. In: Chowdhry BZ, Harding SE, editors. Protein-ligand interactions: hydrodynamics and calorimetry: a practical approach. Oxford: Oxford University Press. 2001, p. 287.
33. Garbett NC, Chaires JB. In: Lee M, Strekowski L, editor. Synthetic and biophysical studies of DNA binding compounds. Kerala: Transworld Research Network. 2007, p. 1.
34. Leng F, Chaires JB, Waring MJ. Nucleic Acids Res. 2003;31:6191.
35. Jelesarov I, Bosshard HR. J Mol Recognit. 1999;12:3.
36. Brandts JF, Lin L-N. Biochemistry. 1990;29:6927.
37. Schellman JA. J Phys Chem. 1958;62:1485.
38. Crothers DM. Biopolymers. 1971;10:2147.
39. McGhee JD. Biopolymers. 1976;15:1345.
40. Spink CH, Wellman SE. Methods Enzymol. 2001;340:193.
41. Chaires JB, Shi X. In: Waring MJ, editor. Sequence-specific DNA binding agents. Cambridge: Royal Society of Chemistry. 2006, p. 130.

42. Bishop GR, Ren J, Polander BC, Jeanfreau BD, Trent JO, Chaires JB. Biophys Chem. 2007;126:165.
43. Freyer MW, Lewis EA. In: Correia JJ, Detrich HW, editors. Methods in Cell Biology Vol. 84: Biophysical tools for biologists: volume 1, in vitro techniques. San Diego, CA: Academic. 2008, p. 79.
44. Wiseman T, Williston S, Brandts JF, Lin L-N. Anal Biochem. 1989;179:131.
45. Sigurskjold BW. Anal Biochem. 2000;277:260.
46. Zhang Y-L, Zhang Z-Y. Anal Biochem. 1998;261:139.
47. Turnbull WB, Daranas AH. J Am Chem Soc. 2003;125:14859.
48. Goldberg RN, Kishore N, Lennen RM. J Phys Chem Ref Data. 2002;31:231.
49. Haq I, Lincoln P, Suh D, Nordén B, Chowdhry BZ, Chaires JB. J Am Chem Soc. 1995;117:4788.
50. Rajput C, Rutkaite R, Swanson L, Haq I, Thomas JA. Chem Eur J. 2006;12:4611.
51. Chaires JB, Leng F, Przewloka T, Fokt I, Ling YH, Perez-Soler R, et al. J Med Chem. 1997;40:261.
52. Leng F, Priebe W, Chaires JB. Biochemistry. 1998;37:1743.
53. Portugal J, Cashman DJ, Trent JO, Ferrer-Miralles N, Przewloka T, Fokt I, et al. J Med Chem. 2005;48:8209.
54. Velazquez-Campoy A, Todd MJ, Freire E. Biochemistry. 2000;39:2201.
55. Velazquez-Campoy A, Kiso Y, Freire E. Arch Biochem Biophys. 2001;390:169.

Chapter 13
Investigating the Biological Significance of Metallointercalators with cDNA Microarrays

Elise P. Wright, Victoria Lyons, Shaoyu Wang, and Vincent J. Higgins

13.1 Central Dogma and Gene Expression

The double helix coded sequence of nucleotide bases with its protective sugar phosphate backbone forms deoxyribonucleic acid (DNA) which is the genetic blueprint of all living things. All the information required for the development, operation and maintenance of cells is contained in a sequence of adenine (A), thymine (T), cytosine (C) and guanine (G) bases, where adenine is paired with thymine and cytosine is paired with guanine [1]. The DNA sequence is made usable by transcription of the nucleotide sequence into single stranded messenger RNA (mRNA). This temporarily stable molecule transports genetic information from the nucleus to the endoplasmic reticulum (ER); where the ribosomes translate the mRNA message into specific proteins (except RNA viruses). This means that the four member nucleic acid base code sequence is converted into a 22 member amino acid code [2]. These amino acids interact to produce a tertiary structure that may require di-sulfide bonds, post-translational modification and/or protein mediated activation to produce a functional protein [1]. This transition from DNA to protein outlines the Central Dogma and describes general gene expression (Fig. 13.1) [2]. Once the protein is active it is able to directly affect proteins and molecules in the cell. Affected molecules that are metabolised, synthesised or catalysed are known as metabolites and are the end result of transcriptional intervention. Under environmental stress, different proteins and metabolites are required to protect the cell and are produced via transcription. Cells are able to "reprogram" their protein complement to counter a detrimental environment or take advantage of a beneficial one [3].

A cell alters its protein complement by regulating gene expression, often through a complex feedback loop [1]. A number of molecular factors are required for this reprogramming process in eukaryotes. The first step is the recruitment and binding of RNA polymerase II, a protein that liaises with an unwound strand of DNA to produce

E.P. Wright (✉)

School of Medicine, College of Health and Science, University of Western Sydney, Penrith South, NSW, Australia
e-mail: E.Wright@uws.edu.au

DNA **RNA** **Protein**

TRANSCRIPTION TRANSLATION
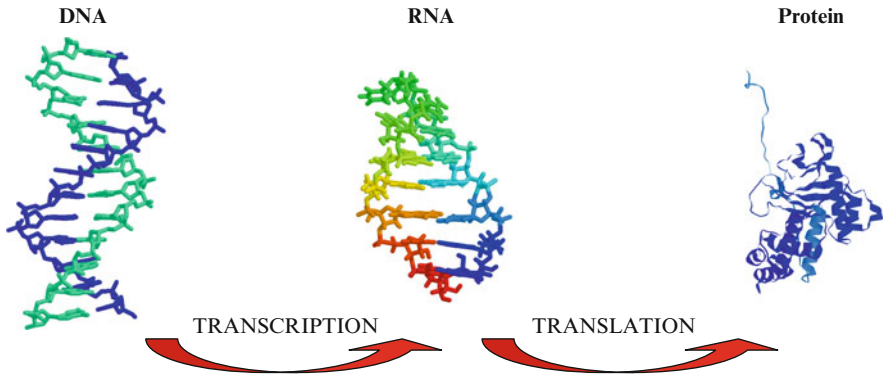
Fig. 13.1 The Central Dogma – DNA is transcribed to RNA which is translated into protein. In this case the examples of DNA, RNA and protein are structures from the protein data base files

RNA. During this process adenine pairs up with uracil (U) bases instead of thymine bases [4]. This change gives the mRNA molecule its necessarily short lifespan; stable mRNA molecules would result in permanent protein transcripts regardless of external stimulus or cellular needs. But first, the RNA polymerase needs to locate a promoter to initiate transcription immediately downstream of the promoter sequence [4]. The RNA polymerase then migrates to the promoter, a sequence of DNA that marks the start of the gene. The RNA polymerase moves down the sequence and reads the complement of the strand it is transcribing. It strings the complementary bases, cytosine for guanine, uracil for adenine and vice versa, onto its growing mRNA strand until it reaches a termination sequence. The polymerase then disassociates from the DNA strand, having completed a mRNA molecule for a particular gene [1]. But how does the RNA polymerase "know" which gene to transcribe? Not only are there proteins that form complexes with RNA polymerase to direct successful promoter interaction, additional proteins bind to specific DNA sequences and can act to enhance or silence DNA transcription [4]. These transcription factors are critical for the initiation of transcription [1].

Once a transcript mRNA is complete, it is shuttled from the nucleus to the ER where it is translated into protein. In this way, the relatively inert gene has been translated into an active molecule that is capable of initiating reactions, catalysing metabolism and contributing to the variety of biological molecules present in and used by the cell [5]. This process by which the transcription of a gene is triggered by a cellular signal is referred to as "up-regulation". Alternatively, gene expression can be down regulated whereby stimulus of either environmental or cellular origin decreases or prevents the transcription and therefore expression of a particular gene [1]. What this means is that examining gene expression profiles gives us an indication of how a particular environment influences the cellular response and this allows us to draw links between gene expression and environmental conditions [6]. As RNA sequences are unique to specific genes, this biomolecule is a prime candidate for assaying gene expression.

13.1.1 Signal Transduction

The ability to up- and down-regulate genes based on external cues depends on the cell's ability to "communicate" between the cell surface and the nucleus [7]. Sensory proteins or receptors situated at the surface of the cell interact with molecules in the cell's external environment. These external molecules may be produced by the cell itself, by surrounding cells (hormones) [8] or be an inorganic molecule from the non-living environment [1]. Once receptors sense these molecular signals in the environment they affect one or more protein targets inside the cell (Fig. 13.2) [9]. These proteins alter other proteins in turn and the signal is passed from the cell's surface to the nucleus; the "message" is sent through a pathway of gene products until a protein capable of interacting with DNA directly is triggered and stimulates gene expression; these proteins are the transcription factors mentioned previously [1, 7]. An additional process for transcription factor activation as a result of extracellular stimulus is also used; extracellular signals can activate transcription factors that reside in the cytoplasm in an inactive form. Once activated, they are then transported into the nucleus where they can act on DNA [9]. This is a simplified account of signal transduction, there are a number of journal resources available if more information is required [7, 8, 10]. However, an understanding of how a cell's DNA, RNA and protein complements can reflect the response to its environment is sufficient and this indicates the main reason for assaying gene expression with microarrays as detailed in this chapter.
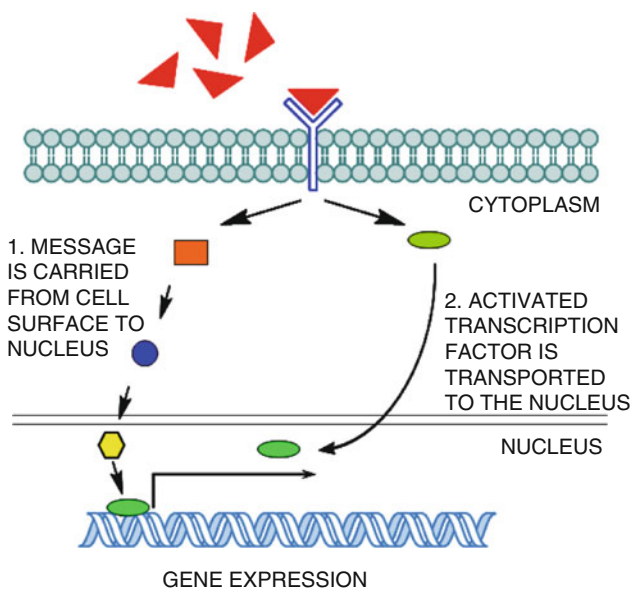
Fig. 13.2 A schematic of signal transduction

13.2   Microarrays

A microarray consists of a glass or nylon platform that is arrayed with micro-quantity spots of particular DNA sequences that are homologous to genes within the cell. Each of the thousands of spots on a microarray features a different sequence and is situated at a known location, i.e., each gene sequence has coordinates (Fig. 13.3a) [11]. A microarray facilitates the simultaneous interrogation of tens of thousands of genes per experiment; first a cellular population is exposed to an environmental change that triggers a cellular reaction [12]. Once this response is underway, the total RNA, the nucleic intermediate between DNA and protein, must be extracted and converted to the more stable double stranded complementary DNA (cDNA) with reverse transcriptase [11]. The conversion of mRNA into cDNA maintains relative abundance and incorporates the fluorophores that label the sample. cDNA samples are then applied to an array with its many different sequences attached to the platform. When the cDNA finds its complement on the platform it binds, or hybridises, to the cDNA spotted onto the glass and attaches the fluorescent signal (Fig. 13.3b). These fluorescent signals can then be used to identify the genes that were transcribed in response to the experimental stimulus and their mRNA levels quantified in terms of relative abundance [11].

With the advent of whole genome sequencing the complete genome can be arranged on a microarray allowing for the global interrogation of gene expression for identification of genetic mechanisms related to chemosensitivity or environmental
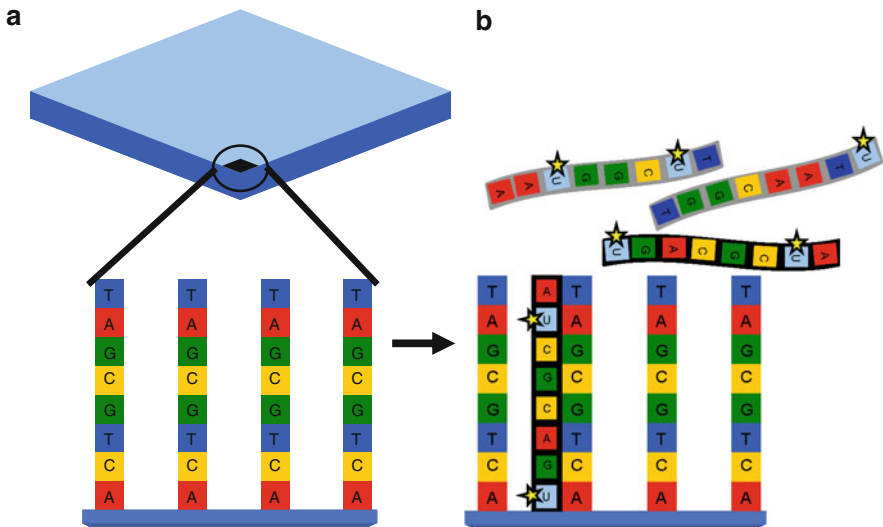
Fig. 13.3 (**a**) Schematic of a microarray and the hybridisation of the complementary strands. Each feature arrayed on a slide has many copies of a single complementary strand of nucleic acid affixed in place. (**b**) When a sample of labelled cDNA is hybridised to the microarray, complementary sequences bind while non-complementary sequences find their specific complement on another feature

susceptibility [13–16]. The Central Dogma describes the pathway from latent gene to active protein via mRNA, a molecule whose presence is the result of active transcription. The process of signal transduction initiates a transcriptional reaction in direct response to an external stimulus [1]. By examining the complement of RNA in a population of cells exposed to the same stimulus, the genes associated with responding to the external stimulus can be identified. Microarrays present a fast and high throughput method of genetic interrogation that has a variety of applications in drug investigations.

Currently, published microarray data is required to meet Minimal Information About a Microarray Experiment (MIAME) standards [17]. These standards ensure that experiments conducted by different groups can be successfully compared and evaluated. Required information includes sufficient description of experimental and array design, samples, hybridisation details, methods measurement and normalisation procedures [17]. There are a number of web-based databases that supply array information to the scientific community. Gene Expression Omnibus (GEO) [18], Array Express [19] and ONCOMINE are a few examples [20].

In an example of the benefits of community-wide access to microarray data, Rhodes et al. [12] performed a meta-analysis of four publicly available microarray datasets. Each of the studies used by Rhodes et al. [12] was attempting to identify differentially expressed genes in prostate cancer. The investigation found that using the p-values generated from statistical analysis of this data identified 50 overexpressed and 103 underexpressed genes in response to prostate cancer. This was despite the differences in microarray platforms, array type and results [12].

13.2.1 Advantages

The advantages associated with arrays are significant. It is possible to globally interrogate a genome's response to a particular stimulus and to quantitate that response in terms of relative transcript abundance. Investigators are granted considerable design freedom that allows for the attachment of particular groups of genes from metabolic pathways, organelles or even proteins with a common sequence that is of interest to an array platform [11, 21]. Each of the nucleotide sequences can be assessed against a real RNA transcript sample from a biological system and they can all be interrogated at once. Many molecular biological suppliers offer automated systems for array manufacture and scanning [15]. Microarrays can also be commercially printed from prepared nucleic material derived from different model organism and/or cell lines [22]. One of the technical advantages associated with array application is the ever shrinking scale of these platforms. Multiple arrays are being placed onto single chips and there is a market trend towards smaller and more compact platforms with increased spot density [6, 23]. Reproducibility has become more readily achievable as automated robotic systems are available for the manufacture, hybridisation and scanning of arrays. Printed genome arrays are commercially available in conjunction with the customisation option, allowing for a more economically flexible investigation [24].

13.2.2   Limitations

The potential limitations are only problematic if care isn't taken to address them in the experimental design. Despite the near uniform design of the dyes used in array technology, the red fluorophore used in two-colour microarrays is more prone to photobleaching than the green dye [11]. This means that once conjugated to your nucleotides, it is possible for a decrease in signal to occur over time in the red labelled samples that will give rise to misleading results. Mathematical correction (channel balancing) can be used to minimise this effect after the fact [11]. Effective experimental design would remediate this problem by including a specific sample quantity of RNA into the hybridisation mix to act as a reference for normalisation [25]. Another simple solution is the inclusion of a dye swap experiment where each dye is switched to the opposite sample and only results that are significant in both experiments are counted as genuine [11].

Arrays are based on global gene expression precursors, the RNA transcripts. These molecules cannot provide information on post-translational modification, enzyme activity or quantity of actively functional protein [26]. Protein abundance and functionality don't always correlate with the gene expression described by microarray results but they still make a significant contribution to systems-based biology.[27]. An additional limitation that must be accounted for is the high rate of false discovery in this method as a result of its high throughput nature [28]. Again, careful experimental design can minimise the effect of false positives on legitimate results. Array results should always be confirmed by independent experiments that corroborate any resultant hypotheses [11, 29]. For example, as part of a confirmation step, Villeneuve et al. [24] used quantitative real time polymerase chain reaction (qRT-PCR) to qualify their results. This technique also quantifies amplified DNA as it is replicated during each sequence of PCR, giving researchers a sense of how much mRNA was present in the initial sample, usually examining only a single gene in each reaction.

Normalisation involves the standardisation of microarray data across an experiment so that all microarrays are comparable to each other. This process is required for meaningful results interpretation and often occurs by a range of methods. This may contribute to a potential source of variation [11]. Cost can also be a limiting factor in microarray application but the high throughput and substantial data produced are worth the expense [30, 31]. These limitations are the subject of diverse attempts to extend the technology and optimise the related processes resulting in the elimination of many of these problems [21].

13.2.3   Applications

Microarrays are utilised in three main areas when applied to metallointercalator investigation. These are elucidating a compounds mechanism of action whether it is

novel or otherwise; identifying patterns of expression that precede or are concurrent with a particular chemotherapeutic response; and optimising drug structure and therefore interaction with biological systems. The main drive of microarray data analysis is to identify a pattern; this may be in terms of a common thread of function amongst up- and down-regulated genes, a differentially expressed gene amongst cancer patients who respond to treatment or a protein that can be targeted by a drug designed to consistently affect its gene expression [30]. Microarrays are a particularly valuable tool for cancer research as they are able to examine the entire transcriptome and its various interactions simultaneously [32].

13.2.3.1 Mechanisms of Action

In this area of application, microarrays can be used to indicate the gene products that interact with carcinogens and identify whether a tumour will be responsive or refractive to treatment. Microarrays have also been used to identify the expressional changes different cell lines undergo when they are dosed with antioxidants [33–35], fatty acids [36–38], non-steroidal anti-inflammatory drugs [39], phytochemicals [40, 41], retinoids [42, 43], selenium [44] and vitamins [45]. Examining drug mechanisms and biological effects in this way allows for a holistic and systematic investigation and facilitates the comparison of known and novel compounds. This information facilitates novel compound classification and drug design optimisation [11].

Arango et al. [46] utilised this application in their study of oxaliplatin, a cisplatin derivative that has demonstrated activity against colon cancer. In this investigation, a cDNA microarray was used to interrogate the expression of 30 colon carcinoma or derivative cell lines. These experiments identified apoptosis and DNA damage repair genes as being important for the response of a cell to oxaliplatin [46]. Ahn et al. [47] focussed on gastric cancer cells and examined their sensitivity and resistance to 5-fluorouracil and cisplatin. 5-Fluorouracil is a pyrimidine analogue which is substituted into DNA strands instead of a pyrimidine (C and T), thus terminating cancer cell replication [48]. Cisplatin binds co-ordinately to DNA and can cause apoptosis. This study also identified genes that were consistently up- and down-regulated in both 5-fluorouracil and cisplatin responses suggesting a common biological mechanism of response involving apoptosis resistance genes [47].

Maxwell et al. [49] interrogated 2,400 breast cancer genes for differential expression in response to 5-fluorouracil exposure. This study identified 619 potential response genes that were up-regulated at least threefold. Many of these genes featured a p53 binding site. This suggests that this master regulatory protein is involved in the cellular response to 5-fluorouracil. Similar general stress response genes showed differential expression when the same MCF-7 breast cancer cell line was exposed to oxaliplatin [49].

Microarrays have also been used to investigate the molecular mechanisms involved in how a drug can affect cells in a different fashion; the response of drug-susceptible and resistant breast cancer cell lines to doxorubicin has been investigated [50]. Exposure to this drug induces double strand breaks as it

irreversibly binds to topoisomerase II [30]. Ahn et al. [50] identified individual genes that showed differential expression when exposed to doxorubicin, a common breast cancer treatment. The tumour necrosis factor gene family and matrix metal-loproteinase 1 were among those implicated [50]. The array results for this study were corroborated by independent qRT-PCT [50]. The study of Kudoh et al. [29] compared the gene expression of doxorubicin resistant MCF-7 cells with that of MCF-7 cells exposed to doxorubicin only briefly. Genes involved in the cell cycle, signal transduction, transcription, ubiquitination and protein secretion were common in both cell lines [29]. Additionally, over 9,000 genes on cDNA microarrays have been used to interrogate doxorubicin-induced growth arrest gene expression and compare it to proliferating doxorubicin resistant cell populations. Genes which have been associated with growth arrested cells include proliferation inhibition genes, tumour suppressors, anti-apoptotic and angiogenic genes [51]. Microarrays provide information about the points where a biological system meets and interacts with a chemotherapeutic; examining this interaction with microarrays facilitates the determination of the specific biological response to an anticancer compound.

13.2.3.2 Markers

The use of markers involves linking gene expression patterns with a clinical outcome [11]. This allows for the recognition of genes that are consistently corre-lated with a patient's response to a drug [52]. Investigators can then predict a patient's response to chemotherapy treatment and facilitate patient specific regimes using microarray measured gene expression [53]. In addition to the patients' genetic variability, the variation in tumour origin and genetics also affects the efficacy of pharmaceutical treatments. Performing a microarray on a tumour cell type allows for its classification based on cellular origin which can be both biologically and clinically important [31]. While there is some conjecture regarding consistently accurate prediction, the use of biomarkers is becoming better defined and more accepted. Some reports describe the use of the alpha-methylacyl CoA racemase (*AMACR*) gene as a biomarker as it is over expressed in prostate cancer [54]. *AMACR* expression has been used to deliver 97% sensitivity and 100% specificity for prostate cancer detection. A study by Varambally et al. [55] found that the RNA and protein of the zeste homolog 2 (EZH2) gene were highly expressed in meta-static prostate cancer and expression patterns predicted the return of cancer after surgery. An additional microarray study assayed overexpressed secretory proteins and following more extensive investigations identified prostasin as more prevalent in ovarian cancer cells and thus a candidate protein for biomarker validation [56].

A study of the anti-mitotic taxane, docetaxel, was able to identify microarray indicators for tumour sensitivity. Recalcitrant tumours showed higher levels of signal transduction gene expression while sensitive tumours expressed cell cycle, protein transport and modification, stress/apoptosis, cytoskeleton and adhesion genes at higher rates. Both tumour types demonstrated elevated levels of transcrip-tion [57]. This study showed a ~90% success rate identifying 10 out of 11 sensitive

tumours accurately [57]. A wider scale approach made use of 39 human cancer cell lines (representing lung, colorectal, gastric, breast, ovarian, renal, prostate cancers, gliomas and melanomas). Expression of over 9,000 genes was examined in these cell lines in order to identify genes that indicate chemotherapeutic sensitivity [58].

MAT-8 was identified as a potential biomarker for 5-fluorouracil resistance as it showed a tenfold increase in expression in 5-fluorouracil-resistant cell lines [49]. Kihara et al. [59] examined gene expression in over 9,000 genes in oesophageal cancers to identify biomarkers for survival after surgical removal and adjuvant chemotherapy. This study compared cancerous tissue to normal cells and identified 52 genes that could be correlated with chemosensitivity to cisplatin or 5-fluorouracil and the patient's survival [59]. In a study to link the gene expression profiles of human cancer xenografts with a response to anticancer compounds, Zembutsu et al. [52] used cDNA microarrays to screen 85 different grafts. Xenografts originating from nine different organs were interrogated for over 23,000 genes. Nine different drugs including cisplatin and 5-fluorouracil, were administered to the xenografts and 1,500 genes were found to have strong correlation with drug sensitivity. Over 300 of these genes were linked with two or more drugs and 32 were related to as many as 6 or 7 of the drugs tested.

In addition to a positive response to treatment, this method could be applied to the identification of toxic response indicators [26]. In addition to gauging the responsiveness of tumours to chemotherapeutics, biomarkers can also be used as early indicators of disease onset [12]. The main driving force behind biomarker research is its ability to facilitate rapid treatment implementation and determine treatment success prior to its initiation. For this reason, the application of biomarkers is a valuable, economical and life saving tool [52].

13.2.3.3   Drug Optimisation

In addition to examining cell response in terms of the biological perspective, microarrays can also be used to fine tune drug design for clinical application [30]. By examining the genes that are up- and down-regulated when an organism is exposed to a compound, target genes can be identified. Gene pathways associated with the drug's function can also be elucidated allowing for the counteraction of resistance by isolating connections between specific gene expression and chemotherapeutic susceptibility [13, 31]. A single drug can be screened against multiple cell lines for activity in cells of different origin, cancer type and mutation. Specifically, this process can be used to identify gene pathways and networks as well as co-regulated gene groups [11]. In addition, a microarray interrogation can facilitate functional assignment for uncharacterised genes in the context of existing gene networks [11, 31].

Screening for sensitivity could also be used to select test subjects in drug trials [21]. This would allow drug trials to be conducted only with individuals who were potentially responsive to treatment rather than include patients who were already genetically predisposed to resistance. This would also allow for the customisation of

treatment to the individual patient [53]. Thus, the best indication of a drugs' possible effectiveness could be determined. Microarrays present a unique opportunity early in drug development to identify the range of drug targets in a tumour. Candidate drugs can also be screened for a minimal response before extensive amounts of time are expended in perfecting the performance of an ineffective drug [26].

Ross et al. [22] used cDNA microarrays to assess the expression of ~8,000 genes across 60 cell lines. This process was able to verify cell origin based on common gene expression. Not only did this allow for the identification of misclassified cell lines but it could also link gene expression information to generation time and drug processing characteristics [22]. This facilitates the design of a drug that is able to inhibit a specific process in tumour growth.

13.3   Model Systems

Many of the molecular processes mentioned in previous sections are conserved across the eukaryotic domain [60]. While investigations are most relevant when applied to human genetics and biological systems, much can be learnt from the utilisation of model organisms. When the complexity of *Homo sapiens* and the ethical issues associated with human experimentation are taken into account, logistical difficulties encourage the investigation of model organisms in lieu of their more complex "cousins" [61].

Genetic models are typically species that are able to represent human cellular processes in a more practicable system [60]. Not only are these model organisms better suited to genetic investigations ethically, they are also easier to grow, house, control and experiment with. Also, the ease with which model organisms can be genetically manipulated has allowed for technological advancement in parallel with their use. As the genome sequences of model organisms became available it was possible to use this information in a variety of applications including microarray investigations, research into aging [62], RNA interference [63] and intronic splicing [64].

All cells with complex cellular structures and membrane enclosed organelles, particularly a well structured nucleus, are called eukaryotes [1]. This classification separates more complex cells, like our own from simpler unicellular organisms like bacteria or algae. Despite this many of the inherently eukaryotic cellular processes are still common between the simpler eukaryotes – yeast, worms, flies and rodents – and the most complex, humans.

13.3.1   Cell Lines

A range of cell lines are available commercially. Not only are most cancer types represented, researchers can also choose the organ of origin and species [22]. This

tailors experimental design to the exact conditions of interest. An exemplar cell line is L1210, a murine leukaemia cell population that is commonly used for IC$_{50}$ assays. Cell lines present a valuable compromise of a single celled organism with all of the biochemical complexity of a multicellular organism. This means that researchers can grow the cell type of interest conveniently in culture without the need to house or care for full scale organisms or consider the ethical problems. It is important to keep in mind however, that trends discovered in cell lines may not reflect actual events in the multicellular organism as all of the structural components that usually surround those cells have been removed [21]. Working with cell lines removes any host input, such as behavioural factors like appetite in a biological response to a chemotherapeutic.[21]. Cell lines can also be susceptible to contamination.

13.3.2 Saccharomyces cerevisiae

Saccharomyces cerevisiae, or bakers yeast, is a single celled eukaryotic organism that shares processes and cellular structures with many higher eukaryotes, including humans [60]. An additional advantage associated with this organism is that its genome is completely sequenced. This has enabled in-depth analysis of the genome such that the function, if known, and location of every open reading frame (ORF) is collated into a database dedicated to yeast (SGD, available at http://www.yeast genome.org) [65]. Furthermore, given the ease with which the yeast genome is manipulated, a complete library of single gene deletion mutants has been constructed [66]. This analytical tool consists of mutants with a single systematic gene by gene deletion that substitutes the target gene with a kanamycin cassette and mutant specific genetic labels [66]. While the amenable nature of yeast to genetic manipulation and its short generation time make for a useful model, yeast cells have a cell wall which sets them apart, structurally, from their mammalian counterparts [1]. Some investigations will require careful design for information to be relevant to the system that is being modelled.

13.3.3 Caenorhabditis elegans

Caenorhabditis elegans is a more complex organism that has a genome of 100 Mb that codes for 14,000 genes [60]. These nematode worms provide a multicellular alternative to *S. cerevisiae* that can be used to examine development and antimicrobial potential (Chap. 15) [67]. These hermaphroditic worms are fully grown after 3.5 days of development with a total lifespan of 1,000 days [68]. They also deliver all of the advantages of working with a simple organism with uncomplicated

needs. As the genomic sequence of *C. elegans* has been available since 1998, microarrays have been used to examine *C. elegans* germline cells, gene expression during development and identify sex related genes through the comparison of males and hermaphrodites [69–71].

13.3.4   Drosophila melanogaster

Drosophila melanogaster, the common fruitfly is used in the study of developmental genetics. As the majority of the genome has been sequenced using shotgun sequencing techniques, these organisms provide another multicellular alternative to *S. cerevisiae* but remain simple to work with [67]. Microarrays have been used to examine *Drosophila* metamorphosis, circadian gene expression and immune response genes [72–75]. The main advantage of using *Drosophila* is that it is an organism that provides insight into early development [67].

13.3.5   Mus musculus *and* Rattus norvegicus

Mus musculus is the scientific name of the common mouse. It is a genetic research workhorse with a lifespan of 3.5 years and has been used to model genetic disorders from cystic fibrosis to various cancer types [76–82]. The mouse is a small scale mammal that shares many processes in common with humans and can be genetically manipulated [83–85]. Mouse arrays have been used to examine circadian rhythms in peripheral tissues, identify protein targets and classify stem cell identity and gene expression [3, 86, 87]. Additionally, mouse and human arrays have been applied to studies of placental, embryonic and uterine gene expression and have been used to study the gene expression effects of alcohol [88–90].

Rattus norvegicus (the common rat), a rodent with a 4 year lifespan, has been used similarly to mice in molecular genetics to model various human conditions [91–93]. Rat arrays have been applied to examining changes in gene expression in the rat aorta when treated with different nitrate sources and identifying c-Myc responsive genes [94, 95]. Studies of the gene expression response to hepatotoxicants and elevated intraocular pressure have also been conducted using rat microarrays [96, 97].

The rodent presents a convenient model that is useful for analogy building research [98, 99]. Using whole multicellular organisms gives an indication of drug specificity and the practicality of drug targets [26]. Limitations associated with using this model include a longer generation time with additional responsibilities involving care and maintenance. Researchers must also comply with stringent ethical guidelines to become authorised to use mice and rats for research. There is also a need to house and maintain the animals that could present logistical and/or scheduling problems.

13.4 Methodologies

In this section, we will cover the basic steps of a successful microarray experiment from experimental design, conducting a microarray experiment, obtaining gene expression data and interpreting that data with bioinformatics. The output generated by a microarray experiment provides simultaneous measurement of the abundance of transcripts representing almost all of the genes in a given genome. The difference in transcript abundance between treatment and control samples reveals genes that are up-regulated and down-regulated in response to their environmental stimulus or differences between the cells being investigated.

This extensive amount of gene expression data can then be used to define specific gene expression signatures to a treatment and to generate testable hypotheses regarding drug mechanisms of action. There are a number of preparatory steps required before hypothesis generating data is reached.

13.4.1 Selecting a Microarray Platform

As mentioned previously, DNA microarrays are nucleic acid probes attached to a physical surface [100]. Each probe represents a gene. Different probes can be attached within micrometers of each other, so it is possible to place a large quantity and variety of probes on a small surface, forming a DNA array that represents part of or the complete genome.

cDNA microarrays are made by spotting nucleic material onto the array platform. In spotted arrays, the probes are mechanically deposited on modified glass slides by robotic contact or inkjet printing. This type of microarray takes the form of glass microscope slides, nylon membranes or silicon wafers [23, 101]. Various sizes of probes can be used and this includes PCR products of 500–2,500 bp or oligonucleotides of 15–70 bp [100]. Array slides, membranes, GeneChips® and bead arrays for many organisms can be purchased from various sources (Table 13.1). For organisms that are without a sequenced genome or commercially available chips, custom made microarrays can often be produced if the research groups are able to supply the nucleic material [102]. Research groups may need to supply the nucleic material in this case.

When using spotted arrays, two different fluorescent dyes, the cyanine dyes Cy3 and Cy5 for example, are needed to label the treatment and control samples. Both of these labelled samples are hybridised to the same chip. This two-colour microarray system requires the competitive hybridisation of two samples onto a single microarray slide, each labelled with a different dye, allowing direct on-slide comparison between the control and treatment. An alternative is the one-colour hybridisation system, such as the GeneChips® from Affymetrix [103]. In this example, each sample is hybridised to a unique chip, with comparison done afterwards by bioinformatic programs. This may seem to be more expensive at first as each condition

Table 13.1 Suppliers and products of common microarray equipment [102]

Company	Products	Website
Affymetrix	GeneChip oligonucleotide arrays, array processing instruments and analytical software	http://www.affymetrix.com
Agilent Technologies	Oligonucleotide arrays, processing hardware and software	http://www.agilent.com
Applied Biosystems	Oligonucleotide arrays, chemiluminescent detection tools, Ambion reagents for sample preparation and labelling	http://www.appliedbiosystems.com
Atactic Technologies	Speciality custom microarrays	http://www.atactictech.com
BioCat	Premade and custom arrays and reagents	http://www.biocat.de
CapitalBio Corporation	Premade expression profiling arrays	http://www.capitalbio.com
Clontech (Takara Bio)	Atlas arrays and products for performing microarray experiments	http://www.clontech.com
Combimatrix	Custom and catalogue arrays, CustomArray synthesizer	http://www.combimatrix.com
Eurogentec	Probe sets for array use, ArrayIt printing tools, array design services	http://www.eurogentec.com
GE Healthcare	CodeLink oligonucleotide arrays and processing tools	http://www.amershambiosciences.com
GenoSensor Corporation	GenoExplorer Biochips for expression analysis, array services	http://www.genosensorcorp.com
Illumina	BeadArray platform for oligonucleotide arrays and associated instruments and reagents	http://www.illumina.com
Integrated DNA Technologies	Custom oligonucleotides for use on arrays	http://www.idtdna.com
Microarrays	Catalogue arrays and custom array printing services	http://www.microarrays.com
Nimblegen	Custom and catalogue array designs, array experimental services	http://www.nimblegen.com
Operon Biotechnologies	Pre-printed oligonucleotide arrays and probe sets for microarray use	http://www.operon.com
Oxford Gene Technology	Oligonucleotide arrays for a variety of applications	http://www.ogt.co.uk
Panomics	cDNA arrays and associated reagents	http://www.panomics.com
Phalanx Biotech	Human OneArray genomic array and hybridization kits	http://www.phalanxbiotech.com
SuperArray	GEArray preprinted arrays, hybridization and analysis services	http://www.superarray.com

Table 13.1 (continued)

Company	Products	Website
Telechem International	ArrayIt oligonucleotide microarrays, scanners and instruments	http://www.arrayit.com
The Ramaciotti Centre (UNSW)	Microarrays, sequencing and high-throughput technologies	http://www.ramaciotti.unsw.edu.au
Zeptosens	Custom oligonucleotide arrays	http://www.zeptosens.com

being tested will require an individual chip. However, each sample can then be compared to every other hybridised sample without being limited to the pair wise comparison of dual dye microarrays. With more complex experimental designs, one-colour chips become the only practical solution. Some companies also sell small arrays for probing genes involved in specific pathways. An advantage of using this type of array is that you are able to pinpoint the exact location of your genes in a biochemical and biological context. A limitation that should be considered, however, is that some knowledge of the process you are investigating is required before you can correctly select the appropriate biochemical pathway array.

Spotted microarrays are effective tools for assaying gene expression, however, a few caveats related to their use must be considered. (1) In the preparation of samples for spotted DNA microarray experiments, cDNA obtained from treatment and control samples will need to be labelled by different fluorescent dyes (quite often Cy5 and Cy3 or other fluorescent dyes). Each slide will also need to receive samples from a treatment and a control. Also, in the case of the cyanine dyes Cy3 and Cy5, Cy5 is more prone to photobleaching [104]. The comparison between sample and control is made spectrometrically during data processing and bioinformatic analysis.

Prior to committing any biological samples to arrays it is important that quality control is conducted. While these dummy experiments will identify flaws in arrays that are not visible to the eye, a visual inspection for scratches and imperfections is also worthwhile. Scanning blank microarrays can also identify extreme background fluorescence and prevent pollution of cDNA signals [105].

13.4.2 Experimental Design

A successful microarray experiment begins with a careful experimental design. The end goal is to find differentially expressed genes and analyse the data to generate useful, biologically significant and testable hypotheses.

A fundamental experimental design principle for microarray experiments has been proposed by Churchill; the most important consideration is sample replicates [25, 106]. A clear distinction between biological and technical replicates needs to be made. A technical replicate involves processing multiple RNA samples from one experiment in replication. Technical replicates are repeated samples of the same

biological material. Relying on this replicate type ensures that any variation caused during sample processing will be amplified [107]. A biological replicate is another type of replication but the RNA sample is obtained from a repeat of the same experiment conducted independently [107]. Biological replicates are samples taken from independent biological materials such as different mouse individuals and different cultures of a cell lines. It is more advantageous in terms of statistical relevance to have biological rather than technical replicates given the same number of slides being used [106]. Lee et al. [108] reports a false positive rate as high as 10% error in microarray experiments; even though this is low it is still important to minimise this with independent biological replicates. Statistical significance is only useful with at least three biological replicates, although many more are desired for clinical studies due to the increased frequency of individual differences and variation.

Several scenarios for investigating the mechanism of action of a potential drug can be formulated: contrast between treatment and control, time course experiments and dosage experiments. In the simple contrast design, treated samples and untreated samples are compared. This comparison establishes gene expression in the cell when exposed to a stimulus and then compares it to gene expression in the absence of that stimulus. In the time course design a zero point sample is taken prior to any drug exposure. This becomes the starting point of your experiment. Following the administration of the drug, samples are taken throughout the exposure. These time point samples are then individually compared with the zero time point to determine which genes have been differentially expressed and by how much. Microarrays also allow for the examination of the dynamic interplay of gene expression changes over time. This type of data can also be compared to that of a solvent exposed series of samples. In the dosage design, different test groups are exposed to different concentrations of the drug and samples are taken at the same time point. A control incubation must also be conducted. It will be necessary to stagger the starting points of each of the incubations in order to maintain accurate sampling times and this experiment can be combined with a time course if planning is careful.

Each of these designs may be more suited to a particular investigation and chosen model organism. For cell models (primary culture, cell lines and yeast culture), the time course and dosage designs are relatively easy to conduct. A similar mouse model analysis, however, may prove to be too costly, ethically ambiguous and difficult to perform. In this case a simple contrast may be more plausible. An additional concern with the use of whole organism samples, especially human, is that subjects have non-homogenous genetic backgrounds; this issue can complicate the identification of mRNA and formulation of species wide hypotheses [109]. Even with the most well thought out experimental plan, details can go wrong in the execution. By producing conservative excesses of samples at each step, it is possible to repeat the flawed experimental stage without repeating the entire experiment from exposure [105]. In addition to allowing for experimental errors it is important to prepare enough cDNA for dye swap experiments. This involves switching the fluorophores between the control and sample and only considering results from both variations as significant. The authors advise that

dye swap experiments always be performed when using two-colour microarrays. Blocking and washing steps can also introduce fluorescent contamination, especially as they contain a fluorescent detergent, sodium dodecyl sulphate (SDS) [100]. Furthermore, the dyes may experience quenching or non-homogenous labelling which will bias control:test ratios and this can be accounted for if a dye swap series of arrays are performed [6]. Dye-swaps can be combined with biological replicates rather than technical ones to reduce microarray costs without compromising on the quality of the results.

13.4.3 Microarray Experimental Method

13.4.3.1 Model Selection

Model selection depends on the biological question that is being posed. It is important to keep financial, facility and personnel limitations in mind when the model organism is selected. Remember that reduced complexity may increase the distance between the model organism and the condition or organism that is being modelled.

13.4.3.2 Drug Exposure

If a biological response to a novel compound is being investigated, drug exposure is a critical factor in the success of microarray experiments. How much drug or compound should be used is a common question. This will depend on the research objectives. If the objective is to understand the interaction between the drug and biological system, then a concentration that kills a model organism too quickly will not allow the examination of this interaction. A good guide is to use IC_{20} (20% inhibition) which is another way of describing a concentration that reduces activity of the biological system or organism being investigated to 80%. Alternatively, a concentration that inhibits growth but does not affect cell viability would also provide a suitable sample. A more familiar use of this term might be half maximal inhibitory concentration or IC_{50}, a concentration that produces a 50% reduction in viability. These values are arrived at by exposing a population to a compound and measuring the loss of viability over time. Multiple concentrations can be investigated simultaneously in order to arrive at a timescale that is amenable to the experiment. Cytotoxic levels that were excessively high would activate genes that are involved in cellular death. It may be possible for these genes to mask relevant results as they become more predominant in the array results over exposure time.

13.4.3.3 RNA Preparation

Following exposure to the drug under investigation the samples from various live sources such as cancer cells, yeast or tissues are collected by centrifugation,

snap-frozen in liquid nitrogen and, if required, stored at −80 °C until RNA extraction. Elimination of residual growth media is crucial at this stage for successful RNA isolation. It is possible to use products, such as RNALater (Qiagen®) to protect tissues or cells from RNA degradation or changes in mRNA amounts, however, this is generally not needed if samples are snap-frozen and RNA isolation is done straight away, especially with RNA from culture sources. These products can be useful when using tissue samples or when liquid nitrogen is not available, although extra care has to be taken to avoid carryover of the solvent into later processes. Due to this risk, the authors recommend using it only when absolutely necessary, although an additional advantage is that "RNALater" can also protect the RNA during freeze/thaw cycles [110].

The main RNA extraction protocols following sample collection are relatively similar and aim to deliver enough RNA for effective hybridisation [21]. One protocol for RNA isolation is presented that makes use of TRIzol®, the Guanidinium thiocyanate–phenol–chloroform extraction method and yields between 200 and 400 μg of RNA [111]. This protocol for RNA isolation should be applicable to most cDNA microarray experiments. This method relies on the liquid-phase partitioning of nucleic acids and proteins. Cells are first lysed in TRIzol®, which is a solution of guanidinium thiocyanate (GuSCN) and phenol. By adding chloroform, an upper aqueous phase and lower organic liquid phase are formed; with the upper aqueous phase containing the RNA and the lower organic phase containing protein and DNA. The RNA is then extracted from the aqueous phase by ethanol precipitation and centrifuged to form a pellet. The protocol detailed below has been used by the authors for RNA extraction from yeast cells, which has routinely worked very well and is very easy to carry out.

A major benefit of this isolation technique is that RNA, DNA and protein can all be extracted from a single sample simultaneously. Even though this technique takes more time than other methods, it provides a higher concentration and better quality RNA. For larger samples (100 mg) higher volumes of reagents will be required to accommodate the increased RNA load. Please refer to the manual if this becomes necessary. Keep in mind that TRIzol® is light and temperature sensitive; avoid unnecessary exposure.

RNA Isolation Method Using TRIzol®

Glass beads were weighed out into 2 mL screw capped tubes at 0.75–1 g per tube. A millilitre of TRIzol® was added to the frozen cell pellets prepared from drug exposed cultures as described above and the cells were allowed to thaw. This conserved the RNA against degradation as the cells defrosted. Once the cell pellets were resuspended, the liquid was transferred to the 2 mL microfuge tubes with glass beads. The tubes were placed in a bead beater/cell smasher and beaten at maximum speed for 2 min at 4 °C. If necessary, the time can be increased to 4 or 6 min, with a 2 min incubation on ice every 2 min to avoid over-heating of the samples. The tubes were incubated at room temperature (RT) for 5 min and then 200 μL of chloroform

were added to each of the tubes. The tubes were vigorously shaken for 15 s before incubating for an additional 3 min at RT. Following this incubation the tubes were centrifuged for 15 min at 12,000 $\times$ g at 4 °C. The clear layer on top (containing the RNA) was transferred to fresh 1.5 mL microcentrifuge tubes and quality can be improved by only transferring 400 μL of this layer and discarding the remainder. Isopropyl alcohol (200 μL) was added to each of the tubes, mixed by inversion and incubated at RT for 10 min. The tubes were centrifuged for 10 min at 12,000 $\times$ g at 4 °C. Pellets should be visible at the bottoms of the tubes. The supernatant was discarded and each pellet was washed with 1 mL of 75% ethanol. Following mixing, the tubes were centrifuged for 5 min at 7,500 $\times$ g at 4 °C. The supernatant was removed and the pellets air-dried for 20 min. Sometimes the pellets may not be visible to the human eye at this stage. Once the pellets were dried, each pellet was resuspended in 50–200 μL of RNase free water. The RNA should be stored at −20 °C for short term or −80 °C for long term storage.

There are some alternatives to the bead beater/glass bead method of breaking open the cells outlined above. One of these involves manually crushing the cells in liquid nitrogen using a mortar and pestle, which works well but is labour-intensive, potentially inconsistent and can lead to DNA contamination (a DNase treatment is recommended). In some cases this may be the best option for RNA extraction of bacteria or plant cells that are extremely tough and resistant to the other less vigorous methods. Care must be taken when using liquid nitrogen in this manner. For cells lacking a cell wall, vortexing the cells in the presence of TRIzol or, more commonly, an enzyme, such as lysozyme, will generally be sufficient to break open the cell.

While the TRIzol protocol has performed more than satisfactorily there are alternatives. These include completely different manual protocols or using RNeasy columns (Qiagen®) which are commercially available. The working principles and references for alternative protocols are given below should the need arise.

13.4.3.4   Alternative Protocols for RNA Isolation

Acid Phenol and GuSCN with Lithium Chloride Extraction Methods

The acid phenol RNA extraction method uses phenol without GuSCN. This is not as effective, with possible RNase problems arising from the use of this method, however, it is very inexpensive. Another method uses GuSCN without phenol for the extraction with lithium chloride used to help separate RNA from DNA. While this is a good method, it involves a lot of steps and was therefore combined with the phenol method to create the GuSCN–phenol–chloroform method.

Boom Method

The Boom method is also a GuSCN-based RNA isolation technique; however, it uses glass or silica particles to bind the RNA in a sample. GuSCN helps to lyse the

cells, prevent RNase activity and gene expression level changes and assists binding to the silica (due to its chaotropic property). Protein and DNA are then removed from the silica by adding Proteinase and DNase, before purified RNA can be eluted from the silica. Diatomaceous earth can also be used, to replace the silica in this method [112].

Spin Column Method

This method relies on a membrane impregnated with silica or finely crushed glass particles. The cell lysate is applied to a spin column containing this membrane and the whole assembly is centrifuged. RNA is retained on the membrane while multiple buffer washes are used to remove nucleic acid impurities, protein and DNA contamination. The RNA is then eluted from the column. Detailed protocols can be obtained from the manufacturers of these columns, such as RNeasy columns (Qiagen®), which are usually supplied as a kit [110, 113]. A variation of this method involves the use of a filtration manifold rather than centrifugation. This can increase the ability for the method to be scaled up for higher throughput, such as using a 96-well filter-bottom plate [114].

13.4.3.5 Assessing RNA Quality

In comparing two experimental samples (such as cells with and without drug exposure), it is essential to purify the RNA under conditions that are as uniform as possible and in triplicate. This ensures that any differential expression observed in the microarray data is legitimately associated with the stimulus. Once the RNA has been extracted, the concentration and quality of the RNA will need to be assessed. Absorbance at 230, 260 and 280 nm is measured by spectrophotometer. The absorbance reading at 260 nm is used to calculate the concentration of RNA, since an absorbance of 1 equals 40 μg/mL. A 260/280 ratio is calculated for each RNA sample; a ratio that is greater than 1.8 indicates good quality RNA, lower indicates protein contamination. The 260/230 ratio also determines quality. It should also be greater than 1.8 and indicates the presence of solvents such as ethanol or TRIzol® as well as sugars (if below 1.8). Gel electrophoresis is also used to graphically present the purity and degradation status of the RNA sample.

As technology has progressed, the amount of sample required for these tests has become smaller. The authors favour the use of the NanoDrop 1000® (Thermo Scientific) for spectrophotometric analysis as it uses only 2 μL of the resuspended RNA. A benefit of the NanoDrop® is that it shows the absorbance over a large range of wavelengths, revealing unexpected peaks. In addition, an Agilent Bioanalyzer 2100® is used for electrophoretic separation and RNA quality control. Its use of capillary action allows for microlitre loading volumes. It also provides cleaner images of the band separation, clearly showing whether the RNA has been degraded. This quality control should follow whatever RNA isolation method is used.

13.4.3.6 Improving RNA

Following RNA extraction it may be necessary to improve the quality of the RNA samples and a DNase treatment would be applied. Such treatment should eradicate any residual genomic DNA that might remain after extraction. This ensures that strands of DNA can't compete with RNA in downstream processes. Solvent contamination can also be problematic downstream. Qiagen® offers an RNeasy column-based clean-up kit (with an optional DNase incubation step), with the protocol described in the manual. The RNeasy columns purify extracted RNA using centrifugation steps that retain RNA in the column matrix allowing impurities to flow through in an application similar to the spin column RNA isolation. Once this is complete, RNA can be eluted, generally using RNase-free water. Purification is optional and can be omitted; however, the authors recommend its inclusion in standard RNA preparations. Usually, finalised NanoDrop® and Bioanalyzer® assessment follows these purification steps.

For some specialised microarrays or where a gene is expressed at very low levels, mRNA can be used instead of total RNA. The simplest way of separating the mRNA out of a sample is to apply it to a column containing oligo dT strands, for instance, to bind to the dA tails, retaining mRNA in the column. One such mRNA enrichment method is the Poly(A)Purist™ kit from Ambion, although there are many available alternative suppliers.

13.4.3.7 cDNA Conversion

As mentioned previously, RNA is an inherently unstable molecule that will degrade rapidly. Converting RNA into cDNA for subsequent array application or qRT-PCR experiments, etc. rather than storing RNA is beneficial; cDNA is significantly more stable than RNA and stores better, leading to more reliable downstream results. The sequence of the RNA remains but it is now in a more stable DNA form. During this process, the cDNA samples are also labelled with a specific fluorophore. At this stage, the authors have used two different commercial products; Alexa Fluors (Invitrogen®) and Cyanine dyes (GE Healthcares®), both of which are indirect labelling reagents. Below, a method of conversion and a variation are presented that are specific for each fluorophore type.

In all biochemical reactions it is vital that reagents and samples are fully defrosted prior to beginning. A brief vortex will homogenise the defrosted samples and following this with a brief centrifugation pulse will gather contents at the bottom of the tube. Thorough mixing at all of the following steps is imperative for a successful conversion.

cDNA Conversion Method for CyDye Application

A master mix that includes enough of all general reagents at the required concentrations for all of the reactions with one volume extra (n + 1) was prepared. This

reaction mixture includes strand buffer (5 × 1st, 8.0 μL), anchored oligo dT primer (T20VN, 1.5 μL) and dithiothreitol (DTT) (0.1 M, 4.0 μL). For each of the reactions a volume of 13.5 μL of master mix was aliquoted into RNase-free 200 μL PCR tubes (or 1.5 mL microcentrifuge tubes if heating blocks are being used for subsequent incubations). RNA was then added (15–20 μg, made up to 18.7 μL with RNase-free water) to each tube and the reactions were mixed. The tubes were then incubated at 65 °C for 5 min (PCR machines and heating blocks work equally well, although PCR machines can be more convenient) and then at 50 °C for 5 min. During the incubation a second master mixture was prepared which included d(ACG)TP (10 mM each, 2.0 μL), dTTP (2.5 mM, 2.6 μL) (10 mM) 5′-(3′aminoallyl-2′-dUTP, (aa-dUTP)) (1.4 μL) and SuperScript III Reverse Transcriptase (2.0 μL).

While at 50 °C, 8 μL of the second master mix was added into each tube and mixed thoroughly. The tubes were then incubated at 50 °C for 2.5–3 h. During this incubation, it was important to check the pH of the 0.25 M NaOH and 0.2 M acetic acid used in the subsequent step to ensure that they neutralise each other (we recommend using the PBI buffer that comes with the Qiagen® QIAquick PCR purification kit – the colour should change from purple to yellow if the pH levels are correct). To hydrolyse the RNA, 5 μL 0.5 M EDTA and 10 μL 0.25 M NaOH was added to each mixture. The tubes were incubated at 65 °C for 20 min and 15 μL of 0.2 M acetic acid was added afterwards to neutralise the reactions. The contents of the tubes were transferred into 1.5 mL microcentrifuge tubes (optional). The cDNA was purified using Qiagen® QIAquick PCR purification kit, following the manufacturer's instructions. However, it is advisable to use PB buffer instead of PBI buffer and 75% ethanol instead of PE buffer. Following elution, the concentration and quality of the cDNA was checked using the NanoDrop® and the samples were dried by vacuum centrifugation to 1–2 μL. We recommend using a cDNA amount of at least 1.6 μg, with a minimum of 0.8 μg required before continuing.

Indirect Coupling with Cyanine Dyes

This and subsequent parts of the protocol were conducted in the dark. The cDNA pellets were resuspended in 9 μL NaHCO$_3$ (0.1 M, pH 9). Monoreactive Cy3 and Cy5 vials were resuspended in enough DMSO to ensure that each sample can be coupled with 2 μL of dye. A total volume of 10 μL is preferable and enough for four arrays while up to 19 μL will serve for nine arrays. Two microliters of resuspended dye were added into each cDNA sample (taking care to consider which samples should be labelled with Cy5 or Cy3 and ensuring that one of each dye will be hybridised onto each array) and the reactions were incubated for 1 h at RT in the dark. The labelled cDNA was purified using the Qiagen® PCR purification columns as described earlier and the samples were again dried using vacuum centrifugation to 1–2 μL. You should have at least 80 pmol of incorporated dye before using this sample to hybridise to a slide.

An alternative method is the kit-based SuperScript™ Plus Indirect cDNA Labeling System from Invitrogen®. It is similar to the method described above,

but uses Alexa Fluor® 555 and 647 dyes instead of Cy3 and Cy5 dyes. The Alexa Fluors® are excellent dyes and more stable than the cyanine dyes. The authors recommend, however, that the purification columns from Qiagen® be used instead of the ones recommended by the kit. Both methods lead to equally successful microarrays. These methods involve indirect labelling, but there are direct labelling methods available, such as the SuperScript™ Plus Direct cDNA Labeling System (Invitrogen®) which involves the incorporation of dye-labelled nucleotides, making it a single-step process and saving time. However, the authors have not yet tested this method.

13.4.3.8   Blocking, Hybridisation, Washing and Scanning

The microarray slides were blocked before use by agitating them in 95 °C 0.1% SDS for 1 min, RT 5% ethanol for 1 min followed by water for 1 min. The slides were dried by tapping them on tissues to remove excess liquid before centrifuging them at $1,000–2,000 \times g$ for 20 s. Coverslips were washed carefully by immersing them in 100% ethanol before rubbing them clean with KimWipes. It is important to wear gloves when handling the slides and coverslips. This should be done during the incubation of the coupling step.

To prepare the hybridisation solution, each sample was resuspended in 50 μL DIG-Easy hybridisation buffer before the relevant samples were combined. Aliquots of 132.5 μg tRNA and 125 μg herring sperm DNA were then added. The samples were incubated at 65 °C for 5 min before centrifuging at $16,000 \times g$ for 5 min.

The microarray slides and coverslips were set up raised over Kimwipes dampened with DIG-Easy hybridisation buffer in a box, creating a humid environment. This can be achieved by laying the microarray horizontally over a few blank microscope slides in a slide box. The hybridisation solution (100 μL total volume) was applied under the coverslip and left in the dark at 37 °C for 14–18 h to hybridise.

Alternatively, hybridisation can utilise specialised hybridisation machines, such as the a-Hyb™ Hybridization Station from Miltenyli Biotec, which pumps the sample over the slide rather than the standard static method described above. While both methods are effective, the movement of the washes by the a-Hyb™ pump ensures uniformity of both the spots and the background of the microarrays.

After hybridisation, the slides were washed by agitating them in $2 \times$ SSC (300 mM sodium chloride, 30 mM sodium citrate), 0.2% SDS for 10 min, then $2 \times$ SSC for 10 min, followed by $0.2 \times$ SSC for 10 min, with all washes performed at RT in a rocking hybridisation oven. The slides can not be washed with water. The slides were tapped on a tissue and centrifuged at $1,000–2,000 \times g$ for 20 s. For optimum results, the slides were scanned within the following few hours. A good scanner to use is the Genepix® 4000B scanner from Axon Instruments. If an array specialist is being considered, options available in Australia include the Ramaciotti Centre (http://www.ramaciotti.unsw.edu.au; based in Sydney) and the Australian Genome Research Facility (http://www.agrf.org.au; main office in Brisbane, nodes in Adelaide, Melbourne and Sydney). Examples of arrays are included in Fig. 13.4.
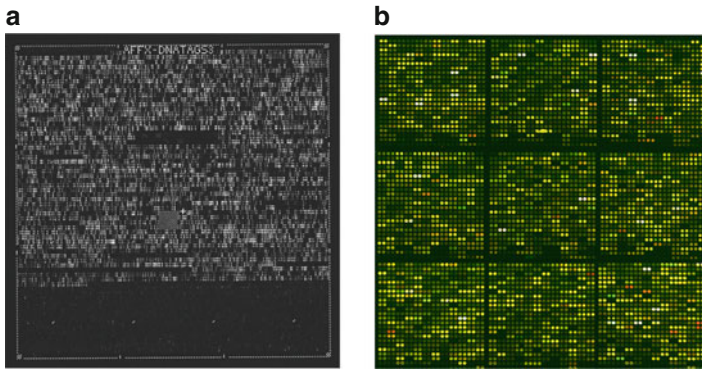
Fig. 13.4 Examples of array data images. (**a**) A single fluorophore Affymetrix Tag Array. (**b**) Nine of the 24 equal-sized blocks of a two colour glass microarray

13.5 Data Analysis

13.5.1 Finding Differentially Expressed Genes

13.5.1.1 Data Pre-Processing

As the process of hybridisation cannot be finitely controlled, some extra processing is required prior to examining results for differentially expressed genes. For spotted arrays, spot quality, i.e., how completely the labelled cDNA has covered the array feature, needs to be assessed prior to bioinformatic analysis. This also allows for the identification and elimination of contaminating dust particles or precipitated label on the array [115]. It is important to distinguish these artefacts from real gene-related fluorescence. During this step it is also necessary to assign gene identities to the spots on the array [115]. Depending on the analytical program used, these functions may be included as part of the image acquisition package, for example GenePix Pro from Axon Inc. At this stage it is also necessary to determine the background levels on the array. This should be calculated locally for each spot as the background noise is rarely homogenous across the whole slide [115]. It is important to look for regions of unexpectedly high background. These areas usually indicate hybridisation problems, precipitation of nucleic material and/or slide dehydration. Again, analytical software usually includes a function capable of assessing background, usually based on the pixels around the spot, and delivers information about its distribution [25, 105].

The fluorescence intensities can now be determined by subtracting the background from each spot. Spot intensity can be calculated using median or mean intensity although improved consistency has been reported with the latter [115]. The exact method will vary with the bioinformatic program used and program suggestions are listed in Table 13.2. Inconsistencies in array printing may become

Table 13.2 Some sources of online array data analysis programs and support

Program	Source	Description
EASE related to DAVID (Database for Annotation, Visualisation and Integrated Discovery)	http://david.abcc.ncifcrf.gov/	The "Expression Analysis Systematic Explorer" is an application that can be downloaded from DAVID and allows for the interpretation of microarray results by offering statistical analytical tools including models for multi-test comparisons
Genemaths XT	http://www.aplied-maths.com/genemaths/genemaths.htm	Statistical program that allows for visualisation, supervised and unsupervised analysis, variance assessment
GeneSpring	http://www.chem.agilent.com/en-US/products/software/lifesciencesinformatics/genespringgx/Pages/default.aspx	Provides analytical tools for visualisation of array data
MicroArray Explorer	http://maexplorer.sourceforge.net	Offers variance assessment, data filters, visualisations, web database interaction
Partek Genomics Suite	http://www.partek.com	Provides statistical analysis with access to visualisations of statistically significant relationships between array results. All microarray platforms are compatible with the software
Regulatory Sequence Analysis Tools	http://rsat.ccb.sickkids.ca/	Program designed to identify regulatory signals in introns
TIGR Spotfinder, Microarray Data Manager (MADAM), MeV, etc.	http://www.tm4.org/index.html	Freely downloadable software suite that allows for the identification of array spots, examination of differential expression and comparison of multiple experiments

apparent at this stage. However, array spots that have tails or have a dark patch in the centre of the spot, like a donut, are still usable with only a marginal effect on successful data generation [105]. Donuts and tail-smearing are generally caused by degradation of the slide coating over time; therefore slides should be used within their expiry period, generally within three months for glass-based arrays.

13.5.1.2 Normalisation

Given our discussion of the necessity of replicates, each microarray experiment will involve multiple chips. The use of multiple arrays introduces variation that can

obscure experimental data [116]. For this reason, array-wide fluorescence has to be normalised. This process ensures that a poorly or excessively hybridising chip doesn't bias the results. Using raw fluorescence ratios can not guarantee a result of legitimate differentially expressed genes [25]. Normalisation also accounts for different starting concentrations of RNA [115]. This process does, however, rely upon some critical assumptions, the foremost being that some genes won't be differentially expressed and the ratio between hybridised and scanned red- and green-labelled samples will be 1 [115]. Assuming this is true for the samples in question; array data can be normalised using housekeeping genes, setting their red: green ratio to 1 and adjusting the remaining fluorescent signals accordingly [115]. Total array-wide fluorescence intensity can also be used. Alternatively, it is possible to spike standards of known concentration into your hybridisation mix and use the fluorescent signal of these markers to normalise multiple arrays [25]. Linear regression can also be used by plotting red fluorescence intensity against green fluorescence intensity for each gene and adjusting the slope of the graph to 1 [115]. The arrays can then be compared as they have been standardised for variation that may have occurred in the labelling, hybridisation or detection processes [115]. A commonly used normalisation method is Locally Weighted Scatterplot Smoothing (LOWESS), a least squares regression normalisation technique used by GeneSpring [117]. The normalisation technique used for one-colour Affymetrix arrays is Robust Multi-chip Average (RMA), a technique used by RMAExpress, BioConductor and Partek [103].

Traditionally, p-values have been used to assess whether an experimental outcome satisfied a hypothesis. While this statistical method has been used to assess microarrays, its ability to tolerate the high through-put hypothesis testing of genome wide arrays has been questioned [28]. Consequently, false discovery rate (FDR) has also been used for the statistical evaluation of microarray data. FDR describes the expected number of genes identified as differentially expressed that are in reality not significantly up- or down-regulated [118]. Excessive control of FDR can increase the false negative rate (FNR) and mask valuable legitimate results [28].

13.5.1.3 Identification of Differentially Expressed Genes

For the successful analysis of microarray data it will be necessary to invest in a program designed specifically for microarray analysis. Typically, this data is in the form of a ratio of the two tested conditions. For example, a single spot would have hybridised the fluorescent signal for a gene from a control sample and the fluorescent signal of the same gene from a drug exposed sample. These values would make up the reported ratio; we suggest using GeneSpring from Agilent for this purpose [25]. One statistical method that is frequently used after normalising raw microarray data is an ANalysis Of VAriance (ANOVA). It is used to make identifying differential gene expression more precise [119]. Taking a measure of experimental error makes it possible to trust the inferences that are made from the experimental data [119]. Successful identification of a legitimate biological effect can only be

carried out when the inherent variation of the experiment is considered and accounted for [25]. Replicate experiments are a simple way to improve certainty as this provides a basis for consensus [25]. Typically, processing array data through one of the programs designed to identify differentially expressed genes produces a gene list. This can be analysed in a variety of ways. The aim of these methods is to assess variance and cluster genes into groups through dimensional categorisation. More than one approach may be required to draw meaning from experimental data.

13.5.2 Analysis of Differentially Expressed Genes and Data Mining

There are a number of tools available to extract biological information from the identified differentially expressed genes. Each of these methods has different levels of complexity and requires differing degrees of computational input.

13.5.2.1 Univariate Analysis

For a simple microarray analysis where minimal treatment conditions (e.g., control and compound exposure) are involved, mapping the genes with Gene Ontology (GO) terms provides a good start towards making sense of the data. GO terms are standard descriptors of biological processes, compartments and mutant behaviour. An advantage of using these terms is that most remain organism-independent and indicate gene function relationships across species divisions. Univariate analysis involves gene by gene examination of array data. Differentially expressed genes are assessed for similarity in general characteristics including function, location and regulation to identify the important biological processes in a drug response [120]. A set of genes with related functions that are all differentially expressed suggests that the process these genes govern is important for the biological response to experimental stimuli [120].

There are a number of resources available that are annotated for a single organism and include links to information on gene homologues in other organisms; YPD is an example of this kind of database and other resources are listed below (Table 13.3) [121]. These genes will be linked by gene ontology terms that specify the role of the gene product in the cell, the metabolic pathways it is involved in and the organelle it is localised to. Not all of these resources are freely available but there is a wide variety that can be accessed on the internet free of charge. Some prominent tools, websites and databases are found in the table below [30].

13.5.2.2 Multivariate Analysis

Multivariate statistical procedures are statistical tools that map relationships between multiple individual genes and their expression simultaneously [120].

Table 13.3 Tools for data mining. Often both databases and tools are combined in many commercially available websites. Some resources are free and others must be subscribed to

Tool	Website and description
BioProspector	http://ai.stanford.edu/~xsliu/BioProspector/
	Predicts regulatory motifs from genes in prokaryotes and lower eukaryotes
Compare-Prospector	http://compareprospector.stanford.edu/inputs.html
	Sister program to BioProspector for use with higher eukaryotes
FunSpec	http://funspec.med.utoronto.ca/
	Allows users to input gene lists and returns a characterisation of each of those genes in terms of function, localisation and interactions. FunSpec also reports a p-value indicating the probability that each gene was included in the collection randomly
GeneCards	http://www.genecards.org/
	Database of genomic, proteomic and transcriptomic information about human genes
Kyoto Encyclopaedia of Genes and Genomes	http://www.genome.jp/kegg/
	Database of biological systems, genomic and chemical information about a variety of genes from different organisms and is able to determine which pathways are enriched in a dataset
SGD	http://www.yeastgenome.org
	A standard yeast database including information about genes with curated references. Includes gene expression data regarding various experimental conditions. Protein data also provided. This database also links out to some tools such as GO
The Gene Ontology	http://www.geneontology.org/
	Bioinformatic Database for the universal application of gene descriptors that allows for the classification of genes based on location, function, complexes, etc
UniGene	http://www.ncbi.nlm.nih.gov/unigene
	Database of transcript sequences with protein homology, expression and location on the genome
Yeast Microarray Global Viewer	http://transcriptome.ens.fr/ymgv
	Database of microarray experiments displayed graphically that allows users to identify conditions which affect specific genes
YPD	http://biobase-international.com/pages/index
	A cross-referenced database of gene information from yeast, *C. elegans*, *Schizosaccharomyces pombe*, and mammalian systems that includes details on gene function, location and known interactions with links to literature. This is a subscribed resource

Using information about a subset of genes, this method aims to gauge how other genes will behave transcriptionally. This produces information about how groups of genes interact to maintain and regulate similar biological pathways and allows for a better perspective of the complex interactions that drive cellular processes [120]. While an indication of gene interaction is extremely valuable when trying to examine an environmental stimulus, even to the stage of connecting previously

disparate biological processes, multivariate analysis is as yet unable to describe the exact nature of these interactions [120, 122]. It is advisable to choose a subset of target genes based on rigorous criteria for more extensive investigation to avoid high levels of computer processing required to analyse genome-wide data.

An example of a multivariate method is Principal Components Analysis (PCA). The application of PCA to microarray analysis aims to explain changes in gene expression by identifying the main factors in the experimental conditions that produce these differences [123]. This is especially useful when examining a large number of samples from different subjects or tissue types. Gender, age, etc. can be coloured as variables, making it easier to see whether separation is based on treatment or another factor that is not related to the tested variables. This method is capable of treating both the genes or the experimental conditions as variables and identifies what characteristics in the variables contribute to the biological response [123]. The assistance of a biostatistician would be a valuable resource when undertaking this analysis.

13.5.2.3 Cluster Analysis

For more complex microarray experiments where there are more than two conditions such as multiple treatments, time-points or dosages, data-mining techniques will be needed to extract biological information from a vast amount of data that is beyond the processing power of a human brain [124]. One approach is cluster analysis. This method examines the expression of the entire data set and groups genes with similar patterns of expression together [124]. The process can be supervised, where classification refers to another characteristic of the gene, like localisation, or unsupervised where data is classified based solely on the expression information yielded by the experiment. Prior to successful classification, similarity must be defined mathematically [124].

Hierarchical clustering is useful when large datasets require analysis; such as when three or more metallointercalators are screened with the aim of finding common biological modules or gene expression patterns among these drugs [124]. Clustering can also be used for time course experiments where gene expression data has been generated from multiple time points. Clustering software can be downloaded from http://rana.lbl.gov/EisenSoftware.htm [30]. Hierarchical clustering is usually graphically presented as a tree diagram where similarly expressed genes are allocated a colour representative of their expression levels and grouped together. The greater the distance between two genes in the diagram the greater the difference in their expression levels [124]. Eisen et al. [124] reported that functionally similar genes frequently clustered together when they studied human fibroblast expression and yeast gene expression during different environmental stresses with spotted cDNA microarrays. This can prove useful for identifying the function of uncharacterised genes by virtue of their clustering with characterised genes [124].

13.5.2.4   Common Regulatory Motifs

While differentially expressed genes may appear completely disparate with only the most tenuous of cellular links between them, they may still be regulated by the same mechanism [4]. By submitting your gene list to online regulatory motif databases, such as RSAT (http://rsat.ccb.sickkids.ca/), it is possible to identify whether any of your genes are regulated by the same sequence.

13.5.2.5   Generating Hypotheses Involving the Initial Objective

At this stage, the array experiment should have delivered a set of differentially expressed genes and the data mining process will have yielded the biological links (function, regulation, localisation, etc.) between these genes. The initial objective to identify gene products involved in the biological response to a compound will have been met. This information forms the foundation for an investigation into the biological response to the compound under examination. The information from the array experiment should only be used to refine the initial hypothesis. Usually genome wide array data will require additional evidential support before hypotheses can be confirmed [6].

13.5.2.6   Further Testing of the Hypothesis

As microarray experiments produce high throughput data, they are more useful for the generation rather than confirmation of hypotheses. For this reason it is important to follow microarrays with confirmatory experiments that are able to corroborate microarray results; likely options include Western and Northern blotting and immunohistochemistry [11, 26]. Western and Northern blotting are techniques used to determine differential gene expression, utilising electrophoresis for separation and a complementary hybridisation probe for detection [125]. Streit et al. [126] demonstrate the application of Northern blotting to determine differential gene expression in pancreatic cancer cells and tissues. This has largely been replaced by qRT-PCR, which along with tissue arrays are also utilised in validating microarray results. Some investigators implement both methods for validation [12]. It may be necessary to focus your study on some critical genes identified in the array data rather than all of the "potentials" in the collection [26].

It is important to consider what the array data is suggesting about how the biological system copes with the compound in question. Is it possible to label the drug and track it by microscopy to the organelle indicated by the arrays? Can mutant studies be used to remove a critical gene product from the organism, increasing its sensitivity to the compound of interest? Consider the best way to prove what is being suggested by the gene expression relationships indicated by the array data. In this way, array interrogation can yield results that are proven in a real context and provide solid evidence for a biological response to a compound. The flowchart below (Fig. 13.5) may help you plan your study with regard to what has been discussed in this chapter.
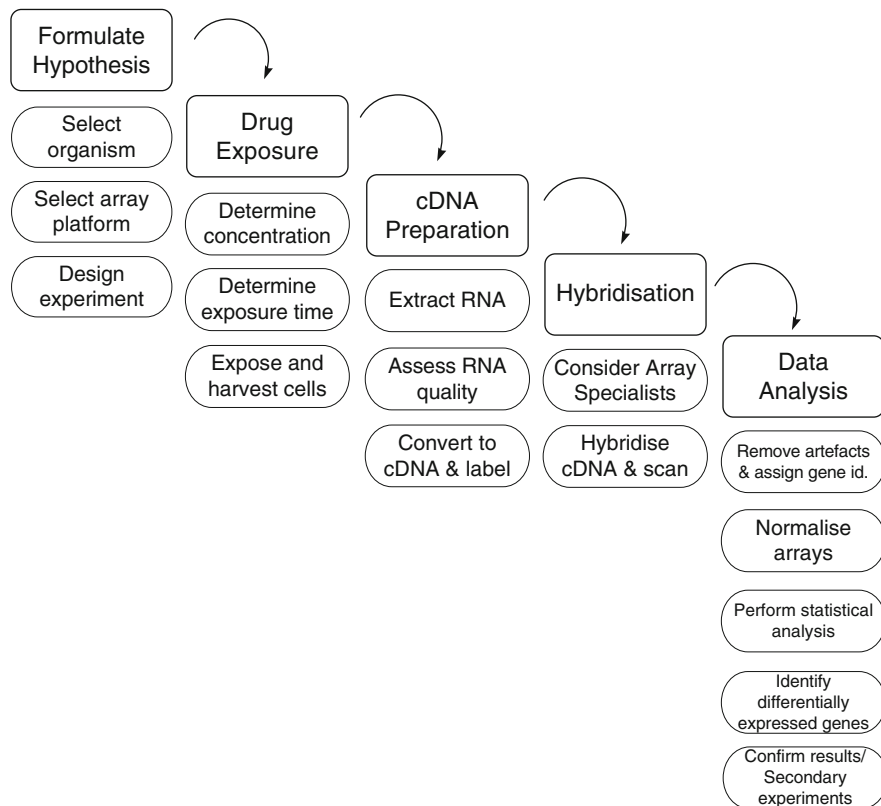
Fig. 13.5 Summary of the microarray process

References

1. Knox B, Ladiges P, Evans B, Saint R. Biology. 2nd ed. Sydney: McGraw-Hill Book Company Australia; 2001.
2. Crick F. Nature. 1970;227:561.
3. Perez-Iratxeta C, Palidwor G, Porter CJ, Sanche NA, Huska MR, Suomela BP, et al. FEBS Lett. 2005;579:1795.
4. Mathews CK, van Holde KE, Ahern KG. Biochemistry. 3rd ed. Canada: Addison-Wesley Publishing Company; 2000.
5. Lodish H, Berk A, Matsudaira P, Kaiser CA, Krieger M, Scott MP, Zipursky SL, Darnell J. Molecular cell biology, 5th ed. New York: NY: WH Freeman and Company, 2004.

6. Afshari CA. Endocrinology. 2002;143:1983.
7. Pertseva M. Comp Biochem Physiol A: Physiol. 1991;100:775.
8. Shpakov AO, Pertseva MN. International review of cell and molecular biology. In: Kwang WJ, editor, vol. 269. London: Academic Press; 2008. p. 151.
9. Rhoads RE. J Biol Chem. 1999;274:30337.
10. Ullrich A, Schlessinger J. Cell. 1990;61:203.
11. Villeneuve DJ, Parissenti AM. Curr Top Med Chem. 2004;4:1329.
12. Rhodes DR, Chinnaiyan AM. Ann N Y Acad Sci. 2004;1020:32.
13. Huang Y, Sadee W. Drug Discov Today. 2003;8:356.
14. Clarke PA, te Poele R, Wooster R, Workman P. Biochem Pharmacol. 2001;62:1311.
15. Hughes TR, Shoemaker DD. Curr Opin Chem Biol. 2001;5:21.
16. Dilda PJ, Don AS, Tanabe KM, Higgins VJ, Allen JD, Dawes IW, et al. J Natl Cancer Inst. 2005;97:1539.
17. Brazma A, Hingamp P, Quackenbush J, Sherlock G, Spellman P, Stoeckert C, et al. Nat Genet. 2001;29:365.
18. Edgar R, Domrachev M, Lash AE. Nucleic Acids Res. 2002;30:207.
19. Brazma A, Parkinson H, Sarkans U, Shojatalab M, Vilo J, Abeygunawardena N, et al. Nucleic Acids Res. 2003;31:68.
20. Rhodes DR, Yu J, Shanker K, Deshpande N, Varambally R, Ghosh D, et al. Neoplasia. 2004;6:1.
21. Ramaswamy S, Golub TR. J Clin Oncol. 2002;20:1932.
22. Ross DT, Scherf U, Eisen MB, Perou CM, Rees C, Spellman P, et al. Nat Genet. 2000;24:227.
23. van Hal NLW, Vorst O, van Houwelingen AMML, Kok EJ, Peijnenburg A, Aharoni A, et al. J Biotechnol. 2000;78:271.
24. Sinicropi D, Cronin M, Liu M-L. BioMEMS & Biomedical Nanotechnology. In: Ferrari M, Ozkan M, Heller MJ, editors, vol. 2. New York: Springer; 2007. p. 23.
25. Newton MA, Kendziorski CM, Richmond CS, Blattner FR, Tsui KW. J Comput Biol. 2001;8:37.
26. Gerhold DL, Jensen RV, Gullans SR. Nat Genet. 2002;32:547.
27. Righetti PG, Castagna A, Antonucci F, Piubelli C, Cecconi D, Campostrini N, et al. J Chromatogr A. 2004;1051:3.
28. Pawitan Y, Michiels S, Koscielny S, Gusnanto A, Ploner A. Bioinformatics. 2005;21:3017.
29. Kudoh K, Ramanna M, Ravatn R, Elkahloun AG, Bittner ML, Meltzer PS, et al. Cancer Res. 2000;60:4161.
30. Chin K-V, Kong ANT. Pharm Res. 2002;19:1773.
31. Bertucci F, Houlgatte R, Nguyen C, Viens P, Jordan BR, Birnbaum D. Lancet Oncol. 2001;2:674.
32. Pusztai L, Ayers M, Stec J, Hortobagyi GN. Oncologist. 2003;8:252.
33. Gustafsson A, Kupershmidt I, Edlundh-Rose E, Greco G, Serafino A, Krasnowska E, et al. BMC Cancer. 2005;5:75.
34. Edlundh-Rose E, Kupershmidt I, Gustafsson AC, Parasassi T, Serafino A, Bracci-Laudiero L, et al. Pathobiology. 2005;72:203.
35. Izzotti A, Bagnasco M, Cartiglia C, Longobardi M, Balansky RM, Merello A, et al. Eur J Cancer. 2005;41:1864.
36. Hilakivi-Clarke L, Olivo SE, Shajahan A, Khan G, Zhu Y, Zwart A, et al. J Nutr. 2005;135:2946S.
37. Xia S-H, Wang J, Kang JX. Carcinogenesis. 2005;26:779.
38. Yang K, Yang W, Mariadason J, Velcich A, Lipkin M, Augenlicht L. J Nutr. 2005;135:2710.
39. Hardwick JCH, van Santen M, van den Brink GR, van Deventer SJH, Peppelenbosch MP. Carcinogenesis. 2004;25:1293.
40. Wang SI, Mukhtar H. Cancer Lett. 2002;182:43.
41. Frantz DJ, Hughes BG, Nelson DR, Murray BK, Christensen MJ. Nutr Cancer. 2000;38:255.

42. Afonja O, Juste D, Das S, Matsuhashi S, Samuels HH. Oncogene. 2004;23:8135.
43. Kong G, Kim H, Wu K, DeNardo D, Hilsenbeck SG, Xu X, et al. Cancer Res. 2005;65:3462.
44. Schlicht M, Matysiak B, Brodzeller T, Wen X, Liu H, Zhou G, et al. BMC Genomics. 2004;5:58.
45. Palmer HG, Sanchez-Carbayo M, Ordonez-Moran P, Larriba MJ, Cordon-Cardo C, Munoz A. Cancer Res. 2003;63:7799.
46. Arango D, Wilson AJ, Shi Q, Corner GA, Aranes MJ, Nicholas C, et al. Br J Cancer. 2004;91:1931.
47. Ahn M-J, Yoo Y-D, Lee K-H, Ahn J-I, Yu D-H, Lee H-S, et al. Cancer Res Treat. 2005;37:54.
48. Longley DB, Harkin DP, Johnston PG. Nat Rev Cancer. 2003;3:330.
49. Maxwell PJ, Longley DB, Latif T, Boyer J, Allen W, Lynch M, et al. Cancer Res. 2003;63:4602.
50. Ahn M-J, Lee K-H, Ahn J-I, Yu D-H, Lee H-S, CHoi J-H, et al. Cancer Res Treat. 2004;36:46.
51. Chang B-D, Swift ME, Shen M, Fang J, Broude EV, Roninson IB. Proc Natl Acad Sci U S A. 2002;99:389.
52. Zembutsu H, Ohnishi Y, Tsunoda T, Furukawa Y, Katagiri T, Ueyama Y, et al. Cancer Res. 2002;62:518.
53. Parissenti AM, Hembruff SL, Villeneuve DJ, Veitch Z, Guo BQ, Eng J. Anti-Cancer Drugs. 2007;18:499.
54. Rubin MA, Zhou M, Dhanasekaran SM, Varambally S, Barrette TR, Sanda MG, et al. J Am Med Assoc. 2002;287:1662.
55. Varambally S, Dhanasekaran SM, Zhou M, Barrette TR, Kumar-Sinha C, Sanda MG, et al. Nature. 2002;419:624.
56. Mok SC, Chao J, Skates S, K-k Wong, Yiu GK, Muto MG, et al. J Natl Cancer Inst. 2001;93:1458.
57. Chang JC, Wooten EC, Tsimelzon A, Hilsenbeck SG, Gutierrez MC, Elledge R, et al. Lancet. 2003;362:362.
58. Dan S, Tsunoda T, Kitahara O, Yanagawa R, Zembutsu H, Katagiri T, et al. Cancer Res. 2002;62:1139.
59. Kihara C, Tsunoda T, Tanaka T, Yamana H, Furukawa Y, Ono K, et al. Cancer Res. 2001;61:6474.
60. Miklos GLG, Rubin GM. Cell. 1996;86:521.
61. Hedges SB. Nat Rev Genet. 2002;3:838.
62. Guarente L, Kenyon C. Nature. 2000;408:255.
63. Buckingham SD, Esmaeili B, Wood M, Sattelle DB. Hum Mol Genet. 2004;13:R275.
64. Deutsch M, Long M. Nucleic Acids Res. 1999;27:3219.
65. Cherry J, Adler C, Ball C, Chervitz S, Dwight S, Hester E, et al. Nucleic Acids Res. 1998;26:73.
66. Delneri D. Curr Genomics. 2004;5:59.
67. Adams MD, Celniker SE, Holt RA, Evans CA, Gocayne JD, Amanatides PG, et al. Science. 2000;287:2185.
68. Mulder C, Schouten AJ, Hund-Rinke K, Breure AM. Ecotoxicol Environ Saf. 2005;62:278.
69. Reinke V, Smith HE, Nance J, Wang J, Van Doren C, Begley R, et al. Mol Cell. 2000;6:605.
70. Jiang M, Ryu J, Kiraly M, Duke K, Reinke V, Kim SK. Proc Natl Acad Sci U S A. 2001;98:218.
71. Ashburner M, Ball CA, Blake JA, Botstein D, Butler H, Cherry JM, et al. Nat Genet. 2000;25:25.
72. Andrews J, Bouffard GG, Cheadle C, Lu J, Becker KG, Oliver B. Genome Res. 2000;10:2030.
73. De Gregorio E, Spellman PT, Rubin GM, Lemaitre B. Proc Natl Acad Sci U S A. 2001; 98:12590.

74. McDonald MJ, Rosbash M. Cell. 2001;107:567.
75. White KP, Rifkin SA, Hurban P, Hogness DS. Science. 1999;286:2179.
76. Gabriel S, Brigman K, Koller B, Boucher R, Stutts M. Science. 1994;266:107.
77. Clarke LL, Grubb BR, Gabriel SE, Smithies O, Koller BH, Boucher RC. Science. 1992;257:1125.
78. Grubb BR, Boucher RC. Physiol Rev. 1999;79:193.
79. Greten FR, Eckmann L, Greten TF, Park JM, Li Z-W, Egan LJ, et al. Cell. 2004;118:285.
80. Arap W, Pasqualini R, Ruoslahti E. Science. 1998;279:377.
81. Wang TC, Dangler CA, Chen D, Goldenring JR, Koh T, Raychowdhury R, et al. Gastroenterology. 2000;118:36.
82. Wilson VL, Smith RA, Ma S, Cutler RG. J Biol Chem. 1987;262:9948.
83. Green LL. J Immunol Methods. 1999;231:11.
84. Matsusaka T, Xin J, Niwa S, Kobayashi K, Akatsuka A, Hashizume H, et al. J Am Soc Nephrol. 2005;16:1013.
85. Metzger D, Feil R. Curr Opin Biotechnol. 1999;10:470.
86. Akhtar RA, Reddy AB, Maywood ES, Clayton JD, King VM, Smith AG, et al. Curr Biol. 2002;12:540.
87. Chauhan BK, Reed NA, Yang Y, Cermak L, Reneker L, Duncan MK, et al. Genes Cells. 2002;7:1267.
88. Bethin KE, Nagai Y, Sladek R, Asada M, Sadovsky Y, Hudson TJ, et al. Mol Endocrinol. 2003;17:1454.
89. Tanaka TS, Jaradat SA, Lim MK, Kargul GJ, Wang X, Grahovac MJ, et al. Proc Natl Acad Sci U S Am. 2000;97:9127.
90. Treadwell J, Singh S. Neurochem Res. 2004;29:357.
91. Pinto YM, Paul M, Ganten D. Cardiovasc Res. 1998;39:77.
92. St-Amand J, Okamura K, Matsumoto K, Shimizu S, Sogawa Y. FASEB J. 2001;15:684.
93. Barja G, Herrero A. FASEB J. 2000;14:312.
94. Wang E, Lee W-I, Brazeau D, Fung H-L. AAPS J. 2002;4:45.
95. Guo QM, Malek RL, Kim S, Chiao C, He M, Ruffy M, et al. Cancer Res. 2000;60:5922.
96. Bulera SJ, Eddy SM, Ferguson E, Jatkoe TA, Reindel JF, Bleavins MR, et al. Hepatology. 2001;33:1239.
97. Ahmed F, Brown KM, Stephan DA, Morrison JC, Johnson EC, Tomarev SI. Invest Ophthalmol Vis Sci. 2004;45:1247.
98. Hardison RC, Oeltjen J, Miller W. Genome Res. 1997;7:959.
99. Wasserman WW, Palumbo M, Thompson W, Fickett JW, Lawrence CE. Nat Genet. 2000;26:225.
100. Bengtsson A, Bengtsson H. BMC Bioinformatics. 2006;7:96.
101. Lenigk R, Carles M, Ip NY, Sucher NJ. Langmuir. 2001;17:2497.
102. Eisenstein M. Nature. 2006;442:1071.
103. Irizarry RA, Bolstad BM, Collin F, Cope LM, Hobbs B, Speed TP. Nucleic Acids Res. 2003;31:e15.
104. Dar M, Giesler T, Richardson R, Cai C, Cooper M, Lavasani S, et al. BMC Biotechnol. 2008;8:86.
105. Eisen MB, Brown PO. Methods Enzymol. 1999;303:179.
106. Churchill GA. Nat Genet. 2002;32:490.
107. Cui X, Churchill GA. Genome Biol. 2003;4:210.1.
108. Lee M-LT, Kuo FC, Whitmore GA, Sklar J. Proc Natl Acad Sci U S A. 2000;97:9834.
109. Seo J, Bakay M, Chen Y, Hilmer S, Shneiderman B, Hoffman EP. Bioinformatics. 2004;20:2534.
110. Qiagen, http://www.qiagen.com, 2003–2009.
111. Chomczynski P, Sacchi N. Anal Biochem. 1987;162:156.
112. Boom R, Sol CJ, Salimans MM, Jansen CL, Wertheim-van Dillen PM, van der Noordaa J. J Clin Microbiol. 1990;28:495.

113. Invitrogen Corporation, 2009.
114. Mahadevappa M, Warrington JA. Nat Biotechnol. 1999;17:1134.
115. Hegde P, Qi R, Abernathy K, Gay C, Dharap S, Gaspard R, et al. Biotechniques. 2000;29:548.
116. Dudoit S. Stat Sin. 2002;12:111.
117. Cleveland WS, Devlin SJ. J Am Stat Assoc. 1988;83:596.
118. Benjamini Y, Hochberg Y. J R Stat Soc Series B Methodol. 1995;57:289.
119. Kerr MK, Martin M, Churchill GA. J Comput Biol. 2000;7:819.
120. Kim S, Dougherty ER, Chen Y, Sivakumar K, Meltzer P, Trent JM, et al. Genomics. 2000;67:201.
121. Costanzo MC, Hogan J, Cusick ME, Davis BP, Fancher AM, Hodges PE, et al. Nucleic Acids Res. 2000;28:73.
122. Kim S, Dougherty ER, Bittner ML, Chen Y, Sivakumar K, Meltzer P, et al. J Biomed Opt. 2000;5:411.
123. Raychaudhuri S, Stuart JM, Altman RB. Pacific Symposium on Biocomputing, vol. 5. Honolulu: World Scientific Press; 2000. p. 455.
124. Eisen MB, Spellman PT, Brown PO, Botstein D. Proc Natl Acad Sci U S A. 1998;95:14863.
125. Burnette WN. Anal Biochem. 1981;112:195.
126. Streit S, Michalski CW, Erkan M, Kleeff J, Friess H. Nat Protoc. 2008;4:37.

Chapter 14
Cytotoxicity Testing: Cell Experiments

Renate Grünert, Aron Westendorf, Magdalena Buczkowska, Mareike Hänsch, Sybil Grüunert, and Patrick J. Bednarski

14.1 Introduction

14.1.1 Cytotoxicity Screening

Screening for new anticancer agents has traditionally been done with *in vitro* cell culture methods. Even in the genomic era of target-driven drug design, screening for cytotoxic activity is still a standard tool in the search for new anticancer agents, especially if the mode of action of a substance is not yet known. A wide variety of cell culture methods with unique end-points are available for testing the anticancer potential of a substance. Each has its advantages and disadvantages, which must be weighed in the decision to use a particular method. Often several complementary methods are used to gain information on the mode of action of a substance. End-points of these assays can be divided into five general classes depending on the method used: transformation and mutagenesis, irritancy (inflammation), cell viability, metabolic, and survival or clonogenic assay [1]. The last three are suitable for screening for anticancer activity and will be discussed here.

The gold standard for *in vitro* testing of potential anticancer agents is widely considered the clonogenic assay because this method records the ability of a substance to halt the formation of cancer cell colonies, which are thought to be the origin of tumorogenesis. Substances that inhibit colonies formation are termed anticlonogenic. However, testing with clonogenic assays is laborious (i.e., counting of stained colonies even with an automatic colony counter is slow) and thus impractical for screening large numbers of compounds. Furthermore, this method is not suited for use with all cell lines because the line must exhibit colony forming growth, which many human cancer cell lines do not (e.g., leukaemia cells).

P.J. Bednarski (✉)

Department of Pharmaceutical and Medicinal Chemistry, Institute of Pharmacy, University of Greifswald, Greifswald, Germany

e-mail: bednarsk@pharmazie.uni-greifswald.de

Nevertheless, it is a useful tool to explore anticancer potential when active substances have been identified by other means.

Vitality assays are widely popular because they yield information about the well-being of cells after treatment with a test substance by measuring the integrity of cell membranes. One very simple method is the so-called dye exclusion test, whereby cells are exposed to anionic azo dyes such as Trypan Blue or Amido Black (Naphthalene Black). In normal, healthy cells these dyes are excluded by the cell membrane and can not penetrate into cytoplasm; thus they are unable to accumulate in the cells and the cells remain colourless. However, cells with damaged cell membranes (e.g., dead cells) take up the dye, which stains the interior of the cells. Cells that take up the dye and those that do not are counted manually with an inverse microscope and the fraction of stained to total cells is determined. This makes the method subjective, error prone, and very laborious to say the least. Thus it is unsuited for screening large numbers of compounds.

Another technique of measuring cell membrane integrity is to assay for leakage of cytoplasmatic enzymes from the cell into the cell culture medium. An enzyme that is typically assayed for is lactate dehydrogenase (LDH), a cytosolic enzyme that easily escapes the cell when membranes are damaged. The activity of this enzyme outside the cell can be measured with a number of colorimetric methods amenable to microtitre assay format.

Assays that measure cell growth (proliferation) are perhaps the most commonly used methods in cytotoxic substance screens. Thus, these assays do not actually measure cytotoxicity but rather cell growth and should more correctly be termed antiproliferative assays. The easiest method to measure cell growth is to count cells. This can be done either manually with an inverse microscope and a haemocytometer slide or with an automatic cell counting device such as a Coulter Counter. Both methods are laborious and unsuitable for screening purposes.

A widely used metabolic assay suitable for measuring cell growth rates is the so-called MTT assay [2]. MTT (diphenyltetrazolium bromide, 3-(4,5-dimethylthiazol-2-yl)-2,5-diphenyltetrazolium bromide), a lemon-yellow water soluble tetrazolium dye, is reduced in healthy cells by cell dehydrogenases to a dark blue-colored, water insoluble formazan product. Cellular dehydrogenases play a critical role in raising the energetic state of the cell; i.e., dead and dying cells can not reduce the dye. Thus, the intensity of the dark blue color, brought into solution through the use of DMSO, is proportional to the number of healthy (i.e., living) cells. The quotient of blue coloration in the treated cells to untreated control cells is used as a vitality index. The advantage of this assay is that it can easily be adapted to microtiter plates, allowing for the screening of many compounds in parallel. Furthermore, it can be used equally with adherent cells (i.e., from solid tumors) as well as cells that grow in suspensions (i.e., leukemias and lymphomas). The chief disadvantage with the MTT assay is the requirement that cellular dehydrogenase activity must be determined immediately at the end of the drug exposure time when the cells are still alive, which requires an additional 3–4 h incubation with dye followed by workup. Thus, the time requirement is a hindrance when many substances are being tested. Furthermore, the formazan product of MTT is light-sensitive and has been reported

to be mutagenic. An alternative method is the use of XTT (Tetrazolium Hydroxide, 2,3-bis(2-methoxy-4-nitro-5-sulfophenyl)-5[(phenylamino)carbonyl]-2*H*-tetrazolium hydroxide), which forms a less toxic, water soluble formazan and thus avoids the use of DMSO as a solubilising agent [2].

Measuring the biosynthesis rates of proteins or DNA can be used as an indirect method for determining metabolic activity and hence growth rates of cells [3]. These methods utilize radioactive precursors (i.e., radiolabelled methionine or thymidine), that become incorporated into the respective biomolecule when the cells are exposed for a short (pulse) time to the radioactive precursor. After washing out the excess radioactive precursor, the level of radioactivity bound up in the cell, obtained by precipitating the cellular material, is proportional to the growth rate. While these methods provide important information about rates of protein and DNA synthesis in growing cells, they are laborious and produce radioactive waste. Furthermore, they are not amendable to microtiter-based assays. Thus, they are not widely used for screening large numbers of substances.

Quantification of protein and nucleic acid (DNA/RNA) content in cells can also be achieved indirectly through staining them with suitable dyes. For protein staining, the negatively charged dye sulforhodamine B (SRB) has been used [4]. For nucleic acid staining, crystal violet (CV), a positively charged dye, is useful [5]. Figure 14.1 shows 5637 bladder cancer cells stained with CV; it is noticeable that most of the stain is localized in or near to the nucleus, where large amounts of DNA and RNA are present, while the cytoplasm retains relatively little dye.

While both SRB and CV are cheap and pose no threat to personnel or the environment, they stain both live cells as well as dead ones, so a method must be used to separate living from dead cells. In the case of adherent cells, dead cells usually lose contact with the plastic surface of the culture material and can simply
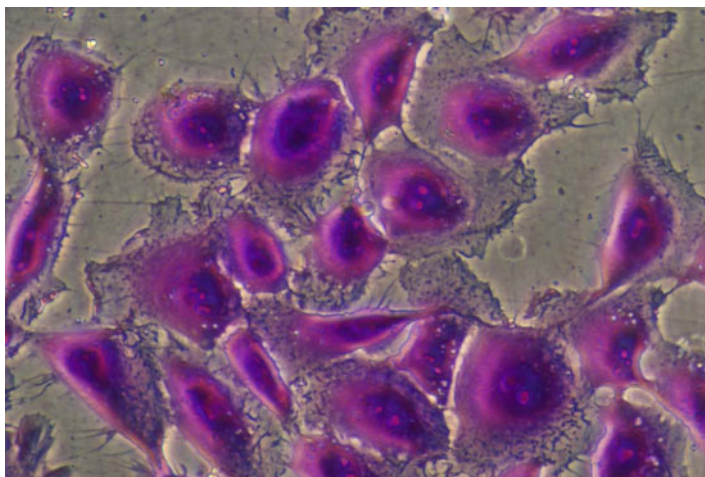
Fig. 14.1 Following embalmation with glutaraldehyde, 5637 cells were stained with Crystal Violet (400-fold magnification)

be washed out with the culture medium at the end of the assay. Cells remaining bound to the plastic are considered "alive and well". The cells can not be immediately stained but can be preserved by treatment with a dilute glutaraldehyde solution, which embalms the cells but does not affect their ability to bind dye later (Fig. 14.1). Plates can be stored at 4 °C until staining; staining of cells can take place days or even weeks after the test was ended, e.g., in one large, simultaneous staining session. With dye staining methods the non-cell bound dye must be washed out before the cell bound dye is extracted out of the cells, typically with ethanol/water, for colorimetric determination. This washing out step proves to be a disadvantage because only adherent cells can be used in microtiter plate-based assays; i.e., if the cells grow in suspension, as is the case with leukaemia cell lines, there is no way to wash out the excess dye without washing out the cells.

Dye-based methods are ideally suited for use in microtiter plate assays and have widely been employed to screen for cytotoxic substances. The NCI uses a SRB dye based microtiter assay to screen substances in 60 cancer cell lines for cytotoxic activity [4]. The experiments described in this chapter are based on a similar CV microtiter assay for measuring antiproliferative activity [6, 7].

14.1.2 Antiproliferative Activity

Proliferating cells are particularly sensitive to the action of anticancer drugs. Because tumor cells tend to have an increased rate of proliferation compared to most non-transformed cells, this makes anticancer drugs somewhat selective towards cancer cells, although rapidly dividing, non-transformed cells (e.g., of the GI-tract, hair follicles, bone marrow) are also vulnerable to the toxic effects of the drug, and this explains many of the common side effects of anticancer therapy.

Events in cell division, the replication of DNA and mitosis particularly, are frequently targets of anticancer drugs. One of the first effects of an anticancer drug is an arrest of the cell cycle at one or more of the various check-points, leading to a reduction in cell division and proliferation. If the damage can be repaired, the cells recover and return to normal proliferation. However, if the cellular insult is too great, the cell can enter into a programmed cell death. Various forms of programmed cell death are known, such as apoptosis, autophagy and mitotic cell death [8]. Antiproliferative assays do not distinguish between the forms of programmed cell death but measure the events as a whole: blockage of cell division and cell death.

Assays that measure antiproliferative effects must take into account a time element when determining end-points. With such assays, it is important to measure cell number or, in the case of microtiter assays, cell density at multiple time points so that reference can be made to the normal growth rate of the cells. In the case of screening large numbers of compounds with microtiter assays, it is usual to measure cell density only at the beginning and end of the assay, either with or without the

test compound [2]. The density of cells at the time of drug application (C_{t0}) serves as a reference value that is subtracted from the densities of cells at the end of the assay (t) for both the treated (T) and untreated cells (C). A percentage, the corrected T/C (%T/C$_{corr}$), is calculated with the equation below to yield the growth rate relative to untreated control after treating cells at a defined concentration of drug:

$$\%\text{T/C}_{\text{corr}} = \frac{(T_t - C_{t0})}{(C_t - C_{t0})} \times 100. \tag{14.1}$$

Based on (14.1), a %T/C$_{corr}$ < 100 and > 0% indicates partial growth inhibition, %T/C$_{corr}$ = 0% indicates total growth inhibition, and %T/C$_{corr}$ < 0% (negative) indicates cytotoxicity. Thus, cytotoxicity is truly achieved only when the cell mass present at the end of the assay is less than when treatment began. Nevertheless, in the literature the term cytotoxicity is frequently used to discuss the effects of substances that do not reduce cell mass (%T/C$_{corr}$ < 0%) but in fact only partial inhibit cell growth. The term GI$_{50}$ (50% Growth Inhibition) was introduced to distinguish an antiproliferative end-point from a simple one-time end-point IC$_{50}$ (50% Inhibitory Concentration) that measures only the number of cells present in the treated compared to the untreated control (T/C) at the end of the assay [2].

For the correct interpretation of the assay, it is important that between the time points t_0 and t, sufficient time is allowed for several rounds of cell division so one is sure that an antiproliferative effect is being measured and not just a toxic one [1]. This is particularly important by cell phase specific drugs like etoposide, methotrexate and vinblastine [3]. Depending on the cell line and how rapidly they divided, exposure to anticancer agents (e.g., cisplatin) can take several days before antiproliferative effects become noticeable, in particular when treatment is with low, therapeutically relevant concentrations of the drug. This is why we allow 96 h to elapse between the beginning of treatment and the end of the assay, which allows the cells (doubling times between 24 and 36 h) 2.5–4 rounds of division on the average [6].

For primary screening purposes, a singular determination of %T/C$_{corr}$ at a chosen concentration is sufficient to identify active compounds. Compounds are active if the %T/C$_{corr}$ is below 50%. The concentration chosen depends on the class of anticancer agents being developed; for platinum complexes we use a cut-off concentration of 20 μM. However, to determine potency, multiple concentrations (preferably five or more) need to be used to establish a dose–response effect. The hypothetical concentration that would lead to a %T/C$_{corr}$ = 50% is the GI$_{50}$ value. This value can be calculated by linear regression analysis of the various %T/C$_{corr}$ versus the log concentration of Pt complex. The %T/C$_{corr}$ values should lie between 10 and 90% to avoid errors in interpolation of the data. We have found that a series of twofold dilutions are more reliable for estimating GI$_{50}$ values than a series of tenfold dilutions [6]. It is critical for the quality of the data that experiments are independently repeated at least in duplicate, better in triplicate or quadruplicate,

because GI_{50} values commonly vary from individual determinations (depending on the cell line) by as much as twofold. The GI_{50} value is commonly used to judge the potency of new substances in relation to known anticancer agents.

14.2 Results

14.2.1 Antiproliferative Activity of Phenanthroline–Pt(II) Complexes

Figure 14.2 shows the structures of the phenanthroline–Pt(II) complexes investigated for antiproliferative activity in human cancer cell lines. These include complexes with diaminoethane (En), *RR*-, *SS*-, or *meso*-2,3-diaminobutane (Bn), and *RR*- or *SS*- 1,2-diaminocyclohexane (Dach) ligands in addition to the phenanthroline ligand. The phenanthroline ligands are either unsubstituted or disubstituted with methyl groups at the 5 and 6 positions. The antiproliferative activities of RRDach/SSDach and 56MERR/56MESS/ have already been reported by us in two previous publications [9, 10]. Here we report continued structure–activity relationship studies with coordination complexes containing 2,3-diaminobutanes as the auxiliary ligands.

A typical dose–response curve for a phenanthroline–Pt(II) complex at five serial dilutions, compared with the dose–response curve for cisplatin in the same cell lines, is shown in Fig. 14.3. These results show clearly, that both phenanthroline–Pt(II)
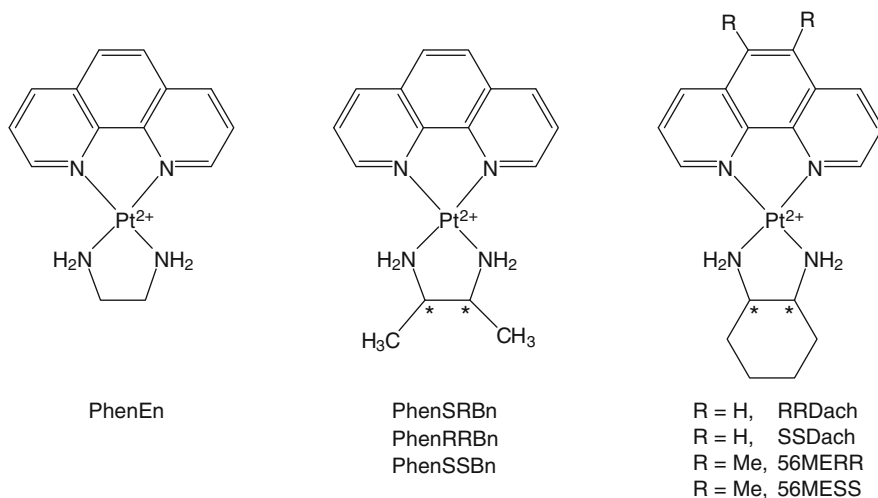
Fig. 14.2 Structures of investigated phenanthroline–Pt(II) complexes. Complexes PhenEn, PhenSRBn, PhenRRBn, PhenSSBn, 56MERR, and 56MESS had chloride as counter ions and racemic-Bn, RRDach and SSDach were perchlorate salts
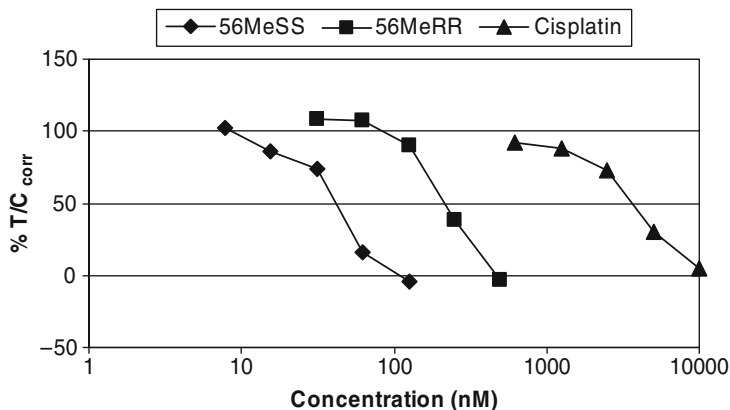
Fig. 14.3 Dose–response curves for the inhibition of cell growth (line A-427) by three Pt coordination complexes. Cells were exposed to substances continuously for 96 h. These results are representative of a single experiment

complexes are considerably more active than cisplatin, and that the *S*,*S*-enantiomer is more active than the *R*,*R*. The curves for the two phenanthroline Pt(II) complexes are somewhat steeper than the one for cisplatin, although the difference is not very great. Toxic compounds generally show very steep curves that drop from 100 to near 0% when the concentration is doubled while anticancer agents like cisplatin generally show broad curves that go from 100 to 0% over 4 or more serial dilutions.

Linear regression analysis with the concentrations of complex that give %T/C$_{corr}$ between 10 and 90% yielded the GI$_{50}$ values of the complexes. Table 14.1 reports the GI$_{50}$ values for a series of phenanthroline–Pt(II) complexes with either En, Bn or Dach as the auxiliary amine ligand. The ethylenediamine complex is the least potent. Substitution of methyl groups at positions 1 and 2 of the ethylenediamine ligand yield the 2,3-diaminobutane ligand, giving rise to complexes with GI$_{50}$ values 25–65 times more potent than PhenEn, depending on the cell line. While there was little difference between the meso and the racemic forms of 2,3-diaminobutane, the enantiomers show a ca. threefold difference in potency with the *R*,*R* enantiomer more active than the *S*,*S* in all four cell lines. The PhenRRBn complex is also considerably more active than cisplatin in all cell lines.

When the Bn ligand was replaced by the Dach ligand as the auxiliary ligand, not only was an increase in potency noted, but interestingly a reversal in the enantioselectivity was observed; the S,S isomer was now more potent than the R,R. (Table 14.1). Furthermore, the difference in potency between the S,S and the R,R enantiomers was considerably greater for the 1,2-diaminocyclohexane compared to the 2,3-diaminobutane complexes. An additional increase in potency could be achieved by substituting methyl groups at the 5 and 6 positions of the phenanthroline ligand, which resulted in a lowering of the GI$_{50}$ values by a factor of fivefold compared to the unsubstituted phenanthroline in the 5637 and A-427 cell lines. Overall, a 500–800-fold increase in antiproliferative potency could be

Table 14.1 Average GI_{50} values ($\mu M \pm$ standard deviation) from 3 to 8 independent determinations, except were otherwise noted

Compounds	Cell lines			
	5637 (bladder)	A-427 (lung)	LCLC-103H (lung)	KYSE 520 (esophagus)
PhenEn	23.7 ± 1.3^{b}	15.1 ± 10.6^{b}	37.4 ± 6.2	43.5 ± 20.2
PhenSRBn	0.75 ± 0.25	1.00 ± 0.24	1.08 ± 0.11	0.96 ± 0.18
PhenRR/SSBn	0.88 ± 0.51	0.78 ± 0.25	1.05 ± 0.25	0.89 ± 0.18
PhenRRBn	0.48 ± 0.17	0.64 ± 0.25	0.78 ± 0.19	0.67 ± 0.08
PhenSSBn	1.01 ± 0.28	1.29 ± 0.26	2.41 ± 0.74	1.83 ± 0.59
RRDach	0.54 ± 0.44^{b}	1.19 ± 0.85^{b}	1.14^{a}	0.69^{a}
SSDach	0.091 ± 0.008^{b}	0.11 ± 0.05^{b}	0.26^{a}	0.16^{a}
56MERR	0.17 ± 0.89^{c}	0.21 ± 0.07^{c}	0.25 ± 0.01^{c}	n.d.
56MESS	0.082 ± 0.029^{c}	0.021 ± 0.011^{c}	0.045 ± 0.013^{c}	n.d.
cisplatin	0.35 ± 0.10^{d}	1.96 ± 0.54^{d}	0.90 ± 0.19^{d}	3.61 ± 1.86^{d}
etoposide	0.54 ± 0.30^{d}	0.127 ± 0.101^{d}	0.42 ± 0.13^{d}	0.413 ± 0.071^{d}

[a] $n = 2$
[b] IG_{50} values are from [9]
[c] GI_{50} values are from [10]
[d] GI_{50} values are from [6]

achieved by making the correct substitutions to the starting En and phenanthroline structure. Compared to cisplatin, the most potent complex, 56MESS, was 10–100-fold more active at inhibiting cancer cell growth. The results illustrate the exquisite structure activity relationships (SAR) present in the class of phenanthroline–Pt(II) complexes.

14.2.2 Effect on the Cell Cycle and Cell Morphologies

Cancer cell growth can be inhibited when the cell cycle is blocked at specific check points. Important check points occur between the four phases of the cell cycle: G1, S, G2 and M. The three most critical phases are the G1/S, S/G2 and G2/M checkpoints. Many anticancer drugs act by arresting the cell cycle specifically at only one of these checkpoints. Flow cytometry, which measures the relative amount of DNA present in a cell, is used to estimate the fraction of cells in the G1, S and G2+M phases of the cycle [11]. Cells in the G1 phase have a normal (diploid) amount of DNA, cells in the G2+M phases have a double amount of DNA and cells in the S phase have an amount of DNA between cells in the G1 and G2+M phases. DNA is typically stained with a fluorescent dye such as propidium iodide; the intensity of the fluorescence is proportional to the amount of DNA in the cell [11, 12].

Figure 14.4 shows a histogram presentation of the cell cycle analysis after HL-60 human leukemia cells were treated with equitoxic concentrations of either etoposide, cisplatin or 56MESSfor 48 h. These concentrations represent an approximate GI_{90} for each of the three agents in the HL-60 cell line. The anticancer drug
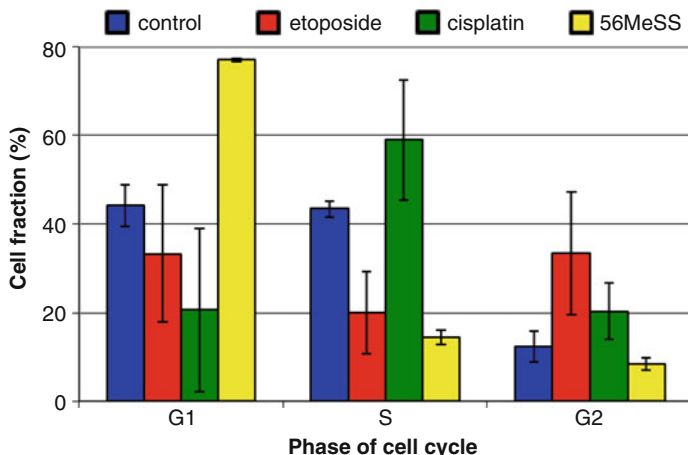
Fig. 14.4 Fraction of HL-60 leukaemia CELLS in either the G1, S or G2+M phase of the cell cycle following exposure to equitoxic concentrations (GI$_{90}$) of etoposide, cisplatin or 56MESS for 48 h. Untreated cells served as a control. Values are averages of three independent determinations and error bars are standard deviations

etoposide, a topoisomerase inhibitor that acts selectively in the S phase of the cell cycle, brings about a decrease in the fraction of cells in the S phase while increasing the fraction of cells in the G2 phase by a comparable amount (Fig. 14.4). This is consistent with a G2 arrest in the cell cycle, as reported earlier [13]. On the other hand, cisplatin, which acts by binding irreversibly to DNA in all phases of the cell cycle, causes a decrease in cells in the G1 phase while the fraction of cells in the S phase increases accordingly (Fig. 14.4). This is consistent with cisplatin causing an arrest in the S phase, as reported earlier [14].

Treatment of HL-60 cells with a GI$_{90}$ concentration (i.e., 2.0 μM) of 56MESS induces a massive accumulation of cells in the G1 phase after 48 h. The G1 cell population increases from 44% in the control to over 77% in the 56MESS treated cells. The S phase cell population decreases to 14% in the treated cells compared to 44% in the control. The G2 phase shows only a small decrease. These changes are consistent with 56MESS causing a G1 arrest. These results indicate that cells damaged by 56MESS are not able to replicate their DNA and halt the cell cycle at the G1/S checkpoint.

Figure 14.5 shows the morphologies of untreated HL-60 cells and compares them with cells treated with equitoxic concentrations of 56MESS or ethoposide. Cells treated with either 56MESS or etoposide show membrane cell shrinkage, blebing and apoptotic bodies, which might indicate apoptosis as the cause of cell death (Fig. 14.5). However, we were not able to detect any activation of caspase 3 in HL-60 cells treated with 56MESS, in contrast to cells treated with etoposide or cisplatin, which brought about strong caspase activation [10]. Thus, another mechanism of programmed cell death independent of caspase activation appears likely for the mode of action of these interesting Pt coordination complexes [8].
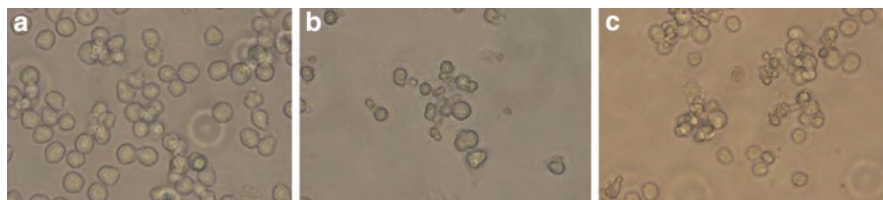
Fig. 14.5 Phase contrast photos (400-fold magnification) of HL-60 cells (**a**) untreated controls, (**b**) exposed to 2.0 µM of etoposide for 24 h (**c**) exposed to 2.0 µM of 56MESS for 24 h

14.3 Experimental Methodologies

14.3.1 Materials

All phenanthroline–Pt(II) complexes were kindly provided by Professor Janice Aldrich-Wright (University of Western Sydney, Australia) and used as received. Cisplatin was obtained from ChemPur (Karlsruhe, Germany) and used as received. Cell culture medium, fetal calf serum (FCS), etoposide, and cell culture grade DMSO and DMF were purchased from Sigma–Aldrich (Taufkirchen, Germany). Cell lines were obtained from the German Collection of Microorganisms and Cell Culture (DSMZ) (Braunschweig, Germany). Water for cell culture work was purified by a Millipore Milli-Q system.

14.3.2 Cytotoxicity Testing

Cells were grown in medium containing 90% RPMI-1640 medium, 10% FCS and supplemented with penicillin G and streptomycin. Cell lines were passaged shortly before confluence in fresh medium. One thousand-fold stock solutions of drugs were prepared in a 1:1 mixture of DMSO/DMF or DMSO/water, except for cisplatin, which was dissolved in DMF only. Stock solutions were stored at −20 °C in the dark. Immediately prior to testing, stock solutions were removed from the refrigerator and serially diluted in DMSO/DMF or DMF (for cisplatin) to concentrations 500-fold the desired concentrations, giving the series of five dilutions.

Testing was done with all cell lines grown in 96 well microtiter plates. Cells were plated out 24 h prior to testing at a density of 1,000 cells/well in 100 µl medium, except for the LCLC-103H cell line, which was plated out at 500 cells/well in 100 µl medium. At the time the substances were added to the cells, one untreated plate for each cell line was removed and this plate served later as the C_{t0} control. The dilution series of substances were diluted 500-fold into culture medium to give concentrations twofold the test concentration. Two or four Pt complexes at

five concentrations per drug and eight or four wells per concentration were tested on each plate. Each concentration was tested in eight or four wells with each plate containing two rows of control wells (i.e., 16 wells).

The method for measuring growth inhibition by crystal violet staining has been described in detail elsewhere [6]. Briefly, after a 96 h incubation with substance, the medium was discarded and replaced for 20 min with a 1% glutaraldehyde-buffer solution to fix the cells. The fixing solution was discarded and the cells stored under PBS at 4 °C until staining. Staining was done for 30 min with a 0.02% solution of crystal violet dissolved in water. After discarding the excess dye and washing the cells for 30 min measured in water, the cell bound dye was re-dissolved in 70% ethanol/water and the optical density measured at $\lambda = 570$ nm with an Anthos 2010 plate reader (Salzburg, Austria) operated with the WinRead software (ver. 2.10). MS-Excel (ver. 2003) was used to calculate the GI_{50} values by linear regression analysis of the log dose versus the corresponding $\%T/C_{corr}$ value [see (14.1)].

14.3.3   Cell Cycle Analysis

For flow cytometry analysis the cell suspension (10^6 cells/ml) was placed in tissue culture flasks. One flask was used as control. Another flask was treated with the GI_{90} value of 2.0 μM for 56MESS, 0.74 μM cisplatin and 0.56 μM etoposide. After incubating for 48 h cells were counted with a Z2 Coulter Counter. One million HL-60 cells were centrifuged for 10 min at 500 g, the supernatant was removed and cell pellets were washed twice with 1 ml phosphate buffered saline (pH 7.4) (PBS). The cells were recentrifuged and the supernatant removed. Cell pellets were resuspended in 500 μl ice cold ethanol (70% v/v) and stored at $-20°C$ overnight. Cells were centrifuged for 10 min, 4,000 U/min at 4°C and the supernatant removed. The cells were resuspended in PBS containing 25 μg/ml propidium iodide and 100 μg/ml RNase, then placed in the dark at RT for 30 min. Samples were analysed on a FACSCalibur flow cytometer (Becton Dickinson) operated with the ModFitLT software (ver. 3.0) with excitation and emission at $\lambda = 488$ and 615 nm, respectively.

14.4   Conclusions

Phenanthroline–Pt(II) complexes represent a potentially new class of non-traditional Pt anticancer agents. These complexes show potent antiproliferative activities in a variety of human solid tumor cell lines as well as leukaemia cell lines. In fact, the *in vitro* potency of these complexes far exceeds that of cisplatin. Interestingly, these complexes appear to be sufficiently stable and do not bind to DNA irreversibly, as cisplatin does. Thus, the mode of action must be very different compared to the traditional *cis*-configured Pt(II) complexes that cross-link DNA.

The complexes also differentiate themselves from cisplatin in their effects on the cell cycle, leading to a G1 arrest, in contrast to the arrest in the S phase by cisplatin. Furthermore, while cell death caused by cisplatin is associated with caspase 3 activation, death by 56MESS is not, even though both complexes cause similar morphological changes in HL-60 cells at GI_{90} concentrations. Another form of programmed cell death other than noticeable apoptosis appears to be operative, like caspases-independent cell death (CICD) [8]. The SAR observed with these new phenanthroline–Pt(II) complexes indicates that specific targets are involved in cytotoxicity. In particular, the enantioselectivity of the various auxiliary diamine ligand is remarkable and strongly suggests that chiral recognition is at the heart of the mode of action of these remarkable coordination complexes. Nevertheless, it is interesting that in spite of the potent *in vitro* antiproliferative activity of these Pt-complexes no *in vivo* antitumour activity was found as reported in Chap. 16.

References

1. Freshney RI. Culture of animal cells. Hoboken, NJ: Wiley-Liss; 2005.
2. Pagé M. In: Cancer Therapeutics: Experimental and Clinical Agents, Ed. Teicher BA. Totowa, NJ: Humana. 1997.
3. Wilson AP. In: Animal Cell Culture: A Practical Approach, Ed. Freshney RI. Oxford: IRL. 1986; p. 183.
4. Boyd MR. In: Cancer Therapeutics: Experimental and Clinical Agents, Ed. Teicher BA. Totowa, NJ: Humana. 1997; p. 23.
5. Saotome K, Morita H, Umeda M. Toxic In Vitro. 1989;3:317.
6. Bracht K, Boubakari R, Grünert P, Bednarski J. Anti-Cancer Drugs. 2006;17:41.
7. Reile H, Birnböck H, Bernhardt G, Spruß T, Schönenberger H. Anal Biochem. 1990;187:262.
8. Blank M, Shiloh Y. Cell Cycle. 2007;6:686.
9. Fisher DM, Bednarski PJ, Grünert R, Turner P, Fenton RR, Aldrich-Wright JR. ChemMedChem. 2007;2:488.
10. Krause-Heuer AM, Grünert R, Kuehne S, Buczkowska M, Wheate NJ, Le Pevelen DD, et al. J Med Chem. 2009;52:5474.
11. Murray A, Hunt T. The cell cycle. Oxford: Oxford University Press; 1993.
12. Morasca L, Erba E. In: Animal Cell Culture: A Practical Approach, Ed. Freshney RI. Oxford: IRL. 1986; p. 125.
13. Facompré M, Wattez N, Kluza J, Lansiaux A, Bailly C. Mol Cell Biol Commun. 2000;4:37.
14. Eastman A. In: Cisplatin: Chemistry and Biochemistry of a Leading Anticancer Drug, Ed. Lippert B. Weinheim: Wiley-VCH. 1999, p. 111.

Chapter 15
Development of Metal Complexes as Potential Antimicrobials

Albert Bolhuis and Adair D. Richards

15.1   Introduction

In 1969, the Surgeon General of the USA said that it was time "to close the book on infectious diseases" on the basis of the prolific success of antibiotics in the previous quarter century that had been widely prescribed [1]. This optimism, whilst seemingly justified at the time, was seriously misjudged, as the intervening 40 years have clearly demonstrated. This is because of the previously disregarded ability of bacteria to genetically mutate to an extent where future generations of bacteria proved immune to the effects of specific antibiotics – hence the need for novel approaches to combating microbial infections is as great as ever.

The rapid development of antibiotic resistance has ensured that resistant strains appear in the clinic very quickly. For example, penicillin resistance was observed in the clinic in 1946, a mere 3 years after it had been licensed for use [2]. Because of this, there is a clear reason to continually develop new types of antibacterial agents that avoid all of the current resistance mechanisms of pathogenic bacteria. By constantly keeping one step ahead of bacterial development, it may be possible to have an appropriate cure for bacterial infections. However, staying ahead of bacterial evolution is proving to be a very challenging task, and whilst huge strides were made in the 1940s and 1950s, with many new types of antibiotics being produced, the last few decades are of note for the very few new types of antibiotic being developed. Research in the area has generally focused and been more successful at adapting existing drugs to counteract the resistance mechanisms evolved by the pathogenic bacteria. This has led to the emergence of multi-drug resistant pathogenic strains such as methicillin-resistant *Staphylococcus aureus* (MRSA) and strains of *Clostridium difficile*, both of which are frequently the cause of nosocomial infections in the developed world and are proving extremely expensive and difficult to treat. For example, the drugs needed to treat multi-drug resistant forms of *Mycobacterium tuberculosis*, which causes tuberculosis, are over

A. Bolhuis (✉)
Department of Pharmacy and Pharmacology, University of Bath, Bath, UK
e-mail: a.bolhuis@bath.ac.uk

100 times more expensive than the first-line drugs used to treat the non-resistant forms [3]. Indeed, the World Health Organization noted that: "*The decline in new antimicrobial development, even if reversed now, is likely to result in the absence of effective therapies for some pathogens within the next ten years*" [3].

15.2   Antibacterial Drug Discovery

Traditionally, there have been four key targets of antibiotics. The first of these is cell wall synthesis, and antibiotics inhibiting this process include penicillin, a β-lactam, and vancomycin, a glycopeptide that is currently a last-line of treatment for MRSA. One reason that inhibition of cell wall synthesis has proved so successful is because of the differences in the cell envelopes between bacterial and human cells. This allows for high doses to be used *in vivo* without affecting cells in the human body. A second target that has been exploited successfully is protein synthesis, which can be inhibited by macrolides, aminoglycosides, and oxazolidinones, all of which bind primarily to peptidyltransferase or sites on the ribosome. The third target is folate synthesis, which can be inhibited with drugs such as sulphonamides. Finally, the fourth key target of antibiotics is the DNA replication and repair mechanisms. This is currently only exploited by the (fluoro)quinolones, which target the topoisomerases DNA gyrase and topoisomerase IV [4], both of which are essential for DNA replication in bacteria. Quinolones cause the formation of irreversible complexes of the topoisomerases with DNA. This in turn causes DNA damage and the generation of DNA breaks, eventually leading to cell death [5]. In particular the newer generations of quinolones are effective on a wide range of Gram-positive and Gram-negative bacteria. Drugs within this class, such as ciprofloxacin, are being used as broad-spectrum antibiotics where exact diagnosis is unclear or multiple-infections are suspected. It was hoped that because of the lack of a transferable mechanism of resistance, clinically resistant strains would not occur. Nevertheless, resistant strains have indeed developed with resistance due to alteration of the targets of these compounds or reduction in drug accumulation through efflux pumps [6], two common methods through which antibiotic resistance is acquired.

There are a number of routes that can be used to identify compounds with antimicrobial activity. In the early days of antibiotic research, Fleming and others thought that the only way to find potential cures for bacterial diseases was through isolation of naturally occurring chemicals from other bacteria, fungi or plants [7]. This has proven to be a very successful way of finding a variety of antibacterial substances, and indeed most antibiotics used clinically today are either isolated from natural sources, or derivatives thereof. A second route of antibiotic discovery is the use of non-natural compounds. Synthetic molecules have been created in laboratories worldwide that have been found, either by accident or by design, to contain significant antibacterial properties. In the past 15 years, research has tended to rely increasingly on automated high-throughput screens of a vast array

of compounds [8]. Typically, a large pharmaceutical firm may screen millions of compounds for efficacy against a particular target, and this can be performed at a rate in excess of 100,000 compounds per week [9]. The library of compounds consists of all the molecules which have been synthesized or isolated for unrelated pharmaceutical projects in the hope that at least one of them will have bacteriostatic (inhibiting bacterial growth) or bactericidal (killing bacteria) properties for a specific strain of bacteria. Synthetic approaches to antibiotics have yielded three important classes of antibiotics: sulpha drugs, quinolones, and the only major breakthrough in antibacterials in the past 30 years, the oxazolidinones [10].

With the advent of the genomic era, it is thought that analysis of bacterial genomes will yield an array of new targets for which molecules can be specifically designed and synthesized. One approach to using genomic data would be to search for essential genes in bacterial pathogens that have no homologues in humans. In various projects numerous potential targets for antibiotics have been identified, but the step from a potential target identification to developing a therapeutic agent is difficult and has not yet been successful [11]. Another approach to the development of novel antibiotics is the concept of using agents that target the bacterial genome itself, i.e., using compounds that bind DNA. This will be explored in more detail in the remainder of this chapter.

15.3   Natural DNA-Binding Antibiotics

DNA-binding compounds have been investigated for several decades and have been synthesized for use as anticancer agents (see also Chaps. 14 and 16). In many cases antibacterial activity has also been reported, albeit that the amount of experimental data presented on this is usually very sparse. At present no DNA-binding compounds are being used in clinical treatments of bacterial infections. One of the problems is the eukaryotic toxicity of some of these compounds, although it is entirely plausible that DNA-binding molecules may be developed that do not have significant effects on eukaryotic cells *in vivo* whilst still promoting their bacteriostatic or bacteriocidal effects.

Binding of compounds to DNA can occur via three primary different modes: external (covalent) association with the phosphate backbone, binding to the minor or major groove, or intercalation between bases [12–14]. This can lead to inhibition of enzymes such as DNA or RNA polymerases [15] and thus affect various processes such as DNA replication, DNA repair, and RNA transcription. If the binding is specific to certain regions of DNA, it is also conceivable that regulation of particular genes is affected.

A number of natural products have been identified that were found to interact with DNA. Many of those were isolated from the Gram-positive soil bacterium *Streptomyces*, the source of so many antibiotics that are currently in clinical use (e.g., streptomycin, vancomycin, and chloramphenicol). Classic studies on those organisms were conducted in the laboratory of Selman Waksman, the 1952 Nobel

laureate (Physiology or Medicine) who coined the term antibiotics. A number of his papers described a simple screening method for antibiotics [16, 17]. Reported in these studies, diluted samples of soil were spread on agar plates, which were then overlaid with a second layer of agar containing pure cultures of *Escherichia coli* or other bacteria. After incubation, the plates were screened for clearing zones in the top layer of agar around single colonies derived from soil bacteria – indicating that these produced one or more antibacterial compounds. From the culture of one soil bacterium, an ether-extractable compound was isolated that was named actinomycin. Over the years a number of actinomycins were isolated, one of which was actinomycin D (isolated from *Streptomyces parvulus*; Fig. 15.1a). This compound, also known as dactinomycin, binds to DNA by intercalation (with a preference for GC-rich sequences) and affects the activity of RNA polymerase, thereby interfering with the elongation of RNA [18]. Because of this strong inhibition of transcription, it is widely used as a tool in molecular biology. Actinomycin D is too toxic to use to treat bacterial infections, but it is used to treat certain types of paediatric cancer such as Wilms' tumour [19] or rhabdomyosarcoma [20].

Another compound produced by a *Streptomyces* species is echinomycin (*Streptomyces echinatus*; Fig. 15.1b) and it was shown that this compound also is a DNA intercalator [21]. Recent studies show that this compound has a very good activity against vancomycin resistant *enterococci* (VRE), with minimal inhibitory concentrations (MIC; see also Sect. 15.5.3) in the range of 0.03–0.25 mg/L for clinical VRE isolates [22]. A problem with echinomycin is, however, its hydrophobicity; more polar derivatives, named YK2000 and YK2005, have been designed, but the increase in polarity (and therefore their solubility) resulted in lower antibacterial activity [22]. Notably, VRE infections are notoriously difficult to treat, so echinomycin and the better of the two derivatives, YK2000 (MIC 0.5–8 mg/L) should still be considered for therapeutic use.

In addition to the DNA intercalators, a number of minor groove binders have also been identified. Examples of these are distamycin and netropsin (Fig. 15.1c) two similarly structured oligopeptides with antibacterial and antiviral activity. Both have a strong preference for AT-rich regions [12]. These substances are currently too toxic for clinical use, but they are useful for biophysical studies into the specificity of minor groove binding [23].

15.4 DNA-Binding Metal Complexes as Antibiotics

Following the line of DNA-binding compounds, we believe it is also possible to develop novel antibiotics through the rational design of synthetic compounds that target DNA. One particular group of compounds that is attractive for that purpose are metal coordination complexes. In these complexes, the metal centre acts as a scaffold, firmly holding a three-dimensional structure of ligands in place so that they can interact with DNA. Metal complexes have great promise in therapeutics as they can have antitumour, antibacterial, antiviral, and antiprotozoal activity. It has

a

b

c
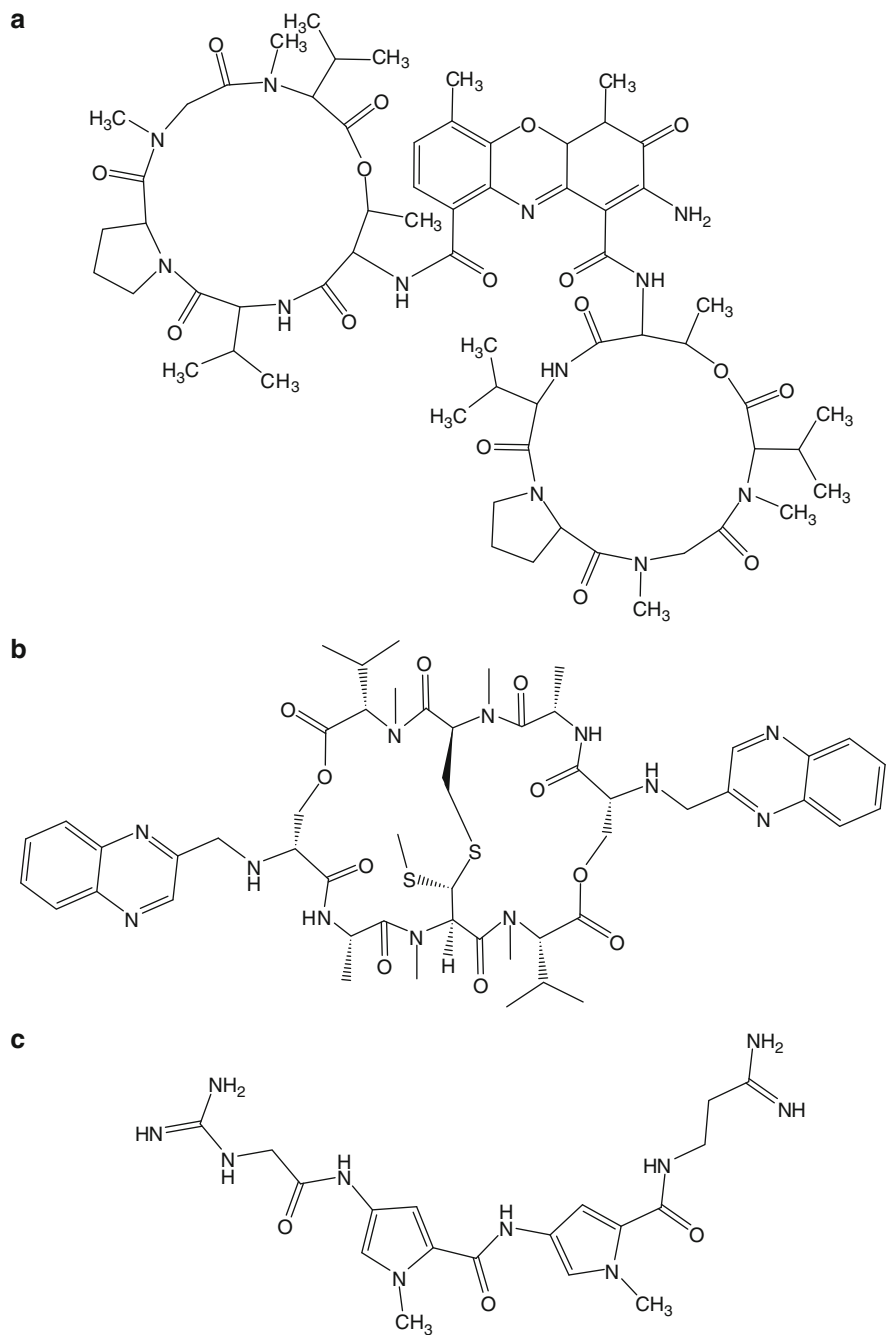
Fig. 15.1 Structures of DNA-binding antibiotics. (**a**), actinomycin D; (**b**), echinomycin; and (**c**), netropsin

been speculated that DNA-binding metallomolecules might be able to be developed into DNA sequence-specific molecules that can then be targeted only to specified cells, but progress on this line of research is only just beginning [24, 25].

Some of the earliest work on the biological activity of metal complexes was done in the laboratory of Francis Dwyer. In the early 1950s, it was shown that an intercalator with the metal ruthenium ($[Ru(phen)_3]^{2+}$, where phen = 1,10-phenanthroline) is active against Gram-positive bacteria [26]. A more detailed and comprehensive study by the same group was later published in the late 1960s which analysed the antimicrobial activity of ruthenium(II) chelates, using 1,10-phenanthroline and 2,2′-bipyridine as ligands. Activity of these complexes was tested against a range of Gram-positive and Gram-negative bacteria, including *M. tuberculosis*, *S. aureus*, *Streptococcus pneumoniae*, *Clostridium perfringens*, *E. coli*, and *Proteus vulgaris*. It was demonstrated that the compounds were more active against the Gram-positive bacteria, with the most sensitive organism being *M. tuberculosis*. Complexes with metals other than Ru(II), such as Ni(II), Fe(II) or Co(II) showed similar activity. Interestingly, progressive methylation of the different compounds increased antibacterial activity, and it was suggested that this was caused either by improved uptake of the compound or improved accumulation at the target sites. Notably, the target sites for these compounds were not determined, so it was unclear whether it was indeed binding to DNA that caused the antibacterial effects. A number of compounds were tested for the treatment of mice or guinea pigs infected with pathogens, but these were found not to be effective when administered intraperitoneally. Notably, however, some of the metal complexes were shown to be useful for the topical treatment of bacterial infections [27].

Another metal with biological activity that is often used is platinum. Early reports in the 1960s showed that electrolysis products from a platinum electrode caused the development of long filaments in *E. coli*, indicating an inhibition of cell division [28]. It was speculated that the product causing the cell-division effect was the ammonium salt of platinum(IV) chloride, $[Pt(NH_4)_2Cl_6]$. However, it was also noticed that fresh preparations of this salt had a significantly lower efficacy than solutions that had remained standing for several days. A later report showed that irradiation of $[Pt(NH_4)_2Cl_6]$ with UV light led to the formation of complexes in which one or more chloride ions were replaced by ammonia molecules [29]. That study demonstrated that it was at low concentrations the *cis* form of the diamminetetrachloroplatinate $[Pt(NH_3)_2Cl_4]$ that inhibited cell division (but not cell growth). The *trans* form, or forms with only one $[Pt(NH_3)Cl_5]^-$ or no ammonia $[PtCl_6]^{2-}$ were not active or were barely active at similar concentrations. Also, *cis* and *trans* forms of diamminedichloroplatinite $[Pt(NH_3)_2Cl_2]$ were synthesised, and again it was the *cis* form that was effective in inhibiting cell division [29]. This form, better known as cisplatin, alongside its derivatives, is currently used clinically to treat various types of cancer. It is known to bind to DNA, leading to a block in DNA replication that in turn leads to a variety of other cellular responses, but it is estimated that in mammalian cells 95% of the drug binds elsewhere – primarily to ribosomes [30]. In *E. coli* cisplatin has been shown to lead to DNA damage [31]. However, a recent proteomics-based study identified 31 proteins in *E. coli* as also

being targets for cisplatin, including proteins involved in DNA repair (e.g., mismatch repair protein MutS and topoisomerase I) and stress-regulated proteins (e.g., the chaperonin GroEL and outer membrane protein OmpA) [32].

In the last two decades or so, most of the research on the biological activity of metal complexes has focussed on their antitumour activity, but in recent years there also appears to be a renewed interest in their potential antibacterial activity. For example, two studies showed that coordination complexes with oxovanadium(IV), some of which were shown to be DNA intercalators in vitro, have good antibacterial activity against a range of Gram-positive and Gram-negative bacteria [33, 34]. Similarly, a number of studies with reference to copper(II) complexes were reported to have antibacterial activity [35, 36]. Some of the studies above identified DNA as a target for these complexes *in vitro* (i.e., using purified DNA), but none showed this also to be the case *in vivo*.

We recently published a study where DNA was shown to be the *in vivo* target [37]. This involved the analysis of the antimicrobial activity of a dinuclear iron (II) supramolecular helicate $[Fe_2L_3]^{4+}$ (where L is (*NE*,*N′E*)-4,4′-methylenebis(*N*-(pyridin-2-ylmethylene)aniline)). $[Fe_2L_3]^{4+}$ is, unusually, a major groove binder (Fig. 15.2). This triple helicate is synthesized as a mixture of two enantiomers (denoted M and P), and it is the M enantiomer in particular that strongly induces coiling of DNA [38]. $[Fe_2L_3]^{4+}$ was shown to have antibacterial activity against both *E. coli* and *Bacillus subtilis*, with the latter being more susceptible. Strikingly, a similar Cu double helicate ($Cu_2L'_2$, where L′ is (*NE*,*N′E*)-4,4′-methylenebis(2,6-diethyl-*N*-(pyridin-2-ylmethylene)aniline)) was not active against those bacteria, which could be due to a differential uptake of the compounds or a different mode of DNA binding [37]. We demonstrated that the Fe helicate reaches its intended target, DNA, *in vivo*, after incubation of *B. subtilis* cells with the compound followed by isolation of chromosomal DNA (Sect. 15.5.5). The Fe helicate was also shown to affect protein synthesis using a method involving radioactive labelling of cells. This effect could be indirect through inhibition of growth because of binding of the compound to DNA, but it is also conceivable the Fe helicate has targets other than DNA and thus inhibits protein synthesis directly [37].

15.5 Methodology to Analyse Antimicrobial Activity

Several techniques can be used to test the efficacy of an antimicrobial compound. In most cases this is done *in vitro*, which means that the effect of a compound is tested on pure cultures of bacteria, which grow in liquid broth or on agar plates. The most commonly used techniques for growth of bacteria and *in vitro* tests on the antimicrobial activity are listed below in Sects. 15.5.1–15.5.4. To enable further development of a drug, it is important to determine its target. In the case of metal intercalators the intended target is DNA, but this needs to be confirmed. Section 15.5.5 therefore gives a procedure for the isolation of chromosomal DNA for bacteria. It should also be noted that it would be rare for a complex to have only

Fig. 15.2 $[Fe_2L_3]^{4+}$ (in *purple*) overlaid on the structure of DNA (in the major groove). The two iron ions are shown as *red spheres*
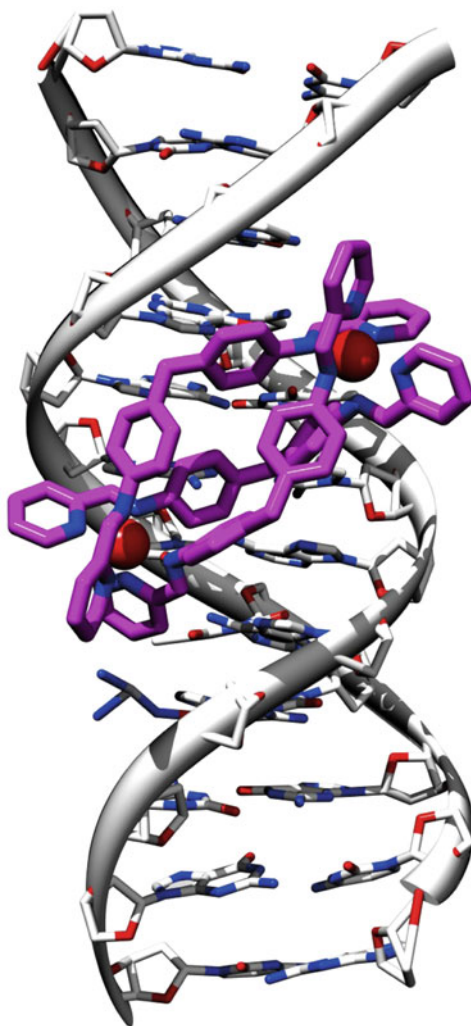
one target. As described above the amount of complex reaching its intended target can be less than 5% in clinically successful drugs. Finally, the efficacy of a drug is ideally also tested in an infection model, which is briefly discussed in Sect. 15.5.6.

15.5.1 Growth Media

A number of different tests can be used to determine the antimicrobial activity of a compound. Before choosing the methods to be used to test the efficacy of the agent,

the growth medium for the bacteria has to be considered. In several cases a general growth medium will suffice. These can include for instance Lysogeny broth (LB, better known as Luria–Bertani broth, containing 1% tryptone, 0.5% yeast extract, and 0.5% NaCl), or nutrient broth (0.3% beef extract, 0.5% peptone). These media can also be purchased as ready-made powders that only need addition of water. For solid media, 1.5% agar should be included.

In past studies it has been shown that there is some effect of the growth medium on the levels of antibiotic resistance [39]. Thus it was recognised that some form of standardisation was important, in particular with reference to various national and international screening programs to monitor antibiotic resistance in clinical isolates. The two media most commonly used to test antibiotic sensitivity of clinical isolates are Isosensitest broth (recommended by the British Society for Antimicrobial Chemotherapy [40]) or Mueller–Hinton broth, both of which can be obtained as ready-made powders from companies such as Oxoid Ltd.

A challenge that may have to be overcome is the solubility of the antibacterial compound to be tested in the growth medium. Traditional growth media contain many charged compounds that could interact with positively charged metal complexes. This was observed with the aforementioned Fe-helicate, which precipitates in LB medium, particularly under gentle centrifugation [37]. For that reason we designed a new growth medium (RB medium) that still promoted growth of organisms such as $E.$ $coli$ and $B.$ $subtilis$, but was reduced in negatively charged molecules [37]. The medium contains 20 g/L glucose, 10 mM NH_4 SO_4, 7 μM $CaCl_2$, 0.5 μM $MnCl_2$, 0.01 μM $ZnCl_2$, 0.05 μM $FeCl_3$, 0.1% casamino acids, 10 mM potassium phosphate at pH 7. The last two ingredients were added separately, with thorough mixing after each addition. For strains deficient in specific components (e.g., amino acids, vitamins), additional factors may have to been added.

Various organisms can be tested for efficacy of antimicrobials. For initial studies non-pathogenic bacteria, such as $E.$ $coli$ K12 and $B.$ $subtilis$, can be used. These two organisms are the best-studied Gram-negative and Gram-positive bacteria, respectively. They are safe to work with, and are good model organisms for the extensive range of pathogens available for testing. This could include opportunistic pathogens that are a major cause for nosocomial infections, such as $S.$ $aureus$, $Enterococcus$ $faecalis$, and $Pseudomonas$ $aeruginosa$. Some of these are also well known for their ability to acquire resistance against various antibiotics, with the best-known examples being MRSA and VRE. Other bacteria such as $C.$ $difficile$ can also be considered, but the latter is more difficult to culture as it is strictly anaerobic.

15.5.2 Disc Diffusion Susceptibility

One common method of analysing susceptibility to antibiotics is the so-called disc diffusion testing, which is also known as Kirby–Bauer testing [41]. This method makes use of small paper discs that are impregnated with specific amount of an

Fig. 15.3 Disc diffusion test.
Here, an isolate of the
opportunistic pathogen
Enterococcus faecium was
spread on an agar plate. Three
discs were then placed on the
plate. The discs contained
10 mg antibiotic:
erythromycin (*top*),
chloramphenicol (*bottom*)
and ampicillin (*right*). Next,
the plate was incubated for
18 h at 37 °C. The particular
strain shown here is sensitive
to erythromycin and
chloramphenicol, and
resistant to ampicillin

antimicrobial agent. Such discs are commercially available with several types of
antibiotics at specific concentrations. For testing novel antimicrobials, cheap home-
made discs (~6 mm) can be prepared very simply using a common hole-punch
(available in book or stationary shops) and good quality chromatography paper such
as Whatman 3MM. These discs need to be sterilised by autoclaving (e.g., packed in
a small container or wrapped in aluminium foil). Next, the discs can be impregnated
with a specific amount of the antimicrobial to be tested.

To measure disk susceptibility, Petri dishes with solid medium have to be
prepared using one of the media above supplemented with 1.5% agar. A suspension
of cells is spread on these plates. After this, a disc with the absorbed antimicrobial
is applied on top of the agar, and then the plate is incubated overnight at the
appropriate temperature. If the compound is active against the plated bacteria, a
clear zone around the disc will be visible with the size of the clearing zone giving an
indication of the efficacy of the compound (Fig. 15.3). For consistent results, the
number of cells that have to be plated should give semi-confluent growth [42].
Confluent growth would lead to smaller clearing zones, while plating out too few
cells could make it more difficult to see the clearing zones properly.

15.5.3   Minimal Inhibitory Concentration

Another important technique to determine efficacy of antimicrobials is the determi-
nation of the minimal inhibitory concentration (MIC) and the minimal bacterio-
cidal concentration (MBC). It is these measures that are most frequently cited in
the literature. In this technique, growth medium mixed with different concentra-
tions of the antimicrobial (usually doubling concentrations in a range from e.g.,
0.25–128 mg/L are inoculated with a specific number of bacterial cells). These can
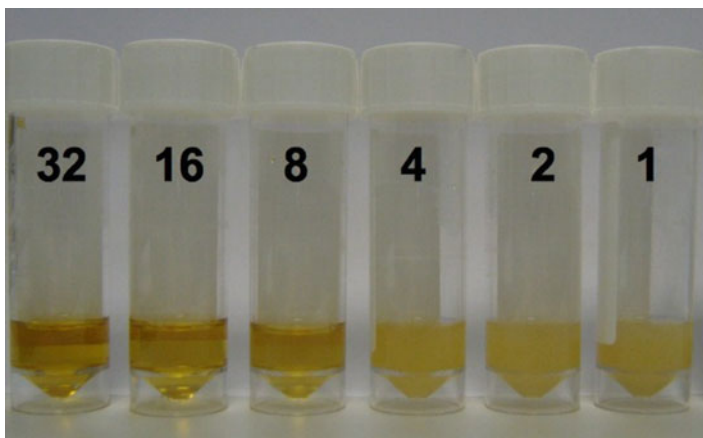
Fig. 15.4 Example of a macrobroth dilution test to determine the minimal inhibitory concentration of an antimicrobial agent, with concentrations indicated in milligram per litre. The agent is added to 5 mL cultures in doubling concentrations, in a range from, for example, 0.5–128 mg/L. In the example given here there is still a bit of turbidity in the tube with 8 mg/L (although difficult to see from the image) so in this case the minimal inhibitory concentration is 16 mg/L

be grown on a 5 mL scale in tubes (macrodilution) or in 96-well plates on a 200 μL scale (microdilution). The cultures are then incubated for 18–20 h, and the tube or well with the lowest concentration of antimicrobial compound that remains visibly clear defines the MIC (Fig. 15.4). Again, for consistent results it is important to start with a specific number of bacteria which has to be in between 10^5 and 10^6 cells/mL [40].

To determine whether an antimicrobial is bacteriostatic or bacteriocidal the MBC is determined. From the MIC experiment above, samples from the tubes or wells that did remain clear are subcultured in liquid broth or on agar plates that is free of antimicrobials and incubated for 18–20 h; the MBC then is defined as the lowest concentration of the compound in which no growth is observed after sub-culturing.

MICs can also be determined using agar plates instead of liquid cultures. In that case, agar plates with differing concentrations of the compound are prepared, and an inoculum containing 10^4 cells is spotted on the plates (e.g., 10 μL of a suspension containing 10^6 cells/mL), followed by incubation. The MIC is defined as the lowest concentration of antibiotic where no growth is observed after 18 h of incubation at the appropriate temperature.

15.5.4 Time-Dependent Killing of Bacteria

A key factor in the treatment of bacterial infections, particularly serious secondary nosocomial infections, is the time it takes for the treatment to work. The majority of

multi-drug resistant infections occur as secondary infections, often in hospitals, to patients who are already unwell [43]. One factor that can play a role is how rapidly an antimicrobial is able to kill a population of cells. Initial experiments into this can be performed by measuring the rate of inactivation of bacterial cells (in a liquid culture) by an antimicrobial agent. Starting with a known number of cells (e.g., 1×10^5 cells/mL), samples should be taken at different time points and then the number of viable cells should be determined by plating serial dilutions of the samples. When taking samples, it is important to stop the action of the antimicrobial agent, as any carry-over of the agent can affect the results – cells could continue to be killed if some of the agent is still present after taking the samples. There are three basic methods to stop the action of an antimicrobial agent [44]. Firstly, the concentration of the agent can be reduced by dilution. Secondly, the agent can be removed by membrane filtration or centrifugation of cells, followed by resuspension of the cells in fresh medium. The third method involves inactivating the antimicrobial using various methods depending on the type of antimicrobial. In some cases inactivation can be done enzymatically, such as β-lactamases that inactivate penicillins, while other compounds can be inactivated with surfactants such as polyoxyethylenesorbitane monooleate (Tween 80) and L-α-phosphatidylcholine (L-α-lecithin) [44]; which inactivator is suitable needs to be tested empirically.

15.5.5 Isolation of Chromosomal DNA

When using DNA-binding metal complexes as an antimicrobial agent it is also of importance to establish that they do indeed interact with their DNA target, although if they are effective at killing bacteria but not eukaryotic cells the mode of action may not be of primary concern from a pragmatic point of view. Certainly many drugs on the market, not least the aforementioned cisplatin, were used clinically before the mode of action was fully understood. However, if the target is known then it provides a better framework for the synthesis of derivatives with, for instance, improved efficacy. To establish whether a complex binds DNA, chromosomal DNA can be isolated, followed by detection of the metal complex. How the compound is detected depends of course on the nature of the complex, but several metal complexes have a distinctive colour and/or fluorescence and thus can be detected by spectrometry.

To test binding to chromosomal DNA, cells from a 10 mL overnight culture should be mixed with the compound and incubated for a specific time. Next, excess compound has to be removed. This can be done by collecting the cells through centrifugation for 15 min at 8,000 g, resuspending in buffer (e.g., 10 mM Tris–HCl at pH 8), and repeating the centrifugation step. The next steps depend somewhat on the bacterial strains used, but the following will work for many types of cells including *E. coli* and *B. subtilis*. Bacteria with very tough cell walls (such as *enterococci*) may require modifications of this protocol.

Cells from a 10 mL culture that have been washed should be resuspended in 1 mL 10 mM Tris–HCl at pH 8 supplemented with 0.5 mg/mL lysozyme. This has to be incubated for 30 min at room temperature (Gram-negative bacteria) or 37 °C (Gram-positive bacteria) to digest the cell walls. Next, 0.5% SDS (from a 10% stock solution) and 0.2 mg/mL proteinase K (from a 20 mg/mL stock solution) are added. After gently mixing, this is then incubated for 1 h at 50–55 °C. At this stage cells should lyse, with the solution becoming clearer accompanied with a marked increase in viscosity because of the release of chromosomal DNA. Chromosomal DNA can then be precipitated by adding 10% the volume of 5 M NaCl and, after gently mixing, 60% volume of isopropanol (or two volumes of ethanol). With gentle mixing the DNA will then precipitate. The DNA can be collected by centrifugation (3 min, 8,000 g) and washed with 70% ethanol. Finally, the pellet can be dried at room temperature and resuspended in 1 mL 10 mM Tris–HCl at pH 8. Presence of the metal complex can than be determined by atomic absorption spectrometry or another suitable technique. It needs to be verified that the compound remains soluble throughout the procedure, and that it is only the compound bound to DNA that is precipitated.

15.5.6 In Vivo *Models of Infection*

It is important to realise that the antimicrobial activity is initially always determined *in vitro*, i.e., in liquid cultures or on agar plates. This may not be a good reflection of a bacterial infection, and the next stage should therefore be to test the antimicrobial activity in an infection model. Cultures of mammalian cells could be used for this purpose, but these lack the complexity of whole animal models [45]. Mice are commonly used for the modelling of infectious disease, such as in the study of the efficacy of linezolid on *S. aureus* infections [46]. The use of rodents does have disadvantages in terms of the ethical and administrative burden, and for that reason a number of alternative non-mammalian models have been developed. These include the amoeba *Dictyostelium discoideum*, the nematode *Caenorhabditis elegans*, the insect *Drosophila melanogaster* (fruit fly), and the fish *Danio rerio* (zebrafish). Note, however, that before any new drug can go into clinical trials their toxicity has to be tested in animal models such as rodents and dogs, but use of alternative non-mammalian models can help in minimise such testing.

One interesting model is that of the fruit fly. The genetics of this organism have been studied for nearly 100 years and are thus very well characterised [47]. Moreover, 77% of proteins involved in human diseases are also conserved in *D. melanogaster* [48], indicating the usefulness of the fruit fly as a model for these diseases. The fruit fly was also shown to be a good model system for infections with bacterial pathogens such as *Vibrio cholerae* (which causes cholera) and *S. aureus* [49, 50]. These bacteria cause lethal infections in *D. melanogaster* that are treatable with antibiotics or other drugs. Probably not surprisingly, differences between mammals and the fruit fly in response to infection were also found. For example,

whereas cholera toxin alone is sufficient to cause disease in humans, the toxin was only lethal in fruit flies when ingested together with pathogenic *V. cholerae* isolates [49].

A second example is that of *C. elegans*. This nematode feeds on bacteria – in the laboratory it is normally grown on a harmless strain of *E. coli*. However, the nematodes die when their diet is switched to certain pathogenic strains, including *E. faecalis*, *P. aeruginosa*, and *S. aureus*. In one study this was used to screen over 7,000 compounds; 25 compounds were identified that promoted survival of *C. elegans* [51]. Interestingly, the *in vivo* efficacy of several of these was significantly higher than their *in vitro* efficacy. Different explanations could be given for this observation. Firstly, some compounds may have been prodrugs that had to be converted by the host into an active compound (which would not occur in a pure bacterial culture). Secondly, some compounds may have affected virulence without affecting growth of bacteria. Thirdly, some of the compounds may have stimulated host immunity. Whichever explanation is correct, the activity of these compounds would never have been found with the traditional *in vitro* screens, clearly demonstrating the value of an infection model for antibiotics screening. Another important advantage of a live-animal screen is that it not only tests for antimicrobial activity, but also for lack of cytotoxicity of the compound against the infection host.

15.6 Concluding Remarks

There is a continuing need for finding novel antimicrobials as there are more and more biological isolates that are resistant against conventional antibiotics. DNA is a target of interest; although used for many years in anticancer therapy, DNA-binding compounds such as metallointercalators have not yet been used to treat bacterial infections clinically. For several compounds antibacterial activity has been reported, but there is a lack of understanding on the mode of action of these compounds. For example, antibacterial activity of the aforementioned cisplatin was reported over 40 years ago, while its targets in *E. coli* were shown only very recently [32]. Strikingly, although cisplatin is a DNA binding compound, several protein targets were identified. The fact that it has several targets may even be an advantage, as it could be more difficult for bacteria to develop resistance. As far as we are aware, bacteria resistant to cisplatin have indeed not been reported, with the exception of hyper-sensitive *E. coli* mutants that can revert, through secondary-site mutations, to normal wild-type resistance [52]. Early studies indicated no development of significant resistance to phenantroline metal chelates by various microorganisms [27], while we have been unable to isolate *B. subtilis* strains resistant to the Fe-helicate (Richards and Bolhuis, unpublished results). We could therefore speculate that it could be difficult for bacteria to develop resistance against DNA-binding complexes for two different reasons. Firstly, having a target as general as DNA could prevent resistance developing through mutation because of the lack of a specific target. Secondly, if metal complexes have, in addition to DNA several other

targets such as RNA or proteins, it may also be difficult to acquire resistance. In either case, resistance could only develop through preventing the uptake of the compounds, but this again is an area on which hardly anything is known. It is therefore clear that future studies into the antimicrobial activity of DNA-binding metal complexes need to focus on uptake by bacterial cells and the mode of action. A pressing need for novel antibacterials has been demonstrated worldwide in recent years with the rise of multi-drug resistant pathogens and we believe that the development of DNA-binding antibiotics will be a key part of the solution.

References

1. Franklin TJ, Snow GA. Biochemistry and molecular biology of antimicrobial drug action. 6th ed. Heidelberg: Springer; 2005.
2. Palumbi SR. Science. 2001;293:1786.
3. W.H. Organization, WHO/CDS/CSR/DRS/2001.2 ed., WHO, Geneva, 2001.
4. Bradbury BJ, Pucci MJ. Curr Opin Pharmacol. 2008;8:574.
5. Hooper DC. Clin Infect Dis. 2000;31 Suppl 2:S24.
6. Rattan A. Natl Med J India. 1999;12:162.
7. Axelsen PH. Essentials of antimicrobial pharmacology. NJ: Humana; 2002.
8. Atkinson Jr AJ, Abernethy DR, Daniels CE, Dedrick RL, Markey SP. Principles of clinical pharmacology. 2nd ed. New York: Academic; 2007.
9. Walsh C. Antibiotics:actions, origines, resistance. Washington, DC: ASM; 2003.
10. Wilcox MH. Expert Opin Pharmacother. 2005;6:2315.
11. Coates AR, Hu Y. Br J Pharmacol. 2007;152:1147.
12. Baraldi PG, Bovero A, Fruttarolo F, Preti D, Tabrizi MA, Pavani MG, et al. Med Res Rev. 2004;24:475.
13. Pindur U, Jansen M, Lemster T. Curr Med Chem. 2005;12:2805.
14. Richards AD, Rodger A. Chem Soc Rev. 2007;36:471.
15. Smolina IV, Demidov VV, Frank-Kamenetskii MD. J Mol Biol. 2003;326:1113.
16. Waksman SA, Woodruff HB. Proc Soc Exp Biol. 1940;45:609.
17. Waksman SA, Woodruff HB. J Bacteriol. 1940;40:581.
18. Sobell HM. Proc Natl Acad Sci USA. 1985;82:5328.
19. Mehta MP, Bastin KT, Wiersma SR. Drugs. 1991;42:766.
20. Walterhouse D, Watson A. Paediatr Drugs. 2007;9:391.
21. Waring MJ, Wakelin LP. Nature. 1974;252:653.
22. Kim JB, Lee GS, Kim YB, Kim SK, Kim YH. Int J Antimicrob Agents. 2004;24:613.
23. Freyer MW, Buscaglia R, Nguyen B, Wilson WD, Lewis EA. Anal Biochem. 2006;355:259.
24. Hannon MJ, Rodger A. Pharma Vis. 2002;autumn issue:14.
25. Nordell P, Westerlund F, Wilhelmsson LM, Nordén B, Lincoln P. Angew Chem Int Ed Engl. 2007;46:2203.
26. Dwyer FP, Gyarfas EC, Rogers WP, Koch JH. Nature. 1952;170:190.
27. Dwyer FP, Reid IK, Shulman A, Laycock GM, Dixson S. Aust J Exp Biol Med Sci. 1969;47:203.
28. Rosenberg B, Vancamp L, Krigas T. Nature. 1965;205:698.
29. Rosenberg B, Van Camp L, Grimley EB, Thomson AJ. J Biol Chem. 1967;242:1347.
30. Boulikas T, Vougiouka M. Oncol Rep. 2003;10:1663.
31. Fram RJ, Cusick PS, Wilson JM, Marinus MG. Mol Pharmacol. 1985;28:51.
32. Will J, Sheldrick WS, Wolters D. J Biol Inorg Chem. 2008;13:421.
33. Panchal PK, Parekh HM, Pansuriya PB, Patel MN. J Enzyme Inhib Med Chem. 2006;21:203.

34. Patel MN, Chhasatia MR, Patel SH, Bariya HS, Thakkar VR. J Enzyme Inhib Med Chem. 2009;24:715.
35. Kumar RS, Arunachalam S, Periasamy VS, Preethy CP, Riyasdeen A, Akbarsha MA. Eur J Med Chem. 2008;43:2082.
36. Song YL, Li YT, Wu ZY. J Inorg Biochem. 2008;102:1691.
37. Richards AD, Rodger A, Hannon MJ, Bolhuis A. Int J Antimicrob Agents. 2009;33:469.
38. Meistermann I, Moreno V, Prieto MJ, Moldrheim E, Sletten E, Khalid S, et al. Proc Natl Acad Sci USA. 2002;99:5069.
39. Raymond EA, Traub WH. Appl Microbiol. 1971;21:192.
40. Andrews JM. J Antimicrob Chemother. 2001;48 Suppl 1:5.
41. Bauer AW, Roberts Jr CE, Kirby WM. Antibiot Annu. 1959;7:574.
42. Andrews JM. J Antimicrob Chemother. 2008;62:256.
43. Struelens MJ. BMJ. 1998;317:652.
44. Russell AD, Ahonkhai I, Rogers DT. J Appl Bacteriol. 1979;46:207.
45. Wiles S, Hanage WP, Frankel G, Robertson B. Nat Rev Microbiol. 2006;4:307.
46. Gill CJ, Abruzzo GK, Flattery AM, Misura AS, Bartizal K, Hickey EJ. Antimicrob Agents Chemother. 2007;51:3434.
47. Rubin GM, Lewis EB. Science. 2000;287:2216.
48. Carroll PM, Dougherty B, Ross-Macdonald P, Browman K, FitzGerald K. Pharmacol Ther. 2003;99:183.
49. Blow NS, Salomon RN, Garrity K, Reveillaud I, Kopin A, Jackson FR, et al. PLoS Pathog. 2005;1:e8.
50. Needham AJ, Kibart M, Crossley H, Ingham PW, Foster SJ. Microbiology. 2004;150:2347.
51. Moy TI, Ball AR, Anklesaria Z, Casadei G, Lewis K, Ausubel FM. Proc Natl Acad Sci USA. 2006;103:10414.
52. Massey A, Offman J, Macpherson P, Karran P. DNA Repair (Amst). 2003;2:73.

Chapter 16
Animal Testing

Johnny Moretto, Bruno Chauffert, and Florence Bouyer

16.1 General Considerations for Animal Testing

The development of a new anticancer drug is a long, complex and multistep process which is supervised by regulatory authorities from the different countries all around the world [1]. Application of a new drug for admission to the market is supported by preclinical and clinical data, both including the determination of pharmacodynamics, toxicity, antitumour activity, therapeutic index, etc. As preclinical studies are associated with high cost, optimization of animal experiments is crucial for the overall development of a new anticancer agent. Moreover, *in vivo* efficacy studies remain a determinant panel for advancement of agents to human trials and thus, require cautious design and interpretation from experimental and ethical point of views.

Preclinical animal testings arise in the "life" of a new molecule when many sensitive, specific, and accurate methods have already been developed to assay its chemosensitivity. Several *in vitro* clonogenic and proliferation assays, cell metabolic activity assays, molecular assays to monitor expression of markers for responsiveness or resistance in naïve and relapsing tumours, and for induction of apoptosis have been achieved [2]. Animal studies include *in vivo* tumour growth and survival assays in metastatic and orthotopic models, *in vivo* imaging assays [3] and early pharmacokinetic evaluation by appropriate screening methods [4]. They play a pivotal role in correlating *in vitro* response, to predicting (at least partially) clinical outcomes [5, 6] for a particular agent, and tailoring chemotherapy regimens to individual patients.

This chapter will deal with the requirements for *in vivo* preclinical studies conducted in rodents, mouse mostly and rat, as they are usually the first type of animals used to assess *in vivo* behaviour of anticancer drugs. Different types of rodent models of cancer will be briefly discussed, focusing on their principle advantages and limits. Then, considerations on how to design and evaluate animal

F. Bouyer (✉)
Equipe Avenir, INSERM, University of Burgundy, UMR 866 Dijon, France
e-mail: florence.bouyer@u-bourgogne.fr

testing and assessing anticancer drug effects will be presented. However, general statements regarding tests of anticancer drugs on rodents are provided by guidelines from regulatory authorities. To finish, examples of anticancer drug assessments will be described in the area of platinum derivatives.

16.1.1   A Brief Discussion on In Vivo Evaluation of Anticancer Drugs

Animal models represent a crucial and necessary basis for the development and testing of new drugs. Interestingly, their development has been closely related to the history of cancer chemotherapy, and can be classified into three main periods.

Before the 1970s, the field of chemotherapy was the most efficient for the treatment of leukemia and lymphoma and many therapeutic successes arose from the treatment of childhood-related diseases. The development of the first models of cancer arose at that time: the L1210 model of acute lymphocytic leukemia was followed by others such as P388 leukemia. Their success relies on their ability to lay the foundations for advancement of clinical experimentation in cancer treatment [7], demonstrating that:

1. An inverse relationship exists between the total charge of leukemic cells in the body and the ability of chemotherapy to cure cancer
2. A dose–response relationship exists whatever the class of anticancer drug used; and was represented by the log-kill model which quantified the relationship between tumour growth and therapeutic regression
3. A given dose of a given drug always kills the same percentage (and not the same number) of leukemic cells originating from different sized populations of leukemia cells

The second step in cancer chemotherapy was marked by its application to the treatment of solid tumours. Despite the development of several classes of anticancer drugs, this era was also characterized by the reality of clinical failure to cure cancer and the occurrence of drug resistance. Many solid-tumour models were developed in a preclinical setting but even given the same histological type of cancer this model was not necessarily able to predict the clinical outcome. Several reasons may explain these differences: the lack of common etiology between tumour models and human disease, even if tumour cells are selected to match the human disease. For example, many rodent models developed from chemically-induced primary tumours (mainly alkylating used as mutagenic agents), differ from the "spontaneous" emergence of human cancer whose inducting factors are less characterized and multiple; the lack of data concerning advanced disease in models; the frequent differences in biochemistry [8] and drug exposure among hosts.

More recently, cancer chemotherapy has embraced new therapeutic approaches called "targeted-directed cancer therapy". Gene-targeting therapy relies on the concept

of developing drugs that affect tumour cells, specifically, avoiding most of the general toxic effects of classical anticancer agents. Such a strategy has required the development of a new generation of animal models, already known as "transgenic models", in which one or several genes are modulated. Transgenic modeling involves a primary step of target validation to demonstrate whether:

1. The target is linked to the disease, and the frequency of this association
2. The target is mechanistically linked to the disease
3. The pharmaco-modulation of the target enables a change in the phenotype of the disease

16.1.2   Animal Models of Cancer

This part will focus on rodent models of solid cancers, and will briefly review some principle features, advantages and limits, and uses for therapeutic experiments [9, 10]. Three main types of animal models have been distinguished: syngeneic rodent tumours, tumour xenograft in nude mice and transgenic mouse models of cancer. Every model has been engineered to duplicate human disease as closely as possible, and or to help the clinician provide more effective treatment for cancer patients [11, 12].

16.1.2.1   Animal Transplantable Syngeneic Rodent Tumours

Syngeneic models are defined as models in which a tumour of mouse (or rat) origin is transplanted into another mouse (or a rat). They were the "quasi-exclusive" models used in the development of most classical antitumour agents [13–15] until the development of nude mice. The most frequently used murine models were the leukemias L1210 and P388, the melanoma B16, and Lewis Lung Cancer (LLC). They were adequate tools to study alkylating agents, and some other DNA interacting drugs [14, 16, 17]. Nowadays, these models remain particularly valuable for studying biological response modifiers or certain agents that need to be evaluated in a syngeneic environment, such as those targeting distant organ metastasis [13].

Their main advantage is compatibility with the host animal, which allowed a level of reproducibility that cannot be reached in immune-deficient animal models. They allow the confirmation of a result obtained in a human tumour-xenograft model in a model in which the animal has a "healthy" immune competent system.

One of their major limitations is the restricted spectrum of transplantable and autochthonous murine tumour models (e.g., melanoma, colon, breast, bladder or lung carcinomas). In addition, most models are based on high-dose regimens of a single genotoxic carcinogen which can induce large-scale genetic damage in a random fashion [18], but that do not generally reflect the gene–environment interactions underlying the pathogenesis of cancer in humans.

16.1.2.2   Human Tumour Xenografts in Nude Mice

Xenograft models involve transplantation of a tumour from a heterologous species (e.g., human) into a mouse. Since the first success obtained with the xenografting of a human tumour into nude mice in 1969, immunodeficient animals became extensively used all over the world. In oncology, their role has continuously increased, and athymic nude mice are a host for many human solid-tumour xenograft [19]. These mice are now extensively used in the development of potential anticancer drugs, new antineoplastic treatment modalities, and studies of tumour biology [14, 15, 20–25]. Moreover, mice with severe combined immunodeficiency (SCID) have enlarged the spectrum of possible applications in cancer research and enabled engraftments of human tumours that were previously difficult to explain, such as those of the Hematopoietic system [26].

Their use is highly recommended by regulatory agencies such as the EMEA (European Agency for the Evaluation of Medicinal products) in the "note for guidance on the preclinical evaluation of anticancer medicinal products" (http://www.eudora.org/emea.html). Xenograft tumours could be classified into two types according to their origin:

– Either from human cultured tumour cells, which generally allowed a higher rate of takes when inoculated into nude mice, but displayed an undifferentiated histology and as a result, are very resistant to most of the standard agents [17]. This is most likely a result of the high selection pressure *in vitro* during long-term culture resulting in aggressive subclones
– Or from human solid tumours of the same histological type transplanted directly from patients. They have demonstrated a high correlation of drug response and drug resistance compared to that in the clinic [27, 28]. This allows for preselection of responsive tumour types in follow-up studies. Human tumour xenografts are the most relevant models to demonstrate that a new drug exhibits a differential selectivity against human tumours compared to the most sensitive normal tissues, because the patient-derived tumours grow as a solid tumour and they develop a stroma and vasculature, as well as central necrosis. Moreover, the tumour-xenograft architecture, the cell morphology and molecular characteristics mirror the original patient cancers, in most cases

16.1.2.3   Transgenic Mouse Models of Cancer

In the 1990s, new development of molecular-directed treatment strategies [29] led to the use of specifically bred transgenic mouse models which are "disease-oriented" and "target-characterized" [30]. Transgenic models were generated by genetically altering the mouse genome to increase tumour occurrence. Animals with specific genetic susceptibilities for tumour development [31] were designed, especially with carcinogenesis-related genes over-expressed or inactivated (e.g., the p53 tumour-suppressor gene, the adenomatous polyposis coli (APC) gene, the

human papillomavirus early genes, etc.). They are useful tools to study the carcinogenesis process [32], and to test preventive strategies that can offset specific and highly relevant genetic susceptibilities to cancer in humans. Many large-scale programs of mouse mutagenesis have been developed since 1997, and have led to the establishment of knock-out and conditional mouse strains for all mouse genes at the International Knockout Mouse Consortium in 2007 [33]. However, transgenic mice are high cost, have a limited availability, and cannot cover all human cancers. For these reasons, they were not suitable for large-scale drug testing.

16.2 Considerations When Designing Animal Tests

16.2.1 Global Strategy

An animal model of cancer is designed to fulfill at least one of these three objectives: cure cancer, prevent cancer or contribute to understanding the carcinogenesis process. The most suitable animal model (e.g., species, strain and tumour type) should be chosen after consideration of *in vitro* sensitivity profiles of the test agent against a panel of different tumour cell lines, the properties of the anticancer drug tested, and the proposed therapeutic indications.

In this section, general statements regarding tests of anticancer drugs in rodents will be discussed, how to organize and how to evaluate these tests will also be examined [34–37]. Animal testing should be designed and evaluated in such a way that a positive therapeutic effect in rodents should accurately predict a positive therapeutic effect in cancer patients.

Whatever the model used, critical factors have to be applied to reduce the potential for false-positive conclusions and minimize the risks of false-negative results. They include selecting an optimal preclinical efficacy model and developing an appropriate experimental design, which includes defining the adequate control, treatment protocols, group sizes and randomization protocols that will provide statistically valuable data. All these parameters critically influence the final conclusions of the study [9], namely the under- or over-estimation of the drug efficacy.

16.2.2 Parameters Influencing the Design of In Vivo Testing

They will be artificially classified into three categories: those related to the choice of the animal model, those related to the experimental protocol, and those determining a good evaluation of collected data.

16.2.2.1   Determination of the Relevant Animal Model

Selection of the tumour model represents the first step in preclinical *in vivo* efficacy evaluation, and involves not only the determination of the type of animal model, but also parameters interfering with tumour growth, such as the type of tumour cells, the number of cells to inoculate, the route of administration and the progression of the disease (e.g., metastases).

Type of Animal Model

Two situations could be distinguished according to the type of anticancer drug evaluated. For "classical" anticancer drugs (not devised in accordance with a principle of drug specificity) [9, 38, 39], two types of animal models are usually brought face to face to evaluate their *in vivo* antitumour activity: xenografts of human cell lines inoculated in immunodeficient mice or tumour cell lines implanted in immunocompetent rodents. The choice depends on the objective of the study. Actually, complex interactions connect chemotherapeutic agents and the immune system [40, 41], the dose of chemotherapeutic drug used can induce a positive or negative effect on the immune system which leads to modulation of the antitumour effects of chemotherapy. Thus, for the same drug, the antitumour effect obtained may be reduced in immunodeficient animal models compared to syngeneic models, as no immune reaction against tumour cells altered by the cytotoxic drug can develop. Moreover, for tumours generated from *in vitro* cultivated cell lines, the presence of the relevant target must be checked in the growing tumours and not only in the cell lines from which they originated. *In vitro* culture can alter target gene and protein expression through changes in environmental pressures. For many agents designed to interfere with a specific molecular target or pathway (targeted strategy) and without broad-spectrum cytotoxic or cytostatic effects [9, 38, 42, 43], the animal model must be capable of responding to alterations in the target pathway, and must fit with the use of a transgenic model as an interesting and adequate alternative for such drug evaluation.

   The adequacy of the animal model might be refined when the potential efficacy of the anticancer drug tested can be compared to a reference drug, usually; a therapeutic agent already available on the market and that has efficacy previously demonstrated in the model. Such a demonstration makes activity in the tumour model more convincing in terms of potential application in clinic, and tumour response to chemotherapy.

Tumour Type

To be reliable, animal models should develop similar characteristics to human cancers. Thus, tumour type and the biological properties of cancer vary enormously

among available rodent models for cancer, from transplantable counterparts in rodents, to chemically induced tumour models or transgenic models.

The location of the tumour also influences tumour growth. According to the route of administration of tumour cells: intravenously, intraperitoneally, intramuscularly, subcutaneously or intracranially, nutrients and oxygen supply and the space available for tumour growth may differ dramatically. Priority should be given to an orthotopic position.

In syngeneic models, tumour type and location strongly determine the rate of tumour uptake. Generally, the rate of uptake correlates closely with the invasive and metastatic capability of the tumour. Moreover, maintenance of an adequate syngeneic tumour-model requires continuous access to the mice of origin and adequate quality controls, such as checking that the passage of tumours in cell culture may not alter the behaviour (genotype, histology, biological behaviour and drug–response characteristics) of the tumours (by increasing genetic instability) when re-implanted in mice.

Tumour Load

The antitumour effect of a drug may be different according to the size of the treated tumour. This is highly dependent on tumour load which can vary by a factor of 10, 100 or more in experimental protocols. Interestingly, and often for regulatory reasons, new drugs are usually recommended to treat advanced cancers that are quite large, drug-resistant, not accessible to surgery or a combination of these factors. In this respect, small tumour loads generally do not reflect the clinical situation, and might be a source of false-positive results in cancer models.

16.2.2.2 Design of an *In Vivo* Experimental Protocol

Determination of the Drug Vehicle

One of the first considerations of any *in vivo* investigation is the careful choice of drug formulation. Generally, formulations are made of a carrier or diluents recognized to be inert to the tumour or the host (e.g., no unexpected toxic effects or pharmacological effect). When new vehicle formulations are developed, they need to be proven as innocuous. Thus, a control group of animals which does not receive the tested drug should not be untreated but rather treated with inert excipients. Such control groups are usually designated as vehicle-treated animals.

Preliminary Studies of the Drug

Antitumour efficacy studies of a drug are often preceded by toxicological evaluation to ensure that the drug has no general or specific toxicity incompatible with

later *in vivo* evaluation. Toxicological investigations should be performed in the same animal species and strain as the one selected to assess antitumour efficacy. The protocol procedure includes the administration of increasing doses of the drug to different groups of animals by an appropriate route of administration followed by their observation over a suitable period of time. Animal behavior, survival, blood Hematology and biochemical parameters as well as histological examinations are important factors to measure during the protocol period. In syngeneic and xenograft models, these studies also allow the determination of the Maximal Tolerated Dose (MTD) which could serve as a reference for later antitumour efficacy studies.

Assessment of Antitumour Effect

The antitumour effect of a drug can be explored by using two types of experiments in murine solid tumours. In the first approach, drug treatment begins prior to tumour development, 1 or 2 days before or the same day of tumour cell implant. This study is referred as tumour-growth-inhibition study. In the second type of experiment, drug treatment is delivered after the development of a tumour nodule (with a size between 50 and 200 mm^3), and corresponds to tumour-growth-delay study. For a drug, exhibiting an effect in a tumour-growth-delay model is stronger data than exhibiting an effect in a tumour-growth-inhibition model, as the first model is more relevant to human clinical situation.

Dose, Schedule and Route of Administration

The treatment protocol must be precise doses and schedules for administration and under the experimental conditions selected, must be based on well-founded criteria. These may include achieving a target plasma concentration, maintaining a minimum exposure time, or giving the maximum amount of drug that does not cause unacceptable toxicity. All treatment parameters need to be detailed for a full understanding of the meaning of the experimental outcomes, and the relevance of the conclusions.

Many protocols performed with cytotoxic drugs are based on the maximum tolerated dose to define the treatment dose and schedule [20]. However, this approach may not be appropriate with target-modulating agents [44, 45] which are expected to be of low toxicity because of their specificity. However, high doses of such agents could lead to over-interpreting the activity of the compound, given that comparable doses would be unlikely in humans. Thus, treatment schedules may be based on parameters such as plasma concentration and exposure time [45].

Drug exposure time should be long enough to avoid discarding an agent wrongly considered as ineffective. For example, a targeted-drug could require long-term continuous exposure to the tumour. In general, biological agents such as antibodies usually have long half-lives, whilst small molecules have short half-lives, especially in rodents [42].

The route of administration is also a key point to consider. The pharmacological effect of a drug may be highly variable depending on a systemic (e.g., intravenous) or a local (e.g., intraperitoneal) route [46] of administration which determines the distribution of the drug in the body, and concentration in the vicinity of the tumour.

16.2.2.3   Parameters Influencing the Validity of the Test Data

Validation of Animal "Handling"

As animal handling can induce a stress response that can alter the experimental outcome, investigators have to become accustomed to animals before the beginning of the experiments. Every surgical intervention has to be validated before undertaking large scale tests.

The choice and validation of anaesthesia are also important considerations, as anaesthesia is necessary for invasive or harmful procedures. Choosing the most appropriate anaesthetic agent for a particular experiment or tumour model is difficult as no ideal agent exists. The choice depends on several factors: the adverse physiological and pharmacological effects of anaesthetics must not interfere with physiological parameters important for the validity of the study, or with tumour and normal tissue homeostasis. Such information requires a careful search of the literature. Inhalant anaesthetics (mostly halogenated anaesthetics: halothane, isoflurane, methoxyflurane, enflurane and the combination of sevoflurane and desflurane) can be safely administered to rats and mice, and have the advantage over injectable anaesthetics (e.g., pentobarbital, urethane, and ketamine) in providing greater control of anaesthetic depth during prolonged experiments [47].

Groups of Animals

The experimental design must also define the number of animals per group. Too few animals can compromise result validity, and too much do not always bring additional benefit. A statistician or statistical software can indicate the minimum number of animals necessary to detect differences in measurable outcomes between groups. Preliminary studies should assess the intragroup heterogeneity of the measured parameter. Then, this value serves as a reference to calculate the group size necessary to determine the statistical significance of the difference in the tested parameter. High intragroup heterogeneity will require sample groups of a larger size.

Randomization and Statistical Evaluation

Animal randomization is an integral part of the experiment to avoid biased selection and later, experimental bias. It could be easily performed by using software.

Criteria of randomization include age considerations because aging can determine heterogeneity of drug response, animal manipulation and operator fatigue, which is of special concern in a complex protocol requiring surgery or difficult route of administration.

Analyses of differences between treated and control groups require appropriate statistical evaluation, depending on the type of experimental model, the design, and endpoints collected [48]. Choice of statistical test relies on the identification of the distribution of data: normal or not. For data normally distributed, a parametric test such as the *t* test and analysis of variance are applicable; otherwise, nonparametric tests such as Wilcoxon, Mann-Whitney, or Kruskal-Wallis tests [49] should be used. The statistical test chosen determines the selecting criteria for analyzing the data, and the criteria for excluding outlying data points. Such an approach leads to an independent interpretation of the data even if it does not fit well with the initial hypothesis.

16.2.3 Analysis of Antitumour Activity

16.2.3.1 Choice of Endpoint Parameters

Endpoints should be defined in the experimental design. The two most common endpoint categories are measurement of antitumour activity and modulation of molecular targets. The effects of a treatment on the tumour can be evaluated in various ways in rodents, but preference is given, as much as possible, to parameters comparable to those used in the clinic. Decreased tumour size, decreased tumour-associated morbidity, improved quality of life, and when possible, lengthened life span can be addressed irrespective of the host species. However, parameters such as long-term survival, improvement or maintenance of quality of life, etc. may be difficult to answer in animal models.

When measuring the antitumour effect of a drug, gradual responses may be recorded and quantified as following:

- The cancer is cured by the drug. In this case, the drug induces a complete tumour regression without tumour recurrence. In practice, in a mouse, that means that no tumour has reappeared in a delay of 60 days after drug treatment
- The cancer is induced into complete remission by the drug, i.e., that the drug allows the complete disappearance of visible tumour at the end of the treatment
- The cancer undergoes partial remission in response to the drug, i.e., the drug induces a decrease of more than 50% of the tumour size (from the origin)
- The cancer growth is stabilised, i.e., the drug induces a variation of the size of the tumour of 50–150% from the origin

Determination of partial or complete tumour regression involves the measurement of two different parameters: the rate and the duration of remission, which are both clinically relevant endpoints [50, 51]. When assessing survival to quantify

a drug effect, care must be taken not to mistake prolongation of survival with tumour growth delay, especially when tumour growth has been slowed down by the drug. Frequently, tumour growth delay could also be indicative of disease progression. Moreover, important information, such as body-weight loss from the treatment, should be provided in the trial to avoid misinterpretation of data. Indeed, many antitumour and toxic agents make a mouse sick enough that it fails to eat adequately or drink fluids sufficiently, causing a non specific weight loss. Weight loss alone can induce substantial growth inhibition of a solid tumour [52].

In transgenic cancer models, experimental endpoints may also include modulation of molecular markers and determination of target protein expression levels. In this case, the characteristics of the sample to analyze should be detailed (e.g., tumour tissue, surrogate tissue such as bone marrow, spleen or skin, serum or plasma) and optimized. Timing of sample collection following anticancer drug exposure also needs to be described and validated, as well as the method of collection (e.g., cryobiopsy, standard needle biopsy, and full or partial tumour resection), storage of the samples, because many markers are unstable and might change with experimental conditions [44, 53]. Moreover, other sample characteristics should include the size or amount of tissue needed to conduct the study, and its stability, as some targets may degrade rapidly postmortem. For endpoint volatile analyses, which are easily affected by stress or manipulation, the quality of the sample may be better preserved by collection under general anesthesia.

16.2.3.2 Evaluation and Presentation of Results

Results may be presented in different ways depending on the endpoint results and cancer model used. A crucial point to remember is that overall efficacy of an anticancer drug depends on the type of cancer treated and on the efficacy of drugs available in clinic.

For example, in models characterized by tumours growing subcutaneously, tumour weights, expressed as percent test/control (% T/C), are commonly assessed. They are usually calculated using a caliper to measure the length and the width of the subcutaneous tumours. Accurate measurements require tumour size bigger than 5 mm in either dimension [54], a mouse strain with thin skin and measurements performed by the same manipulator during the entire protocol. Other possible endpoint parameters include the determination of tumour growth delay, time to reach a specified number of tumour doublings or to reach a defined tumour weight, and tumour regression [39, 54]. In addition, subcutaneously growing tumours provide data from multiple time points, and the statistical significance of differences in tumour size are assessed at each time point. In such cases, if data is only presented as a single time point, the choice of that specific time point should be carefully made and explained.

In models with viscerally growing tumours, weight cannot be monitored as easily at different time points during the protocol as it requires resection from the body. New imaging technologies, such as magnetic resonance imaging, ultrasound

and bioluminescence have provided highly sensitive methods that have strongly improved tumour assessments and increased the number of possible time points for tumour growth measurements. Moreover, careful tumour resection must define the same tumour borders in all mice included in the protocol. For tumours growing within organs, it could be easier to resect and weigh the entire organ to avoid resection bias. For accuracy, tumour weight should be measured only when tumour mass is big enough to provide statistically valid differences between treatment groups, and needs preliminary validation of time measurements. Histopathological analyses could provide valuable data on the presence and characterisation (number and size) of visceral lesions, especially in metastatic cancer models, e.g., murine Lewis lung cancer, B16 melanoma, and M5076 sarcoma [55].

Whatever the experimental endpoint chosen, calculations must provide mean values and SD, SE or 95% CI so that intra- and inter-group variability can be easily ascertained. Results are usually reported on graphs presenting data from drug-treated group(s) versus drug-vehicle treated group(s). Plots for tumour growth data for each treatment group can be presented in two principle ways: as weights expressed as medians or averages [9, 38, 39, 54, 56–58], or as relative tumour weight arising from a calculated percent of control or starting tumour weight. Frequently, tumour growth data are more understandable when weights are plotted rather than relative weight. Presentation of tumour weights as median or average values allows for the unambiguous reporting of tumour weights from the beginning to the end of the post-treatment period.[59] Data presentation as relative weight can be misleading because they do not provide an insight into the real effect of the drug on tumour. For example, a tumour that is 400% of its initial weight can correspond to a tumour of 40 mg as well as a tumour of 4,000 mg, depending on whether the initial tumour weight was 10 or 1,000 mg.

16.3   Examples of Platinum Compounds Evaluation

16.3.1   *Examples from the Literature*

Since the discovery of cisplatin at the end of the 1960s, the diversity of animal models available to assess *in vivo* efficacy of platinum compounds has grown extensively from the first syngeneic models to the more recent xenograft and transgenic models. In this section, the main animal models used for classical (cisplatin, oxaliplatin and carboplatin) and more recent (satraplatin, picoplatin) platinum compound evaluation are briefly reviewed (Table 16.1).

The antitumour effect of cisplatin (*cis*-diamminedichloroplatinum(II)) was first evaluated in several syngeneic models. After promising preliminary results were obtained in BDF1 mice (a cross between female C57BL/6 and male DBA/2) with leukemia L1210, Rosenberg et al. demonstrated that cisplatin was able to cure 60–100% of Swiss white mice bearing sarcoma 180 [60, 61]. This cytotoxic

Table 16.1 Summary of animal testing performed with cisplatin, carboplatin, oxaliplatin, picoplatin and satraplatin

Compounds	Type of tumours	Type of animal	Tumour implantation	Route of administration	Results	References
Cisplatin	Sarcoma 180	Swiss white mice	Subcutaneous	IV	Cure = 63–100%	Rosenberg et al. [60]
	P388 leukemia	BDF1 mice	Peritoneum (IP)	IV	ILS = 635%, cure = 40%	Rosenberg et al. [61]
	L1210 leukemia	BDF1 mice	Peritoneum (IP)	IV	ILS = 293%	Kociba et al. [63]
	Walker 256 Carcinosarcoma	Fischer 344 rat	Peritoneum (IP)	IP	Cure = 100%	
	DMBA-induced mammary carcinoma	Sprague–Dawley rat	DMBA IV injection	IV	Total regression = 77%	Welsch et al. [64]
	Ehrlich ascitic tumour	BALBC/c rat	Peritoneum (IP)	IP	ILS = 300%	Howle et al. [62]
Carboplatin	L1210 leukemia	Wistar rat	Peritoneum (IP)	IP	T/C = 15%	Harrap et al. [65]
	ADJ/PC6 plasmacytoma	Wistar rat	Peritoneum (IP)	IP	TI = 12.4	
	Yoshida ascitic tumour	Wistar rat	Peritoneum (IP)	IP	T/C = 34%	
	xg. P246 epidermoid carcinoma	Nude mice	Subcutaneous	IP	ILS = 60%	
	L1210 leukemia	Mice				Lelieveld et al. [66]
	C22LR osteosarcoma	Mice				
Oxaliplatin	L1210 leukemia	CD2F1 mice	Peritoneum (IP)	IP/IV	T/C = 80–250%	Tashiro et al. [69]
	P388 leukemia	CD2F1 mice	Peritoneum (IP)	IP/IV	T/C = 120–220%	
	B16 melanoma	B6D2F1 mice	Subcutaneous	IP/IV	T/C = 130–200%	
	Lewis lung carcinoma	B6D2F1 mice	Subcutaneous	IP/IV	T/C = 100–160%	
	Colon 28 adenocarcinoma	CD2F1 mice	Peritoneum (IP)	IP/IV	T/C = 100–140%	
	Colon 26 adenocarcinoma	CD2F1 mice	Peritoneum (IP)	IP/IV	T/C = 115–150%	
	L40 AkR leukemia	CD2F1 mice	Peritoneum (IP)	IV	T/C = 140–170%	Mathé et al. [68]
	LGC lymphoma	CD2F1 mice	Peritoneum (IP)	IV	Cure >50%	
	L1210 leukemia	CD2F1 mice	Brain	IV	T/C = 165%	
Picoplatin	ADJ/PC6 plasmacytoma	Balb/c-mice	Subcutaneous	IV, IP, PO	TI = 14 (IP), 90 (PO)	Raynaud et al. [72]
	L1210 leukemia	DBA2 mice	Peritoneum (IP)	IV, IP, PO	ILS = 54%	
	xg. ovarian HX100	Nude mice	Subcutaneous	IP	Growth delay > 139 days	
	xg. ovarian CH1	Nude mice	Subcutaneous	IP		Jones et al. [73]

(*continued*)

Table 16.1 (continued)

Compounds	Type of tumours	Type of animal	Tumour implantation	Route of administration	Results	References
Satraplatin	ADJ/PC6 plasmacytoma	Balb/c-mice	Subcutaneous	IP, PO	Growth delay = 65 days	Kelland et al. [71]
	L1210 leukemia	DBA$_2$ mice	Peritoneum (IP)	IP, PO	TI = 5 (IP), 57 (PO) ILS = 40%(IP), 20%(PO)	
	xg. ovarian PXN/109T/C	Nude mice	Subcutaneous	PO	Growth delay = 45 days	
	xg.ovarian HX100	Nude mice	Subcutaneous	PO	Growth delay = 30 days	
	xg. ovarian OVCAR-3	Nude mice	Subcutaneous	PO	Growth delay = 40 days	

xg. xenograft, *IV* intravenous, *IP* intraperitoneal, *PO* per os, *ILS* increased life span, *T/C* percent of tumour mass in treated animal/tumour mass in control animals, *TI* therapeutic index = maximal tolerated dose/efficacy dose 90

effect was later confirmed in other transplantable tumour models as well as in chemically- or viral-induced tumours by United State National Cancer Institute (NCI) and various teams [62–64].

Nevertheless, side effects and clinical resistance have limited the clinical use of cisplatin, and stimulated the synthesis and screening of new platinum complexes. From the multitude of compounds synthesized, only two derivates successfully passed clinical trials and were commercially available all around the world: oxaliplatin (1R,2R-diaminocyclohexane oxalatoplatinum(II)) and carboplatin (cis-diammine-[1,1-cyclobutanedicarboxylato] platinum(II)).

Preclinical antitumour assessment of carboplatin has been conducted primarily by the NCI, Bristol-Myers company, and the Institute of Cancer Research, Surrey, in the United Kingdom. Antitumour evaluation was conducted using two leukemic models (e.g., L1210, P388) and several solid tumour models (e.g., B16 melanoma, colon-38 carcinoma, Lewis lung carcinoma, C22LR osteosarcoma) including human tumour xenografts in athymic mice (e.g., epidermoid carcinoma P246) [16, 65, 66]. Comparison of carboplatin and cisplatin efficacy at equivalent doses established that carboplatin antitumour effect was at least equivalent to cisplatin in over two thirds of the studied models. Moreover, carboplatin was active against tumours resistant to cisplatin (P388/DDP) [16].

On the other hand, oxaliplatin, the first DACH-platinum used in a therapeutic protocol such as the FOLFOX regimen, was synthesized and selected by Kidani et al. in the 1970s because of its greater cytotoxicity in leukemic L1210 cell lines and in the derived L1210/DDP-bearing mice (up to 40 times higher than cisplatin with an equivalent dose schedule). Ten years later, Mathe et al., in collaboration with Kidani, confirmed the high antitumour efficacy of oxaliplatin against solid tumour models (e.g., B16 melanoma, Lewis lung carcinoma, colon 26 and 28 adenocarcinoma, M5076 fibrosarcoma) and hematological (e.g., L1210 and AkR leukemia, LGC lymphoma) malignancies in mice using an optimal dose determined previously [67–69].

Thus, the animal models and strategy used to evaluate oxaliplatin and carboplatin *in vivo* efficacy laid the foundations for clinical trials. Other animal models, including xenograft and transgenic animals, have been used mainly to assess new therapeutic strategies or to identify tumour markers of prognosis or treatment effectiveness. Since marketing of carboplatin and oxaliplatin, two exciting platinum agents have been brought to phase III clinical trials in recent years: satraplatin to treat hormone-refractory prostate cancer and picoplatin in small-cell lung cancer [70].

Satraplatin (*bis*-acetato-ammine-dichloro-cyclohexylamine platinum(IV)) or JM216 has been developed to be an orally active platinum complex, and picoplatin (*cis*-amminedichloro,2-methylpyridine,platinum(II)) or AMD473 is a sterically hindered platinum complex. Both were screened by Kelland et al. on the same cell lines, and exhibited cytotoxic effects in cisplatin-resistant cells, cell lines with enhanced DNA repair or cell lines with increased tolerance to platinum-DNA adducts [71, 72]. *In vivo* investigations were undertaken in tumour-bearing mice (e.g., subcutaneous ADJ/PC6 and ADJ/PC6cisR variant plasmacytoma in

Balb/c- mice, intraperitoneal L1210 and L1210cisR variant in DBA$_2$ mice) and in mice with various ovarian cell xenografts (e.g., CH1 and CH1cisR, HX/62 and HX/110, PXN/65, SKOV-3). Picoplatin exhibited a powerful activity against acquired-resistant tumours (ADJ/PC6cisR, L1210CisR, HX/110 and CH1cisR) and an activity at least equivalent to cisplatin in all xenograft models [71–73]. Satraplatin efficacy was higher than cisplatin only in tumour-bearing mice, and was equivalent to intraperitoneal cisplatin administration in xenograft models.

Antitumour assessment of platinum compounds also includes the determination of toxicological and pharmacokinetic profiles of the drugs before potentially switching to phase I clinical trials. Several animal models treated by different dose schedules are selected according to international guidelines. Both acute and dose-repeated toxicities together with hematological, renal and hearing injuries are assessed mainly in mouse, rat, guinea-pig, dog or monkey. Additional mutagenic and teratogenic studies are also conducted on several species including at least one mammal.

16.3.2 Our Experience on the Evaluation of a New Metallointercalator: The 56MESS

Metallointercalators represent a particular class of new platinum–intercalator conjugates which combine a structure different from classical platinum derivates used in the clinic, with original mechanisms of action [74, 75]. Many of these compounds exhibited cytotoxic activity against different cell lines *in vitro* [74–78] and some displayed antitumour efficacy [79] *in vivo*. Various metallointercalators with substituted 1,10-phenanthroline synthesized by Prof. Aldrich-Wright and co-workers [74–77] were assessed *in vitro* [80] and the compound with the highest cytotoxicity: the [(5,6-dimethyl-1,10-phenanthroline) (1S,2S-diaminocyclohexane) platinum(II)] complex (56MESS) was evaluated *in vivo* in a syngeneic model of peritoneal carcinomatosis in the rat [81] and compared to the reference molecule cisplatin (Fig. 16.1).

16.3.2.1 Preliminary Studies with 56MESS

In vivo toxicological studies were carried out to assess whether 56MESS could be used for later antitumour evaluation, including the determination of general and specific toxicity, and the dose rate for antitumour studies.

Experimentally, 3–5 months old male and female BD-IX rats were split in several groups. Each group received a bolus intravenous injection of 56MESS at increasing doses, and was observed for 1 month. 56MESS was highly soluble in sterilized 0.9% NaCl solution, and rats from the control group received an IV injection of sterilized 0.9% NaCl solution. An "early" preliminary study was
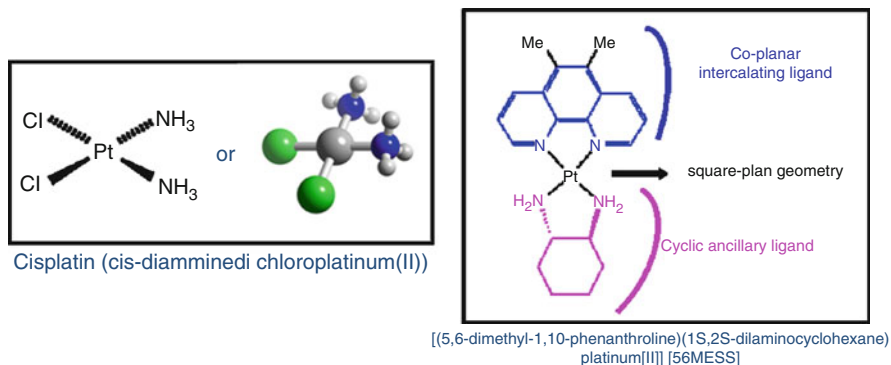
Fig. 16.1 Chemical structures of cisplatin and [(5,6-dimethyl-1,10-phenanthroline)(1*S*,2*S*-dia-minocyclohexane) platinum(II)]$^{2+}$ (56MESS)
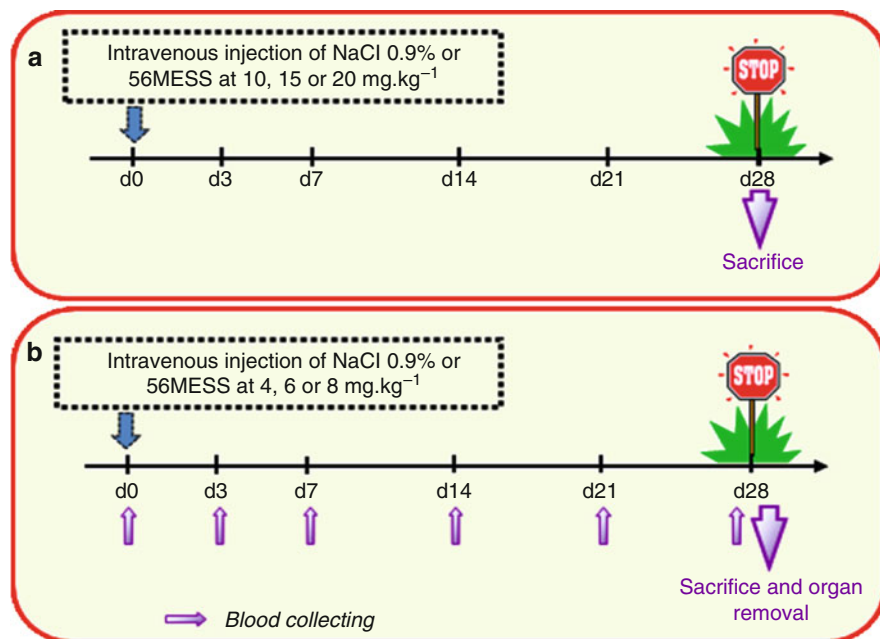
Fig. 16.2 Protocols performed to assess 56MESS toxicological behaviour. (**a**) Preliminary study. (**b**) Main toxicological study. *d = day*

conducted with three groups of two animals treated by 0, 10, 15 or 20 mg of 56MESS per kilogram of rat (Fig. 16.2a). Rats treated with 15 or 20 mg/kg of 56MESS died in the first 24 h, and rats treated with 10 mg/kg of 56MESS died in the first week following injection. This first study was followed by the main toxicological
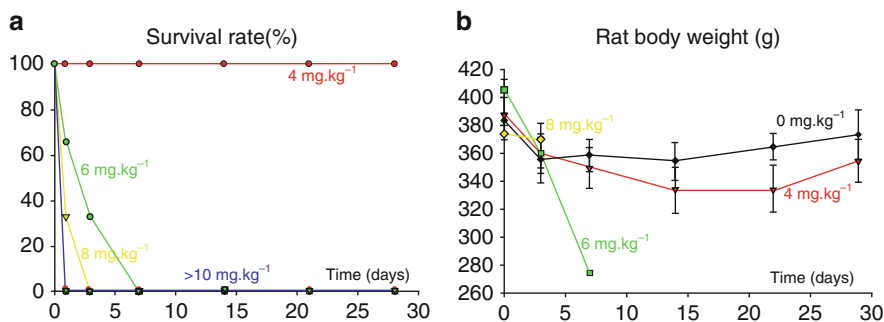
Fig. 16.3 Determination of general parameters in rats treated by increasing doses of 56MESS during the main toxicological study. (**a**) Measurement of survival rate, which allowed the determination of the Maximal Tolerated Dose (MTD). (**b**) Measurement of rat body weight during the protocol period

experiment in which four groups of BD-IX rats received 0, 4, 6 or 8 mg of 56MESS per kg, respectively, by intravenous injection (Fig. 16.2b). During the protocol, body weight, behaviour and survival rate were regularly assessed. Blood was collected at the tail or by cardiac puncture (under anaesthesia with isoflurane) at days 0, 3, 7, 14, 21 and 28 for biochemical and Hematological analyses. At day 28, animals were sacrificed and liver, kidney, heart, intestine and lung were removed for histological analyses (with buffered formol fixation, paraffin inclusion and hematoxylin/eosin stain).

Rats treated with 56MESS at doses above 4 mg/kg died during the first week following IV injection, whilst no death occurred in the group of rats treated at 4 mg/kg or below. Thus, a Maximum Tolerated Dose (MTD), which corresponds to the maximal dose for which no death occurs, was estimated at 4 mg/kg for 56MESS in BD-IX rat (Fig. 16.3).

Considering blood hematologic parameters (Fig. 16.4), rats treated by 56MESS at 4 mg/kg displayed a polynucleosis with inversion of the rates of blood neutrophils and lymphocytes from day 7 to day 14, but no abnormality occurred in other white cell populations (monocytes, basophils, eosinophils), platelets, erythrocytes or associated parameters (hemoglobinemia, hematocrit, Mean Corpuscular Volume, and Mean Corpuscular Hemoglobin Content). Biochemical measurements illustrated in Fig. 16.5 highlighted a hypoalbuminemia in a context of hypoproteinemia from day 3, without changes in blood glucose level or hepatic markers (Alanin aminotransferase, Aspartate aminotransferase, alkaline phosphatase, total bilirubin and gamma glutamyl transpeptidase). Iono-gram abnormality consisted in an isolated hypokaliema, occurring from day 3 (Fig. 16.6). Moreover, major elevations of plasma creatinine and urea were observed between day 3 and day 14, with a maximum at day 7 (up to ten times more than normal) (Fig. 16.6). These abnormalities were associated with kidney injuries at day 28. Histological lesions were characterized by a tubulopathy with macrophage and lymphocyte infiltrates and fibrous development of renal
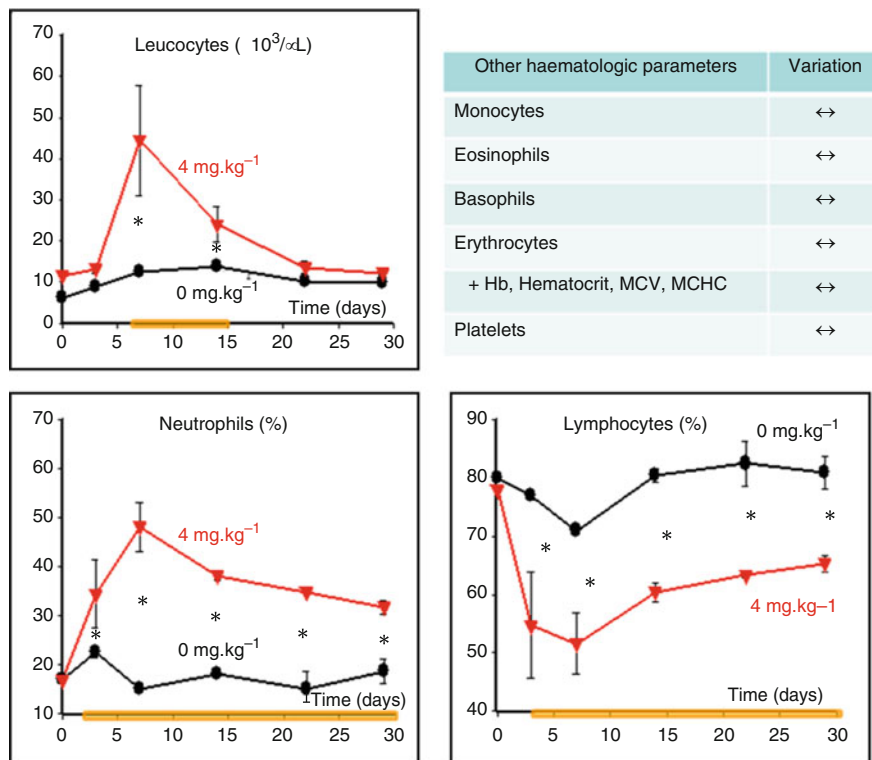
Fig. 16.4 Evolution of blood hematological parameters in rats treated by increasing doses of 56MESS during the main toxicological study. *Hb* hemoglobinemia, *MCV* Mean Corpuscular Volume, *MCHC* Mean Corpuscular Hemoglobin Content, orange box = significant statistical differences between control and 56MESS-treated groups: *$p < 0.05$

interstitium (Fig. 16.7). However, no abnormality was detected in the heart, the lung, the liver, and the large intestine (Fig. 16.8).

As renal toxicity was detected, a complementary study was assessed to better characterize acute renal injuries. BD-IX rats were treated with a supra-pharmacological dose of 56MESS of 6 mg per kg by IV injection and histological analyses were performed 24 h and 48 h after 56MESS injection (Fig. 16.9a). Although no abnormality was detected at day 1, treated rats displayed a significant increase in plasma creatinine and urea (Fig. 16.9b), associated with signs of Hemorrhagic tubular necrosis at day 2 (Fig. 16.9c).

Thus, these *in vivo* data disclosed many features of 56MESS: a renal toxicity associated to a hypokaliemia characteristic of tubular lesions, similar to toxic effects of cisplatin, already evaluated in the BD-IX rat in our laboratory [82]. However, 56MESS did not display major hematologic toxicity, or hepatic lesions. The Maximal Tolerated Dose was also determined at 4 mg/kg for antitumour investigations.

Blood biochemical parameters	Variation
Blood glucose	↔
Alanin aminotransferase	↔
Aspartate aminotransferase	↔
Alkaline phosphatases	↔
Total bilirubin	↔
Gamma glutamyl transpeptidase	↔
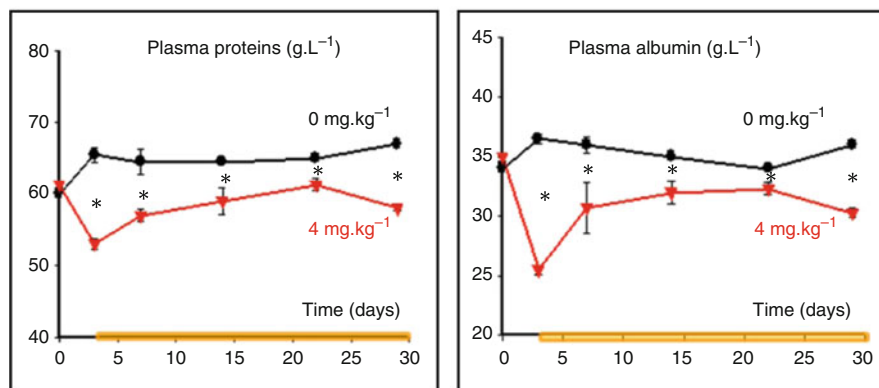
Fig. 16.5 Evolution of blood biochemical parameters in rats treated by increasing doses of 56MESS during the main toxicological study. Orange box = significant statistical differences between control and 56MESS-treated groups: *$p < 0.05$

16.3.2.2   Evaluation of 56MESS in a Peritoneal Carcinomatosis Model in the Rat

The Syngeneic Model of Colon Cancer in the Rat

This model was generated in the laboratory in the early 1980s [81] to evaluate chemotherapeutic agents or regimens for the treatment of digestive cancers. Many chemically induced models for colon carcinogenesis were generated at that time. These developments satisfied experimental requirements as spontaneous epithelial tumours of the colon are relatively rare in experimental animals, as are virally induced large bowel tumours.

In our model, colon tumours were induced in rats of BD-IX strain by using 1,2-dimethyl-hydrazine (DMH) [81]. DMH, an analog of cycacin, is an effective carcinogen that has been intensively used for the specific induction of tumours of the colon and rectum in rats and mice [83–88]. Results from rodent colon cancer generated with DMH are relatively consistent despite protocol heterogeneity (with regard to doses, schedules, and animal strains) between laboratories. The spectrum of colon epithelial lesions induced by DMH is similar to various types of neoplastic
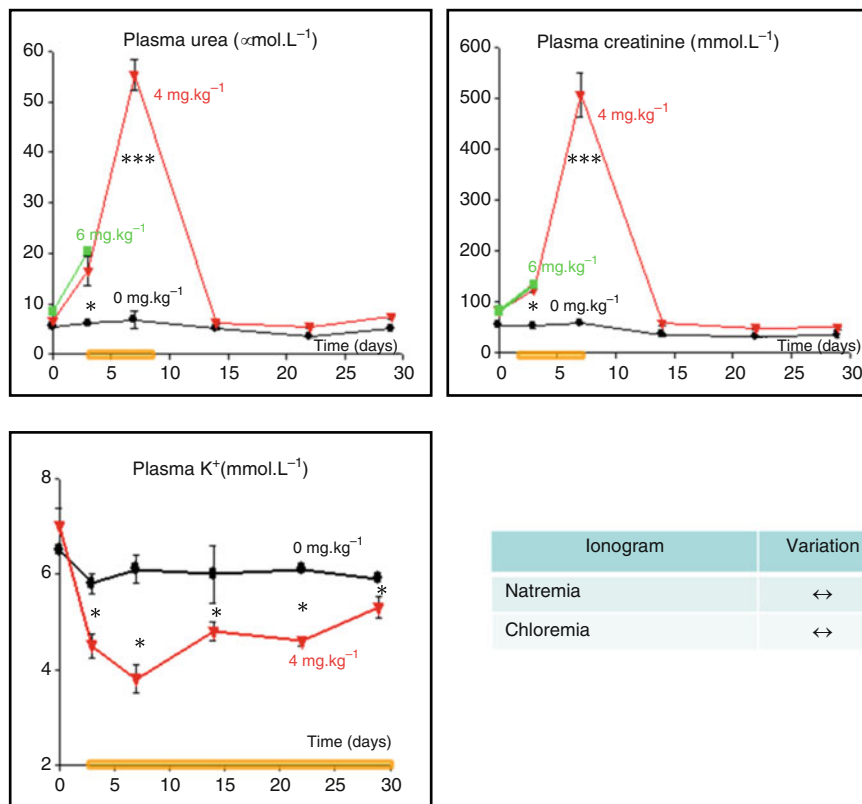
Fig. 16.6 Determination of blood renal parameters and ionogram in rats treated by increasing doses of 56MESS during the main toxicological study. Orange box = significant statistical differences between control and 56MESS-treated groups: $*p < 0.05$, $***p < 0.001$

lesions in the colorectum of humans, in term of histopathology, regional distribution of nodules and clinical manifestations [88]. The main limitation associated with this model is that induction of colon tumours requires multiple injections of DMH.

In our model, the original cell line arisen from DMH-induced colon tumour was called DHD/K12. It was subdivided into two main clones: the PROb clone was chosen for its regular tumourigenicity when injected into syngeneic rats [81]. After a stage of cell multiplication in culture, PROb cells were suspended in serum-free Ham's F10 medium and then implanted intraperitoneally (2×10^6 cells per rat) into anesthetized BD-IX rats.

The size of the peritoneal tumour nodules depended upon time and upon the clone injected. With PROb cells, no tumour nodules were visible at day 2 and multiple nodules of 0.5–3 mm were seen throughout the mesenteric and parietal peritoneum at day 14 after cell injection. At day 21, corresponding to an advanced carcinomatosis, tumour nodules were confluent in the epiploic area and extended to the entire peritoneum wall, including the diaphragmatic areas. Untreated rats
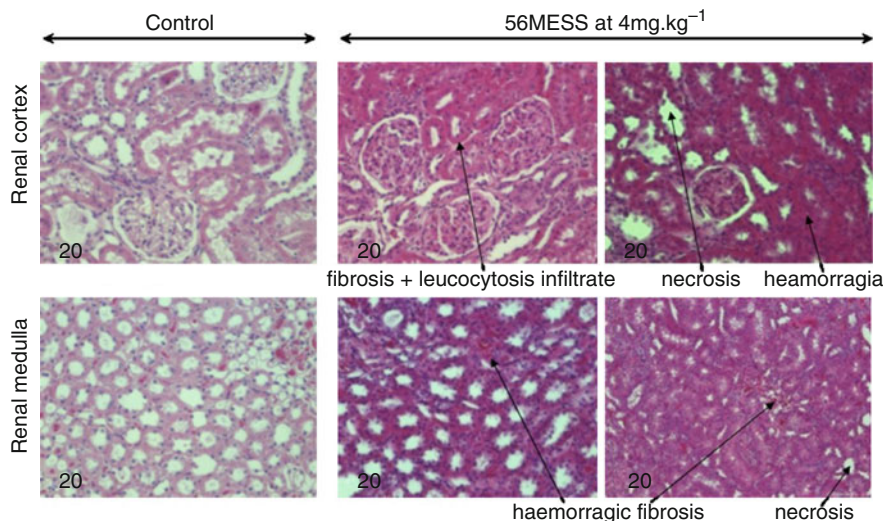
Fig. 16.7 Histologic characteristics of kidney in rats treated by 0 (control) or 4 mg/kg of 56MESS removed at the end of the main toxicological study. Microscopic analyses were performed on renal cortex and medulla. Tissues were stained by hematoxylin/eosin coloration
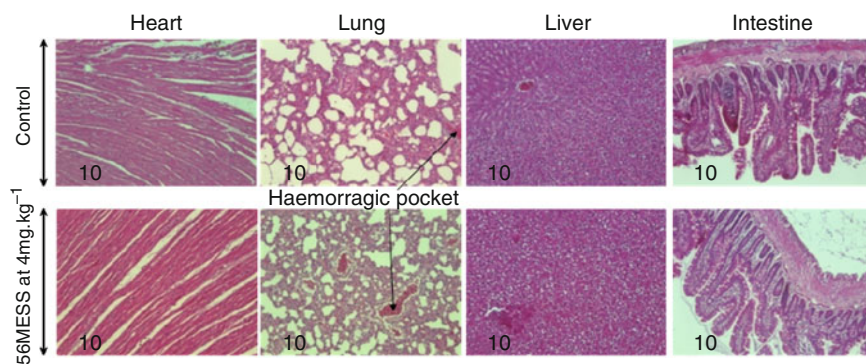
Fig. 16.8 Histologic characteristics of heart, lung, liver and large intestine in rats treated by 0 (control) or 4 mg/kg of 56MESS. Organs were removed at the end of the main toxicological study. Microscopic analyses were performed after hematoxylin/eosin coloration

regularly died an average of 40 days after cell injection from extensive peritoneal carcinomatosis with hemorrhagic ascites, but without macroscopically evident extraperitoneal metastases, notably in the liver or in the lungs.

Experimental Protocol

BD-IX rats received an intraperitoneal injection of 2×10^6 PROb cancer cells and 3 days later rats were selected randomly for vehicle-treated (control) or drug-treated
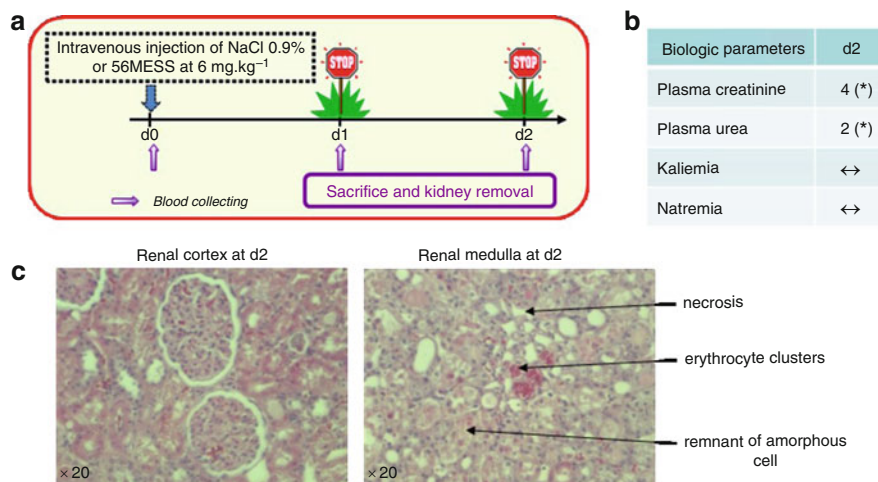
Fig. 16.9 Toxicological experiments assessing acute renal injuries in rats treated with 0 (control) or 6 mg/kg of 56MESS. (**a**) Protocol used. (**b**) Measurement of blood parameters in rats treated by 56MESS compared to control group at day 2. (**c**) Histologic lesions of kidney at day 2 after 56MESS treatment. Microscopic analyses were performed on renal cortex and medulla, stained with hematoxylin/eosin. *d = day, significant statistical differences between control and 56MESS-treated groups: *p < 0.05*

(56MESS or cisplatin) groups, each group consisted of five animals (Fig. 16.10a). Treated rats received an intravenous or intraperitoneal injection of cisplatin or 56MESS, as a single bolus, at their Maximal Tolerated Dose, which was previously determined to be of 4 mg/kg body weight for cisplatin and 56MESS.

Treatments were delivered under anaesthesia by isoflurane. Intravenously treated rats received drug in a volume of 1 mL of isotonic saline through the penis vein for male and through the femoral vein for female. Rats under conventional intraperitoneal treatment received a single intraperitoneal bolus of 56MESS or cisplatin in 20 mL of isotonic saline. Control animals received an intravenous or intraperitoneal injection of sterilized 0.9% NaCl solution. Animals were examined for 30 days after PROb cancer cell injection.

Experimental Endpoints

The ability of 56MESS or cisplatin to cure or decrease tumour growth was investigated 30 days after a single dose injection of drug or its vehicle. Quantification was made using a tumour scale score from CP0 (no peritoneal carcinomatosis left) to CP1 (few millimetre sized nodules present) to CP2 (many supra-millimetre sized nodules mainly in the epiploic area) and CP3 (advanced carcinomatosis with multiple peritoneal, parietal and diaphragmatic nodules)
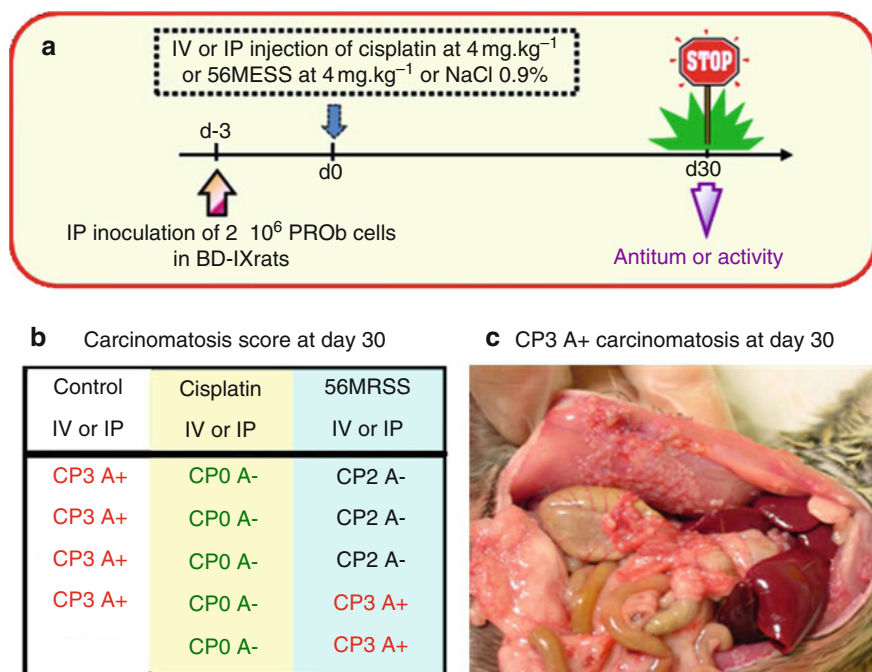
Fig. 16.10 Evaluation of antitumoural activity of 56MESS versus the reference molecule cisplatin in a rat syngeneic model of colon cancer. (**a**) Protocol performed to assess antitumoural effect of 56MESS versus cisplatin. (**b**) Carcinomatosis scores obtained 30 days after 56MESS or cisplatin treatment. (**c**) Illustration of a CP3 A+ peritoneal carcinomatosis in BD-IX rat 33 days after PROb cell inoculation. *IV intravenous*, *IP intraperitoneal*

(Fig. 16.10c). The additional letter A indicates the presence of hemorrhagic ascites: A+, or its absence: A−.

In Vivo Potential of 56MESS in a Syngeneic Model of Carcinomatosis

In the control group, rats displayed an advanced peritoneal carcinomatosis with hemorrhagic ascites at day 30, characterized by tumour nodules extended to the entire peritoneal wall, classified as score CP3 A+ (Fig. 16.10b).

Treatment by 56MESS at 4 mg/kg did not cure rats whatever the route of administration used (systemic or local). At autopsy, 40% of rats exhibited extensive peritoneal carcinomatosis, scored CP3 A+, and 60% of rats displayed several nodules, scored CP2 A- (Fig. 16.10b). Comparatively, rats treated by cisplatin at MTD completely recovered from cancer as illustrated by the absence of nodules in all surviving rats scored CP0 A- (Fig. 16.10b).

16.3.2.3 Concluding Remarks

56MESS did not display any antitumour effect in this syngeneic model of peritoneal carcinomatosis in the BD-IX rat. Hypotheses to explain this result are that there is a possible inactivating metabolism of 56MESS in the body or a low diffusion of 56MESS in tumour nodules. These hypotheses are under investigation [89].

Animal testing remains essential for anticancer drug evaluation, and may reveal discrepancies between *in vitro* and *in vivo* results. These inconsistencies are an argument for *in vivo* investigations of drugs at early stages of development to better predict their potential effect in a whole mammalian organism.

16.4 Conclusions

Animal testing is a crucial step in the discovery of new anticancer drugs, as it strongly influences the "stop and go" of this agent down the drug development pathway. Appropriate interpretation of results from animal studies relies on careful selection of the type of animal model used, after consideration of its principle features, limits, and relevance to the human disease in terms of histopathology, molecular and genetic lesions during early and progression stages of carcinogenesis. The experimental design must provide detailed explanation and validation of protocols. Presentation of the experimental data should allow the reader to properly assess the experiment, and cautious interpretation of data should be provided based on scientifically justified hypotheses.

Recently, new *in vivo* imaging technologies, including nanotechnologies [90], such as ultrasound [91], magnetic resonance imaging [92, 93], or positron emission tomography [3, 94] have highly improved investigations of cancer in animal models, especially when tumours grow in visceral localizations. Even if their utilization is restricted to some tumour growth sites, they have considerably increased the sensitivity of detection and the assessment of visceral tumour growth. Moreover, earlier and more precise pharmacokinetic and pharmacodynamic profiles can be attempted using these new tools, for a better evaluation of novel anticancer agents and a better prediction of tumour response to this agent.

In conclusion, animal models are powerful tools for anticancer drug evaluation, and the benefits of this type of experiment are reinforced by technological improvements that facilitate an increase in data collection without the sacrifice of the animal. However, precise guidelines for evaluation of anticancer drugs on animal models are difficult to establish because of the diversity among cancers and the cost and ethical considerations associated with animal experiments.

References

1. Marchetti S, Schellens JH. Br J Cancer. 2007;97:577.
2. Newell DR. Br J Cancer. 2001;84:1289.
3. Hammond LA, Denis L, Salman U, Jerabek P, Thomas Jr CR, Kuhn JG. Invest New Drugs. 2003;21:309.
4. Smith NF, Raynaud FI, Workman P. Mol Cancer Ther. 2007;6:428.
5. Johnson JI, Decker S, Zaharevitz D, Rubinstein LV, Venditti JM, Schepartz S, et al. Br J Cancer. 2001;84:1424.
6. Voskoglou-Nomikos T, Pater JL, Seymour L. Clin Cancer Res. 2003;9:4227.
7. Laszlo J. The cure of childhood leukemia – into the age of miracles. New Brunswick, NJ: Rutgers University Press; 1995.
8. Schabel Jr FM, Griswold Jr DP, Laster Jr WR, Corbett TH, Lloyd HH. Pharmacol Ther. 1977;1:411.
9. Teicher BA. Mol Cancer Ther. 2006;5:2435.
10. Teicher BA. Tumour models in cancer research. Totowa, NJ: Humana; 2002.
11. Ottewell PD, Coleman RE, Holen I. Breast Cancer Res Treat. 2006;96:101.
12. de Jong GM, Aarts F, Hendriks T, Boerman OC, Bleichrodt RP. J Surg Res. 2009;154:167.
13. Bibby MC. Br J Cancer. 1999;79:1633.
14. Ovejera AA. Rodent tumour models in experimental cancer therapy. Kallman RF, editor. New York: Pergamon; 1987. p. 218.
15. Staquet MJ, Byar DP, Green SB, Rozencweig M. Cancer Treat Rep. 1983;67:753.
16. Goldin A, Venditti JM, Macdonald JS, Muggia FM, Henney JE, Devita Jr VT. Eur J Cancer. 1981;17:129.
17. Fiebig HH, Dengler WA, Roth T. In: Fiebig HH, Burger AM, editors. Relevance of tumour models for anticancer drug development, Vol. 54, Contrib Oncol, Basel: Karger; 1999. p. 29.
18. Huggins CB. J Lab Clin Med. 1987;109:262.
19. Rygaard J, Povlsen CO. Acta Pathol Microbiol Scand. 1969;77:758.
20. Kerbel RS. Cancer Biol Ther. 2003;2:S134.
21. Fomchenko EI, Holland EC. Clin Cancer Res. 2006;12:5288.
22. Dutt A, Wong KK. Clin Cancer Res. 2006;12:4396s.
23. Boivin GP, Washington K, Yang K, Ward JM, Pretlow TP, Russell R, et al. Gastroenterology. 2003;124:762.
24. Ovejera AA, Houchens DP, Barker AD. Ann Clin Lab Sci. 1978;8:50.
25. Venditti JM, Weseley RA, Plowman J. In: Garattini S, Goldin A, Hawking F, editors. Advances in pharmacology and chemotherapy, Vol. 20. New York: Academic. 1984; p. 2.
26. Fichtner I, Goan S, Becker M. Baldy C, Borgmann A, Stackelberg A. In: Fiebig HH, Burger AM, editors. Relevance of tumour models for anticancer drug development, Vol. 54, Contrib Oncol, Basel: Karger. 1999; p. 207.
27. Fiebig HH, Schmid JR, Bieser W, Henss H, Lohr GW. Eur J Cancer Clin Oncol. 1987;23:937.
28. Fiebig HH, Berger DP, Dengler WA, Wallbrecher E, Winterhalter BR. In: Fiebig HH, Berger DP, editors. Immunodeficient mice in oncology, Vol. 42, Contrib Oncol. Basel: Karger. 1992; p. 321.
29. Sausville EA, Feigal E. Ann Oncol. 1999;10:1287.
30. Malakoff D. Science. 2000;288:248.
31. Hursting SD, Slaga TJ, Fischer SM, DiGiovanni J, Phang JM. J Natl Cancer Inst. 1999;91:215.
32. Carver BS, Pandolfi PP. Clin Cancer Res. 2006;12:5305.
33. Gondo Y. Nat Rev Genet. 2008;9:803.
34. Den Otter W, Steerenberg PA, Van der Laan JW. Regul Toxicol Pharmacol. 2002;35:266.
35. Hollingshead MG. J Natl Cancer Inst. 2008;100:1500.
36. Anisimov VN, Ukraintseva SV, Yashin AI. Nat Rev Cancer. 2005;5:807.
37. Schuh JC. Toxicol Pathol. 2004;32 Suppl 1:53.
38. Suggitt M, Bibby MC. Clin Cancer Res. 2005;11:971.

39. Plowman J, Dykes DJ, Hollingshead M, Simpson-Herren L, Alley MC. In: Teicher BA, editor. Anticancer drug development guide: preclinical screening, clinical trials and approval. Totowa, NJ: Humana. 1997; p. 101.
40. Menard C, Martin F, Apetoh L, Bouyer F, Ghiringhelli F. Cancer Immunol Immunother. 2008;57:1579.
41. Salama P, Platell C. ANZ J Surg. 2008;78:745.
42. Hermiston TW, Kirn DH. Mol Ther. 2005;11:496.
43. Peterson JK, Houghton PJ. Eur J Cancer. 2004;40:837.
44. Kinders RJ, Hollingshead M, Khin S, Rubinstein L, Tomaszewski JE, Doroshow JH, et al. Clin Cancer Res. 2008;14:6877.
45. Luo FR, Yang Z, Camuso A, Smykla R, McGlinchey K, Fager K, et al. Clin Cancer Res. 2006;12:7180.
46. Goodman J, Walsh V. The story of Taxol: nature and politics in the pursuit of an anticancer Drug. New York, NY: Cambridge University Press; 2001.
47. Meyer RE, Braun RD, Dewhirst MW. In: Teicher BA, editor. Tumour models in cancer research. Totowa, NJ: Humana. 2002; p. 407.
48. Snedecor GW, Cochran WG. Statistical methods. 7th ed. Ames, IA: The Iowa State University Press; 1980.
49. Motulsky H. Intuitive biostatistics. New York, NY: Oxford University Press; 1995.
50. Martin DS, Stolfi RL, Sawyer RC. Cancer Treat Rep. 1984;68:1317.
51. Stolfi RL, Stolfi LM, Sawyer RC, Martin DS. J Natl Cancer Inst. 1988;80:52.
52. Laster Jr WR, Schabel Jr FM, Skipper HE, Wilcox WS, Thomson JR. Cancer Res. 1961;21:895.
53. Baker AF, Dragovich T, Ihle NT, Williams R, Fenoglio-Preiser C, Powis G. Clin Cancer Res. 2005;11:4338.
54. Alley MC, Hollingshead M, Dykes DJ, Waud WR. In: Teicher BA, Andrews PA, editors. Cancer drug discovery and development guide: preclinical screening, clinical trials, and approval. 2nd ed. Totowa, NJ: Humana. 2004; p. 125.
55. Kakeji Y, Teicher BA. Invest New Drugs. 1997;15:39.
56. Waud WR, Gilbert KS, Shepherd RV, Montgomery JA, Secrist 3rd JA. Cancer Chemother Pharmacol. 2003;51:422.
57. Carter CA, Chen C, Brink C, Vincent P, Maxuitenko YY, Gilbert KS, et al. Cancer Chemother Pharmacol. 2007;59:183.
58. Corbett TH, White K, Polin L, Kushner J, Paluch J, Shih C, et al. Invest New Drugs. 2003;21:33.
59. Kelland LR. Eur J Cancer. 2004;40:827.
60. Rosenberg B, VanCamp L. Cancer Res. 1970;30:1799.
61. Rosenberg B, VanCamp L, Trosko JE, Mansour VH. Nature. 1969;222:385.
62. Howle JA, Gale GR. Biochem Pharmacol. 1970;19:2757.
63. Kociba RJ, Sleight SD, Rosenberg B. Cancer Chemother Rep. 1970;54:325.
64. Welsch CW. J Natl Cancer Inst. 1971;47:1071.
65. Harrap KR. Cancer Treat Rev. 1985;12(Suppl A):21.
66. Lelieveld P, Van der Vijgh WJ, Veldhuizen RW, Van Velzen D, Van Putten LM, Atassi G, et al. Eur J Cancer Clin Oncol. 1984;20:1087.
67. Kidani Y, Noji M, Tashiro T. Gann. 1980;71:637.
68. Mathe G, Kidani Y, Noji M, Maral R, Bourut C, Chenu E. Cancer Lett. 1985;27:135.
69. Tashiro T, Kawada Y, Sakurai Y, Kidani Y. Biomed Pharmacother. 1989;43:251.
70. Shah N, Dizon DS. Future Oncol. 2009;5:33.
71. Kelland LR, Barnard CF, Evans IG, Murrer BA, Theobald BR, Wyer SB, et al. J Med Chem. 1995;38:3016.
72. Raynaud FI, Boxall FE, Goddard PM, Valenti M, Jones M, Murrer BA, et al. Clin Cancer Res. 1997;3:2063.
73. Jones M, Siracky J, Kelland LR, Harrap KR. Br J Cancer. 1993;67:24.

74. Fisher DM, Bednarski PJ, Grunert R, Turner P, Fenton RR, Aldrich-Wright JR. ChemMed-Chem. 2007;2:488.
75. Kemp S, Wheate NJ, Buck DP, Nikac M, Collins JG, Aldrich-Wright JR. J Inorg Biochem. 2007;101:1049.
76. Brodie CR, Collins JG, Aldrich-Wright JR. Dalton Trans. 2004:1145
77. Jaramillo D, Buck DP, Collins JG, Fenton RR, Stootman FH, Wheate NJ, Aldrich-Wright JR. Eur J Inorg Chem 2006:839
78. Margiotta N, Papadia P, Fanizzi FP, Natile G. Eur J Inorg Chem. 2003;6:1136.
79. Fisher DM, Fenton RR, Aldrich-Wright JR. Chem Commun. 2008:5613
80. Grünert R, Westendorf A, Buczkowska M, Hänsch M, Kühne S, Bednarski PJ. In: Aldrich-Wright JR, editor. Metallointercalators – synthesis, techniques to probe their interaction with biomolecules. 2011;361.
81. Caignard A, Martin MS, Michel MF, Martin F. Int J Cancer. 1985;36:273.
82. Polycarpe E, Arnould L, Schmitt E, Duvillard L, Ferrant E, Isambert N, et al. Int J Cancer. 2004;111:131.
83. Enker WE, Jacobitz JL. J Surg Res. 1976;21:291.
84. Pozharisski KM, Likhachev AJ, Klimashevski VF, Shaposhnikov JD. Adv Cancer Res. 1979;30:165.
85. Reddy BS, Watanabe K, Weisburger JH. Cancer Res. 1977;37:4156.
86. Reddy BS, Weisburger JH, Wynder EL. J Natl Cancer Inst. 1974;52:507.
87. Rogers AE, Newberne PM. Nature. 1973;246:491.
88. Pozharisski KM. In: Turuso V, Mohr U, editors. Pathology of tumours in laboratory animals, Vol. 1. Tumours of the rat. Lyon: IARC Scientific Publication; 1990. p. 159.
89. Kemp S, Wheate NJ, Pisani MJ, Aldrich-Wright JR. J Med Chem. 2008;51:2787.
90. Bentolila LA, Ebenstein Y, Weiss S. J Nucl Med. 2009;50:493.
91. Barati AH, Mokhtari-Dizaji M, Mozdarani H, Bathaie SZ, Hassan ZM. Ultrasound Med Biol. 2009;35:756.
92. Pickup S, Chawla S, Poptani H. Acad Radiol. 2009;16:341.
93. Serkova NJ, Hasebroock KM, Kraft SL. Methods Mol Biol. 2009;520:315.
94. Medarova Z, Rashkovetsky L, Pantazopoulos P, Moore A. Cancer Res. 2009;69:1182.

Index